Springer Series in Materials Science 180

M. S. Ramachandra Rao
Tatsuo Okada *Editors*

ZnO Nanocrystals and Allied Materials

Springer Series in Materials Science

Volume 180

Series Editors

Robert Hull, Charlottesville, VA, USA
Chennupati Jagadish, Canberra, ACT, Australia
Richard M. Osgood, New York, NY, USA
Jürgen Parisi, Oldenburg, Germany
Zhiming M. Wang, Chengdu, P.R. China

For further volumes:
http://www.springer.com/series/856

The Springer Series in Materials Science covers the complete spectrum of materials physics, including fundamental principles, physical properties, materials theory and design. Recognizing the increasing importance of materials science in future device technologies, the book titles in this series reflect the state-of-the-art in understanding and controlling the structure and properties of all important classes of materials.

M. S. Ramachandra Rao
Tatsuo Okada
Editors

ZnO Nanocrystals and Allied Materials

Editors
M. S. Ramachandra Rao
Department of Physics
Indian Institute of Technology Madras
Chennai
Tamil Nadu
India

Tatsuo Okada
Department of Electrical Engineering
Kyushu University
Fukuoka
Japan

ISSN 0933-033X ISSN 2196-2812 (electronic)
ISBN 978-81-322-1159-4 ISBN 978-81-322-1160-0 (eBook)
DOI 10.1007/978-81-322-1160-0
Springer New Delhi Heidelberg New York Dordrecht London

Library of Congress Control Number: 2013945152

© Springer India 2014
This work is subject to copyright. All rights are reserved by the Publisher, whether the whole or part of the material is concerned, specifically the rights of translation, reprinting, reuse of illustrations, recitation, broadcasting, reproduction on microfilms or in any other physical way, and transmission or information storage and retrieval, electronic adaptation, computer software, or by similar or dissimilar methodology now known or hereafter developed. Exempted from this legal reservation are brief excerpts in connection with reviews or scholarly analysis or material supplied specifically for the purpose of being entered and executed on a computer system, for exclusive use by the purchaser of the work. Duplication of this publication or parts thereof is permitted only under the provisions of the Copyright Law of the Publisher's location, in its current version, and permission for use must always be obtained from Springer. Permissions for use may be obtained through RightsLink at the Copyright Clearance Center. Violations are liable to prosecution under the respective Copyright Law.
The use of general descriptive names, registered names, trademarks, service marks, etc. in this publication does not imply, even in the absence of a specific statement, that such names are exempt from the relevant protective laws and regulations and therefore free for general use.
While the advice and information in this book are believed to be true and accurate at the date of publication, neither the authors nor the editors nor the publisher can accept any legal responsibility for any errors or omissions that may be made. The publisher makes no warranty, express or implied, with respect to the material contained herein.

Printed on acid-free paper

Springer is part of Springer Science+Business Media (www.springer.com)

Foreword

New opportunities are opening up for innovative materials research across physics, electrical sciences, chemistry, surface science, and nanotechnology. Keeping in line with this, the Department of Physics at IIT Madras organized a two-day workshop on ZnO nanocrystals and allied materials. This two-day conference was conducted by Indian collaborators from IIT Madras and Japanese collaborators from Kyushu University, Japan. Researchers from the academic world of India and Japan presented their recent results on the development of nanostructured ZnO and allied materials and their applications in key areas of Applied Physics and Electrical Engineering. The work presented by all the experts during the workshop has been compiled into this book form with carefully written contributory articles. This book thus presents complete articles summarizing 17 invited talks and contributions. It is well complemented by research work from various scientists well known in the field of ZnO and Allied Materials.

Progress in the nano-research based on ZnO, during the last decade, has been very fast. Various research programs have been renewed and revisited and efforts are on to remove the deadlocks with the help of accurate research on ZnO nanostructures and applied materials for routine use in industry worldwide. It was therefore considered timely to organize an Indo–Japan workshop. It takes a good collaborative effort to understand and explore the varied physical properties and to envisage device applications of ZnO in thin films, heterostructures, and nanostructures. ZnO has been the central theme of research in the past decade due to its potential as UV/blue light emitting diode material that can replace GaN if only the *p*-type doping problem is resolved. In nanostructured form, it offers ample opportunities to realize tunable optical and optoelectronic properties and it was also termed as a potential material to realize room temperature ferromagnetism. ZnO can be easily deposited in high quality thin film form by sputtering, CVD, and laser ablation methods at low temperatures. It can be easily fabricated into devices and its lattice is amenable to 3d and 4f element doping. ZnO is biocompatible and exhibits many interesting applications in textile and biomedical industries. Doping in ZnO can bring about changes in optical emissivity and by virtue of controlling the oxygen vacancies, ZnO lattice can be used for light emission in a wide spectral range. Al doped ZnO competes well with ITO for easy fabrication of conducting

back electrodes for solar cells. ZnO quantum dots open new technological avenues for the fabrication of photonic crystal lattices. ZnO heterostructures can play a key role in band gap engineering. Alloys of MgZnO are useful in tuneable band gap systems and many of its allied material systems can be used in gas sensing applications.

The fundamental challenge, however, remains the same: more stable *p*-type ZnO and its application to larger systems, and access to new materials properties. Responding to these challenges will require substantial effort at various levels.

Being the workshop organizers and editors of this book, we would like to thank all the contributors (especially those who accepted the burden of writing full chapter articles) and the members of the Advisory Board for helping to organize such an effective program. We are sure that this book with an assortment of articles will be quite useful for researchers in this area.

M. S. Ramachandra Rao
Tatsuo Okada

Preface

Functional nanostructures are attracting much interest for use in sensing, energy harvesting, and flexible electronics. ZnO is a versatile material system that offers potential applications in high power and high temperature electronics, UV/Visible light emitting diodes for domestic lighting, and in colour displays. Due to its radiation hardness property, it also finds application in radiation hard transistors for high temperature sensors and spaceflight instrumentation. There have been many recent advances in this field, concerning nanostructure synthesis. ZnO has also been reported as an active channel material for thin-film transistors because of its high electron mobility even for room temperature deposition in ZnO (as the semiconducting active layer)-based field effect transistors. ZnO has also attracted significant attention as a new candidate for transparent electrodes due to its good conductivity, high optical transparency, and surface smoothness.

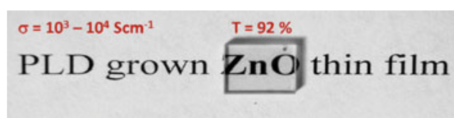

This book brings together articles contributed by experts working on various aspects of ZnO and allied materials detailing all the important recent advances. The topics begin with a brief review of ZnO followed by an important article on nano-Soldering of ZnO nanowires and GaN thin films for the fabrication of hetero *p*-*n* junction using laser. The book also presents works on photoluminescence processes of ZnO thin films and quantum structures, Li–Ni co-doped ZnO films grown by pulsed laser deposition for realizing stable *p*-type conducting material, lasing characteristics of an optically pumped single ZnO nanocrystal, and nanomachining for controlling oscillation wavelength, deposition of Al-doped ZnO films by ICP-assisted sputtering. Advances in nanoparticle-assisted pulsed laser deposition, synthesis of silicon carbide (SiC) thin films using pulsed laser deposition, ZnO-based phosphors, related bio-material applications, experimental

and theoretical investigations of dopants, and defects in ZnO nanoparticles have also been discussed. The purpose of the book is to present a summary of the current state-of-the-art research aspects that can pave the way for new areas for future research.

M. S. Ramachandra Rao
Tatsuo Okada

Acknowledgments

Prof. M. S. R. Rao would like to thank the Department of Science and Technology (DST) funding that facilitated the establishment of Nano Functional Materials Technology Centre (NFMTC) at IIT Madras.

Prof. Okada would like to thank the financial support under the program of Special Coordination Funds for Promoting Science and Technology from Japan Science and Technology Agency (JST).

Our special thanks to Dr. Shubra Singh for careful editing and proof reading of the manuscripts.

Contents

1 Zinc Oxide: The Versatile Material with an Assortment of Physical Properties 1
E. Senthil Kumar, Shubra Singh and M. S. Ramachandra Rao

2 Laser Nano-Soldering of ZnO Nanowires and GaN Thin Film for Fabrication of Hetero *p-n* Junction 39
Tetsuya Shimogaki, Yuki Ishida, Kota Okazaki, Mitsuhiro Higashihata, Daisuke Nakamura and Tatsuo Okada

3 Photoluminescence Processes in ZnO Thin Films and Quantum Structures 49
L. M. Kukreja and P. Misra

4 Effect of Oxygen Pressure on Photoluminescence Spectra and Hall Coefficients of Li–Ni Co-Doped ZnO Films Grown by a Pulsed Laser Deposition 91
K. Sakai, K. Ishikura, D. Ohori, D. Nakamura, A. Fukuyama, T. Okada, M. S. Ramachandra Rao and T. Ikari

5 Lasing Characteristics of an Optically-Pumped Single ZnO Nanocrystal and Nanomachining for Controlling Oscillation Wavelength 101
K. Okazaki, T. Shimogaki, I. A. Palani, M. Higashihata, D. Nakamura and T. Okada

6 Deposition of Aluminum-Doped ZnO Films by ICP-Assisted Sputtering 125
Yoshinobu Matsuda, Akinori Hirashima, Kenji Mine, Takuhiro Hashimoto, Daichi Matsuoka, Masanori Shinohara and Tatsuo Okada

7 Control of ZnO Nano-Crystals Synthesized by Nanoparticle-Assisted Pulsed Laser Deposition Using Buffer Layer and Laser Irradiation 149
Daisuke Nakamura, Tetsuya Shimogaki, Kota Okazaki, I. A. Palani, Mitsuhiro Higashihata and Tatsuo Okada

8 Influence of Sb as a Catalyst in Synthesize of Sb Doped ZnO Nanostructures Using Nanoparticle Assisted Pulsed Laser Deposition for UV LED Applications 175
I. A. Palani, D. Nakamura, K. Okazaki, M. Highasiata and T. Okada

9 Time and Spatially Resolved Luminescence Spectroscopy of ZnO Nanostructures 195
Hideaki Murotani, Yoichi Yamada, Daisuke Nakamura and Tatsuo Okada

10 Synthesis of Polycrystalline Silicon Carbide (SiC) Thin Films Using Pulsed Laser Deposition 217
B. Venkataramesh and Nilesh J. Vasa

11 Preparation and Characterization of ZnO Nanorods, Nanowalls, and Nanochains 233
T. Premkumar, Y. F. Lu and K. Baskar

12 Synthesis and Characterization of ZnO-Based Phosphors and Related Phosphor Composites in Bulk, Thin Film and Nano Form 247
P. Thiyagarajan, M. Kottaisamy and M. S. Ramachandra Rao

13 Zinc Oxide Nanomaterials as Amylase Inhibitors and for Water Pollution Control 269
Rohini Kitture, Sandip Dhobale and S. N. Kale

14 Zinc Oxide: From Optoelectronics to Biomaterial—A Short Review 289
R. Suryanarayanan

15 On the Optical and Magnetic Properties of Doped-ZnO 309
J. Kumar, S. Ramasubramanian, R. Thangavel and M. Rajagopalan

16 Low-Temperature Photoluminescence of Sb-doped ZnO Nanowires Synthesized on Sb-coated Si Substrate by Chemical Vapor Deposition Method 331
K. Sakai, K. Ishikura, A. Fukuyama, I. A. Palani, M. S. Ramachandra Rao, T. Okada and T. Ikari

17 Experimental and Theoretical Investigations of Dopant, Defect, and Morphology Control on the Magnetic and Optical Properties of Transition Metal Doped ZnO Nanoparticles 341
O. D. Jayakumar, C. Persson, A. K. Tyagi and C. Sudakar

Editors Biography 371

Author Index 373

Chapter 1
Zinc Oxide: The Versatile Material with an Assortment of Physical Properties

E. Senthil Kumar, Shubra Singh and M. S. Ramachandra Rao

Abstract Zinc oxide has the potential to replace GaN as the next-generation white light emitting diode material. This wide bandgap semiconductor with an excitonic binding energy of $\sim$60 meV has been researched extensively in the last decade due to its immense potentiality for blue/UV light emitting devices. ZnO lattice is amenable to doping with transition metal ions (TM) and 4*f*-elements. Such a doping activity in ZnO has been mainly aimed at the realization of *n* and *p*-type conductivity and room temperature diluted magnetic semiconducting behavior. Several doping studies have been attempted in order to get an insight into the changes in physical properties with the emphasis on fabricating of all ZnO *p*–*n* junctions for white light/UV emission. The challenge is to obtain highly stable *p*-ZnO with doping. Our group has been working on doping studies in ZnO. Ni doping shows a dramatic decrease in resistivity in polycrystalline ZnO. Stable and low resistive *p*-type conduction in ZnO was not possible with monovalent ion (Li, Ag etc.) doping. Recent work indicated the possibility of inducing shallow holes into ZnO lattice using co-doping route. We used Li and Ni co-doping to realize a low resistive, *p*-type and magnetic ZnO. Aligned 1-dimensional ZnO nanowires can also be obtained using PLD and other methods. Our research group at IIT Madras has been working closely with Kyushu University and other partner universities in Japan to make research in ZnO a worthwhile attempt aimed at device applications. We will present, in this chapter, overall physical properties of ZnO with our important results related to the doping aspects in ZnO.

E. Senthil Kumar · M. S. Ramachandra Rao (✉)
Department of Physics, Nano Functional Materials Technology Centre,
and Materials Science Research Centre, Indian Institute of Technology (IIT) Madras,
Chennai 600036, India
e-mail: msrrao@iitm.ac.in
URL: www.physics.iitm.ac.in/~msrrao

S. Singh
Crystal Growth Centre, Anna University, Chennai 600025, India

M. S. R. Rao and T. Okada (eds.), *ZnO Nanocrystals and Allied Materials*,
Springer Series in Materials Science 180, DOI: 10.1007/978-81-322-1160-0_1,
© Springer India 2014

1.1 Introduction

In the past two decades, optoelectronics research was mainly focused on the crystal growth and conductivity control of semiconductors such as SiC, II–VI chalcogenides, III–V compound semiconductors, and II–VI metal oxides [1–3]. Despite the successful fabrication of SiC-based blue light-emitting diodes (LEDs) and considerable research efforts devoted to the fabrication of *p*-type ZnSe and II–VI blue-green lasers, these two semiconductors were rapidly outshined by the superior electronic properties and light emission efficiency of nitride-based thin-film devices (Morkoc et al. 1994). Furthermore, the external quantum efficiency of nitride-based LEDs in the blue region was found to surpass that of SiC LEDs (41 % for nonpolar InGaN/GaN LEDs vs 0.3 % for SiC LEDs) [4]. The success of III–V nitrides was due to the achievement of stable *p*-type behavior and low resistivity in GaN thin films doped with Mg [5]. These breakthroughs led to the possible fabrication of small sized and high-brightness blue light emitting devices and laser diodes [6]. These devices find applications in high-storage capacity optical recording media (e.g., Blu-ray disks) and optical communication. There is also a large potential in lighting and illumination such as traffic signals, automobile interior panel lighting, high-resolution printers, video game consoles, ophtalmics, and biophotonics [7].

In parallel with nitrides, oxide semiconductors continue to receive considerable attention due to their low cost of fabrication, chemical robustness, and high thermal conductance [8]. Transparent conducting oxide thin films such as Sn-doped In_2O_3 (ITO), F-doped SnO_2, and Al-doped ZnO are usually fabricated on transparent substrates such as glass or sapphire [9, 10]. These semiconductors always exhibit *n*-type conduction with a resistivity of 10^{-4}–10^{-5} Ω cm and are widely used as transparent electrodes in thin film transistors, organic light emitting diodes, and solar cells. The lack of transparent *p*-type oxide material has always been a major obstacle to the fabrication of oxide-based *p–n* homo and hetero-junction devices.

Zinc oxide (ZnO) is a II–VI transparent conducting oxide touted as a material of choice for short wavelength optoelectronics. Similar to GaN, ZnO has a direct band gap of 3.37 eV at 300 K that can be engineered via dilute alloying with BeO, MgO, and CdO [11–13], while retaining its wurtzite structure. As shown in Fig. 1.1, the more tightly bound exciton in ZnO (60 meV) compared with other compound semiconductors (20 meV for GaN) opens the possibility for ZnO-based optoelectronic devices to operate well above 300 K. Lasing in optically pumped ZnO has already been demonstrated at 300 K in high-quality epilayers, poly-crystalline films (random lasers), quantum well superlattices, and nanowire arrays [14–16]. Furthermore ZnO, which shows electron and proton radiation hardness capabilities, can be of potential use in high-irradiation conditions such as space-based environments.

ZnO and its ternary alloys have the potential to compete with III–V nitrides for optoelectronic applications. However, fabrication of the ZnO-based optoelectronic

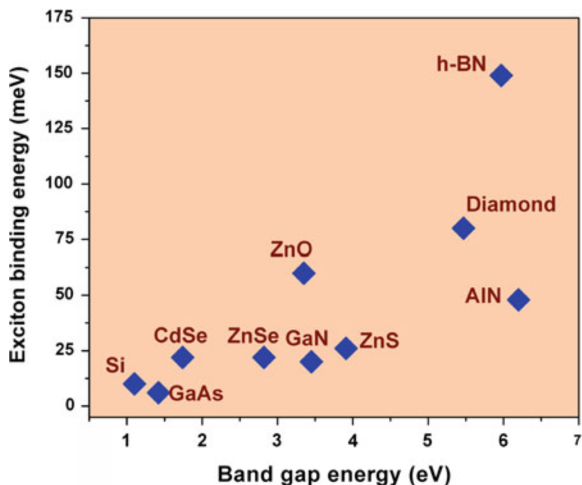

Fig. 1.1 The exciton binding energy as a function of the band gap energy for compound semiconductors

devices is still a problem to deal with due to the difficulty in obtaining *p*-type ZnO. The quest for stable, *p*-type ZnO is a challenging one because the electrical and optical properties of ZnO are very sensitive to minute concentrations of dopants, impurities, and to microscopic perturbations of the lattice [17]. It will be explained in the subsequent sections that the reasons for the difficulties to achieve *p*-type ZnO come from its asymmetric defect chemistry, ionicity, and the complex roles of impurities and crystal defects.

The observation of ferromagnetism in (Ga, Mn) As has inspired a great deal of research interest in the field of spintronics [18]. The main challenge for practical application of the diluted magnetic semiconductor (DMS) materials is the attainment of Curie temperature (T_C) at or preferably above room temperature. Transition metal (TM) ion-doped ZnO became the most extensively studied topical material, since the prediction by Dietl et al. [19], as a promising candidate to realize Curie temperature above room temperature. The particular predictions are on the assumption that hole mediated exchange interaction is responsible for magnetic ordering. The additional advantages of ZnO-based DMSs are that they can be readily incorporated into the existing semiconductor heterostructure systems, in which a number of optical and electronic devices have been realized, thus allowing the exploration of the underlying physics and applications based on previously unavailable combinations of quantum structures and magnetism in semiconductors.

Low-dimensional self-assembled ZnO nanostructures have shown a great advantage in fabrication of devices in the nanometer regime. In particular, one-dimensional (1D) ZnO nanowires/rods have been used to fabricate the field emission devices, piezoelectric nanogenerators, photonic devices, and light emitting diodes [20]. When the sizes of the ZnO nanostructures are comparable with that of exciton Bohr radius, excellent quantum confinement effects have been seen in the optical and electrical properties of ZnO (Song et al. 2007).

Table 1.1 Comparison of physical properties of some key compound semiconductors

Material	Crystal structure	Lattice constants a and c (Å)	Band gap (eV)	Energy of fusion (K)	Exc. binding energy (meV)	Dielectric constant ε (0) and ε (∞)
ZnO	Wurtzite	3.25 5.21	3.37	2,248	60	8.75 3.75
ZnS	Wurtzite	3.82 6.26	3.8	2,103	30	9.6 5.7
ZnSe	Zinc blende	5.66	2.7	1,793	20	9.1 6.3
GaAs	Zinc blende	5.65	1.43		4.2	12.9 10.9
GaN	Wurtzite	3.19 5.19	3.39	1,973	21	8.9 5.35
SiC	Wurtzite	3.18 15.12	2.86	>2,100	–	9.66 6.52

Hence, in this article we have made an effort to explore the electrical, magnetic, and optical properties of doped and undoped ZnO thin films and nanostructures. Table 1.1 shows the summary of the physical properties of some key compound semiconductors used for the optoelectronic applications. It is evident that the ZnO is the only oxide counterpart to GaN in terms of band gap and exciton binding energy. In addition, ZnO is one of the promising transparent conducting oxide used for as transparent electrode in solar cells.

1.2 Physical Properties of ZnO

In this section, crystal structure, electronic band structure, doping studies, transport properties, magnetic properties, and optical properties of the ZnO will be discussed in detail.

1.2.1 Crystal Structure

ZnO is a II–VI compound semiconductor, which crystallizes into three different structures viz., wurtzite (B4), zinc blende (B3), and rocksalt (B1) under different growth conditions. Where B1, B3, and B4 denote *strukturbericht* designations for the three phases [21]. Among these structures, the wurtzite structure is thermodynamically most stable phase under ambient conditions. The zincblende structure can be stabilized by growing on cubic substrates like MgO and Pt/SiO_2/Si [11]. However, the rocksalt (NaCl) structure can be realized only by applying very high

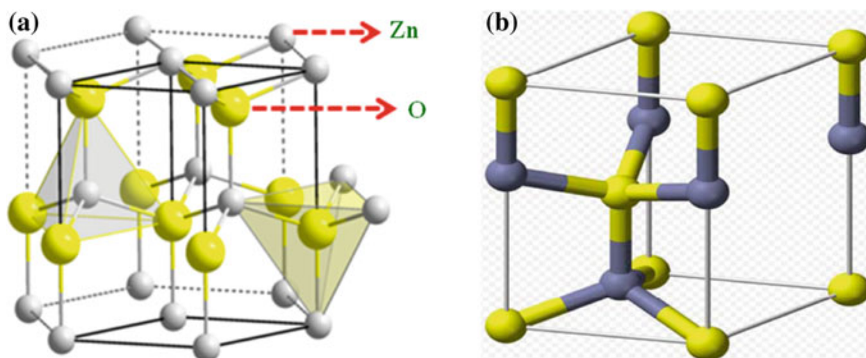

Fig. 1.2 **a** Wurtzite crystal structure of ZnO showing the tetrahedral coordination of the Zn and O atoms. **b** Unit cell of wurtzite structure (figure: courtesy http://www.en.wikipedia.org/wiki/Zinc_oxide)

pressures [22]. When compared with zincblende and rocksalt structures, wurtzite ZnO has shown intriguing optical, electrical, and optoelectronic properties in thin film and nanostructured form. Hence, a lot of research work has been mainly focused on the study of doped and undoped wurtzite ZnO thin films and nanostructures.

The wurtzite ZnO belongs to the space group of C_{6v}^{4} in the Schoenflies notation and $P6_3mc$ in Hermann–Mauguin notation [23]. Figure 1.2 shows the crystal structure and unit cell of the wurtzite ZnO. The structure is composed of two interpenetrating hexagonal close packed (hcp) sublattices, each of which consists of one type of atom displaced with respect to each other along the three fold c-axis by the amount $u = 3/8 = 0.375$, where the parameter u is defined as the anion–cation bond length parallel to the c-axis. The measured lattice parameters of the hexagonal wurtzite ZnO are $a = 3.249$ Å and $c = 5.206$ Å. In the wurtzite ZnO, each sublattice consists of four atoms per unit cell and each atom of one kind is surrounded by four atoms of the other kind. In other words, both Zn and O atoms are tetrahedrally coordinated to each other. This tetrahedral coordination gives rise to polar symmetry along the c-axis.

The polar nature of the ZnO is responsible for many interesting properties viz., piezoelectricity, spontaneous polarization, crystal growth, etching, and defect generation. In ZnO, both Zn terminated (0001) and O terminated $(000\bar{1})$ faces are polar in nature. The other important faces in the wurtzite ZnO structure are nonpolar $(11\bar{2}0)$ and $(10\bar{1}0)$. Figure 1.3 gives the important planes and orientations that are commonly seen in wurtzite structure.

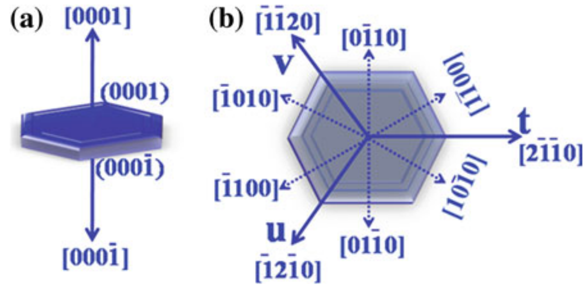

Fig. 1.3 **a**, **b** Various polar and nonpolar planes in ZnO hexagonal wurtzite structure

1.2.2 Electronic Band Structure

Numerous theoretical calculations have been employed to calculate the band structure of ZnO by a number of groups [24]. Figure 1.4 shows the calculated band structure of wurtzite crystal of ZnO. Location of the Zn 3*d* levels was unambiguously determined using the local density approximation (LDA) and incorporating atomic self-interaction corrected pseudo-potentials (SIC-PP). In ZnO, both the valence band maxima and the conduction band minima occur at the Γ point $k = 0$ indicating that ZnO is a direct band gap semiconductor. The bottom 10 bands, occurring around −9 eV (not shown in figure), correspond to Zn 3*d* levels [23]. The next six bands, from −5 to 0 eV, correspond to O 2*p* levels. The first two conduction band states are strongly Zn localized and correspond to empty Zn 3*s* states. The O 2*s* bands, associated with core-like energy states, occur around −20 eV. Using the above calculation, the band gap was determined as 3.77 eV. In addition to theoretical calculations, the electronic band structure was experimentally carried out [25], at the surface of wurtzite ZnO, using the data obtained from electron energy loss spectroscopy (EELS) and ultraviolet photoelectron spectroscopy (UPS). It was observed that the Zn face possesses more covalent character, arising from the Zn 4*s* – O 2*p* states, while the O face is more ionic.

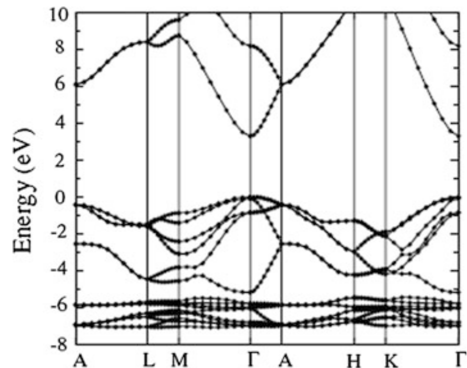

Fig. 1.4 Calculated band structure of the wurtzite ZnO using HSE hybrid functional method. Reprinted after permission from IOP publishing group (*Rep. Prog. Phys.* 72, 126501 (2009))

1.3 Doping Studies in ZnO

The physical properties of ZnO are strongly affected by the dopant impurities and defects. ZnO exhibits intriguing electrical, optical, and magnetic properties when doped with TM ions and other elements [23]. These properties can be tuned by carefully controlling the defects and concentration of dopant impurities in the system. The future optoelectronic applications of ZnO will depend on the ability to dope it into *n*-type and *p*-type material. Band gap of the ZnO can be engineered by doping with Cd and Mg.

1.3.1 Defects in ZnO

The electrical and optical properties of ZnO are still not well understood, which implies that the role of various extrinsic as well as intrinsic defects have not been clearly understood yet. In this section, some of the experimental as well as theoretical approaches to illustrate the presence of defects will be explained. An old age saying in materials science goes as, "materials are like people; it is the defects that make them interesting". Defects play an important role in determining the electronic and optoelectronic properties of semiconducting materials. However, we need to identify and quantify these defects in order to understand the microscopic processes involved. Different types of defects come into effect due to different growth conditions, doping, and growth techniques. Occurrence of electronic defects, involved in optical recombination processes, depends on structure, particle size, composition as well as crystallinity of the sample. A fundamental understanding of the physics of various defects can help in improving emission properties of ZnO as well as in achieving *p*-type conduction in this compound. Appreciable amount of work have been reported on the intrinsic as well as extrinsic defect species present in this compound [26–31]. However, most of these papers present controversial results. Sun et al. studied the intrinsic defects in ZnO by using full potential linear muffin-tin orbital method, and concluded that zinc interstitial is the dominant donor owing to its shallower defect level [32–34]. Kohan and Van de Walle [33, 34] seperately studied different possible native point defects in ZnO by the plane-wave pseudopotential method in the LDA. Kohan et al. [33] used the first-principles pseudopotential method to determine the electronic structure, atomic geometry, and formation energy of native point defects in ZnO and showed that both the Zn and O vacancies are the relevant defects in ZnO. Zhang et al. [35] also calculated the formation energies of native defects in ZnO by the plane-wave pseudopotential method in the LDA. Oxygen and zinc vacancies were found to have the lowest formation energies in their calculations, but the formation energies of most defects have a considerable difference from Kohan's results. Oba et al. [36] calculated the electronic structure of native defects in ZnO by the plane-wave pseudo potential method in the generalized gradient

approximation (GGA), and showed that oxygen vacancies and zinc vacancies act as dominant donor and acceptor defects with deep levels, in agreement with Kohan's and Zhang's LDA studies and that zinc interstitials and zinc antisites are shallow donors. Other theoretical analyses have also shown that Zn interstitial is actually a shallow donor [35, 36] which was further supported by electron irradiation measurements. Kohan et al. [33] also show that oxygen vacancies have lower formation energy than the zinc interstitial defects and hence should be more abundant. Mahan's [26] interpretation of Hagemark's [29] experimental measurements agrees well with the results of Kohan et al. [33]. When there is excess Zn, the native donors are the oxygen vacancies and when there is Zn depletion, Zn vacancies are present [the formation energy of a Zn interstitial is at least 1.2 eV higher than that of an oxygen vacancy]. The formation energy of Zn and oxygen antisites has been found to be higher than that found in the case of Zn and O vacancy defects and hence the antisites are less likely to form [33]. For ZnO exposed to hydrogen during growth, it (hydrogen) was considered as the main donor (as it can ionize easily with low formation energy) [37]. The differences in concentrations of relevant point defects are determined by differences in formation energies of intrinsic point defects in wurtzite ZnO [38]. Electronic structure, formation energies, transition levels, and concentration of intrinsic defects in wurtzite ZnO were investigated by the projector augmented wave (PAW) method and it was found that oxygen and zinc vacancies are the dominant intrinsic donor and acceptor defects in ZnO [38]. Presence of defects can also affect the carrier concentration in ZnO [38]. In a solid, the defect is a function of the chemical potential of the species involved. At thermodynamic equilibrium, the concentration of defects in a crystal is given by the expression:

$$C_{\mathrm{d}} = N_{\mathrm{sites}} N_{\mathrm{config}} - \left(E_f / k_{\mathrm{B}} T\right) \tag{1.1}$$

Here, E_{f} is the formation energy of the defect. N_{sites} is the number of sites in the lattice (per unit volume) where the defect can be produced; N_{config} is the number of equivalent configurations. For a perfect ZnO crystal, the carrier concentration is

$$n_{\mathrm{e}} = n_{\mathrm{h}} = (N_{\mathrm{C}} N_{\mathrm{V}})^{1/2} \exp\left(-E_{\mathrm{g}} / 2k_{\mathrm{B}} T\right) \tag{1.2}$$

where n_{e} and n_{h} are the concentration of free electrons and holes respectively, k_{B} is the Boltzmann constant and T is the temperature. N_{C} and N_{V} are the effective density of states of the conduction and valence band respectively. For a ZnO crystal with defects, the carrier concentration depends upon the Fermi level in the following way:

$$n_e = N_C \exp\left[-\left(E_g - E_F\right)/k_B T\right], \quad n_h = N_V \exp(-E_F/k_B T) \tag{1.3}$$

Here, the Fermi level E_{F} is determined by the overall charge neutrality [39], i.e.

$$\sum q(i) N_{\mathrm{s}}(i) \exp\left[-E_{\mathrm{f}}^{(q)}(i) \Big/ k_{\mathrm{B}} T\right] = N_{\mathrm{C}} \exp\left[-\left(E_{\mathrm{g}} - E_{\mathrm{F}}\right)/k_{\mathrm{B}} T\right] - N_{\mathrm{V}} \exp(-E_{\mathrm{F}}/k_{\mathrm{B}} T) \tag{1.4}$$

Here, $E_f^{(q)}$ (i) is the formation energy of defect i at charge state q and $N_s(i)$ is the number of sites where defect i can be formed per unit volume. In the oxygen deficient condition, the most abundant native defect in ZnO is the oxygen vacancy, which acts as the dominant intrinsic donor. In the oxygen rich condition, the zinc vacancy is the most abundant native defect and serves as the dominant intrinsic acceptor. Zinc interstitial was also found to act as a dominant intrinsic donor in some studies [29, 30]. However, calculations by Zhao et al. [38] indicate that the zinc interstitial is at least 1.0 eV higher in formation energy than the oxygen vacancy. They also found that the formation energy of the oxygen interstitial is about 1 eV higher than that of the zinc vacancy. Some of the authors pointed out Zn interstitials as the dominant defects in ZnO, on the basis of ionic diffusion or size considerations [29, 40, 41], whereas others indicated that it was oxygen vacancies, based on the calculation of reaction rates, diffusion experiments, or electrical conductivity and Hall effect measurements [26].

Bulk ZnO crystals, grown by the seeded vapor phase and melt technique, have been found to have low concentration of defects, dominant one being the Zn vacancies Tuomisto and Look (2007). Zn vacancies as well as high concentrations of O vacancies have been observed in ZnO bulk crystals grown by conventional chemical vapor transport and hydrothermal methods [31].

The luminescence properties of ZnO have also been related to various crystalline lattice defects [42]. The internal absorption is not expected to affect the visible emission spectrum in wide bandgap semiconductors, hence the intensity of deep level emission should be roughly proportional to the density of defects present. Bond lengths associated with the host compounds are affected by the presence of defects (which can be explained in terms of size and charge effects). As for example Zn, vacancy defect implies the removal of a small positively charged Zn ion. Thus, we expect that other positively charged Zn ions will move closer to the vacant sites because of the availability of space and reduced electrostatic repulsion. Oxygen neighbors are no longer electrostatically attracted to the vacancy and consequently move farther away [33].

1.3.2 Electrical Properties of ZnO

Defect chemistry plays a very important role in controlling the electrical transport properties of ZnO [43]. ZnO belongs to a group of transparent conducting oxide (TCO) materials that show strong doping asymmetry (unipolarity) i.e., inability to dope both n and p-type carriers into the lattice.

Table 1.2 gives the summary of the electrical properties such as electron concentration and mobilities of the bulk ZnO and thin films grown by various techniques. Normally, these samples show n-type conductivity due to various defects present in the lattice.

Table 1.2 Summary of the electrical properties of the bulk ZnO and thin films grown by various techniques

Sample	Carrier concentration (cm^{-3})	Electron mobility ($cm^2 V^{-1} s^{-1}$)	Reference
Bulk ZnO grown by vapor-phase transport	6.0×10^{16}	205	Look et al. [46]
Bulk ZnO grown by pressurized melt method	5.05×10^{17}	131	Nause and Nemeth et al. [117]
Bulk ZnO grown by hydrothermal method	8×10^{13}	200	Maeda et al. [118]
PLD grown ZnO thin films on *c*-plane sapphire	2.0×10^{16}	155	Kaidashev et al. [119]
MBE grown ZnO thin films on *c*-plane sapphire	1.2×10^{17}	130	Kato et al. [44]
MBE grown ZnO thin films on *a*-plane sapphire	7.0×10^{16}	120	Iwata et al. [45]
PLD grown $Zn_{0.9}Mn_{0.1}O$/ZnO heterostructure on sapphire	8.8×10^{14}	130	Edahiro et al. [120]
MBE grown ZnO thin film on ZnO/MgO double buffer layers	1.2×10^{17}	145	Miyamoto et al. [121]
ZnO film grown on MgZnO-buffered ScAlMgO4 by PLD	1×10^{16}	440	Ohtomo and Tsukazaki [122]

1.3.2.1 *n*-Type Doping

Naturally, unintentionally doped ZnO shows *n*-type conduction with an electron concentration $\sim 10^{17}$–10^{21} cm^{-3} [44, 45]. It was believed that the *n*-type conduction originates due to native defects such as oxygen vacancies (O_v) and zinc interstitials (Zn_i). Look et al [46] suggested that zinc interstitials (Zn_i) are the dominant shallow donors, rather than O_v, with an ionization energy of about 30–50 meV. However, first-principle calculations show that both O_v and Zn_i have high formation energies in *n*-type ZnO, and therefore none of these native defects are shallow donors [33]. Van de Walle [37] has theoretically shown that H is likely to be the dominant background shallow donor in ZnO materials that are exposed to H during growth. Since the H mobility is large, it can easily diffuse into ZnO in any kind of growth technique. A recent theoretical calculation of Kim and Park [47] suggests that the columbic attraction between O_v and Zn_i acts as shallow donors in ZnO. Nevertheless, the origin of *n*-type conductivity in unintentionally doped ZnO is still a controversial and has not been completely understood.

Besides the native defects and H donors, the *n*-type doping of ZnO can be easily achieved by group-III elements and group-VII elements. Group-III elements such as Al, Ga and In can be easily substituted at Zn site with doping concentration $\sim 10^{20}$ cm^{-3} (Makino et al. 2004). Al-doped ZnO thin films grown by metal organic chemical vapor deposition (MOCVD) and pulsed laser deposition (PLD) methods have shown a low resistivity of 6.2×10^{-4} and 8.5×10^{-5} Ω cm

respectively [48, 49]. Ga-doped ZnO thin films grown by CVD method showed room temperature resistivity of $1.2 \times 10^{-4}\ \Omega$ cm [50]. These films are found to be transparent to visible light with transparency >90 %. Hence, Al or Ga-doped ZnO thin films can be an alternative for Indium Tin Oxide (ITO) for commercial applications in solar cells and flat panel displays due to their low cost, chemical and thermal stability, and nontoxicity.

1.3.2.2 *p*-Type Doping

Most of the wide bandgap semiconductors such as GaN, ZnO, ZnS, and ZnSe can be easily doped into *n*-type, while *p*-type doping is difficult [51]. ZnO has proven to exhibit strong unipolarity (*n*-type) i.e., doping asymmetry. The problem of *p*-type doping in ZnO can arise for several reasons such as (i) acceptor dopants may be compensated by the native donors (O_v and Zn_i) and background *H* impurities, (ii) low solubility of the dopant impurities, and (iii) high activation energy of acceptors (deep impurity level) [52]. The self compensation problem is the most challenging phenomenon in ZnO that leads to the instability of *p*-ZnO and reverting to *n*-type within a matter of days.

The possible *p*-type dopants in ZnO are group-IA and -IB elements (Li, Na, K, Ag, and Cu), group-V elements (N, P, Sb, and As), and Zn vacancies (Zn_v) [53–55]. However, many of these form deep acceptor levels and do not contribute significantly to the *p*-type conduction. It has been believed that the most promising dopants for *p*-type ZnO are the group-V elements, although theoretical studies suggest some difficulty in achieving shallow acceptor levels [56]. In order to understand the microscopic aspects of *p*-type doping in ZnO, numerous theoretical studies have been made using first-principle calculations [57]. It was shown that group-I elements may be better *p*-type dopants than group-V elements in terms of the shallowness of acceptor levels. However, in contrary, group-I elements tend to occupy interstitial sites rather than substitutional sites because of their small ionic radii [38]. Doping with K and Na increases the Zn–O bond length that leads to the formation of compensating donor defects. Similarly, P and As doping in ZnO increases the bond length and hence they form antisites, A_{Zn}, which are well-known donors in ZnO [57]. N substitution at the O site is believed to be the best *p*-type doping in ZnO [53, 58]. However, a few theoretical and experimental reports show that N can form a deep acceptor level in ZnO [56, 56]. Moreover, the stability of N in ZnO is found to be low [59].

Yamamoto and Yoshida [52] proposed a codoping method to solve the unipolarity in ZnO, based on ab-initio electronic band structure calculations. Codoping acceptors (N) with donor impurities (Ga, Al and In) in the 2:1 ratio in ZnO was suggested to stabilize the N in appropriate lattice site through acceptor–donor–acceptor (N–Ga–N) formation [60]. The enhancement of solubility limit was explained in terms of the formation of ionic pairs between donor and acceptor ions as a consequent reduction in Madelung energy. The calculated differences in Madelung energy (E_{Mad}) between (i) undoped and group-III doped, (ii) undoped

Table 1.3 Calculated differences in Madelung energy (E_{Mad}) between undoped and *n* or *p*-type doped ZnO

n-type doping		*p*-type doping		Codoping	
Element	E_{Mad}	Element	E_{Mad}	Element	E_{Mad}
Al	−6.44	N	+0.79	(Al, 2 N)	−3.95
Ga	−13.72	Li	+13.56	(Ga, 2 N)	−11.27
In	−9.73	As	+12.61	–	–

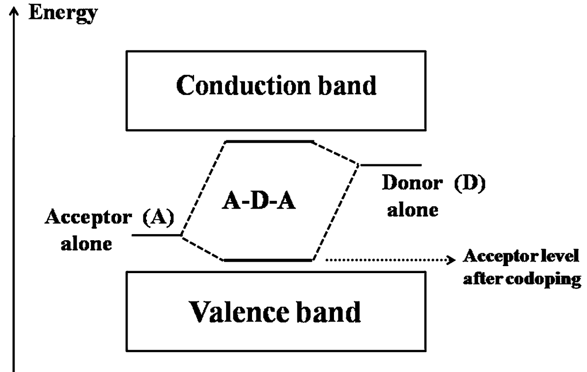

Fig. 1.5 Schematics depicting a change in acceptor and donor energy levels in the band gap due to the strong interaction between acceptors and reactive donors

and group-V doped, and (iii) undoped and Group-III and V codoped ZnO system are shown in Table 1.3. It is very clear from the table that the Madelung energy decreases with the group-III elements (Al, Ga, and In) for *n*-type doping, whereas it increases with group- I and V elements (Li, N and As) for *p*-type doping.

Yamamoto [60] have shown that the codoping method causes the formation of the complexes including acceptors and donors in the crystals, and contributes (i) to reduce the Madelung energies and enhance the incorporation of acceptors because the strong acceptor–donor attractive interaction overcomes the repulsive interactions between the acceptors and (ii) to lower the energy levels of the acceptors in the band gap due to the strong interaction between the acceptors and donors by forming an acceptor–donor–acceptor complex as shown in Fig. 1.5, and (iii) to increase the carrier mobility due to the short-range dipole-like scattering mechanism (long-range Coulomb scattering is dominated in the case of doping of acceptors alone). Thus, the *p*-type codoped semiconductors exhibit low resistivity with high carrier density and high mobility. Numerous experimental results have been successfully reported based on the codoping theory (Joseph et al. 1999) [9, 61].

Lee et al. [39] have suggested that codoping Li with H will be ideal for getting low resistive *p*-ZnO. However formation of the complexes, such as Li_{Zn}–Li_i, Li_{Zn}–H, and Li_{Zn}–AX, will limit the *p*-type doping concentration [62]. Zeng et al. [38] have reported a low resistivity of 16.4 Ω cm with a carrier mobility of 2.65 $cm^2\ V^{-1}\ s^{-1}$ by Li monodoping. The same group [63] has tried Li–N dual-acceptor doping in ZnO (ZnO: Li–N) and achieved a resistivity of 0.93 Ω cm and a Hall mobility of 0.75 $cm^2\ V^{-1}\ s^{-1}$ with an acceptor activation energy of 95 meV. Shubra et al. [64]

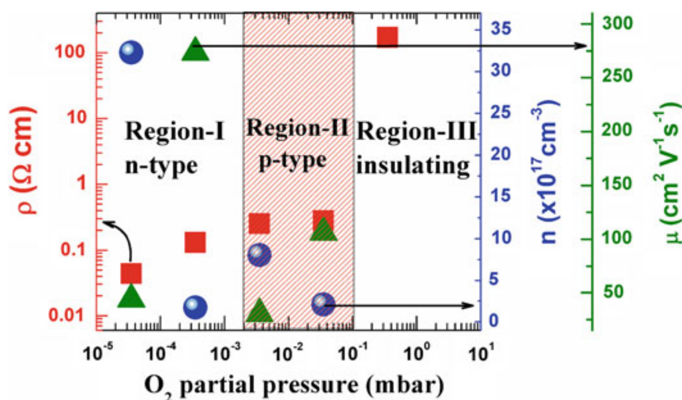

Fig. 1.6 Room temperature electrical transport properties of Li–Ni codoped ZnO thin films grown at various oxygen partial pressures. Reprinted after permission from American Institute of Physics (*Appl. Phys. Lett.* 96, 232504 (2010))

have reported a dramatic decrease in the bulk resistivity of Ni-doped ZnO. This was attributed to the impurity *d*-band splitting of Ni ion in the tetrahedral crystal field of ZnO. Recent experimental and theoretical reports [65, 66] show that incorporation of Li in TM ion-doped ZnO will stabilize the ferromagnetic ordering thereby increase the Curie temperature. However, what happens to the stability of *p*-type conduction when a TM ion is incorporated in Li-doped ZnO lattice, remains to be seen. This question has motivated us to examine the codoping of Li–Ni to achieve a stable and low resistive *p*-type ZnO. Hence Li–Ni codoped ZnO thin films were grown on sapphire substrates using PLD technique at a substrate temperature of 400 °C at with different oxygen partial pressures.

Room temperature electrical resistivity (ρ) of the Li–Ni codoped ZnO thin films is found to increase with the increase in oxygen growth pressure. The films grown at 10^{-5}, 10^{-4}, 10^{-3}, 10^{-2} and 10^{-1} mbar of oxygen partial pressure showed room temperature electrical resistivity of 0.044, 0.132, 0.254, 0.281, and 172 Ω cm, respectively. A dramatic jump in the electrical resistivity from 0.281 to 172 Ω cm is observed while increasing the oxygen partial pressure from 10^{-2} to 10^{-1} mbar. This is because at high O_2 partial pressures, a significant amount of Li occupies the interstitial sites (Li_i) and compensates the acceptors (Li_{Zn}), leading to an increase in the resistivity dramatically [62].

Room temperature Hall effect measurements on the Li–Ni codoped ZnO thin films grown at various oxygen partial pressures were carried out at a magnetic field of 8 T. Figure 1.6 shows the room temperature electrical transport properties of the Li–Ni codoped ZnO thin films as a function of oxygen growth pressure. We have observed three interesting conductivity regimes. The films grown at oxygen partial pressure in the range 10^{-5} and 10^{-4} mbar show *n*-type conductivity and exhibited electron concentrations of 3.2×10^{18} to 2.4×10^{17} cm^{-3}. The films grown at oxygen partial pressures $\geq 10^{-1}$ mbar exhibited insulating nature. Because of the high resistivity of these films, Hall effect measurements could not

be performed on these insulating films. However, we observed an interesting narrow window of growth pressure between 10^{-3} and 10^{-2} mbar, in which the films showed stable *p*-type conduction with a room temperature hole concentration of 8×10^{17} to 2.4×10^{17} cm^{-3} [67].

1.3.3 Magnetic Properties of ZnO

Diluted Magnetic Semiconductors (DMS) are semiconducting materials in which a fraction of the host cations can be substitutionally replaced by magnetic ions [68]. Much of the attention on DMS materials is due to its potential application in what is now called spintronic devices, in which both charge and spin can be simultaneously controlled [69, 70]. The III–V and II–VI semiconductors can be magnetically doped using the 3*d* TM ions and 4*f* rare-earth ions [71]. The discovery of hole mediated ferromagnetism in (Ga, Mn) As has paved the way for a wide range of possibilities for integrating magnetic and spin-based phenomena in microelectronics and optoelectronics [18]. However, the highest Curie temperature, T_C, reported in (Ga, Mn) As grown by molecular beam epitaxy (MBE), is $\sim$170 K [72]. In order to realize practical applications of spintronic devices, the DMS materials must exhibit ferromagnetism with a Curie temperature (T_C) above room temperature.

ZnO has attracted intense attention in the search for high T_C ferromagnetic DMS materials, since Dietl et al. [19] predicted that Mn-doped *p*-type ZnO-based DMSs could exhibit ferromagnetism above room temperature. This is due to the strong *p*–*d* hybridization between the *p*-states of the valence band and the Mn 3*d* levels. The values of T_C computed by assuming 5 % of Mn and $p = 3.5 \times 10^{20}$ cm^{-3}.

This prediction has stimulated considerable research in wide bandgap semiconductors, resulting in the observation of a spontaneous magnetic moment at room temperature in TM ion-doped nitrides and oxides. The wide bandgap semiconductors, which tend to have smaller lattice constants, exhibit strong *p*–*d* hybridization and small spin orbit interaction, and hence large Curie temperatures. In addition to the prediction of Dietl et al. [19], ferromagnetism in magnetic ion (V, Cr, Mn, Fe, Co, and Ni) doped ZnO has been theoretically investigated using ab-initio calculations based on the LDA by Sato et al. (2000, 2001). Their results suggest that ferromagnetic ordering can be possible even in *n*-type TM:ZnO thin films and bulk polycrystalline powders.

1.3.3.1 Origin of Ferromagnetism in TM Ion Doped ZnO

In a DMS material, presence of magnetic ions (TM ions) affects the free carrier behavior through the *sp*–*d* exchange interaction between the localized magnetic moments and the spins of the itinerant carriers [73]. Generally, 3*d* transition-metal ions substitute for the cations of the host semiconductors, i.e., Zn sites in ZnO.

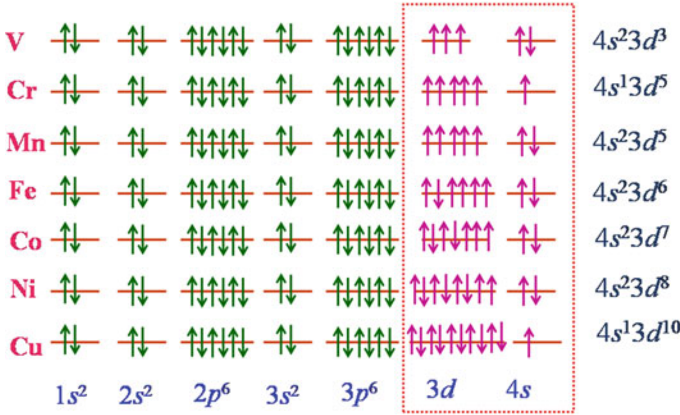

Fig. 1.7 Electronic configuration of the 3*d* states and 4*s* states of TM elements

In ZnO, the particular transition-metal element, for example, Mn, contributes its 4 s^2 electrons to the sp^3 bonding, and can therefore substitutionally replace the Zn in the tetrahedral bonding to form a TM^{2+} charge state. The 3*d* band of the Mn^{2+} ion is exactly half-filled with five electrons among the 10 available states. For other TM ions such as Fe, Co and Ni, one of the bands is usually partially filled (up or down), as shown in Fig. 1.7. The TM-*d* bands of the TM hybridize with the host valence bands (O-*p* bands in ZnO) to form the tetrahedral bonding. This hybridization gives rise to the exchange interaction between the localized 3*d* spins and the carriers in the host valence band. In this simple picture, the *s* band of the conduction band does not mix with the TM-*d* bands, but it is still influenced by the magnetic ion.

Few mechanisms proposed to understand the ferromagnetic properties of DMS materials are direct superexchange (antiferromagnetic), indirect superexchange (ferromagnetic), carrier mediated exchange (ferromagnetic) that include the double exchange mechanism and bound magnetic polarons (BMPs). In the Zener model, the direct interaction (superexchange) between the *d* shells of the adjacent Mn ions leads to antiferromagnetic nature. However, the indirect coupling between the spins of Mn ions and the conduction electrons is ferromagnetic (indirect superexchange) in nature [74]. In Ruderman–Kittel–Kasuya–Yoshida (RKKY) model, the interaction is based on the coupling between the magnetic ion and the conduction electron. However, if the electrons are localized, the RKKY interaction becomes weak and unrealistic. The mean-field Zener model proposed by Dietl et al. [19] is based on the original Zener model and the RKKY interaction and takes into account the anisotropy of the carrier mediated exchange interaction associated with the spin–orbit coupling in the host material. The Curie temperature (T_C) predicted by the mean-field Zener model in DMS material like (Ga, Mn) As is given by,

$$T_C = C N_{Mn} \beta^2 m^* p^{1/3} \tag{1.5}$$

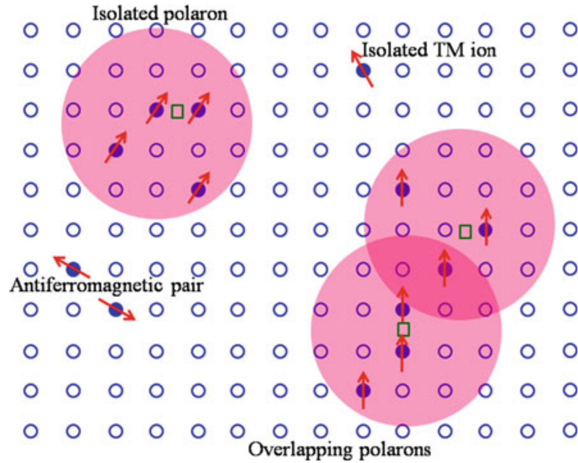

Fig. 1.8 Representation of magnetic polarons. A donor electron couples its spin antiparallel to impurities with a half-full or more than half-full 3*d* shell. Cation sites are represented by *small circles*. Oxygen is not shown; the unoccupied oxygen sites (F-center vacancies) are represented by *open squares*. Reproduced after permission from Nature Publishing group (*Nater. Mater*. 4, 175 (2005))

where N_{Mn} is the concentration of uncompensated Mn spins, β is the coupling constant (*p*–*d* coupling), m^* is the effective mass of the holes and *p* is the hole concentration.

First-principle ab initio calculations of electronic band structure by Sato and katayama-Yoshida [75] are based on the double exchange mechanism for the carrier-induced ferromagnetism. In the DMS material, if neighboring TM ions magnetic moments are in the same direction, the TM-*d* band is widened by the hybridization between the up–spin states. Therefore, in the ferromagnetic configuration the band energy can be lowered by introducing carriers in the *d* band. In these cases, the 3*d* electron in the partially occupied 3*d*-orbitals of the TM is allowed to hop into the 3*d*-orbitals of the neighboring TM, if neighboring TM ions have parallel magnetic moments. As a result, the *d*-electron lowers its kinetic energy by hopping in the ferromagnetic state. This is the so-called double exchange mechanism.

In addition to the above-mentioned models, the most recently proposed mechanism for the understanding of the ferromagnetic ordering of the TM ion due to the localized carriers is the BMP model [76]. The BMPs are formed by the alignment of the spins of many transition-metal ions with that of much lower number of weakly bound carriers such as excitons within a polaron radius. The basic idea is schematically illustrated in Fig. 1.8. The localized holes of the polarons act on the transition-metal impurities surrounding them, thus producing an effective magnetic field and aligning all spins. As temperature decreases, the interaction distance (boundary) grows. The neighboring magnetic polarons overlap and interact via magnetic impurities forming correlated clusters of polarons. One observes a ferromagnetic transition when the size of such clusters is equal to the size of the sample.

This model is inherently attractive for low-carrier density systems such as many of the electronic oxides. The polaron model is applicable to both *p*- and *n*-type host

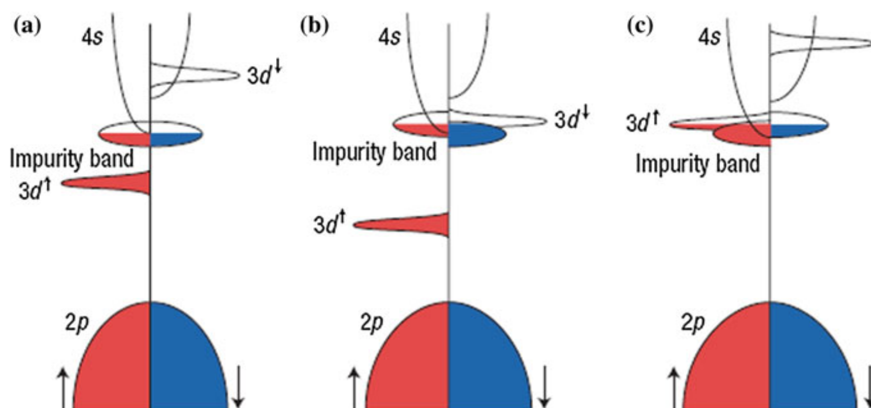

Fig. 1.9 Schematic band structure of an oxide with 3*d* impurities and a spin split donor impurity band. **a** The position of the 3*d* level for low Curie temperature T_C, when the splitting of the impurity band is small **b** and **c** show positions of the minority and majority spin 3*d* bands respectively that lead to high T_C. Reprinted after permission from Nature Publishing group (*Nater. Mater.* 4, 175 (2005))

materials. Even though the direct exchange interaction of the localized holes is antiferromagnetic, the interaction between BMPs may be ferromagnetic for sufficiently large concentrations of magnetic impurities. The ferromagnetic exchange is thus mediated by charge carriers in a spin–split impurity band formed by extending donor states. Coey et al. [76] have showed that for Sc, Ti, and V, the spinup states are aligned with the impurity levels and for Fe, Co, and Ni doping, the spindown states are aligned with the impurity levels. Mn and Cr dopings were said to have a small hybridization thereby leading to a weak magnetization. Figure 1.9 shows the schematic band structure of an oxide with 3*d* impurities and a spin–split donor impurity band.

1.3.3.2 Experimental Results of TM Ion Doped ZnO Thin Films and Bulk Polycrystalline Powders

Experimental attempts have led to various conflicting reports of room temperature ferromagnetism in ZnO [77, 78]. Both paramagnetism (Sharma et al. 2003) and ferromagnetism [79] have been observed in ZnO with TM^{2+} substituted at Zn^{2+}. Norton et al. [80] have showed the evidence of ferromagnetism with a Curie temperature around 250 K in Mn implanted *n*-type ZnO:Sn single crystal. High saturation magnetic moment of 1.4 μB/Mn is observed at room temperature in (Mn, N) codoped ZnO thin films grown by inductively coupled plasma enhanced chemical vapor deposition [81]. *Monte Carlo* simulation studies of Souza et al. [82] have showed that the *p*-type conductivity is essential for observing ferromagnetism in Mn-doped ZnO thin films. Hou et al. [83] have observed room temperature ferromagnetism in *n*-type Cu-doped ZnO thin films grown by DC

reactive magnetron sputtering. Sudakar et al. (2008) have shown room ferromagnetism in CuO–ZnO multilayers. Room temperature ferromagnetism has been observed in Co-doped ZnO single crystalline thin films [71, 84], bulk polycrystalline powders [86] and nanoparticles [87]. Liu et al. [63, 88] have reported that the room temperature ferromagnetism can be tuned by controlling the Ni concentration in PLD grown thin films. Ni-doped colloidal ZnO nanoparticles showed above room temperature (~350 K) ferromagnetism (Schwartz et al. 2004). V and Cr-doped ZnO thin films have also shown room temperature ferromagnetism [89, 90]. Room temperature ferromagnetism has been reported in C-doped ZnO thin films and nanostructures [91, 92] prepared by PLD technique. Room temperature ferromagnetism has been observed even in nonstoichiometric ZnO thin films and bulk polycrystalline powders [93, 94]. Moreover, recent theoretical calculations [66] show that incorporation of acceptor defects in Ni:ZnO lattice will enhance the ferromagnetic ordering, and hence increase the Curie temperature. Hence we have made a systematic effort to study the magnetic properties of Li–Ni codoped ZnO thin films in the *n*-type, *p*-type and insulating regimes to understand the origin of ferromagnetism, if any, in ZnO.

Magnetic measurements were carried out on the Li–Ni-codoped ZnO thin films grown at different oxygen partial pressures and showed change in carrier type from *n* to *p* and insulating nature. Figure 1.10 shows the magnetization measurements (M–H) of the films grown at 10^{-5} mbar (*n*-type), 10^{-3} mbar (*p*-type), 10^{-2} mbar (*p*-type) and 10^{-1} mbar (insulating) at 300 K. All the films showed clear saturated M–H curves at room temperature. Both the *n*-type and *p*-type thin films exhibited hysteresis loops opening with a coercive field of ~45 Oe in the M–H curve indicating room temperature ferromagnetic nature. However, the insulating film, grown at 10^{-1} mbar, showed zero coercive field indicating superparamagnetic nature [67].

Very interestingly, we have observed that the saturation magnetization (M_s) of the Li–Ni-codoped ZnO thin films strongly depends on the oxygen growth pressure and the carrier concentration and not on the carrier type. The *n*-type film with an electron concentration of $\sim 3.3 \times 10^{18}$ cm^{-3} exhibited a maximum saturation magnetization (M_s) ~ 0.12 μ_B/Ni. The *p*-type Li–Ni-codoped ZnO thin films with

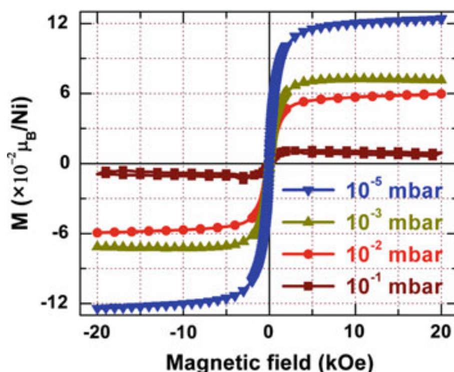

Fig. 1.10 Room temperature M–H curves of the Li–Ni codoped ZnO thin films after subtracting the substrate contribution. Reprinted after permission from American Institute of Physics (*Appl. Phys. Lett.* 96, 232504 (2010)

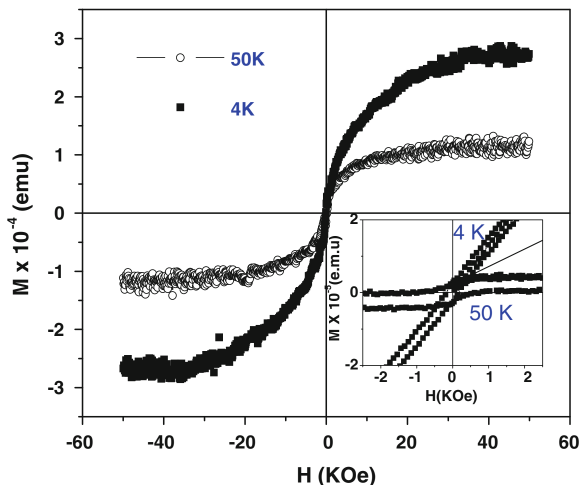

Fig. 1.11 M–H plots of 1 mol% Co doped thin film at 4 and 50 K. *Inset* shows the magnified plot of hysteresis loops at different temperatures

a hole concentration of 8.1×10^{17} and 2.1×10^{17} cm^{-3} showed $M_s \sim 0.07$ and 0.06 μ_B/Ni, respectively. The insulating film that was grown at a high oxygen partial pressure of 10^{-1} mbar showed $M_s \sim 0.009$ μ_B/Ni. This clearly shows that the oxygen vacancies and carrier concentration play a crucial role in determining ferromagnetic ordering. Hence, the oxygen vacancy (donor defect) related ferromagnetism can be more suitably explained using defect mediated mechanism—the so-called BMP mechanism [76]. Hence, Ni substitution in the zinc cation site and the oxygen vacancies are jointly responsible for the observed ferromagnetism. This study clearly reveals that the type of carrier does not influence the ferromagnetic nature of the films and higher the carrier density (*n* or *p*), higher the saturation magnetization.

We have also investigated the magnetic properties of the polycrystalline TM ion-doped ZnO. Figure 1.11 illustrates the M–H curves of 1 mol% Co and Mn-doped ZnO films respectively. For Co-doped thin film hysteresis loops were observed at 4 and 50 K, though in the presence of some noise because of weak signal. The coercivity was measured to be about 100 Oe at 4 K. According to our experimental results, low-temperature hysteresis loops could be realized even for 1 mol% doped samples of Co and Mn-doped ZnO. However, at higher temperatures the M–H curve did not show any sign of saturation. The source of magnetism of ZnO-doped with Co at low concentration is still not totally understood. In our view, metal clusters may not be the source of magnetism at low Co concentration, as this concentration is well below the solid solubility limit of Co in ZnO. It is known that ferromagnetism is the usual explanation for hysteresis. However, it is worth noting that spin glass and superparamagnetism below a blocking temperature can also be the cause of the hysteresis loop. An investigation of magnetization dependence on temperature can give us a clear idea of the exact nature of the magnetic behavior. However, due to low signal from the films, the nature of M–T

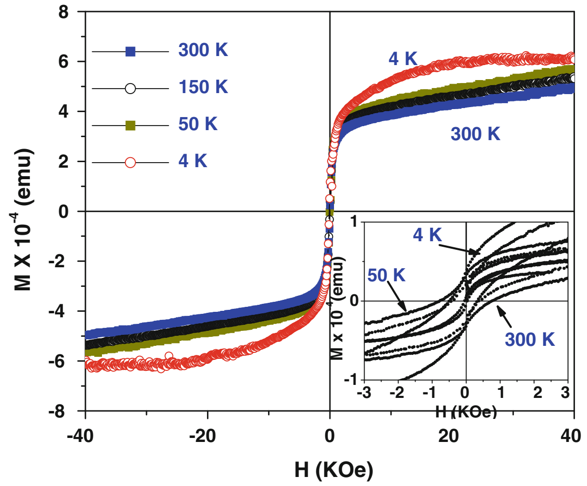

Fig. 1.12 M–H plot of 1 mol% Mn doped thin film at different temperatures. Inset shows the magnified plot of hysteresis loops at different temperatures

data obtained from VSM was very noisy. So at this point, it was difficult to determine the nature of magnetization in our sample.

Mn-doped sample hysteresis loops (Fig. 1.12) were observed from 4 to 300 K. The coercivity was measured to be about 300 Oe. At higher temperatures (>4 K), the M–H plot did not show saturation. Thin films corresponding to other dopants (Ni, Ti, V and Cr) were paramagnetic in nature.

The thin films of doped ZnO samples do not show ferromagnetism. Though Co, Fe, and Mn samples showed hysteresis loops at low temperatures (>50 K), there were no signs of room temperature ferromagnetism in the samples.

1.4 Optical Properties of ZnO

The application of semiconductors in electro-optical devices relies on their ability to efficiently emit or detect light. The optical properties of ZnO are heavily influenced by the energy band structure and lattice dynamics. If photons of energy greater than or equal to the band gap are incident on a semiconductor, they can excite an electron from the valence band to the conduction band. In this process, the photon that is absorbed creating an electron-hole pair. In the reverse process, an electron in a conduction band may return to the valence band and recombine with a hole thereby emitting a photon. As the energies of the electron and hole will be very close to the bottom of the conduction band and the top of the valence band respectively, the emitted photon energy will be approximately equal to the band gap energy of the semiconductor.

Optical properties of ZnO have been intensively studied because of its wide and direct band gap (3.35 eV), high exciton binding energy (60 meV), and efficient

radiative recombination. The large exciton binding energy paves the way for an intense near-band-edge (NBE) excitonic emission at room and even higher temperatures, because this value is 2.4 times the room temperature thermal energy (25 meV) [21, 23]. Hence, laser operation based on excitonic transitions is highly expected in ZnO. The optical absorption and emission properties of ZnO are strongly influenced by the excitonic processes (free and bound excitons) and dopant or impurity states in the band gap. The electronic states of the bound excitons (BE), which may be bound to neutral or charged donors and acceptors, strongly depend on the band structure of ZnO. For a shallow neutral donor–bound exciton (DBE), the two electrons in the bound exciton state are assumed to pair off into a two electron state with zero spin. The additional hole is then weakly bound in the net hole attractive Coulomb potential set up by this bound two electron aggregate [21]. Similarly, neutral shallow acceptor–bound excitons (ABE) are expected to have a two-hole state derived from the topmost valence band and one electron interaction. The commonly observed optical spectra are free to bound (electron–acceptor), bound to bound (donor–acceptor) and the so-called yellow and green luminescence (Look et al. 2001). The well-known green band observed around 500–530 nm is related to the singly ionized oxygen vacancies.

Optical transitions in ZnO can be studied using a variety of experimental techniques such as optical absorption, transmission, reflection, ellipsometry, photoluminescence (PL), and cathodoluminescence. In general, luminescence from the bulk ZnO extends from the band edge to green spectral range. The sharp lines dominating band edge region of the spectra originate from various bound exciton recombinations (excitons bound to neutral and ionized donors, D^0X and D^+X) followed by longitudinal optical (LO) phonon replicas with an energy separation of 72 meV. On the high energy side of the bound excitons, free exciton transitions appear with the A-valence band (FX_A) positioned at 3.377 eV (Teke et al. 2004). At lower energies from 3.33 to 3.31 eV, two electron satellite (TES) recombination lines of the neutral DBEs have been reported.

From the transition energies of the intrinsic excitons, the exciton binding energy, exciton Bohr radius, and the dielectric constant can be calculated. Assuming the exciton has hydrogen like set of energy levels, the exciton binding energy (E_B) can be calculated from Kelsall et al. (2005),

$$E_n = E_g - \frac{E_B}{n^2} \tag{1.6}$$

where n is the main quantum number and $E_B = 4/3\ (E_2–E_1)$ is the exciton binding energy. Where E_1 and E_2 are energies correspond to $n = 1$ and $n = 2$ levels respectively. E_B can also be expressed in terms of the low frequency dielectric constant ε_0 and the reduced exciton mass μ^*_{ex}, Planck's constant $\hbar$ and electronic charge e as,

$$E_B = \frac{e^4 \mu^*_{ex}}{2h^2 \varepsilon_0^2} = 13.6 \frac{\mu^*_{ex}}{\varepsilon_0^2} (\text{eV}) \tag{1.7}$$

The exciton Bohr radius can be expressed as,

$$a_{\mathrm{B}} = \frac{\hbar^2 \varepsilon_0}{\mu_{\mathrm{ex}}^* e^2} n^2 \tag{1.8}$$

1.4.1 Photoluminescence (PL) of ZnO

In order to reduce the power consumption and increase the brightness of phosphors used in flat panel displays, we need to optimize the properties of phosphors (light emitting solids). To achieve this, a basic physical understanding of the luminescence processes of the phosphor materials is essential. ZnO is a well-known greenish white light emitting phosphor for low-voltage vacuum display devices with a relatively high luminescent efficiency [95]. A broad defect-related peak extending from ~1.9 to ~2.8 eV is a common optical feature of ZnO. A typical PL spectra of ZnO sample are shown in Fig. 1.13. The origin of this green luminescence band is still not well understood and it has been attributed to the presence of a variety of different impurities and defects present in the ZnO lattice. Moreover, ZnO due to its bio-compatible character would be a suitable phosphor material (by doping) in biological labeling applications [96]. Many researchers have investigated the emission properties of ZnO films, including ultraviolet and green emission. Green luminescence of ZnO is the characteristic of phosphors fired in air or under reducing conditions (H_2, ZnS, CO, etc.).

In high-quality bulk ZnO substrates, the neutral shallow defect band emission often dominates because of the presence of donors due to unintentionally doped impurities and/or shallow donor-like defects. Lin et al. [97] reported green luminescent center in undoped zinc oxide films deposited on silicon substrates by DC-reactive sputtering. The intensity of the green peak depends markedly on annealing conditions; however, the intensity of the UV peak varies little with annealing

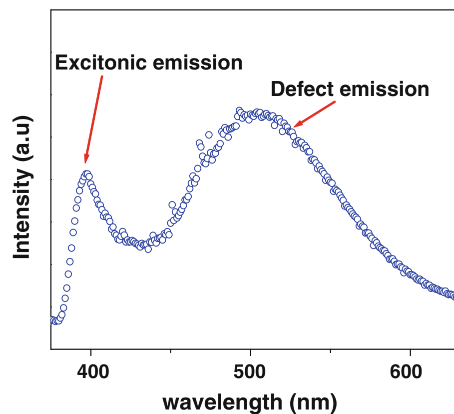

Fig. 1.13 PL emission from ZnO thin film. Intense excitonic defect free emission is desirable from ZnO thin films for optical pumping, light emission and optoelectronic applications

conditions. Liu et al. [98] investigated the green and yellow luminescence centers in ZnO and Mn-doped ZnO. It was seen that water vapor enhanced green luminescence of ZnO in the surface, and causes a two-band luminescence phenomenon (green and yellow in the bulk). Photoluminescence spectra of the ZnO films deposited by Fang et al. (2004) showed the blue emission peak centered at 430 nm.

Mordkovich et al. reported the discovery and optimization of ZnO-based phosphors using a combinatorial method [99]. The efficiency of these phosphors in low-voltage cathodoluminescence was found to be high and promises their prospective use in advanced flat panel display and lighting applications. ZnO exhibited luminescence defect centers such as oxygen vacancies, as donors, located at 50 and 190 meV below the conduction band edge and zinc interstitials as acceptors located at 2.5 eV below the conduction band edge [100]. The visible PL of ZnO is related to the defects, such as oxygen vacancies and zinc interstitials in the films and the green PL comes from oxygen deficient films as reported by Vanheusden et al. [101, 102]. The emission peak around 375 nm has been attributed to donor–acceptor pair emission [103]. At room temperature, the bound exciton emission changes to the free-exciton recombination.

1.4.2 Band Gap Engineering in ZnO

It has been experimentally demonstrated that the band gap of ZnO can be tuned from 2.1 to 6.0 eV by developing $Cd_xZn_{1-x}O$ and $Mg_yZn_{1-y}O$ alloys respectively. The energy gap of the ternary semiconductor $A_xZn_{1-x}O$ (where A = Mg or Cd) is determined by the following equation [21],

$$E_g(x) = (1 - x)\,E_{ZnO} + xE_{AO} - bx\,(1 - x) \tag{1.9}$$

where b is the bowing parameter and E_{AO} and E_{ZnO} are the bandgap energies of compounds AO and ZnO, respectively. The bowing parameter b depends on the difference in electronegativities of the end binaries AO and ZnO.

Ohtomo et al. [104] have reported the growth of $Mg_xZn_{1-x}O$ thin films using PLD technique with Mg content varying from $x = 0$ to 0.33. The band gap E_g linearly increases with x up to 4.15 eV. Choopun et al. [11] have shown the phase diagram for wurtzite and cubic $Mg_xZn_{1-x}O$ thin films while varying x from 0 to 1. They have also shown the increase in the band gap up to 6.0 eV. Makino et al. [12] have demonstrated the single phase $Cd_yZn_{1-y}O$ alloy thin films grown by PLD on sapphire (0001) and $ScAlMgO_4$ (0001) substrates with Cd content of up to 7 %. The band gap energy decreases to 3.0 eV as Cd content increases to 7 %. However, Vigil et al. [105] have shown the decrease in band gap up to 2.51 eV when y varies from 0 to 1.

1.5 Optoelectronic Properties of ZnO

One of the unique properties of direct band gap semiconductors that revolutionized the optoelectronics field is their ability to produce light emission in response to excitation mainly by means of electrical or optical injection of minority carriers. When an external voltage is applied across a forward biased *p*–*n* junction, electrons and holes that are injected from their respective ends recombine resulting in light emission called electroluminescence (EL). The exciton binding energy of ZnO (60 meV) is three times higher than that of GaN (20 meV) and the band gap (3.35 eV) is also comparable with that of GaN (3.45 eV) (Pearton et al. 2008). Hence, ZnO is the ideal–oxide counterpart to III–V group semiconducting LEDs, in particular GaN-based LED devices.

The first ZnO-based heterostructure LED was fabricated by Drapak (1968) using Cu_2O as a *p*-type layer. Numerous heterostructures have been fabricated using *n*-ZnO thin films with various possible *p*-type semiconducting materials [106, 107]. All ZnO-based light emitting devices have also been reported after the successful fabrication of N-doped *p*-type ZnO thin films using temperature modulation epitaxy method [53]. However, hole concentration of *p*-ZnO thin films is relatively low, and hence the injection is dominant from the highly doped *n*-ZnO into lightly doped *p*-ZnO. Hence, the recombination takes place in *p*-ZnO layer that degrades the emission efficiency as the quality of *p*-layer is inferior. Later, near-band-edge EL has also been reported from ZnO-based homojunction devices using P, N, As, and Sb as a *p*-type dopants [4, 84, 85, 108, 109]. Random lasing action has been observed from the ZnO-based homojunctions and multi quantum wells [13, 110, 111]. Figure 1.14 shows the random lasing action observed in Sb:ZnO/MgZnO/Ga:ZnO heterostructure diode observed by Chu et al. [109]. Recently, Nakahara et al. [58] showed intense UV light output from Mg-doped ZnO-based heterostructures.

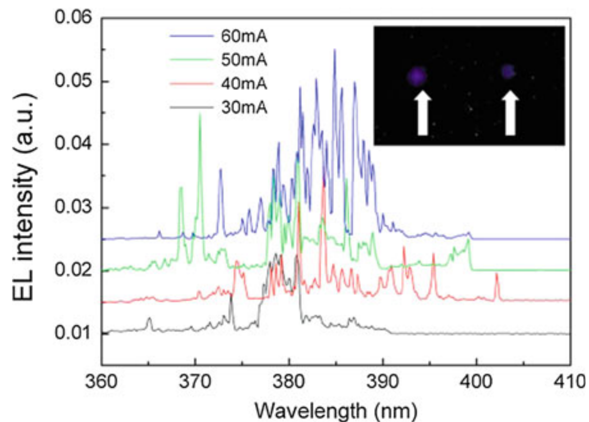

Fig. 1.14 EL spectra at higher injection currents depicting the random lasing action in the near UV region. Reprinted after permission from American Institute of Physics (*Appl. Phys. Lett.* 93, 181106 (2008))

1.6 ZnO Nanostructures

In recent years, low dimensional self-assembled ZnO nanostructures have received intense research interest in optoelectronics, piezoelectrics, mechanics, and biomedical sciences [112]. Among these ZnO nanostructures, 1D nanorods and nanowires have shown great advantage in the fabrication of devices in nanometer regime. Vertically aligned morphology is essential for nanoelectronics and nanooptoelectronics, such as field emission, light emitting diode-based on crossed *p*-type and *n*-type nanowires, nanosensors, nanowire integrated *p–n* junctions, nanowire lasers, and piezoelectric nanogenerators [20]. The lack of center of symmetry in wurtzite structure resulted in strong piezoelectric and pyroelectric properties in ZnO. By coupling the piezoelectric and semiconducting properties of the ZnO nanorods, a new field “nanopiezotronics” has emerged. Since ZnO is a biocompatible and biosafe material, it can be useful for implantable biosensors [112]. The higher exciton binding energy (60 meV) of ZnO ensures the room temperature lasing action. Furthermore, the lasing conditions can be further improved with low-dimensional 1D ZnO nanostructures, which enhance the exciton oscillator strength and quantum efficiency. Size of the nanowires and nanorods is the critical parameter, for achieving quantum confinement effects, and should be of the order of exciton Bohr radius (a_B) of ZnO and is 2.34 nm for bulk material.

Due to different chemical activities of its polar and nonpolar facets, ZnO is one of the materials known to exhibit nanostructures with different morphologies viz. nanorods, nanowires, nanobelts, nanocages, nanocoms, nanosaws, nanospirals, nanosprings, nanorings and nanohelix etc. (Kong et al. 2004; Gao et al. 2003). ZnO nanowires/nanorods can be grown using vapor phase transport (VPT) process, MBE, MOCVD, PLD, hydrothermal method, sol gel, electrodeposition, template-assisted growth etc. Generally, 1D nanowires/nanorods grow along the *c*-axis [0001] of the hexagonal wurtzite structure [21]. Selective area ZnO nanostructures also can be grown using a patterned substrates [85, 113].

Nanocrystalline diamond (NCD) thin films have always been of great interest because of their futuristic applications in electronic devices as thermal spreaders (Thermal conductivity $\sim$2000 W m^{-1} K^{-1}), in mechanical parts as wear resistance coatings and in flat panel displays as field emitters. Hence, realizing ZnO-based nanostructures on NCD coated substrates (normally Si) are of great interest (Liu et al. 2008) [114]. For example, realizing ZnO nanostructure-based devices on NCD substrates will find promising applications in heat free electronics in near future. In this article, we report on the growth of ZnO nanostructures on NCD thin films using NAPLD technique. We have investigated various stages and growth processes of ZnO nanostructures and propose a mechanism of growth of 1D nanostructures originating from two-dimensional hexagonal stacks.

Unintentionally doped ZnO nanowires were grown on nanocrystalline diamond (NCD) thin films using nanoparticle-assisted pulsed laser deposition (NAPLD) technique. A KrF excimer laser was used for the growth of nanowires with an

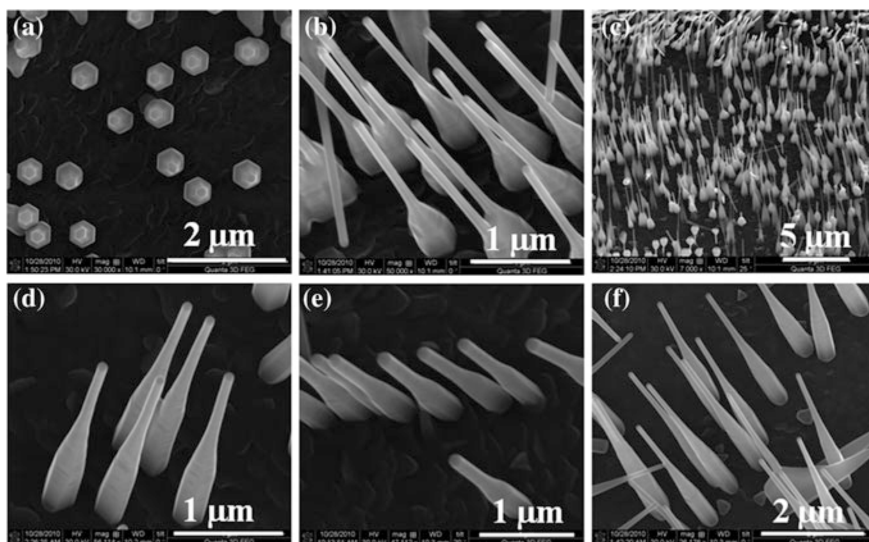

Fig. 1.15 HRSEM images of **a** stacking of ZnO hexagonal base and **b**–**f** nanowires with base diameter to tip diameter ratio ranging from 4 to 5

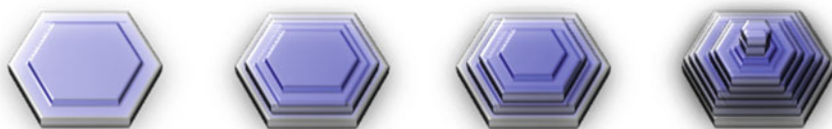

Fig. 1.16 Schematic representation of the formation of 1D nanowires on the 2D hexagonal stacking

energy density on the target $\sim$4 J cm^{-2} and frequency of 20 Hz. During the growth, the substrate temperature was maintained at 1000 °C with Ar flow of 27.5 sccm, which maintains the chamber pressure of 260 mTorr. The growth happens over a period of 30 min.

Figure 1.15 shows HRSEM images of ZnO nanostructures with different morphologies recorded at different places of the substrate. Figure 1.15a clearly shows formation of the base of the nanowires by the stacking of two-dimensional hexagons. The nanowires with a length of 1–2 μm and a diameter of around 50–70 nm were observed in most of the structures Fig. 1.15b–f. Three kinds of ZnO nanowires were observed with the ratio of the base height to wire length varying from 1 to 4.

The growth mechanism of the 1D ZnO nanorods on two-dimensional hexagons is shown schematically in Fig. 1.16. The six facets of hexagonal ZnO are generally bounded by the $\langle 10\bar{1}0 \rangle$ family of planes and the growth rate of different family of planes follow the sequence $(0001) > (10\bar{1}1) > (10\bar{1}0) > (000\bar{1})$ [63, 115].

In general, rod or wire like structures, which are bounded by six $(10\bar{1}0)$ facets will grow along (0001) direction. Also, ZnO is a polar material with a chemically active positively charged (0001) Zn^{2+} layer and chemically inactive negatively charged $(000\bar{1})$ O^{2-} layer. Thus, the base is the O^{2-} layer and top is the Zn^{2+} layer. A step-by-step growth process of the 1D nanorods on the two-dimensional hexagonal stacking can be understood as follows: A two-dimensional hexagon with (0001) basal plane, bounded by six crystallographic equivalent $\{0\bar{1}10\}$ faces, is formed at the beginning of the growth process with a size ~400–500 nm. Then the next hexagon, with smaller size, starts forming on the first basal hexagon and hexagons with decreasing size stack up along the [0001] direction. The stacking of these two-dimensional hexagons happens with decrease in size till the top hexagon size reaches ~75 nm. Since the surface diffusion is the most important rate limiting process in the ZnO crystal growth, the (0001) plane easily disappears and instead it is capped with the lower surface energy facet of $\{01\bar{1}1\}$ surfaces [116]. After the growth of $\{01\bar{1}1\}$ facet, the Zn-terminated (0001) plane is the most likely remaining facet which tends to form a uniformly sized hexagonal nanowire (~50 nm) on the top hexagon. In general, ZnO grows preferentially along the [0001] direction because of the faster growth rate in this direction than in other directions.

1.6.1 Synthesis and Characterization of Nanocrystalline ZnO Powders

To synthesize nanocrystalline ZnO bulk samples, 10.97 g of zinc acetate was added to 70 ml of water and kept under constant stirring using a magnetic stirrer. 6 g of urea was then added followed by the addition of 1.39 g of PVP (polyvinylpyrrolidone). The solution was stirred for about 2 h and then stirred under heating conditions until a gel was obtained. It was then calcined at two different temperatures (500 and 600 °C). To grow thin films 0.1 mol of zinc acetate solution was added to 50 ml of diethylene glycol (DEG) and 10 ml of ethanol. Similarly, 0.1 mol of NaOH solution was mixed with 50 ml of DEG and 10 ml of ethanol. The two solutions were mixed and stirred for 3 h at 60 °C. Two glass substrates were then dip coated for 5 and 10 times respectively and dried after each coating at 80 °C. The as deposited films were then annealed at 600 °C.

Figure 1.17 shows the XRD patterns of bulk nanocrystalline ZnO samples prepared from Zn acetate and PVP, and Fig. 1.18 shows the XRD patterns of bulk nanocrystalline ZnO thin films prepared by Zn acetate and PVP. The as prepared samples are single phase and do not contain any impurity phase.

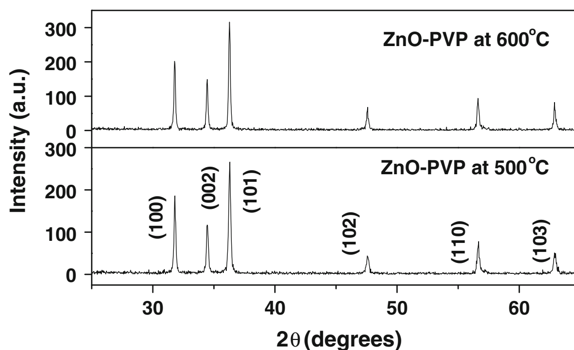

Fig. 1.17 XRD patterns of bulk nanocrystalline ZnO powders prepared by Zn acetate and PVP

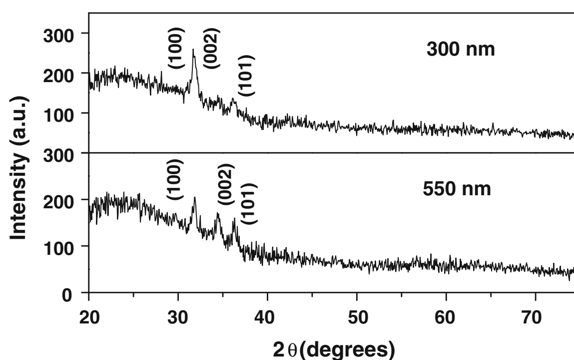

Fig. 1.18 XRD patterns of bulk nanocrystalline ZnO thin films of different thickness prepared by Zn acetate and PVP

1.6.2 Microstructural and Optical Studies

Figure 1.19 shows SEM images of bulk nanocrystalline ZnO thin films prepared by Zn acetate and PVP. The sample calcined at 500 °C shows formation of distorted hexagons, while the sample calcined at 600 °C shows formation of perfect hexagons. Both the samples consist of particles with average diameter of 150 nm. Few white patches seen in the SEM images are agglomerated ZnO powder. Figure 1.19c is a magnified image of sample calcined at 600 °C. EDX on the two samples (Fig. 1.20) show the composition as $Zn_{1-\delta}$ O, where $\delta = 0.2$ for the sample calcined at 500 °C, and $\delta = 0.38$ for the sample calcined at 600 °C.

Photoluminescence emission from these two samples. For an excitation wavelength of 365 nm, the UV emission at 395 nm merges along with the defect emission around 450 nm giving a broad emission. This defect emission around 410 and 450 nm can be attributed to the Zn vacancies in the structure as is also evident from the EDX spectra. Figure 1.21 shows the diffuse reflectance spectra measured on nanostructured ZnO powder samples prepared using Zn acetate and PVP and

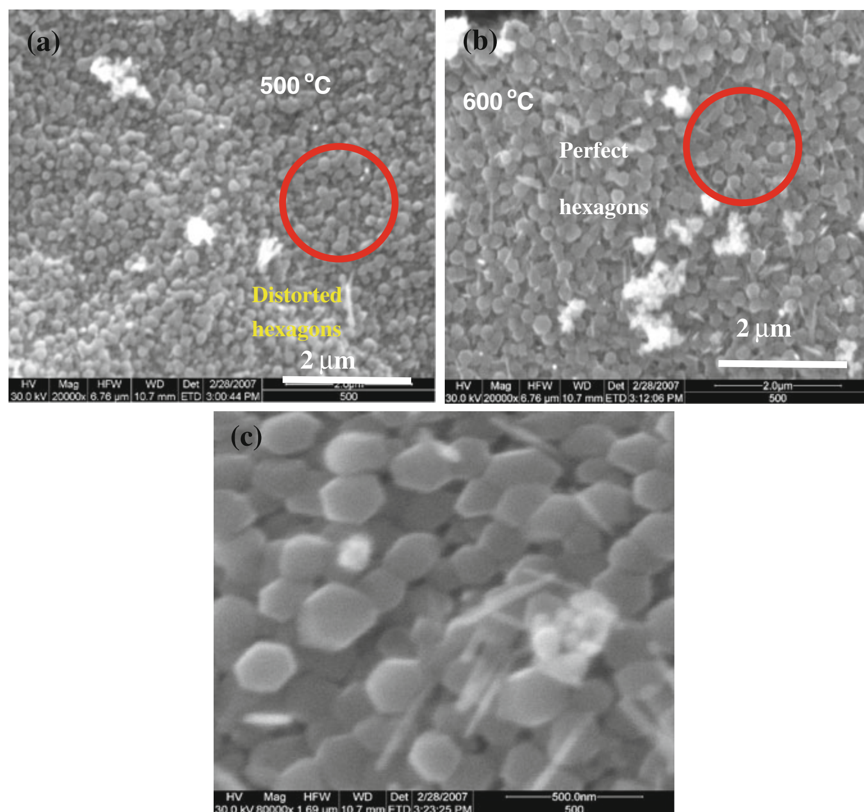

Fig. 1.19 SEM images of bulk nanocrystalline ZnO powders prepared from Zn acetate and PVP and calcined at **a** 500 °C, **b** 600 °C. Figure 1.19(c) is a magnified image of sample calcined at 600 °C

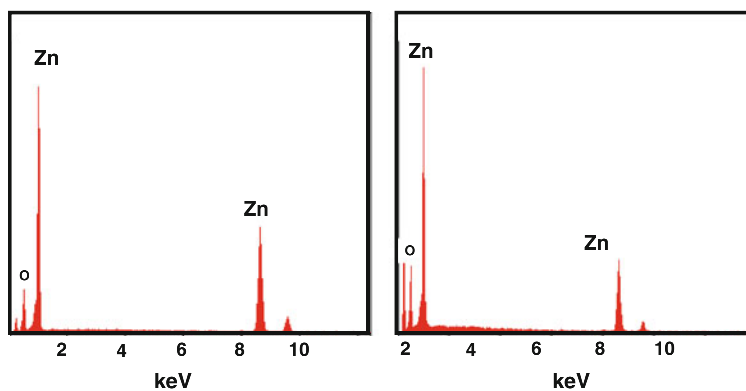

Fig. 1.20 EDX patterns on bulk nanocrystalline ZnO powders prepared from Zn acetate and PVP and calcined at 500 and 600 °C

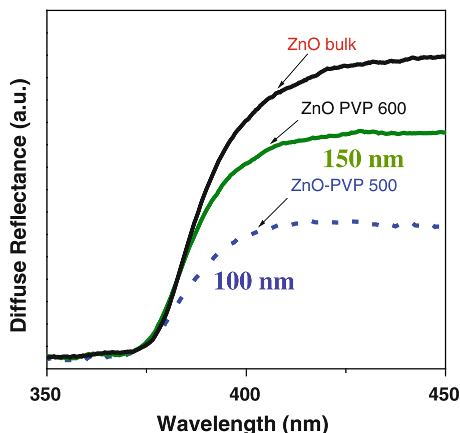

Fig. 1.21 Diffuse reflectance spectra measured on nanostructured ZnO powder samples prepared using Zn acetate and PVP and calcined at **a).** 500 °C and **b).** 600 °C

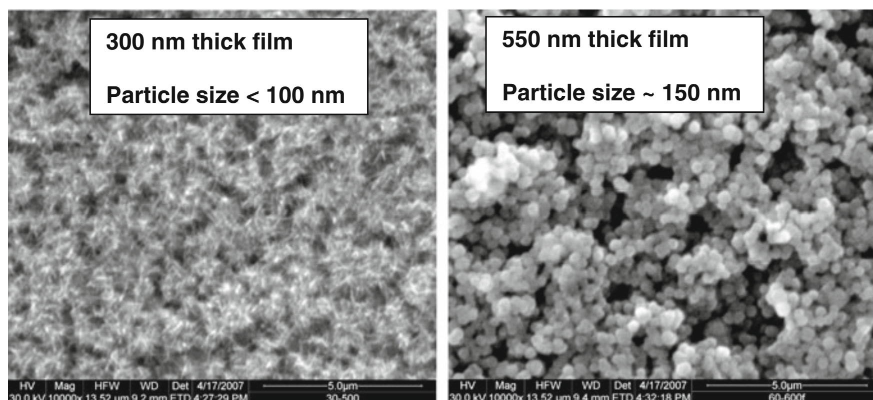

Fig. 1.22 SEM images of bulk nanocrystalline ZnO thin films prepared using Zn acetate and NaOH, with different thickness (annealed at 600 °C)

calcined at (a) 500 and (b) 600 °C. It is observed that the reflectance intensity decreases as the particle size reduces. This can be attributed to the increased absorbtion by lower particle sizes for samples calcined at lower temperatures. Microstructural studies on nanostructured thin films were carried out by SEM. Figure 1.22 shows the SEM images of nanocrystalline ZnO thin films prepared from Zn acetate and NaOH with different thickness annealed at 600 °C. EDX on the two samples (Fig. 1.23) show the composition as $Zn_{1-\delta}O$, where $\delta = 0.27$ for the sample with particle size of 150 nm, and $\delta = 0.4$ for the sample with particle size less than 100 nm.

Photoluminescence of nanocrystalline ZnO thin films (Fig. 1.24) clearly shows the difference in defect emission from these two samples as surface area increases

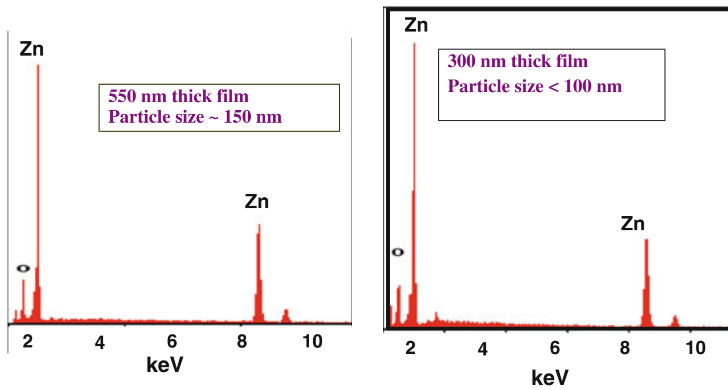

Fig. 1.23 EDX patterns on nanocrystalline ZnO thin films prepared from Zn acetate and NaOH and with different particle sizes

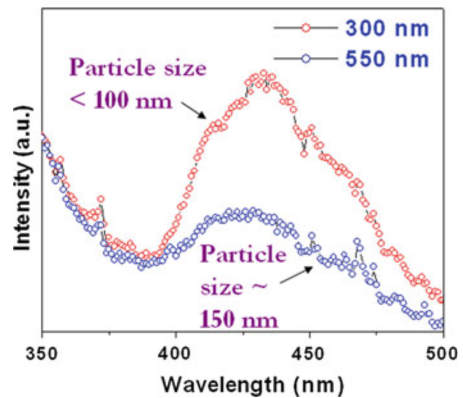

Fig. 1.24 PL spectra on nanocrystalline ZnO thin film samples prepared from Zn acetate and NaOH with different particle sizes

for sample with particle size less than 100 nm. Smaller particle size, hence larger surface area, gives rise to larger bulk density of dangling bands. Thus, the total PL intensity goes up with the decrease in particle size.

Figure 1.25 shows the HRSEM images of the ZnO nanostructures grown by vapor phase deposition technique. The size of the nanoparticles varies largely depending on the synthesis route and the parameters involved and can be controlled by varying any one of the parameters at a time. A variety of micronanostructures have been synthesized using various techniques. However, the size and shape of these structures depended on the techniques used and the parameters involved. To conclude, presumably different growth directions were found to be favored depending on different experimental conditions. Fabrication of such micronanostructures of undoped and doped ZnO, using simple methods, leading to interesting optical properties is important from the view point of a number of optical applications of ZnO.

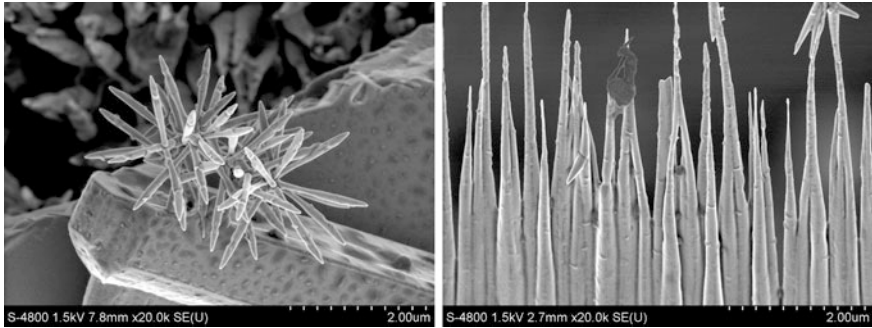

Fig. 1.25 HRSEM images of various other ZnO nanostructures deposited by vapor phase deposition technique

Acknowledgments S. Singh would like to acknowledge Dr. M. Kottaisamy from Materials Science Research Centre, IIT Madras for the useful discussion on synthesis techniques of nanostructures.

References

1. S. Nakamura, T. Mukai, M. Senoh, High-power GaN *p–n* junction blue light emitting diodes. Jpn. J. Appl. Phys. **30**, L1998–L2001 (1991)
2. A.M. Haase, J. Qiu, J.M. Depuydt, H. Cheng, Blue-green laser diodes. Appl. Phys. Lett. **59**, 1272–1274 (1991)
3. A.J. Edmond, H.S. Kang, C.H. Carter, Blue LEDs, UV photodiodes and high-temperature rectifiers in 6H-SiC. Phys. B **185**, 453–460 (1993)
4. C.K. Kim, M.C. Schmidt, H. Sato, F. Wu, N. Fellows, M. Saito, K. Fujito, J.S. Speck, S. Nakamura, S.P. DenBaars, Improved electroluminescence on nonpolar *m*-plane InGaN/GaN quantum wells LEDs. Phys. Status Solidi (RRL) **1**, 125–127 (2007)
5. S. Nakamura, T. Mukai, M. Senoh, N. Iwasa, Thermal annealing effects on *p*-type Mg-doped GaN films. Jpn. J. Appl. Phys. **31**, L139–L142 (1992)
6. S. Nakamura, M. Senoh, T. Mukai, P-GaN/N-InGaN/N-GaN double-heterostructure blue-light-emitting diodes. Jpn. J. Appl. Phys. **32**, L8–L11 (1993)
7. B.G. Stringfellow, M.G. Craford, *Applications for High-brightness Light-Emitting Diodes* (Academic Press, London, 1997)
8. T. Minami, Transparent conducting oxide semiconductors for transparent electrodes. Semicond. Sci. Technol. **20**, S35 (2005)
9. G.C. Granqvist, Window coatings for the future. Thin Solid Films **193**, 730–741 (1990)
10. T. Minami, H. Nanto, S. Takata, Highly conductive and transparent aluminum doped zinc oxide thin films prepared by RF magnetron sputtering. Jpn. J. Appl. Phys. **23**, L280–L282 (1984)
11. S. Choopun, R.D. Vispute, W. Yang, R.P. Sharma, T. Venkatesan, H. Shen, Realization of band gap above 5.0 eV in metastable cubic-phase $Mg_xZn_{1-x}O$ alloy films. Appl. Phys. Lett. **80**, 1529–1531 (2002)
12. T. Makino, Y. Segawa, M. Kawasaki, A. Ohtomo, R. Shiroki, K. Tamura, T. Yasuda, H. Koinuma, Band gap engineering based on $Mg_xZn_{1-x}O$ and $Cd_yZn_{1-y}O$ ternary alloy films. Appl. Phys. Lett. **78**, 1237–1239 (2001)

13. Y. Ryu, T.S. Lee, J.A. Lubguban, H.W. White, B.J. Kim, Y.S. Park, C.J. Youn, Next generation of oxide photonic devices: ZnO-based ultraviolet light emitting diodes. Appl. Phys. Lett. **88**, 241108 (2006)
14. D.H. Li, S.F. Yu, A.P. Abiyasa, C. Yuen, S.P. Lau, H.Y. Yang, E.S.P. Leong, Strain dependence of lasing mechanisms in ZnO epilayers. Appl. Phys. Lett. **86**, 261111 (2005)
15. H. Cao, Y.G. Zhao, H.C. Ong, S.T. Ho, J.Y. Dai, J.Y. Wu, R.P.H. Chang, Ultraviolet lasing in resonators formed by scattering in semiconductor polycrystalline films. Appl. Phys. Lett. **73**, 3656–3658 (1998)
16. A. Ohtomo, K. Tamura, M. Kawasaki, T. Makino, Y. Segawa, Z.K. Tang, G. Wong, Y. Matsumoto, H. Koinuma, Room-temperature stimulated emission of excitons in ZnO/(Mg, Zn)O superlattices. Appl. Phys. Lett. **77**, 2204–2206 (2000)
17. S. Limpijumnong, S.B. Zhang, S.H. Wei, C.H. Park, Doping by large-size-mismatched impurities: the microscopic origin of arsenic- or antimony-doped *p*-type zinc oxide. Phys. Rev. Lett. **92**, 155504 (2004)
18. H. Ohono, Making nonmagnetic semiconductors ferromagnetic. Science **281**, 951 (1998)
19. T. Dietl, H. Ohno, F. Matsukura, J. Cibert, D. Ferrand, Zener model description of ferromagnetism in zinc-blende magnetic semiconductors. Science **287**, 1019–1022 (2000)
20. L.Z. Wang, J. Song, Piezoelectric Nanogenerators based on zinc oxide nanowire arrays. Science **312**, 242–246 (2006)
21. H. Morkoc, U. Ozgur, *Zinc Oxide: Fundamentals, Materials and Device Technology* (Wiley-VCH Verlag GmbH & Co, Wienheim, 2007)
22. M. Kunisu, I. Tanaka, T. Yamamoto, T. Suga, T. Mizoguchi, The formation of a rock-salt type ZnO thin film by low-level alloying with MgO. J. Phys.: Condens. Matter. **16**, 3801–3806 (2004)
23. C. Jagadish, S.J. Pearton, *Zinc Oxide Bulk, Thin Films and Nanostructures* (Elsevier, New York, 2006)
24. A. Ashrafi, C. Jagadish, Review of zincblende ZnO: stability of metastable ZnO phases. J. Appl. Phys. **102**, 071101 (2007)
25. I. Ivanov, J. Pollmann, Electronic structure of ideal and relaxed surfaces of ZnO: a prototype ionic wurtzite semiconductor and its surface properties. Phys. Rev. B. **24**, 7275–7296 (1981)
26. G.D. Mahan, Intrinsic defects in ZnO varistors. J. Appl. Phys. **54**, 3825 (1983)
27. J.W. Hoffman, I. Lauder, Diffusion of oxygen in single crystal zinc oxide Trans. Faraday Soc. **66**, 2346c (1970)
28. E. Ziegler, A. Heinrich, H. Oppermann, G. Stover, Electrical properties and non-stoichiometry in ZnO single crystals. Phys. Status Solidi A **66**, 635 (1981)
29. K.I. Hagemark, Defect structure of Zn-doped ZnO. J. Solid State Chem. **16**, 293 (1976)
30. D.C. Look, J.W. Hemsky, J.R. Sizelove, Residual native shallow donor in ZnO. Phys. Rev. Lett. **82**, 2552 (1999)
31. F. Tuomisto, V. Ranki, K. Saarinen, D.C. Look, Evidence of the Zn vacancy acting as the dominant acceptor in *n*-type ZnO. Phys. Rev. Lett. **91**, 205502 (2003)
32. Y. Sun, P. Xu, C. Shi, F. Xu, H. Pan, E. Lu, A FP–LMTO study on the native shallow donor in ZnO. J. Electron Spectrosc. Relat. Phenom. 114–116, 1123 (2001)
33. F.A. Kohan, G. Ceder, D. Morgan, C.G. Van de Walle, First-principles study of native point defects in ZnO. Phys. Rev. B. **61**, 15019–15027 (2000)
34. C.G. Van de Walle, Defect analysis and engineering in ZnO. Phys. B **308–310**, 899 (2001)
35. S.B. Zhang, S.H Wei, A. Zunger, Intrinsic *n*-type versus *p*-type doping asymmetry and the defect physics of ZnO. Phys. Rev. B 63, 075205 (2001)
36. F. Oba, S.R. Nishitani, S. Isotani, H. Adachi, I. Tanaka, Energetics of native defects in ZnO. J. Appl. Phys. **90**, 824 (2001)
37. C.G. Van de Walle, Hydrogen as a cause of doping in Zinc oxide. Phys. Rev. Lett. **85**, 1012–1015 (2000)
38. J.Y. Zeng, Z.Z. Ye, W.Z. Xu, D.Y. Li, J.G. Lu, L.P. Zhu, B.H. Zhao, Dopant source choice for formation of *p*-type ZnO: Li acceptor. Appl. Phys. Lett. **88**, 062107 (2006)

39. C.E. Lee, K.J. Chang, Possible *p*-type doping with group-I elements in ZnO. Phys. Rev. B **70**, 1152010 (2004)
40. J.S. Choi, C.H. Yo, Study of the nonstoichiometric composition op zinc oxide. J. Phys. Chem. Solids **37**, 1149 (1976)
41. A.W. Sleight, R. Wang, Nonstoichiometry and Doping of Zinc Oxide. MRS Proceedings **453**, 323. doi:10.1557/PROC-453-323 (1996)
42. S.A.M. Lima, F.A. Sigoli, M. Jafelicci Jr, M.R. Davolos, Luminescent properties and lattice defects correlation on zinc oxide. Int. J. Inorg. Mater. **3**, 749 (2001)
43. A. Janotti, C.G. Van de Walle, Fundamentals of ZnO as a semiconductor. Rep. Prog. Phys. **72**, 126501 (2009)
44. H. Kato, K. Miyamoto, T. Yao, Effect of O/Zn flux ratio on crystalline quality of ZnO films grown by plasma-assisted molecular beam epitaxy. Jpn. J. Appl. Phys. **42**, 2241–2244 (2003)
45. K. Iwata, P. Fons, S. Niki, A. Yamada, K. Matsubara, K. Nakahara, H. Takasu, Improvement of electrical properties in ZnO thin films grown by radical source (RS)-MBE. Phys. Status Solidi A **180**, 287–292 (2000)
46. C.D. Look, D.C. Reynolds, J.R. Sizelove, R.L. Jones, C.W. Litton, G. Cantwell, W.C. Harsch, Electrical properties of bulk ZnO. Solid State Commun. **105**, 399–401 (1998)
47. Y.S. Kim, C.H. Park, Rich variety of defects in ZnO via an attractive interaction between O vacancies and Zn interstitials: Origin of *n*-type doping. Phys. Rev. Lett. **102**, 086403 (2009)
48. Y.S. Myong, S.J. Baik, C.H. Lee, W.Y. Cho, K.S. Lim, Extremely transparent and conductive ZnO:Al thin films prepared by photo-assisted metalorganic chemical vapor deposition (photo-MOCVD) using $AlCl_3(6H_2O)$ as new doping material. Jpn. J. Appl. Phys. **36**, L1078–L1081 (1997)
49. S. Yata, Y. Nakashima, T. Kobayashi, Improved crystallinity of ZnO thin films grown by the Aurora PLD method. Thin Solid Films **445**, 259–262 (2003)
50. M.B. Ataev, A.M. Bagamadova, A.M. Djabrailov, V.V. Mamedov, R.A. Rabadanov, Highly conductive and transparent Ga-doped epitaxial ZnO films on sapphire by CVD. Thin Solid Films **260**, 19–20 (1995)
51. B.S. Zhang, S.H. Wei, A. Zunger, A phenomenological model for systematization and prediction of doping limits in II–VI and I–III–VI2 compounds. J. Appl. Phys. **83**, 3192–3196 (1998)
52. T. Yamamoto, H. Katayama-Yoshida, Unipolarity of ZnO with a wide band gap and its solution using codoping method. J. Crys. Growth **214**, 552–555 (2000)
53. A. Tsukazaki, A. Ohtomo, T. Onuma, M. ohtani, T. Mahino, M. Sumiya, K. Ohtani, S.F. Chichibu, S. Fuke, Y. Segawa, H. Ohno, H. Koinuma, M. Kawasaki, Repeated temperature modulation epitaxy for *p*-type doping and light emitting diode based on ZnO. Nat. Mater. **4**, 42–46 (2005)
54. R.J. Duclerea, M. Novotnyb, A. Meaneya, R.O. Hairea, E. McGlynna, M.O. Henrya, J.P. Mosniera, Properties of Li-, P- and N-doped ZnO thin films prepared by pulsed laser deposition. Superlattices Microstruct. **38**, 397–404 (2005)
55. H.S. Jeong, D.G. Yoo, D.Y. Kim, N.E. Lee, J.H. Boo, Physical properties and etching characteristics of metal (Al, Ag, Li) doped ZnO films grown by RF magnetron sputtering. Thin Solid Films **516**, 6598–6603 (2008)
56. L.J. Lyons, A. Janotti, C.G. Van de Walle, Why nitrogen cannot lead to *p*-type conductivity in ZnO. Appl. Phys. Lett. **95**, 252105 (2009)
57. H.C. Park, S.B. Zhang, S.H. Wei, Origin of *p*-type doping difficulty in ZnO: the impurity perspective. Phys. Rev. B. **66**, 073202 (2002)
58. K. Nakahara, S. Akasaka, H. Yuji, K. Tamura, T. Fujii, Y. Nishimoto, D. Takamizu, A. Sasaki, T. Tanabe, H. Takasu, H. Amaike, T. Onuma, S.F. Chichibu, A. Tsukazaki, A. Ohtomo, M. Kawasaki, Nitrogen doped $Mg_xZn_{1-x}O$/ZnO single heterostructure ultraviolet light emitting diodes on ZnO substrates. Appl. Phys. Lett., 97, 013501 (2010)
59. M.T. Barnes, K. Olson, C.A. Wolden, On the formation and stability of *p*-type conductivity in nitrogen-doped zinc oxide. Appl. Phys. Lett. **86**, 112112 (2005)

60. T. Yamamoto, Codoping for the fabrication of *p*-ZnO. Thin Solid Films **420**, 100–106 (2002)
61. M.J. Bian, X.M. Li, X.D. Gao, W.D. Yu, L.D. Chen, Deposition and electrical properties of N–In codoped *p*-type ZnO films by ultrasonic spray pyrolysis. Appl. Phys. Lett. **84**, 501–543 (2004)
62. G.M. Wardle, J.P. Goss, P.R. Briddon, Theory of Li in ZnO: A limitation for Li based *p*-type doping. Phys. Rev. B **71**, 155205 (2005)
63. L.W. Liu, M. Shamsa, I. Calizo, A.A. Balandin, V. Ralchenko, A. Popovich, A. Saveliev, Thermal conduction in nanocrystalline diamond films: effects of the grain boundary scattering and nitrogen doping. Appl. Phys. Lett. **89**, 171915 (2006)
64. S. Shubra, N. Rama, M.S. Ramachandra Rao, Influence of d–d transition bands on electrical resistivity in Ni doped polycrystalline ZnO. Appl. Phys. Lett. **88**, 222111 (2006)
65. D.O. Jayakumar, I.K. Gopalakrishnan, S.K. Kulshreshtha, Surfactant-assisted synthesis of Co- and Li-doped ZnO nanocrystalline samples showing room-temperature ferromagnetism. Adv. Mater. **18**, 1857–1860 (2006)
66. G. Pei, C. Xia, B. Wu, T. Wang, L. Zhang, Y. Dong, J. Xu, Studies of magnetic interactions in Ni-doped ZnO from first-principles calculations. Comput. Mater. Sci. **43**, 489–494 (2008)
67. E. Senthil Kumar, S. Venkatesh, M.S. Ramachandra Rao, Oxygen vacancy controlled tunable magnetic and electrical transport properties of (Li, Ni) codoped ZnO thin films. Appl. Phys. Lett. **96**, 232504 (2010)
68. C. Liu, F. Yun, H. Morkoc, Ferromagnetism of ZnO and GaN: A review. J. Mater. Sci: Mater. Elec. **16**, 555–597 (2005)
69. H.A.M. Macdonald, P. Schiffer, N. Samarth, Ferromagnetic semiconductors: moving beyond (Ga, Mn) As. Nat. Mater. **4**, 195–202 (2005)
70. J.X. Wang, I.A. Buyanova, F. Zhao, D. Lagarde, A. Balocchi, X. Marie, C.W. Tu, J.C. Harmand, W.M. Chen, Room-temperature defect-engineered spin filter based on a non-magnetic semiconductor. Nat. Mater. **8**, 198–202 (2009)
71. Z. Lu, H.S. Hsu, Y. Tzeng, J.C.A. Huang, Carrier mediated ferromagnetism in single crystalline (Co, Ga) codoped ZnO films. Appl. Phys. Lett. **94**, 152507 (2009)
72. D. Chiba, K. Takamura, F. Matsukura, H. Ohno, Effect of low temperature annealing on (Ga, Mn)As trilayer structures. Appl. Phys. Lett. **82**, 3020 (2003)
73. K.J. Furdyna, Diluted magnetic semipconductors. J. Appl. Phys. **64**, R29–R64 (1988)
74. C. Zener, Interaction between the d-shells of the transition metals. II Ferromagnetic compounds of manganese with perovskite structure. Phys. Rev. **82**, 403–405 (1951)
75. K. Sato, H.K. Yoshida, First principles materials design for semiconductor spintronics. Semicond. Sci. Technol. **17**, 367 (2002)
76. J.M.D. Coey, M. Venkatesan, C.B. Fitzgerold, Donor impurity band exchange in dilute ferromagnetic oxides. Nat. Mater. **4**, 173–179 (2005)
77. T. Wakano, N. Fujimura, Y. Morinaga, N. Abe, A. Ashida, T. Ito, Magnetic and magneto-transport properties of ZnO:Ni films. Phys. E **10**, 260–264 (2001)
78. K. Ando, H. Saito, Z. Jin, T. Fukumura, M. Kawasaki, Y. Matsumoto, H. Koinuma, Magneto-optical properties of ZnO-based diluted magnetic semiconductors. J. Appl. Phys. **89**, 7284–7286 (2001)
79. R. Janisch, P. Gopal, N.A. Spaldin, Transition metal-doped TiO_2 and ZnO-present status of the field. J. Phys.: Condens. Matter. **17**, R657–R689 (2005)
80. P.D. Norton, S.J. Pearton, A.F. Hebard, N. Theodoropoulou, L.A. Boatner, R.G. Wilson, Ferromagnetism in Mn-implanted ZnO:Sn single crystals. Appl. Phys. Lett. **82**, 239–241 (2003)
81. Z. Yan, Y. Ma, D. Wang, J. Wang, Z. Gao, L. Wang, P. Yu, T. Song, Impact of annealing on morphology and ferromagnetism of ZnO nanorods. Appl. Phys. Lett. **92**, 081911 (2008)
82. M.C. Souza, I.C. Lima, M.A. Boselli, Carrier induced ferromagnetism in Mn doped ZnO: Mante Carlo simulations. Appl. Phys. Lett. **92**, 152511 (2008)
83. L.D. Hou, X.J. Ye, H.J. Meng, H.J. Zhou, X.L. Li, C.M. Zhen, G.D. Tang, Magnetic properties of *n*-type Cu doped ZnO thin films. Appl. Phys. Lett. **90**, 142502 (2007)

84. B.Y. Zhang, S. Li, G.K.L. Goh, S. Tripathy, Hydrothermal epitaxy of ZnO:Co diluted magnetic single crystalline thin films. Appl. Phys. Lett. **93**, 102510 (2008)
85. P.B. Zhang, N.T. Binh, K. Wakatsuki, Y. Sekawa, Y. Yamada, N. Usami, M. Kawazaki, H. Koinuma, Formation of highly oriented ZnO tubes on sapphire (0001) substrates. Appl. Phys. Lett. **84**, 4098–4010 (2004)
86. T. Zhu, W.S. Zhan, W.G. Wang, J.Q. Xiao, Room temperature ferromagnetism in two step prepared Co doped ZnO bulks. Appl. Phys. Lett. **89**, 022508 (2006)
87. B. Martínez, F. Sandiumenge, L. Balcells, J. Arbiol, F. Sibieude, C. Monty, Role of the microstructure on the magnetic properties of Co-doped ZnO nanoparticles. Appl. Phys. Lett. **83**, 103113 (2005)
88. X. Liu, F. Lin, L. Sun, W. Cheng, X. Ma, W. Shi, Doping concentration dependence of room temperature ferromagnetism for Ni doped ZnO thin films. Appl. Phys. Lett. **88**, 062508 (2006)
89. H. Liu, X. Zhang, L. Li, Y.X. Wang, K.H. Gao, Z.Q. Li, R.K. Zheng, S.P. Ringer, B. Zhang, X.X. Zhang, Role of point defects in room temperature ferromagnetism of Cr doped ZnO. Appl. Phys. Lett. **91**, 072511 (2007)
90. H.S. Liu, H.S. Hsu, C.R. Lin, C.S. Lue, J.C.A. Huang, Effect of hydrogenated annealing on structural defects, conductivity and magnetic properties of V doped ZnO powders. Appl. Phys. Lett. **90**, 222505 (2007)
91. S. Zhou, Q. Xu, K. Potzger, G. Talut, R. Grötzschel, J. Fassbender, M. Vinnichenko, J. Grenzer, M. Helm, H. Hochmuth, M. Lorenz, M. Grundmann, H. Schmidt, Room temperature ferromagnetism in C implanted ZnO. Appl. Phys. Lett. **93**, 232507 (2008)
92. S.T. Herng, S.P. Lau, C.S. Wei, L. Wang, B.C. Zhao, M. Tanemura, Y. Akaike, Stable room temperature ferromagnetism in *p*-type carbon doped ZnO nanoneedles. Appl. Phys. Lett. **95**, 133103 (2009)
93. M. Khalid, M. Ziese, A. Setzer, P. Esquinazi, M. Lorenz, H. Hochmuth, M. Grundmann, D. Spemann, T. Butz, G. Brauer, W. Anwand, G. Fischer, W.A. Adeagbo, W. Hergert, A. Ernst, Defect-induced magnetic order in pure ZnO films. Phys. Rev. B **80**, 035331 (2009)
94. K. Potzger, S. Zhou, J. Grenzer, M. Helm, J. Fassbender, An easy mechanical way to create ferromagnetic defective ZnO. Appl. Phys. Lett. **92**, 182504 (2008)
95. S. Shionoya, W.M. Yen (ed.), *Phosphor Hand Book* (CRC Press, Boca Raton, 1999), p. 565
96. R. Xie, D. Li, H. Zhang, D. Yang, M. Jiang, T. Sekiguchi, B. Liu, Y. Bando, Low-temperature growth of uniform ZnO particles with controllable ellipsoidal morphologies and characteristic luminescence patterns. J. Phys. Chem. B **110**, 19147 (2006)
97. B. Lin, Z. Fu, Y. Jia, Green luminescent center in undoped zinc oxide films deposited on silicon substrates. Appl. Phys. Lett. **79**, 943 (2001)
98. M. Liu, A.H. Kitai, P. Mascher, Point defects and luminescence centres in zinc oxide and zinc oxide doped with manganese. J. Lumin. **54**, 35 (1992)
99. Z.V. Mordkovich, H. Hayashi, M. Haemori, T. Fukumura, M. Kawasaki, Discovery and optimization of new ZnO-based phosphors using a combinatorial method. Adv. Funct. Mater. **13**, 519 (2003)
100. J.H. Egehaaf, D. OelKrug, Luminescence and nonradiative deactivation of excited states involving oxygen defect centers in polycrystalline ZnO. J. Cryst. Growth **161**, 190 (1996)
101. K. Vanheusden, C.H. Seager, W.L. Warren, D.R. Tallant, J.A. Voigt, Correlation between photoluminescence and oxygen vacancies in ZnO phosphors. Appl. Phys. Lett. **68**(3), 403 (1996)
102. K. Vanheusden, W.L. Warren, C.H. Seager, D.R. Tallant, J.A. Voigt, B.E. Gnade, Mechanisms behind green photoluminescence in ZnO phosphor powders. J. Appl. Phys. **79**, 7983 (1996)
103. Y. Sun, J.B. Ketterson, G.K.L. Wong, Excitonic gain and stimulated ultraviolet emission in nanocrystalline zinc-oxide powder. Appl. Phys. Lett. **77**, 2322 (2000)
104. A. Ohtomo, M. Kawasaki, T. Koida, K. Masubuchi, H. Koinuma, Y. Sakurai, Y. Yoshida, T. Yasuda, Y. Segawa, $Mg_xZn_{1-x}O$ as a II–VI widegap semiconductor alloy. Appl. Phys. Lett. **72**, 2466–2468 (1998)

105. O. Vigil, L. Vaillant, F. Cruz, G. Santana, A.M. Acevedo, G.C. Puente, Spray pyrolysis deposition of cadmium–zinc oxide thin films. Thin Solid Films **361**, 53–55 (2001)
106. I.Y. Alivov, J.E. Van Nostrand, D.C. Look, M.V. Chukichev, B.M. Ataev, Observation of 430 nm electroluminescence from ZnO/GaN heterojunction light-emitting diodes. Appl. Phys. Lett. **83**, 2943–2945 (2003)
107. H. Ohta, K. Kawamura, M. Orita, M. Hirano, N. Sarukura, H. Hosono, Current injection emission from a transparent *p–n* junction composed of *p*-$SrCu_2O_2$/*n*-ZnO. Appl. Phys. Lett. **77**, 475–477 (2000)
108. Y. Yang, X.W. Sun, B.K. Tay, G.F. You, S.T. Tan, K.L. Teo, A *p–n* homojunction light emitting diode formed by As ion implantation. Appl. Phys. Lett. **93**, 253107 (2008)
109. S. Chu, M. Olmedo, Z. Yang, J. Kong, J. Liu, Electrically pumped ultraviolet ZnO diode lasers on Si. Appl. Phys. Lett. **93**, 183106 (2008)
110. D. Hofstetter, R. Théron, A.H. El-Shaer, A. Bakin, A. Waag, Demonstration of a ZnO/MgZnO-based one-dimensional photonic crystal multiquantum well laser. Appl. Phys. Lett. **93**, 101109 (2008)
111. K.H. Liang, S.F. Yu, H.Y. Yang, Directional and controllable edge emitting ZnO ultraviolet random laser diodes. Appl. Phys. Lett. **91**, 101116 (2010)
112. X. Wang, J. Song, J. Liu, Z.L. Wang, Direct-current nanogenerator driven by ultrasonic waves. Science **316**, 102–105 (2007)
113. B. Liu, H.C. Zeng, Room temperature solution synthesis of mono dispersed single-crystalline ZnO nanorods and derived hierarchical nanostructures. Langmuir **20**, 4196–4204 (2004)
114. C.J. Madaleno, M.K. Singh, E. Titus, G. Cabral, J. Grácio, L. Pereira, Electron field emission from patterned nanocrystalline diamond coated *a*-SiO_2 micrometer-tip arrays. Appl. Phys. Lett. **92**, 023113 (2008)
115. T. Ghoshal, S. Kar, S. Chaudhuri, Synthesis and optical properties of nanometer to micrometer wide hexagonal cones and columns of ZnO. J. Crys. Growth **293**, 438–446 (2006)
116. R.O. Guo, J. Nishimura, M. Ueda, M. Higashihata, D. Nakamura, T. Okada, Vertically aligned growth of ZnO nanonails by nanoparticle-assisted pulsed-laser ablation deposition. Appl. Phys. A **89**, 141–144 (2007)
117. J. Nause, B. Nemeth, Pressurized melt growth of ZnO boules. Semicond. Sci. Technol. **20**, S45–S48 (2005)
118. K. Maeda, M. Sato, I. Niikura, T. Fukuda, Growth of 2 inch ZnO bulk single crystal by the hydrothermal method. Semicond. Sci. Technol. **20**, S49 (2005)
119. M.E. Kaidashev et al., High electron mobility of epitaxial ZnO thin films on *c*-plane sapphire grown by multistep pulsed-laser deposition Appl. Phys. Lett. **82**, 3901 (2003)
120. T. Edahiro, N. Fujimura, T. Ito, Formation of two-dimensional electron gas and the magnetotransport behavior of ZnMnO/ZnO heterostructure. J. Appl. Phys. **93**, 7673 (2003)
121. K. Miyamoto, M. Sano, H. Kato, T. Yao, High-electron-mobility ZnO epilayers grown by plasma-assisted molecular beam epitaxy. J. Cryst. Growth **265**, 34 (2004)
122. A. Ohmoto, A. Tsukazaki, Pulsed laser deposition of thin films and superlattices based on ZnO. Semicond. Sci. Technol. **20**, S1 (2005)
123. E.J. Jaffe, A.C. Hess, Hartree-Fock study of phase changes in ZnO at high pressure. Phys. Rev. B **48**, 7903–7909 (1993)
124. U. Rossler, Energy bands of hexagonal II–VI semiconductors. Phys. Rev. **184**, 733–738 (1969)
125. T.Y. Chen, C.L. Cheng, Y.F. Chen, Giant white and blue light emission from Al_2O_3 and ZnO nanocomposites. Nanotechnology **19**, 445707 (2008)
126. X.P. Gao, Z.L. Wang, Substrate atomic-termination-induced anisotropic growth of ZnO nanowires/nanorods by the VLS process. J. Phys. Chem. B **108**, 7534–7537 (2004)
127. S.B. Kang, S.J. Pearton, F. Ren, Low temperature (<100 °C) patterned growth of ZnO nanorod arrays on Si. Appl. Phys. Lett. **90**, 083104 (2007)
128. R.W. Kelsall, I.W. Hamley, M. Geoghegan, *Nano Science and Technology* (Wiley, 2004)

129. G.J. Lu, Y.Z. Zhang, Z.Z. Ye, L.P. Zhu, L. Wang, B.H. Zhao, Q.L. Liang, Low resistive, stable *p*-type ZnO thin films realized using a Li–N dual acceptor doping method. Appl. Phys. Lett. **88**, 222114 (2006)
130. G.J. Lu, Z.Z. Ye, J.Y. Huang, L.P. Zhu, B.H. Zhao, Z.L. Wang, S. Fujita, ZnO quantum dots synthesized by a vapor phase transport process. Appl. Phys. Lett. **88**, 063110 (2006)
131. M.C. Tarun, M.Z. Iqbal, M.D. McCluskey, Nitrogen is a deep acceptor in ZnO. AIP Adv. **1**, 022105 (2011)
132. Y.J. Zhang, P.J. Li, H. Sun, X. Shen, T.S. Deng, K.T. Zhu, Q.F. Zhang, J.L. Wu, Ultraviolet electroluminescence from controlled arsenic-doped ZnO nanowire homojunctions. Appl. Phys. Lett. **93**, 021116 (2008)
133. J.L. Zhao, W. Zhang, X.M. Li, J.W. Feng, X. Shi, Convergence of the formation energies of intrinsic point defects in wurtzite ZnO: first-principles study by projector augmented wave method. J. Phys.: Condens. Matter **18**, 1495 (2006)

Chapter 2
Laser Nano-Soldering of ZnO Nanowires and GaN Thin Film for Fabrication of Hetero *p-n* Junction

Tetsuya Shimogaki, Yuki Ishida, Kota Okazaki, Mitsuhiro Higashihata, Daisuke Nakamura and Tatsuo Okada

Abstract We have investigated the laser nano soldering between ZnO nanowires and the *p*-type GaN thin film for the realization of the hetero *p-n* junction with low thermal loading. When the ZnO nanowires were irradiated with 355 nm laser beam at a fluence of 0.25 J/cm^2, only a tip of the nanowires was melted due to the field enhancement effect near the tip of the nanowires, and a small bead with a diameter of 40 nm was formed at the tip of each nanowires. This phenomenon was applied to solder the junction between the ZnO nanowires and a *p*-type GaN thin film, by irradiating the junction through the GaN film with 375 nm laser beam which is transparent for the *p*-type GaN thin film but opaque for the ZnO nanowires. As a result, the improvements of the *I–V* characteristics of the junction and the increment of the UV electro-luminescence were clearly observed, demonstrating the effectiveness of the nano soldering in fabrication of the hetero *p-n* junction between the ZnO nanowires and the GaN thin film.

2.1 Introduction

Due to its wide band gap and large exciton-binding energy, ZnO has been attracting continuous interest for the application to opto-electronic devices such as ultra-violet (UV) emitters, sensors, TFTs, and so on. Especially, one-dimensional ZnO nanowires are attractive due to its unique structure [1]. A variety of method have been reported for the growth of the ZnO nanowires, including catalyst-assisted chemical vapor deposition, hydrothermal liquid method, high pressure laser ablation, and so on [2]. The hydrothermal method can grow the ZnO nanowires at a relatively low temperature around 400 K, but usually their optical

T. Shimogaki · Y. Ishida · K. Okazaki · M. Higashihata · D. Nakamura · T. Okada (✉)
Department of Electrical Engineering, Kyushu University, Ito 744, Fukuoka 819-0395, Japan
e-mail: okada@ees.kyushu-u.ac.jp

M. S. R. Rao and T. Okada (eds.), *ZnO Nanocrystals and Allied Materials*, Springer Series in Materials Science 180, DOI: 10.1007/978-81-322-1160-0_2,
© Springer India 2014

quality is poor, showing greenish fluorescence due to large oxygen-related defects [1]. We have also succeeded in growing vertically aligned high-quality ZnO nanowires without any catalyst by the nano-particle assisted high pressure pulsed laser deposition [3–5].

ZnO nanowires can be used as the building blocks for UV light emitting diodes. Unfortunately, the synthesis method of the *p*-Type ZnO nanowires has not been well established and is still a challenging subject [6], while the ZnO nanowires usually show the *n*-type conduction due to the defect-related states. Therefore, the realization of the hetero *p*-*n* junction has been extensively studied, using already existing *p*-type semiconductors, for instance, like *p*-Si [7], *p*-GaN [8, 9], *p*-type polymer [10], and so on.

In this study, we have firstly investigated the influence of the growth temperature on the direct growth of ZnO nanowires on *p*-type GaN film. Furthermore, we have investigated the laser nano soldering of ZnO nanowires and the *p*-type GaN thin film for the realization of the hetero *p*-*n* junction with low thermal loading. We also investigated the structural change of the ZnO nanowires irradiated by laser beam. The electrical and emission characteristics of the hetero junction with the ZnO nanowires and the *p*-type GaN film were also investigated with and without laser nano soldering.

2.2 Growth of ZnO Nanowires on P-GaN Film for Hetero LED

ZnO nanowires used in this study were prepared by nanoparticles-assisted pulsed laser deposition methods [11]. A sintered ZnO target was ablated by a KrF excimer laser at a fluence of 4 J/cm^2 in a quartz furnace filled with Ar background gas. The operational conditions are as follows: the temperature of the furnace is 1170–1270 K and an Ar gas pressure was 35 kPa. ZnO nanowires were grown on a *p*-GaN film deposited on a *c*-cut sapphire substrate placed in front of the target. The vertically aligned nanocrystals were successfully grown after 20 min. deposition, as shown in Fig. 2.1. The diameters of the crystals are in the range from 100 to 300 nm.

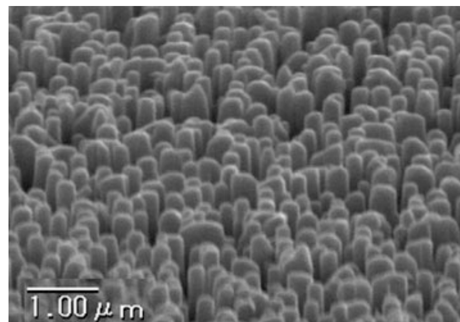

Fig. 2.1 SEM image of ZnO crystals grown on *p*-GaN film

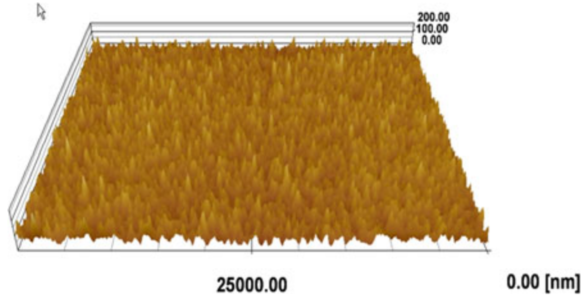

Fig. 2.2 AFM image of *p*-GaN film heat-treated at 1270 K

We have investigated the influence of the growth temperature on the crystallinity of the *p*-GaN film. Figure 2.2 shows an AFM image of the *p*-GaN surface heat treated at 1270 K in the atmosphere. It can be seen that the surface became rough with a root-mean-square roughness of 25 nm.

Figure 2.3 shows the XRD pattern of the *p*-GaN film heat treated at 1270 K. At a temperature lower than 1170 K, only the diffraction peaks from (002) and (004) planes were observed other than that from the sapphire substrate. As can be seen in Fig. 2.3, however, a new diffraction peak was observed from the *p*-GaN film heat treated at 1270 K, as indicated by the arrow in Fig. 2.3. These observations suggest that the *p*-GaN film is damaged during the growth of the ZnO nanocrystals by NAPLD, where the process temperature of more than 1170 K is required to obtain good crystallinity.

Next, we have fabricated the LED structure, in order to evaluate the electrical properties on the hetero p-n junction between *p*-GaN film and ZnO nanowires. For the purpose, the spin on glass was coated on *p*-GaN film by spin coating as shown in Fig. 2.4, in order to isolate the *p*-GaN film from the electrode on the ZnO nanowires. The measured *I*–*V* characteristics using the ZnO nanowires grown at 1170 K are shown in Fig. 2.5 along with the CCD image of the emission shown in the inset. A rectifying characteristics was obtained with a forward threshold voltage of 6 V and a reverse breakdown voltage of about 20 V, and the emission can be seen by naked eyes with a bright spot of about 5 mm in diameter.

2.3 Laser Nano-Soldering

As described in the previous section, the direct growth of ZnO nanowires on *p*-GaN films causes the damage in the *p*-GaN film. In order to solve this problem, we have investigated the possibility for joining the ZnO nanowires and the *p*-GaN films by the laser irradiation on the interface between them with low thermal loading. Prior to the nano joining, the interaction of the ZnO nanowires and the laser beam was investigated. ZnO nanowires on a sapphire substrate were irradiated by the third harmonics of a Q-switched Nd:YAG laser. The laser beam was irradiated in parallel to the nanowires from the top surface of the substrate.

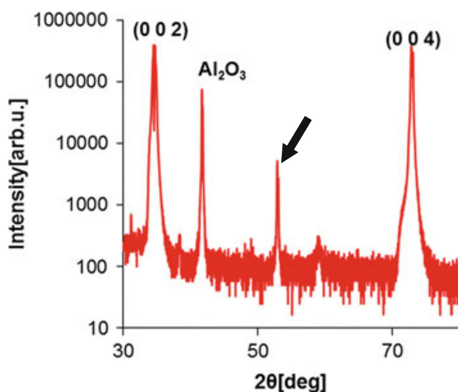

Fig. 2.3 XRD pattern of p-GaN film heat treated at 1270 K. The new diffraction peak indicated by the arrow appears after heat treatment, indication the damage of p-GaN film

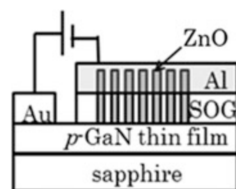

Fig. 2.4 Schematic image of LED

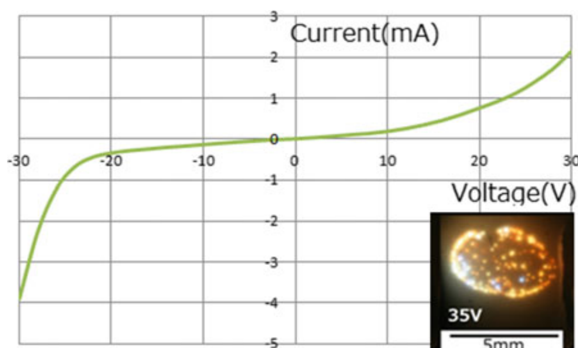

Fig. 2.5 Measured *I–V* characteristics and CCD image

The SEM images of ZnO nanowires irradiated with different irradiation fluences of 0.25 J/cm^2, 0.38 J/cm^2, and 0.72 J/cm^2 are shown in Fig. 2.6a, b and c. When irradiation fluence was 0.25 J/cm^2, a small bead with a diameter of 40 nm was observed at the tip of each nanowire. The magnified SEM image of the tips is shown in the inset of Fig. 2.6a. This indicates that only a tip of the nanowires was melted and a small bead was formed by the re-solidification. When the influence was increased to 0.38 J/cm^2, the melting zone was extended to an entire region of the nanowires and the structure of the nanowires was almost disappeared. When irradiation fluence is further increased up to 0.72 J/cm^2, the nanowires completely have melted and a net-like structure was formed by re-solidification.

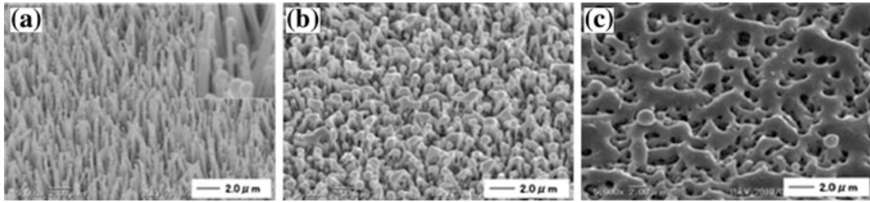

Fig. 2.6 SEM images of ZnO nanowires irradiated with different irradiation fluences of (**a**) 0.25 J/cm^2, (**b**) 0.38 J/cm^2 and (**c**) 0.72 J/cm^2. The *inset* of Fig. 2.6(**a**) is a image magnified of the tip of nanowires

In order to understand the formation of the bead at the tip of nanowires with a lower fluence of 0.25 J/cm^2, the intensity distribution of the laser beam near the tip of a nanowire was simulated with a three-dimensional electromagnetic field simulator. Figure 2.7 shows that intensity distribution of the laser beam near the tip of nanowires, where the top surface of a nanowire is perpendicular to the laser beam. It is clearly observed that the intensity distribution of laser beam was enhanced at the nanowire tip by a factor of two. For the sake of the near field effect, only the tip of nanowires could be melted.

In order to examine the crystallinity of the re-solidified beads, the nanowire was observed with a transmission electron microscope (TEM). Figure 2.8 shows an electron beam diffraction images of a re-solidified bead and a nonmelting part of the same nanowire. The same diffraction pattern was observed for both parts of the bead and the nanowires after laser irradiation. It was confirmed that the re-solidified beads were single crystal.

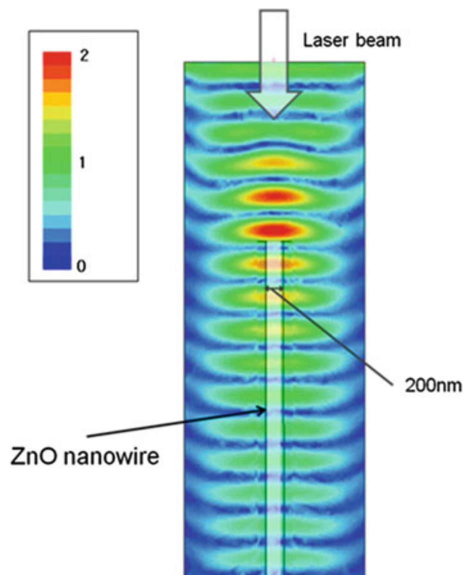

Fig. 2.7 Electric field distribution around laser-irradiated ZnO nanowire simulated by HFFS code

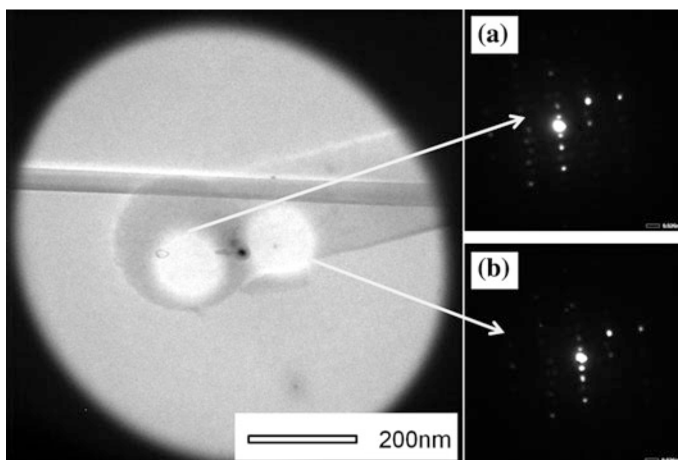

Fig. 2.8 Site selected diffraction images observed by TEM, (**a**) for the resolidified head after laser irradiate. (**b**) for original nanowire

The phenomenon that only the tip of the nanowires can be melted with proper irradiation fluence was applied to the nano soldering between the ZnO nanowires and a *p*-type GaN thin film. Figure 2.9 shows an experimental arrangement for the laser nano soldering. ZnO nanowires were mechanically contacted onto the GaN film and a laser beam for the soldering was irradiated through the GaN film on the sapphire substrate. For this purpose, the selection of the laser wavelength is very important. Figure 2.10 shows relative transmission spectra of the *p*-type GaN thin film and the ZnO nanowires on a sapphire substrate. The *p*-type GaN thin film has an absorption band below 370 nm. On the other hand, the ZnO nanowires have an absorption band below 390 nm. Since the sapphire substrate is transparent down to 200 nm, the transmission spectra reflected those of the *p*-type GaN and the ZnO nanowires. Therefore, when the laser beam at a wavelength of 375 nm is irradiated through the *p*-type GaN film, the laser beam can be absorbed at the tip of the ZnO nanowires contacted with the *p*-type GaN film. In the following experiment, the

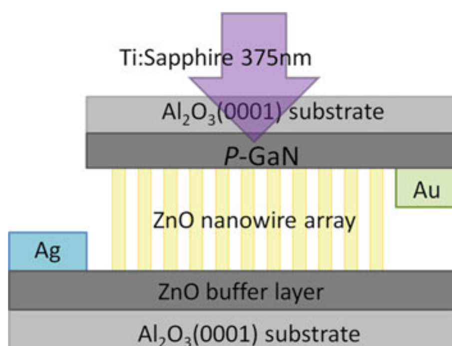

Fig. 2.9 Experimental arrangement for the laser nano soldering

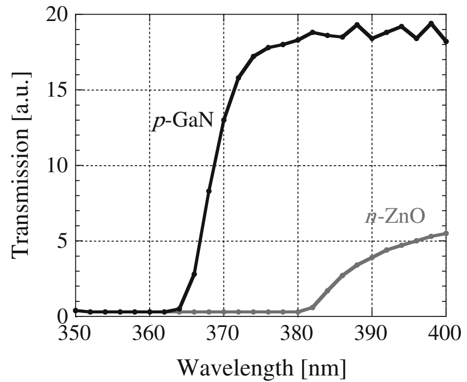

Fig. 2.10 Relative transmission spectra of the *p*-type GaN thin film and the ZnO nanowires on a sapphire substrate

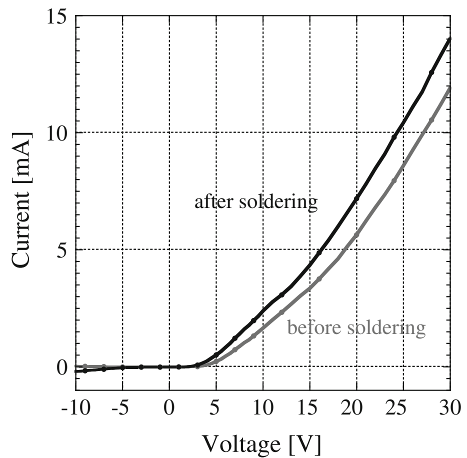

Fig. 2.11 *I-V* characteristics through the junction between the ZnO nanowires and the *p*-type GaN thin film

laser beam at a wavelength of 375 nm was used for the nano soldering, that was generated by the second harmonic of a Q-switched Ti:sapphire laser.

The *I–V* characteristics through the junction between the ZnO nanowires and the *p*-type GaN thin film were investigated before and after the laser soldering, as summarized in Fig. 2.11. In both cases, rectification characteristics were observed. After soldering, the threshold voltage was reduced from 6 to 3 V and the forward current was increased by a factor of 1.2 at a bias voltage of 30 V. At the same time, the electroluminescence form the junction was increased after the soldering, as shown in Fig. 2.12a and b, which shows the CCD images of the electroluminescence from the junction before and after the soldering.

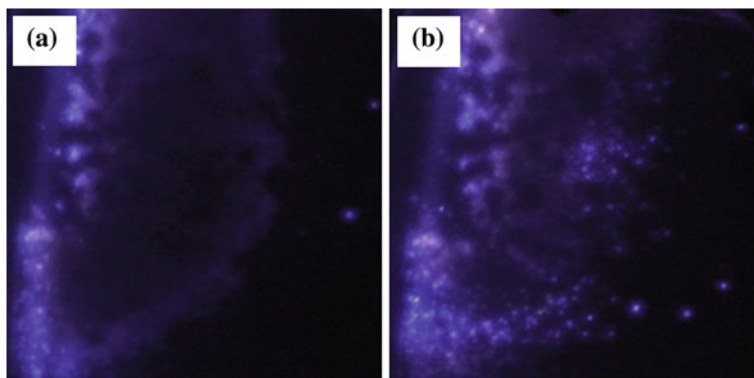

Fig. 2.12 CCD images the electro-luminescence from the junction (**a**) before and (**b**) after the soldering

2.4 Conclusion

The interaction between the ZnO nanowires and the laser beam has been investigated for the nano soldering between ZnO nanowires and *p*-type GaN thin film for the fabrication of hetero LED. When the ZnO nanowires were irradiated with a 355 nm laser beam at a fluence of 0.25 J/cm^2, only a tip of the nanowires was melted and a small bead with a diameter of 40 nm was formed at the tip of each nanowires. This phenomenon can be understood as a result of the near-field effect, based on a full-wave electro-magnetic simulation code. This phenomenon was applied to solder the junction between the ZnO nanowires and *p*-type GaN thin film, by irradiating the junction through the GaN film with 375 nm laser beam which is transparent for the *p*-type GaN thin film but opaque for the ZnO nanowires. As a result, the improvements in I–V characteristics of the junction and the intensity of the UV electroluminescence were clearly observed, demonstrating the effectiveness of the nano soldering.

This work was supported in part by a Grant-in-Aid for Scientific Research from the Japan Society of Promotion of Science (No. 24656053) and Special Coordination Funds for Promoting Science and Technology from Japan Science and Technology Agency. We also would like to thank Research Laboratory for High Voltage Electron Microscopy, Kyushu University for TEM observation.

References

1. M. Willander, O. Nur, Q.X. Zhao, L.L. Yang, M. Lorenz, B.Q. Cao, J. Zuniga Perez, C. Czekalla, G. Zimmermann, M. Grundmann, A. Bakin, A. Behrends, M. Al-Suleiman, A. El-Shaer, A. Che Mofor, B. Postels, A. Waag, N. Boukos, A. Travlos, H.S. Kwack, J. Guinard, D. Le Si Gang, Nanotechnology **20**, 332001 (2009)

2. Y.W. Heo, D.P. Norton, L.C. Tien, Y. Kwon, B.S. Kang, F. Ren, S.J. Pearton, J.R. LaRoche, Mater. Sci. Eng. **R47**, 1 (2004)
3. A.B. Hartanto, A. Ning, Y. Nakata, T. Okada, Appl. Phys. **A78**, 299 (2004)
4. R.Q. Guo, J. Nishimura, M. Ueda, M. Higashihata, D. Nakamura, T. Okada, Appl. Phys. **A89**, 141 (2007)
5. R.Q. Guo, J. Nishimura, M. Matsumoto, M. Higashihata, D. Nakamura, J. Suehiro, T. Okada, Appl. Phys. **A90**, 539 (2008)
6. S.S. Lin, J.I. Hong, J.H. Song, Y. Zhu, H.P. He, Z. Xu, Y.G. Wei, Y. Ding, R.L. Snyder, Z.L. Wang, Nano Lett. **9**, 3877 (2009)
7. J.Y. Zhang, Q.F. Zhang, T.S. Deng, J.L. Wu, Appl. Phys. Lett. **95**, 211107 (2009)
8. R.Q. Guo, J. Nishimura, M. Matsumoto, M. Higashihata, D. Nakamura, T. Okada, Appl. Phys. **B94**, 33 (2009)
9. A.M.C. Ng, Y.Y. Xi, Y.F. Hsu, A.B. Djurisic, W.K. Chan, S. Gwo, H.L. Tam, K.W. Cheah, P.W.K. Fong, H.F. Lui, C. Surya, Nanotechnology **20**, 445201 (2009)
10. A. Wadeasa, O. Nur, M. Willander, Nanotechnology **20**, 065710 (2009)
11. R.Q. Guo, M. Matsumoto, T. Matsumoto, M. Higashihata, D. Nakamura, T. Okada, Appl. Surf. Sci. **255**, 9671 (2009)

Chapter 3
Photoluminescence Processes in ZnO Thin Films and Quantum Structures

L. M. Kukreja and P. Misra

Abstract ZnO, a well-known direct and wide bandgap semiconductor is found to show intricate photoluminescence (PL) spectra in thin films and quantum structures such as quantum wells and quantum dots (QDs). In ZnO, thin films grown on sapphire substrates using pulsed laser deposition (PLD) an intense PL in the UV region at about 3.35 eV was observed, which corresponded to near band-edge emission due to the excitonic recombinations. The deep level emission in the visible spectral region of 2–3 eV, which is found to be due to off stoichiometry of the ZnO films, i.e., oxygen vacancies, zinc interstitial, and other structural defects, was almost negligible compared to the near band-edge emission. The strong near band-edge emission in UV spectral region was found to have fine structures consisting of various peaks mainly due to donor and acceptor bound excitons and their phonon replicas, which changed their position and intensity with temperature. In ZnO/$Mg_xZn_{1-x}O$ multi-quantum wells (MQWs) with well layer thickness in the range of $\sim$4 to 1 nm on (0001) sapphire substrates also grown using PLD under the optimized conditions, we observed size-dependent blue shift in ZnO bandgap due to the quantum confinement effect. The PL spectra of these ZnO MQWs recorded at 10 K showed that line width of the PL peaks increased with decreasing well layer thickness, which was attributed to fluctuations in the well layer thickness. The temperature-dependent PL peak positions for the MQWs were found to shift gradually toward red end of the spectrum with increase in temperature up to 300 K due to the temperature-dependent thermal expansion/dilation of the lattice and carrier-phonon scattering. This dependance was found to be consistent with the well-known Varshni's empirical relation. Ensembles of alumina capped ZnO quantum dots (ZQDs) also grown using pulsed laser deposition with mean radii comparable to and smaller than the pertinent excitonic Bohr radius ($\sim$2.34 nm), called ultra-small QDs showed size-dependent optical absorption edges. These absorption spectra were found to be consistent with the strong confinement model,

L. M. Kukreja (✉) · P. Misra
Laser Materials Processing Division, Raja Ramanna Centre for Advanced Technology,
P.O. CAT, Indore 452 013, India
e-mail: kukreja@rrcat.gov.in

M. S. R. Rao and T. Okada (eds.), *ZnO Nanocrystals and Allied Materials*,
Springer Series in Materials Science 180, DOI: 10.1007/978-81-322-1160-0_3,
© Springer India 2014

in which the confinement energy and Coulombic interaction energy of the localized electron-hole pairs are taken to be significantly higher than their correlation energy and the optical transitions are perceived to be non-excitonic in nature. In PL spectra of such ZQDs of mean radius of ~2.3 nm at temperatures of ~6 K and above the primary recombinations were found to be due to the surface bound and Al donor bound electron-hole pairs. The near band-edge recombination peaks of the PL spectra appeared at the sample temperature of ~70 K and beyond. These peaks were found to be ~166 meV Stoke and/or thermally red shifted with respect to the experimentally observed absorption edge. Almost all the PL spectra of the ZQDs at different temperatures showed the LO and 2 LO phonon replicas of the primary transitions, which suggests strong coupling between the recombining charge carriers and the LO phonons. The temperature-dependent spectral positions of the PL peaks for the ZQDs also followed the above stated Varshni's relation with fitting parameters close to that of the bulk ZnO. The intensity of the PL peaks was found to follow the normal mechanism of thermal quenching which could be fitted with the Arrhenius type of equation having activation energy of ~10 meV. Temperature dependence of FWHM of the PL peaks when fitted with the Hellmann and O'Neill models did not result in a close match. Although one could estimate a value of the carrier-LO phonon coupling coefficient of ~980 meV from this fit, but this was found to be much higher than that reported earlier for the ZQDs. These studies are expected to provide deeper insight into the basic optical processes in ZnO thin films, quantum wells, and QDs.

3.1 Introduction

Currently, wide bandgap semiconductor ZnO and its variants are of substantial interest for their applications in UV-blue photonic and transparent electronic devices [1–7]. ZnO is a well-known II–VI oxide semiconductor, which is pyroelectric, piezoelectric, piezooptic, luminescent, and good thermal conductor. It has a direct and wide bandgap of ~3.34 eV at room temperature (RT) and hence transparent in the visible spectral region. It has a large excitonic binding energy of ~60 meV [8] which is more than two times larger than the room temperature thermal excitation energy of ~26 meV. Therefore excitonic transitions can be observed in ZnO at temperatures much larger than room temperature. ZnO naturally crystallizes in rugged hexagonal wurtzite structure and is nominally *n*-type. The high cohesive energy of ZnO, which is ~1.89 eV makes it highly stable and perhaps one of the most radiation hard materials among the direct bandgap semiconductors' family [9, 10], which ensures a long life and a high degradation threshold of ZnO-based devices. The high melting point of ZnO (~1975 °C) allows one to explore variety of heat treatments required for alloying purpose and device formation. Moreover, ZnO is free from the oxidation problem, which can

severely affect the device performance in the case of oxidation prone semiconductors.

Conventionally, ZnO has been used for transparent conducting electrodes, surface acoustic wave devices, varistors, oxygen sensors, green phosphor for display devices, UV screens, and cosmetics etc. [11, 12]. The current spurt in ZnO research is motivated to develop the futuristic robust and environment friendly technology for the photonic devices operating in short wavelength regimes, i.e., UV-blue spectral region such as light-emitting diode (LED), diode laser, solar blind UV photodetectors, transparent electronics, and magneto optical devices. These devices could be based on ZnO epitaxial thin films and/or quantum structures of different dimensionality [1, 2, 5, 13]. The observation of stimulated emission and laser oscillations at RT at a low threshold of optical pumping in high-quality ZnO thin films grown on sapphire substrates indicated that the exciton related-transitions at room temperature could be utilized for optoelectronic and nonlinear optical devices [14]. The size-dependent quantum confinement effects in ZnO quantum structures also result in large oscillator strength, enhanced excitonic binding energy, tunability of operating wavelength, and low threshold of lasing [15, 16].

The excitonic transitions are very sensitive to the crystalline quality of the material and therefore growth of thin films and nanostructures with high crystalline quality and stoichiometry are crucial to observe an efficient and stable light emission in the UV-blue spectral region due to recombination of free excitons [17]. Since optoelectronic devices such as light-emitting diodes and laser diodes are based on the fundamental processes of emission, it is imperative to study the optical emission characteristics of high-quality ZnO thin films and low dimensional structures in detail.

In the following sections, we discuss the basics of various photoluminescence (PL) processes occurring in ZnO in general such as recombination of free and bound excitons, LO phonon-assisted recombination of excitons, deep level transitions and effect of quantum confinement on the PL processes in ZnO. The details about the experimental setup used for the PL spectroscopy of ZnO will be presented. This will be followed by a detailed discussion on the results of our studies on the PL spectroscopy of ZnO thin films, quantum well, and dots. Various existing theoretical models have been applied to understand the experimental observations and those will also be presented and discussed in this chapter.

3.2 Fundamentals of Photoluminescence Processes in ZnO

In direct bandgap semiconductors like ZnO, the emission of photon results due to a process reverse of the absorption [18]. The photons of the incoming light beam are absorbed in the semiconductor material to produce free electrons and holes in the conduction and valence band, respectively, which result in the formation of free excitons. Under equilibrium conditions, excitons make transition to an empty

ground state and emit electromagnetic radiation of photon energy equal to the bandgap. This process is commonly known as PL. The energy distribution of photon (PL) is measured to determine properties of the material, including defect species, defect concentrations, possible stimulated emission [18], etc. In intrinsic ZnO, the near band-edge PL process is dominated by excitonic recombination and their longitudinal optical (LO) phonon-assisted transitions. To understand the PL processes in ZnO, it is imperative to discuss the physics of excitons in ZnO and their recombination dynamics. In the following sections, we will give a brief introduction to the ZnO band structure, free and bound excitons and their phonon replicas, deep level transitions, and effect of quantum confinement on the PL processes in ZnO thin films.

3.2.1 Band Structure and Excitons

Since ZnO is a direct bandgap ($\sim$3.3 eV at room temperature) semiconductor, the maxima of valence band and the minima of conduction band in ZnO lie at the same point in the Brillouin zone, namely at $K = 0$, i.e., at the Γ-point. The ZnO conduction band (CB) is mainly constructed from the empty 4 s states of Zn^{+2} ions and has Γ_7 symmetry. The valence band (VB) in ZnO originates from the occupied 2p orbitals of O^{-2} ions and is split into three doubly degenerated bands due to the influence of crystal-field and spin–orbit interactions [3, 14, 15]. A schematic of the ZnO band structure is shown in Fig. 3.1a, b. The three valence bands are labeled from top to bottom suffixes A, B, and C, respectively. The top valence band A has Γ_7 symmetry while the two lower bands B and C have Γ_9 and Γ_7 symmetries, respectively [3, 14]. The splitting of the A and B valence bands and B and C valence bands are of the order of $\sim$6 and $\sim$38 meV, respectively [2, 8, 19, 20]. The transitions from the two upper valence bands VB_A (Γ_7) and VB_B (Γ_9) to the conduction band CB (Γ_7) are allowed only for the light polarized in the orientation $E \perp c$ and the transitions from the CB (Γ_7) to VB_C (Γ_7) is allowed only for the light polarized in the orientation $E//c$ [2, 20]. These transitions are explicitly shown in Fig. 3.1a. The effective electron mass m_e^* has value $\sim(0.28 \pm 0.02)\ m_0$ and is almost isotropic [21]. The effective hole masses for the A and B valence bands are also isotropic and have similar value of $m_h^*(\perp, //)_{A,B} = 0.59\ m_0$, while for C valence bands the effective hole mass has typical value of $m_h^*//c = 0.31 m_0$ and $m_h^* \perp c = 0.55 m_0$ [20].

Generally in high-quality ZnO crystals and epitaxial thin films and at low excitation density, the electrons and holes generated by the absorption of a photon of suitable energy can pair due to Coulombic attraction to form an exciton [18, 21]. This electron-hole system coupled through Coulumbic interaction is known as free exciton. The energy of the free excitons can be calculated by introducing Coulumbic interaction term in the Schrödinger equation and is expressed as [18, 21]:

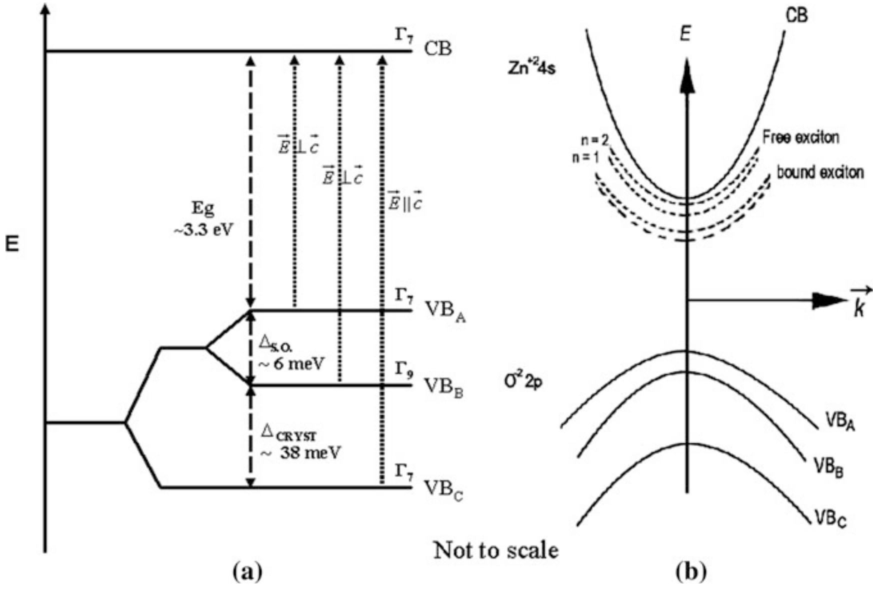

Fig. 3.1 Schematic of ZnO band structure **a** energy level diagram showing the allowed upward transitions with *dotted lines* and **b** *E–K* diagram showing free and bound exciton energy levels below conduction band with *dotted* and *dashed lines* respectively

$$E_{\text{ex}} = \frac{m_r^* q^4}{2h^2\varepsilon^2} \cdot \frac{1}{n^2} = -E_B \cdot \frac{1}{n^2} \tag{3.1}$$

where n is an integer and represents different energy states of the excitons and m_r^* is the reduced mass of exciton, which can be given by the following relation:

$$\frac{1}{m_r^*} = \frac{1}{m_e^*} + \frac{1}{m_h^*} \tag{3.2}$$

where m_e^* and m_h^* are the effective masses of electron and hole, respectively. The reduced mass of free exciton is always lower than that of the effective mass of free electron or free hole.

The exciton energy levels E_{ex} are defined with respect to conduction band-edge and the bottom of the conduction band is treated as continuum ($n = \infty$). A schematic representation of the free exciton energy levels corresponding to different n and with respect to the E–K diagram is shown in Fig. 3.1b by dotted lines. The separation E_{ex} ($n = \infty$) – E_{ex} ($n = 1$) is equal to the binding energy (E_B) of free exciton [18]. The binding energy of exciton is the measure of its stability against temperature. At sufficiently high temperatures, with corresponding thermal energy larger than that of the free exciton binding energy, the excitons dissociate into free electrons and holes.

The free exciton as a pair of opposite charges is free to move in the crystal and hence posses kinetic energy. The kinetic energy of the free excitons can be represented as [18, 21]:

$$E_{\mathrm{ke}} = \frac{\hbar^2 K^2}{2(m_e^* + m_h^*)} \tag{3.3}$$

where K is the exciton wavevector associated with the motion of centre of gravity of excitons. The total energy of exciton including the kinetic energy can be represented as:

$$E_{\mathrm{ex}} = E_g - \frac{E_B}{n^2} + E_{\mathrm{ke}} \tag{3.4}$$

where E_g is the bandgap of the material. Addition of kinetic energy to the exciton energy results in the broadening of excitonic energy levels [18, 21].

The formation of excitons usually appears as narrow peak in the absorption of the direct bandgap semiconductors at photon energies [18, 21]:

$$hv = E_g - E_B\left({}^1\!/\!_{n^2}\right) \tag{3.5}$$

where E_B is the binding energy of free excitons. Similarly the excitons generated during the optical absorption process recombine, emitting a narrow spectral line at a photon energy given by Eq. 3.5. Since excitons can have series of excited states, hence free excitonic absorption or emission spectra consist of series of narrow lines or peaks occurring at values given by Eq. 3.5. However, the intensity of the higher order peaks decreases rapidly with increasing n [19]. The excitonic absorption and luminescence in semiconductors are governed by the fact that creation or annihilation of exciton is possible only close to $K = 0$, i.e., at zone center due to negligible momentum of involved photon, hence at $K = 0$ it is very pronounced transition which broadens with temperature. Due to delta function like density of states and narrow spectral width the excitonic recombination is of particular importance for the laser diode applications [19].

Besides free excitons, excitons bound to shallow impurities play an important role for the optical properties close to the band-edge of ZnO at low temperatures [18, 21]. A free exciton can combine with the impurity or defects to form bound exciton. For example, a free exciton can combine with a donor or acceptor impurities (neutral or ionized) to form a donor or acceptor like bound excitons. The binding energy of the bound exciton is much smaller than that of the free exciton; therefore, they are observed at very low temperatures. Both the free and the bound excitons may occur simultaneously in the semiconductor and can be differentiated by their energy positions and line widths [18, 21]. The energy level of the bound exciton is below the free exciton energy by an amount equal to the binding energy of bound exciton and can be given by the following equation:

$$hv = E_g - E_B - E_D \tag{3.6}$$

where E_g, $E_{B,}$ and E_D are the bandgap and binding energy of free and bound excitons, respectively. The energy position of the bound excitons is also shown in Fig. 3.1b. The bound excitonic transitions are characterized by extremely narrow spectral width and are generally observed at low temperatures [18]. With increasing temperature, the bound excitons disappear due to thermal dissociation of excitons from the defect complexes. Like free excitons, the bound excitons can also recombine by emission of one or more LO phonons, however the interaction of LO phonons with bound excitons is generally very weak.

3.2.2 LO Phonon Replicas and Deep Level Transitions

In polar semiconductors such as ZnO, one of the channels of the excitonic recombination is through mediation of optical phonons [2, 18, 21]. In ZnO with partial ionic bonding, a long-range polarization field is created due to the vibration of cation and anion against each other in longitudinal mode. This results in strong scattering of LO phonons with excitons and modifies the optical recombination and emission characteristics especially at elevated temperatures [21]. In such cases, the excitons recombine by emission of one or more LO phonons as the LO phonons are possible at $K = 0$. Hence the narrow emission spectrum of exciton is replicated at several lower photon energies represented as [21]:

$$hv = E_g - E_{\text{ex}} - mE_p \tag{3.7}$$

where m is the number of optical phonons involved and E_p is their energy. Like free excitons, the bound excitons can also recombine by emission of one or more LO phonons; however, the interaction of LO phonons with bound excitons is generally very weak.

Other than band to band transitions of excitons and their phonon replicas, which are responsible for the VU-Blue PL, there are also mid-gap PL emissions from ZnO in the visible spectral region. These recombination processes occur due to the formation of donor, acceptor, or other structural defect related states in ZnO bandgap. The various downward electron transitions responsible for yellow, blue, green, and red luminescence observed in ZnO are found to be due to (a) deep acceptor defect levels (b) shallow Oxygen vacancy induced defect levels, (c) Singly ionized Oxygen vacancies induced defect levels, and (d) Zn interstitials induced defect levels. Depending on the defects and other conditions prevailing in the sample to be investigated and the measurement parameters, PL transition corresponding to some or all of the above-mentioned mechanisms are observed.

3.2.3 Effect of Quantum Confinement

The quantum confinement effects in low dimensional ZnO structures modify its optical properties significantly. A confined structure is the one, which has one or more of its dimensions reduced to the size of confinement regime, i.e., of the order of de Broglie wavelength, which is normally in nanometers. If the confinement occurs in one dimension only (say z direction) and the charge carriers have free motion in other two directions (x and y), such a structure is known as two dimensional (2D) quantum structure or a quantum well. In practice, a quantum well consists of a low bandgap semiconductor layer flanked by two layers of a higher bandgap semiconductor of nearly similar crystal structure on either side. These layers are called the barrier layers and are invariably thicker than the confinement layer, which is of thickness in the nanometer regime. In this case, the motion of the charge carries is restricted along the film thickness (z direction) due to potential barriers created by high bandgap semiconductor layers and has two degrees of freedom.

The energy states of charge carries in semiconductor quantum structure of different dimensionality can be calculated by solving the Schrödinger equation with appropriate boundary conditions. The energy of charge carriers in three dimensions is the sum of the kinetic energy due to its free motion in all the three dimensions and can be represented with following expression in usual terms:

$$E_{\text{Total}}^{3D} = \frac{\hbar^2}{2m}(k_x^2 + k_y^2 + k_z^2) \tag{3.8}$$

In case of 2D quantum wells and under infinite potential well approximation, the total energy of the electron, which is the sum of quantized energy (in confined direction z) and the kinetic energy due to its (x, y) motion (in unconfined directions) is given as:

$$E_{\text{Total}}^{\text{2D}} = En_z + \frac{\hbar^2}{2m}(k_x^2 + k_y^2) \tag{3.9}$$

where En_z is the energy of electron in the confinement direction and can be expressed as:

$$En_z = \frac{\hbar^2}{2m}\left(\frac{n_z \pi}{a}\right)^2 \tag{3.10}$$

where $\hbar$ is Plank's constant, a is the size of the well in the confinement direction, and n_z is quantum number having values $n_z = 1, 2, 3, \ldots$.

It is obvious from Eq. 3.10 that quantum confinement results in discreteness of the energy levels, which are dependent on the size of the confinement dimension. The energies and wave functions for the first two quantized states of a quantum well are shown in Fig. 3.2. A blue shift in the semiconductor's bandgap is a natural consequence of the quantization of energy levels, which increases with decreasing size. A similar size dependence of the energy states can also be expected for holes in the valance band.

If the barrier potential is finite, the wave function decays exponentially into the barrier region and is a Sine or Cosine function in the quantum well. By matching the wave function and its derivatives at the boundaries, the energy and wave function can be obtained by the solution to the following set of transcendental equations [22, 23] using usual symbols

$$\begin{aligned}\alpha \tan\frac{\alpha\omega}{2} &= \beta \\ \alpha \cot\frac{\alpha\omega}{2} &= -\beta\end{aligned} \tag{3.11}$$

where

$$\alpha = \sqrt{\frac{2m^3 E}{\hbar^2}} \quad \text{and} \quad \beta = \sqrt{\frac{2m^3 (V-E)}{\hbar^2}}$$

V is the finite barrier height and m is the effective mass of carriers. These equations can be solved numerically to get the energy and wave function for a 2D quantum wells with finite barrier heights.

The size confinement also modifies the excitonic behavior discussed in Sect. 3.2.1. The excitonic binding energy increases significantly with reducing size of the semiconductor [21–23]. The energy states of free excitons in 2D quantum well structures can be calculated by solving Schrödinger equation including both Coulombic interaction between the carriers and confining potential due to the potential barriers [21, 22], which can be expressed as:

$$E_{\text{ex}}^{\text{2D}} = \frac{E_B}{(n-\frac{1}{2})^2} \quad (n \geq 1) \tag{3.12}$$

where E_B is the binding energy of free excitons in three dimensions (Eq. 3.10) and n is an integer. For $n = 1$ the binding energy of exciton in 2D structures can be given as:

$$E^{\text{2D}} = 4E_B \tag{3.13}$$

Hence binding energy of the exciton in two dimensions increases theoretically ~4 times the bulk value. However, experimentally it has been observed that the binding energy varies between E_B to *3* E_B due to leakage of the electron wave

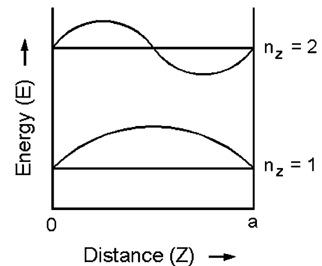

Fig. 3.2 Schematic of energy levels and wave functions of electron in a quantum well

function in the barrier region because of finite confining potential. Quantum confinement also modifies the excitonic Bohr radius [21]. The Bohr radius of the exciton in two dimensions can be given as:

$$a_B^{2D} = \frac{a_B^{3D}}{2} \tag{3.14}$$

Hence, the exciton Bohr radius in the 2D quantum well decreases compared to the three dimensional case. Since the relative separation of electron and hole of the exciton reduces in nanostructured semiconductors due to spatial confinement as compared to the three dimensional solid, the oscillator strength of the optical transitions increases significantly in low dimensional semiconductors. However, at sufficiently low thickness of quantum well layer, i.e., well layer thickness much lesser than the excitonic Bohr radius, the excitons behave like bulk excitons. The 0D confinement effect on the excitons is still under intense investigation both theoretically and experimentally. From elementary and also involved theoretical calculations it has been established that excitonic binding energy should enhance further with size in case of 0D structures compared to their 2D and 1D counterparts. However they exist at interesting size regime in which size of the QDs is smaller than the excitonic Bohr radius. It is currently a matter of intense investigation whether the optical transitions in these ultra-small QDs are of excitonic nature or excitons do not exist at all in such structures. Our investigations in this area which are presented in subsequent sections below have given a clue that possibly the optical transitions in such structures are mainly due to unbound electron-hole pairs which are strongly confined and interacting through columbic interaction.

3.3 Photoluminescence Spectroscopy Setup

Photoluminescence spectroscopy is a contactless, nondestructive method of probing the electronic structure of materials and is a useful technique for the characterization of photoemissive processes occurring in materials [18, 21, 24]. Photoluminescence spectroscopy is based upon the principle of measuring the energy distribution of emitted photons due to radiative recombination of free carriers or excitons after optical excitation. In direct bandgap semiconductors, the emission of photon is a reverse process of the absorption. Figure 3.3 shows schematic of the experimental setup for PL spectroscopy. The PL is excited with an intense pump laser beam of photon energy greater than the bandgap of the semiconductor sample which generates free electrons and holes in the conduction and valence bands, respectively, or free excitons. The emitted PL is dispersed with a high-resolution monochromator (MC1) and detected by using suitable detector such as Charge Couple Device (CCD) or photomultiplier tube (PMT). Normally, a PMT is used as a detector to get higher gain while CCD is used to get faster

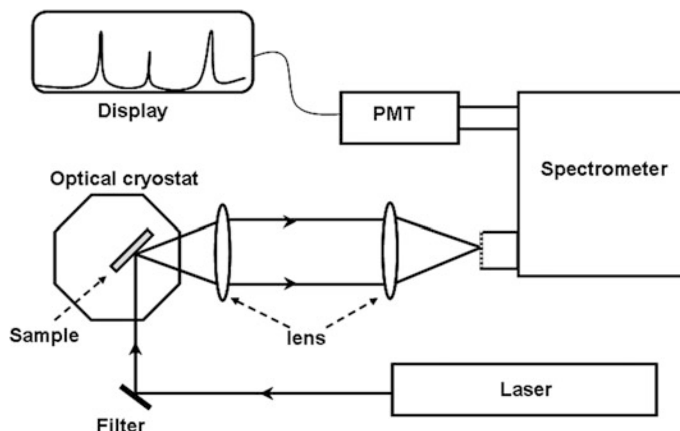

Fig. 3.3 Schematic of the experimental setup of PL spectroscopy

response. In-phase detection of the PL signal is performed with the help of a lock-in amplifier and a mechanical chopper capable of chopping the laser light at desired frequency. A long pass filter is used to block the scattered laser light.

The main strength of the PL spectroscopy technique lies in its sensitivity to detect very weak signal, i.e., high signal-to-noise ratio, which depends on the quality of the sample. It provides a direct measure of the optical quality of the samples and the compositional as well as spatial homogeneity of the epitaxial layers. Its main limitation is a weak or no PL signal for indirect bandgap materials. It provides only the lowest excited state information for quantum structures and requires low temperatures to suppress the luminescence from defects in case of poor quality samples. Photoluminescence technique for semiconductor characterization has achieved significant success and popularity partly due to the simplicity of the technique and the no requirement of sample processing. Photoluminescence signal from a grown structure is directly related to its optical quality needed to make the light-emitting devices. Time-resolved PL spectroscopy provides Information about recombination kinetics, surface recombination, and transport dynamics. Spatially resolved PL spectroscopy is sensitive to sample inhomogeneities and transport processes. Photoluminescence spectroscopy is useful in quantifying, (a) optical emission efficiencies, (b) composition of the material (i.e., alloy composition), (c) impurity content, and (d) quantum size effect etc.

3.4 Photoluminescence Spectroscopy of ZnO Thin Films

We carried out a detailed study of the PL emanating from high-quality ZnO thin films grown on sapphire substrates in the temperature range of 10–300 K to understand various recombination mechanisms and their relative weight on the

light emission from ZnO. Photoluminescence processes due to recombination of free (F_X) and bound (B_X) excitons and associated with the LO phonon mediated transitions were observed and studied as a function of temperature. The results of these studies are presented and discussed in this chapter.

The ZnO thin films, multiple quantum wells, and multilayer matrices of Alumina capped ZnO quantum dots used in this study were grown on epi-polished (0001) Sapphire substrates having rms surface roughness <0.5 nm using pulsed laser deposition (PLD). A third harmonic Q-switched Nd:YAG laser (355 nm, 6 ns, and 10 Hz) was used at a fluence of $\sim$2 J/cm^2 to ablate the ZnO target which was prepared by palletization and sintering of its high purity (99.9995 %) powder. The growth was carried out in high purity (99.999 %) Oxygen ambient at a partial pressure of $\sim 1 \times 10^{-5}$ Torr and at a substrate temperature of $\sim$750 °C. Thickness of these films as measured by step profiler was $\sim$500 nm. Details of the growth process have been described elsewhere [25, 26]. Crystalline quality of the grown films was studied using Phillips make high-resolution X-ray diffractometer (HRXRD) with a resolution of 0.05° which revealed highly crystalline and c-axis oriented growth [25, 26] with c-axis lattice parameter of $\sim$5.209 Å in close agreement with the reported bulk value of 5.20661 Å [27], indicating nearly strain-free films. The full width at half maxima (FWHM) of ω-rocking curve of (0002) ZnO peak was $\sim$0.11° which compared favorably with the value of $\sim$0.13° reported earlier by Ohtomo et al. [28]. The Φ-scans of HRXRD revealed 30° in-plane rotated growth of ZnO lattice on Sapphire when grown at 750 °C in conformity to the strain free nature of the films [25, 26].

The temperature-dependent PL measurements were carried out in the range of 10–300 K using a 20 mW He–Cd laser operating at 325 nm as an excitation source [27]. The PL signals were recorded by a photomultiplier tube in photon counting mode after dispersing it through a 1 m long monochromator. Figure 3.4 shows the PL spectrum from ZnO film in broad spectral energy range of 1 to 4 eV at 10 K. A strong luminescence in the UV region at around 3.35 eV, corresponds

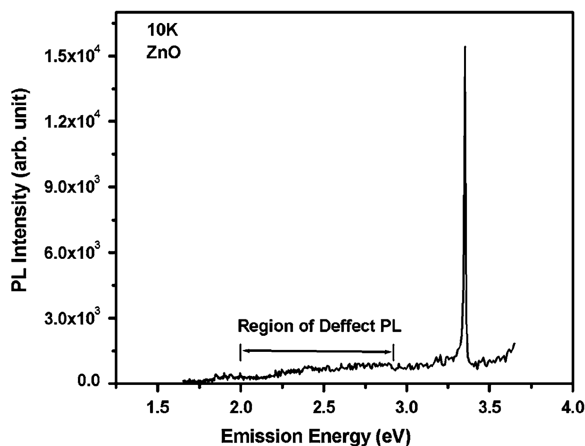

Fig. 3.4 PL spectrum from ZnO film at 10 K in broad spectral range of 1–4 eV

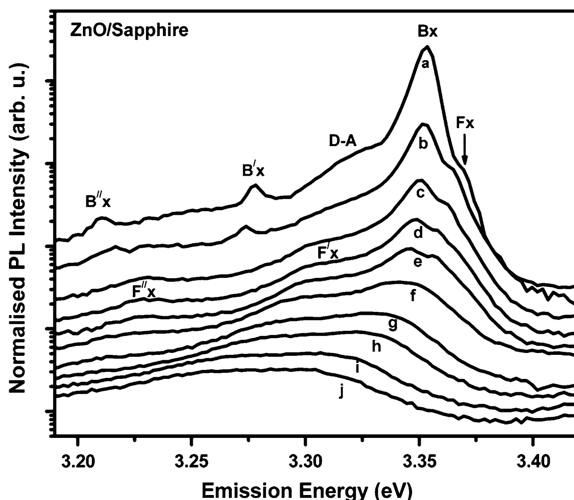

Fig. 3.5 PL spectra of ZnO thin film taken at different temperatures **a** 10, **b** 50, **c** 70, **d** 90, **e** 110, **f** 150, **g** 190, **h** 210, **i** 250, and **j** 300 K. The spectra are plotted in logarithm scale, multiplied and vertically displaced for clarity

to ZnO bandgap due to excitonic recombination. It is interesting to note that the deep level emission in the visible spectral region, which is considered to be due to off stoichiometry, i.e., oxygen vacancies, zinc interstitial, and other structural defects is almost negligible, indicating nearly defect free and stoichiometric growth of ZnO on sapphire. However, the strong near band-edge emission in UV spectral region has fine structures containing various peaks which changed their position and intensity with temperature. To get deeper insight of the PL processes occurring in ZnO, we have carried out the PL measurements at different temperatures in the broad temperature range from 10 to 300 K.

Photoluminescence spectra of a ZnO film recorded at different temperatures in the range of 10 to 300 K are shown in Fig. 3.5. As can be seen in this figure, the PL spectra contained various emission features, corresponding to different recombination mechanisms of excitons. To determine the individual peak positions and its intensity within a spectrum, we reconstructed the spectrum using multiple standard Gaussian profiles. It can be seen that at low temperatures the near band-edge emission was dominated by radiative decay of donor bound excitons (B_X) that peaked at ~3.357 eV at 10 K with a line width of ~6 meV as commonly observed in the low temperature PL of ZnO [1, 21, 29–31]. The PL spectral feature from the free exciton recombination (F_X) at ~3.374 eV appeared as a shoulder with intensity almost two orders of magnitude smaller than that of the bound exciton emission. It is also evident that the intensity of the F_X peak increases at the expense of B_X peak with increase in temperature and finally disappears.

To understand the temperature dependence of the F_X and B_X peaks, the respective PL peak intensities were plotted as a function of temperature which is shown in Fig. 3.6. As seen in this figure, the B_X peak intensity decreases rapidly with increasing temperature and disappears completely at ~130 K in the background of F_X; however, the F_X peak intensity initially increases steadily with temperature from 10 to ~110 K and then gradually decreases up to 300 K. The rapid decrease in the

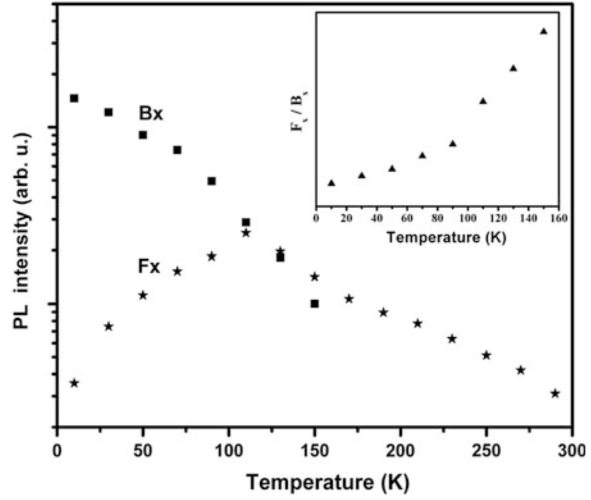

Fig. 3.6 PL peak intensity of bound excitons (B_X) and free excitons (F_X) as a function of temperature. The inset shows the variation of the ratio (F_X/B_X) with temperature

intensity of B_X and monotonic increase in the intensity of F_X with temperature up to 130 K can be attributed to the enhanced thermal dissociation of bound excitons into free excitons with increasing temperature [21, 30, 31]. Accordingly, the ratio of PL peak intensity of F_X and B_X increased monotonically with increasing temperature in the range of 10–300 K. This is explicitly shown in the inset of Fig. 3.6. The temperature-dependent quenching of B_X and F_X intensity can be used to estimate their activation energy using the following equation:

$$I(T) = I_0/[1 + A\exp(-E_a/k_B T)] \tag{3.15}$$

where E_a is the activation energy of the thermal quenching process, k_B is Boltzman constant, T is temperature, I_0 is the integrated intensity of B_X at 0 K, and A is a constant.

Figure 3.7a, b shows the natural logarithm of the integrated intensity of B_X and F_X as a function of 1000/T. From a fit to the experimental data as shown by solid line in Fig. 3.7a, E_a for bound exciton was estimated to be ~17 meV, consistent with the binding energy obtained from the difference in the B_X and F_X peak positions at 10 K and reported values of binding energy (10–20 meV) of donor-bound exciton complexes in case of bulk ZnO [29–31]. Similarly, the binding energy of the exciton was estimated to be ~59 meV closely matching with the theoretical value.

In addition to the near band-edge excitonic emissions at 10 K, two other weak features in the PL spectrum shown in Fig. 3.5 are at ~3.284 and ~3.214 eV. These peaks are ~72 and 144 meV away, respectively, from the B_X peak as can be seen in Fig. 3.5. These approximately equidistant PL features could be attributed to the 1 and 2-LO phonon-mediated recombination of the bound excitons [21] and are represented by B'_X and B''_X, respectively. However, the PL peak intensities of B'_X and B''_X quenched more rapidly with temperature compared to that of the B_X

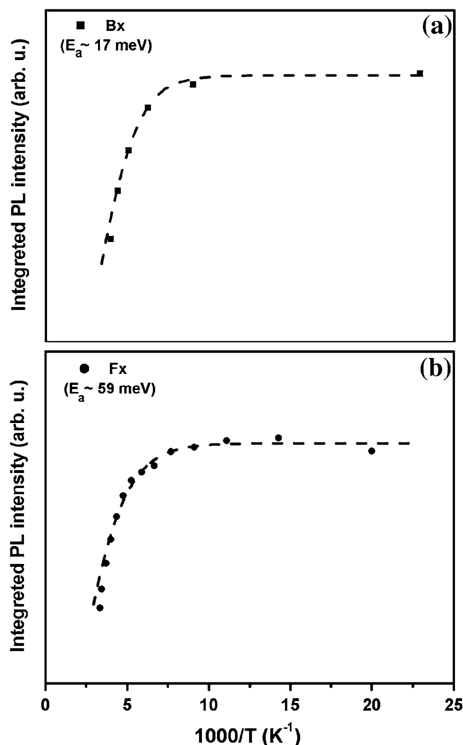

Fig. 3.7 Integrated PL intensity of the **a** B_X and **b** F_X as a function of 1000/T. The plotted data was fitted using Eq. 3.15 as shown by broken line to estimate respective activation energies

and they disappeared at ~70 K. The broad emission feature at ~3.32 eV located between the bound exciton emission and its 1-LO phonon replica at 10 K which quenched rapidly with temperature and disappeared at ~50 K, has been attributed to the recombination arising from the donor-to-acceptor pair transitions [27, 30, 32]. However with increasing temperature beyond 50 K, two other PL peaks due to 1 and 2 LO phonon-mediated recombination of free excitons represented by F'_X and F''_X, respectively appeared. The intensity of these PL peaks increased gradually relative to F_X with increasing temperature as seen in Fig. 3.5.

Figure 3.8 shows the variation of the ratio of the PL peak intensity of F'_X and F_X. It can be seen that this ratio increases monotonically close to unit with increasing temperature up to RT.

At RT, the dominant transitions were found to be due to F_X and F''_X. The line width of the F_X at RT was found to be ~93 meV which is lower than the reported value of ~117 meV for ZnO grown on Sapphire by MBE [33] and ~120 meV by MOCVD [34]. The deep level emission in ZnO, which has been attributed to the crystal defects [35] such as oxygen vacancies, zinc interstitials, and oxygen anti-sites was negligible in our case, both at low and room temperatures. Narrow width of the free excitonic PL peak at RT along with the negligible deep level emissions are clear indications of high structural and optical qualities of the ZnO films grown by PLD.

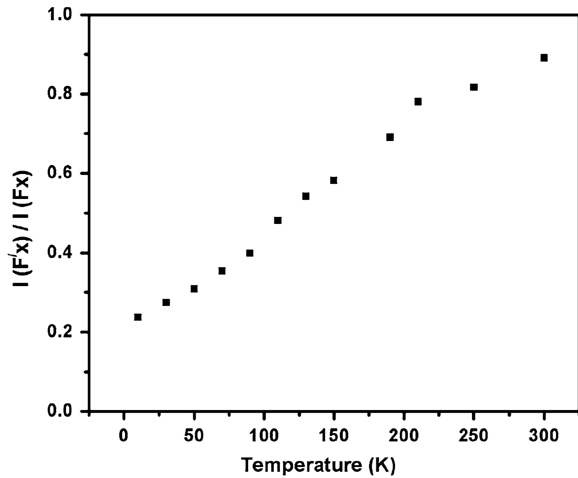

Fig. 3.8 Variation of ratio of intensity of free exciton and its first LO phonon replica as a function of temperature

Temperature dependence of the spectral position of various PL peaks from the ZnO film is shown in Fig. 3.9. It can be seen that peaks corresponding to B_X and F_X and their associated phonon replicas are monotonically red shifted with increasing temperature at different rates. The shift in the exciton energy essentially results from the bandgap shrinkag and thermal dissociation of bound excitons assuming that exciton binding energy is independent of temperature. The dependence of the bandgap on temperature can be explained using the well-known Varshni's empirical relationship [27] as follows:

$$E(T) = E(0) - \frac{\alpha T^2}{\beta + T} \tag{3.16}$$

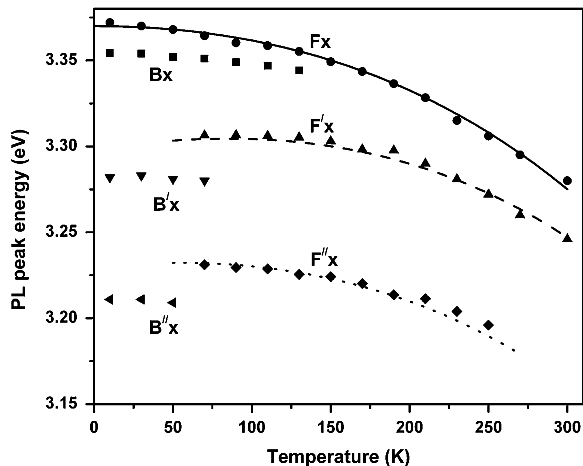

Fig. 3.9 Temperature dependence of energy positions of F_X, B_X, F'_X, B'_X, F''_X, and B''_X PL peaks. Solid line shows the fit to the F_X peak values according to Varshni's empirical relation. Dashed and dotted lines show the fit to the F'_X and F''_X considering free exciton kinetic energy

where $E(0)$ is the bandgap of the material at 0 K, α and β are the fitting parameters, and β is related to the Debye temperature θ_D. If we assume binding energy of the exciton to be independent of temperature, then the same Eq. 3.16 can be used to explain the temperature-dependence of energy state of the free excitons. The best fit to the experimental data for the F_x peak of ZnO film, as shown by the solid lines in Fig. 3.9 was obtained for $\alpha = 8.2 \times 10^{-4}$ eV/K and $\beta = 1070$ K and $E(0) \sim 3.38$ eV [28].

However, the B_X peak position is red shifted gradually with temperature compared to F_X and hence the separation (F_X–B_X) reduced from ~17 to ~11 meV with increasing temperature from 10 to 130 K. The observed decrease in the separation (F_X–B_X) with temperature can be explained considering the excitonic fine structure in bulk single crystals of ZnO [36]. According to this finding, the emission band due to recombination of bound excitons in bulk ZnO is composed of many closely spaced transitions associated with various unintentionally introduced donors and/or donor like defects. The relative intensities of these emission peaks depend upon the temperature and nature of defects [37]. We suggest that with increase in temperature from 10 to 130 K the bound excitons at 10 K with activation energy of ~17 meV dissociate and transform into bound excitons associated with shallow donor defects. This leads to the successive population of shallow donor bound exciton states with comparatively less binding energy as the temperature is increased. Therefore, a decrease in the separation (F_X–B_X) with increasing temperature is observed. The observed values of the separation (F_X–B_X) at different temperatures in the range of 10–130 K are in good agreement with the reported values of binding energies of donor bound exciton complexes which lie in the range of ~10–20 meV [30, 36].

The energy separation between the PL peaks F_X and it's LO phonon replica F'_X, which is the characteristic energy of the LO phonon in ZnO (~72 meV) showed an unusual temperature dependence. It can be seen from Fig. 3.9 that the PL energy position of F'_X (first phonon replica of F_X) show much stronger temperature dependence than F''_X (second phonon replica of F_X) and F_X in the range of 50–300 K and the separation between the F_X and F'_X, i.e., (F_X–F'_X) was found to decrease more rapidly than the separation between the F_X and F''_X, i.e., (F_X–F''_X). The strong temperature dependence of energy separation between the F_X and its LO phonon replicas could be attributed to following two mechanisms (i) shift in the energy of phonon with either temperature [38] and/or stress [39] and (ii) due to the increase in kinetic energy of the free excitons with temperature [21].

The phonon energy in solids is known to decreases with increasing temperature due to thermal expansion of the lattice and can contribute to the observed temperature dependence of the energy separations in the present case [38]. The change in the energy of the LO phonons in ZnO films with increasing temperature up to RT was calculated using the formulation of Alim et al. [38] taking into account the thermal expansion and anharmonic coupling effects. All the required parameters were taken from the same Ref. [28]. The estimated shift of LO phonon energy due to change in the temperature from 10 to 300 K was as small as ~1.7 meV and

hence inadequate to explain the observed temperature dependence of energy separation. Similarly the change in the LO phonon energy in ZnO film due to residual strain is also negligible as the HRXRD measurements revealed nearly strain free ZnO films on sapphire.

The other possible factor responsible for the observed behavior is the exciton-phonon coupling mechanism. According to the paradigms of Permogorov's [40] and Klingshirn [21], which deal with the asymmetric spectral shape of the phonon-assisted luminescence in polar semiconductors taking into account the kinetic energy of the free excitons, a general relationship for the energies of the emission lines involving phonons and excitons could be written as:

$$F_X^n = F_X - n\hbar\omega_{\mathrm{LO}} + \Delta E \tag{3.17}$$

where F_X^n is the energy position of the spectral peak corresponding to the nth phonon replica, F_X is the free exciton energy at $K = 0$, h is the Planck's constant, and ω_{LO} is the LO phonon energy which is $\sim$72 meV. The term ΔE is related to the kinetic energy of the gas like free excitons in the crystal [21]. Since the excitons with kinetic energy ΔE move away from $K = 0$ in E–K space, therefore they require mediation of phonons of suitable energy and momentum to recombine. The transition probability of excitons with kinetic energy ΔE is proportional to $(\Delta E)^L$ where L is an integer and hence the kinetic energy of excitons can be approximated to $(L + 1/2)KT$ where the integer L is 0 or 1 [21]. Therefore the energy separation between the free exciton peak and its nth LO phonon replica can be represented in terms of usual and predefined symbols as:

$$F_X^n = F_X - n\hbar\omega_{\mathrm{LO}} + \left(L + \frac{1}{2}\right)KT \tag{3.18}$$

The best fit to the observed temperature dependence of the energy position of F'_X peak was obtained for $L = 1$ resulting in a slope of $\sim -3/2\ KT$, which is shown by the dashed line in Fig. 3.9. For F''_X, a reasonable fitting of the experimental data, as shown by the dotted line in Fig. 3.9, was obtained for $L = 0$ indicating that the transition probability was independent of the excitonic kinetic energy in this case. The insignificant variation with temperature in the energy of B'_X and B''_X compared to that of F'_X and F''_X seen in Fig. 3.9 indicates that there is a significant difference in the scattering mechanisms between free excitons–phonons and bound excitons–phonons.

3.5 Photoluminescence Processes in ZnO Quantum Wells

Research and studies on ZnO quantum wells is important for the development of next generation nanophotonic and electronic devices [41, 42]. In general, quantum structures exhibit fascinating size-dependent physical properties such as large oscillator strength of optical transitions, enhanced excitonic binding

energy, tunability of operating wavelength, very low threshold of lasing, and quantum transport properties. The ZnO quantum structures are also ideal systems for studying the effect of dimensionality on the excitonic recombination mechanisms. The nonlinear optical response such as third-order nonlinear susceptibility can be enhanced significantly in ZnO nanostructures compared to that of bulk due to confinement effects [2].

We carried out studies on the PL processes in one dimensional confined structure of ZnO such as multiple quantum wells (MQWs), which are important for the development of modern optoelectronic devices based on quantum confinement effects. Since the excitonic Bohr radius for ZnO is ~2.1 nm, the size-dependent quantum confinement effects in ZnO nanostructures can be observed only if the size of structures is less than ~4.2 nm. We have accomplished the growth of high-quality ZnO/$Mg_xZn_{1-x}O$ MQWs with well layer thickness in the range of ~4 to 1 nm on (0001) on sapphire substrates by using PLD under optimized conditions and observed size-dependent blue shift in ZnO bandgap due to the quantum confinement effect. To the best of our knowledge, we have observed for the first time, efficient luminescence at room temperature (RT) from these MQWs grown on sapphire substrates [43].

Growth of ZnO multiple quantum wells was carried out on sapphire substrates using pulsed laser deposition technique. It is well known that the ZnO/$Mg_xZn_{1-x}O$ hetero interfaces are stable below 650 °C [44]. However the high crystalline quality of ZnO and its alloys can be achieved at high growth temperature of 750 °C and above due to 30° rotated growth with respect to sapphire through domain epitaxy as discussed in Refs. [26, 27, 45]. To accomplish these contradictory growth requirements, we evolved a buffer-assisted growth methodology [26] wherein a ZnO buffer layer of ~50 nm thickness was first grown on Sapphire substrate at 750 °C and the subsequent growth of barrier and well layers was carried out on this ZnO template at a lower temperature of ~600 °C. This ensured a high crystalline quality of the barrier and well layers along with the physically and chemically sharp interfaces. Ternary alloy $Mg_{0.34}Zn_{0.66}O$ film with bandgap of ~4.1 eV at room temperature was deposited using sintered pellet of MgZnO as barrier layer. Depositions were carried out at a laser fluence of ~0.6 J/cm^2 by sequentially ablating the ZnO and MgZnO targets mounted on a multi-target carousal in the PLD chamber. The growth chamber was initially evacuated to a base pressure of $\sim 1 \times 10^{-7}$ Torr using a Turbo Molecular Pump and depositions were carried out in high purity (99.9995 %). Oxygen ambient at a partial pressure of $\sim 1 \times 10^{-5}$ Torr. The typical growth rate at this fluence, which was measured in separate experiments, was found to be ~0.1 nm/s for ZnO and ~0.08 nm/s for MgZnO targets, respectively. These growth rates were subsequently used to determine the barrier and well layer thicknesses. Ten periods of ZnO/$Mg_xZn_{1-x}O$ layers were grown with a constant $Mg_xZn_{1-x}O$ barrier layer thickness of ~8 nm and variable thickness of ZnO well layer in the range of ~1 to 4 nm in separate MQWs. The schematic of the ZnO MQWs grown by us is shown in Fig. 3.10. The Mg concentration in the $Mg_xZn_{1-x}O$ barrier layer was found to be ~34 % using Energy Depressive X-ray Analysis.

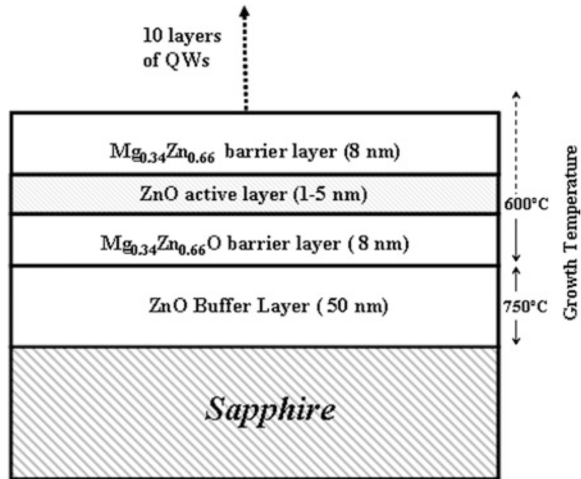

Fig. 3.10 Schematic of the ZnO/$Mg_xZn_{1-x}O$ multiple quantum wells

The optical properties of the ZnO multiple quantum wells were studied using an absorption photo-spectrometer (SHMADZU, UV-3101PC) at room temperature and temperature dependent PL spectroscopy. For PL measurements a 5 mW He–Cd laser operating at 325 nm was used as an excitation source and the resulting luminescence was collected through a ¼ m monochromator with a band pass of ~0.5 nm in the temperature range of 10 K to RT.

All the MQW samples appeared highly transparent and shining to the naked eyes with an average transmission ~80 % in the visible spectral region. Figure 3.11 shows the room temperature optical absorption spectra of these MQWs in the photon energy range of ~2 to 5 eV. Absorption spectra of ~200 nm thick ZnO and MgZnO thin films directly grown on Sapphire substrate are also shown in the same figure for reference. The latter two spectra show the band-edge of ZnO and $Mg_{0.34}Zn_{0.66}O$ bulk at ~3.3 and 4.1 eV, respectively, along with conspicuous excitonic humps. It can be seen from Fig. 3.11 that each absorption spectrum of the MQWs consists of three well resolved features. The broad shoulder at ~3.3 eV obviously corresponds to the ZnO buffer layer grown prior to every multiple quantum wells. The shoulder at ~4.1 eV corresponds to the absorption due to $Mg_{0.34}Zn_{0.66}O$ barrier layers. It is noteworthy here that the constant position of the absorption edge corresponding to the barrier layers of $Mg_{0.34}Zn_{0.66}O$ in all the MQW samples is indicative of negligibly small inter-diffusion of chemical species at the ZnO/$Mg_{0.34}Zn_{0.66}O$ interfaces. The central peak in these absorption spectra is found to correspond to the $n = 1$ excitonic transition of the ZnO quantum wells. It can be seen that this peak undergoes monotonic blue shift with decreasing well layer thickness from ~4 to 1 nm as expected from the size-dependent quantum confinement effect. The band-edge of ZnO/$Mg_{0.34}Zn_{0.66}O$ MQWs at different well layer thicknesses was estimated from their first derivative absorption spectra. The first derivatives of the absorption spectra of the ZnO MQws with different well layer thicknesses are shown in the

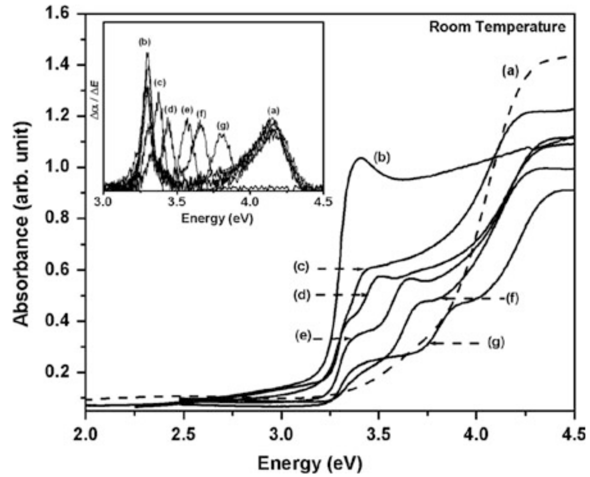

Fig. 3.11 Room temperature optical absorption spectra of **a** 200 nm thick $Mg_{0.34}Zn_{0.66}O$ barrier layer **b** 200 nm thick ZnO layer and ZnO MQWs of different well layer thickness **c** 4, **d** 2.5, **e** 2, **f** 1.5, and **g** 1.0 nm. The corresponding first derivatives of the absorption spectra are shown in the *inset*

inset of Fig. 3.11. The spectra show clear peaks corresponding to the $n = 1$ excitonic transitions, which shift toward shorter wavelength on decreasing the well layer thickness. The bandgap energy of the MQWs of different well layer thicknesses can be obtained from the peak positions in the corresponding first derivative absorbance spectrum.

The PL spectroscopy of ZnO MQWs of different well layer thickness was carried out at different temperatures in the range of 10–300 K to study the optical emission processes in ZnO MQWs. A 5 mW He–Cd laser operating at 325 nm was used as an excitation source. The sample was kept in a close cycle optical cryostat for temperature-dependent measurements. The PL signal was collected through a ¼ m monochromator with a band pass of $\sim$0.5 nm and was detected by a photomultiplier tube.

Figure 3.12 shows 10 K PL spectra of ZnO MQWs grown on sapphire with different well layer thickness along with 200 nm thick ZnO layer. The PL from $Mg_xZn_{1-x}O$ barrier layers and 1 nm thick ZnO MQW could not be observed because their bandgap which was estimated to be $\sim$4.1 and 3.8 eV, respectively, at room temperature from their absorption spectra exceeded the energy of the excitation photons from the He-Cd laser. A weak PL from the underlying ZnO buffer layer was indeed observed at $\sim$3.37 eV in each sample but not shown in the graph. It can be seen that as the well layer thickness was decreased from $\sim$4 to 1.5 nm the PL peak shifted from $\sim$3.41 to $\sim$3.78 eV in line with size-dependent quantum confine effects. It can also be seen that the line width of the PL peaks increases with decreasing well layer thickness. The broadening of PL peak with decreasing well layer thickness was attributed to fluctuations in well layer thickness within the MQW structures, which increased as the well layer thickness was decreased.

To measure the PL spectra of ZnO MQWs having well layer thickness less that 1.5 nm, we have used an ArF excimer laser operating at 193 nm. Figure 3.13 shows the 10 K PL spectra of ZnO MQW having well layer thickness 1, 1.2, and 1.8 nm respectively [45]. The 1.2 and 1.8 nm thick MQWs were also grown by us

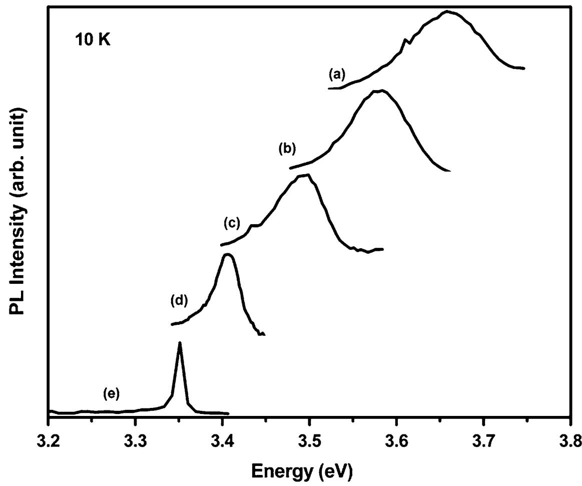

Fig. 3.12 10 K PL from ZnO MQWs of different well layer thickness **a** 1.5 nm, **b** 2 nm, **c** 2.5 nm, **d** 4 nm, and **e** 200 nm thick ZnO film

but not included in absorption spectra shown in Fig. 3.11 for the sake of clarity in the graph. It can be seen from Figs. 3.12 and 3.13 that bandgap of ZnO MQWs shifts toward blue with decreasing well layer thickness up to 1 nm due to quantum confinement effect.

The dependence of bandgap on the well layer thickness of ZnO MQWs is explicitly shown in Fig. 3.14, wherein the bandgap values obtained from 10 K PL

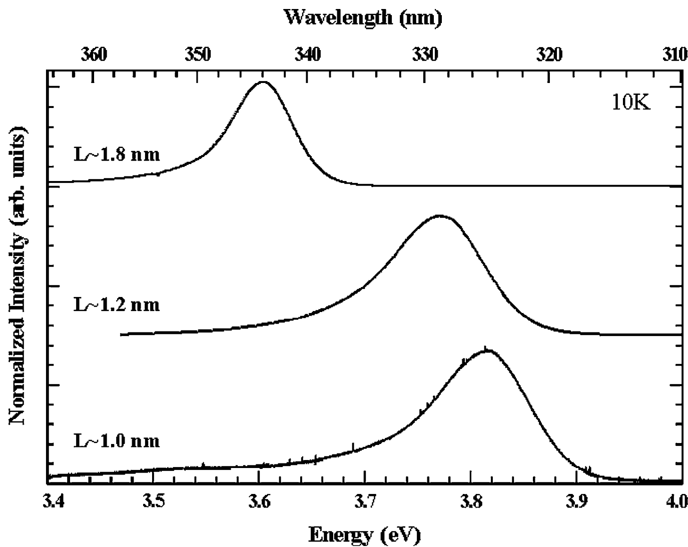

Fig. 3.13 10 K PL from ZnO MQWs with well layer thicknesses down to 1 nm

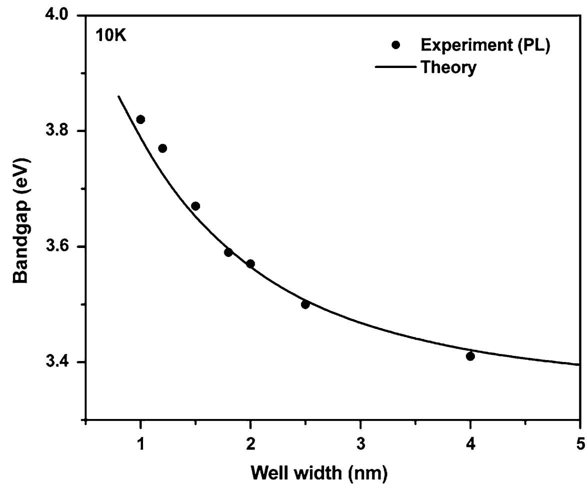

Fig. 3.14 Bandgap of ZnO MQWs obtained from 10 K PL measurements as a function of well layer thickness

spectra of different MQWs excited using either He–Cd or ArF lasers are plotted as a function of active layer thickness. To understand this dependence, we calculated the QW bandgap at different well layer thicknesses at 10 K by solving the time-independent Schrödinger equation using finite square potential well approximation as discussed in previous Sect. 3.2.3. The binding energy of excitons was assumed to be constant with respect to temperature and well layer thickness. The calculated values are shown by the continuous curve in Fig. 3.14, which shows a reasonable agreement with the experimental values obtained from PL measurements.

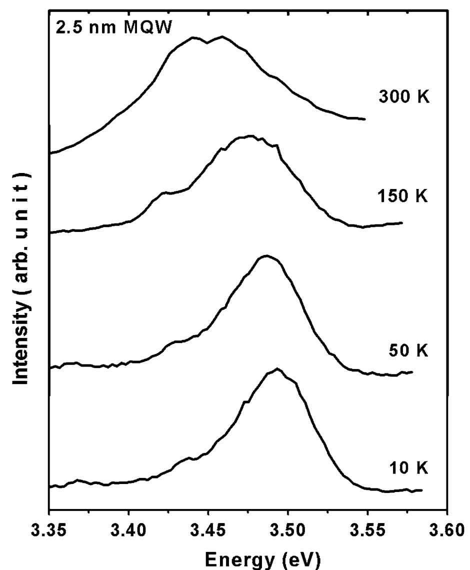

Fig. 3.15 PL spectra of ZnO MQWs at a constant well layer thickness ~2.5 nm at four different temperatures up to room temperature

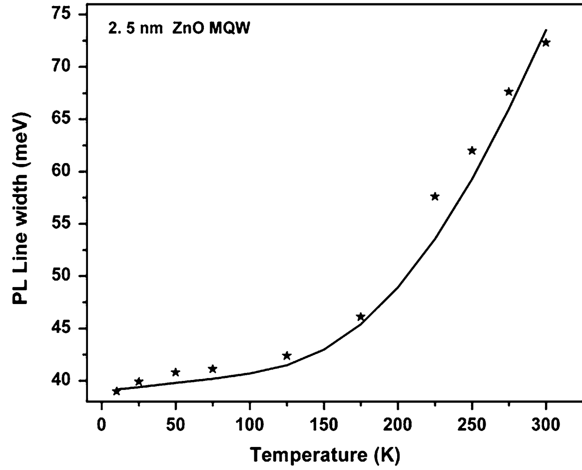

Fig. 3.16 Variation of PL spectral line width with temperature from ZnO MQWs of well layer thickness of ~2.5 nm. Solid line shows the fitted theoretical dependence

The temperature dependence of PL spectra from ZnO MQWs with a particular well layer thickness of ~2.5 nm is shown in Fig. 3.15 for four different temperatures down to RT. It can be seen that the PL peak position shifts toward red and its line width increases gradually with increase in temperature up to RT. The temperature dependence of the FWHM of the excitonic emission peak for a 2.5 nm thick ZnO MQW is shown in Fig. 3.16. It can be seen from Fig. 3.16 that the line width of the PL peak increases gradually up to ~120 K and then exponentially up to RT. The temperature-dependent broadening of the PL peak has been interpreted in terms exciton-phonon scattering in different temperature regimes using theoretical formulation developed by Hellmann et al. [46] and O'Neill et al. [47], which is as follows:

$$\Gamma(T) = \Gamma_{\mathrm{inh}} + \gamma_{\mathrm{ph}} T + \frac{\Gamma_{\mathrm{LO}}}{\exp\left(\frac{h\omega_{\mathrm{LO}}}{kT}\right) - 1} \tag{3.19}$$

where $\hbar\omega_{L0}$ is the LO phonon energy, Γ_{inh} is the inhomogeneous line width at 0 K, γ_{ph} is the coupling strength of exciton-acoustic phonon interaction [46], Γ_{LO} is the parameter related to the strength of exciton-LO phonon coupling [47], and exp $[(\hbar\omega_{L0}/kT)-1]^{-1}$ is the population of LO phonons of energy $\hbar\omega_{\mathrm{LO}}$ at temperature T. The dotted line in Fig. 3.16 shows the fitted result based on the O'Neill and Hellmann formulations. The best fit was obtained for the parameter values of $\Gamma_{\mathrm{inh}} = 39$ meV, $\Gamma_{\mathrm{LO}} = 450$ meV and $\gamma_{\mathrm{ph}} = 160$ μeV/K. As explained through the Hellmann's formulation [46], the gradual increase of the line width in the low temperature regime up to ~120 K is attributed to the exciton scattering with the acoustic phonons while the exponential rise at higher temperatures to that with the LO phonons [46]. Because the temperature dependence of the line width in the present case could be explained using O'Neill and Hellmann formulations, meant exclusively for the excitonic transitions, it indicates that all the PL transitions

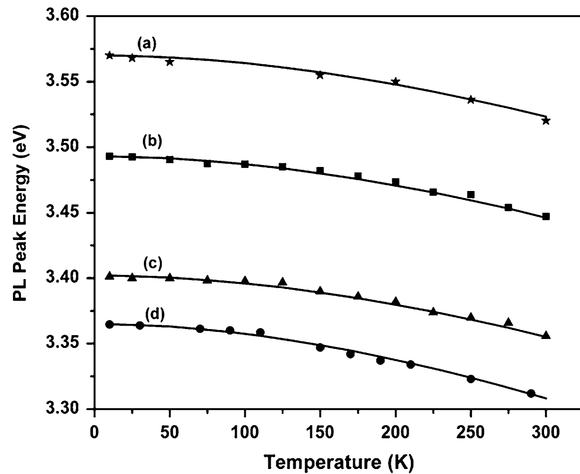

Fig. 3.17 Temperature dependence of the PL peak position of ZnO MQWs with different well layer thicknesses **a** 2, **b** 2.5, **c** 4 nm, and **d** 200 nm thick ZnO film. Solid lines show the fit to the respective experimental data using the Varshani's relation (Eq. 3.16)

observed in MQWs of different well layer thicknesses up to RT were excitonic in nature [46, 47].

The temperature-dependent PL peak positions for the MQWs with three different active layer thicknesses along with that of ~200 nm thick ZnO film are shown in Fig. 3.17. The PL peak positions were found to shift gradually toward red with increase in temperature up to 300 K. The red shift in the semiconductor bandgap with temperature results from the temperature-dependent thermal expansion/dilation of lattice and carrier-phonon scattering. The variation of the bandgap of ZnO MQWs with temperature was studied using Varshni's empirical relation [48] discussed in Eq. 3.16. The best fit to the experimental data for different MQWs, as shown by the solid lines in Fig. 3.17, were obtained for $\alpha = 8.2 \times 10^{-4}$ eV/K and $\beta = 1070$ K where α and β are the fitting parameters [49]. It can be seen from Fig. 3.17 that the MQWs with different well layer thicknesses and 200 nm thick ZnO film show similar functional form of the temperature dependence. The fact that all the MQWs followed the same functional form of the temperature dependence of bandgap, which also matched with that of the 200 nm thick ZnO film, indicates that the strain effects are minimal in these MQWs [50]. The negligible strain effects in these MQWs can be attributed to our optimized high temperature buffer assisted growth scheme which provided 30° in-plane rotated, highly crystalline, smooth, and relaxed ZnO template layers even on the mismatched sapphire substrate [26] for the growth of ZnO quantum structures. The successive low temperature growth of ZnO MQWs over this high temperature grown template layer not only ensured chemically and physically sharp interfaces and smooth surfaces of multilayer structures but also the high structural characteristics.

The room temperature PL spectra of the ZnO MQWs with different well layer thicknesses down to ~2 and about 200 nm thick ZnO film are shown in Fig. 3.18. The PL peak intensity for the ZnO MQWs with active layer thickness bellow 2 nm

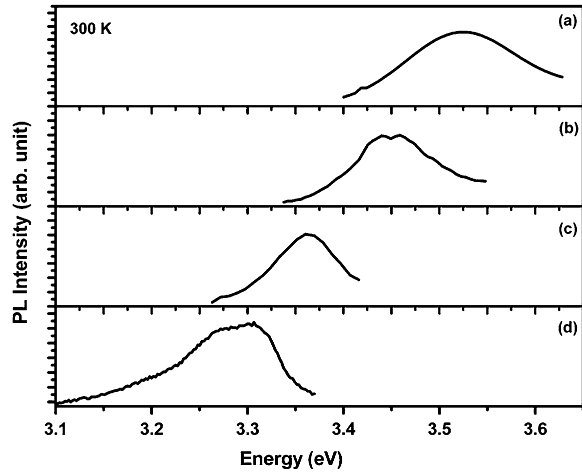

Fig. 3.18 Room temperature PL from ZnO MQWs with different well layer thicknesses of **a** 2, **b** 2.5, **c** 4 nm, and **d** 200 nm thick ZnO film

was negligibly small at RT and hence could not be recorded with the present PL setup. A feeble PL from the underlying ZnO buffer layer was observed (not shown in the figure) at ~3.3 eV in each sample. It can be seen in Fig. 3.18 that as the well layer thickness was decreased from ~4 to 2 nm, the PL peak shifted from ~3.36 to 3.52 eV in line with size-dependent quantum confinement effects. Although there are some reports on the observation of room temperature PL from ZnO MQWs but in these reports lattice match $ScMgAlO_4$ substrates were used instead of sapphire. To the best of our knowledge, this is for the first time that efficient PL has been observed at room temperature from ZnO MQWs grown on commonly used sapphire substrates [47]. The reduced interface roughness, high crystalline quality along with the minimal strain effects obtained by using high temperature buffer assisted PLD methodology adopted by us appear to be responsible for the observation of an efficient room temperature PL and well resolved absorption edges in RT absorption spectra in these MQWs.

The size-dependence of bandgap obtained from the room temperature absorption and PL measurements of the ZnO MQWs are shown in Fig. 3.19. The bandgap was calculated theoretically at each well layer thickness by solving Schrödinger equation using one dimensional square potential well approximation with finite well depth as discussed in Sect. 3.2.3. The calculated values are shown by the continuous curve in the same figure, which shows a reasonable agreement with the experimental values obtained from absorption spectra as already discussed above. However, the corresponding PL data showed some stoke shift compared to the values obtained from absorption spectra which increased with decreasing well layer thickness. In our views, a clear understanding for such a Stoke shift in ZnO MQWs is not yet well established although some authors have earlier attributed it to the local physical and compositional fluctuations in the barrier layers of ZnO and GaAs [51] MQWs.

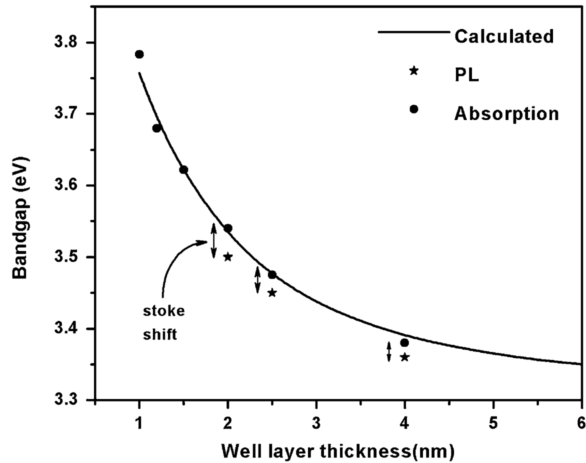

Fig. 3.19 Bandgap of ZnO MQWs obtained from room temperature PL and absorption measurements as a function of well layer thickness

3.6 Photoluminescence from Quantum Dots of ZnO

The evolution of next generation photonic devices and sensors etc. necessitated research on ZnO quantum structures. Although a significant amount of research on ZnO-based quantum wells has been reported in the literature; the work on ZnO Quantum Dots (ZQDs) grown on solid substrates is quite scanty. A study on ZQDs grown on solid substrate is important not only to understand the three dimensional quantum confinement effects on the excitonic transitions but also to create new forms of this material which could open more frontiers for its applications. As an example, by growing quantum dots (QDs) one can enhance the linear and non-linear responses in ZnO significantly.

Earlier the ZQDs were grown mainly using wet chemical methods [52–56]. About a decade ago, Ohkubo et al. [57] reported a study on the growth and characteristics of a single layer of ZQDs on atomically flat alumina substrates using PLD technique. To the best of our knowledge, we have grown for the first time, multilayer of ZQDs of varying size by PLD embedded in alumina matrix on optically polished c-axis oriented Sapphire substrates [58–60] and observed size-dependent blue shift in the ZnO bandgap due to 0D quantum confinement effect in line with theoretically calculated values. Recently, there have been a few reports on the PL spectroscopy studies on ZQDs; however, exact details of underlying optical transitions responsible for PL, especially if the dot's size is less than the excitonic Bohr radius, are not yet discussed in detail. We have recently found that some of the PL processes in ZnO dot's size less than the excitonic Bohr radius hereafter called ultra-small QDs show anomalous behaviors compared to their larger counterpart [59]. The basic question which arises from these studies that if at all the excitons exist in such ultra-small QDs? Our experiments suggests that the bandgaps of ultra-small QDs deviate significantly from the excitonic model and the LO phonon coupling with the recombining electron-hole pairs enhances.

These findings make us propose that excitons may not exist in ultra-small ZQDs and the optical transitions originate from the localized electron-hole pairs. The results of these studies are presented and discussed in the following sections.

Alternate ablation of the sintered targets of ZnO and Al_2O_3 was used to grow a multilayer matrix of alumina capped ZnO nanoparticles. Followed by the deposition of a base layer of alumina on the (0001) Sapphire substrates, 10-layer structure of alternate ZnO nanoparticles and alumina layer was grown at room temperature. While the alumina layer was grown for 120 s in all the samples, the deposition time of ZnO in different samples was varied in the range of ~ 10 to 120 s to grow the nanoparticles of different mean sizes [59]. The deposition of both these materials was carried out at a fluence of ~ 0.6 J/cm^2 in oxygen ambient at a pressure of about 10^{-2} Torr for good stoichiometry. The optical characteristics of ZQDs were studied using the optical absorption and PL spectroscopy studies of the multilayer structures at room temperature. Size and shape of these QDs were studied using Transmission Electron Microscopy and Atomic Force Microscopy. The size-dependent quantum confinement energy was calculated using the effective mass approximation (EMA) to understand the experimentally observed variation of the bandgap with in-plane quantum dot size. Results of these studies are discussed in following sections.

Figure 3.20a shows typical TEM viewgraph of ensemble of the ZQDs wherein it can be seen that these ZQDs are polydisperse and mostly of irregular shape with density of the order of $\sim 10^{13}$ cm^{-2}. While most of the ZQDs are isolated but at a few locations those are also coalesced. The inset of Fig. 3.20a shows the selected area electron diffraction (SAED) pattern which confirmed that the QDs were composed of ZnO. The presence of speckles in the SAED pattern indicate growth of certain specific planes in the ZQDs which were identified to be (0002), $(11\overline{2}0)$, (0004), and $(20\overline{2}3)$ from the observed SAED patterns. Although these ZQDs are of irregular shape, we approximated those to be somewhat circular at the base and hemispherical in three dimensions [60] to work out their theory. The size distribution of these ZQDs is shown in the histogram of Fig. 3.20b. From such histograms the mean radii of the ZQDs were calculated. These mean radii were used for correlating the average band-edges of the ensembles of ZQDs with their corresponding mean sizes, which is presented and discussed later.

The normal θ–2θ X-ray diffraction pattern of the ZQDs of mean radius of ~ 2.3 nm is shown in Fig. 3.21. One can see in this figure the presence of (0002), (0004), and $(20\overline{2}3)$ peaks of ZnO with dominant (0002) ZnO peak indicating most of the ZQDs are c-axis oriented hexagonal wurtzite structures. Presence of these peaks and their narrow line width are indicative of good crystalline quality of these ZQDs. Since this XRD pattern is of polydisperse ZQDs, the peak line width is contributed not only by the size of the particles which in present case in the nm regime but also by the large size distribution and crystalline defects of the particles as shown TEM measurements in Fig. 3.20b. Further it is expected that the larger sized ZQDs will contribute more intensity of the diffracted X-rays than their smaller counterparts and hence the peak line width is weighted more in favor of

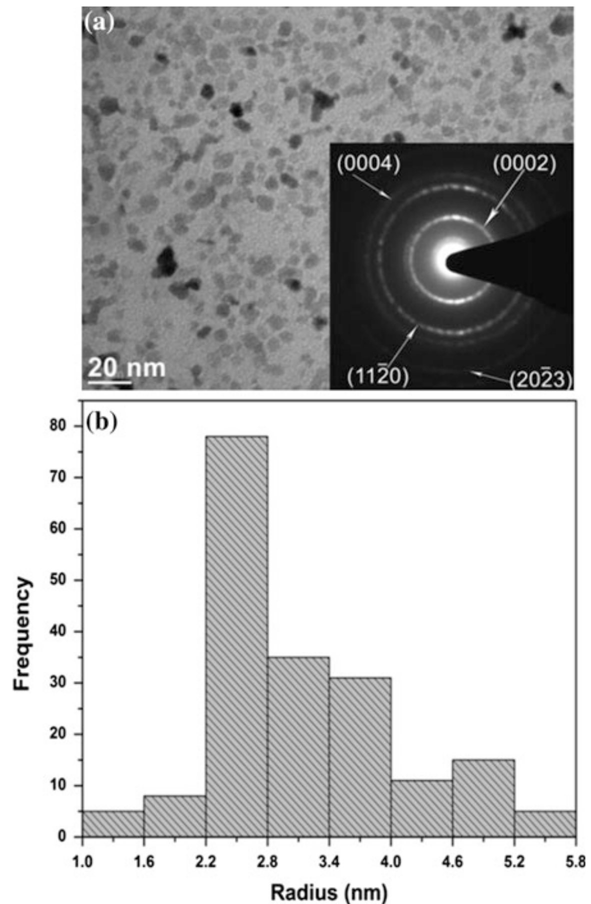

Fig. 3.20 **a** TEM viewgraph of a typical ensemble of the polydisperse ZQDs grown by pulsed laser deposition. Inset shows the selected area electron diffraction pattern of these dots. **b** Histogram showing size dispersion of the ZQDs. [Reprinted with permission from Kukreja et al. [59]. Copyright 2011 American Vacuum Society]

larger ZQDs. The calculated mean radius of the ZQDs using Debye–Scherrer formula for the dominant (0002) peak of Fig. 3.21 is ~5 nm, which is not very off from the mean radius of ~2.3 nm measured from the TEM data.

Figure 3.22 shows the room temperature absorption spectra of the multilayer matrices of alumina capped ZQDs of different mean radii. As can be seen these absorbance spectra do not show a series of isolated absorption peaks rather each spectrum, corresponding to a particular growth time and hence a mean size exhibits a broad absorption feature which is expected due to the broad distribution of ZQD sizes and is found to be due to the $1s_e$–$1s_h$ transition. Average values of the band-edges were obtained from the first derivative of these spectra and plotted as function of mean size of the ZQDs as shown in the inset of Fig. 3.22. It can be clearly seen from these spectra that the band-edge undergoes a monotonic blue shift with decreasing mean size of the ZQDs as expected from the quantum confinement effects [60, 61]. The bandgap of bulk ZnO at room temperature was taken to be ~3.3 eV, which is also shown in this figure for comparison. In this

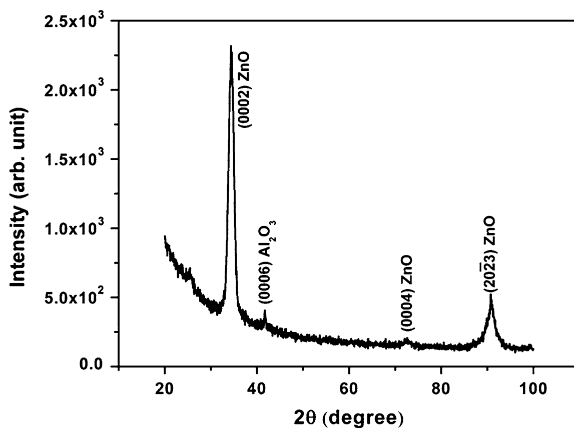

Fig. 3.21 X-ray diffraction pattern of the ZQDs. The weighted mean radius of these dots measured from the TEM data was about 2.3 nm. [Reprinted with permission from Kukreja et al. [59]. Copyright 2011 American Vacuum Society]

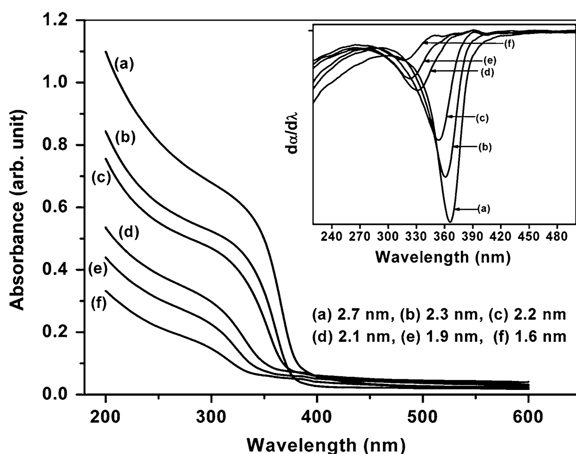

Fig. 3.22 Optical absorption spectra of the ZQDs of different mean radii. Inset shows the first derivative of these spectra. Spectral position of the lowest tip of these derivative spectra was taken as the average band-edge of the ZQDs' ensemble. [Reprinted with permission from Kukreja et al. [59]. Copyright 2011 American Vacuum Society]

figure, one can clearly see a drastic increase in the bandgap with decreasing size of the ZQDs in the range smaller than the excitonic Bohr radius (a_B) for ZnO which is calculated to be ~2.3 nm. In the size range greater than the excitonic Bohr radius, the variation of the bandgap is rather subdued as can be seen in this figure.

To understand these observations in two size-domains, i.e., the dot size shorter than the excitonic Bohr radius and other one with the dot size larger than the excitonic Bohr radius; we have used the effective mass approximation with strong confinement and weak confinement, respectively. In the size domain where the dot size is smaller than the excitonic Bohr radius, it is plausible that the exciton may not exist and therefore holes and electrons will experience a strong confinement with a characteristic reduced mass and a Coulombic interaction term. Therefore, the bandgap under these circumstances was calculated using the following expression [62–64]:

$$E = E_g + \frac{\hbar^2\pi^2}{2eR^2}\left(\frac{1}{m_e} + \frac{1}{m_h}\right) - \frac{1.786e}{4\pi\varepsilon_0\varepsilon_r R} - 0.248E_{\mathrm{ex}} \tag{3.20}$$

where E is the bandgap of the dots, E_g the bulk bandgap, R the dot size, m_e and m_h the effective masses of electron and hole, respectively. The last term, i.e., 0.248 E_{ex} represents the correlation energy, which can be expressed in terms of the excitonic binding energy E_{ex} [62]. We took $m_e = 0.24\ m_0$, $m_h = 0.45\ m_0$, $E_g = 3.359$ eV, $E_{\mathrm{ex}} = 59$ meV, and $\varepsilon_r = 6.01$ for ZnO [54–56]. The plot of the Eq. 3.20 is shown in Fig. 3.23 by solid lines. It can be seen that the match between the theoretical curve and the experimental data is reasonably good except for the case of 1.8 nm dots. This is attributed to the extremely low dot density at this deposition time and therefore a large scatter in the experimental data.

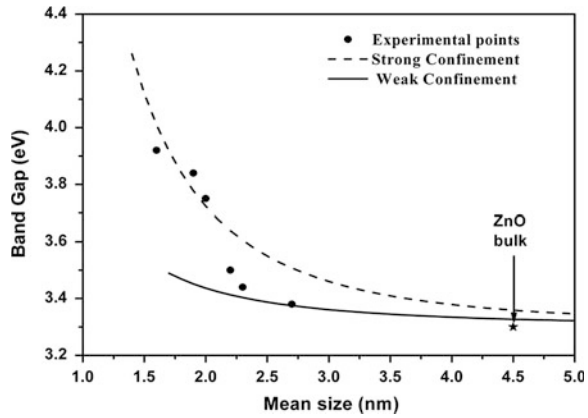

Fig. 3.23 Variation of average band-edge of the ZQDs' ensemble as a function of the mean radius. Experimental data are shown by filled circles while the fitting curves are plots of theoretically calculated values. The location of bandgap of bulk ZnO is also shown. [Reprinted with permission from Kukreja et al. [59]. Copyright 2011 American Vacuum Society]

In case of the dot size greater than the excitonic Bohr radius, the excitons can exist and therefore the Coulombic interaction term is replaced by the excitonic binding energy. Further, since the exciton is free to move in the dot, we need to take the translational mass in place of the reduced mass in Eq. 3.21. Thus in weak confinement region, the bandgap of the ensemble of the dots is calculated using the following expression [62]:

$$E = E_g + \frac{\hbar^2\pi^2}{2eMR^2} - E_{\mathrm{ex}} \tag{3.21}$$

where M is the translational mass of the exciton, which is the algebraic sum of the electron and hole effective masses, and R is the mean dot size. As can be seen here that the blue shift in the bandgap as a function of R in this case is much weaker than in the previous case of the strong confinement. A plot of the Eq. 3.21 is also shown in Fig. 3.23. Thus it can be seen in Fig. 3.23 that while the measured band-edge of the ZQDs of mean size of ~2.7 nm lies on this curve, the band-edges for ZQDs of sizes ~2.3 nm and shorter which we call ultra-small ZQDs tend to

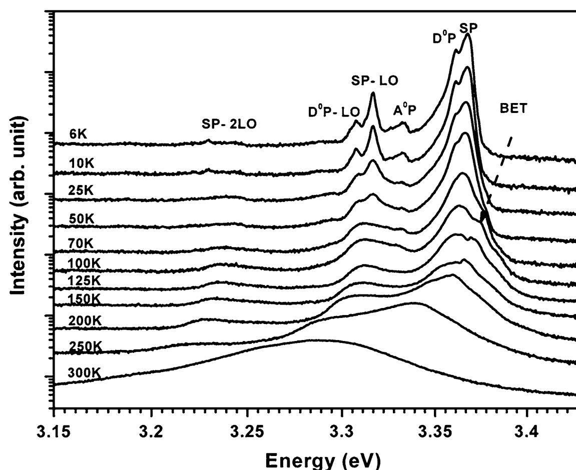

Fig. 3.24 PL spectra of the ZQDs' ensemble of mean radius of about 2.3 nm at different temperatures. [Reprinted with permission from Kukreja et al. [59]. Copyright 2011 American Vacuum Society]

deviate from this curve toward the curve for the strong confinement. It may be noted here that the in case of strong confinement it was assumed that the electrons and holes are not in the form of excitons as in case of bulk ZnO or QZDs of larger sizes but rather they are in the unbound state though interacting strongly through Coulomb forces and localized in the QDs. Although one can find a number of models in the literature [62, 63, 65–67] to understand the bandgap versus size behavior of the dots, but we find that the classic model of the effective mass approximation as seen separately in strong and weak confinement regimes explained our experimental data rather satisfactorily.

Figure 3.24 shows the temperature-dependent PL spectra from the multilayer matrix of ZQDs of mean radius of about 2.3 nm in a broad range of 6–300 K. It can be seen that the PL spectra of ZQDs exhibit various spectral features which conspicuously broaden and shift toward red with increasing temperature. As can be seen in Fig. 3.24, the PL spectra were dominated by two sharp peaks at ~3.368 (SP) and ~3.360 eV (D^0P) in the temperature range of 6–50 K.

Adjacent to these peaks one can see a weak PL feature (A^0P) peaking at ~3.333 eV. Beyond these primary PL peaks there are prominent LO phonon replicas of SP and D^0P peaks seen at ~3.296 and 3.288 eV, respectively, and the corresponding 2LO phonon replicas at ~3.224 and 3.216 eV, respectively, which are which are ~72 and 144 meV away, respectively, from the parent PL peaks. Presence of LO and 2LO phonon replicas of the primary PL transitions is a noteworthy observation. As the sample temperature was increased, the primary PL peaks of SP, D^0P, and A^0P diminished, broadened, merged, and shifted to lower energies and at about 70 K a new feature appeared at ~3.376 eV. At temperatures beyond 70 K, this new feature started dominating over the merged feature of SP and D^0P as can be seen in Fig. 3.24.

In literature one can find number of reports on the PL spectroscopy of ZQDs but most of them are for ZQDs with mean size larger than the excitonic Bohr radius [68–70]. To the best of our knowledge, there is no detailed report on the

temperature-dependent PL characteristics of alumina capped ultra-small ZQDs grown by PLD whose mean size is smaller than the excitonic Bohr radius. Hence an assignment of various PL spectral features to understand their thermal dynamics shown in Fig. 3.24 of the present experiments is based on the existing literature on PL from the ZQDs grown mostly by wet chemical methods or bulk ZnO. It may also be noted here that the PL spectral features in case of ultra-small ZQDs are expected to be blue shifted compared to those in the larger ZQDs and that of the bulk ZnO but this blue shift might be mostly counterbalanced by the red shift due to the significant Stoke shift [59, 68] and/or the heating of the ZQDs by the laser beam used as excitation source. Hence the spectral positions of the PL features of the ultra-small ZQDs may not be very different from their larger counterparts. Another important point to be illustrated here is that the optical transitions in the ultra-small ZQDs are expected to be non-excitonic in nature while in case of ZQDs of larger sizes, the PL features are described and interpreted in terms of excitonic transitions. Hence in the present case of ultra-small QDs, the emanating PL has been considered as those due to the electron-hole pairs which are localized in the QDs and hence strongly interacting with each other but unbound. The PL peak SP at ~3.368 eV in the temperature range of 6–50 K could be attributed to the recombination due to surface O_V donor-bound electron-hole pairs [71, 72], while the peak D^2P at ~3.360 eV could be due to the recombination of electron-hole pairs bound to the Al donors [73]. The presence of aluminum donors in the ZQDs is expected as Al_2O_3 has been used as capping as well as buffer layer in the ZQD multilayer structures. The PL peak A^0P at ~3.333 eV in the literature has been attributed to the stacking faults bound electron-hole pair recombinations [73]. The PL feature at ~3.376 eV, which appeared at ~70 K and red shifted with increasing sample temperature could be assigned to the band-edge transition (BT) of the ZQDs' ensemble. The spectral position of the band-edge measured from the pertinent experimental photo-absorption spectrum shown in Fig. 3.23 for the ZQDs of mean radius 2.3 nm was at ~3.45 eV. It may be noted here that the energy difference between the location of BET at low temperature and the experimentally measured absorption band-edge at room temperature is about 166 meV, which has been attributed mainly to the Stoke shift of the BET in the ZQDs expected in the ultra-small ZQDs due to the large electrostatic attractive field between the confined electron and holes [68]. As also discussed above, the other possibility for this red shift of BET compared to absorption band-edge at room temperature could be the rise in local temperature of the ZQDs due to the absorption of the excitation light from the He–Cd laser. Alim et al. have shown that the local temperature of ZnO can significantly rise at this power level [38] which can correspondingly contribute to the red shift of the PL band-edge of the ZQDs' also.

To ascertain the origin of these spectral features, the chemical state of different elemental constituents of the ZQDs was studied using XPS. The XPS profiles of the 4 nm thick layer of ZnO originally sandwiched between the buffer and the capping layers of alumina is shown in Fig. 3.25. For this measurement, the capping layer of alumina was completely removed in situ by etching the sample

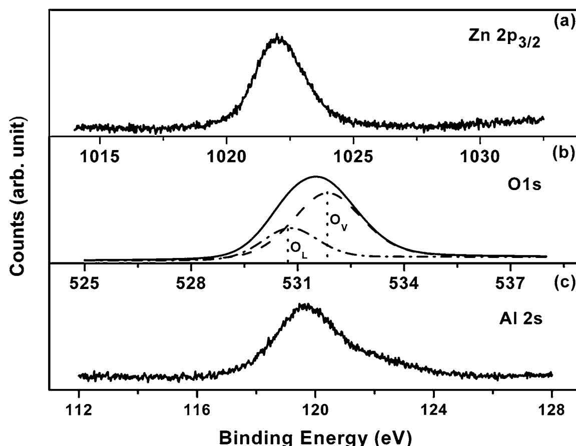

Fig. 3.25 X-ray photoelectron spectra of Zn 2p3/2 **a** O1 s and **b** and Al 2 s **c** levels from 4 nm thick layer of ZnO originally sandwiched between buffer and capping layers of alumina. The capping layer was removed by in situ etching before recording these spectra. [Reprinted with permission from Kukreja et al. [59]. Copyright 2011 American Vacuum Society]

surface before measurements. The elemental presence of Zn, O, and Al in the ZnO layer can clearly be seen in Fig. 3.25 through the observed Zn $2p_{3/2}$, O 1 s, and Al 2 s XPS peaks at binding energies ~1022, 531.5, and 119.5 eV, respectively [74, 75]. Incorporation of Al in ZnO is possible due to interdiffusion and mixing of constituents at the interfaces of the buffer/capping layer and the ZnO layers during the PLD [25]. The spectrum corresponding to O1S has been deconvoluted accurately when fitted with two peaks of Lorentzian mixed with Gaussian. The peak at ~530.15 eV designated as O_L has been attributed to O^{2-} ions on the lattice sites of hexagonal Zn^{2+} ion array and the peak at ~531.25 eV designated as (O_V) is associated with O^2-ions in the oxygen deficient regions within the matrix of ZnO [76]. As can be seen in Fig. 3.25, the peak corresponding to O_V which is the measure of the O^{2-} vacancies dominates over the peak corresponding to O_L. It has been reported in the literature that the oxygen vacancies which act as donors in ZnO are abundantly concentrated in the surface region [74, 76] and hence significant presence of donor-bound charge carriers in the surface region of the ZQDs is expected. In addition, the large surface to volume ratio of QDs supports the surface related recombination features further in the PL of ultra-small ZQDs.

The spectral positions of various PL peaks as a function of temperature are shown in Fig. 3.26. As can be seen at low temperatures, the PL recombinations are dominated by the SP peak and beyond ~125 K this peak merged with the higher energy feature corresponding to BET as mentioned earlier. The spectral position of the D^0P transition as a function of temperature is shown in limited temperature range in which this transition was conspicuously observed. Spectral positions of the phonon replicas of SP and BET transitions are also shown in Fig. 3.26.

The variation of these spectral PL features can be fitted using the Varshni relation discussed in Eq. 3.16. The best fit with the experimental values, shown by the dotted curve in Fig. 3.26, was obtained with the fitting parameters $\alpha = 8.2 \times 10^{-4}$ eV/K and $\beta = 1070$ K. These values of fitting parameters matched well with those for bulk ZnO reported in the literature [68]. It can also be

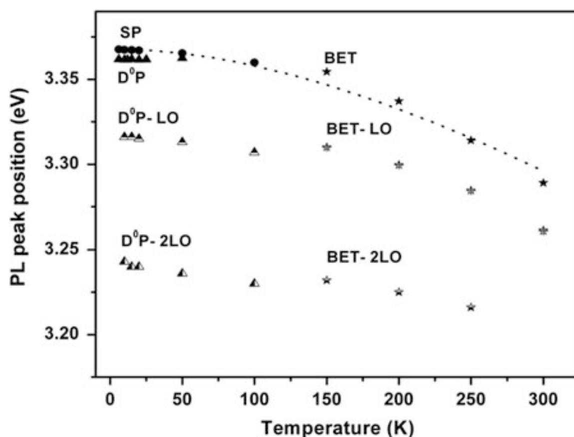

Fig. 3.26 Spectral positions of different PL peaks from ZQDs as a function of temperature. The points are experimental values and the dotted curve is a theoretical fit based on Varshni's equation (Eq. 3.16). [Reprinted with permission from Kukreja et al. [59]. Copyright 2011 American Vacuum Society]

seen in Fig. 3.26 that the energy gap between the spectral positions of SP and BET PL peaks and that for their LO phonon replicas slightly decreased with the increase in the sample temperature. This can be attributed to the existence of bound exciton complexes in which the electron-hole pairs are bound to the surface defects and the transition shifts from one complex to another as the temperature increases. This possibility has been discussed in detail by Teke et al. for the single crystalline bulk ZnO [36].

The activation energy of SP transition at $\sim$3.368 eV was estimated by plotting the integrated intensity of SP peak as a function of inverse temperature of the sample as shown in Fig. 3.27a. It can be clearly seen in this figure that the peak intensity follows the Arrhenius type of dependence on temperature given by the Eq. 3.15. The plot of the above equation is theoretical fit to data shown by the solid curve in Fig. 3.27a and from this fitting the activation energy E_a was found to be $\sim$10 meV. This value of the activation energy corresponds to binding energy of electron-hole pairs with the donor type surface defects of the QDs and is comparable to the one reported in the literature [72].

The line width (FWHM) of the PL peaks as a function of temperature corresponding to the SP and BET recombinations is shown in Fig. 3.27b. The observed FWHM of these PL peaks is attributed to three broadening mechanisms which have been described by Hellmann and O'Neill formulation [46, 47] discussed in Eq. 3.19. In case of ZQDs, the Γ_{inh} is the inhomogeneous broadening due to the size variation of the ZQDs [60]. The second term in Eq. 3.19 is linear in temperature and is governed by the corresponding phonon scattering coefficient γ_{ph} and represents broadening due to scattering with acoustic phonons. The third term corresponds to the broadening due to scattering of charge carriers with LO phonons. In the original formulation of Hellmann and O'Neill [46, 47], they took excitons as recombining charge carriers and the third term actually corresponds to the coupling of LO phonons with excitons as per their formulation [46, 47]. However, since in the present case we think that optical transitions are non-excitonic in the ultra-small ZQDs, the coupling of LO phonons with the

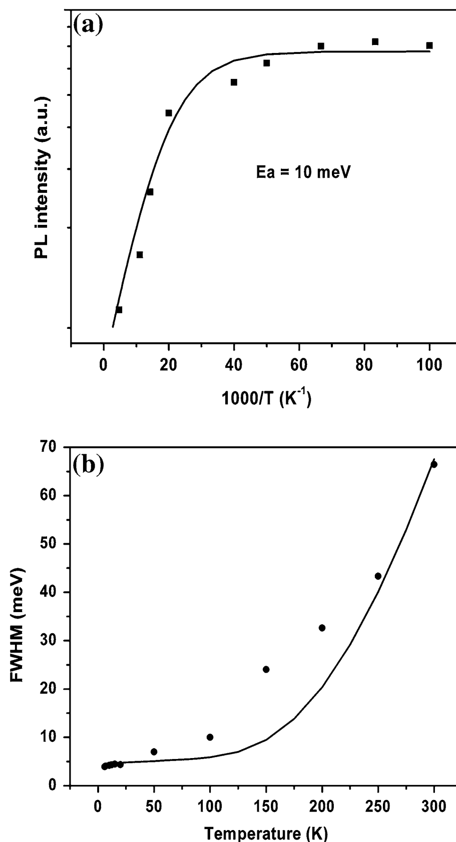

Fig. 3.27 **a** Variation of peak intensity of the PL originating from the surface bound electron-hole pairs' recombination (SP) with inverse of temperature *T*. **b** Line width (FWHM) of the SP (up to 100 K) and band-edge transition BET (beyond 100 K) as a function of temperature. Discrete points are experimental values and continuous curves are theoretical fits. [Reprinted with permission from Kukreja et al. [59]. Copyright 2011 American Vacuum Society]

electron-hole pairs is expected to be different from that with the excitons as proposed by Hellmann and O'Neill in their formulations mainly due to the fact that excitons are bosons and unbound electrons and holes being Fermions will not follow the Bose statistics. To the best of our knowledge, the formulation of LO phonon coupling with the unbound electron-hole pairs does not exist in the literature. In the absence of any such model, we used the Hellmann and O'Neill model based on excitons. The best fit of the above equation with the FWHM shown in Fig. 3.27b was obtained for $\gamma_{ph} = 12$ μV/K and $\Gamma_{LO} = 980$ meV. Two points are worth noting here. First that the LO phonon coupling coefficient Γ_{LO} is significantly large and comparable to that of bulk ZnO [69]. The value of Γ_{LO} for isolated free standing ZQDs of $\sim$4 nm diameter prepared by wet chemical method reported by Fonoberov is much lower than this [69]. Second, despite our best efforts to get a good fit, the calculated curve did not match very well with most of the experimental points in the intermediate range as can be seen in Fig. 3.27b. These observations lead to important conclusions for the ultra-small ZQDs. One is that the coupling of LO phonons with the recombining electron-hole pairs is significantly strong in the ultra-small ZQDs grown in the alumina host compared

to free standing ZQDs grown by wet chemical methods. This is contrary to the prevailing understanding that with decreasing size, the LO phonon coupling decreases [69, 71]. The strong coupling of the recombining electron-hole pairs with LO phonons is also clear from the presence of LO phonon replicas of SP and BET transitions seen in Fig. 3.24. This strong coupling of LO phonons with the recombining electron-hole pairs might be attributed to the quantum confinement effect, strain, and/or enhanced Coulombic interaction between the localized electrons and holes and the resulting Fröhlich interactions etc. In case of self-organized InAs/GaAs, Heitz et al. have shown that the interaction of LO phonon with excitons increased for such strained low-symmetry QDs because of the quantum confinement and piezoelectric effect [77]. Richters et al. have shown that coating of ZnO nanowire core with alumina shell strongly reduced the defects and enhanced the phonon interaction of the charged deep centers with the surrounding crystal lattice [78]. The other reason for this mismatch between the theoretical curve and the experimental points shown in Fig. 3.27b might be that the PL recombinations are non-excitonic in the present case. Since the theoretical formulation described by Hellmann and O'Neill is meant for the coupling of free excitons with LO phonons [46, 47], it may not match with the experimental points of the present experiment.

3.7 Conclusions

In conclusion, the temperature-dependent PL processes of the ZnO thin films grown on sapphire by PLD in the broad temperature range of 10–300 K gives insight into the various mechanisms and their relative influence on light emission, which in turn are related to the structural and crystalline quality of the films. In the present case since the dynamics of the PL processes was similar to that observed in bulk crystals of ZnO, it means reasonably good crystalline and structural quality of the PLD grown films on sapphire substrates. At low temperatures, the prominent PL peaks were due to neutral donor bound exciton and it is LO phonon-assisted transitions. With increasing temperatures, the free excitonic PL and associated phonon replicas dominated the PL spectra. The unusual temperature dependence of 1 and 2 LO phonon-assisted transitions of the F_X PL was explained by taking into account the kinetic energy of the gas like free excitons.

Photo luminescence spectroscopic investigation of ZnO MQWs of different well layer thicknesses grown on (0001) sapphire using an in-house developed buffer-assisted PLD scheme in the broad temperature range of 10 K to RT. Growth of ZnO/MgZnO MQWs was carried out on sapphire substrates using in-house developed buffer assisted PLD scheme. The 8 nm thick $Mg_{0.34}Zn_{0.66}O$ alloy films with bandgap of $\sim$4.1 eV was used as barrier layer and ZnO well layer thickness was varied in the range from $\sim$1 to 4 nm. Efficient room temperature PL was achieved on these MQWs which blue shifted with decreasing ZnO well layer thickness due to putative quantum confinement effects. The optical absorption

spectra of MQW structures showed monotonic blue shift in ZnO absorption edge and excitonic features entwined with the band-edges, which pointed to the excitonic nature of the PL transitions. At room temperature, the band-edge of these MQWs shifted from $\sim$3.36 to 3.78 eV on decreasing the well layer thickness from $\sim$4 to 1 nm in agreement with theoretically calculated values. In the range from 10 K to RT, the PL spectral line width increased and the peak shifted monotonically toward red with increasing temperature. The red shift of the PL peak with increasing temperature was attributed to the bandgap shrinkage in accordance with the Varshni's empirical relation. The increase in spectral line width with temperature was explained by considering the scattering of excitons with acoustic and optical phonons in different temperature regimes.

PL processes occurring in ensembles of alumina capped ZQDs grown using pulsed laser deposition were studied using temperature-dependent PL spectroscopy. The PL processes in alumina capped ultra-small ZQDs are different than those observed in their uncapped smaller or larger counterparts grown mostly by wet chemical routes. One basic difference is that the PL in alumina capped ultra-small ZQDs appears to be due to the localized electron-hole pairs instead of excitons. Therefore it is expected that the PL recombinations would be due to the electron-hole pairs and not through the excitonic recombinations. At low temperatures the PL spectra were dominated by the surface bound electron-hole pairs' recombinations mainly because of large surface to volume ratio and presence of oxygen vacancies in the surface region of the ultra-small ZQDs. The Al donor bound electron-hole pair recombinations are also observed because of the sputtering based mixing at the interfaces during the PLD and the diffusion of Al from the capping and/or buffer layers of alumina into the ZQDs. The band-edge PL transitions, red shifted by $\sim$166 meV with respect to the experimentally observed absorption band-edge due to Stokes shift and/or local heating of the ZQDs was observed only when the sample temperature was 70 K and higher. A small PL peak due to the defect bound recombination at $\sim$3.333 eV was also observed. The LO phonon coupling with the electron-hole pairs responsible for the PL emission is significantly large in the alumina capped ultra-small ZQDs. This is also evident from the presence of LO and 2LO phonon replicas in the PL spectra and the FWHM of the PL peak as a function of temperature. This is in contrast to the popular thought that LO phonon coupling with excitons deceases with decreasing size of the ZQDs.

Acknowledgments It is a pleasure to thank Prof. C. Klingshirn of University of Karlsruhe, Germany, Dr. G. M. Prinz and Dr. K. Thonke of Institut für Halbleiterphysik, Universität Ulm, Germany, and Dr. T. K. Sharma, Mr. Sanjay Porwal, and Dr. S. M. Oak of Raja Ramanna Centre for Advanced Technology, Indore for their help with the PL measurements and many fruitful discussions. We also thank Dr. T. Ganguli, Dr. A. K. Shrivastava, and Dr. S. K. Deb of our centre for their help with HRXRD and TEM measurements and Dr. D. M. Phase and Mr. A. Wadikar of UGC—DAE Centre for Scientific Research, Indore for their help with the XPS measurements. LMK thanks Alexander von Humboldt foundation of Germany for the financial support to visit University of Karlsruhe and Universität Ulm where low temperature PL studies were carried out.

References

1. Ü. Özgür, Ya.I. Alivov, C. Liu, A. Teke, M. A. Reshchikov, S. Doðan, V. Avrutin, S.-J. Cho, H. Morkoç, J. Appl. Phys. **98**, 041301 (2005)
2. C. Klingshirn, Chem. Phys. Chem. **8**, 782 (2007)
3. A. Tsukazaki, A. Ohtomo, T. Onuma, M. Ohtani, T. Makino, M. Sumiya, K. Ohtani, S.F. Chichibu, S. Fuke, Y. Segawa, H. Ohno, H. Koinuma, M. Kawasaki, Nat. Mater. **4**, 42 (2005)
4. Y.R. Ryu, T.S. Lee, J.A. Lubguban, H.W. White, Y.S. Park, C.J. Youn, Appl. Phys. Lett. **87**, 153, 504 (2005)
5. W.I. Park, J.S. Kim, G.-C. Yi, H.-J. Lee, Adv. Mater. **17**, 1393 (2005)
6. P. Misra, A.K. Das, L.M. Kukreja, Phys. Status Solidi C **7**(6), 1718 (2010)
7. P. Sharma, A. Mansingh, K. Sreenivas, Appl. Phys. Lett. **80**, 553 (2002)
8. A. Mang, K. Reimann, St. Rubenacke, Solid State Commun. **94**, 251 (1995)
9. A.Y. Polyakov, N.B. Smirnov, A.V. Govorkov, E.A. Kozhukhova, V.I. Vdovin, K. Ip, M.E. Overberg, Y.W. Heo, D.P. Norton, S.J. Pearton, J.M. Zavada, J. Appl. Phys. **94**, 2895 (2003)
10. S.O. Kucheyev, J.S. Williams, C. Jagadish, J. Zou, C. Evans, A.J. Nelson, A.V. Hamza, Phys. Rev. B **67**, 094115 (2003)
11. V.A. Coleman, C. Jagadish, *Basic Properties and Applications of ZnO*, in *Zinc Oxide Bulk, Thin Films and Nanostructures: Processing, Properties, and Applications*, ed. by C. Jagadish, S.J. Pearton (Elsevier, 2006)
12. R. Triboulet, J. Perriere, Prog. Cryst. Growth Charact. Mater. **47**, 65 (2003)
13. T. Fukumura, H. Toyosaki, Y. Yamada, Semicond. Sci. Technol. **20**, S103–S111 (2005)
14. D.M. Bagnall, Y.F. Chen, Z. Zhu, T. Yao, S. Koyama, M.Y. Shen, T. Goto, Appl. Phys. Lett. **70**, 2230 (1997)
15. A. Ohtomo, K. Tamura, M. Kawasaki, T. Makino, Y. Segawa, Z.K. Tang, G.K.L. Wong, Y. Matsumoto, H. Koinuma, Appl. Phys. Lett. **77**, 2204 (2000)
16. H.D. Sun, T. Makino, N.T. Tuan, Y. Segawa, Z.K. Tang, G.K.L. Wong, M. Kawasaki, A. Ohtomo, K. Tamura, H. Koinuma, Appl. Phys. Lett. **77**, 4250 (2000)
17. T. Ohnishi, A. Ohtomo, M. Kawasaki, K. Takahashi, Y. Yoshimoto, Appl. Phys. Lett. **72**, 824 (1998)
18. J.I. Pankove, *Optical Processes in Semiconductors* (Dover Publications, New York, 1971)
19. L. Birman, Phys. Rev. Lett. **2**, 157 (1959)
20. *Landolt-Bçrnstein*, New Series, Group III, vol. 17 B, 22, 41B, ed. by U. Rçssler, (Springer, Heidelberg, 1999)
21. C. Klingshirn, *Semiconductor Optics*, 3rd edn. (Springer, Heidelberg, 2006)
22. J.H. Davies, *The Physics of Low-Dimensional Semiconductors* (Cambridge University Press, Cambridge, 1998)
23. P. Harrison, *Quantum Wells* (Wires and Dots, New York, 2000)
24. P.K. Basu, *Theory of Optical Processes in Semiconductors: Bulk and Microstructures* (Clarendon Press, Oxford, 1997)
25. L.M. Kukreja, B.N. Singh, P. Misra, *Pulsed Laser Deposition of Nanostructured Semiconductors*, in *Bottom-up Nanofabrication: Supramolecules, Self-Assemblies and Organized Films*, ed. by K. Ariga, H.S. Nalwa, (American Scientific, California, 2008)
26. P. Misra, L.M. Kukreja, Thin Solid Films **485**(1–2), 42 (2005)
27. P. Misra, T.K. Sharma, L.M. Kukreja, Curr. Appl. Phys. **9**(1), 179 (2009)
28. A. Ohtomo, M. Kawasaki, T. Koida, K. Masubuchi, H. Koinuma, Y. Sakura, Y. Yashida, T. Yashuda, Y. Segawa, Appl. Phys. Lett. **72**, 2466 (1998)
29. C. Klingshirn, Phys. Status Solidi B **71**, 547 (1975)
30. D.C. Reynolds, D.C. Look, B. Jogai, C.W. Litton, T.C. Collins, W. Harsch, G. Cantwell, Phys. Rev. B **57**, 12151 (1998)
31. D.W. Hamby, D.A. Lucca, M.J. Klopfstein, G. Cantwell, J. Appl. Phys. **93**, 3214 (2003)

32. C. Solbrig, E. Mollwo, Solid State Commun. **5**, 625 (1975)
33. Y. Chen, D.M. Bagnall, H.-J. Koh, K.-T. Park, K. Hiraga, Z. Zhu, T. Yao, J. Appl. Phys. **84**, 3912 (1998)
34. D.M. Bagnall, Y.F. Chen, M.Y. Shen, Z. Zhu, T. Goto, T. Yao, J. Cryst. Growth **184/185**, 605 (1998)
35. S. Bethke, H. Pan, B.W. Wessels, Appl. Phys. Lett. **52**, 138 (1998)
36. A. Teke, Ü. Özgür, S. Doğan, X. Gu, H. Morkoç, B. Nemeth, J. Nause, H.O. Everitt, Phys. Rev. B **70**, 195207 (2004)
37. Douglas B. Chrisey, Graham K. Hubler, *Pulsed Laser Deposition of Thin Films*, (Wiley-interscience, 1994)
38. A. Alim Khan, A. Fonoberov Vladimir, A. Balandin Alexander, Appl. Phys. Lett. **86**, 053103 (2005)
39. M.S. Liu, L.A. Bursill, S. Prawer, K.W. Nugent, Y.Z. Tong, G.Y. Zhang, Appl. Phys. Lett. **74**, 3125 (1999)
40. E. Gross, S. Permogorov, B. Razbirin, J. Phys. Chem. Solids **27**, 1647 (1966)
41. T. Makino, Y. Segawa, M. Kawasaki, H. Koinuma, Semicond. Sci. Technol. **20**, 78 (2005)
42. M.H. Huang, S. Mao, H. Feick, H. Yan, Y. Wu, H. Kind, A. Dadgar, E. Weber, R. Russo, P. Yang, Room-temperature ultraviolet nanowire nanolasers. Science **292**, 1897 (2001)
43. P. Misra, T.K. Sharma, S. Porwal, L.M. Kukreja, Appl. Phys. Lett. **89**, 161912 (2006)
44. A. Ohtomo, A. Tsukazaki, Semicond. Sci. Technol. **20**, 1 (2005)
45. P. Misra, T.K. Sharma, G.M. Prinz, K. Thonke, L.M. Kukreja, in Proceedings IUMRS-ICAM, Banglore, Oct 7–12 2007, pp. V11–12
46. R. Hellmann, M. Koch, J. Feldmann, S.T. Condiff, E.O. Gobel, D.R. Yakovlev, A. Waag, G. Landwehr, Phys. Rev. B **48**, 2847 (1993)
47. M. O'Neill, M. Oestreich, W.W. Ruhle, D.E. Ashenford, Phys. Rev. **48**, 8980 (1993)
48. Y.P. Varshni, Physica **34**, 149 (1967)
49. B.P. Zhang, N.T. Binh, K. Wakatsuki, C.Y. Liu, Y. Segawa, N. Usami, Appl. Phys. Lett. **86**, 032105 (2005)
50. T. Mozume, J. Kasai, J. Appl. Phys. **95**, 1050 (2004)
51. P. Misra, T.K. Sharma, L.M. Kukreja, Superlattices Microstruct. **42**(1–6), 212–217 (2007)
52. U. Koch, A. Fojtik, H. Weller, A. Henglein, Chem. Phys. Lett. **122**, 507 (1985)
53. L. Spanhel, M.A. Anderson, J. Am. Chem. Soc. **113**, 2826 (1991)
54. E.M. Wong, J.E. Bonevich, P.C. Searson, J. Phys. Chem. B **102**, 7770 (1998)
55. J.J. Cavaleri, D.E. Skinner, D.P. Colombo Jr, R.M. Bowman, J. Chem. Phys. **103**, 5378 (1995)
56. E.M. Wong, P.C. Searson, Appl. Phys. Lett. **74**, 2939 (1999)
57. I. Ohkubo, Y. Matsumoto, A. Ohtomo, T. Ohnishi, A. Tsukazaki, M. Lippmaa, H. Koinuma, M. Kawasaki, Appl. Surf. Sci. **159–160**, 514 (2000)
58. S. Barik, A.K. Srivastava, P. Misra, R.V. Nandedkar, L.M. Kukreja, Solid State Commun. **127**, 463 (2003)
59. L.M. Kukreja, P. Misra, A.K. Das, J. Sartor, H. Kalt, J. Vac. Sci. Technol., A **29**(3), 120 (2011)
60. L.M. Kukreja, S. Barik, P. Misra Jr, Cryst. Growth **268**(3–4), 531 (2004)
61. L.M. Kukreja, P. Misra, J. Fallert, J. Sartor, H. Kalt, C. Klingshirn, IEEE Photon. Global **1** (2009)
62. L.E. Brus, J. Chem. Phys. **80**, 4403 (1984)
63. Y. Kayanuma, Phys. Rev. B **38**, 9797 (1988)
64. Y. Kayanuma, Phys. Rev. B **38**, 9797 (1988)
65. M.V. Rama Krishna, R.A. Friesner, Phys. Rev. Lett. **67**, 629 (1991)
66. P.E. Lippens, M. Lannoo, Phys. Rev. B **39**, 10935 (1989)
67. S.V. Nair, L.M. Ramaniah, K.C. Rustagi, Phys. Rev. B **45**, 5969 (1992)
68. K.-F. Lin, H.-M. Cheng, H.-C. Hsu, L.-J. Lin, W.-F. Hsieh, Chem. Phys. Lett. **409**, 208 (2005) and references cited therein
69. V.A. Fonoberov, K.A. Alim, A.A. Balandin, F. Xiu, J. Liu, Phys. Rev. B **73**, 165317 (2006)

70. W.-T. Hsu, K.-F. Lin, W.-F. Hseih, Appl. Phys. Lett. **91**, 181913 (2007)
71. V.V. Travanikov, A. Freiberg, S.F. Savikhin, J. Lumin. **47**, 107 (1990)
72. L. Wischmeier, T. Voss, I. Ruckmann, J. Gutowski, Nanotechnology **19**, 135705 (2008)
73. B.K. Meyer et al., Phys. Status Solidi B **241**, 231 (2003)
74. M. Chen, X. Wang, Y.H. Yu, Z.L. Pei, X.D. Bai, C. Sun, R.F. Huang, L.S. Wen, Appl. Surf. Sci. **158**, 134 (2000)
75. N. Ohtsu, M. Oku, T. Shishido, K. Wagatsuma, Appl. Surf. Sci. **253**, 8713 (2007)
76. M.N. Islam, T.B. Ghosh, K.L. Chopra, H.N. Acharya, Thin Solid Films **280**, 20 (1996)
77. R. Heitz, I. Mukhametzhanov, O. Stier, A. Madhukar, D. Bimberg, Phys. Rev. Lett. **83**, 4654 (1999)
78. J.-P. Richters, T. Voss, D.S. Kim, R. Scholz, M. Zacharias, Nanotechnology **19**, 305202 (2008)

Chapter 4
Effect of Oxygen Pressure on Photoluminescence Spectra and Hall Coefficients of Li–Ni Co-Doped ZnO Films Grown by a Pulsed Laser Deposition

K. Sakai, K. Ishikura, D. Ohori, D. Nakamura, A. Fukuyama, T. Okada, M. S. Ramachandra Rao and T. Ikari

Abstract Since the co-doping method is a key technique for the realization of *p*-type ZnO films, we grew samples by the co-doping of Li and Ni impurities using a pulsed laser deposition technique to investigate the formation of a possible acceptor level. The effect of the oxygen gas pressure on the physical properties is discussed. The electrical and optical properties of the films were investigated through Hall and photoluminescence (PL) measurements. Although *p*-type conduction was not observed, we were able to observe the change in conduction type from *n*-type to insulating upon increasing the oxygen pressure. PL spectra of co-doped samples were investigated at 10 K by comparison with those of mono-doped samples. Co-doping drastically changes the PL spectral shape and reveals additional peaks at 2.4 and 3.0 eV, which could not be observed in the spectra of mono-doped samples. The experimental results showed that the acceptor level was indeed formed by the co-doping of Li and Ni.

K. Sakai (✉)
Center for Collaborative Research & Community Cooperation, University of Miyazaki, 1-1 Gakuen Kibanadai-nishi, Miyazaki, Japan
e-mail: k-sakai@cc.miyazaki-u.ac.jp

K. Ishikura · D. Ohori · A. Fukuyama · T. Ikari
Faculty of Engineering, University of Miyazaki, 1-1 Gakuen Kibanadai-nishi, Miyazaki, Japan

D. Nakamura · T. Okada
Graduate School of Information Science and Electrical Engineering, Kyushu University, 744, Motooka, Nishi-ku, Fukuoka, Japan

M. S. Ramachandra Rao
Department of Physics, Nano Functional Materials Technology Centre and Materials Science Research Centre, Indian Institute of Technology Madras, Chennai 600036, India

M. S. R. Rao and T. Okada (eds.), *ZnO Nanocrystals and Allied Materials*, Springer Series in Materials Science 180, DOI: 10.1007/978-81-322-1160-0_4,
© Springer India 2014

4.1 Introduction

Zinc oxide (ZnO) semiconductors are promising materials for application to ultraviolet (UV) emitting and sensing devices. ZnO is a direct bandgap semiconductor with a bandgap energy of 3.37 eV at room temperature (RT) [1]. The large exciton binding energy of about 60 meV promises efficient exciton emission even at RT [1]. It is known that the conventionally grown ZnO crystal shows *n*-type conduction, probably due to the presence of donors caused by oxygen vacancies. Therefore, the fabrication of *p*-type ZnO semiconductors has been motivated by the need for the development of semiconductor devices such as homo-polar ZnO light-emitting diodes (LEDs). There is a co-doping method that is a key technique for the realization of *p*-type doping in ZnO semiconductors. It has been shown that *p*-type conduction can only be realized by the co-doping of group I or group V elements with a reactive donor [2–4]. At the same time, intriguing results of room-temperature ferromagnetism have been shown by doping with transition metal (TM) ions in ZnO [2–4]. More recent reports have also shown that oxygen vacancies play a key role in controlling *p*-type conductivity and ferromagnetism in ZnO [5–7]. Kumar et al. successfully grew *p*-type Li and Ni (Li–Ni) co-doped ZnO thin films by using pulsed laser deposition (PLD), and reported the appearance of ferromagnetism [8]. They grew thin-film samples with a thickness of 300 nm on c-sapphire substrates at 400 °C with an oxygen pressure between 3.5×10^{-3} and 10^{-2} mbar by PLD. The contents of Li–Ni impurities were fixed to 2 mol%. These ZnO thin films exhibited *p*-type conduction in a narrow region of the oxygen growth pressure (10^{-3}–10^{-2} mbar). Electrical, magnetic, and magnetotransport studies of these Li–Ni co-doped ZnO materials suggested that both *p*-type conductivity and ferromagnetic ordering could be tuned by carefully controlling the oxygen vacancies. Moreover, they clearly showed that the observed room-temperature ferromagnetism did not depend on the charge carrier type, but on the oxygen vacancies and carrier density [8].

However, reports on the systematic characterization of the optical properties were very scarce for Li–Ni co-doped ZnO thin films. It is usually important to study the electronic structures of semiconductors for a discussion of both the electrical and optical properties. Since the conductivity is strongly affected by impurities and/or defect levels formed in the bandgap, the PL technique, with its high sensitivity and high spatial resolution, is a powerful tool for investigation of the electronic states in the semiconductors. In this paper, we report on the photoluminescence properties of Li–Ni co-doped ZnO films grown under various O_2 background gas pressures. The relation between the conduction type and induced impurity levels formed in the bandgap region of ZnO by the co-doping of Li and Ni are discussed.

4.2 Experimental Procedures

Li–Ni co-doped ZnO films were grown on c-sapphire substrates at 400 °C with various O_2 background gas pressures (0.32, 0.5, 1, 2, 3, 5, and 10 Pa) using PLD. Following that reported by Kumar et al. [8], a *p*-type ZnO film was expected to be formed in this region. The pulsed laser used was a neodymium-doped yttrium aluminum garnet (Nd:YAG) laser ($\lambda = 355$ nm) operated at a repetition rate of 10 Hz with a laser fluency of 2.7 J/cm^2. The contents of Li–Ni impurities in the ZnO ablation target were fixed to 2 mol%. At the same time, Li–Ni mono-doped samples were also grown with a doping level of 2 mol% to allow a discussion of the effect of co-doping.

We estimated the carrier concentrations of our Li–Ni co-doped ZnO film by the Van der Pauw method at RT. Hall measurements were performed under a magnetic field of 0.5 T. The electrodes for the ohmic contact with the ZnO film were obtained from indium or gold.

For the PL measurements, a He–Cd laser (325 nm) was used as the excitation light source. The laser beam was focused on the sample through a light chopper. The sample was placed in a cryostat for the low-temperature measurements. The PL signal dispersed by a monochromator was detected by a photomultiplier and a lock-in amplifier. The PL measurements were performed at 10 K.

4.3 Results and Discussion

The electron carrier concentration, resistivity, mobility, and conduction type of these films were determined by Hall measurements. The results are shown in Table 4.1. Above 2 Pa, we could not observe the Hall measurement data because of the high resistivity of the sample. Therefore, we considered that the conduction type was insulating in this region. Below 1 Pa, Hall measurements could be carried out, and we found that the conduction types of the samples were *n*-type, and the carrier concentrations were of the order of 10^{18}. The *p*-type conduction could not be obtained in this O_2 pressure region for any of the samples. For the Ni mono-doped ZnO film, *n*-type conduction appeared, and the electron carrier concentrations were 3.0×10^{17} cm^{-3}. However, for the Li mono-doped ZnO film, the resistivity was too high for the Hall voltage to be observed. We considered this Li-doped sample to be insulating.

Figure 4.1 shows the PL spectrum of the Ni mono-doped ZnO film at 10 K. A broad peak was observed at around 3.35 eV. The PL peak at 3.376 eV of the nondoped ZnO nanowire single crystal observed in our previous measurements at 10 K, and we considered this to be due to the free exciton recombination [1]. Donor and acceptor bound excitons were also observed in the PL spectra at around 3.36 eV [1]. Therefore, we considered that this broad peak observed at 3.35 eV in Fig. 4.1 was due to a group of donor- or acceptor-bound excitons caused by Ni and

Table 4.1 Electrical properties of Li–Ni co-doped ZnO films at room temperature

O_2 pressure (Pa)	Carrier concentration (cm^{-3})	Resistivity (Ω cm)	Mobility (cm^2/Vs)
0.32	2.0×10^{19} (n)	4.4×10^{-2}	7.4
0.5	1.9×10^{18} (n)	8.1×10^{-2}	4.1
1	7.9×10^{18} (n)	1.9×10^{-1}	4.0
2	Insulating	–	–
3	Insulating	–	–
5	Insulating	–	–
10	Insulating	–	–

unintentionally incorporated impurities. Hereafter, we refer to this as the near-band-edge (NBE) transition. Moreover, note that the observed PL peak intensities of the NBE transition were very weak compared with those for the single crystal [1]. This is because the present ZnO film samples were grown at a lower temperature (400 °C) than before, and were polycrystalline. Since the photoexcited carriers are scattered or recombined at the crystal grain boundary and the lifetime became small, the PL intensity gets weaker. We could not observe the PL spectrum at RT because of the rapid thermal quenching of the PL signal.

It is especially noted in Fig. 4.1 that the PL signal related to defect levels such as oxygen vacancies was not observed. Qui et al. [9] reported the PL spectra of 5 % Ni-doped ZnO films at RT. They observed a broad peak that was decomposed into two Gaussian curves centered at 3.23 (384 nm) and 2.64 eV (470 nm), which were attributed to the emissions from free excitons and from Ni^{3+}-related and/or interstitial-oxygen-related impurity transitions, respectively [9]. Our PL spectral shape obtained for Ni-doped ZnO film in Fig. 4.1 is similar to the PL spectra of these materials. The temperature shift of the bandgap energy of the nondoped ZnO crystal was estimated to be 65 meV from 300 to 10 K, as determined from our PL

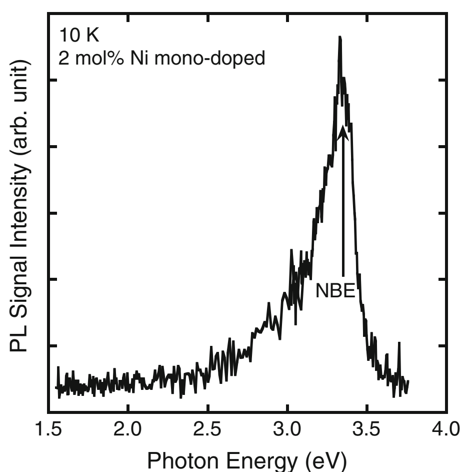

Fig. 4.1 PL spectra of 2 mol% Ni mono-doped ZnO film. Near-band-edge (NBE) is indicated by the *arrows* in the figure

data of nondoped ZnO nanowire single-crystal samples grown by the nano-particle-assisted pulsed-laser deposition (NAPLD) technique [1]. This indicates that our NBE peak should appear at around 3.29 eV at RT, and is about 60 meV higher than that observed by Qui et al. Although there is a large tail on the lower energy side of the NBE transition, as shown in Fig. 4.1, the Ni^{3+}-related peak at 2.64 eV (RT) reported by Qui et al. was not observed. This may be because of the small Ni concentration in our ZnO crystal.

We next discuss why the conduction of the Ni mono-doped sample is *n*-type despite the fact that there is no PL peak related to defect levels such as oxygen vacancies, known to be a dominant source of donors, for our Ni-doped ZnO film. X-ray photoelectron spectroscopy (XPS) measurements confirmed the existence of Ni^{3+} and Ni^{2+} bonds in the Ni mono-doped ZnO film. When the Zn atom is substituted by the Ni atom and ionized to Ni^{3+} by the interaction between other atoms or vacancies in the ZnO lattice, this Ni atom can release an electron. This is because the Ni^{3+} ion behaves as a source of free electrons for *n*-type conduction.

From PL observations, Tong et al. [10] reported that Ni doping leads to a decrease in the concentration of intrinsic defects such as oxygen vacancies. Another report showed that oxygen vacancies played an important role in the magnetic origin for oxide diluted magnetic semiconductors (DMSs) [11]. Oxygen vacancies can result in a considerable change in of the band structure of host oxides and the formation of bound magnetic polarons (BMPs), which explain the origin of the ferromagnetism [8, 12]. When BMPs are formed by the interaction of a Ni atom and an oxygen vacancy, the PL peak related to the oxygen vacancy should be observed more strongly in Ni-doped ZnO than that in the nondoped material [12]. However, we considered that this was not the case. The oxygen vacancy may not act as a donor because it releases an electron to form the BMPs. Therefore, the PL peak related to defect levels such as oxygen vacancies is not observed in the present case.

Figure 4.2 shows the PL spectrum of the Li mono-doped ZnO sample. The broad peak around 3.35 eV is considered to be the NBE transition, as in the case of the Ni-doped sample. In addition to this, a broad luminescence band was observed below the NBE transition. Although the green luminescence (GL) around 2.5 eV caused by oxygen vacancies is well-known [13], the peak position in the present spectrum was centered at 2.1 eV. This may be yellow luminescence (YL) due to the deep Li acceptor level [13]. According to the results reported by Schirmer et al., the YL is polarized at low temperatures and is explained by the two metastable orientations of the Li_{Zn} center in the ZnO lattice [14]. Ozgur et al. [13] also reported that the YL band is quenched at temperatures above 200 K with an activation energy of about 0.5 eV. This may be the case in our sample. Since the observed PL intensity of the Li mono-doped sample became very weak at higher temperatures, the activation energy of the YL could not be estimated for this sample.

According to the electronic band-structure calculations by Yamamoto and Katayama-Yoshida [15], the acceptor impurity states introduced by Li doping are considerably delocalized and form a shallow acceptor level. However, the increase

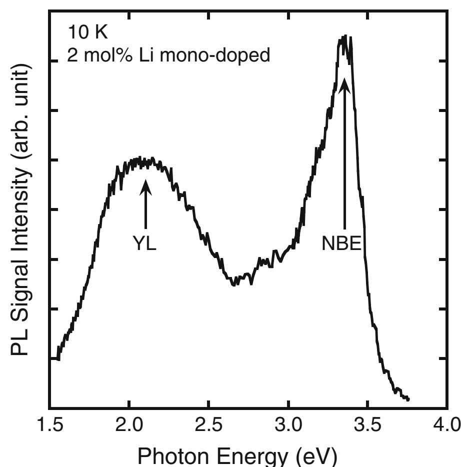

Fig. 4.2 PL spectra of 2 mol% Li mono-doped ZnO film. Near-band-edge (NBE) and yellow band emissions (YL) are indicated by the *arrows* in the figure

in Madelung energy upon doping with Li causes the formation of oxygen vacancies at the same time [15]. The oxygen vacancies, acting as donors, are located near the Li sites [15]. Although the PL related to the acceptor-bound excitons could not be resolved owing to the broadening of the emission line of the NBE transition, our PL results could be explained by the above discussion. Thus, the conductivity of this sample showed insulating behavior because of the self-compensation between the Li acceptors and the donors originating from the oxygen vacancies.

Figure 4.3 shows some PL spectra measured from different irradiation positions on the sample surface for the Li–Ni co-doped ZnO sample grown at 0.32 Pa. The numbers labeled on each spectrum in Fig. 4.3 show the measurement times for each irradiation position. Three PL peaks were observed between 1.5 and 3.8 eV, as shown by the arrows in Fig. 4.3. However, it was found that the intensity ratios of these three PL peaks were different for different irradiation positions, indicating that the ZnO film was not homogeneous. To investigate the origin of these peaks, we decomposed the PL spectrum into three components by the Gaussian fitting procedure. Then, the ratio of each PL peak was compared with the samples deposited under various O_2 background gas pressures.

It was found that the PL signal observed in Fig. 4.3 decomposes into three PL peaks at 2.4, 3.0, and 3.32 eV. An example of these Gaussian fitting simulations is shown in Fig. 4.4 with the curves drawn as dashed lines. The sum of the three PL peaks is shown by the open circles. As shown in Fig. 4.4, the experimental PL data and the sum of the simulated peaks were in good agreement. Moreover, the PL integrated intensity ratio of each peak was estimated, so that the sum of the three peak intensities became one. The dependence of the observed PL peak intensities of the co-doped samples on the oxygen background gas pressure is shown in Fig. 4.5. The regions for the conduction types are also shown in Fig. 4.5, with *n*-type and insulating conductions observed below and above 1 Pa, respectively. The PL intensity ratio of the 3.32 eV peak as a function of O_2 pressure has a

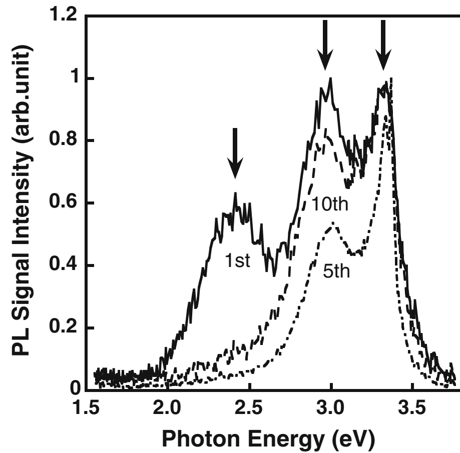

Fig. 4.3 Some PL spectra measured by changing the irradiation position of the excited laser for the Li–Ni co-doped ZnO sample grown at 0.32 Pa

maximum at around 1 or 2 Pa. This peak was due to the bound exciton luminescence near the bandgap of ZnO. This indicates that there was a suitable O_2 background gas pressure for ZnO crystal growth. The bound exciton, which has a low binding energy, is dissociated in the crystal when the crystallinity is poor.

On the other hand, we observed a new dominant PL peak at 3.0 eV for the co-doped samples, which was not observed for the (Fig. 4.1) Li–Ni mono-doped (Fig. 4.2) samples in the present study. This PL peak intensity was dominant for all O_2 background gas pressures as shown in Fig. 4.5. The conduction type changed from *n*-type to insulating in this O_2 pressure region. However, the PL peak at 3.0 eV was always observed for the samples that showed *n*-type conduction. Thus, it is reasonable to consider that this peak is due to the donor level formed by the co-doping of Li and Ni.

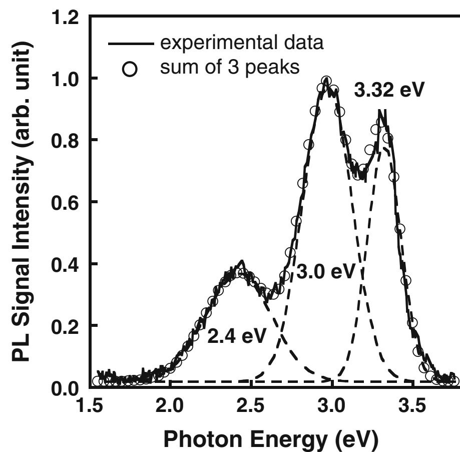

Fig. 4.4 Gaussian curve fitting results for PL spectrum of Li–Ni co-doped ZnO sample grown at 0.32 Pa

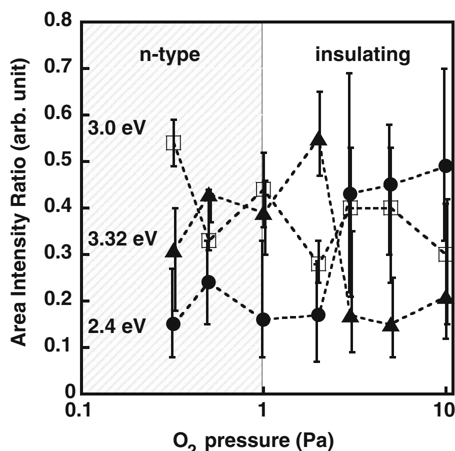

Fig. 4.5 Dependence of the observed PL peaks of the Li–Ni co-doped ZnO film on the O_2 background gas pressure. The regions of the conduction types of the samples are also shown in this figure

The observed PL peak at 2.4 eV, or the so-called GL, may be caused by defect levels such as oxygen vacancies [13]. Since the GL peak could not be observed in the Ni mono-doped sample, the appearance of the GL peak in Fig. 4.1 is due to the effect of co-doping of Li and Ni. However, this assignment is not reasonable in the case of the co-doped sample, because the PL signal intensity ratio of the 2.4 eV peak increases drastically above 2 Pa. The Hall measurements showed that in this region, the conduction type changed from *n*-type to insulating. Moreover, the donor level at 3.0 eV existed for all O_2 background gas pressures. Therefore, it is reasonable to consider that this peak is due to the acceptor level caused by the co-doping of Li and Ni. Although the deep acceptor level around 2.1 eV is formed in the bandgap of ZnO in the case of Li mono-doping [13], the formation of donors due to oxygen vacancies is drastically reduced by Ni mono-doping through the formation of BMPs, and a new deep acceptor level is formed at around 2.4 eV by the co-doping of Li and Ni. Consequently, the conduction shows insulating behavior because of the self-compensation between the acceptor and donor levels.

4.4 Conclusion

We tried to use PLD to develop Li–Ni co-doped ZnO films with *p*-type conduction under various O_2 background gas pressures. We also investigated the electrical and luminescence properties of these films to clarify the mechanism for the materialization of *p*-type conduction. In the present study, we could not observe the *p*-type behavior of ZnO thin films from Hall measurements. However, we observed a change in the conduction type from *n*-type to insulating upon increasing the oxygen pressure. Moreover, we observed a drastic change in the PL spectra of co-doped ZnO films by comparing them with those of mono-doped ZnO films. The additional PL peaks observed at 2.4 and 3.0 eV are due to the acceptor

and donor levels formed upon co-doping, and come from the relations between the electrical and optical properties, respectively. It is concluded that these impurity levels determine the conduction type of co-doped ZnO films.

Acknowledgments This work was supported by the Special Coordination Funds for Promoting Science and Technology from the Japan Science and Technology Agency, and also by a Grant-in-Aid from the Ministry of Education, Science, Sports and Culture, Japan.

References

1. K. Sakai, K. Noguchi, A. Fukuyama, T. Ikari, T. Okada, Jpn. J. Appl. Phys. **48**, 085001 (2009)
2. J.G. Lu, Y.Z. Zhang, Z.Z. Ye, L.P. Zhu, L. Wang, B.H. Zhao, Q.L. Liang, Appl. Phys. Lett. **88**, 222114 (2006)
3. A. Tsukazaki, A. Ohtomo, T. Onuma, M. Ohtani, T. Mahino, M. Sumiya, K. Ohtani, S.F. Chichibu, S. Fuke, Y. Segawa, H. Ohno, H. Koinuma, M. Kawasaki, Nat. Mater. **4**, 42 (2005)
4. Z. Jin, T. Fukumura, M. Kawazaki, K. Ando, H. Saito, T. Sekiguchi, Y.Z. Yoo, M. Murakami, Y. Matsumoto, T. Hasegawa, H. Koinuma, Appl. Phys. Lett. **78**, 3824 (2001)
5. F.X. Xiu, Z. Yang, L.J. Mandalapu, J.L. Liu, Appl. Phys. Lett. **88**, 152116 (2006)
6. S. Ramachandran, J. Narayan, J.T. Prater, Appl. Phys. Lett. **88**, 242503 (2006)
7. G. Xing, D. Wang, J. Yi, L. Yang, M. Gao, M. He, J. Yang, J. Ding, T.C. Sum, T. Wu, Appl. Phys. Lett. **96**, 112511 (2010)
8. E.S. Kumar, S. Venkatesh, M.S.R. Rao, Appl. Phys. Lett. **96**, 232504 (2010)
9. D.J. Qui, H.Z. Wu, A.M. Feng, Y.F. Lao, N.B. Chen, T.N. Xu, Appl. Surf. Sci. **222**, 263 (2004)
10. L. Tong, T. Cheng, H. Han, J. Hu, X. He, Y. Tong, C.M. Schneider, J. Appl. Phys. **108**, 023906 (2010)
11. J.M.D. Coey, M. Venkatesan, C.B. Fitzgerald, Nat. Mater. **4**, 173 (2005)
12. J. Iqbal, B. Wang, X. Liu, D. Yu, B. He, R. Yu, New J. Phys. **11**, 063009 (2009)
13. Ü. Özgür, Y.I. Alivov, C. Liu, A. Teke, M.A. Reshchikov, S. Doğan, V. Avrutin, S.-J. Cho, H. Morkoç, J. Appl. Phys. **98**, 041301 (2005)
14. O.F. Schirmer, D. Zwingel, Solid State Commun. **8**, 1559 (1970)
15. T. Yamamoto, H. Katayama-Yoshida, Phys. B 302–303, 155 (2001)

Chapter 5
Lasing Characteristics of an Optically-Pumped Single ZnO Nanocrystal and Nanomachining for Controlling Oscillation Wavelength

K. Okazaki, T. Shimogaki, I. A. Palani, M. Higashihata, D. Nakamura and T. Okada

Abstract Lasing characteristics from a single ZnO nanocrystal excited by third harmonic of a Q-switched Nd:YAG laser beam (355 nm, 5 ns) were investigated for the application to ultraviolet (UV) laser diode (LD) by using ZnO nanocrystals as building blocks. Those ZnO nanocrystals were synthesized on a silicon substrate with a catalyst of gold by a carbothermal chemical vapor deposition (CVD) method. ZnO nanowires and ZnO nanosheets were synthesized by changing the synthesis conditions and the dependence of lasing characteristics on the different forms were investigated. The emission spectra observed from a single ZnO nanowire and ZnO nanosheet showed the obvious lasing characteristics having mode structure and a threshold for lasing on the input–output characteristics. The threshold power density of a ZnO nanowire and a ZnO nanosheet was measured to be about 150 and 50 kW/cm^2, respectively. Then, the oscillation mechanisms were discussed on those ZnO nanocrystals, and it was concluded that each lasing mechanism was attributed to the microcavity effect due to the strong UV light confinement caused by the high refractive index of ZnO ($\approx$2.4) for UV light. ZnO can be a superior UV laser medium and an UV nano-laser source also can be expected. However, the observed lasing spectra from both ZnO nanocrystals had mode structure, and a single longitudinal mode lasing would be required for the stabilization of the output power and the prevention of light dispersion. Therefore, we considered the possibilities of the single longitudinal mode lasing from a single ZnO nanowire using distributed Bragg reflector lasing machined by focused ion beam with Ga ions focused up to 7 nm and a single ZnO nanosheet using subwavelength machining by Fresnel diffraction for 2D photonic crystal. We also observed the laser-induced motions (LIM) of ZnO nanocrystals dispersed on a substrate in the air when they were excited by the UV laser beam at high excitation power over several MW/cm^2 which could be attributed

K. Okazaki · T. Shimogaki · I. A. Palani · M. Higashihata · D. Nakamura · T. Okada (✉)
Graduate School of Information Science and Electrical Engineering,
Kyushu University, 744 Motooka, Nishi-ku, Fukuoka 819-0395, Japan
e-mail: okada@ees.kyushu-u.ac.jp

M. S. R. Rao and T. Okada (eds.), *ZnO Nanocrystals and Allied Materials*,
Springer Series in Materials Science 180, DOI: 10.1007/978-81-322-1160-0_5,
© Springer India 2014

to the electromotive force due to piezo effects of ZnO nanocrystals, and a simple alignment method of ZnO nanocrystals was considered by the use of the LIM and voltage-applied electrodes on a substrate.

5.1 Introduction

Zinc oxide (ZnO) is one of the most promising semiconductor materials in ultraviolet (UV) region. ZnO belonging to compound II–VI semiconductor has a wide band gap of approximately 3.37 eV at room temperature and a large exciton binding energy of approximately 60 meV that is significantly larger than the thermal energy at room temperature which corresponds to 26 meV. It can ensure an efficient exciton emission at room temperature with a low excitation energy. Gallium nitride (GaN) with the band gap of 3.44 eV at room temperature has already been used for UV devices such as light emitting diode (LED), laser diode (LD). ZnO and GaN have remarkably similar characteristics each other. Both ZnO and GaN are hexagonal wurtzite crystals. In addition, the lattice constants of ZnO are $a = 0.325$ nm and $c = 0.521$ nm, and the ones of GaN are $a = 0.312$ nm and $c = 0.519$ nm. However, ZnO has some superior conditions to GaN, including the larger exciton binding energy of ZnO than the exciton binding energy of GaN which is 24 meV and a great deal of resources of ZnO. From these advantages, ZnO is a promising material replacing GaN for UV applications.

Nanostructured ZnO has attracted a great interest due to their importance in both scientific research and potential technological applications. Considerable efforts have been made on the synthesis and study of nanostructured ZnO. For example, various nanostructured ZnO crystals have been synthesized by various approaches, such as nanowires by nanoparticle-assisted pulsed-laser deposition (NAPLD) [1–5] and physical vapor deposition [6], nanorods by chemical vapor deposition (CVD) [7] and molecular beam epitaxy [8], nanosheets by CVD [9], electrodeposition method [10, 11] and soft-solution route [12]. Those ZnO nanocrystals have an excellent crystalline due to the small volume.

Due to the excellent crystalline, UV-stimulated emission at room temperature from optically pumped ZnO nanocrystals has been reported. A lot of investigations on the lasing from a ZnO nanowire and nanorod have been reported, which is responsible for a microcavity effect of the nanowire itself [13–15]. The lasing from a number of optically pumped ZnO nanosheets was also reported [11, 12]. In addition, there is a different lasing mechanism on a random lasing from ZnO nanorods [16] or nanoparticles [17], where closed loops between a number of nanocrystals were formed and the random laser oscillation took place in the closed loop. In the case of random lasing, relatively higher excitation power around several MW/cm^2 $\sim$ is needed for laser oscillation than the excitation power of the microcavity lasing. Recently, a lasing from electrically pumped ZnO nanocrystals has also been reported [17–19]. Those reports indicate that ZnO nanocrystals can be candidates for excellent UV laser mediums.

However, there are some major challenges to be solved for a practical UV LD application, including comparison of microcavity lasing characteristics on the different forms of the nanocrystals, a multi-longitudinal mode lasing from those ZnO nanocrystals, an alignment method of ZnO nanocrystals on a substrate and unstable output from an electrically pumped ZnO nanocrystals.

In this study, we report on the further investigations of the lasing characteristics such as oscillation spectra and a threshold power density from a single ZnO nanocrystal excited by an UV laser beam. In concrete terms, two different forms of a ZnO nanowire and a ZnO nanosheet synthesized by a carbothermal CVD method were examined. Even though the lasing spectra form both of ZnO nanocrystals were observed, the spectra had a modal structure due to the microcavity effect. Since the practical application to UV LD will require a single longitudinal mode lasing, the realization was considered by the use of distributed Bragg reflector (DBR) laser on a ZnO nanowire which can be machined by a focused ion beam focused up to 10 nm below. The DBR laser for a ZnO nanowire is 1D photonic crystal, and 2D photonic crystal would be required for a ZnO nanosheet. From the calculation, the machining resolution below 100 nm will be needed, and therefore subwavelength machining method was considered by the use of an electrical field propagation simulator. As a demonstration, a silica glass substrate was machined at the subwavelength resolution by a CO_2 laser beam ($\lambda = 10.6$ μm), and a simple and high-throughput method with a laser processing was suggested. If the technique is applied to an UV excimer laser, the nanomachining below 100 nm can be realized. Finally, alignment methods of ZnO nanocrystals on a substrate were considered by the use of laser-induced motions (LIM) of ZnO nanocrystals and voltage-applied electrodes.

5.2 Synthesis of ZnO Nanocrystals with a Carbothermal CVD Method

ZnO nanocrystals were synthesized by a carbothermal CVD method. The mixed powder of ZnO and graphite was used, in which graphite worked as a promoter of evaporation of ZnO. A silicon substrate was used for the deposition of ZnO, and a gold layer of 1 nm thickness, as a catalyst, was evaporated on the silicon surface in advance. The mixed source of ZnO and graphite was placed in an alumina boat, and then the silicon substrate was located about 1 cm above the sample where the gold-evaporated surface was facing the sample. After the prepared alumina boat was inserted to the center of a silica glass vacuum chamber, the air in the chamber was evacuated up to several Torr by a vacuum pump. Mixed gas of argon (Ar) and oxygen (O_2) were allowed to pass with the fixed flow rate of 100 and 3 sccm, respectively. Various ZnO nanocrystals are easily synthesized on the silicon substrate by changing the synthesis conditions. ZnO nanowires were synthesized at the temperature of 1,000 °C, the ambient gas pressure of 100 Torr and the synthesis time of 30 min.

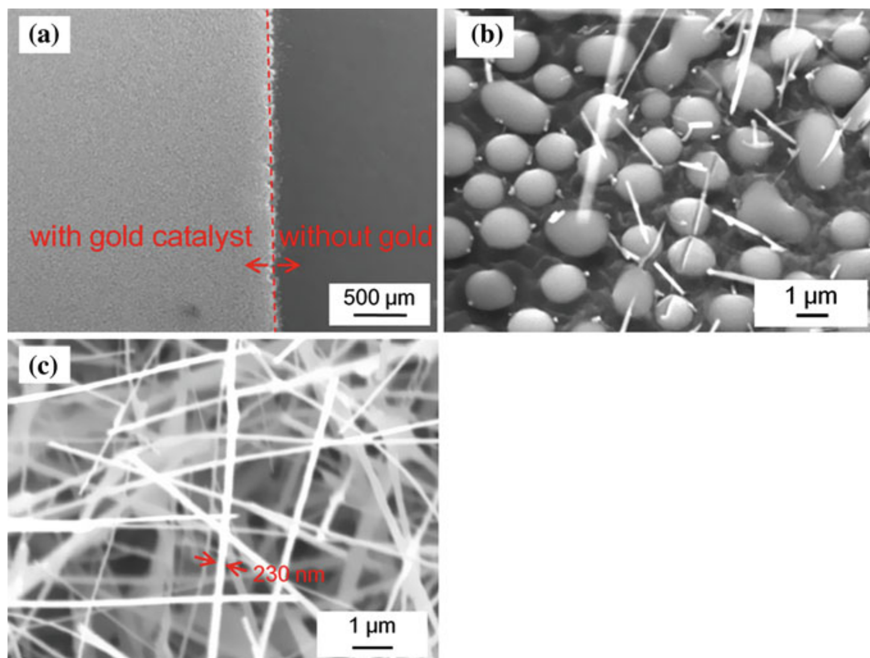

Fig. 5.1 ZnO nanowires synthesized on a silicon substrate with the gold catalyst by a CVD method. A large quantity of nanowires were synthesized just only on gold-evaporated side (a), and ZnO nuclei from which ZnO nanowires grew were obviously formed by the help of a gold catalyst (b), and the ZnO nanowires have the length of several dozen μm, and the width of about 230 nm (c)

Figure 5.1 shows a scanning electron microscope (SEM) (KEYENCE, VE-7800S) image of the silicon substrate where ZnO nanowires were synthesized specifically on the gold-evaporated side and did not grow without gold catalyst. Figure 5.1b shows the ZnO nuclei formation at the boundary of the area with and without gold and the nanowires seem to grow from those nuclei. Since the nuclei were only formed on the gold-evaporated side, it can be assumed that they are formed with the help of gold catalyst. Figure 5.1c shows the magnified image of the ZnO nanowires in Fig. 5.1a. The length of the nanowires synthesized by a CVD method was relatively long, and those were several dozen μm in length, and the diameter of the nanowire was about 200 nm as shown in Fig. 5.1c.

ZnO nanosheets were synthesized when the synthesis conditions of the temperature and the ambient gas pressure were changed into 1,100 °C and 300 Torr, respectively. Figure 5.2 shows SEM images of the ZnO nanosheets. ZnO nanosheets were synthesized in a form of an island as shown in Fig. 5.2a, and the magnified image was shown in Fig. 5.2b, and it seems that the nanosheets require several steps to grow. First, the nanowire grows as a principal axis. Next, the

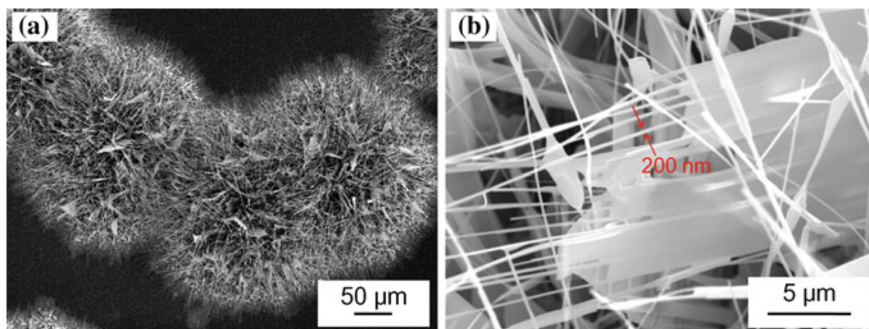

Fig. 5.2 **a** Mixed ZnO nanosheets and ZnO nanowires were synthesized on a silicon substrate in a form of islands. **b** A magnified image of a single nanosheet which has frameworks of parallel nanowires of about 200 nm

multi-parallel nanowires grow perpendicular to the main nanowire, and the configuration like a comb is formed. Finally, the spaces between the parallel nanowires are filled with ZnO nanoparticles. Thus, the ZnO nanosheets are formed by a framework of ZnO nanowires. The thickness of the nanosheets in Fig. 5.2b was almost same as that in the framework (200 nm).

In addition, relatively thick nanosheets were also synthesized on the same substrate as shown in Fig. 5.3a, b, where the thickness was about 570 nm. The ZnO nanosheet was observed by a transmission electron microscopy (TEM) (JEOL, JEM-1300NEF) as shown in Fig. 5.4. The ZnO nanosheet was single crystalline and the lattice spacing in the planar direction was 0.26 nm corresponding to the distance between (0002) planes.

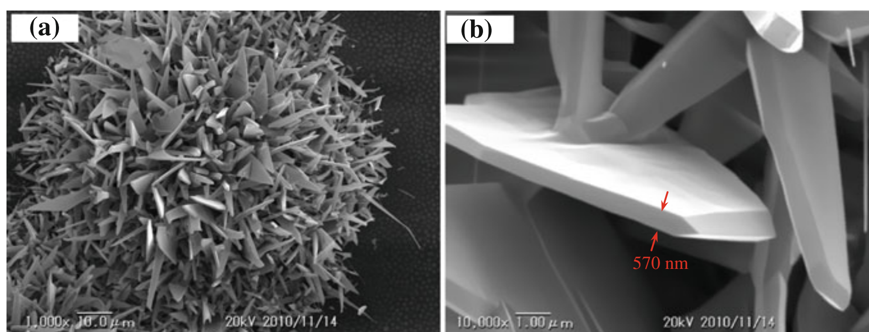

Fig. 5.3 **a** Thick ZnO nanosheets synthesized on the same silicon substrate as Fig. 5.2. **b** A magnified image of the nanosheet which has a thickness of about 570 nm

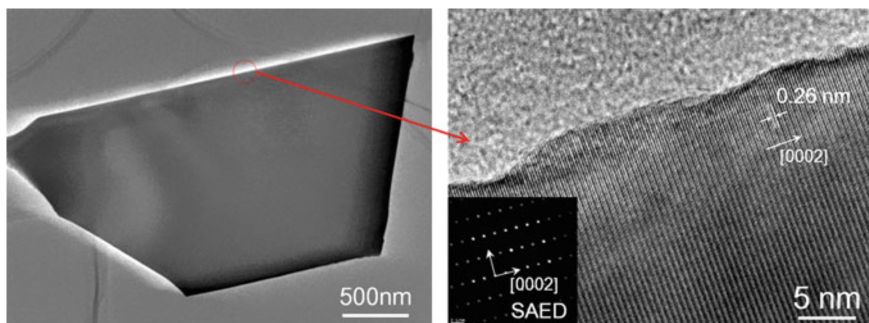

Fig. 5.4 Transmission electron microscope (TEM) image and selected area electron diffraction (SAED) pattern of a ZnO nanosheet

5.3 Experimental Arrangement for Observation of Lasing Characteristics from a Single ZnO Nanocrystal

Lasing characteristics of the ZnO nanocrystals were examined by an observation of emission spectra from a single ZnO nanocrystal excited by an UV laser beam. In advance, ZnO nanocrystals on a silicon substrate were dispersed into ethanol solution with an ultrasonic cleaner method and a few drops were put on a silica glass substrate. After the ethanol solution dried, the ZnO nanocrystals on the substrate were observed by a conventional optical microscope as shown in Fig. 5.5 which was applied for a detailed observation of the emission light from a single ZnO nanocrystal and positioned with the micrometers under the optical microscope. The ZnO nanocrystals were excited by third harmonic of a Q-switched Nd:YAG laser beam (355 nm, 5 ns). The excitation laser was injected through the silica glass substrate, and then the emission light from a ZnO nanocrystal was

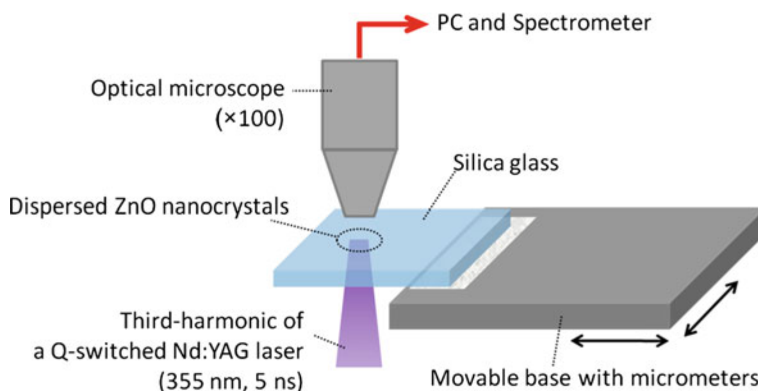

Fig. 5.5 An experimental configuration for an observation of emission spectra from a single ZnO nanocrystal

collected by the optical microscope with a magnification factor of 100 and transferred to a spectrometer with a coupled light fiber. The light-collected area by the optical microscope was approximately 15 μm in diameter, and therefore the emission light from a single ZnO nanocrystal could be observed by adjusting the position with the micrometers in this setup.

5.3.1 Lasing Characteristics of a Single ZnO Nanowire

First, lasing on a single ZnO nanowire was examined. Figure 5.6a shows an optical microscope image of a single ZnO nanowire on a silica glass substrate. Figure 5.6b shows the nanowire excited by the third-harmonic of the Q-switched Nd:YAG laser beam when the excitation power density was 450 kW/cm^2. The emission light from one end of the excited nanowire, as marked with a red-dotted circle in Fig. 5.6b, was observed by the spectrometer. The nanowire was observed by an

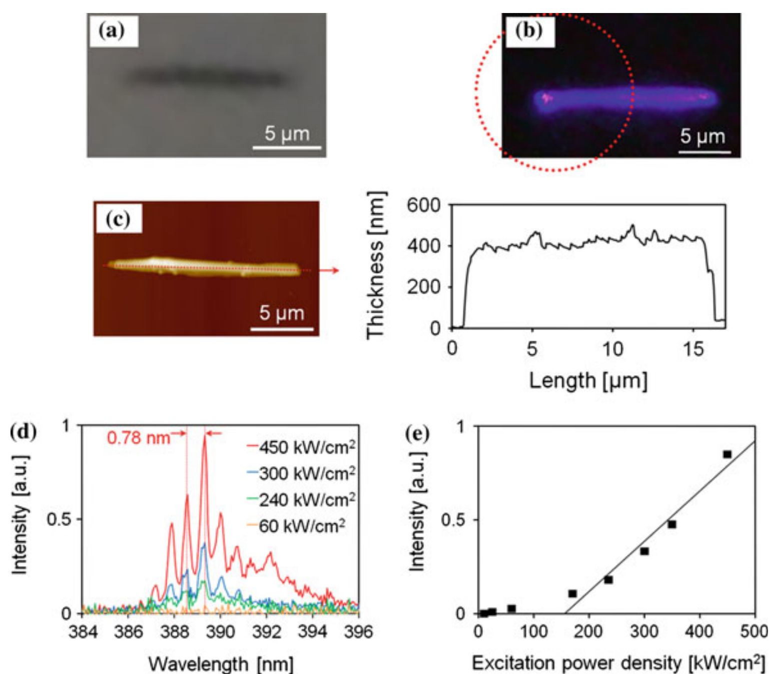

Fig. 5.6 **a** A CCD image of a single ZnO nanowire on silica glass substrate. **b** A CCD image of a single ZnO nanowire excited by a third harmonic of a Q-switched Nd:YAG laser (355 nm, 5 ns). **c** AFM image of the nanowire, and emission light from the *red-dotted circle* was observed by the spectrometer. **d** Emission spectra from the single ZnO nanowire for the different excitation power densities. **e** Input–output characteristics as a function of the excitation power density at 389.3 nm in Fig. 5.2d. The lasing threshold was estimated to be about 150 kW/cm^2

atomic force microscope (AFM) (KEYENCE, VN-8000 M/8010 M) as shown in Fig. 5.6c. The diameter and the length were 400 nm and 15 μm, respectively.

The observed spectra were plotted in Fig. 5.6d for different excitation power densities. Upon increasing the excitation power density, the model structure could be observed. The spectral width of each mode was limited by the spectral resolution of the detection system, which was 0.34 nm. The mode spacing was observed to be about 0.78 nm. The peak intensities for the mode at 389.3 nm in Fig. 5.6d were plotted as a function of the excitation power density as shown in Fig. 5.6e, where the threshold behavior was clearly observed. The threshold power density for lasing was estimated to be about 150 kW/cm^2. The peaks due to lasing at the longer wavelength appeared as the excitation power densities were increased. This is probably due to the band-gap renormalization caused by the interaction between the high-density electrons and holes created by the optical excitation [20].

These observations clearly indicate that the lasing took place within the single ZnO nanowire, due to its microcavity effect. The mode spacing in a FP cavity is given by $\Delta\lambda = \lambda^2[2L(n - \lambda \cdot \mathrm{d}n/\mathrm{d}\lambda)]^{-1}$, where L is the cavity length, n is the refractive index at the wavelength of λ, and $\mathrm{d}n/\mathrm{d}\lambda$ indicates the dispersion of light [21]. The refractive index and the length of the ZnO nanowire are $n = 2.4$ at $\lambda = 389$ nm and $L = 15$ μm, respectively. With $\Delta\lambda = 0.78$ nm as shown in Fig. 5.6d, the dispersion of light is calculated to be $\mathrm{d}n/\mathrm{d}\lambda \approx -0.010\ \mathrm{nm}^{-1}$, which is in reasonable agreement with the value of $\mathrm{d}n/\mathrm{d}\lambda \approx -0.012\ \mathrm{nm}^{-1}$ reported by Zimmler et al. [15]. Therefore, it is concluded that the cavity is formed by the FP cavity formed by two ends of the nanowire in the present experiment.

From the AFM result, the diameter of the nanowire was about 400 nm. When the nanowire is regarded as a cylindrical waveguide surrounded by air for simplicity, the normalized frequency V, which is an indicator to determine the propagation modes, inside the nanowire is given by $V = 2\pi a(n_{\mathrm{ZnO}}^2 - n_{\mathrm{air}}^2)^{1/2}/\lambda$, where a is the radius of the nanowire. The refractive indices of air and ZnO at $\lambda = 389$ nm are $n_{\mathrm{air}} = 1.0$ and $n_{\mathrm{ZnO}} = 2.4$ [22], respectively. Thus, the normalized frequency of the ZnO nanowire in Fig. 5.6b is calculated to be $V = 7.0$, and it indicates that a number of modes exist inside the nanowire [13, 15]. However, since the mode structure in Fig. 5.6d was regular, the lasing took place only on the fundamental mode, and the effective refractive index (n_{eff}) is close to the refractive index of the material.

5.3.2 *Lasing Characteristics of a Single ZnO Nanosheet*

Next, lasing in a single ZnO nanosheet was examined as well. The optical microscope image of the tested single nanosheet on a silica glass is shown in Fig. 5.7a, and the corresponding AFM image is shown in Fig. 5.7b. As a result, the size of the nanosheet with a triangular shape was about 150 nm in thickness and 15 μm in length. The CCD image of the nanosheet excited by the third harmonic

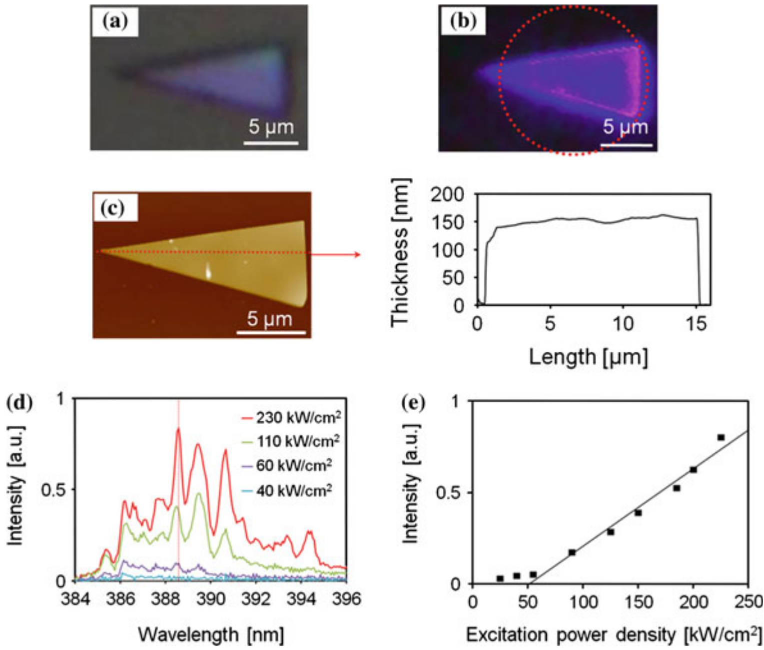

Fig. 5.7 **a** A CCD image of a single ZnO nanosheet on silica glass substrate. **b** A CCD image of the single ZnO nanosheet excited by third harmonic of a Q-switched Nd:YAG laser (355 nm, 5 ns). **c** AFM image of the nanosheet, and emission light from the *red-dotted circle* was observed by the spectrometer. **d** Emission spectra from the single ZnO nanosheet in changing the excitation power densities. **e** Plotted-peak intensities as a function of the excitation power density at *red-broken line* in **d**. The lasing threshold was estimated to be about 50 kW/cm^2

of the Q-switched Nd:YAG laser beam at 450 kW/cm^2 is shown in Fig. 5.7c. PL from the red-dotted circle in Fig. 5.7c was observed by the spectrometer. The observed PL spectra are shown in Fig. 5.7d for different excitation power densities. The spectra showed the modal structure as well as the spectra from a single ZnO nanowire at a higher excitation power of 60 kW/cm^2 indicating, the onset of lasing. The red shift of the peak wavelength was also observed in this case, due to the band-gap renormalization under high excitation power density. The peak intensities at the red-broken line in Fig. 5.7d were plotted as a function of the excitation power density, as shown in Fig. 5.7e. The threshold power density for lasing was estimated to be about 50 kW/cm^2.

For the sake of simplicity, the nanosheet can be regarded as a slab waveguide with a thickness of $t = 150$ nm surrounded by air due to a gap between the nanosheet and the substrate, because the nanosheet was simply dispersed without any adhesions. In the slab waveguide, the relation between t/λ and n_{eff} is expressed as $t/\lambda = [2\tan^{-1}(\alpha_2/\alpha_1) + m\pi]/(2\pi\alpha_1)$, where m is an integer, $\alpha_1 = (n_{\mathrm{ZnO}}^2 - n_{\mathrm{eff}}^2)^{1/2}$ and $\alpha_2 = (n_{\mathrm{eff}}^2 - n_{\mathrm{air}}^2)^{1/2}$. TE$_m$ and TM$_m$ modes exist inside the slab where the mode number corresponds to the integer m in the above equation. When the wavelength

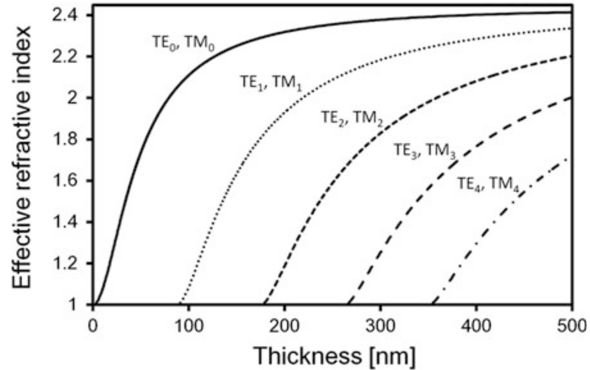

Fig. 5.8 An relationship of transverse-mode propagating in a slab waveguide of ZnO surrounded by air and the thickness of the waveguide, regarded the propagation wavelength as 390 nm

was regarded as $\lambda = 390$ nm, the relationship of the thickness and the mode was shown in Fig. 5.8. From the result, multi-mode oscillation of TE_0, TE_1, TM_0, and TM_1 can propagate inside the nanosheet.

Concerning ZnO nanosheets, there are only a few reports on lasing. Wang et al. [11] reported the stimulated emission based on the narrowing of PL spectra from ZnO nanosheets excited by a laser beam excitation with a Ti: Sapphire laser ($\lambda = 266$ nm, $\tau = 120$ fs). Those ZnO nanosheets were grown by cathodic electrodeposition. In addition, Jang et al. [12] have also reported that lasing based on the narrowing of PL spectra from ZnO nanosheets excited by a Q-switched YAG laser ($\lambda = 355$ nm, $\tau = 6$ ns) was observed. Those ZnO nanosheets were synthesized by a solution process, and the oscillation mechanism of a WGM type phenomenon inside the nanosheet was suggested. In these studies, a large number of ZnO nanosheets on a substrate were totally examined by the PL method. However, we investigated detailed PL characteristics from a single ZnO nanosheet, and then the obviously clearer lasing spectra due to modal structure were obtained as well as the lasing spectra from a single ZnO nanowire. The threshold power density for lasing of the ZnO nanosheet (50 kW/cm^2) was lower than that of the ZnO nanowire (150 kW/cm^2) as well as the above report (25 kW/cm^2) [12]. It indicates that a ZnO nanosheet can be a superior laser medium compared to a ZnO nanowire.

For further consideration, electrical-field propagations inside the nanosheet were simulated by a high-frequency structure simulator (Ansoft, HFSS ver. 11). A single ZnO nanosheet was prepared on the x–y plane as shown in Fig. 5.9, which corresponded to the nanosheet in Fig. 5.7. The nanosheet has the size of 150 nm in thickness and 100 nm at the tip according to the AFM result. Incident light was planar wave with the wavelength of 385 nm linearly polarized in the z-axis, and those were injected from the bottom side to the tip side of the nanosheet. The absorption of the light was neglected for the observation of the propagation inside the nanosheet surrounded by air.

According to the simulation results, the incident light propagates inside the nanosheet by the total reflection at the boundary of ZnO and air, and then the reflection at the tip due to the narrow waveguide behavior was also observed.

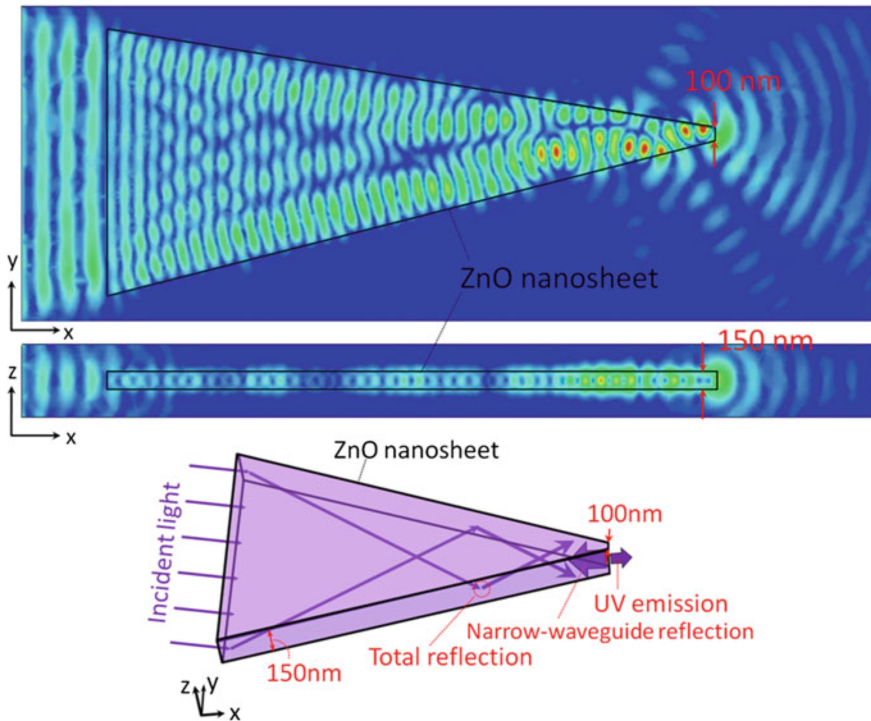

Fig. 5.9 Simulation on electrical-field propagation inside a ZnO nanosheet placed on the x–y plane. The nanosheet has a thickness of 150 nm and the tip size of 100 nm. Incident light was planar wave with a wavelength of 385 nm being linearly polarized in the z-axis. The light absorption was neglected for the observation of the propagation

Therefore, it is considered that oscillation routes inside the nanosheet would be intricately formed by a FP type resonator between both ends with the help of total reflection at the lateral sides. It is also worthwhile noting that the present triangular-shaped nanosheet will be very useful as a UV nano-light source, which can be coupled from the tip.

5.4 Consideration on a Nanomachining of DBR Structure for a Single Longitudinal Mode Lasing

ZnO nanocrystals can be excellent UV laser mediums as discussed above. However, the lasing spectra had mode structure due to its microcavity effect, and the single longitudinal mode lasing would be required for the practical application to the UV LD. Therefore, the possibilities of the single longitudinal mode lasing from a ZnO nanocrystal were considered by a DBR laser machined on a ZnO nanocrystal surface.

In the case of ZnO nanowire, oscillation mechanism can be regarded as a Fabry–Perot cavity and both the tips of the nanowire play the role of mirrors. Therefore, periodic structure with adequate pitch on the ZnO nanowire surface will serve as a grating and regulate the propagation wavelength inside the nanowire in accordance with a DBR laser. The DBR periodic cycle pitch L is expressed as $L = \lambda/2n_{eff}$, where λ is the wavelength propagating inside the nanocrystal, and n_{eff} is effective refractive index of the ZnO nanowire. When the propagating wavelength $\lambda = 390$ nm, the minimum periodic cycle $L_{min} = 81$ nm supposing $n_{eff} = 2.4$ which is a refractive index of a bulk ZnO. The nanostructure can be machined by the use of focused ion beam (FIB) (Quanta 3D 200i, FEI) in which Ga ion beam can be focused up to 7 nm in minimum.

As a demonstration, periodic structure with $L = 81$ nm was machined on a single ZnO nanowire by the FIB as shown in Fig. 5.10. Figure 5.10a shows a typical FIB image of a machined ZnO nanowire in which one side of a nanowire lying on an ITO thin film were shown, and 20 lines were machined on the surface by the Ga ion irradiation accelerated by the voltage of 30 kV. However, the emission intensity from the nanowire considerably decreased after the FIB machining due to the ion-irradiation damage. Figure 5.10b shows an emission intensity from a single ZnO nanowire before and after FIB machining. However, the observed nanowire in Fig. 5.10b was different from the nanowire in Fig. 5.10a, and the dose amount of Ga ions in Fig. 5.10b were too small to confirm the machined area. The emission intensity decreased after the FIB machining even though the excitation intensity was very high at 3.3 MW/cm^2.

So far, the single longitudinal mode lasing was not realized after the FIB machining, which would be attributed to the inadequate DBR pitch of 81 nm, the large damage due to the ion irradiation and the less number of repetitions of the periodic structure. In this case, the effective refractive index was regarded as a refractive index of a bulk ZnO, and therefore more considerations on the different value of n_{eff} will be required. Furthermore, the damage was too large, because the

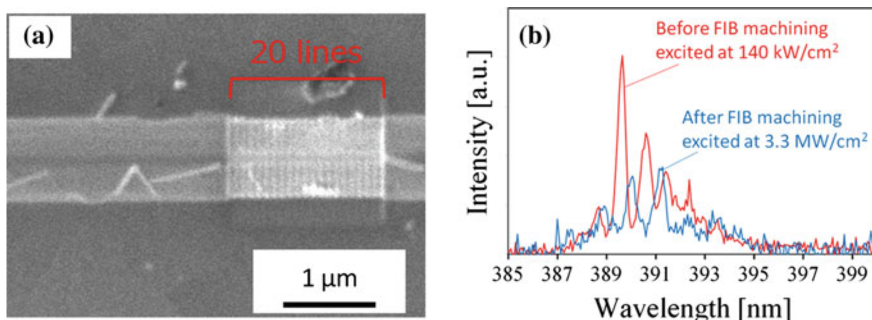

Fig. 5.10 **a** FIB image of a nanowire lying on a ITO thin film. DBR periodic structure with a pitch of 81 nm and 20 lines were machined on the surface. **b** Lasing spectra before and after FIB machining. The single longitudinal mode lasing could not be realized after the DBR machining

heavy ion of Ga was used for the machining. If a light ion or electrons are used for the machining, the damage can be suppressed. In order to make the interference effect strong, the number of repetitions of DBR should be increased and distributed feedback (DFB) lasing would be effective, which meant that the entire surface of the nanowire should be machined to realize the single longitudinal mode lasing. In principle, the machining resolution was sufficiently small to machine the nano-periodic structure, the single longitudinal mode lasing could be realized if the above conditions were optimized.

5.4.1 Consideration on Nanomachining of a 2D Photonic Crystal for Controlled Laser Action

In the case of ZnO nanowire, DBR or DFB lasing for a single longitudinal mode would be effective as discussed above. However, two-dimensional periodic structure would be needed for a single longitudinal mode lasing from a ZnO nanosheet. In order to realize a nanomachining below 100 nm, subwavelength nanomachining will be required when a ZnO nanosheet is machined by a laser processing which has some advantages of low cost and a high throughput. However, it is difficult to process at a subwavelength resolution because of the diffraction limit.

Even though the subwavelength nanomachining would be difficult by the use of an optical lens, the nanomachining could be realized by the use of Fresnel diffraction of a laser beam using a mask with apertures about the size of the irradiation wavelength. Electrical field propagation of Fresnel diffraction at UV light was simulated by the use of Ansoft, HFSS Ver.11 which is a commercial full-wave electromagnetic solver. Figure 5.11 shows a simulation of electrical field propagation of a planar wave with a wavelength of 243 nm and a polarization in x-axis, and the planar wave was entered in the direction of z-axis through a copper mask with square apertures having the size of 486 nm. The incident light was focused just below the mask apertures due to the Fresnel diffraction of the light at the apertures as shown in Fig. 5.11. It is considered that subwavelength nanomachining with the metal mask can be realized by the use of the hot spots generated by the interferences of the Fresnel diffraction light.

In order to confirm the possibilities of subwavelength machining, we demonstrated the subwavelength machining with infrared light of CO_2 laser beam ($\lambda = 10.6\ \mu m$) and a copper grid mask with apertures of several tens μm in size which is used for a typical TEM observation. A silica glass substrate was used for the observation of the machining, because the absorption coefficient of silica glass for infrared light was very high.

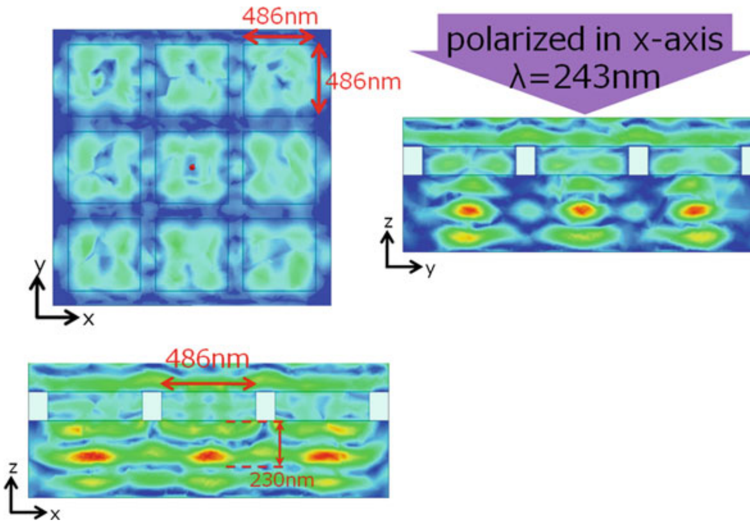

Fig. 5.11 Electrical field distribution of UV light through a metal mask for subwavelength machining using the intense points below the mask generated by the Fresnel diffraction. The incident light was planar wave with the wavelength of 243 nm linearly polarized in x-axis and propagated along z-axis

5.4.2 Demonstration of Sub-Wavelength Machining by Using Fresnel Diffraction of Infrared Laser Beam

Figure 5.12 shows the experimental configuration for the machining of a silica glass. A TEA CO_2 laser (λ = 10.6 μm) (Lambda Physik, EMG201MSC) was used as an ablation laser. The TEA CO_2 laser has a gain-switched peak pulse with a duration of 50 ns and a tail part of 1 μs. A silica glass substrate was placed on an Al plate holder, and a metal grid mask was attached to the silica glass surface. The mask was a copper grid mask which has the aperture size of 20 × 20 μm^2 and bar of 5 μm where the aperture (A) and bar (B) were indicated in Fig. 5.12. The second layer was a copper grid mask with the aperture size of 12 × 12 μm^2 apertures and bar of 5 μm. These masks have the same thickness of 2 μm. The silica glass substrate was irradiated by the TEA CO_2 laser through the mask aperture. The silica glass surface machined by the laser irradiation through the mask was observed by a conventional optical microscope, an AFM (KEYENCE, VN-8000 M/8010 M).

First, the copper grid mask with the apertures of 20 × 20 μm and bar of 5 μm was attached to the silica glass and the silica glass was irradiated by the CO_2 laser beam at the fluence of 0.96 J/cm^2. Figure 5.13a shows an optical microscope image of the irradiated surface after single-shot irradiation. Circular holes were formed on silica glass surface after the laser beam irradiation where every hole was located at the center of apertures. Figure 5.13b shows the cross-sectional

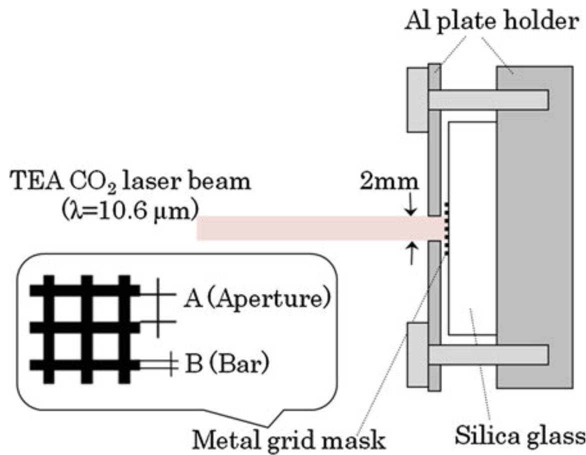

Fig. 5.12 An experimental configuration for a sub-wavelength machining of silica glass substrate by the use of Fresnel diffraction of an infrared laser beam through a metal grid mask

profile of the machined surface along the red-dashed line in Fig. 5.13a. The diameter and depth of the hole were about 7.3 μm and 600 nm, respectively. The machined diameter of the hole was smaller than the wavelength of 10.6 μm, and the subwavelength micromachining was realized by the Fresnel diffraction of the laser beam. It was also observed that there were swellings around the holes with a height of about 50 nm as shown in Fig. 5.13b.

The machined forms were different from place to place under the mask. The minimum diameter of the machined holes were shown in Fig. 5.14. The diameter and depth of the machined hole were 3.4 μm and 60 nm, respectively. The micromachining of the holes with a diameter less than one-third of the wavelength of 10.6 μm was succeeded in this technique.

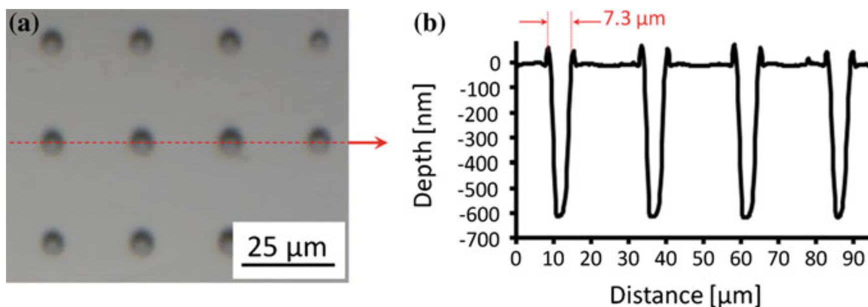

Fig. 5.13 **a** An optical microscope image of a silica glass surface ablated by the TEA CO_2 laser beam (λ = 10.6 μm) through the copper grid mask of the apertures of 20 × 20 μm^2 at a single shot. **b** The cross-sectional profile along *red-dashed line* in **a**

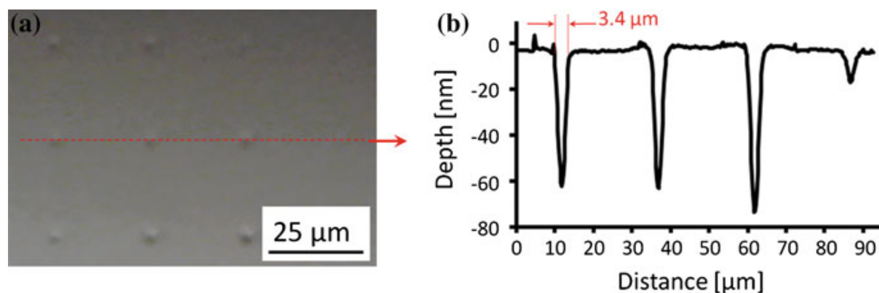

Fig. 5.14 **a** An optical microscope image of the silica glass surface with the minimum diameter ablated by the TEA CO_2 laser beam (λ = 10.6 µm) through the copper grid mask of the apertures of 20 × 20 µm^2 at a single shot. **b** The cross-sectional profile along *red-dashed line* in **a** where the diameter of 3.4 µm is below the one-third of the wavelength of CO_2 laser (λ = 10.6 µm)

Next, the effects of several shots irradiation were investigated using the same copper mask of 20 × 20 µm^2. Figure 5.15a, b show the optical microscope image of the irradiated surface and the cross-sectional profile of the surface after 10 shots irradiation at the fluence of 0.96 J/cm^2, respectively. Circular holes without swellings were formed on the silica glass surface. The diameter and depth of the hole were about 9.4 µm and 500 nm, respectively. The diameter of the holes after 10 shots irradiation is broader than that of single shot. The depth of the holes is, however, almost the same as the depth of single-shot irradiation, indicating that the depth does not depend on the number of laser irradiation. With regard to the disappearance of the swellings around the machined holes, it is considered that the swellings are gradually ablated by the irradiation of 10 times.

Figure 5.16 shows the different area on the same sample as Fig. 5.15, there are also small ablated points between the broader holes which would be covered by the grid mask's bar. The diameter and the depth of the broader hole were about 10.8 µm and 400 nm, respectively, and the diameter and the depth of the small

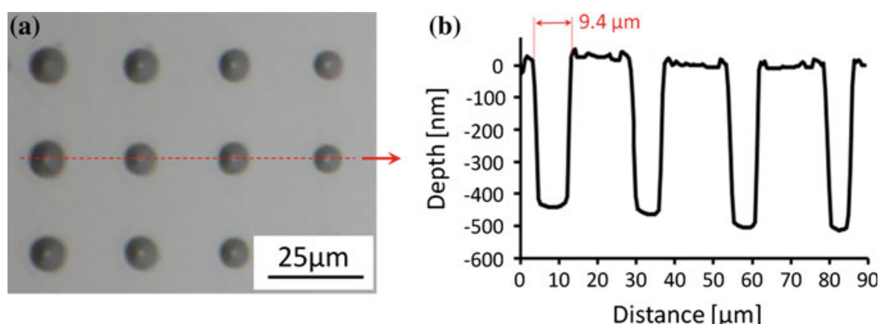

Fig. 5.15 **a** An optical microscope image of a silica glass surface ablated by the TEA CO_2 laser beam (λ = 10.6 µm) through the copper grid mask of the apertures of 20 × 20 µm^2 at 10 shots. **b** The cross-sectional profile along *red-dashed line* in **a**

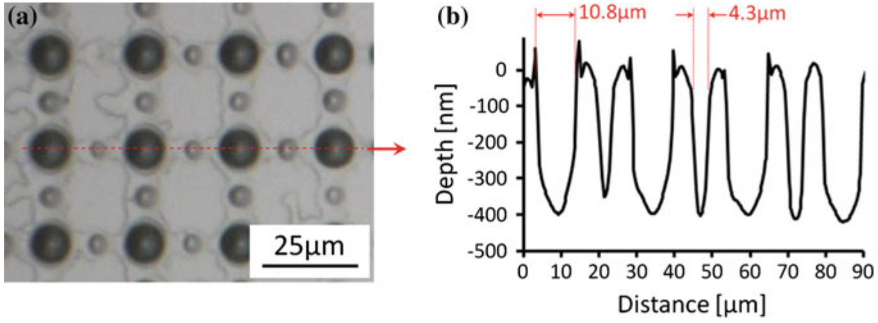

Fig. 5.16 **a** An optical microscope image of a silica glass surface at a different area from Fig. 5.15 where small holes were formed between big holes. **b** The cross-sectional profile along *red-dashed line* in **a**

machined point were about 4.3 μm and 400 nm, respectively. The formation of small ablated points is attributed to the laser light intensities through the mask at silica glass surface, which vary from point to point because of the distortion of the mask. Since the laser light through the neighboring apertures interfere with one another, small intense points appear under the grid mask's bar.

The electric field distributions of the CO_2 laser light through a copper mask were simulated as well as the simulation in Fig. 5.11 as shown in Fig. 5.17. The copper mask has square apertures of $20 \times 20\ \mu m^2$, bars of 5 μm and a thickness of 2 μm. The incident light was supposed to be a planar wave at the wavelength of 10.6 μm propagating along z-axis and linearly polarized in x-axis. This simulation result indicates that hot spots appear 9.0 μm below the mask at the center of every

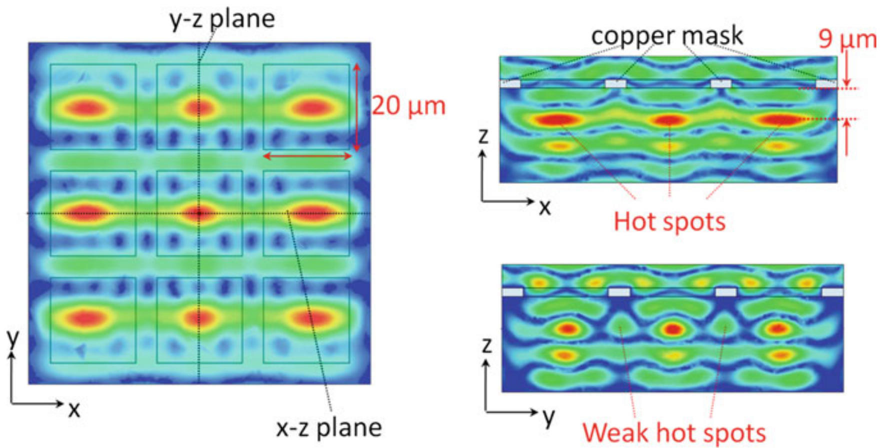

Fig. 5.17 The electric field distributions of CO_2 laser light (10.6 μm) through the copper grid mask with the apertures of $20 \times 20\ \mu m^2$, bars of 5 μm and thickness of 2 μm. Incident light conditions are planar wave propagating along the z-axis and linearly polarized in the x-axis

aperture. The circular machined holes on the silica glass beyond the diffraction limit were formed by the Fresnel diffraction. Furthermore, weak hot spots also appear under the mask bars in y–z plane due to the interference with the lights through the neighboring apertures. However, these interferences cannot be seen in x–z plane. It would depend on the polarization state. These results correspond to the experimental result as shown in Fig. 5.16 where small ablated holes were formed at the middle of the large holes. In the experiment, small holes were formed not only along y-axis but also x-axis, because the CO_2 laser light has a random polarization.

Next, the copper grid mask with the apertures of $12 \times 12\ \mu m^2$ and bars of 5 μm was used to investigate the dependence of the aperture size. However, even though the laser irradiation is at the same conditions as shown in Fig. 5.11, no holes were formed on the silica glass surface. At a high fluence about $1.0 \times 10\ J/cm^2$, no holes were formed and the mask was deformed due to melting. This result indicates the CO_2 laser light did not penetrate the mask aperture, because the aperture was too small and comparable size with its wavelength.

The simulation was performed using the copper grid mask with a thickness of 2 μm, the apertures of $12 \times 12\ \mu m^2$ and bars of 5 μm, and the other conditions were the same as Fig. 5.17. The results are shown in Fig. 5.18, and the hot spots using the mask apertures of $12 \times 12\ \mu m^2$ are considerably weaker than the hot spots using the mask apertures of $20 \times 20\ \mu m^2$. Furthermore, the hot spots appeared at 2.6 μm below the mask. It seems that the smaller the mask aperture size is, the closer to the mask the hot spots are. Therefore, it would be difficult to machine the silica glass by the use of apertures of $12 \times 12\ \mu m^2$, because the hot spots were weaker and closer to the mask. These simulation results have a good agreement with the experimental results, and therefore it is important that the mask should be correctly designed based on the simulation.

Subwavelength machining of silica glass was achieved by the Fresnel diffraction of infrared laser light using a metal grid mask. The minimum diameter was

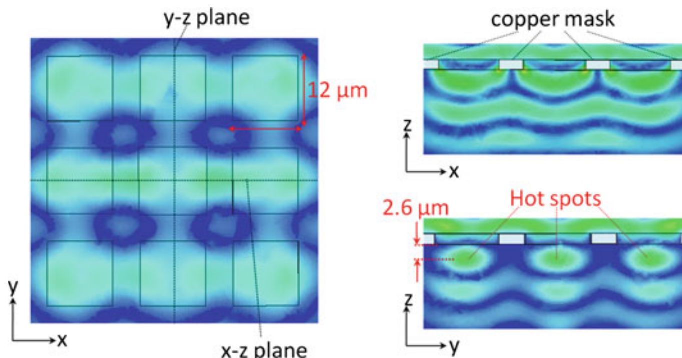

Fig. 5.18 The electric field distributions of CO_2 laser light (10.6 μm) through the copper grid mask with the apertures of $12 \times 12\ \mu m^2$, bars of 5 μm and thickness of 2 μm. Incident light conditions are planar wave propagating along the z-axis and linearly polarized in the x-axis

about 3.4 μm as shown in Fig. 5.14, which was about one-third of the wavelength of 10.6 μm. From this result, subwavelength nanomachining of ZnO nanosheet below 100 nm for 2D photonic crystal can be realized by the use of a mask and an UV laser beam. When a laser beam with the wavelength of 243 nm is used as the machining laser beam as shown in Fig. 5.11, one-third of 243 nm, estimated to be about 81 nm, can be realized. Furthermore, if a vacuum UV laser beam such as a F_2 excimer laser with the wavelength of 157 nm is used, the resolution of 52 nm may be achieved. However, since the machined patterns depend on the mask pattern, the mask pattern should be well designed and the mask positions including the distortion of the mask and the distance between the mask and the target should be well controlled.

In this technique, a subwavelength machining was demonstrated by the Fresnel diffraction of infrared radiation with a mask, and the technique might have a potential for the application to a machining of ZnO nanosheet for 2D photonic crystal because of the machining resolution below 100 nm.

5.5 Laser-Induced Motions of ZnO Nanocrystals

During the lasing observation of ZnO nanocrystals, we have observed motions of nanocrystals irradiated by the excitation laser beam at relatively high excitation power density over several MW/cm^2. The observed examples are shown in Figs. 5.19 and 5.20, which are the snapshots during the LIM in the air. In Fig. 5.19, a nanosheet horizontally placed on a silica glass substrate stood up vertically by the excitation laser irradiation, where the snapshots were taken every 0.5 s. In Fig. 5.20, a ZnO nanocrystal was rotated by the laser irradiation, where the snapshots were taken every 1 s.

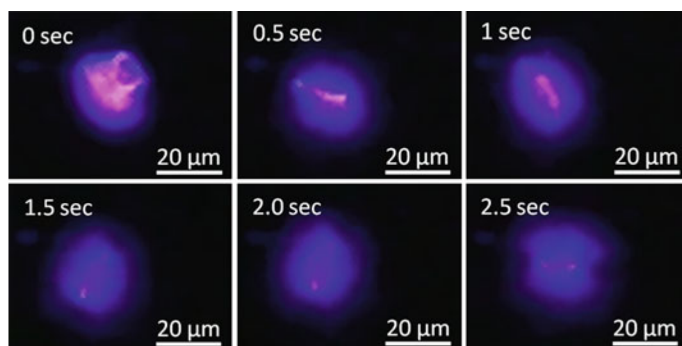

Fig. 5.19 Time course images of a ZnO nanosheet stood up by a laser irradiation on a silica glass. The motion would be attributed to piezo effects of the nanosheet and a resultant electrostatic force

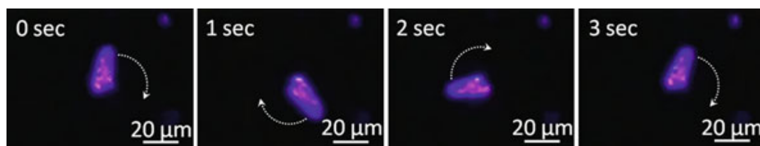

Fig. 5.20 Time course images of a ZnO nanosheet rotated by a laser irradiation on a silica glass. The motion also would be attributed to piezo effects of the nanosheet and a resultant electrostatic force

The detailed mechanism of these motions is not clear, but we believe that they are related to the laser-induced piezo (Zn^{2+}/O^{2-}) effects [23] and a resultant electrostatic force plays a major role in the motion. When the ZnO nanocrystal was irradiated by the UV laser beam, ZnO nanocrystal absorbed the light which results in thermal expansion. Then, the expansion would induce the following electromotive force due to the piezo effect, and therefore the nanocrystal would be moved because of the electrostatic force against the silica glass substrate.

In a previous study, we have demonstrated an electrical trap of a ZnO nanowire between voltage-applied gold electrodes, where the ZnO nanowires were dispersed in ethanol solution with an ultrasonic cleaning method and trapped between the electrodes with a dielectrophoretic method [5]. Since ZnO nanocrystals can be moved with a laser irradiation by an electrostatic force, more accurate alignment of ZnO nanowires will be expected with the LIM. Therefore, we demonstrated the alignment method by LIM and the gold-evaporated silica glass substrate as shown in Fig. 5.21. The voltage of 30 V was applied between the gold electrodes with a gap of 7 µm as shown in Fig. 5.21a, and then the excitation laser was irradiated to the ZnO nanocrystal thorough the silica glass substrate. A single ZnO nanowire as marked by red-dotted line in Fig. 5.21b was moved by the LIM and trapped between the gap of electrodes, and immediately after being trapped, electrical

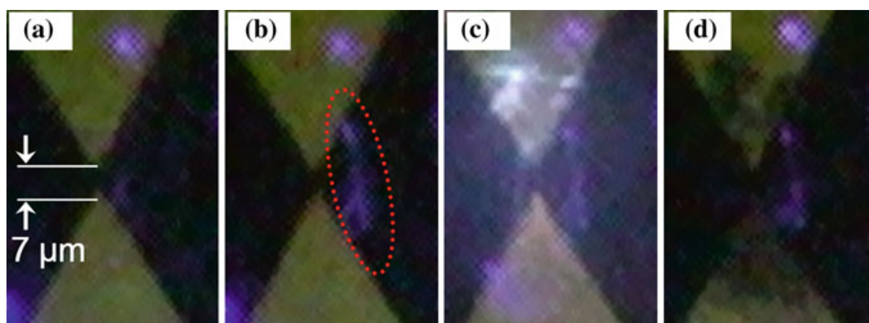

Fig. 5.21 Before applying a voltage (a), and a single ZnO nanowire was moved by the LIM and trapped between the gap of electrodes (b), and immediately after being trapped, electrical current was discharged (c), as the result, the electrodes were broken because of high current (d)

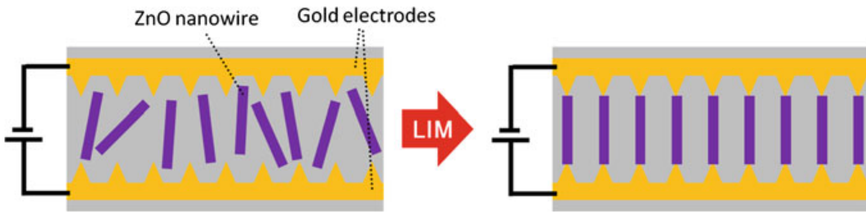

Fig. 5.22 A schematic image of an alignment method by voltage-applied electrodes and LIM of ZnO nanocrystals

current was discharged as shown in Fig. 5.21c. As the result, the electrodes were broken because of high current.

If the technique of trapping ZnO nanocrystals as demonstrated above is well controlled, a simple alignment method can be expected as shown in Fig. 5.22, and it will be useful for the fabrication of ZnO nanocrystal devices for UV applications such as UV LD, UV LED, UV sensor, and etc.

5.6 Conclusion

The lasing characteristics of a single ZnO nanowire and a single ZnO nanosheet were investigated by an optical pumping with third harmonic of a Q-switched Nd:YAG laser (355 nm, 5 ns). These ZnO nanocrystals were synthesized by a carbothermal CVD method. Laser oscillation spectra from both the ZnO nanowire and the ZnO nanosheet were observed, and the threshold power density were 150 and 50 kW/cm^2, respectively. It indicated that the ZnO nanocrystals have an excellent crystalline quality, and especially, a ZnO nanosheet can be a superior laser medium to a ZnO nanowire because of the low lasing threshold. For the practical application to UV LD, a single longitudinal mode lasing with the DBR laser for a ZnO nanowire was considered, and then the DBR structure with the pitch of 81 nm was machined by the use of focused ion beam with Ga ions. However, since the single longitudinal mode lasing could not observed so far, optimization of experimental conditions was necessary. In addition, subwavelength machining with the Fresnel diffraction was considered based on electrical field simulation for 2D photonic crystal of ZnO nanosheet, and the demonstration of subwavelength machining with a TEA CO_2 laser beam ($\lambda = 10.6$ µm) was performed. As the result, the minimum resolution below one-third of the wavelength, the nanomachining below 100 nm can be realized by the use of an UV laser beam such as F_2 excimer laser beam ($\lambda = 157$ nm). Finally, an alignment method of ZnO nanocrystals lying on a substrate was proposed using a combination of voltage-applied electrodes and LIM which would be related to an electrostatic force between the ZnO nanocrystals and the substrate. According to those results discussed above, a simple and useful method making UV devices such as UV

LED, UV LD without any cumbersome procedures in lithographic processes can be expected by the use of those ZnO nanocrystals as building blocks of UV laser mediums.

Acknowledgments The authors would like to thank Dr. T. Daio in the research laboratory for high voltage electron microscopy in Kyushu University, for his assistance in the experiments. A part of this work was supported by a Grant-in-Aid for Scientific Research from the Japan Society for the Promotion of Science (JSPS, No. 20360142) and Special Coordination Funds for Promoting Science and Technology from Japan Science and Technology Agency is also acknowledged.

References

1. T. Okada, K. Kawashima, Y. Nakata, X. NING, Synthesis of ZnO nanorods by laser ablation of ZnO and Zn targets in He and O_2 background gas. Jpn. J. Appl. Phys. **44**, 688 (2005)
2. R.Q. Guo, J. Nishimura, M. Ueda, M. Higashihata, D. Nakamura, T. Okada, Vertically aligned growth of ZnO nanonails by nanoparticle-assisted pulsed-laser ablation deposition. Appl. Phys. **A 89**, 141 (2007)
3. R.Q. Guo, J. Nishimura, M. Matsumoto, D. Nakamura, T. Okada, Catalyst-free synthesis of vertically-aligned ZnO nanowires by nanoparticle-assisted pulsed laser deposition. Appl. Phys. **A 93**, 843 (2008)
4. R.Q. Guo, J. Nishimura, M. Matsumoto, M. Higashihata, D. Nakamura, T. Okada, Density-controlled growth of ZnO nanowires via nanoparticle-assisted pulsed-laser deposition and their optical properties. Jpn. J. Appl. Phys. **47**, 741 (2008)
5. R.Q. Guo, M. Matsumoto, T. Matsumoto, M. Higashihata, D. Nakamura, T. Okada, Aligned growth of ZnO nanowires by NAPLD and their optical characterizations. Appl. Surf. Sci. **255**, 9671 (2009)
6. Y.C. Kong, D.P. Yu, B. Zhang, W. Fang, S.Q. Feng, Ultraviolet-emitting ZnO nanowires synthesized by a physical vapor deposition approach. Appl. Phys. Lett. **78**, 407 (2001)
7. J.J. Wu, S.C. Liu, Low-temperature growth of well-aligned ZnO nanorods by chemical vapor deposition. Adv. Mater. **14**, 215 (2002)
8. Y.W. Heo, V. Varadarajan, M. Kaufman, K. Kim, D.P. Norton, F. Ren, P.H. Fleming, Site-specific growth of Zno nanorods using catalysis-driven molecular beam epitaxy. Appl. Phys. Lett. **81**, 3046 (2002)
9. J.H. Park, J.G. Park, Synthesis of ultrawide ZnO nanosheets. Curr. Appl. Phys. **6**, 1020–1023 (2006)
10. L. Xu, Y. Guo, Q. Liao, J. Zhang, D. Xu, Morphological control of ZnO nanostructures by electrodeposition. J. Phys. Chem. **B 109**, 13519–13522 (2005)
11. F. Wang, R. Liu, A. Pan, L. Cao, K. Cheng, B. Xue, G. Wang, Q. Meng, J. Li, Q. Li, Y. Wang, T. Wang, B. Zou, The optical properties of ZnO sheets electrodeposited on ITO glass. Mater. Lett. **61**, 2000–2003 (2007)
12. E.S. Jang, X. Chen, J.H. Won, J.H. Chung, D.J. Jang, Y.W. Kim, J.H. Choy, Soft-solution route to ZnO nanowall array with low threshold power density. Appl. Phys. Lett. **97**, 043109 (2010)
13. M.H. Huang, S. Mao, H. Feick, H. Yan, Y. Wu, H. Kind, E. Weber, R. Russo, P. Yang, Room-temperature ultraviolet nanowire nanolasers. Science **292**, 1897–1899 (2001)
14. L.K. Vugt, S. Rhle, D. Vanmaekelbergh, Phase-correlated nondirectional laser emission from the end facets of a ZnO nanowire. Nano Lett. **6**, 2707–2711 (2006)
15. M.A. Zimmler, F. Capasso, S. Muller, C. Ronning, Optically pumped nanowire lasers: invited review. Semicond. Sci. Technol. **25**, 024001 (2010)

16. S.F. Yu, C. Yuen, S.P. Lau, Random laser action in ZnO nanorod arrays embedded in ZnO epilayers. Appl. Phys. Lett. **84**, 3241–3243 (2004)
17. E.S.P. Leong, S.F. Yu, S.P. Lau, Directional edge-emitting UV random laser diodes. Appl. Phys. Lett. **89**, 221109 (2006)
18. S. Chu, M. Olmedo, Z. Yang, J. Kong, J. Liu, Electrically pumped ultraviolet ZnO diode lasers on Si. Appl. Phys. Lett. **93**, 181106 (2008)
19. S. Chu, G. Wang, W. Zhou, Y. Lin, L. Chernyak, J. Zhao, J. Kong, L. Li, J. Ren, J. Liu, Electrically pumped waveguide lasing from ZnO nanowires. Nat. nanotechnol. **6**, 506–510 (2011)
20. J.C. Ryan, T.L. Reinecke, Band-gap renormalization of optically excited semiconductor quantum wells. Phys. Rev. **B 47**, 9615–9620 (1993)
21. A.E. Siegman, *Lasers* (University Science Books, Mill Valley, 1986)
22. S. Adachi, Optical Constants of Crystalline and Amorphous Semiconductors: Numerical Data and Graphical Information (Kluwer Academic Publishers, Boston, 1999), Chap. D2
23. J. Zhoua, Z. Wang, A. Grots, X. He, Electric field drives the nonlinear resonance of a piezoelectric nanowire. Sol. State Comm. **144**, 118 (2007)

Chapter 6
Deposition of Aluminum-Doped ZnO Films by ICP-Assisted Sputtering

Yoshinobu Matsuda, Akinori Hirashima, Kenji Mine, Takuhiro Hashimoto, Daichi Matsuoka, Masanori Shinohara and Tatsuo Okada

Abstract Inductively coupled plasma (ICP) assisted DC sputter deposition was used for the deposition of Al-doped ZnO (AZO or ZnO:Al) thin films. With increasing ICP RF power, film properties including deposition rate, crystallinity, transparency, and resistivity were improved. To understand the plasma-surface interaction, several plasma diagnostics were performed. Heat fluxes to the substrate were measured by thermal probes, number densities of sputtered metallic atom species were measured by absorption spectroscopy using hollow cathode lamps (HCL) and light emitting diodes (LEDs), and neutral gas temperatures were measured by external cavity diode laser (ECDL) absorption spectroscopy. As a result, it was revealed that the high-density ICP heated the substrate through a high heat flux to the substrate, resulting in a high-quality film deposition without the need for intentional substrate heating. The heat flux to the substrate was predominantly contributed by the plasma charged species, not by the neutral Ar atoms which were also significantly heated in the ICP. The substrate position where the highest quality films were obtained was found to coincide with the position where the substrate heat flux took the maximum value.

Y. Matsuda (✉) · T. Hashimoto · D. Matsuoka · M. Shinohara
Graduate School of Engineering, Nagasaki University, Bunkyo 1-14,
Nagasaki 852-8131, Japan
e-mail: ymat@nagasaki-u.ac.jp

A. Hirashima · K. Mine
Graduate School of Science and Technology, Nagasaki University, Bunkyo 1-14,
Nagasaki 852-8131, Japan

T. Okada
Graduate School of Information Science and Electrical Engineering,
Kyushu University, Fukuoka 812-8581, Japan

M. S. R. Rao and T. Okada (eds.), *ZnO Nanocrystals and Allied Materials*,
Springer Series in Materials Science 180, DOI: 10.1007/978-81-322-1160-0_6,
© Springer India 2014

6.1 Introduction

Transparent conducting oxide (TCO) thin films with high transparency in the visible and near-infrared spectral region and low resistivity [1, 2] have been widely used as transparent conducting electrodes for various optoelectronic devices such as solar cells, flat panel displays, etc. Some TCO materials such as SnO_2 and In_2O_3 have already been put to practical use in industry. In particular, Sn-doped In_2O_3 (ITO) has been widely used so far due to its high transparency in the visible region, high chemical stability and low resistivity. Metal-doped ZnO which first appeared around 1980 has recently received attention as one of the alternatives to the ITO. Doped ZnO thin films with In (IZO), Ga (GZO), and/or Al (AZO) have high carrier densities of 10^{20}–10^{21} cm^{-3} and low electric resistivity of 10^{-2}–10^{-4} Ω cm. The origin of conductivity, nonstoichiometry, and coloration for TCOs has recently been gradually understood [3–5]. We focus here on AZO thin films, since the AZO has advantages over ITO and other doped ZnO in environment resistance and resource cost. To actually replace the ITO with the AZO, however, reproducible and highly reliable fabrication processes of good quality polycrystalline AZO thin films have to be developed.

The polycrystalline AZO films have been prepared by a variety of techniques such as reactive and nonreactive magnetron sputtering [6], high-density plasma assisted (or superimposed) magnetron sputtering [7–12], chemical vapor deposition [13], pulsed-laser deposition [14], evaporation [15], spray pyrolysis [16], Sol–gel preparation [17], and electrochemical deposition [18]. Among them, magnetron sputtering is one of the dominant deposition techniques for the deposition of good quality, large area coating with relatively low substrate temperature [6].

High-density ICP-assisted magnetron sputtering [19–23] is also a promising technique, because it requires no intentional substrate heating due to high plasma density. The advantages of ICP-assisted sputtering are summarized as follows: (1) the target is sputtered with low target voltage and high target current, (2) the usage efficiency of the target is significantly improved due to the expansion of erosion area, (3) ionization and excitation of the sputtered particles are enhanced in the ICP and the enhanced ion fluxes to the substrate promote the crystallinity of thin films without intentional substrate heating, (4) lateral homogeneity of the deposited film is greatly improved, and (5) abnormal discharge (arcing) [24, 25] is drastically suppressed. However, previous research showed the lowest resistivity of AZO films prepared by the ICP-assisted sputtering is limited around 10^{-3} Ω cm [9–12]. To understand the ICP-assisted sputter-deposition mechanism and to improve the AZO film quality, we have investigated AZO film deposition process by using ICP-assisted DC magnetron sputtering [26–30].

This paper summarizes the experimental results on the basic discharge characteristics, heat flux to the substrate, sputtered atom densities and the neutral gas temperatures in the bulk plasma, and the film properties (deposition rate, resistivity, transparency, crystallinity, and elemental ratio) of prepared AZO films in

the ICP-assisted sputter-deposition process. The effect of ICP superimposing on the bulk plasma and the film properties is discussed.

6.2 Experimental Setup and Procedure of ICP-Assisted Magnetron Sputtering

Figure 6.1 shows the experimental setup for the ICP sputter-deposition of Al doped ZnO thin films [26–30]. A 3 inch DC planar magnetron, an Ar gas supply system, and a pumping system (turbo molecular pump and rotary pump combination) were attached to the vacuum chamber (300 mm in diameter and 300 mm in height). After the base pressure of around 10^{-6} Torr was attained, Ar was introduced by a mass flow controller. Then, the working pressure was set at 4 Pa by tuning the conductance of the main valve. A disk target of ZnO:Al_2O_3 (2 wt%) of 60 mm diameter and 6 mm thick was used as a target, and a glass substrate was set on an earthed substrate holder with a gap length of 80 mm. Between the target and the substrate, a single turn coil antenna of 100 mm diameter was installed and used for producing 13.56 MHz ICP. The antenna was covered with insulator and water cooled. The distance from the target to the RF coil (T-C distance) and the distance from the RF coil to the substrate (C-S distance) were both 40 mm. The magnetron plasma was generated by applying negative DC voltage to the target electrode, and the ICP was generated by applying 13.56 MHz RF power to the coil antenna through a matching circuit. After the thin film deposition, the substrate was taken out from the vacuum chamber and cut to several pieces. Characteristic of each thin film (film thickness, resistivity, transmission, crystallinity, and elemental ratio) and their lateral distribution on the substrate were evaluated.

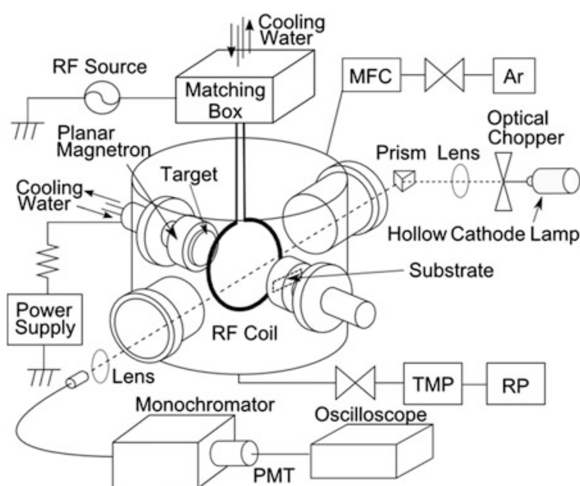

Fig. 6.1 Experimental setup for ICP-assisted DC magnetron sputter deposition and for hollow cathode absorption measurement

The film thickness was measured by a stylus profilemeter (Mitsutoyo, SV-400). The electric conductivity was measured by a four point probe and the film resistivity was evaluated by multiplying the experimental surface resistance by a geometrical correction factor determined by the film thickness, substrate shape and size, and distance between the probe tips. The optical transmission was measured by a spectral photometer consisting of a halogen lamp and an optical fiber spectrometer (Ocean Optics, HR4000CG). In this work, we evaluated the optical transmittance of AZO films by using "the overall transmittance" that was averaged over visible wavelength range (380–780 nm) and further averaged over lateral spatial distribution. However, since the overall transmittance mentioned above depends on the film thickness, we judged the optical property utilizing the absorption coefficient α (absorbance per unit thickness) by $\alpha = \ln(1/T)/d$, where T is the overall averaged transmittance, *and d* is the film thickness. For example, let $d = 300$ nm and $T = 90$ %; it gives $\alpha = 0.4\ \mu m^{-1}$. The crystallinity of thin films was investigated by X-ray diffraction (RINGAKU, RINT2000). The elemental ratio in the film was measured by X-ray photoemission spectroscopy (SHIMADZU-KRATOS, AXIS-HS). Details of the plasma diagnostics will be explained in Sect. 6.4.

6.3 ICP Assisted Sputter Deposition of Aluminum Doped Zinc Oxide Thin Films

6.3.1 Influence of Distance Between Target, ICP Coil, and Substrate on Film Properties

First, the optimum geometry conditions concerning (a) target voltage, (b) target current, (c) deposition rate, (d) resistivity, and (e) transmittance were investigated by varying the T-C distance from 10 to 50 mm and the C-S distance from 30 to 70 mm, respectively. Figure 6.2 shows the results of the investigation for the condition of 4 Pa Ar discharges with a DC target power of 40 W and ICP–RF power of 200 W. As can be seen from (a) and (b) in Fig. 6.2, the target voltage decreases and the target current increases with increasing T-C distance; i.e., the impedance of the discharge increases with increasing the gap length between the target and the ICP coil. This is predominantly explained by the fact that the diffusion loss of charged particles in the plasma is enhanced by decreasing the T-C distance, because the ground shield of the magnetron target works as a sink of plasma particles. The T-C distance dependence of the target discharge impedance shown in Fig. 6.2a, b does not hold for the larger T-C distances. For the larger T-C distances, the target discharge impedance will decrease and get closer to that for the planar magnetron discharge because the magnetron plasma is isolated from the ICP. The C-S distance dependence of the target voltage and the target current is minimal compared with the T-C distance dependence. From a view point of thin

film deposition, low discharge impedance is favorable because of low bombarding damage of the films. Thus, longer T-C and C-S are favorable. As can be seen from Fig. 6.2c, however, the deposition rate decreases with increasing T-C and C-S distances, i.e., the deposition rate and the discharge impedance have a "trade-off" relationship. In addition, we can see there is a trade-off between the film resistivity and the transmittance. Thus, as a result of compromise between the trade-offs, we determined the optimal values for both the T-C distance and the C-S distance to be 4 cm. We confirmed that the AZO film with a resistivity of 2×10^{-3} Ω cm and a transmittance of more than 80 % can be obtained with good reproducibility under this condition at ICP RF power of 200–300 W.

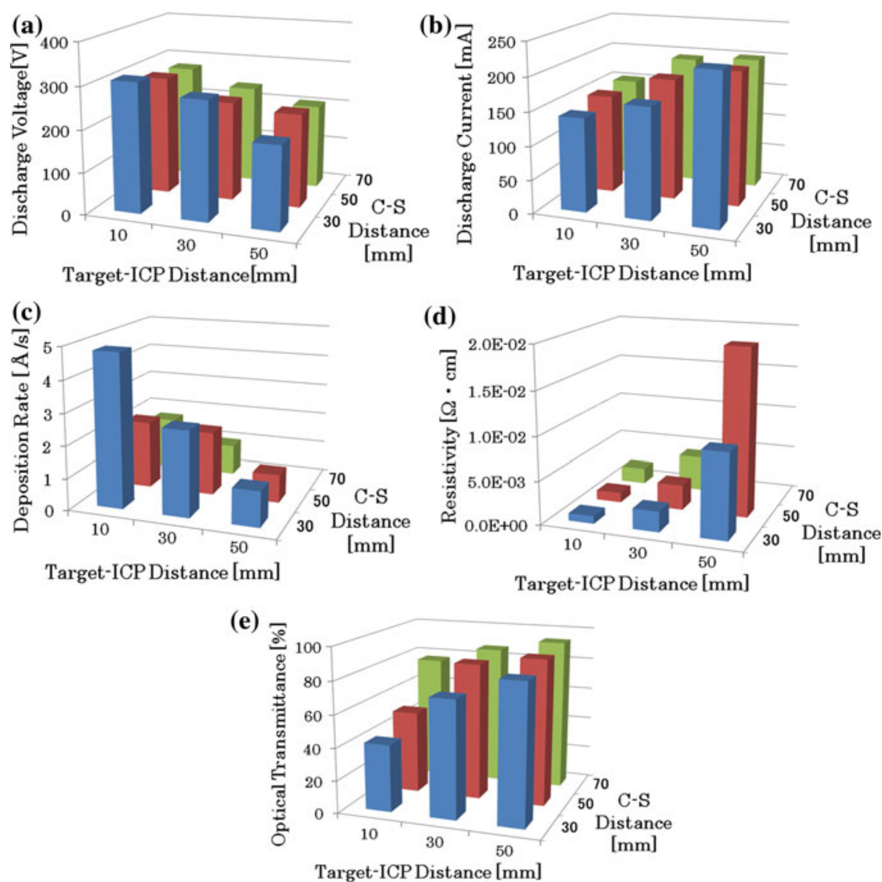

Fig. 6.2 **a** Target voltage, **b** target current, **c** deposition rate, **d** resistivity and **e** transmittance against the target-ICP coil distance and the ICP-coil and substrate distance

6.3.2 Effect of ICP RF Assist Power

Figure 6.3 shows the ICP RF power dependence of the target discharge voltage and the target discharge current for the constant target input power at 45 W. The target discharge voltage decreases and the discharge current increases with increasing ICP RF power. Therefore, the impedance for the sputtering discharge decreases with the increase in ICP RF power. This is because the plasma density near the planar magnetron target is increased by the presence of ICP, whose density almost increases linearly with the ICP RF power. The decrease in the target discharge impedance under the ICP-assisted sputtering is extremely effective, because the low voltage sputtering is directly connected to the reduction of film damage on the substrate. Moreover, the low voltage sputtering is very effective for suppressing arcing. ICP-assisted sputtering is effective for the improvement in the usage efficiency of the target and the uniformity of thin film characteristics, because the sputtering area expands to the whole target surface.

The change in the plasma emission intensity with and without ICP superimposing was investigated. It was found that predominant optical emission lines are only due to the electron impact excitation of sputtered Zn atoms within the wavelength range from 200 to 400 nm without ICP assist. In the case of ICP-assisted magnetron discharges, optical emission intensities for the Zn I lines are significantly increased, and additional optical emission lines from much higher excited states of Zn atoms and from excited states of Al atoms were identified. Thus, the ICP-assisted sputter deposition with promoted excitation and ionization is effective for enhancing the crystallinity of deposited AZO films.

Figure 6.4 shows the ICP RF power dependence of the spatial distribution of deposition rate. It is found that the deposition rate increases by 20–30 % with increasing ICP RF power from 0 to 300 W. This tendency can be explained by the increased sputtered particle flux due to self sputtering effect. With increasing ICP RF power, ionized degree of sputtered Al and Zn atoms is increased and the Al and Zn ions bombard the target as well as the substrate, resulting in self sputtering that enhances the sputtered flux. However, since the increase in the deposition rate with

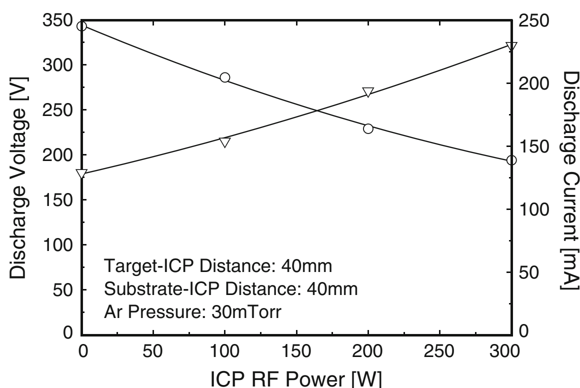

Fig. 6.3 ICP RF power dependence of discharge voltage (*circle*) and discharge current (*triangle*) during ICP assist magnetron sputtering at the working pressure of 4 Pa and at a constant target power of 45 W

increasing ICP RF power is much smaller than that of sputtered Zn atom density that will be described in the Sect. 6.4.2, we can consider that a re-evaporation of Zn atoms from the substrate likely occurred during the deposition process.

Figure 6.5 shows the ICP RF power dependence of the spatial distribution of film resistivity. The resistivity is very high about 2×10^{-1} Ω cm for the planar magnetron discharge without ICP at the pressure 4 Pa. However, the resistivity is drastically decreased and the uniformity is improved with increasing ICP RF power. It is well-known that for DC magnetron sputtering operating at below 1 Pa the resistivity of the film is comparatively low at both the center and peripheries, while the resistivity is high at the substrate positions facing the target erosion. However, in the ICP-assisted sputtering with operating pressures at around 4 Pa, the spatial profile of resistivity is more uniform. The drastic decrease in the resistivity due to the ICP assist is explained as follows. When the ICP RF power increases, the film damage decreases because the target voltage decreases, and the energies of charged and neutral species incident to the substrate decrease. In addition to this effect, total ion flux to the substrate with moderate energies of about 10–20 electron volts increases due to the increase in plasma density with increasing ICP RF power. The increased energy flux to the substrate heats the substrate surface up to a temperature around 200 °C or more and the film crystallinity is improved. In this research, conductive AZO films with resistivity of 2×10^{-3} Ω cm were obtained with good spatial uniformity. Hall measurement result showed the carrier density and carrier mobility were typically 5×10^{20} cm^{-3} and 6–7 $cm^2/(Vs)$ for the AZO films deposited at ICP RF power of 300 W. To decrease more the resistivity of AZO films deposited in this scheme, further increase in the mobility is needed.

Assisting ICP RF power is effective for increasing film transparency. Figure 6.6 shows the ICP RF power dependence of the absorption coefficient of deposited AZO films. The vertical axis of Fig. 6.6 is the averaged absorption coefficient α as explained in the Sect. 6.2. We judged the films with absorption coefficients less

Fig. 6.4 ICP RF power dependence of deposition rate of AZO thin films

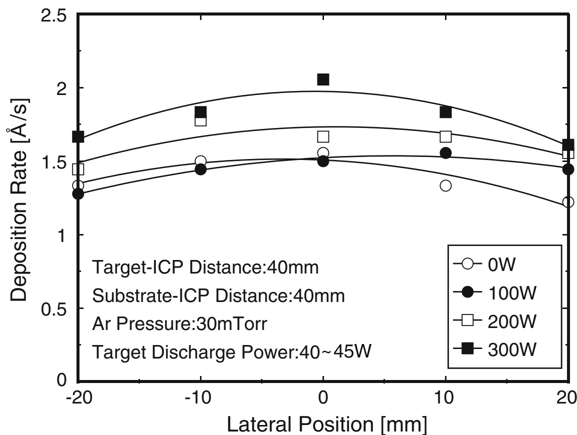

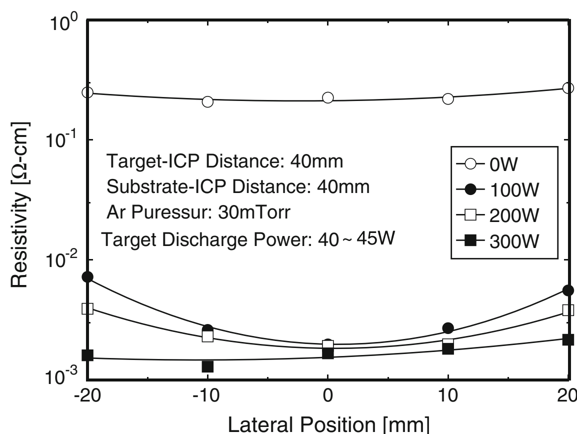

Fig. 6.5 ICP RF power dependence of resistivity of AZO thin films

than 0.5 μm^{-1} have excellent optical transparency. Though the optical transmittance of deposited films is satisfactory for any ICP RF power, the transparency is much improved for ICP RF power more than 100 W as is shown in Fig. 6.6.

Figure 6.7 shows the change in the X-ray diffraction pattern of AZO films with the same thickness of about 300 nm obtained at 5.33 Pa for the ICP RF power of 0, 100, 200, and 300 W. The strong (002) diffraction peak indicates that the films are highly texturized with the c-axis perpendicular to the substrate surface, which is well-known structure for good quality polycrystalline ZnO [3]. The intensity and the width of this peak indicate the fraction of crystallization and the grain size. From Fig. 6.7, we find that the intensity of (002) peak is enhanced with increasing ICP RF power, but the grain size depends weakly on the ICP RF power. The crystallinity of film is promoted with increasing ICP RF power, since the sputtered particles are more excited and ionized and ion fluxes to the substrate are increased in the ICP, resulting in the elevation of substrate surface temperature. However, the number of initial nucleation is already determined at the early deposition stage, resulting in a weak ICP RF power dependence of the grain size. It suggests that the

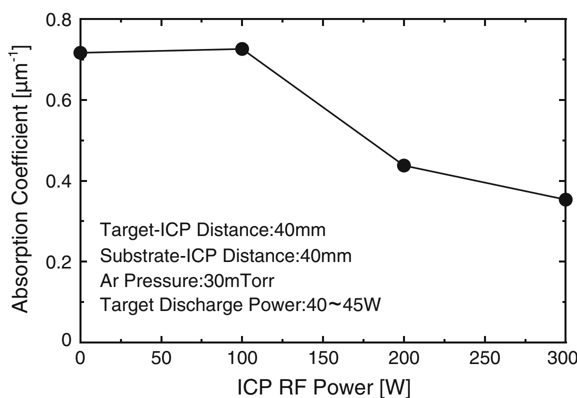

Fig. 6.6 ICP RF power dependence of averaged absorption coefficient of AZO thin films

control of initial nucleation density is important to get large grain sizes that will be effective for increasing carrier mobility.

Figure 6.8 shows the ICP RF power dependence of the elemental ratio of Al and resistivity in the AZO films. The elemental ratio of Al was obtained from the XPS analysis of Al 2p signal. With increasing ICP RF power, the elemental ratio of Al in the film increases and the resistivity decreases. Since the ZnO:Al_2O_3 (2 wt%) target contained 1.56 at% Al, it is found that the fraction of Al in the deposited AZO films changed depending on the ICP RF power. The ICP RF power dependence of the elemental ratio of Al in the film is in agreement with the ICP RF power dependence of the relative gas-phase density of Al to Zn atoms. This will be shown in the later Sect. 6.4.2, which is understood by a large evaporation pressure of Zn. The carrier density of AZO depends on the number densities of donor Al ions and O vacancies, while the carrier mobility depends on the crystallinity of thin films. Thus, it is considered that a rapid decrease in the resistivity is caused not only by the increase in carrier density due to the increase in content of Al atom, but also by the increases in the number density of O vacancies and carrier mobility due to the promotion of crystallinity of thin film as shown in Fig. 6.8. We have also investigated on an AZO target containing 4 wt% Al_2O_3 (or 3.1 at% Al), but the resistivity of AZO (4 wt% Al_2O_3) was several times larger than that of AZO (2 wt% Al_2O_3) for the same ICP RF power range. It is reported that the excess Al fraction in the film causes a decrease in mobility possibly due to the increase in ionized impurity scattering [3].

6.3.3 *Effect of Hydrogen Addition*

In conventional RF sputtering, it is well-known that the electric conductivity of the AZO film is increased when hydrogen gas is added to Ar [31]. Thus, we have

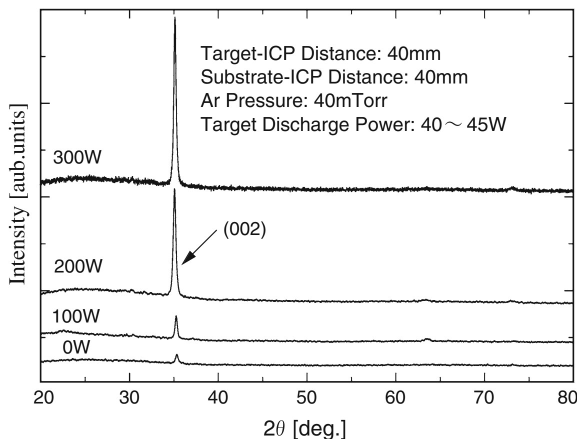

Fig. 6.7 ICP RF power dependence of X-ray diffraction pattern

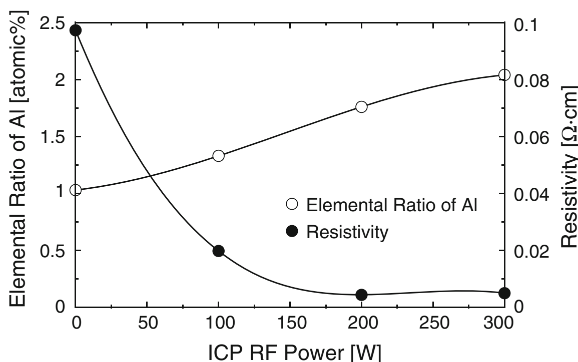

Fig. 6.8 ICP RF power dependence of elemental ratio of Al in the film and resistivity

investigated the effect of hydrogen addition on the electric conductivity, optical transmittance, and deposition rate of the AZO thin films deposited by ICP-assisted sputter deposition. A small amount of hydrogen was mixed with Ar and the total gas pressure was fixed at 4 Pa. The amount of hydrogen addition was changed by setting the preset partial pressure of hydrogen before each deposition. The fraction of hydrogen defined by C_H (=[H_2]/([Ar] + [H_2])) was varied in steps 0, 0.25, 0.5 and 1 %. The ultimate pressure in the chamber was 3×10^{-6} Torr or less. The flow rate of Ar was adjusted to 50 sccm. The sputtering power (target power) and the ICP RF power were fixed at 44 and 200 W, respectively. Deposition time was 30 min for all samples.

Figures 6.9 and 6.10 show the change in resistivity, transmittance, and deposition rate of ZnO films against the hydrogen mixture fraction. From Fig. 6.9, it is found that the film conductivity is slightly improved; the minimum resistivity of 1.8×10^{-3} Ω cm was obtained at $C_H = 0.25$ %. Excess addition of hydrogen over than 0.5 %, however, decreased the film conductivity. The decrease in film resistivity at $C_H = 0.25$ % is explained by the increase in the carrier density, i.e., free electron density due to the increased production of oxygen vacancy. On the other hand, the increase in film resistivity at $C_H = 0.5$ and 1.0 % is explained by the decrease in the carrier mobility due to the degraded crystallinity owing to the excess subtraction of oxygen atoms by the hydrogen atoms. The dependence of the resistivity on hydrogen mixture ratio directly correlates with those of the transmittance and the deposition rate shown in Fig. 6.9. A drastic decrease in the optical transmittance and the deposition rate at $C_H = 1.0$ % is considered to be due to the influence of the excess hydrogen atom density in the AZO thin films as well as in the plasma.

It is reported that the lowest resistivity of 2.8×10^{-4} Ω cm, which is a half or a thirds of the value without hydrogen addition, was obtained when the partial pressure ratio of hydrogen is $C_H = 10$ % [31]. In Ref. [31], a conventional 4 inch RF magnetron was used and the optimum working pressure and RF power were 0.4 Pa and 100 W. However, our experimental condition is very different from that of Ref. [31] in that the sputter deposition was done at much higher pressure around 4 Pa, with lower sputtering power and with additional ICP RF power of 200 W.

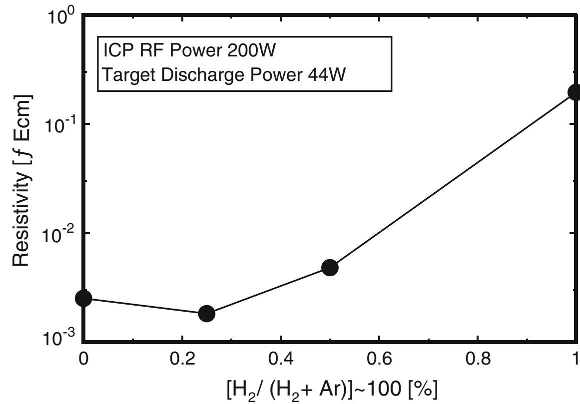

Fig. 6.9 Hydrogen mixture ratio dependence of resistivity of AZO films

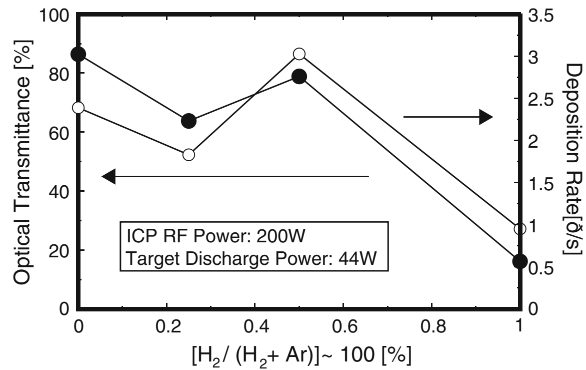

Fig. 6.10 Hydrogen mixture ratio dependence of optical transmittance and deposition rate of AZO films

In the ICP, hydrogen molecules are efficiently dissociated and the flux ratio of atomic hydrogen atoms to the sputter-deposited species would be much higher compared with the CCP case of Ref. [31]. This is the reason why the effect of hydrogen addition appeared at much smaller amount of hydrogen addition than that reported in Ref. [31].

6.4 Diagnostics of ICP-Assisted Sputter-Deposition Processes

As mentioned in the Sect. 6.3.2, crystallization with high orientation along (002) is promoted without intentional substrate heating in the ICP-assisted sputter deposition with increasing ICP RF power. To understand the sputter-deposition mechanism and to improve the film quality further, it is important to reveal the reactions in the gas phase and on the surface. Thus, we have developed several plasma diagnostic systems and applied them as follows: (6.4.1) heat flux

measurement by home-made thermal probes (TPs), (6.4.2) density measurement of sputtered Al and Zn atoms by absorption spectroscopy with hollow cathode lamps (HCLs) and light emitting diodes (LEDs), and (6.4.3) gas temperature measurement by absorption spectroscopy with a tunable external cavity diode laser (ECDL). These are explained below.

6.4.1 *Measurement of Spatial Distribution of Heat Flux to the Substrate*

Energy flux to a substrate was measured by many researchers using variety of TPs in the past in the RF plasma [32–37], RF magnetron plasma [38, 39], and DC grow discharge plasma [40]. However, no measurement of the energy flux to the substrate during the ICP-assisted sputtering has been done to our knowledge. Thus, we have made several TPs with the help of many references [32–40] to grasp the energy flux onto a substrate during the ICP-assisted sputtering.

The energy flux (energy per unit area per second) J to a substrate can be measured with a TP via two different ways: steady-state operation or pulse operation depending on the "plasma on" time duration. In the steady-state operation, plasma is turned on much longer than the thermal relaxation time of the TP, and the temperature gradient ($\Delta T/\Delta x$) on the TP is measured after the TP is thermally equilibrated. Then, the equilibrium J is simply evaluated by the equation

$$J = -k\frac{\Delta T}{\Delta x}, \tag{6.1}$$

where k[W/(m K)] is thermal conductivity. Thus, absolute value of J is measured, even though it takes a long time. Conversely, in the case of the pulse operation, plasma is turned on in a short period of time (shorter than the thermal time constant) and then turned off. From a transient change of the probe tip temperature, J is evaluated by the following equation [32–35]:

$$J = \frac{mc}{S}\left[\left(\frac{\mathrm{d}T_s}{\mathrm{d}t}\right)_{\mathrm{on}} - \left(\frac{\mathrm{d}T_s}{\mathrm{d}t}\right)_{\mathrm{off}}\right]_{T_S}, \tag{6.2}$$

where mc is the thermal capacity (m: mass of probe head, c: specific heat), S is the probe surface area, and $[(\mathrm{d}T_s/\mathrm{d}t)_{\mathrm{on}} - (\mathrm{d}T_s/\mathrm{d}t)_{\mathrm{off}}]$ is the difference in temperature gradient at common substrate temperature T_s during heating and cooling period.

6.4.1.1 Development of a Thermal Probe for Absolute Energy Flux Measurement

Figure 6.11 shows a schematic of a TP made in this work [41–43]. The TP is composed of a Cu plate (10 mm in diameter, 0.1 mm in thickness) facing to the

plasma, a ceramics rod (6 mm in diameter, 10 mm in length) producing temperature gradient, an Al rod (6 mm in diameter, 350 mm in length) connected to the outer heat sink, and outer tubes (Teflon and stainless steel tubes) for thermal and electric insulation, which prevents the energy flux coming in from the side of the TP. The Cu plate, ceramic rod, and Al rod were tightly bonded. The first thermocouple was attached to the ceramic rod at the distance of 6 mm from the joint plane between the ceramic and the Al rod, and the second thermocouple was attached on the Al rod with a distance of 10 mm from the joint plane. The other end of the Al rod was water cooled outside the vacuum vessel. The outer stainless steel tube for heat insulation was grounded to cut the electrical coupling between the TP and plasmas. The greatest thermal gradient appears on the ceramic rod that has a thermal conductivity of 1.6 W/(m K). The length of the ceramics rod was determined by the trade-off between the requirements of a smaller thermal time constant of the ceramic rod and a larger temperature difference at the both ends of the ceramic rod. The thermal time constant is expressed as follows:

$$\tau = CR = \rho c V \frac{L}{kS} = \frac{\rho c}{k} L^2, \tag{6.3}$$

where C is thermal capacity, R is thermal resistance, ρ[kg/m^3] is mass density, c [J/(kg K)] is specific heat, k[W/(m K)] is thermal conductivity, V [m^3] is volume, S [m^2] is cross-section area, and L [m] is length of the TP body. The shorter the length of ceramic rod, the smaller the thermal time constant. The copper plate of TP was biased by connecting a lead wire. As a result of investigation of the influence of film deposition on probe surface, we confirmed that the measured value decreased 4 % by a film deposition thickness of 100 nm. To clean the copper plate surface, the bias voltage of −100 V was applied for 15 min before each experiment.

The TP was set 8 cm from the target surface in the axial direction, and 3 cm from the center axis of magnetron. Figure 6.12 shows a temporal change of difference in temperature measured by the two thermocouples on the TP for the ICP RF power 100 and 200 W when plasma on period was 60 s (pulse operation) and

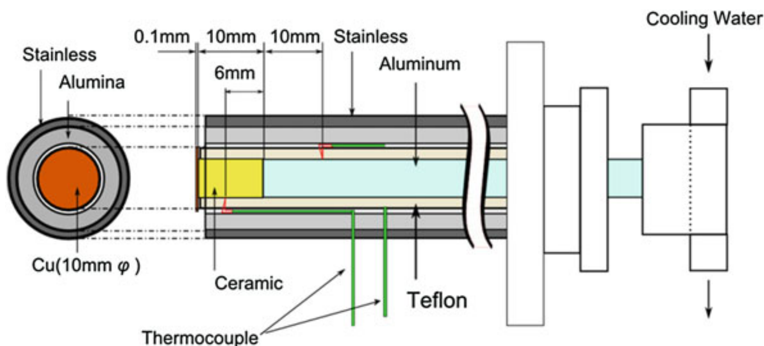

Fig. 6.11 Schematic of a TP that can measure the absolute heat flux

700 s (steady-state operation). The data in Fig. 6.12 indicate that the difference in temperature is mostly saturated with a time constant τ of 160 s and the thermal equilibrium condition is reached at the time after 3–4 τ seconds. In the steady-state operation, the energy flux was evaluated by Eq. (6.1), however, it should be considered that the time interval between each measurement took about 1–2 h, because the heating time of 3–4 τ and the cooling time of several tens of τ were required. In the pulse operation, the energy flux was estimated by Eq. (6.2) by calibrating mc/S with the absolute value of energy flux measured in the steady-state operation. Thus, the time interval between each measurement was reduced by one order of magnitude.

To evaluate the validity of the energy flux measurement in the pulse operation, we compared the variation of the term $[(\mathrm{d}T_s/\mathrm{d}t)_{\mathrm{on}} - (\mathrm{d}T_s/\mathrm{d}t)_{\mathrm{off}}]$ against common substrate temperature difference T_s. As a result, it was found that the term $[(\mathrm{d}T_s/\mathrm{d}t)_{\mathrm{on}} - (\mathrm{d}T_s/\mathrm{d}t)_{\mathrm{off}}]$ in Eq. (6.2) was almost constant within the error of ±5 % when the T_s was taken in the range of 30–100 % of the maximum temperature difference. Thus, the mc/S of the TP was correctly calibrated by dividing the absolute energy flux measured at the same sampling point in the steady-state operation by the constant value of $[(\mathrm{d}T_s/\mathrm{d}t)_{\mathrm{on}} - (\mathrm{d}T_s/\mathrm{d}t)_{\mathrm{off}}]$.

Figure 6.13 shows ICP RF power dependence of energy flux for different target (sputtering) power of 0 W (only ICP discharge) and 40 W (ICP-assisted magnetron discharge). The energy flux to the TP for the 40 W planar magnetron discharge (ICP RF power 0 W) is only 70 W/m^2. The energy flux increases with increasing ICP RF power, and it reaches 3000 W/m^2 for the ICP RF power 200 W and target power 40 W. The contribution of the target (sputtering) power to the total heat flux to the substrate is less than 5 %; i.e., the energy flux in the ICP-assisted sputtering is predominantly determined by the ICP RF power.

The change in energy flux against substrate bias was investigated experimentally and theoretically. The experimental values for the ICP RF power 200 W are plotted with white circles in Fig. 6.14. According to Kersten et al. [35], the total energy influx to a substrate J is the sum of the fluxes due to electrons (J_{e}), ions (J_{i}), neutrals (J_{n}), and photons (J_{p}). In our case, the contributions due to the neutrals

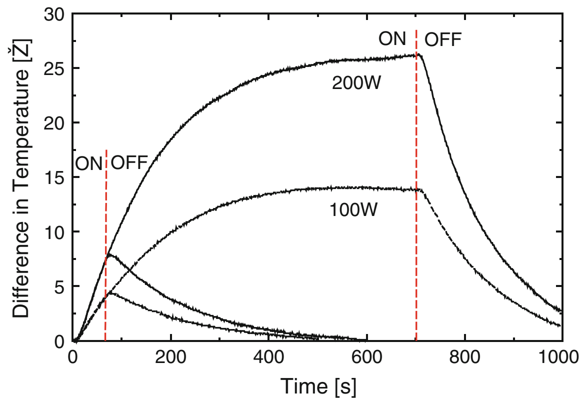

Fig. 6.12 Temporal change in temperature difference obtained by a TP during plasma on and off period for ICP RF power of 100 and 200 W

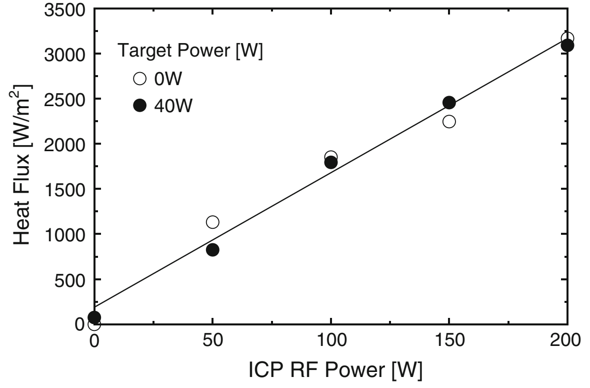

Fig. 6.13 ICP RF power dependence of energy flux (ICP assisted sputtering)

and photons were ignored because of high-density ICP at 4 Pa. Thus, the total energy influx to a substrate J was simply assumed as the sum of J_i due to the kinetic energy of positive ions, J_e due to the kinetic energy of electrons, and J_{rec} due to the recombination of positive ions and electrons at the substrate surface as shown in Eq. (6.4). Here, the contribution of hot neutral species is considered to be negligible. Each contribution is expressed in Eqs. (6.5)–(6.7).

$$J = J_i + J_e + J_{rec}, \tag{6.4}$$

$$J_i = j_i E_i = j_i e_0 (V_{pl} - V_s) = n_e \sqrt{\frac{kT_e}{m_i}} \exp(-0.5) e_0 (V_{pl} - V_s), \tag{6.5}$$

$$J_e = n_e \sqrt{\frac{kT_e}{2\pi m_e}} \exp\left(-\frac{e_0 V_{bias}}{kT_e}\right) 2kT_e, \tag{6.6}$$

$$J_{rec} = j_i E_{rec} = j_i (E_{ionization} - \phi). \tag{6.7}$$

Here, n_e is the electron density, kT_e the electron temperature, m_i the mass of ion, m_e the mass of electron, e_0 the base of natural logarithm, j_i the particle flux of ions,

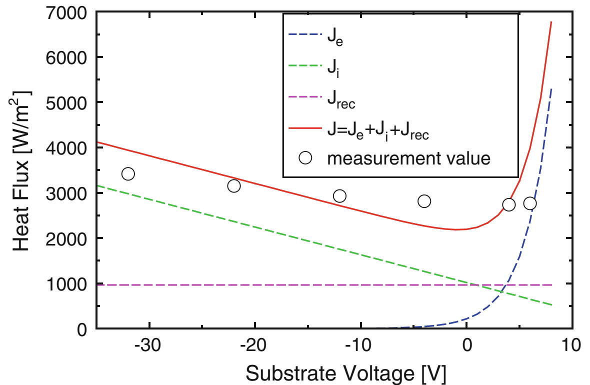

Fig. 6.14 Substrate bias dependence of calculated and measured energy fluxes

V_{pl} the plasma space potential, V_s the substrate potential, V_{bias} (=V_{pl}–V_s) the potential fall from plasma to the substrate that also equals the ion kinetic energy E_i, E_{rec} (=$E_{ionization}-\phi$) the recombination energy of a positive ion, $E_{ionization}$ the ionization energy of Ar ions, and ϕ the work function of the substrate material.

Theoretical energy flux onto a substrate J was calculated for the pure ICP by using the experimental data on n_e, kT_e, and V_{pl}. Electron temperature, electronic density, floating potential and plasma potential were measured by a Langmuir probe respectively 2.5 eV, 2.58×10^{17} m^{-3}, 4.2 eV and 16.8 V for the condition of ICP RF power 200 W at 4 Pa. Thus, we obtained J by substituting the measured values and the physical constants such as m_e, m_i, E_{rec} (=15.7 eV for argon ion) into Eqs. (6.5)–(6.7). Thus, the theoretical energy fluxes of J_i, J_e, J_{rec} and the total J for 200 W ICP were calculated against V_{bias}, which are shown by colored four curves in Fig. 6.14. The experimental substrate bias dependence of the energy flux shown by open circles is in good agreement with the calculated total J. The result indicates that J_i, J_e, and J_{rec} dominantly contribute to the energy flux onto the substrate. It is noted that the heat flux has a minimum of 2,800 W/m^2 at a floating potential of 4 V.

6.4.1.2 Spatial Distribution of Heat Flux to the Substrate in ICP Assisted Sputter-Deposition

To enable space resolved measurements of a directional energy flux in a short time, a new TP was developed. The new TP had a compact and simple structure of a small sampling Cu plate directly soldered to a small K type thermocouple wire with a stainless steel crank tube (6.35 mm diameter) behind it. The lead wire of the thermocouple was covered with alumina tubes for the radial thermal insulation in the crank tube, and connected to a digital multi-meter to monitor temperature. The TP with crank tube was inserted from the substrate side, and the collecting electrode surface was directed to the target and ICP. Spatial distributions of directional heat fluxes were measured with the TP by rotating and transferring the crank tube. Figure 6.15a shows a time response of this TP during plasma on (ICP RF power 200 W for 10 s) and off then after. The decay curve is composed of fast and slow components. Although the slow decay indicates that the thermal protection of the TP is imperfect, it does not affect the determination of the heat flux.

The experimental results for the spatial profile of the directional heat flux in the ICP are shown in Fig. 6.15b. Here, the target and ICP coil are located in the left at $x = -5$ and 0 cm. Figure 6.15b shows that the high heat flux region is at distances 3–5 cm from the coil, which is the same as the empirically optimized substrate positions to get high transparent and high conductive AZO films. Spatial distributions of plasma parameters such as electron density, electron temperature, plasma, and floating potentials were also measured by a movable Langmuir probe. As a result, it was confirmed that the spatial profile of heat flux is similar to that of ion saturation current, and agrees rather well with the calculated heat flux profile by using these plasma parameters.

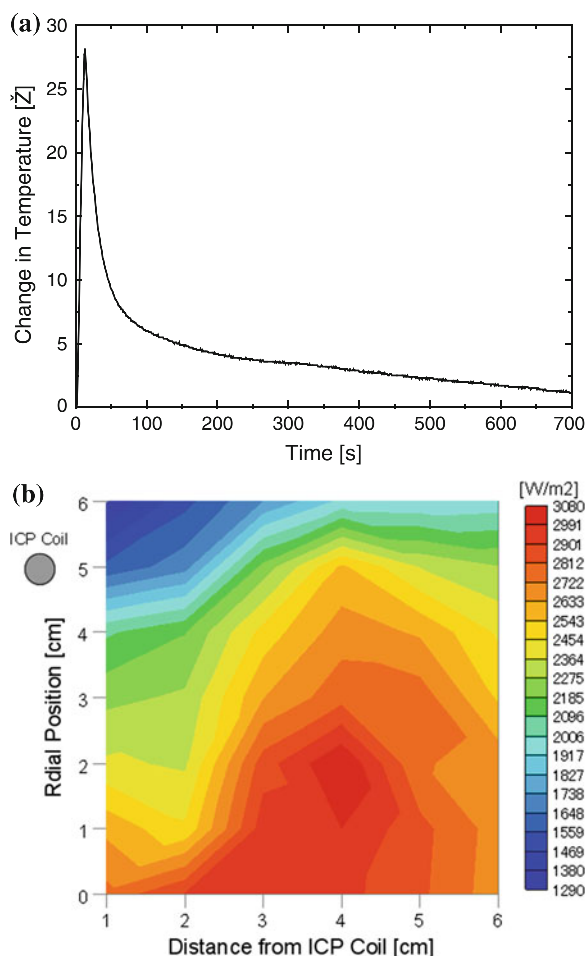

Fig. 6.15 **a** Temporal change in temperature obtained by a compact TP during plasma on (ICP RF power 200 W for 10 s) and off, **b** spatial distribution of the directional heat flux measured by the movable TP

6.4.2 Measurement of Al and Zn Atom Density Using a Hollow Cathode Lamp and UV-LEDs

The behavior of sputtered particles in the gas phase was investigated via optical emission spectroscopy and absorption spectroscopy [44]. The optical emission spectra from the excited species were monitored by employing an optical fiber spectrometer (Ocean Optics, HR4000CG-UV-NIR). For the purpose of estimating the sputtered neutral particle flux to the substrate, sputtered Al and Zn atom densities were investigated by the absorption spectroscopy using two different absorption systems: one consisting of a HCL [45–49], monochromator and photomultiplier tube (HCL-M-PMT) and the other of a LED [50, 51], spectrometer, and a multichannel CCD detector (LED-S-CCD).

6.4.2.1 Measurement of Sputtered Atom Density with HCL-M-PMT System

Ground-state densities of Al and Zn atoms sputtered from the AZO target were measured by the absorption spectroscopy using HCL-M-PMT [47–49]. Optical emission from a HCL (Hamamatsu Photonics, L233-30NQ (Zn) or L233-13NB (Al)) was passed through an optical chopper (NF, 5584A), and guided to a monochromator (JASCO, CT25) through the ICP-assisted sputtering chamber by lens, prism, and optical fiber optics. The time modulated output signal from the PMT was monitored and averaged for 1,024 times on a digital oscilloscope. By comparing the difference in the modulated amplitude of PMT output between plasma ON and OFF phases, absorbance was measured. The sputtered atom density was obtained by comparing the experimental absorbance and the theoretical absorbance that was calculated using assumed gas temperatures (400 K) in light source and plasma reactor and assumed optical path length (0.3 m). The absorption measurements were done for Zn with 307.6 nm ($4s^2\ ^1S_0 \rightarrow 4s4p\ ^3P^o_1$) and for Al with 396.15 nm ($3s^2 3p\ ^2P^o_{3/2} \rightarrow 3s^2 4s\ ^2S_{1/2}$), respectively. It is noted here that the Zn 307.6 nm line used in the experiment is a forbidden line. The use of absorption at the resonant line of Zn (213.856 nm, $4s^2\ ^1S_0 \rightarrow 4s4p\ ^1P^o_1$) was impossible in this experiment due to too strong an absorption.

Figure 6.16 shows the ICP RF power dependence of metal atom densities in gas phase. Both Zn and Al atom densities increase with increasing ICP RF power, but there is a difference in the ICP RF power dependence between Zn and Al atom densities. Al atom density linearly increases with increasing ICP RF power, while Zn atom density increases four times with increasing ICP RF power from 0 to 100 W, then saturates for ICP RF power more than 100 W. The ICP RF power dependence of the ratio of Al to Zn density in the gas-phase correlates well with that of the elemental ratio in the AZO films. The measured Al density is reliable, because the Al atom flux to the substrate was estimated $3\text{–}5 \times 10^{13}\ \mathrm{cm^{-2}\ s^{-1}}$ from the measured Ar density and these values were very close to those calculated from the deposition rate of AZO. Conversely, the measured Zn density was at least two orders of magnitude greater than the expected one; i.e., the Zn atom flux of $2\text{–}8 \times 10^{17}\ \mathrm{cm^{-2}\ s^{-1}}$ was deduced from the measured Zn density and the Zn atom flux of $\sim 10^{15}\ \mathrm{cm^{-2}\ s^{-1}}$ was estimated from the deposition rate. We have not yet identified the cause of this behavior, but we believe that it is due to the large evaporation pressure of Zn, re-evaporation of ZnO due to small formation energy compared to Al_2O_3 [52], blending of absorption by another species such as OH with Zn absorption, or another unknown factor.

6.4.2.2 Measurement of Sputtered Atom Density with LED-S-CCD System

Absorption measurement of Al atoms was also performed using a LED-S-CCD in a DC planar magnetron discharge with Al target [51]. An example of the result is

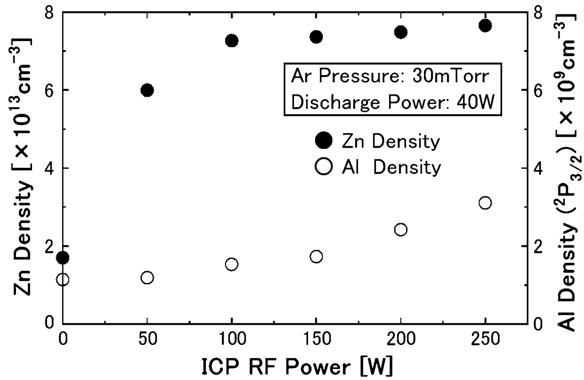

Fig. 6.16 ICP RF power dependence of sputtered Al and Zn atom density in front of the AZO target in ICP-assisted sputtering

shown in Fig. 6.17, indicating clear absorption lines at 394.40 and 396.15 nm of Al. The experimental absorbance using LED-S-CCD was two orders of magnitude smaller than that using HCL-M-PMT under the same conditions as expected from the theoretical estimation, but absorption limit of 2×10^{-4} could be detected owing to the stable operation of LED and CCD. Figure 6.18 shows the discharge power dependence of sputtered Al atom density measured by HCL-M-PMT and LED-S-CCD during magnetron sputtering. Both Al densities agreed well, indicating the Al density was measured with high reliability.

6.4.3 Measurement of Gas Temperature Using an Extra Cavity Diode Laser Absorption

High-resolution diode laser absorption spectroscopy is a powerful tool to diagnose particle density and temperature in plasmas [44, 53]. With the progress in diode laser technology, inexpensive tunable single mode diode lasers with external

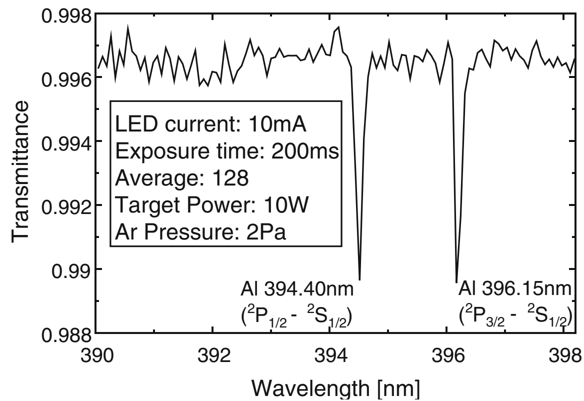

Fig. 6.17 Absorption spectrum of Al atom measured with LED-S-CCD in a DC planar magnetron discharge

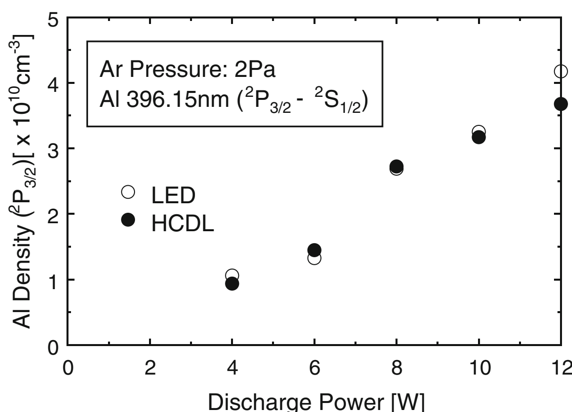

Fig. 6.18 Discharge power dependence of sputtered Al atom density using HCL-M-PMT and LED-S-CCD during magnetron sputtering at 2 Pa

cavity which are also called as ECDLs [54–58] have recently been applied for the measurements of velocity distributions of In [59], He [60], Ar [61], Al [62], and O [63], etc. To grasp the neutral Ar gas temperature in the ICP-assisted sputtering, we have measured the distribution functions of metastable Ar by using a home-made ECDL with Littrow configuration. The ECDL was composed of a diode laser (Opnext HL6738MG), a grating (1800 grooves/mm) for rough tuning and a piezo element for fine tuning. The ECDL delivered a single mode output power of $\sim$5 mW at 696.735 nm of the metastable Ar absorption transition (4s $^2[3/2]^0_2 \rightarrow$ 4p $^2[1/2]_1$). The wavelength was monitored by a 25 cm spectrometer and the spectral scanning was monitored by a scanning Fabry–Perot interferometer (THORLABS SA200-6A). The power of the diode laser beam was attenuated below 10 μW to avoid saturation. The spectral bandwidth of the laser was less than 25 MHz. The laser beam path was set at a position of 3 from the target.

Space average gas temperature (T_{Ar}) and metastable Ar density ($N_{Ar}{}^{m}$) were obtained by a curve fitting of the experimental data with the theoretically calculated absorption line profile function taking into account the saturation of absorption. It is noted that the temperature of metastable Ar ($T_{Ar}{}^{m}$) is the same as that of the ground state Ar (T_{Ar}) because the translational motion is the same in both species. An example of the experimental absorption line profile (obtained at a pressure of 10 mTorr, at a sputtering power of 40 W and ICP RF power of 300 W) is shown in Fig. 6.19 with a calculated fitting line profile, where T_{Ar} and $N_{Ar}{}^{m}$ were estimated to be 410 K and 4.7 × 10^{10} cm^{-3}, respectively. The T_{Ar} was in proportion to ICP RF power, and the T_{Ar} and $N_{Ar}{}^{m}$ were 320 K and 4.5 × 10^{9} cm^{-3}, respectively for the 10 mTorr Ar ICP without the magnetron discharge. The detection limit of $N_{Ar}{}^{m}$ was about 10^{9} cm^{-3}.

Figure 6.20 shows the ICP RF power dependence of Ar gas temperature measured by the homemade ECDL using the 4s $^2[3/2]^0_2 \rightarrow$ 4p $^2[1/2]_1$ transition of metastable Ar at a pressure of 30 mTorr with a magnetron power of 0 W (closed triangle) and 40 W (closed circle). For the 30 mTorr magnetron discharge with the AZO target at a sputtering power of 40 W, T_{Ar} and $N_{Ar}{}^{m}$ were measured to be

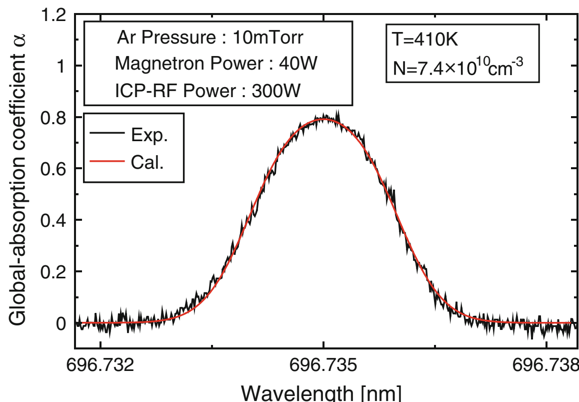

Fig. 6.19 Absorption line profile of the 4s $^2[3/2]_2^0 \rightarrow$ 4p $^2[1/2]_1$ transition of Ar observed in ICP-assisted sputtering at ICP RF power of 300 W, magnetron power of 40 W, at 10 mTorr

440 K and 4 × 10^9 cm^{-3}. With superimposing the ICP RF power from 0 to 300 W on the magnetron discharge, T_{Ar} monotonically increased from 440 to 620 K with increasing ICP RF power as shown in Fig. 6.20; however, $N_{Ar}{}^m$ increased from 4 × 10^9 cm^{-3} to 8 × 10^{10} cm^{-3} for increasing ICP RF power from 0 to 100 W then saturated for the further increase in ICP RF power. The increase in T_{Ar} is due to the gas heating effect in high-density plasmas [64, 65]. ICP RF power dependence of T_{Ar} for the sole ICP without magnetron discharge is also shown in Fig. 6.20 for comparison. We find that T_{Ar} is increased by 80 K with the mixing of sputtered metal atoms. Since the T_{Ar} and $N_{Ar}{}^m$ were observed to increase considerably in the ICP-assisted sputter deposition, we have estimated the heat flux to the substrate by the neutral Ar atoms. As a result, we found that the contribution of the ground state and metastable Ar atoms to the total heat flux to the substrate was negligible.

As described above, our understanding of the ICP-assisted sputter deposition has been gradually increasing. For the moment, however, the film resistivity of our AZO films deposited with ICP-assisted sputter deposition is several times higher than those obtained with other deposition techniques. However, novel ideas to

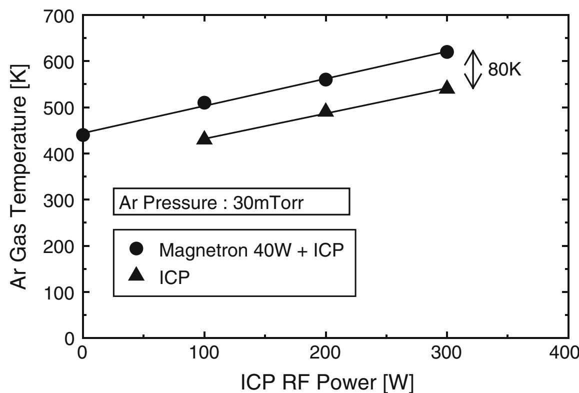

Fig. 6.20 ICP RF power dependence of Ar gas temperature measured by the homemade ECDL using the 4s $^2[3/2]_2^0 \rightarrow$ 4p $^2[1/2]_1$ transition of metastable Ar at a pressure of 30 mTorr with the magnetron power of 0 W (*closed triangle*) and 40 W (*closed circle*)

improve film quality such as the solid-phase crystallization from amorphous phase [66] have been reported. By employing and combining these new ideas with ICP-assisted sputtering, we expect to further improve the film conductivity of AZO, as the ionized sputter deposition has not been fully cultivated.

6.5 Summary

ICP-assisted DC sputter deposition was used for the deposition of Al-doped ZnO (AZO or ZnO:Al) thin films. With increasing ICP RF power, film properties such as deposition rate, crystallinity, transparency, and resistivity were improved. To understand the plasma-surface interaction, several electrical and optical plasma diagnostics were carried out. It was revealed that the high-density ICP heated the substrate through a high heat flux to the substrate, resulting in a high-quality film deposition without the need for intentional substrate heating. The heat flux to the substrate was predominantly contributed by the plasma ions and electrons, not by the neutral Ar atoms which were also significantly heated up in the ICP. The substrate position where the highest quality films were obtained was found to coincide with the position where the substrate heat flux took the maximum of about 3000 W m^{-2}.

Acknowledgments The authors wish to thank T. Iwata, K. Komine, R. Kan, K. Uehara, R. Shindo, H. Kitagawa for their help in the experiment, and Prof. K. Sakai of Miyazaki University for performing the XRD and XPS analyses of AZO films. This research was partially supported by a Grant-in-Aid for Scientific Research (C) from the Japan Society for the Promotion of Science (No. 20540485) in 2008–2010 and by Special Coordination Funds for Promoting Science and Technology sponsored by Japan Science and Technology Agency (JST) in 2009–2011.

References

1. K.L. Chopra, S. Major, D.K. Pandya, Thin Solid Films **102**, 1–46 (1982)
2. T. Minami, H. Sato, K. Ohashi, T. Tomofuji, S. Takata, J. Cryst. Growth **117**, 370–374 (1992)
3. K. Ellmer, A. Klein, B. Rech, *Transparent conductive zinc oxide: basics and applications in thin film solar cells* (Springer, Berlin, 2008)
4. S. Lany, A. Zunger, Phys. Rev. Lett. **98**, 045501 (2007) [4 pages]
5. K. Ellmer, R. Mientus, Thin Solid Films **516**, 5829–5835 (2008)
6. B. Szyszka, in *Transparent conductive zinc oxide: basics and applications in thin film solar cells*, ed. K. Ellmer, A. Klein, B. Rech (Springer, Berlin, 2008), pp. 187–233
7. K. Iwata, T. Sakemi, A. Yamada, P. Fons, K. Awai, T. Yamamoto, M. Matsubara, H. Tampo, S. Niki, Thin Solid Films **445**, 274–277 (2003)
8. K. Yamaya, Y. Yamaki, H. Nakanishi, S. Chichibu, Appl. Phys. Lett. **72**, 235–237 (1998)
9. Y.H. Han, S.J. Jung, J.J. Lee, J.H. Joo, Surf. Coat. Technol. **174–175**, 235–239 (2003)
10. S.J. Jung, Y.H. Han, B.M. Koo, J.J. Lee, J.H. Joo, Thin Solid Films **475**, 275–278 (2005)

11. S. Iwai, Y. Matsuda, M. Shinohara, H. Fujiyama, in *Abstracts and Full-Paper CD of the 18th International Symposium on Plasma Chemistry*, Kyoto, Japan, August 26–31 2007, 396 [4 pages]
12. Y. Matsuda, R. Kan, T. Iwata, K. Komine, K. Uehara, T. Shibasaki, M. Shinohara, in *Proceedings CD of the 19th International Symposium on Plasma Chemistry (ISPC19)*, edited by A. von Keudell, J. Winter, M. Boke, V. Schulz-von der Gathen, Bochum, Germany, July 26–31 2009, P.2.2.20 [4 pages]
13. S. Fay, A. Shah, in *Transparent Conductive Zinc Oxide: Basics and Applications in Thin Film Solar Cells*, ed. K. Ellmer, A. Klein, B. Rech (Springer, Berlin, 2008), pp. 235–302
14. M. Lorentz, in *Transparent Conductive Zinc Oxide: Basics and Applications in Thin Film Solar Cells*, ed. K. Ellmer, A. Klein, B. Rech (Springer, Berlin, 2008), pp. 303–357
15. A. Kuroyanagi, Jpn. J. Appl. Phys. **28**, 219–222 (1989)
16. A.F. Aktaruzzaman, G.L. Sharma, L.K. Malhotra, Thin Solid Films **198**, 67–74 (1991)
17. W. Tang, D.C. Cameron, Thin Solid Films **238**, 83–87 (1994)
18. M. Kemell, F. Dartigues, M. Ritala, M. Leskelä, Thin Solid Films **434**, 20–23 (2003)
19. M. Yamashita, Jpn. J. Appl. Phys. **26**, 721–727 (1987)
20. S.M. Rossnagel, J. Hopwood, Appl. Phys. Lett. **63**, 3285–3287 (1993)
21. J. Hopwood, F. Qian, J. Appl. Phys. **78**, 758–765 (1995)
22. Y. Matsuda, Y. Koyama, K. Tashiro, H. Fujiyama, Thin Solid Films **435**, 154–160 (2003)
23. Y. Matsuda, M. Iwaya, Y. Koyama, M. Shinohara, H. Fujiyama, Thin Solid Films **457**, 64–68 (2004)
24. A. Anders, Thin Solid Films **502**, 22–28 (2006)
25. A.L. Garner, Appl. Phys. Lett. **92**, 011505 (2008) [3 pages]
26. S. Iwai, Y. Matsuda, M. Shinohara, H. Fujiyama, in *Abstracts and Full-Paper CD of the 18th International Symposium on Plasma Chemistry*, Kyoto, Japan, 26–31 August 2007 [4 pages]
27. Y. Matsuda, R. Kan, T. Iwata, K. Komine, K. Uehara, T. Shibasaki, M. Shinohara, in *Proceeding CD of the 19th International Symposium on Plasma Chemistry (ISPC19)*, edited by A. von Keudell, J. Winter, M. Boke, V. Schulz-von der Gathen, Bochum, Germany, 26–31 July 2009, P. 2.2.20 [4 pages]
28. Y. Matsuda, R. Kan, T. Iwata, T. Kitagawa, R. Shindo, M. Shinohara, in *Abstract Book of the 5th DAE-BRNS National Symposium on Pulsed Laser Deposition of Thin Films and Nanostructured Materials (PLD-2009)*, IIT Madras, Chennai India, IRT11, 2–4 December 2009, p 27
29. Y. Matsuda, R. Shindo, A. Hirashima, M. Shinohara, *Inductively Coupled Plasma Assisted Sputter-Deposition of Al-doped ZnO Thin Films*, Bulletin of the American Physical Society, 63rd Annual Gaseous Electronics Conference and 7th International Conference on Reactive Plasmas, Paris France, 4–8 October 2010, Volume **55**, Number 7, DTP.00036 [2 pages]
30. Y. Matsuda, A. Hirashima, K. Mine, T. Hashimoto, D. Matsuoka, M. Shinohara, T. Okada, *Deposition of Transparent Conductive Aluminum-Doped ZnO Films Using RF Superposed DC Sputtering*, Joint IIT Madras-Japan Symposium on ZnO nano-crystals and related materials, IIT-Madras Madras India, 8–10 January 2012 [1page]
31. R. Dsa, K. Adhikary, S. Ray: Jpn. J. Appl. Phys. **47**(3), 1501–1506 (2008)
32. H. Kersten, G.M.W. Kroesen, R. Hippler, Thin Solid Films **332**, 282–289 (1998)
33. H. Kersten, D. Rohde, J. Berndt, H. Deutsch, R. Hippler, Thin Solid Films **377–378**, 585–591 (2000)
34. H. Kersten, E. Stoffels, W.W. Stoffels, M. Otte, C. Csambal, H. Deutsch, R. Hippler, J. Appl. Phys. **87**, 3637–3645 (2000)
35. H. Kersten, H. Deutsch, H. Steffen, G.M.W. Kroesen, R. Hippler, Vacuum **63**, 385–431 (2001)
36. A.L. Thomann, N. Semmar, R. Dussrt, J. Mathias, Rev. Sci. Instrum. **77**, 033501 (2006)
37. R. Dussart, A.L. Thomann, Appl. Phys. **93**, 131502 (2008)
38. R. Wendt, K. Ellmer, K. Wiesemann, J. Appl. Phys. **82**, 2115–2122 (1997)
39. L. Sirghi, G. Popa, Y. Hatanaka, Thin Solid Films **515**, 1334–1339 (2006)
40. H. Matsuura, T. Jida, Contrib. Plasma Phys. **46**, 406–410 (2006)

41. Y. Matsuda, H. Kitagawa, K. Mine, M. Shinohara, Bulletin of the American Physical Society, 63rd Annual Gaseous Electronics Conference and 7th International Conference on Reactive Plasmas, Paris France, 4–8 October 2010, Volume **55**, Number 7, CTP.00010 (2010) [2 pages]
42. H. Kitagawa, R. Kan, K. Mine, M. Shinohara, Y. Matsuda, in *TENCON 2010 IEEE Region 10 Conference*, Fukuoka Japan, 21–24 November 2010. T2-5.P2, pp. 2208–2212 (ISBN: 978-1-4244-6888-1
43. H. Kitagawa, K. Mine, M. Shinohara, Y. Matsuda, T. Okada, in *Proceeding of the 20th International Symposium on Plasma Chemistry (ISPC20)*, Philadelphia USA, 24–29 July 2011, FDM56, ID537 [4 pages]
44. Vladimir N. Ochkin, *Spectroscopy of Low Temperature Plasma* (Wiley-VCH, Germany, 2009)
45. A. Kono, S. Takashima, M. Hori, T. Goto, J. Nucl. Mater. **76**, 460–464 (2000)
46. E. Castanos-Martinez, M. Moisan, Spectrochimica Acta Part B **65**, 199–209 (2010)
47. T. Iwata, R. Shindo, M. Shinohara, Y. Matsuda, in *Proceedings of 31st International Symposium on Dry Process*, Busan Exhibition and Convention Center, Busan, Korea, 24–25 September 2009, 5-P11, pp. 151–152
48. T. Iwata, R. Sindo, K. Komine, M. Shinohara, Y. Matsuda, in *Proceedings CD of the 27th Symposium on Plasma Processing*, Kaiyo Kinen Kaikan, Yokohama, 1–3 February 2010, P1–15, pp. 157–158
49. R. Shindo, T. Iwata, A. Hirashima, M. Shinohara, Y. Matsuda, in *TENCON 2010 IEEE Region 10 Conference*, Fukuoka Japan, 21–24 November 2010, T2-7.3, pp. 1002–1006 (ISBN: 978-1-4244-6888-1)
50. G. Cunge, D. Vempaire, M. Touzeau, N. Sadeghi, Appl. Phys. Lett. **91**, 231503 (2007) [3 pages]
51. R. Shindo, A. Hirashima, M. Shinohara, Y. Matsuda, K. Sakai, T. Okada, in *Proceedings of the 20th International Symposium on Plasma Chemistry (ISPC20)*, Philadelphia USA, 24–29 July 2011, FDM55, ID536 [4 pages]
52. G.V. Samsonov, "*The Oxide Hand Book*" chapter II (IFI/PLENUM, New York, 1973)
53. K. Tachibana, H. Harima, Y. Urano, J. Phys. B: At. Mol. Phys. **15**, 3169 (1982)
54. K.B. MacAdam, A. Steinbach, C. Wieman, Am. J. Phys. **60**(12), 1098–1111 (1992)
55. D. Wandt, M. Laschek, K. Przyklenk, A. Tunnermann, H. Welling, Opt. Com. **130**, 81–84 (1996)
56. S. Eriksson, A.E.M. Lindberg, B. Stahlberg, Opt. Laser Technol. **31**, 473–477 (1999)
57. X.M. Zhang, A.Q. Liu, C. Lu, D.Y. Tang, J. Quant. Electron. **41**(2), 187–197 (2005)
58. B. Mroziewicz, Opto-Electron. Rev. **16–4**, 347–366 (2008)
59. L. Hildebrandt, R. Knispel, S. Stry, J.R. Sacher, F. Schael, Appl. Opt. **42**(12), 2110–2118 (2003)
60. R.F. Boivina, E.E. Scime, Rev. Sci. Instrum. **74**, 4352–4361 (2003)
61. A. Bol'shakov, B.A. Cruden, Technical Physics **53**(11), 1423–1432 (2008)
62. M. Wolter, H.T. Do, H. Steffen, R. Hippler, J. Phys. D: Appl. Phys. **38**, 2390–2395 (2005)
63. K. Sasaki, Y. Okumura, R. Asaoka, Int. J. Spectrosc. (2010). doi: 10.1155/2010/627571
64. M.W. Kiehlbauch, D.B. Graves, Appl. Phys. **91**, 3539–3546 (2002)
65. D.B. Hash, D. Bose, M.V.V.S. Rao, B. A. Cruden, M. Meyyappan, S.P. Sharma, J. Appl. Phys. **90** (5), 2148–2157 (2001)
66. N. Itagaki, K. Kuwahara, K. Nakahara, D. Yamashita, G. Uchida, K. Koga, M. Shiratani, Appl. Phys. Exp. **4**, 011101 (2011) [2 pages]

Chapter 7
Control of ZnO Nano-Crystals Synthesized by Nanoparticle-Assisted Pulsed Laser Deposition Using Buffer Layer and Laser Irradiation

Daisuke Nakamura, Tetsuya Shimogaki, Kota Okazaki, I. A. Palani, Mitsuhiro Higashihata and Tatsuo Okada

Abstract Various ZnO nanocrystals, such as nanowires, nanorods, and nanowalls, have been successfully synthesized by a nanoparticle-assisted pulsed laser deposition (NAPLD). In this study, we have succeeded in controlling the growth density and position of the ZnO nano crystals with a ZnO buffer layer and a buffer layer patterned by interference laser irradiation, respectively. Vertically aligned ZnO nanowires with low lateral density were grown on the ZnO buffer layer, and each nanowire was grown at the tip of the hexagonal cone-shape ZnO core formed on the layer. The lateral density of the ZnO nanowires can be controlled by the buffer layer thickness. In addition, laser irradiation to the buffer layer can also control the density, because the density of the nanowire grown on the laser-irradiated layer was clearly decreased as compared with no-irradiated layer. Furthermore, patterned growth of ZnO nano crystals was demonstrated using four beam interference patterning. The buffer layer and interference laser irradiation can be used as one of the effective additives to control the growth of the ZnO nano crystals synthesized by NAPLD.

7.1 Introduction

Zinc oxide (ZnO) is an attractive material for many different kinds of applications because of piezoelectric [1, 2], spintronic [3], catalytic, electronic, and optoelectronic properties. In addition, one-dimensional ZnO nanostructure has been attracting a lot of attention as building blocks for nanodevices such as ultraviolet

D. Nakamura (✉) · T. Shimogaki · K. Okazaki · M. Higashihata · T. Okada
Graduate School of Information Science and Electrical Engineering, Kyushu University, 744 Motooka, Nishi-ku, Fukuoka 819-0395, Japan
e-mail: dnakamura@ees.kyushu-u.ac.jp

I. A. Palani
Indian Institute of Technology, Indore, India

M. S. R. Rao and T. Okada (eds.), *ZnO Nanocrystals and Allied Materials*, Springer Series in Materials Science 180, DOI: 10.1007/978-81-322-1160-0_7,
© Springer India 2014

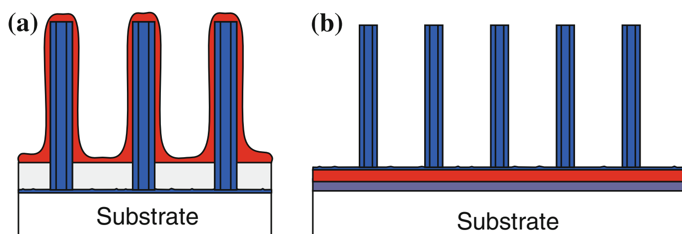

Fig. 7.1 Schematic of the layer-structured ZnO nanowires, **a** core/shell structure and **b** film-wire structure

(UV) lasers [4], laser diodes [5], light emitting diodes (LEDs) [6–12], gas sensor [13], strain sensors [14], and UV photodetectors [15, 16] because of their unique properties. Especially, ZnO nanowire has attracted a great attention, because it has not only superior crystalline quality, but also freedom to choose substrate and large surface area to volume ratio.

For the practical optoelectronic applications based on the ZnO nanowires; however, fabrication of layered structures for *p–n* junction and control of nanowire growth direction, shape, density, and position are essentially required. In our study, we have succeeded in synthesizing various nanostructures, nanorods [17, 18], nanowalls [19], and the vertically and horizontally aligned ZnO nanowires [20–24] by a nanoparticle-assisted pulsed laser deposition (NAPLD) without any catalyst. Besides, the density-controlled growth of vertically aligned ZnO nanowires has been successfully achieved by varying substrate–target distance, repetition rate, and laser energy [25]. Recently, we realized the growth of layer-structured nanowires in a simple step process by changing the growth pressure. Typically, ZnO nanowires are grown at a pressure of 20–40 kPa by NAPLD. On the other hand, a ZnO thin film is also deposited with decreasing the pressure to several Pa in a conventional PLD process using the same vacuum chamber. For instance, core/shell ZnO nanowires, as shown in Fig. 7.1a, can be fabricated by deposition of the film after growth of the nanowires. When a thin film is deposited as a buffer layer before growth of the nanowires, film-wire layered structure can be obtained, as shown in Fig. 7.1b. In addition, we demonstrated the periodic growth of ZnO nano crystals in a two-step process, which combines interference laser irradiation to the buffer layer and NAPLD. In this paper, we describe influence of the buffer layer and laser irradiation on ZnO nanocrystals synthesized by NAPLD.

7.2 Experiments

7.2.1 Experimental Setup

Figure 7.2 shows the schematic of the experimental setup for synthesis of laser structured ZnO nanowire by NAPLD. In this experiment, sintered targets of pure

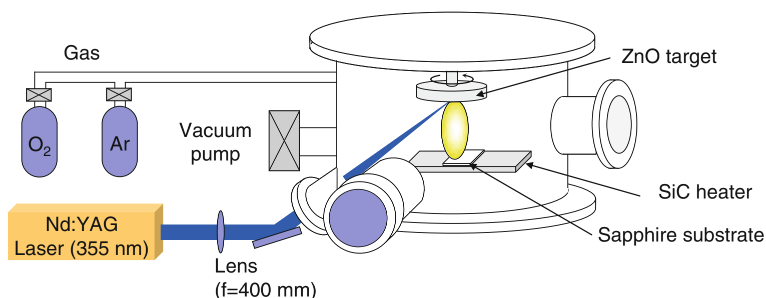

Fig. 7.2 Experimental setup for synthesis of layer structured ZnO nanowire by NAPLD

ZnO, Sb-doped ZnO, and Li–Ni codoped ZnO were prepared in synthesizing ZnO nano crystals. A *c*-plane or an *a*-plane sapphire substrate (10 mm × 10 mm) was put on a SiC heater in a vacuum chamber and the target–substrate distance was set to be 40 mm. The substrate was heated to 400–800 °C in the vacuum chamber filled with a background gas of argon or oxygen. The ZnO target was ablated with the third harmonics of a Q-switched Nd:YAG laser at 355 nm with a repetition rate of 10 Hz and a fluence of about 0.5–1.0 J/cm^2.

In this experimental setup, various ZnO nanostructures could be synthesized by just changing the growth conditions. Table 7.1 shows the typical parameters for synthesis of ZnO nanostructures by NAPLD. In addition, we introduced a multi-target changer, as shown in Fig. 7.3, in the experimental setup. Four kinds of targets could be fixed on it. Since targets can be changed without disturbing ambient growth condition during synthesis of ZnO nanowires, it is expected to be fabricated layer-structured ZnO nanocrystals consisting of different material layers.

The morphology of the as deposited products was analyzed by scanning electron microscopy (SEM). The optical properties of the ZnO nanowires were investigated by observing the room temperature photoluminescence (PL) using a He-Cd laser as the excitation light source.

Table. 7.1 Typical parameters for synthesis of ZnO nanostructures by NAPLD

	ZnO Film	ZnO nanowire	ZnO nanorod
Temprature (°C)	~650	700–800	600–800
Gas (20 sccm)	O_2	Ar	O_2
Pressure	~3 Pa	~40 kPa	~2 kPa

Fig. 7.3 Photograph of the multi-target changer

7.3 Results and Discussion

7.3.1 Influence of ZnO Buffer Layer on Growth of ZnO Nanowires

At first, a difference between ZnO nanowires with and without a ZnO buffer layer was investigated using a pure ZnO target. Figure 7.4 shows the SEM image of pure ZnO nanowires synthesized on bare *c*-plane sapphire substrate. ZnO nanowires were grown at a background argon pressure of 26.7 kPa and a substrate temperature of 800 °C for 20 min. Vertically aligned ZnO nanowires with high lateral density were grown on the substrate. The lengths of the nanowires are around 2 μm and the diameters are about 100 nm.

By contrast, the low-density ZnO nanowires were synthesized on the ZnO buffer layer, as shown in Fig. 7.5. A ZnO buffer layer of about 400 nm thickness was deposited on a sapphire substrate at a background oxygen pressure of 3.3 Pa and a substrate temperature of 650 °C for 5 min before growth of ZnO nanowires. Subsequently, the background gas was changed from oxygen to argon and ZnO nanowires were grown on the ZnO buffer layer at a pressure of 26.7 kPa and a substrate temperature of 800 °C for 15 min without breaking vacuum.

Almost all nanowires were vertically well aligned and grown on hexagonal cone-shape ZnO cores. The size of the cores formed at the bottom of the nanowires was not uniform and the nanowires having no cores also exist. Achievement of the density decrease by introducing a ZnO buffer layer has been reported by Cao et al. [26]. They say that ZnO buffer layer seems to prevent nanowire nucleation and growth, since the incoming ZnO incorporates much more effectively into the ZnO buffer layer. A similar tendency was observed in our experiment.

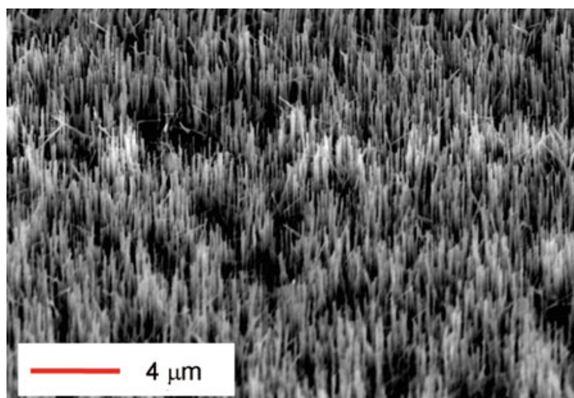

Fig. 7.4 SEM image (45° tilted view) of ZnO nanowires grown on the substrate

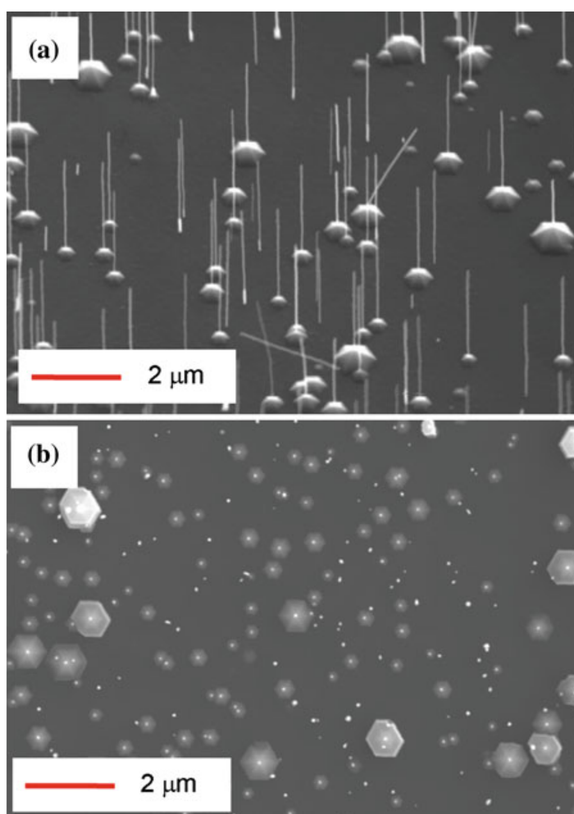

Fig. 7.5 SEM image of ZnO nanowires synthesized on the ZnO buffer layer, **a** 45° tilted view and **b** top view

Regarding alignment of the nanowires, previously we have been succeeded in synthesizing the vertically and horizontally aligned ZnO nanowires using a pre-annealed sapphire substrate [20–22]. The pre-annealing process greatly improves

the substrate surface morphology, so that drastic change in surface morphology is obtained from the irregularly roughened surface to the atomically flat surfaces with atomic steps. On the other hand, the introduction of the buffer layer may increase surface roughness. However, vertically aligned ZnO nanowires are grown on the buffer layer.

Next, in order to investigate the influence of the ZnO buffer layer thickness on growth of the ZnO nanowires, four samples were prepared with different thickness of the buffer layer. The buffer layers were deposited on the sapphire substrates with the deposition times of 1, 3, 5, and 10 min at a background oxygen pressure of 3.3 Pa and a substrate temperature of 650 °C. After deposition of the buffer layer, ZnO nanowires were subsequently grown on the buffer layer at a background argon gas of 26.7 kPa and a substrate temperature of 750 °C for 30 min.

Figure 7.6 shows the SEM images of ZnO nanowires synthesized on the buffer layer with a deposition time of 1 min. Vertically aligned ZnO nanowires with high density are grown on the buffer layer. The lengths and diameters of the nanowires were about 1 μm and 100 nm, respectively. Figure 7.7 shows the SEM images of ZnO nanowires synthesized on the buffer layer with a deposition time of 3 min. The density of the nanowires decreased with increasing the deposition time of the buffer layer. Figure 7.8 shows the SEM images of ZnO nanowires synthesized on the buffer layer deposited for 5 min. Very low density nanowires are grown on the thicker buffer layer. The hexagonal cone-shape cores at the bottom of the nanowires were formed. It is found that the hexagonal cores also exist in Figs. 7.6b and 7.7b, though it is hard to distinguish the cores due to the high density. When the deposition time of the buffer layer was 10 min, the nanowire density was further decreased, as shown in Fig. 7.9.

Figure 7.10 shows the surface profiles of the buffer layers with different deposition times. The surface roughness increased with increasing the deposition time. Table 7.2 shows the surface roughness (rms) of the buffer layers. In general, the grain size increases with increasing the film growth time [27, 28]. These large grains probably prevent the nucleation of the nanowire, because the incoming ZnO nanoparticles may be incorporated effectively into the large grains. Though the growth mechanism of the nanowire on the ZnO layer by NAPLD have been under investigation, the buffer layer can be used as one of the effective additives to control the growth density of the ZnO nanowires synthesized by NAPLD.

The optical property of the ZnO nanowires was characterized with PL spectra measurement at room temperature by a spectrometer (multi-channel analyzer C10027, HAMAMATSU photonics). Figure 7.11 shows the PL spectra from the ZnO nanowires grown on the buffer layer. The spectra are normalized to the UV peak centered at 380 nm. Not only the UV emission but also broad visible emission was observed from the ZnO nanowires. The UV emission band is due to a near-band-edge (NBE) recombination of ZnO, which is the emission of excitons through an electron-hole recombination process. The broad visible emission peak of ZnO is a typical defect-related emission, which is usually attributed to the deep-

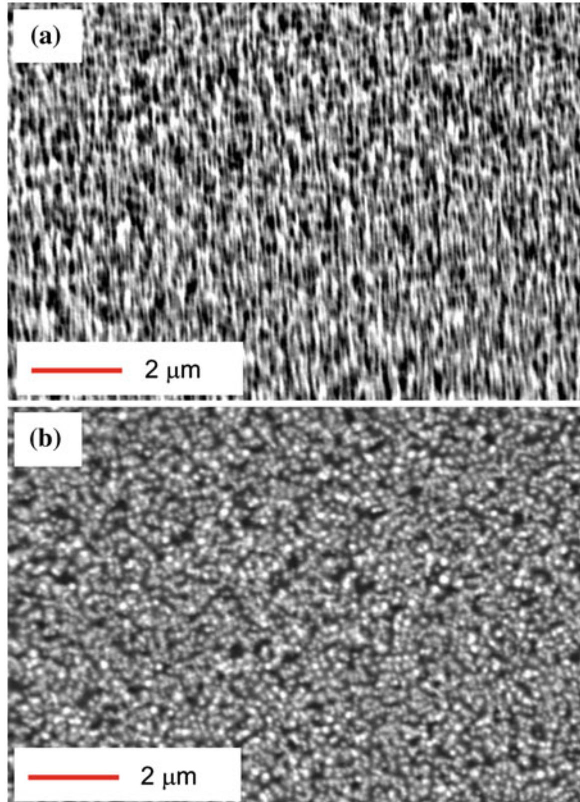

Fig. 7.6 SEM images of ZnO nanowires synthesized on the ZnO film with a deposition time of 1 min, **a** 45° tilted view and **b** top view

level oxygen vacancy in the surface and subsurface lattices of ZnO materials. A red-shift in the visible emission peak is observed by increasing the buffer layer thickness. The visible emission may be attributed to the defects in the buffer layer because an intensity ratio of visible emission to NBE from the ZnO nanowires increases with increasing the layer thickness.

7.3.2 Crystal Quality of the ZnO Nanowire

Crystal quality of the synthesized ZnO nanowires was analyzed with TEM. Figure 7.12 shows a high-magnification TEM image of the ZnO nanowire. ZnO nanowires are single crystalline with the wurzite hexagonal phase and grown along the (0001) direction. In addition, the nanowires are preferentially oriented in the (0002) direction from the XRD analysis, as shown in Fig. 7.13.

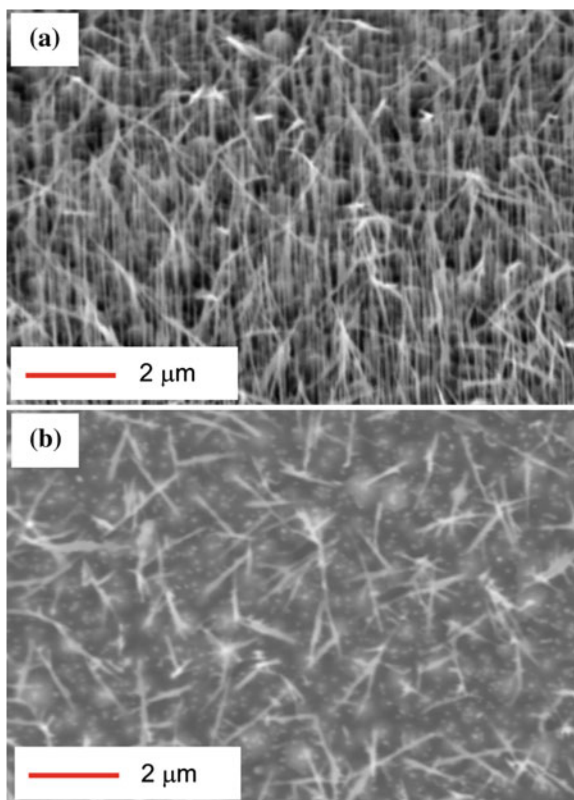

Fig. 7.7 SEM images of ZnO nanowires synthesized on the ZnO film with a deposition time of 3 min, **a** 45° tilted view and **b** top view

7.3.3 Synthesis of Core/Shell-Structured ZnO Nanowire

It is important to fabricate layered structure in not only the nanowire axial direction but also the radial direction, because core/shell nanowires are expected to be more efficient in emitting due to low thermal quenching and large surface effect [26]. Figure 7.14a shows the SEM image of the ZnO nanowires grown on the ZnO buffer layer at the same deposition condition as that of Fig. 7.5. Figure 7.14b, c shows the top view and 45° tilted view SEM images of ZnO nanowires after growth of the shell for 5 min at the temperature of 650 °C and an oxygen gas pressure of 3.3 Pa. The ZnO nanowires grew uniformly in the radial direction, indicating that ZnO shell coats homogeneously the entire nanowire. Figure 7.14d shows the SEM image of the ZnO nanowires after growth of the ZnO shell for 20 min. The diameter of the ZnO nanowire was further increased uniformly with increasing the deposition time. Thus, it was found that thickness of the shell could be controlled by the deposition time and expected that core/shell structure consisting of different material layers could be fabricated using different kinds of targets [29].

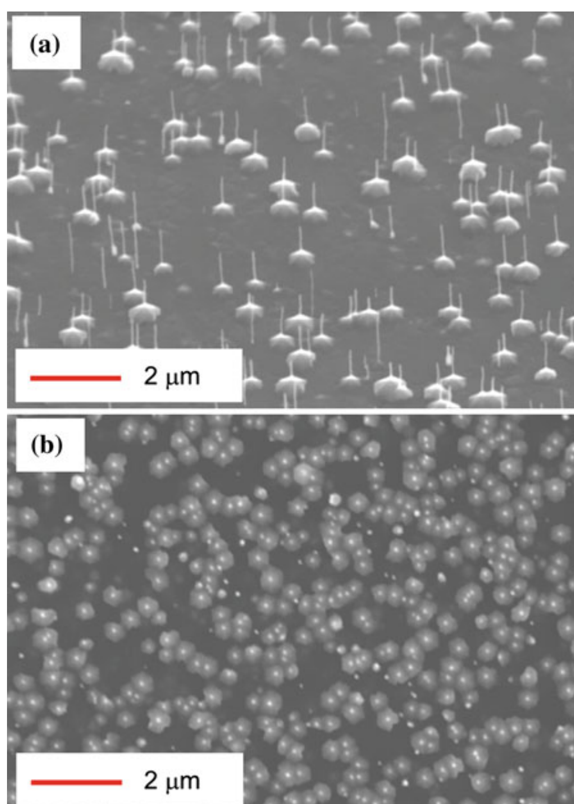

Fig. 7.8 SEM images of ZnO nanowires synthesized on the ZnO film with a deposition time of 5 min, **a** 45° tilted view and **b** top view

7.3.4 Synthesis of Layer-Structured ZnO Nanowires Consisting of Different Material Layers Using Doped ZnO Target

The layer-structured ZnO nanowires, which are a film-wire structure and a core/shell structure, consisting of different material layers also could be synthesized using a pure and a Li–Ni codoped ZnO targets. Li–Ni codoped ZnO is one of the promising targets for *p*-type ZnO thin film [30–32]. Figure 7.15 shows the SEM images of the ZnO nanowires synthesized on the Li–Ni codoped ZnO buffer layer. The Li–Ni codoped ZnO film was deposited on a *c*-plane sapphire substrate at a temperature of 400 °C and an oxygen gas pressure of 3.3 Pa. After deposition of the film for 5 min, the nanowires were subsequently synthesized on the buffer layer at a temperature of 750 °C and an argon gas pressure of 26.7 kPa in the same chamber without breaking vacuum. The growth time of the ZnO nanowires was 15 min. The vertically aligned ZnO nanowires with a diameter of 50–100 nm and a length of around 2 μm were formed.

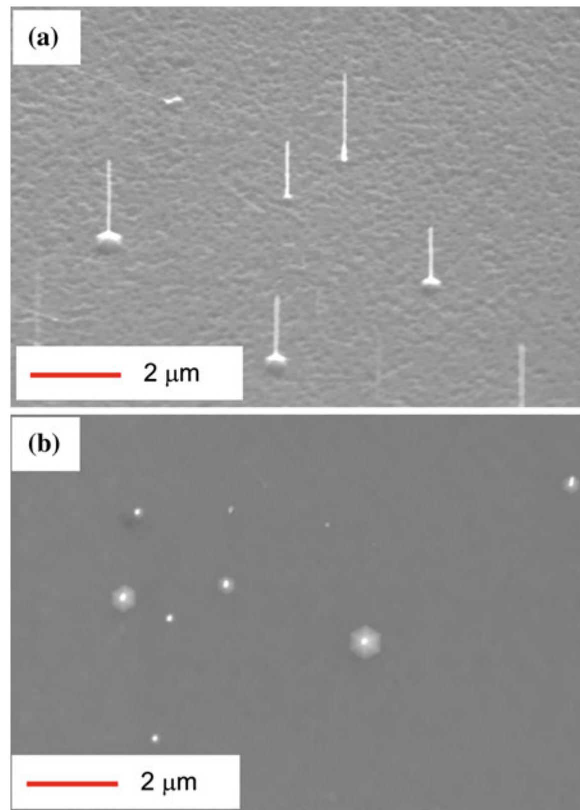

Fig. 7.9 SEM images of ZnO nanowires synthesized on the ZnO film with a deposition time of 10 min, **a** 45° tilted view and **b** top view

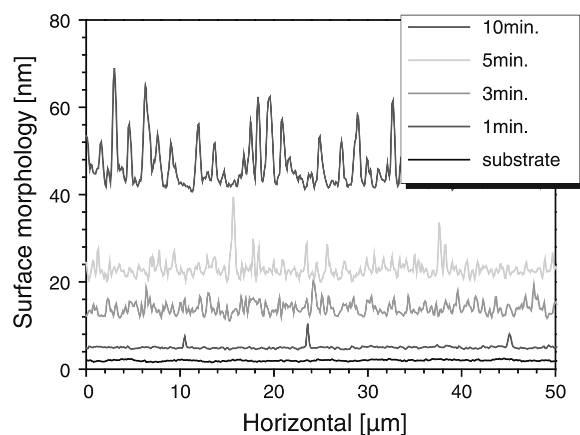

Fig. 7.10 Surface profiles of the buffer layers with different deposition times of 1, 3, 5, and 10 min

The core/shell-structured ZnO nanowires consisting of different materials also could be synthesized. Figure 7.16a shows the SEM image of the pure ZnO nanowires synthesized after deposition of the ZnO film. Figure 7.16b shows the

Table 7.2 The surface roughness rms of the ZnO buffer layer with different deposition times

Deposition time (min)	1	3	5	10
RMS (nm)	0.4	1.5	4.3	8.1

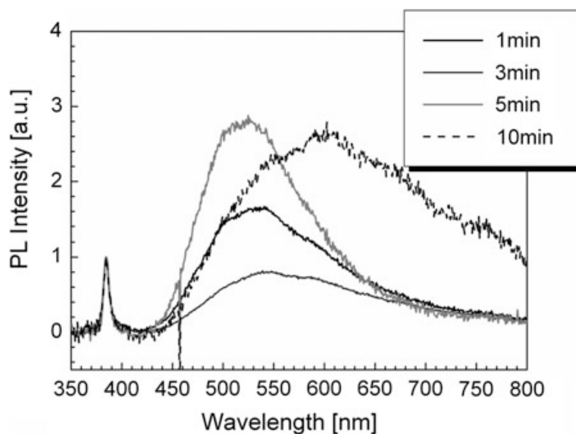

Fig. 7.11 PL spectra from the ZnO nanowires on the buffer layer deposited with different deposition times

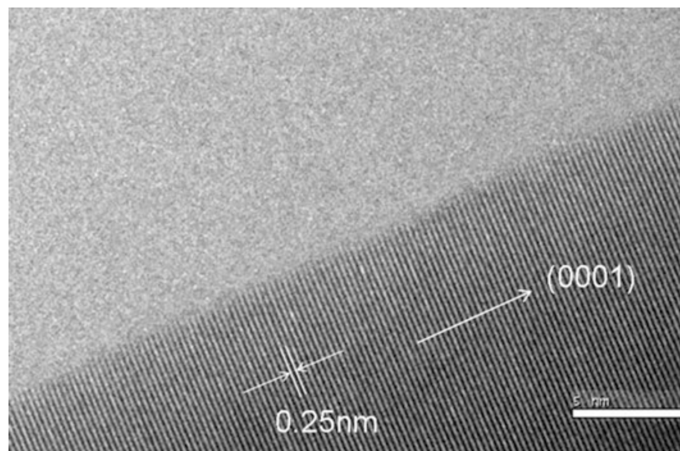

Fig. 7.12 High-magnification TEM image of the ZnO nanowire taken from the side part of the nanowire grown on the *a*-plane sapphire substrate

SEM image of the ZnO/Li–Ni codoped ZnO core/shell-structured ZnO nanowires after growth the shell for 10 min at a temperature of 400 °C and an oxygen gas pressure of 3.3 Pa.

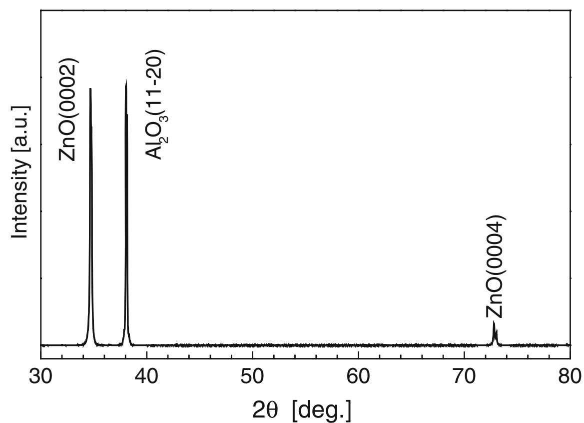

Fig. 7.13 XRD results of the ZnO nanowires grown on the *a*-plane sapphire substrate

Fig. 7.14 SEM images of **a** ZnO nanowires on the buffer layer and core/shell-structured ZnO nanowires, where the growth time of the shell layer were 5 min (**b** top view, **c** 45° tilted view), and **d** 20 min

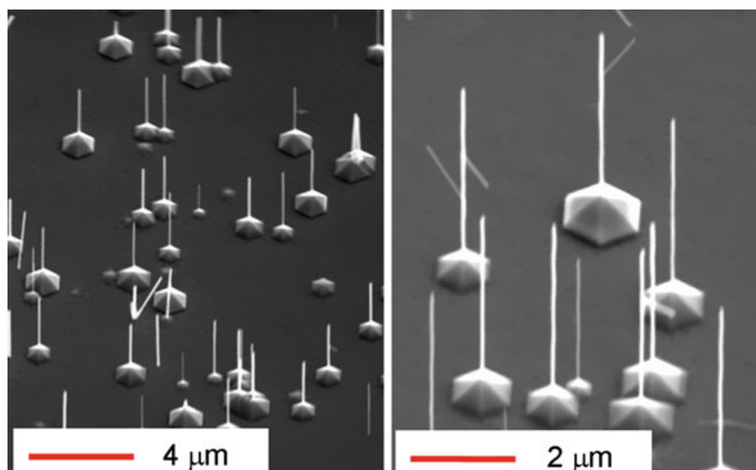

Fig. 7.15 SEM images of the ZnO nanowires synthesized on the Li–Ni codoped ZnO buffer layer

Figure 7.16c, d shows the 45° tilted view and top view SEM images of the ZnO nanowires after growth of the ZnO shell for 20 min. The diameter of the ZnO nanowires increased uniformly with increasing the deposition time of the shell. On the other hand, the hexagonal cone-shape cores were buried in the Li–Ni codoped ZnO film as shown in Fig. 7.16b, c. Thus, the incoming Li–Ni codoped ZnO seems to incorporate much more effectively into the ZnO buffer film layer than the nanowires. These results show that the core/shell structure consisting of different materials is also able to be fabricated by the multi-target changer system.

The optical property of the layer-structured ZnO nanowires was investigated at room temperature. Figure 7.17 shows the PL spectra from the ZnO nanowires synthesized on the Li–Ni codoped ZnO and the pure ZnO buffer layer. The spectra are normalized at the UV peak for easy comparison. A strong UV peak centered at 380 nm and a weak broad visible emission with a peak at about 500 nm were observed from the ZnO nanowires of the pure ZnO film. The UV emission band is due to a NBE recombination of ZnO, which is the emission of excitons through an electron-hole recombination process [33]. The broad green emission peak of ZnO is a typical defect-related emission, which is usually attributed to the deep-level oxygen vacancy in the surface and subsurface lattices of ZnO materials [34]. The intensity of the broad visible emission from the nanowires grown on the Li–Ni codoped ZnO film is higher than that on the pure ZnO film. The results show that the Li–Ni thin film might cause an increase of deep-level defects inside ZnO lattices [35]. However, as an intensity ratio of green emission to NBE from the ZnO nanowires is less than 0.4, the fact that the UV emission is strong and the defect emission is weaker shows the good crystal quality both of ZnO nanowires on the pure and Li–Ni codoped films.

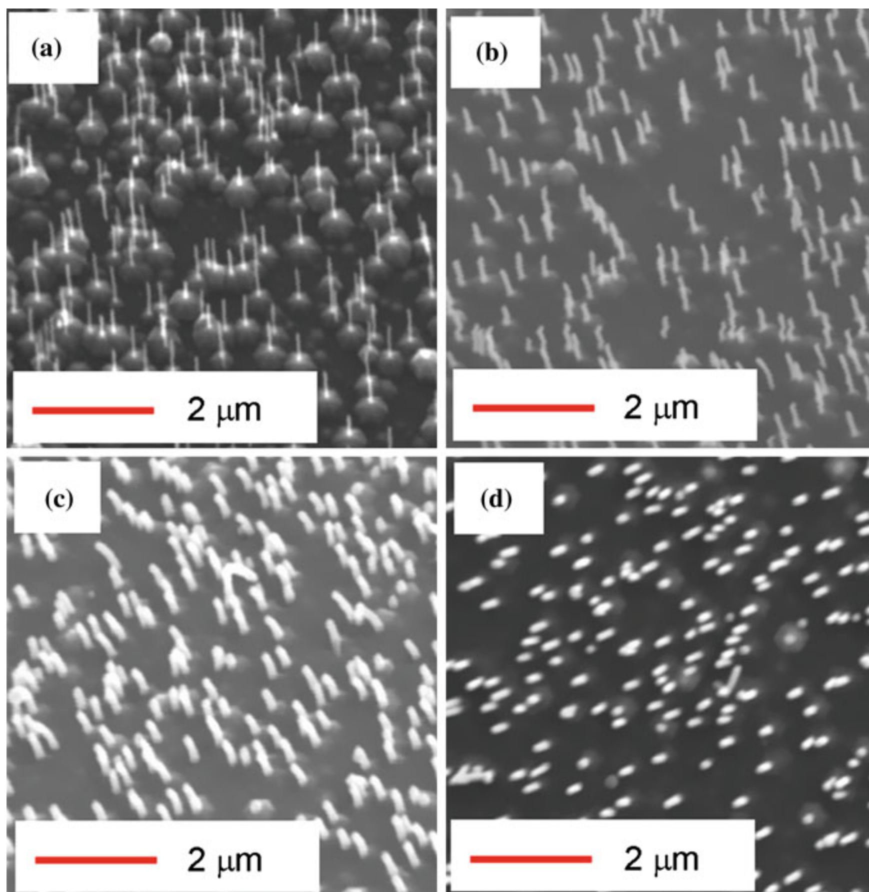

Fig. 7.16 SEM images of (**a**) ZnO nanowires on the film and the ZnO/Li–Ni codoped ZnO core/shell-structured ZnO nanowires, where the growth time of the Li–Ni codoped ZnO shell layer were (**b**) 10 and 20 min (**c** 45° tilted view, **d** top view)

The PL characteristic of the core/shell-structured ZnO nanowires, as shown in Fig. 7.16, was also investigated. The PL was measured in two different configurations, as shown in Fig. 7.18. Figure 7.19 shows the PL spectra of the core/shell-structured ZnO nanowires. A visible light emission at green emission band and very low UV emission were observed. On the other hand, no emission was detected under excitation from the nanowire side, as shown in Fig. 7.18b. The results indicate that the Li–Ni codoped ZnO film would absorb UV emission. To fabricate a ZnO-based homo-junction LED using the Li–Ni codoped ZnO as a *p*-type material, an intrinsic layer would be inevitably required between the *p*–*n* junction, which is a PIN (*p*-type-Intrinsic-*n*-type) diode structure, in order to prevent absorption of the UV emission around the Li–Ni codoped ZnO.

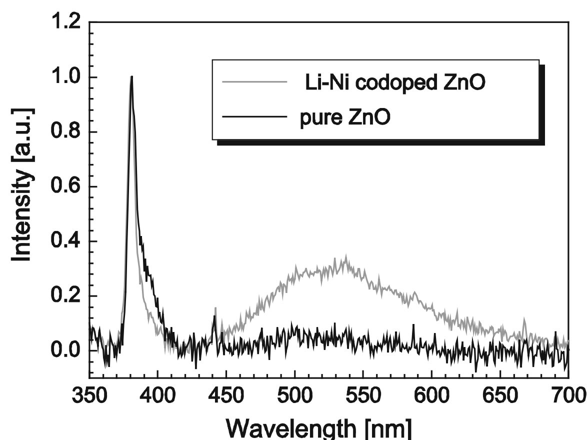

Fig. 7.17 PL spectrum of the ZnO nanowires on the ZnO and the Li–Ni codoped ZnO thin film

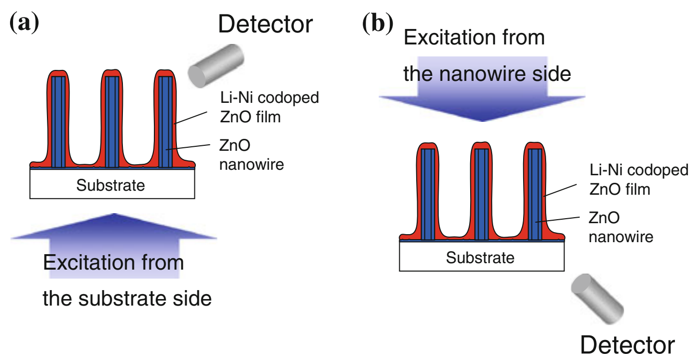

Fig. 7.18 Schematic of the PL measurement from the ZnO/Li–Ni codoped ZnO core/shell-structued ZnO nanowires

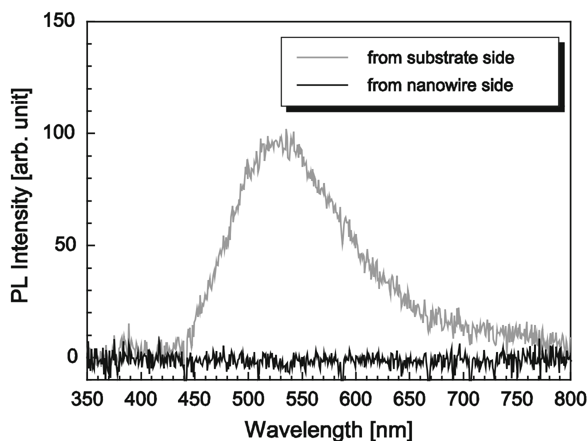

Fig. 7.19 PL spectrum of the core/shell-structured ZnO nanowire

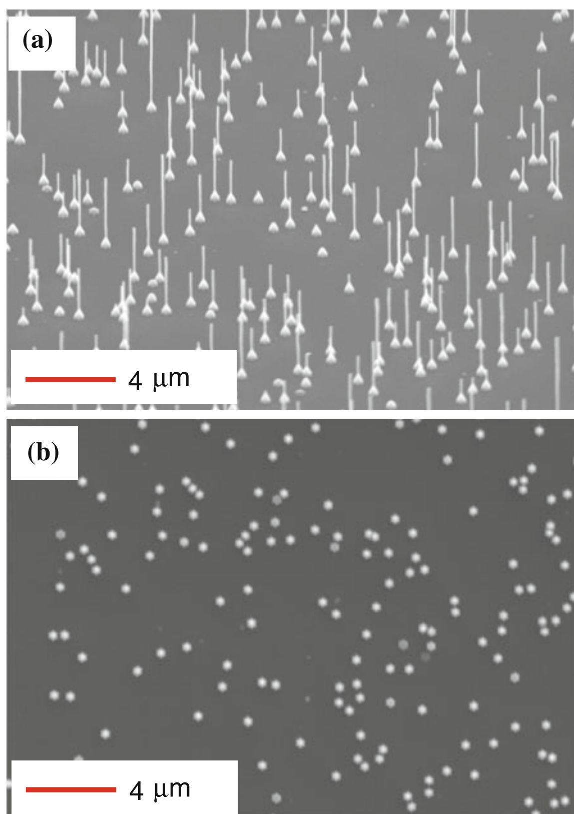

Fig. 7.20 SEM images of ZnO nanowires synthesized on the ZnO layer using Sb_2O_3 ZnO target, **a** tilted view and **b** top view

Next, influence of Sb on growth of the ZnO nanowires in NAPLD was investigated using a ZnO target doped with 5 wt % Sb_2O_3 [36]. Sb is attracted as a one of the promising *p*-type dopant in ZnO. Recently, Sb-doped ZnO film [37, 38] and ZnO nanostructures have been reported [39, 40]. In addition, Sb can be used as an effective additive to control the morphology of ZnO nanostructure [41] and grain [42]. Figure 7.20 shows the SEM images of the Sb-doped ZnO nanowires. A ZnO buffer layer was deposited on an *a*-plane sapphire substrate at a background oxygen pressure of 3.3 Pa and a substrate temperature of 650 °C for 1 min before growth of ZnO nanowires. Subsequently, the background gas was changed from oxygen to argon and ZnO nanowires were continuously grown on the ZnO buffer layer at a pressure of 40 kPa and a substrate temperature of 750 °C for 30 min. Vertically well-aligned ZnO nanowires with low density were grown on the substrate.

The core size was more uniform than that of the pure ZnO target, as shown in Fig. 7.20b. Figure 7.21b shows size histograms of the hexagonal cone-shape core shown in Fig. 7.20 and that of pure ZnO is also shown in Fig. 7.21a for comparison. While the core sizes of the pure ZnO nanowires are broadly distributed in the range of 0–600 nm, the size distribution of Sb-induced ZnO nanowires is

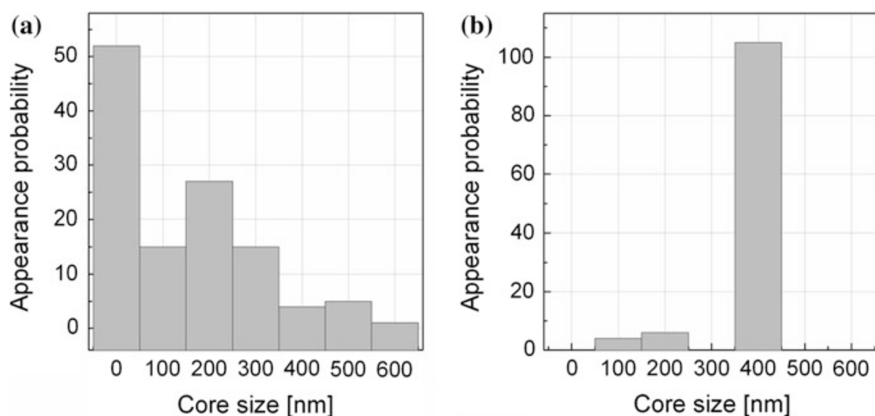

Fig. 7.21 The size histograms of hexagonal cone-shape cores grown with **a** pure ZnO and **b** Sb_2O_3 ZnO

sharpened at 400 nm, namely more than 90 % of the cone-shape cores are formed in the same size of 400 nm using the Sb-doped ZnO target. Li et al. report the tapered ZnO nanocone arrays synthesized by thermal evaporation with Sb_2O_3. They show that the tapering of the ZnO nanocones is related to the doping of Sb_2O_3 [41]. In our experiment, the taper angles of the cone-shape cores does not seem to be uniform in the case of pure ZnO nanowires. On the other hand, since the cone-shape cores have almost the same taper angles of about 60° as in the case of Sb-doped ZnO nanowires (Fig. 7.20a), Sb seems to affect the nucleation process. Hence, Sb_2O_3 can be used as one of the effective additives to control the morphology and alignment of ZnO nanowires from this result.

Further, crystal quality of the synthesized ZnO nanowires was analyzed with TEM. It is found that the Sb-induced ZnO nanowires are also single crystalline with the wurzite hexagonal phase and grown along the (0001) direction. Figure 7.22 shows the XRD results of the ZnO nanowires grown with pure and Sb_2O_3

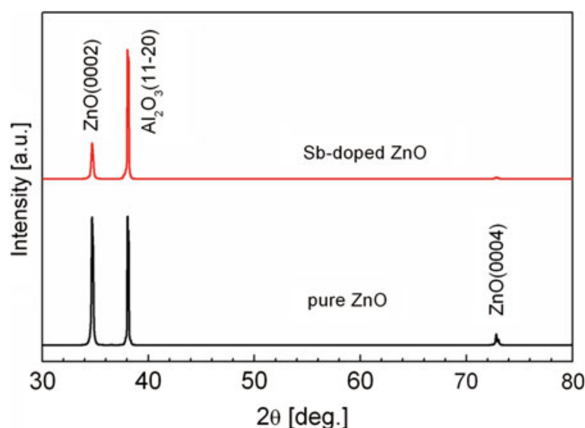

Fig. 7.22 XRD results of the ZnO nanowires with pure and Sb_2O_3 doped ZnO target

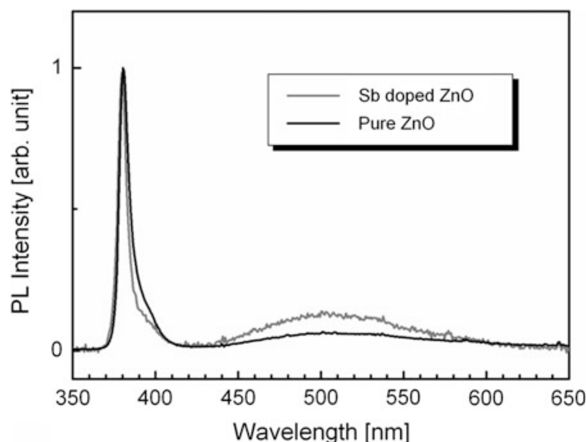

Fig. 7.23 Room temperature PL spectra of the ZnO nanowires with pure and Sb_2O_3 doped ZnO target

doped ZnO targets, indicating the nanowires are preferentially oriented in the (0002) direction. In addition, Sb doping concentration in the nanowire is not so high, because no shift in the XRD diffraction angles was observed for the pure and Sb-induced ZnO nanowires.

PL spectra of the Sb-induced ZnO nanowires were also measured at room temperature. Figure 7.23 shows the PL spectra from pure and Sb-induced ZnO nanowires. A strong UV emission centered at 380 nm and a weak, broad visible emission with a peak at about 504 nm was observed from the nanowires. No broadening and shifting of the NBE peak and green emission was observed between the PL spectra of pure and Sb-induced ZnO. The broadening and red-shift of the NBE peak from Sb-doped ZnO nanobelts and nanocones should be due to the narrowing of E_g and the band tailing induced by doping [41, 43]. It is regarded that the ZnO nanowires is slightly doped with Sb in our experiments, corresponding to the TEM and XRD analysis. However, an intensity ratio of green emission to NBE of Sb-doped ZnO nanowires is slightly higher than that of pure ZnO nanowires [44]. Here, the fact that UV emission is strong and the defect emission is weaker shows the good crystal quality both of pure and Sb-induced ZnO nanowires.

7.3.5 Introduction of Laser Irradiation to ZnO Buffer Layer (Treatment of Buffer Layer by Laser Irradiation)

It was demonstrated that the buffer layer affects the nucleation and the alignment of the nanowires. As another approach to control the nanowire density, laser irradiation to the buffer layer was introduced. A ZnO buffer layer was deposited on the sapphire substrate at a background oxygen pressure of 3.3 Pa and a substrate temperature of 650 °C for 2 min. After deposition of the buffer layer, the sample was taken out from

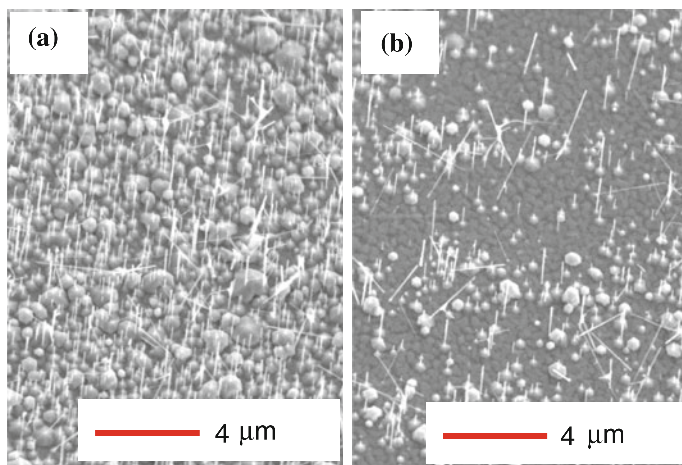

Fig. 7.24 SEM images of ZnO nanowires on **a** the buffer layer and **b** the laser-irradiated buffer layer

the chamber and irradiated by a single Nd:YAG laser pulse of 355 nm with a fluence of 120 mJ/cm^2. Subsequently, the irradiated sample was placed in the chamber again, and then ZnO nanowires were grown on the buffer layer at background argon gas of 26.7 kPa and a substrate temperature of 750 °C for 20 min. Figure 7.24 shows the SEM images of ZnO nanowires on the buffer layer and the laser-irradiated buffer layer. The nanowire density was clearly decreased by laser irradiation to the buffer layer. The surface roughness of the laser irradiated buffer layer decreases with increasing the laser fluence, as shown in Fig. 7.25. On the other hand, there was no modification of the surface roughness after thermal annealing at 800 °C using an electric furnace. It is considered that the ZnO grains constituting the buffer layer connected each other due to transient melting and re-solidification by the laser irradiation. The enlarged ZnO grains might prevent the nucleation of the nanowires,

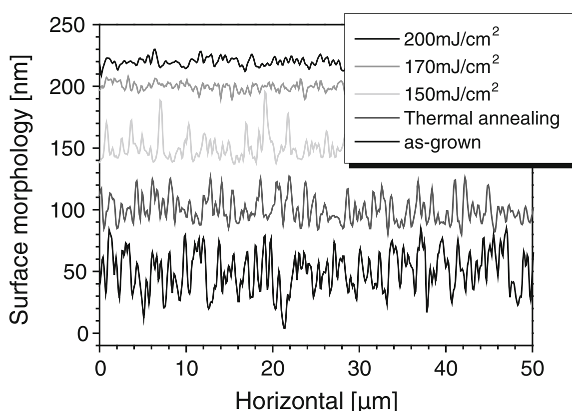

Fig. 7.25 Surface profiles of as-grown and the laser-irradiated buffer layers with different laser fluences of 150, 170, and 200 mJ/cm^2

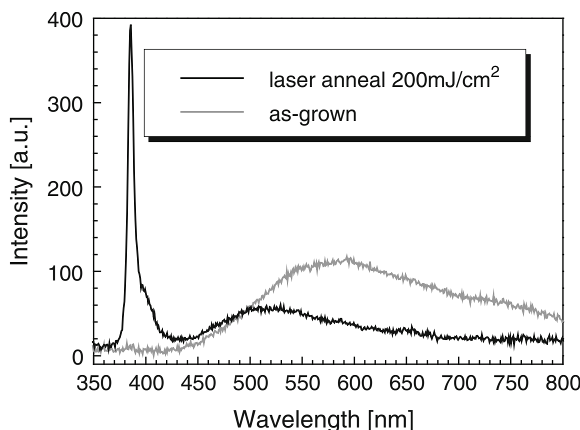

Fig. 7.26 SEM images of the nano-crystals grown on the buffer layer irradiated with the interfering laser beams

corresponding to the former results. Thus, ZnO nanowire density can be controlled by laser irradiation to the buffer layer.

The optical properties of the laser-irradiated buffer layer were investigated at room temperature. Figure 7.26 shows the PL spectra from as-grown and the laser-irradiated ZnO buffer layer. A very weak NBE and a relatively high visible emission are observed from as-grown layer. On the other hand, intense NBE emission was observed with low visible emission from the laser-irradiated layer. Since dramatic improvement of optical properties has been achieved by the laser irradiation, the laser irradiation can be one of the effective techniques for fabrication of ZnO-based optoelectronic materials.

Based on the results of laser irradiation to the buffer layer, we applied four-beam interference irradiation [45, 46] to control the growth position of the ZnO nano-crystals. Figure 7.27 shows the schematic of the experimental setup for four-beam interference irradiation. A TEM grid (400 mesh, 63.5 μm pitch) was used as a transmission beam splitter. Four beams were correlated on the surface of the buffer layer through two lenses configuring a demagnification system. The pitch of the interference pattern can be calculated by $(f_2/f_1)d_1/\sqrt{2}$, where f_1, f_2 are the focal lengths of the lenses and d_1 is the period of the transmission beam splitter.

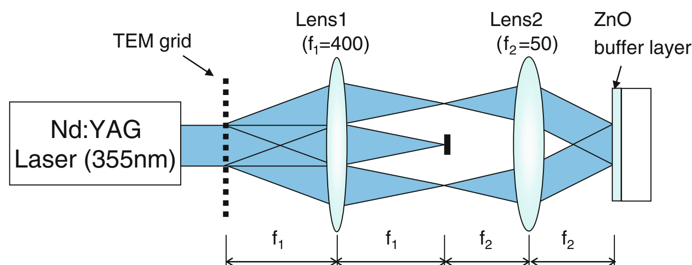

Fig. 7.27 Schematic of four-beam laser interference irradiation

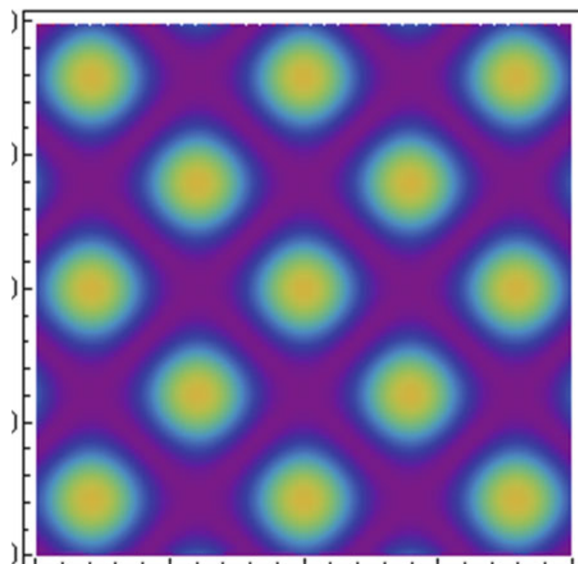

Fig. 7.28 The calculated 4-beam interference pattern

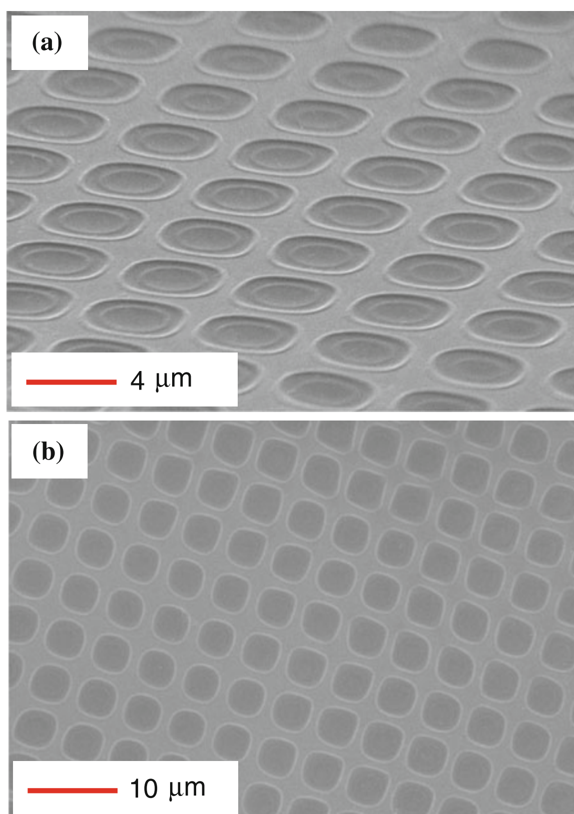

Fig. 7.29 SEM image of ZnO nanowires synthesized on the ZnO film with a deposition time of 10 min, **a** 45° tilted view and **b** top view

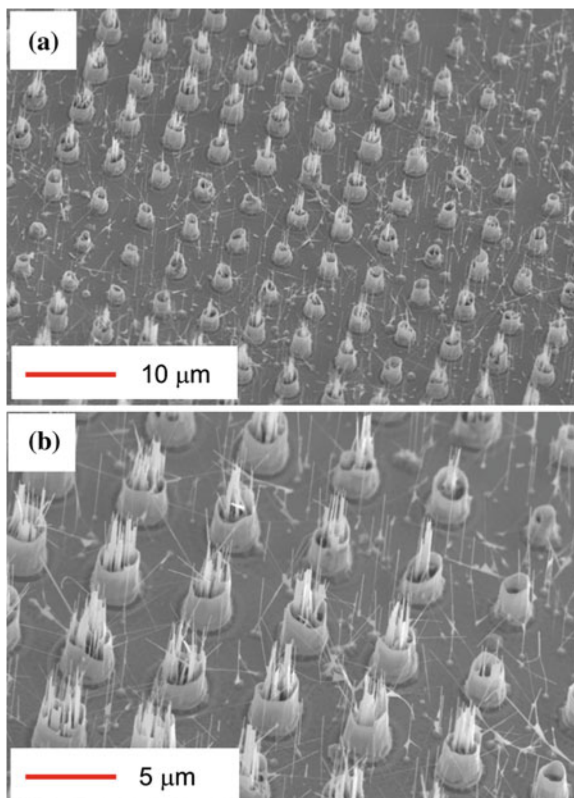

Fig. 7.30 SEM images of the nano crystals grown on the patterned buffer layer by the interfering laser beams, **a** low-magnification and **b** high-magnification

Figure 7.28 shows a calculated interference pattern by four beam. In the experiment, since the lenses of $f_1 = 400$ mm and $f_2 = 50$ mm were used, the pitch of the pattern was estimated to be 5.6 μm.

After the interference irradiation to the buffer layer, the periodic pattern was formed on the buffer layer, as shown in Fig. 7.29. In this case, the buffer layer was ablated at a center of the irradiated spot due to the high laser fluence of more than 800 mJ/cm^2 and re-solidified ZnO was formed around each spot. The pitch of periodic pattern formed on the buffer is almost the same as the calculated pitch of 5.6 μm.

The ZnO nanocrystals were grown on the periodically patterned buffer layer for 20 min. Figure 7.30 shows the SEM images of the nano crystals grown on the patterned buffer layer by the interfering laser beams. Periodic structures were formed on the laser-irradiated buffer layer. ZnO nanowalls were synthesized on the edge of each irradiation spot. At different area of the same sample, dense nanowires were grown along the edge of the laser-irradiation spot. Though we need to investigate the relation between the laser fluence and growth of the ZnO nano crystals, interference laser irradiation can be used as one of the effective technique to control the growth position and morphology of the ZnO nano crystals synthesized by NAPLD.

7.4 Conclusions

To summarize, we have succeeded in synthesizing vertically aligned ZnO nanowires on the ZnO buffer layer by NAPLD. The influence of the buffer layer on ZnO nanowire growth was investigated. The nanowire density decreases with increasing the deposition time of the buffer layer. Layer-structured ZnO nanowires, such as the film-wire structure and the core/shell structure, consisting of different materials were realized in the simple step process by changing the growth pressure. In the case of Sb-induced ZnO nanowire, vertically well-aligned ZnO nanowires were grown on the uniform hexagonal cone-shape cores, namely more than 90 % of the pyramid cores were formed in the same size of 400 nm. Thus, Sb seems to affect the nucleation process and can be used as one of the effective additives to control the morphology and alignment of ZnO nanowires from this result. In addition, laser irradiation to the buffer layer was introduced to control the growth of ZnO nanowires. The lateral density of the nanowire grown on the laser-irradiated layer was clearly decreased as compared with no-irradiated layer. Furthermore, we demonstrated the patterned growth of the ZnO nano-crystals by four-beam interference irradiation. Though the growth mechanism of the nanowire on the ZnO buffer layer by NAPLD has been under investigation, the buffer layer and interference laser irradiation can be used as one of the effective technique to control the growth position and morphology of the ZnO nano crystals synthesized by NAPLD.

Acknowledgments A part of this study has been financially supported by Special Coordination Funds for Promoting Science and Technology from Japan Science and Technology Agency and Agency and Grant-in-Aid for Young Scientist (B) from the Japan Society for the Promotion of Science (No. 23760036, 24656053). We are also indebted to the Research Laboratory of High Voltage Electron Microscope of Kyushu University for the use of TEM and the Center of Advanced Instrumental Analysis, Kyushu University for the use of XRD.

References

1. Z.L. Wang, J. Song, Piezoelectric nanogenerators based on zinc oxide nanowire arrays. Science **312**, 242 (2006)
2. S. Xu, Y. Qin, C. Xu, Y. Wei, R. Yang, Z.L. Wang, Self-powered nanowire devices. Nat. Nanotechnol. **5**, 366 (2010)
3. S.J. Pearton, D.P. Norton, Y.W. Heo, L.C. Tien, M.P. Ivill, Y. Li, B.S. Kang, F. Ren, J Kelly, A.F. Hebard, ZnO spintronics and nanowire devices. J. Elec. Mat. **35**(5), 862 (2006)
4. M.H. Huang, S. Mao, H. Feick, H. Yan, Y. Wu, H. Kind, E. Weber, R. Russo, P. Yang, Room-temperature ultraviolet nanowire nanolasers. Science **292**, 1897 (2001)
5. E.S.P. Leong, S.F. Yu, S.P. Lau, Directional edge-emitting UV random laser diodes. Appl. Phys. Lett. **89**, 221109 (2006)
6. Y.I. Alivov, E.V. Kalinina, A.E. Cherenkov, D.C. Look, B.M. Ataev, A.K. Omaev, M.V. Chukichev, D.M. Bagnall, Fabrication and characterization of n-ZnO/p-AlGaN heterojunction light-emitting diodes on 6H-SiC substrates. Appl. Phys. Lett. **83**, 4719 (2003)

7. W.I. Park, G.C. Yi, Electroluminescence in n-ZnO nanorod arrays vertically grown on p-GaN. Adv. Mater.**16**, 87 (2004)
8. R. Guo, J. Nishimura, M. Matsumoto, M. Higashihata, D. Nakamura, T. Okada, Electroluminescence from ZnO nanowire-based p-GaN/n-ZnO heterojunction light-emitting diodes. Appl. Phys. B **94**, 33 (2009)
9. X.-M. Zhang, M.-Y. Lu, Y. Zhang, L.-J. Chen, Z.L. Wang, Fabrication of a high-brightness blue-light-emitting diode using a ZnO-nanowire array grown on p-GaN thin film. Adv. Mater. **21**, 2767 (2009)
10. M.-C. Jeong, B.-Y. Oh, M.-H. Ham, J.-M. Myounga, Electroluminescence from ZnO nanowires in n-ZnO film/ZnO nanowire array/p-GaN film heterojunction light-emitting diodes. Appl. Phys. Lett. **88**, 202105 (2006)
11. H. Gao, F. Yan, J. Li, Y. Zeng, J. Wang, Synthesis and characterization of ZnO nanorods and nanoflowers grown on GaN-based LED epiwafer using a solution deposition method. J. Phys. D Appl. Phys. **40**, 3654 (2007)
12. Y. Yang, X.W. Sun, B.K. Tay, G.F. You, S.T. Tan, K.L. Teo, A p-n homojunction ZnO nanorod light-emitting diode formed by As ion implantation. Appl. Phys. Lett. **93**, 253107 (2008)
13. T. Okada, J. Suehiro, Synthesis of nano-structured materials by laser-ablation and their application to sensors. Appl. Sur. Sci. **253**, 7840 (2007)
14. Y. Yang, J.J. Qi, Y. Zhang, Q.L. Liao, L.D. Tang, Z. Qin, Controllable fabrication and electromechanical characterization of single crystalline Sb-doped ZnO nanobelts. Appl. Phys. Lett. **92**, 183117 (2008)
15. C. Soci, A. Zhang, B. Xiang, S.A. Dayeh, D.P.R. Aplin, J. Park, X.Y. Bao, Y.H. Lo Wang, ZnO nanowire UV photodetectors with high internal gain. Nano Lett. **7**, 1003 (2007)
16. J. Suehiro, N. Nakagawa, S. Hidaka, M. Ueda, K. Imasaka, M. Higashihata, T. Okada, M. Hara, Dielectrophoretic fabrication and characterization of a ZnO nanowire-based UV photosensor. Nanotechnology **17**, 2567 (2006)
17. M. Kawakami, A.B. Hartanto, Y. Nakata, T. Okada, Synthesis of ZnO nanorods by nanoparticle assisted pulsed-laser deposition. Jpn. J. Appl. Phys. **42**, L33 (2003)
18. T. Okada, A.B. Hartanto, Y. Nakata, ZnO nano-rods synthesized by nano-particle-assisted pulsed-laser deposition. Appl. Phys. A **79**, 1417 (2004)
19. B.Q. Cao, T. Matsumoto, M. Matsumoto, M. Higashihata, D. Nakamura, T. Okada, ZnO nanowalls grown with high-pressure PLD and their applications as field emitters and UV detectors. J. Phys. Chem. C **113**, 10975 (2009)
20. R.Q. Guo, J. Nishimura, M. Ueda, M. Higashihata, D. Nakamura, T. Okada, Vertically aligned growth of ZnO nanonails by nanoparticle-assisted pulsed-laser ablation deposition. Appl. Phys. A **89**, 141 (2007)
21. R.Q. Guo, J. Nishimura, M. Ueda, M. Higashihata, D. Nakamura, T. Okada, Substrate effects on ZnO nanostructure growth via nanoparticle-assisted pulsed-laser deposition. Appl. Sur. Sci. **254**, 3100 (2008)
22. R.Q. Guo, J. Nishimura, M. Matsumoto, M. Higashihata, D. Nakamura, T. Okada, Aligned growth of ZnO nanowires and lasing in single ZnO nanowire optical cavities. Appl. Phys. B **90**, 539 (2008)
23. R.Q. Guo, J. Nishimura, M. Matsumoto, D. Nakamura, T. Okada, Catalyst-free synthesis of vertically-aligned ZnO nanowires by nanoparticle-assisted pulsed laser deposition. Appl. Phys. A **93**, 843 (2008)
24. R. Guo, M. Matsumoto, T. Matsumoto, M. Higashihata, D. Nakamura, T. Okada, Aligned growth of ZnO nanowires by NAPLD and their optical characterizations. Appl. Sur. Sci. **255**, 9671 (2009)
25. R.Q. Guo, J. Nishimura, M. Matsumoto, M. Higashihata, D. Nakamura, T. Okada, Density-controlled growth of ZnO nanowires via nanoparticle-assisted pulsed-laser deposition and their optical properties. Jpn. J. Appl. Phys. **47**, 741 (2008)

26. B.Q. Cao, J. Zúñiga-Pérez, N. Boukos, C. Czekalla, H. Hilmer, J. Lenzner, A. Travlos, M. Lorenz, M. Grundmann, Homogeneous core/shell ZnO/ZnMgO quantum well heterostructures on vertical ZnO nanowires. Nanotechnology **20**, 305701 (2009)
27. S. Kishimoto, T. Yamamoto, Y. Nakagawa, K. Ikeda, H. Makino, T. Yamada, Dependence of electrical and structural properties on film thickness of undoped ZnO thin films prepared by plasma-assisted electron beam deposition. Superlattices Microstruct. **39**, 306 (2006)
28. J.L. Yang, S.J. An, W.I. Park, G.-C. Yi, W. Choi, Photocatalysis using ZnO tin films and nanoneedles grown by metal-organic chemical vapor deposition. Adv. Mater. **16**, 1661 (2004)
29. D. Nakamura, T. Matsumoto, A. Kumeda, K. Toya, M. Higashihata, T. Okada, Synthesis of ZnO nanowire heterostructures by laser ablation and their photoluminescence. J. Laser Micro/Nanoeng. **6**, 23 (2011)
30. D. Nakamura, K. Okazaki, K. Kubo, K. Tsuta, M. Higashihata, T. Okada, Synthesis of Core/Shell nanowires using doped ZnO targets. J. Laser Micro/Nanoeng. **7**, 109 (2012)
31. E.S. Kumar, S. Venkatesh, M.S.R. Rao, Oxygen vacancy controlled tunable magnetic and electrical transport properties of (Li, Ni)-codoped ZnO thin films. Appl. Phys. Lett. **96**, 232504 (2010)
32. E.S. Kumar, J. Chatterjee, N. Rama, N. DasGupta, M.S.R. Rao, A codoping route to realize low resistive and stable p-type conduction in (Li, Ni):ZnO thin films grown by pulsed laser deposition. Appl. Mater. Interfaces **3**, 1974 (2011)
33. B.Q. Cao, W.P. Cai, H.B. Zeng, Temperature-dependent shifts of three emission bands for ZnO nanoneedle arrays. Appl. Phys. Lett. **88**, 161101 (2006)
34. S.B. Zhang, S.-H. Wei, A. Zunger, Intrinsic n-type versus p-type doping asymmetry and the defect physics of ZnO. Phys. Rev. B **63**, 075205 (2001)
35. X. Liu, X. Wu, H. Cao, R.P.H. Chang, Growth mechanism and properties of ZnO nanorods synthesized by plasma-enhanced chemical vapor deposition. J. Appl. Phys. **95**, 3141 (2004)
36. D. Nakamura, K. Okazaki, I.A. Palani, M. Higashihata, T. Okada, Influence of Sb on a controlled-growth of aligned ZnO nanowires in nanoparticle-assisted pulsed-laser deposition. Appl. Phys. A **103**, 959 (2011)
37. F.X. Xiu, Z. Yang, L.J. Mandalapu, D.T. Zhao, J.L. Liu, W.P. Beyermann, High-mobility Sb-doped p-type ZnO by molecular-beam epitaxy. Appl. Phys. Lett. **87**, 152101 (2005)
38. X. Pan, Z. Ye, J. Li, X. Gu, Y. Zeng, H. He, L. Zhu, Y. Che, Fabrication of Sb-doped p-type ZnO thin films by pulsed laser deposition. Appl. Surf. Sci. **253**, 5067 (2007)
39. C.H. Zang, D.X. Zhao, Y. Tang, Z. Guo, J.Y. Zhang, D.Z. Shen, Y.C. Liu, Acceptor related photoluminescence from ZnO:Sb nanowires fabricated by chemical vapor deposition method. Chem. Phys. Lett. **452**, 148 (2008)
40. X. Fang, J. Li, D. Zhao, B. Li, Z. Zhang, D. Shen, X. Wang, Z. Wei, Structural and photoluminescence properties of aligned Sb-doped ZnO nanocolumns synthesized by the hydrothermal method. Thin Solid Films **518**, 5687 (2010)
41. S. Li, X. Zhang, L. Zhang, Sb_2O_3-Induced tapered ZnO nanowire arrays: the kinetics of radial growth and morphology control. J. Phys. Chem. C **114**, 10379 (2010)
42. T. Senda, R.C. Bradt, Grain growth of zinc oxide during the sintering of zinc oxide-antimony oxide ceramics. J. Am. Ceram. Soc. **74**, 1296 (1991)
43. Y. Yang, J.J. Qi, Q.L. Liao, Y. Zhang, L.D. Tang, Z. Qin, Synthesis and characterization of Sb-doped zno nanobelts with single-side zigzag boundaries. J. Phys. Chem. C **112**, 17916 (2008)
44. X. Fang, J. Li, D. Zhao, B. Li, Z. Zhang, D. Shen, X. Wang, Z. Wei, Structural and photoluminescence properties of aligned Sb-doped ZnO nanocolumns synthesized by the hydrothermal method. Thin Solid Films **518**, 5687 (2010)
45. A.A. Maznev, T.F. Crimmins, K.A. Nelson, How to make femtosecond pulses overlap. Opt. Lett. **23**, 1378 (1998)
46. Y. Nakata, N. Miyanaga, T. Okada, Effect of pulse width and fluence of femtosecond laser on the size of nanobump array. Appl. Sur. Sci. **253**, 6555 (2007)

Chapter 8
Influence of Sb as a Catalyst in Synthesize of Sb Doped ZnO Nanostructures Using Nanoparticle Assisted Pulsed Laser Deposition for UV LED Applications

I. A. Palani, D. Nakamura, K. Okazaki, M. Highasiata and T. Okada

Abstract The paper deals with synthesis of Sb and Sb–Al co-doped ZnO nanowires using nanoparticle assisted pulsed laser deposition (NAPLD) by considering Sb as a catalyst. The mechanism of the growth initiation of nanostructures from the Sb droplets is analyzed at varying growth temperature. Nanowires and nanosheets of different orientation were synthesized. With ZnO:Al target and Sb coated Si as substrates, at a growth temperature of 750 °C, random oriented high density nanowires with a diameter of about 1 μm and a length up to a few tens of micrometer were synthesized. The suppression of A_1T modes and E_1(L0) modes from Raman spectroscopy confirming that depletion of oxygen vacancies. XPS analysis confirming that the Sb would substitute for Zn(Sb_{zn}) instead of oxygen Al–O bonds, leading to excess of oxygen, neutralizing the oxygen vacancies. The Sb–Al co-doped nanowires annealed at 650 °C showed a strong UV emission and reduction in visible emission as compared to the Sb–Al co-doped nanowires annealed at 450 °C. This confirms that the Sb–Al co-doped posses high stoichiometric nature, good structural and optical properties. To investigate the p-type conductivity of the Sb–Al co-doped nanowires, a homo *p–n* junction was prepared by synthesizing Sb–Al co-doped ZnO nanowires on the pure ZnO surface. The I–V characteristics of the homo *P–N* junction were investigated and a rectifying behavior was observed confirming the formation of *p*-type. Hence the Sb mono-doped and co-doped ZnO nanowires synthesized by using Sb as catalyst posses good structural and optical properties with good crystallization quality and high stoichiometry nature, hence it is highly suitable for light emitting device applications.

I. A. Palani (✉)
Department of Mechanical Engineering, Indian Institute of Technology,
Indore, India
e-mail: palaniia@iiti.ac.in

I. A. Palani · D. Nakamura · K. Okazaki · M. Highasiata · T. Okada
Graduate School of Information Science and Electrical Engineering,
Kyushu University, Fukuoka, Japan
e-mail: okada@ees.kyushu-u.ac.jp

M. S. R. Rao and T. Okada (eds.), *ZnO Nanocrystals and Allied Materials*,
Springer Series in Materials Science 180, DOI: 10.1007/978-81-322-1160-0_8,

© Springer India 2014

8.1 Introduction

Quasi-one-dimensional ZnO nanomaterials such as nanowires, nanorods, and nanobelts have attracted much attention due to their remarkable morphology dependent properties and potential applications in nano-optoelectronic devices. One-dimensional ZnO nanostructures posses a wide band gap (3.37 eV) and large exciton binding energy (60 meV) at room temperature [1–3]. This makes ZnO an ideal material for studying the transport processes in one-dimensionally confined object, which are important for the development of high performance nanodevices, including sensors, ultra violet/blue emission devices, field emission devices, and so on. *P*-type doping of ZnO nanostructures can be tailored for specific desired applications which is of particular interest [4, 5].

It is well-known that the most suitable dopant for *p*-type doping in ZnO are the group-V atoms (N, P, As, and Sb) substituting for O [9, 10]. Among them there are few reports in the literature which demonstrate the growth of Sb doped ZnO nanowires [6, 7], synthesized by molecular beam epitaxy (MBE), nanoparticle assisted pulsed laser deposition (NAPLD), and Carbothermal evaporation methods [8–12].

In addition to single element doping, a donor–acceptor co-doping method has been also proposed to realize heavy *p*-type doping [13–15]. The co-doping methods simultaneously using group-V acceptors (N and P) and group-III reactive donors (Al and In) was also proposed to increase the solubility of acceptors in ZnO [16–18]. Al–As co-doped ZnO thin film synthesized using magnetron sputtering and Sb–Al co-doped ZnO thin films synthesized using sol–gel also confirms the *p*-type doping of the samples [19, 20].

However, in all these studies the dopant is introduced either in gaseous state or as a source target. But as an alternative approach dopant can also be used as a catalyst. Since these catalyst has high affinity toward occupying the space lattice. The solid metallic Sb dopant powders can be easily coated on the substrate using thermal evaporation method, these Sb particles can act as a dopant source to synthesize Sb doped ZnO nanostructures [21]. Hence Sb coated substrate can be used to synthesize Sb doped ZnO nanostructures from Carbothermal evaporation method and also by NAPLD. This Sb catalyst/dopant will act as a seed layer to control the growth of nanostructures. In addition it can also be used to develop Sb:Al co-doped ZnO nanostructures, to realize stable *p*-type characteristics. So as to develop omo *P–N* junction for UV LED applications.

8.2 Mechanism of Sb Doping of ZnO Nanostructures from Catalyst Through Vapour–Liquid–Solid Technique

Basically, Sb doped ZnO nanowires are developed using Carbothermal evaporation method by introducing Sb as a precursor [22], but during growth at high temperature the Sb particle may get evaporated, and may fail to diffuse into the

Zn sites. Hence an alternative approach employing solid metallic Sb dopant powders coated on the substrate can also act as a dopant source to synthesize Sb doped nanostructures.

The catalyst Sb coated on the silicon forms a droplet during processing and starts to initiate the growth process by the VLS mechanism. Figure 8.1 shows the mechanism of growth initiation of the nanowires synthesized in Carbothermal evaporation method by considering Sb coated Si as the substrate and ZnO mixed with graphite and Sb as a precursor.

Figure 8.1 shows the representative morphologies of as synthesized samples grown at different temperature conditions as revealed by SEM images. To investigate the mechanism of growth initiation of the nanowires on the sandwich type substrate, the experiments were performed at different temperature conditions ranging from 700 to 900 °C which is slightly higher than the melting point of Sb. Figure 8.1a shows the droplet formation of Sb and Au on the surface of Si, when the samples are kept at a growth temperature of 700 °C. This droplet acts as a seed to initiate the growth of nanowires. When the growth temperature was increased to 800 °C, initiation of nanowires from the droplets was observed in Fig. 8.2b. When the growth temperature was increased to 900 °C random-oriented nanowires with a diameter of about 1 μm and a length up to a few tens of micrometer were observed, as shown in Fig. 8.2c. Figure 8.2d shows the SEM morphology of the

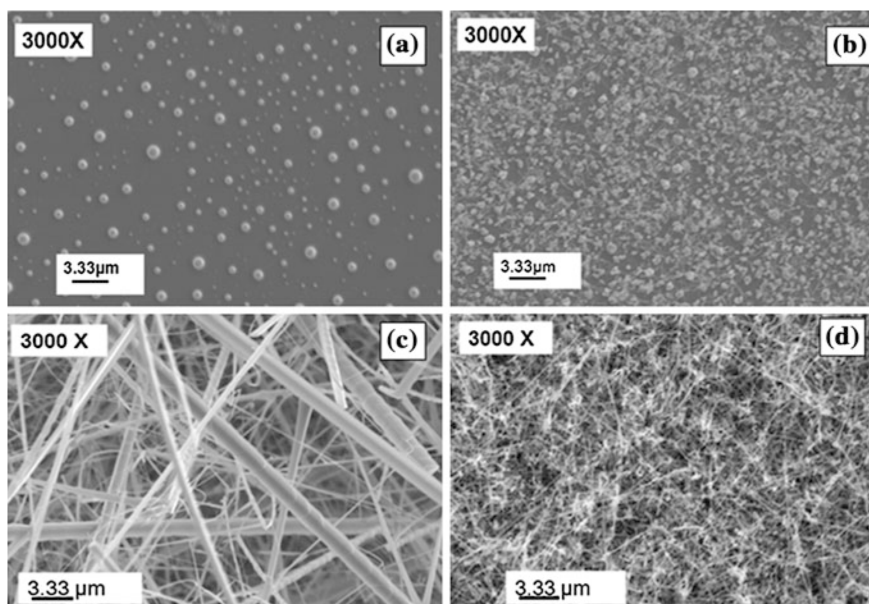

Fig. 8.1 SEM micrograph representing **a** formation of droplets from sandwich substrate at 700 °C; **b** growth initiation of Sb doped ZnO nanowires from sandwich type substrate at 800 °C; **c** synthesis of Sb doped ZnO nanowires with sandwich type substrate at 900 °C; and **d** pure ZnO nanowires synthesized from Si coated with Au substrate at 900 °C

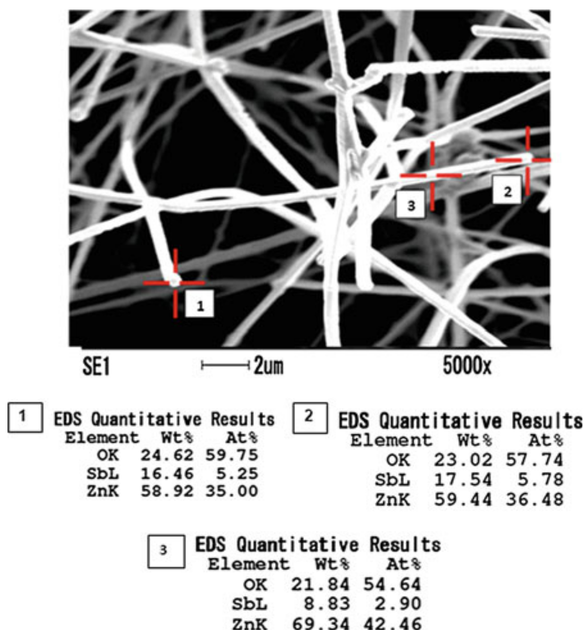

Fig. 8.2 EDX analysis of the Sb doped nanowires at higher magnification

pure ZnO nanowires synthesized without the influence of Sb and by using only Au as catalyst. The synthesis was carried out at similar growth conditions as of Fig. 8.2c. The size of the nanowire generated in absence of Sb ranged from 100 to 200 nm which is thinner as compared to the nanowires synthesized on the sand-wich type substrate in presence of Sb.

Figure 8.2 shows the EDX analysis of the nanowires at different positions. Position 1 and 2 refers to the tip of the nanowire and position 3 refers to the stem of the nanowire. The Sb wt% measured from the tips is quite high as compared to the EDX analysis from the stem. This confirms that the growth process of these nanowires is through VLS mechanism [23, 24]. Thus by controlling the growth condition, the structure and properties of the nanostructures can be varied. This concept has been investigated though a NAPLD setup, where Si coated with Sb is used a Substrate.

8.3 Influence of Catalyst Sb on Development of Horizontally Grown ZnO Nanowires and Nanosheets Using NAPLD

Figure 8.3 shows the schematic layout of NAPLD experimental setup. In these experiments, a sintered intrinsic ZnO target with 99.99 % in purity was used as source material to synthesis nanowires and nanosheets. Intrinsic Si wafer ($\sim$15 $\times$ 15 mm) coated with Sb to thickness of 100–200 nm using thermal

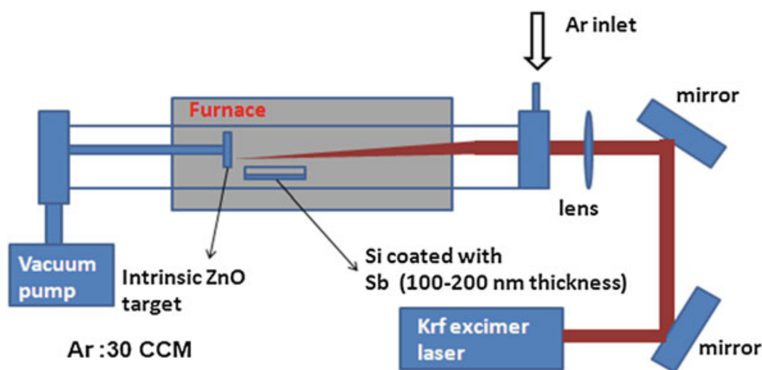

Fig. 8.3 Schematic layout of NAPLD experimental setup

evaporation method was used as a substrate. The substrate was mounted on a layer of SiC and inserted into the horizontal quartz tube chamber. The target to substrate distance was 15 mm. For one growth run 36,000 KrF excimer laser pulses with 20 Hz repetition frequency were applied. The laser energy density on the target was about 3 J/cm^2 in the presence of argon gas at a pressure of 100 Torr and a constant flow rate of 27.5 sccm. The temperature conditions were optimized for efficient growth of nanowires and nanosheets. The nanowires were synthesis at a growth temperature varying from 680 to 880 °C with growth duration for period of 20 min and at a growth temperature of more than 750 °C, nanosheets were observed along with the nanowires.

8.3.1 Temperature Dependent Sb Cataltyzed ZnO Nanostructures

As discussed in the previous section, the catalyst Sb coated on the silicon forms a droplet during processing and starts to initiate the growth process by the VLS mechanism. This droplet is highly sensitive to temperature conditions.

Figure 8.4 shows the formation of Sb catalyzed ZnO nanowires synthesized by raising the temperature from 680 to 880 °C for a period of 20 min. However, maintaining a temperature of 750 °C for a period of 20 min resulted in the formation of nanosheets among the nanowires (Fig. 8.4c). When the processing temperature exceeds the melting temperature of Sb, island like formation are observed as shown in Fig. 8.4b, d.

8.3.2 Nanowire Versus Nanosheets

Figure 8.5 shows the Raman spectroscopic analysis of the nanowires and nanosheets. From Fig. 8.5a, in the case of nanowires, dominant peaks were at 101, 439,

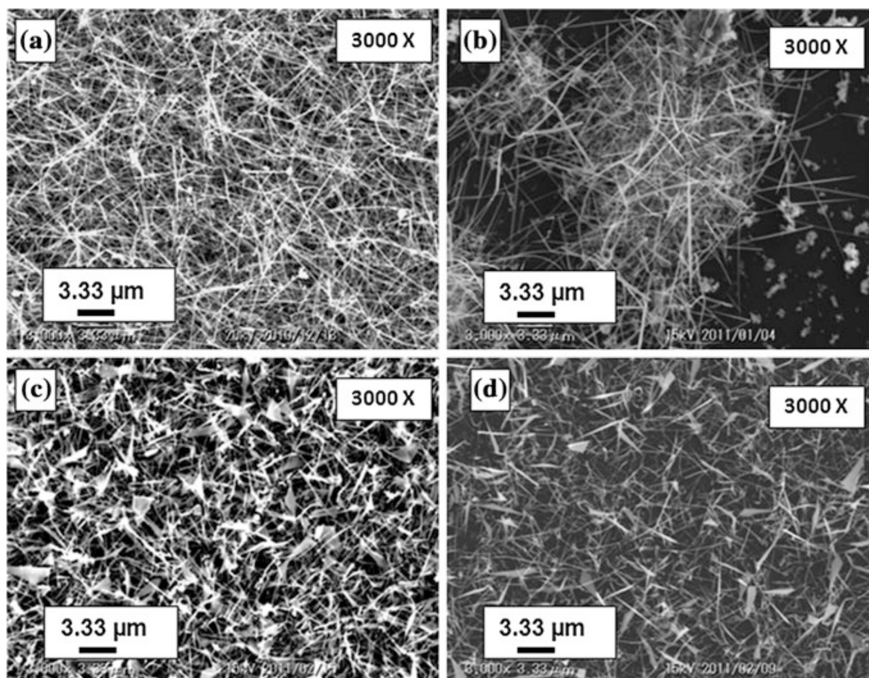

Fig. 8.4 SEM micrograph of **a** Sb doped ZnO nanowires grown at a range of 680–880 °C; **b** nanowires grown at a range of 750–950 °C; **c** Sb doped ZnO nanosheets at 750 °C; and **d** Sb doped ZnO nanosheets at 850 °C

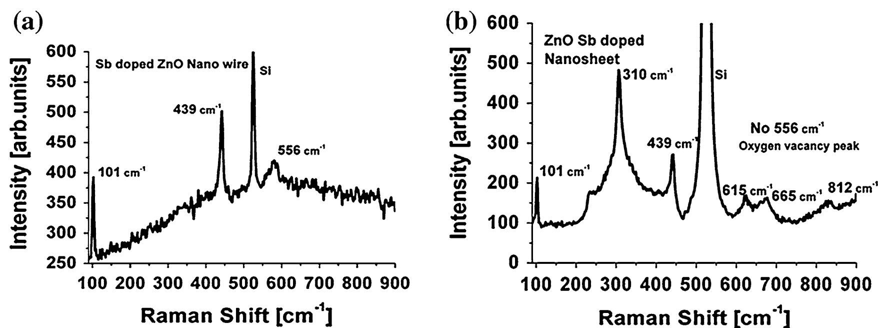

Fig. 8.5 Raman spectra of Sb catalyzed/doped ZnO. **a** Nanowires. **b** Nanosheets

and 522 cm^{-1}. The 522 cm^{-1} corresponds to the crystalline silicon substrate peak. The first peak 101 cm^{-1} is related to the E_2(low) phonon frequency and 439 cm^{-1} corresponds to the E_2(High) mode of nonpolar optical phonon. These two peaks from Raman spectroscopy indicate that the ZnO nanostructures are crystals with hexagonal wurtzite structures [25, 26]. A small peak suppressed at 556 cm^{-1} attributes to the E_1(L0) mode which is associated with the structural defects related

to oxygen vacancies [27, 28]. Similar standard peaks at 101 and 439 cm^{-1} were also observed in nanosheets as shown in Fig. 8.5(b). In addition to the standard peaks, some other peaks were observed at 310, 615, 665, and 812 cm^{-1}. The 310 cm^{-1} peak corresponds to the lattice deformation induced by the presence of Sb in the ZnO lattice. The peaks at 615, 665, and 812 cm^{-1} represents the classical second order Raman modes of ZnO TA+TO, TA+LO, LA+LO. Generally, this second order Raman modes are not very obvious and not observed even in standard ZnO structures.

Figure 8.6 shows the optical spectra measured by room temperature PL spectroscopy. In the case of nanowires, as shown in Fig. 8.6a, a near band edge (NBE) emission at 380 nm and sharp deep level emission at 490 nm were observed. The deep level emission (DLE) peak is dominant than the near band edge emission. In the case of nanosheets, however, as shown in Fig. 8.6b, the PL spectrum of the samples exhibit a dominant peak at 390 nm and a weak DLE with a broad peak located between 450 and 700 nm

From Fig 8.6, the origin of DLE, that is the green emission, appeared due to the radial recombination of a photogenerated hole with electron of the ionized oxygen vacancies in the surface lattice of the ZnO. It is also considered that the radiative transitions between shallow donors (related to oxygen vacancies) and deep acceptor (zinc vacancies) can create defect in the luminescence spectra [29, 30]. Thus the PL green emission peak at 520 nm originates from the single ionized oxygen vacancies. This is due to the increase of layer defect during nucleation processes [31]. Whereas in the case of nanosheets, a sharp UV emission is observed and no visible luminescence was observed. This has also been confirmed with Raman spectroscopic analysis in Fig. 8.5a that an oxygen deficient peak is observed at 556 cm^{-1}, and this peak is absent in case of nanosheets.

From the above discussion, it is clear that the nanostructures synthesized from catalyst Sb possess UV emission. But due to the lattice and thermal mismatches from the substrate, the nanostructures possess lattice defects as pointed from Raman spectroscopic analysis (Fig. 8.5). These can be rectified by introducing a pure ZnO buffer layer instead of Si so as to improve the structural and optical properties.

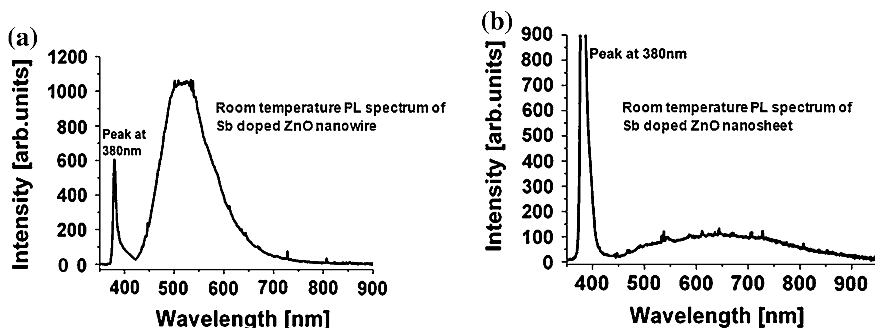

Fig. 8.6 Pl spectra of Sb catalyzed/doped ZnO. **a** Nanowires. **b** Nanosheets

8.4 Influence of Buffer Layer Thickness on Generation of Vertically Aligned ZnO Nanowires

Figure 8.7 shows the stages in synthesis of Sb catalyzed/doped ZnO nanowires on ZnO buffer layer using NAPLD. In this experiment, a sintered source target of pure ZnO with 99.99 % in purity (Kojundo Chemical Laboratory, Japan) was used for synthesizing buffer layer and nanowires. A silicon substrate (1 cm × 1 cm) was put on a SiC heater in a vacuum chamber and the target–substrate distance was set to be 40 mm. The ZnO target was ablated with the third harmonics of a Q-switched Nd:YAG laser (Spectra Physics, Quanta-Ray, GCR-290) at 355 nm with a repetition rate of 10 Hz and a fluence of about 1.3 J/cm^2. A ZnO buffer layer was deposited at a background oxygen pressure of 3.3 Pa with a substrate temperature of 650 °C for 1.5 min, for the growth of 100 nm, 10 min for 800 nm thick, and 20 min for 1600 nm thick layer. The Si deposited ZnO buffer layer was coated with Sb (99.999 % pure (Nilaco corporation, Japan)) to a thickness of 80–100 nm using thermal evaporation method. ZnO nanowires were continuously grown on the Sb coated ZnO buffer layer at 40 kPa with a substrate temperature of 750 °C for 30 min.

8.4.1 Change in Surface Morphology at Different Buffer Layer Thickness

The influence of ZnO buffer layer at varying thickness in generation of Sb doped ZnO nanowires. Horizontally grown nanowires combined with vertically aligned nanowires were observed in the samples grown on the ZnO buffer layer as observed in Fig. 8.8. Figure 8.8 shows the Sb catalyzed doped nanowires synthesized on a buffer layer of 100 nm thickness. The vertically aligned ZnO nanowire with a length of 200 nm and a core diameter of around 100 nm was observed. With increase in buffer layer thickness to 800 nm, there is a slight increase in length and diameter of nanowires to about 0.5 μm and 400 nm, respectively. With further increase in buffer layer to thickness of 1600 nm, increase in core diameter of the nanowires of around 800 nm was observed.

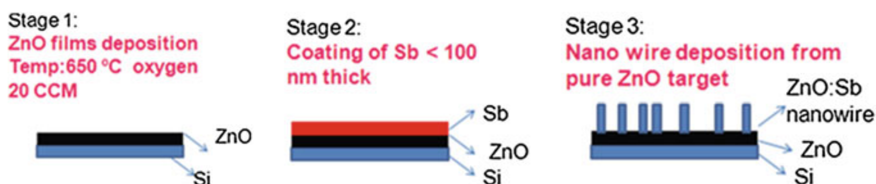

Fig. 8.7 Stages in synthesis of Sb catalyzed/doped ZnO nanowires using nano particle assisted pulsed laser deposition (NAPLD)

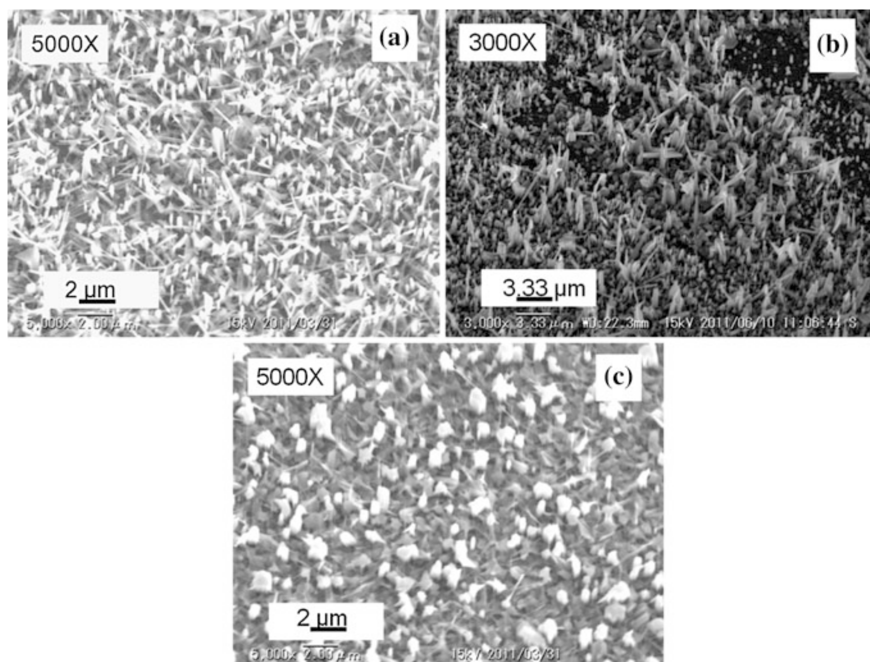

Fig. 8.8 Surface morphology of ZnO nano structures synthesized at different buffer layer with a thickness of **a** 100 nm, **b** 800 nm, **c** 1600 nm

The structural characteristics of the Sb catalyzed/doped ZnO nanowire coated on a ZnO buffer layer of 1,600 nm thick were investigated through XRD. The phases of the as-grown nanowires were identified by XRD. The XRD results of the pure ZnO and Sb doped ZnO are shown in Fig. 8.9 for comparison. The XRD pattern of the Sb doped ZnO indicates that the nanowires have the wurtzite structure and no secondary phase was found as compared to the XRD spectrum of pure ZnO. The Sb doping in ZnO causes significant change in the lattice constants, resulting in measurable lower angle shift of about 0.06° in the (100) and (101) peaks as compared to the pure ZnO nanowires [32, 33].

Figure 8.10 shows low and high magnification TEM images of the Sb doped ZnO nanowire and the corresponding fast Fourier transform (FFT) patterns as in the insets. It was observed that the nanowires are structurally uniform with a lattice fringe spacing of 0.54 nm, which confirms that the grown nanostructure is preferentially oriented in the [0001] (c-axis) direction [34]. The wider lattice fringe spacing is due to the incorporation of Sb in ZnO lattice.

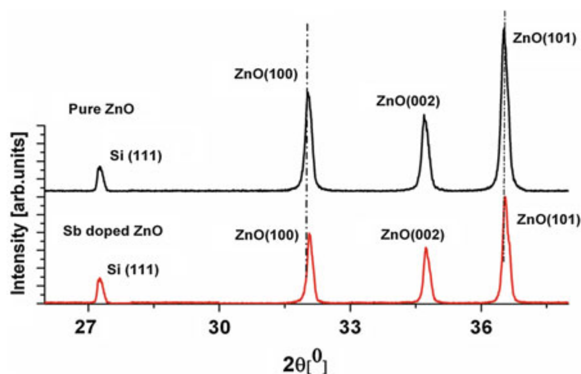

Fig. 8.9 X-Ray diffraction analysis of the pure and Sb catalyzed/doped ZnO nanowires

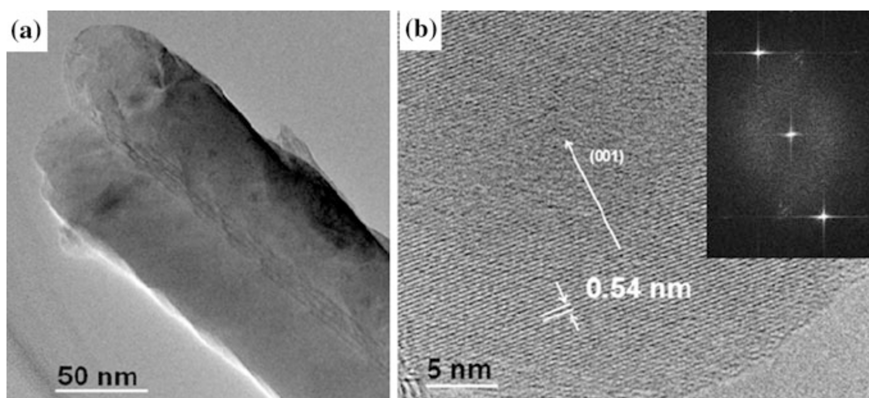

Fig. 8.10 TEM analysis of Sb catalyzed/doped ZnO nano wire on 1600 nm buffer layer. **a** Low-magnification and **b** high resolution taken from the side of the nanowire. The *inset* is the corresponding fast fourier transform (FFT pattern)

8.4.2 Improvement in UV Emission with Increase in Thickness of Buffer Layer

Figure 8.11a shows the room temperature PL spectrum of the pure ZnO thin film which acts as a buffer layer The PL spectra of the ZnO film exhibit UV peak emission i.e., the NBE emission at around 380 nm and a broad DLE corresponding to the visible emission is observed. Figure 8.11b shows the Pl spectrum of the Sb catalyzed/doped ZnO layer synthesized on buffer layers with different thickness. A sharp UV emission with absence of visible emission peak was observed from the Sb catalyzed/doped ZnO samples. The intensity of UV emission increases with respect to the buffer layer thickness. This confirms that the layer defects are considerably reduced with increase in buffer layer thickness [35].

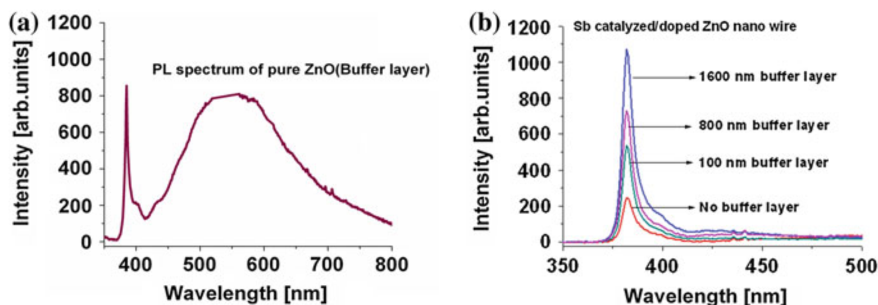

Fig. 8.11 Room temperature PL Spectroscopic analysis of **a** Sb catalyzed/doped ZnO nano wire at different size of the buffer layer, **b** pure ZnO

In addition to single element doping, the technique of Sb catalyst/doping can also be extended in fabrication of Sb:Al co-doped ZnO nanostructures to realize p-type characteristics.

8.5 Synthesis Sb–Al Co-doped ZnO Nanowires Using Sb as Catalyst

The deliberate co-doping of donors with acceptors is essential for the enhancement of the solubility of the acceptors with the stabilization of the ionic charge and distributions and the reduction of acceptor binding energies. The co-doping methods simultaneously use group-V acceptor (Sb) and group-III reactive donors (Al) to increase the solubility of the acceptor in ZnO [36]. However, development of co-doped ZnO nanostructures is highly complex. Hence dopant Sb is introduced from the substrate and the dopant Al is introduced from the target [37].

Sb:Al co-doped ZnO nanostructures were synthesized by using sintered intrinsic ZnO:Al target. Intrinsic Si wafer ($\sim 15 \times 15$ mm) coated with Sb to a thickness of 60–100 nm using thermal evaporation method was used as a substrate. The substrate was mounted on a layer of SiC and inserted into the horizontal quartz tube chamber. The target to substrate distance was 15 mm. For one growth run 36,000 KrF excimer laser pulses with 20 Hz repetition frequency was applied. The laser energy density on the target was about 3 J/cm^2 in the presence of argon gas at a pressure of 100 Torr and a constant flow rate of 27.5 sccm. The Sb–Al co-doped ZnO nanowires were synthesized at a growth temperature of 750 °C with growth duration for period of 20 min. After synthesis, to activate the dopant, the samples were post annealed for a period of 30 min at different temperatures in the ambient condition.

To investigate the mechanism of growth initiation of the nanowires from the Sb coated substrate, the experiments were performed at different temperature conditions ranging from 550 to 750 °C which is slightly higher than the melting point of Sb.

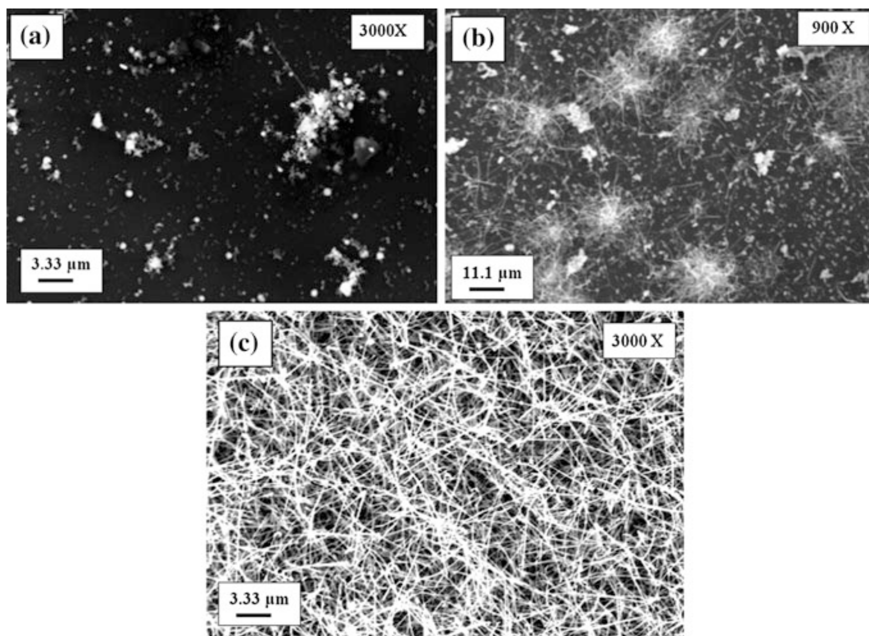

Fig. 8.12 SEM micrograph representing **a** formation of droplets from Sb coated substrate at 550 °C, **b** Growth initiation of Sb–Al co-doped ZnO nanowebs from Sb coated substrate at 650 °C, **c** Synthesize of high density Sb–Al co-doped ZnO nanowebs at 750 °C

The representative morphologies of as synthesized samples grown at different temperature conditions are revealed by SEM images. Figure 8.12 (a) shows the cluster formation of Sb on the surface of Si, when the samples are kept at a growth temperature of 550 °C. These clusters act as a seed to initiate the growth of nanowires. When the growth temperature was increased to 650 °C, growth of nanowires from the clusters was observed as shown in Fig 8.13b. When the growth temperature was increased to 750 °C, randomly oriented high density nanowires with a diameter of about 0.75 µm and a length up to a few tens of micrometers were observed as shown in Fig. 8.14c. When the growth temperature was increased beyond 850 °C density of the nanowires were considerably decreased.

8.5.1 Mechanism of Sb–Al Co-doping in ZnO Nanowires

Figure 8.13a shows the XPS analysis on the content of Sb. Two $Sb_{3d3/2}$ bands are observed at a binding energy of 536.9 and 539.5 eV, respectively. The 536.9 eV is close to binding energy of metal Sb, and the 539.5 eV is the near binding energy of Sb–O bond. From XPS it is clear that the deducted Sb possesses two kinds of chemical environment, one is metal Sb, which is located at grain boundaries of the

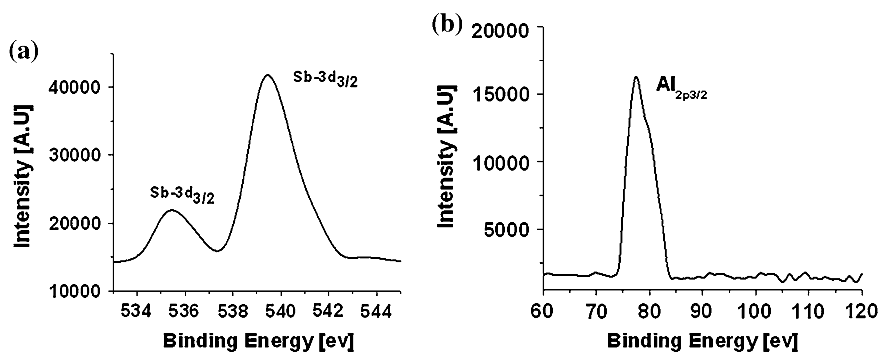

Fig. 8.13 **a** $Sb_{3d3/2}$, **b** $Al_{2p3/2}$ narrow scan XPS spectra of Sb–Al co-doped ZnO nanowires annealed at 650 °C

Fig. 8.14 Raman spectra of Sb–Al co-doped ZnO nanowires annealed at **a** 450 °C, **b** 650 and 750 °C

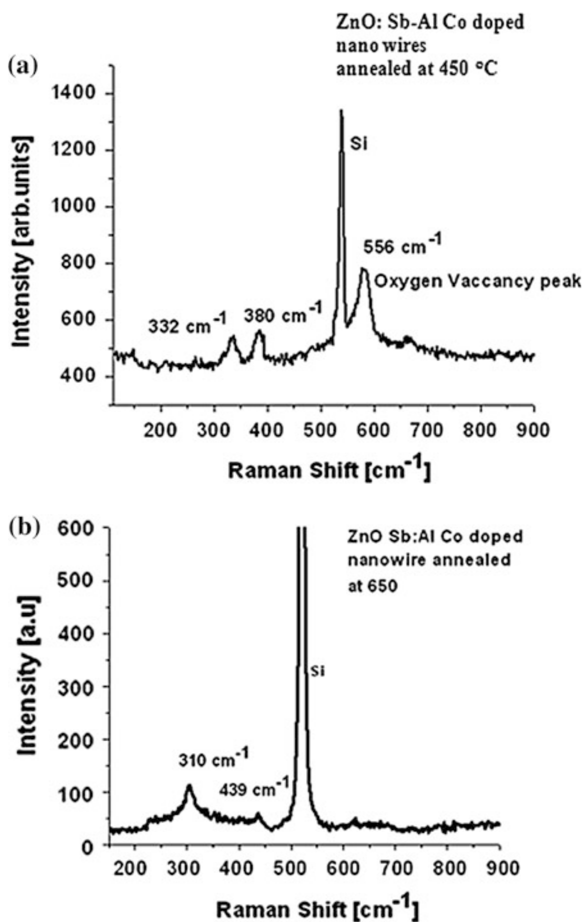

ZnO and another substitution of Sb at Zn site (Sb_{zn}). Based on Fig. 8.13a, the Sb content is estimated to be 0.9 % in a form of Sb and 4.5 % in the form of Sb_{Zn}. Thus it is proposed that Sb would substitute for Zn(Sb_{zn}) instead of oxygen in the Sb doped ZnO and then produce two corresponding Zn vacancies(V_{zn}), which forms a Sb_{zn}–$2V_{zn}$ complex acceptor [38].

Figure 8.13b corresponds to the $Al_{2p3/2}$ core level and the fraction of Al is estimated to be around 0.56 %. The $Al_{2p3/2}$ peaks at 76.2 eV are possibly related to Al–O bonds, supporting the fact that Al-Induced donors are presented in the co-doped films [39]. In order to investigate the secondary phase segregation and the influence of impurity doping on the lattice fringe property of the Sb–Al co-doped ZnO nanowires, Raman spectroscopic analysis was performed on the Sb–Al co-doped ZnO nanowires annealed at 450 and 650 °C.

Figure 8.14a shows the Raman spectroscopic analysis of the Sb-Al co-doped ZnO nanowires annealed at 450 °C. Dominant peak at 332, 380, and 556 cm^{-1} was observed. Figure 8.14b, shows the Raman spectroscopic analysis annealed at 650 °C and the dominant peaks are observed at 310 and 439 cm^{-1}. The 522 cm^{-1} corresponds to the crystalline silicon substrate peak. The peak at 332 cm^{-1} in Fig. 8.14a and 439 cm^{-1} in Fig. 8.14b corresponds to E_{2H}-E_{2L} and E_2H modes of nonpolar optical phonon, respectively. These two peaks confirm that the Sb-Al co-doped ZnO nanowires possess good crystal structure. The peak at 380 cm^{-1} corresponds to the A_1T modes. This is not observed on Sb–Al co-doped samples annealed at 650 °C, However, we observe a peak at 310 cm^{-1} peak corresponding to the lattice deformation induced by the presence of Sb in the ZnO lattice. A small peak suppressed at 556 cm^{-1} attributes to the E_1(L0) modes which are associated with the structural defects related to oxygen vacancies. The optical properties of the Sb-Al co-doped ZnO nanowires were investigated for different annealed samples using Room temperature PL.

8.5.2 Optical Properties of Sb–Al Co-doped ZnO Nanowires

Figure 8.15 shows the room temperature PL spectrum of Sb–Al co-doped ZnO nanowires. The PL spectra of the ZnO nanowires annealed at 450 °C exhibit weak UV peak emission i.e., the NBE emission at around 380 nm and a broad DLE corresponding to the visible emission is observed. With increase in annealing temperature to 650 °C, increase in intensity of the UV emission was observed. Thus the formation of the single ionized oxygen vacancies has been considerably reduced [40].

From the XPS analysis it is clear that the presence of Sb 539.5 eV is near binding energy of Sb–O bond, confirming that the Sb would substitute Zn(Sb_{zn}) instead of oxygen in the Sb doped ZnO and then produce two corresponding Zn vacancies (V_{zn}), which forms a Sb_{zn}–$2V_{zn}$ complex acceptor [33]. The presence of $Al_{2p3/2}$ peaks at 76.2 eV is possibly related to Al–O bonds leading to excess of oxygen neutralizing the oxygen vacancies [34].

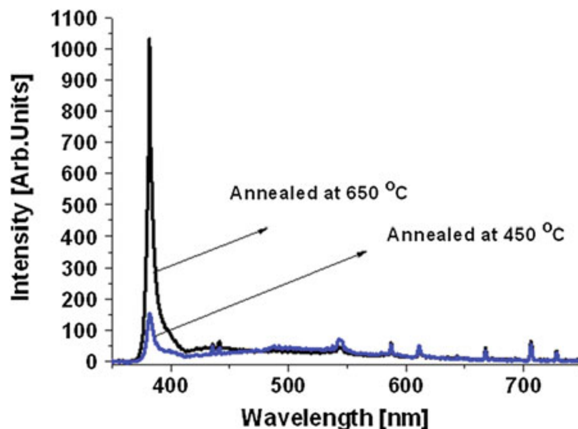

Fig. 8.15 Room temperature PL spectroscopic analysis of Sb–Al co-doped ZnO nanowires annealed at 450 and 650 °C

The annealing of these Sb–Al co-doped samples also has their own influence in the depletion of oxygen vaccines. This has been confirmed from the Raman spectroscopic analysis. The suppression of A_1T modes at 380 cm^{-1} and $E_1(L0)$ modes at 556 cm^{-1} is observed in the Sb–Al co-doped nanowires annealed at 650 °C as compared to the samples annealed at 450 °C. The A1T modes corresponds to lattice irregularities such as oxygen defect or the dopant atom along the c-axis and $E_1(L0)$ modes are associated with the structural defects related to oxygen vacancies [41]. The suppression of these modes will lead to reduction in visible emission and improvement in UV emission as observed in room temperature PL [42]. This confirms that the Sb–Al co-doped samples possess high stoichiometric nature, good structural and optical properties. The p-type conductivity of the Sb–Al co-doped ZnO nanowires can be investigated by fabricating ZnO/ZnO:Sb–Al (co-doped) homo *p–n* Junction.

8.6 ZnO/ZnO:Sb–Al (co-doped) Homo *p–n* Junction

To fabricate homo *p-n* junction pure ZnO was deposited on silicon surface using PLD. A sintered source target of pure ZnO target with 99.99 % in purity (Kojundo Chemical Laboratory, Japan) was used for synthesizing the buffer layer. The ZnO target was ablated with the third harmonics of a Q-switched Nd:YAG laser (Spectra Physics, Quanta-Ray, GCR-290) at 355 nm with a repetition rate of 10 Hz and a fluence of about 1.3 J/cm^2. A ZnO buffer layer was deposited at a background oxygen pressure of 3.3 Pa with a substrate temperature of 650 °C for 1.5 min for the growth of 100 nm, 10 min for 800 nm thick, and 20 min for 1,600 nm thick sample. The Si deposited ZnO buffer layer was coated with Sb (99.999 % pure (Nilaco corporation, Japan)) to a thickness of 80–100 nm using thermal evaporation method. The ZnO nanowires were continuously grown on the Sb coated ZnO buffer layer at 40 kPa with a substrate temperature of 750 °C for

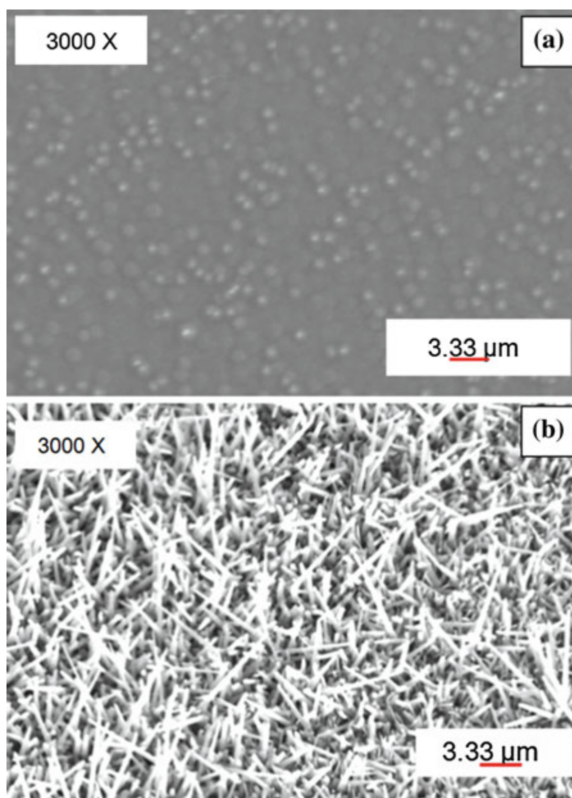

Fig. 8.16 SEM micrograph of **a** ZnO buffer layer, **b** Sb–Al co-doped nanowire on the buffer layer

30 min. Sb:Al co-doped ZnO nanostructures were synthesized by using Sintered intrinsic ZnO:Al target.

The target to substrate distance was 15 mm. For one growth run 36000 KrF excimer laser pulses with 20 Hz repetition frequency were applied. The laser energy density on the target was about 3 J/cm^2 in the presence of argon gas at a pressure of 100 Torr and a constant flow rate of 27.5 sccm. The Sb–Al co-doped ZnO nanowires were synthesized at a growth temperature of 750 °C with growth duration for period of 20 min. After synthesis, to activate the dopant, the samples were post annealed for a period of 30 min at different temperatures in the ambient condition.

Figure 8.16a shows the SEM micrograph of the ZnO buffer layer were granules of microdots are observed. Due to the influence of the ZnO buffer layer a vertically aligned layer along with horizontally grown argon Sb:Al co-doped nanowires were observed as shown in Fig. 8.16b. The diameter of the nanowires synthesized on the ZnO buffer layer is quite high as compared to the nanowires synthesized on the Si surface.

To investigate the electrical properties I–V characteristics were performed. The contacts were taken from the silver paste deposited on the pure ZnO buffer layer and gold paste on the Sb:Al co-doped nanowires.

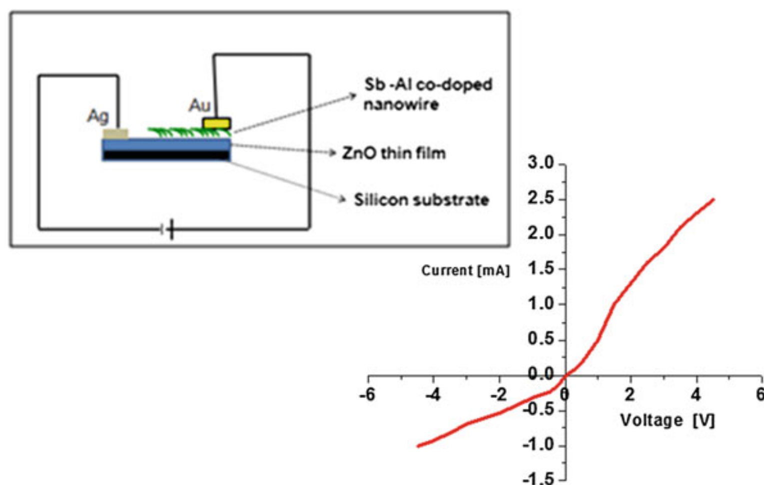

Fig. 8.17 Room temperature PL spectroscopic analysis of Sb–Al co-doped ZnO nanowires annealed at 450 and 650 °C

Figure 8.17 shows the current voltage characteristics showing a diode behavior with large amount of leakage current, which might be due to the improper diffusion of Sb from. However, the rectifying diode behavior confirms the formation of p-type characteristics in the Sb–Al co-doped nanowires

8.7 Summary

The methodology on usage of Sb as catalyst to initiate the growth of ZnO nanostructures has been proposed and demonstrated. The mechanism of the growth initiation of nanostructures from the Sb droplets and the growth is through VLS mechanism. The catalyst Sb is highly sensitive to temperature conditions, thus resulting in synthesis of Sb doped ZnO nanowires and nanosheets at different temperature condition. The Sb catalyzed nanowires showed a strong green emission due to the defect state of ZnO interstitial as oxygen vacancies. This has been confirmed by the Raman peak at 556 cm^{-1}. In the case of Sb catalyzed nanosheets, the formation of oxygen vacancies decreases; resulting in improved UV emission and absence of visible emission as observed from room temperature PL, thus confirming that the nanosheets synthesized possess good structural and optical properties as compared to the nanowires.

In order to rectify the structural defects, Sb doped ZnO nanowires were synthesized on ZnO buffer layer at varying thickness using Sb as catalyst. Vertically grown with horizontally grown Sb doped ZnO nanowires were observed. The Sb doped ZnO nanowires showed a significant change in the lattice constant of about 0.06° from XRD, widening of lattice fringe spacing of 0.054 nm from TEM,

confirms the diffusion of Sb in ZnO lattice. With the increase in buffer layer thickness of 1600 nm, a strong intensity of UV emission with absence of visible emission was observed. This confirms that the defects during the nucleation process is completely rectified resulting in generation of high quality Sb doped ZnO nanowires.

In addition to single element doping, the technique of dopant diffusion form the substrate can be used to develop co-doped ZnO structures. Sb-Al co-doped ZnO nanowires have been successfully synthesized using Nanoparticle Assisted Pulsed Laser Deposition (NAPLD), by using ZnO:Al target and Sb coated Si as substrates. At a growth temperature of 750 °C, random-oriented high density nanowires with a diameter of about 1 μm and a length up to a few tens of micrometer were synthesized. The suppression of A_1T modes and E_1(L0) modes from Raman spectroscopy confirming that depletion of oxygen vacancies. XPS analysis confirming that the Sb would substitute for $Zn(Sb_{zn})$ instead of oxygen Al–O bonds leading to excess of oxygen, neutralizing the oxygen vacancies. Thus Sb-Al co-doped nanowires annealed at 650 °C showed a strong UV emission and reduction in visible emission as compared to the Sb-Al co-doped nanowires annealed at 450 °C. This confirms that the Sb–Al co-doped possess high stoichiometric nature, good structural and optical properties. To investigate the p-type conductivity of the Sb–Al co-doped nanowire, a homo *p–n* junction was prepared by synthesizing Sb–Al co-doped ZnO nanowires on the pure ZnO surface. The I–V characteristics of the homo *P–N* junction were investigated and a rectifying behavior was observed confirming the formation of *p*-type.

In conclusion the Sb mono-doped and co-doped ZnO nanowires synthesized by using Sb as catalyst possess good structural and optical properties with good crystallization quality and high stoichiometry nature, hence it is highly suitable for light emitting device applications.

Acknowledgments A part of this work was supported by the Special Coordination Funds for Promoting Science and Technology from Japan Science and Technology Agency.

References

1. G. VijayaPrakash, K. Pradeesh, A. Kumar et al., Fabrication and optoelectronics characterization of ZnO photonic structure. Mater. Lett. **62**, 1183–1186 (2008)
2. L. Cao, M.K. Li, M. Lub, W. Zhang, Q. Wei, Z.B. Liu, The fabrication and electrical characteristics of ZnO twinned nanowires. Mater. Sci. Semicon. Process. **11**, 25–29 (2008)
3. Y.S. Lim, J.W. Park, S.-T. Hong, J. Kim, Carbothermal synthesis of ZnO nanocomb structure. Mater. Sci. Eng. B. **129**, 100–103 (2006)
4. Z. Xiaohui, Y. Xiaoqin, Z. Jing, Q. Zi, Z. Yue et al., Structure and photoluminescence of S-doped ZnO nanorods arrays. Mater. Lett **63**, 444–446 (2009)
5. A. Ishizumi, Y. Takahashi, A. Yamamoto, Y. Kanemitsu, Fabrication and optical properties of Eu3+-doped ZnO nanospheres and nanorods. Mater. Sci. Eng. B. **146**, 212–215 (2008)
6. P. Xiuhua, Y. Zhizhen, L. Jiesheng, G. Xiuquan, Yujia et al., Fabrictaion of Sb-doped P-type ZnO thin films by pulsed laser deposition. Appl. Surf. Sci. **253**, 5067–5069 (2003)

7. H. Benelmadjat, N. Touka, B. Harieche, B. Boudine et al., Study of structural and optical properties of Sb doped ZnO thin films deposited by spin coating method. Opt. Mater. **32**, 764–767 (2010)
8. D. Yu, L. Hu, J. Li, H. Hu, H. Zhang, Z. Zhao, Q. Fu, Catalyst-free synthesis of ZnO nanorod arrays on InP (001) substrate by pulsed laser deposition. Mater. Lett. **62**, 4063–4065 (2008)
9. I.A. Palani, D. Nakamura, K. Okazaki, M. Higashihata, T. Okada, Influence of Sb as a catalyst in the growth of ZnO nanowires and nano sheets using Nanoparticle Assisted Pulsed Laser Deposition (NAPLD). Mater. Sci. Eng. **176**, 1526–1530 (2011)
10. Z. Guo, D.X. Zhao, Y. Liu, D. Shen, J. Zhang, B. Liu, Visible and ultraviolet light alternative photodetector based on ZnO nanowire/n-Si heterojunction. Appl. Phys Lett. **93**, 163501–163503 (2008)
11. H. Guo, J. Zhou, Z. Lin, ZnO nanorod light-emitting diodes fabricated by electrochemical approaches. Electrochem. Commun. **10**, 146–150 (2008)
12. Y. Li, L. You, R. Duan, P. Shi, G. Qin, Oxidation of a ZnS nanobelt into a ZnO nanotwin belt or double single-crystalline ZnO nanobelts. Solid State Commun. **129**, 233–238 (2004)
13. T. Yamamoto, H.K. Yoshida, Solution using a co-doping method to unipolarity for the fabrication of p-type ZnO. Jpn J. Appl. Phys. **38**, 166–169 (1999)
14. K. Nakahara, H. Takasu, P. Fons, A. Yamada, K. Iwata, K. Matsubara, R. Hunger, S. Niki, Interaction between gallium and nitrogen dopants in ZnO films grown by radical source molecular beam epiatxy. Appl. Phys. Lett. **79**, 4139–4141 (2001)
15. A. Tsukazaki, H. Saito, K. Tamura, M. Ohtani, H. Koinuma, M. Sumiya, S. Fuke, T. Fukumura, M. Kawasaki., Systematic examination of carrier polarity in composition spread ZnO thin films codoped with Ga and N. Appl. Phys. Lett. **81**, 235–238 (2002)
16. Y.Z. Zeng, Z.Z. Ye, J.G. Lu, L.P. Zhu, D.Y. Li, B.H. Zao, J.Y. Huang, Appl. Surf. Sci. **249**, 203 (2005)
17. H.P. He, F. Zhuge, Z.Z. Ye, L.P. Zhu, F.Z. Wang, B.H. Zhao, J.Y. Huange, Stain and its effect on optical properties of Al–N co-doped ZnO films. J. Appl. Phys. **99**, 023503 (2006)
18. F. Zhuge, L.P. Zhu, Z.Z. Ye, J.G. Lu, H.P. He, B.H. Zao, Al concentration dependence of electrical and photoluminescent properties of co-doped ZnO films. Chem. Phys. Lett. **437**, 203 (2007)
19. E. Jung Yun, H.S. Park, K.H. Lee, H.G. Nam, M. Jung, Charecterization of Al–As Co-Doped p-type ZnO films by magnetron cosputtering deposition. J. Appl. Phys. **103**, 073507-1-3 (2006)
20. W.W. Zho, F.M. Liu, L.G. Cai, C.C. Zhou, P. Ding, H. Zhang, Annealing effect of co-doping with Al and Sb on structure and optical-electrical properties of the ZnO thin films. J. Alloys Compd. **499**, 265–268 (2010)
21. D. Nakamura, K. Okazaki, I.A. Palani, M. Highasiata, T. Okada, Influence of Sb on a controlled-growth of aligned ZnO nanowires in nanoparticle-assisted pulsed-laser–deposition. doi:10.1007/s00339-011-6401-5
22. N.J. Vasa, I.A. Palani, M. Singaperumal, T. Okada, Laser assisted doping and smiulatneous texturization of amorphous Si film for tandem photovoltaic cells. Opt. Precis. Engg. **19**, 2263–2270 (2011)
23. R. Yousefi, B. Kamaluddin, M. Ghoranneviss, F. Hajakbari, Auger and photoluminescence analysis of ZnO nanowires grown on AlN thin film. Appl. Surf. Sci. **255**, 6985–6988 (2009)
24. R. Yousefi, B. Kamaluddin, Effect of S- and Sn-doping to the optical properties of ZnO nanobelts. Appl. Surf. Sci. **255**, 9376–9380 (2009)
25. R. Yousefi, A.K. Zak, Growth and characterization of ZnO nanowires grown on the Si(1 1 1) and Si(1 0 0) substrates: optical properties and biaxial stress of nanowires. Mater. Sci. Semicon. Proc. doi:10.1016/j.mssp.2011.02.007
26. S. Xin, Z. Zhengjun, W. Yuquan, Z. Minmin, Synthesis and photoluminescence of aligned ZnO nanorods by thermal decomposition of Zinc acetate at a substrate temperature of 250 °C. J. Phys. D: Appl. Phys. **38**, 3934–3937 (2005)

27. C. Bing, W. Xiufeng, L. Liying, G. Litong, Growth mechanism and morphology dependent luminescence properties of ZnO nano structures prepared in aqueous solution. Mater. Lett. **62**, 3099–3102 (2008)
28. R. Yousefi, B. Kamaluddin, The effects of annealing temperature on structural and optical properties of S-doped ZnO nanobelts. Solid State Sci. **12**, 252–256 (2010)
29. W.Q. Peng, S.C. Qu, G.W. Cong, Z.G. Wang, Structure and visible luminescence of ZnO nanoparticles. Mater. Sci. Semicond. Process. **9**, 156–159 (2006)
30. P.T. Hsieh, Y.C. Chen, C.M. Wang, Y.Z. Tsai, C.C. Hu, Structural and PL characteristics of ZnO films by room temperature sputtering and rapid thermal annealing processes. Appl. Phys. A **84**, 345–349 (2006)
31. S. Senthilkumaar, K. Rajendran, S. Banerjee, T.K. Chini, V. Sengodan, Influence of Mn doping on the microstructure and optical property of ZnO. Mater. Sci. Semicond. Process. **11**, 6–12 (2008)
32. Y. Ya, J. Qi, Q. Lioa, Y. Zhnag, L. Tang, Z. Qin, Synthesis and characterization of Sb doped ZnO nanobelts with single side zigzag boundaries. J. Phy. Chem. C **112**, 17916–17919 (2008)
33. J.Y. Li, L. Li, J. Xu, Z. Xiaosong, L. Haiyan, Z.J. Yan, Controlled growth of ZnO nanorods bypolmer template and their Photoluminescence properties. Sci. China Ser. E-tech. Sci. **52**, 888–892 (2009)
34. M. Gomi, N. Oohira, K. Ozaki, M. Koyano, Photoluminescent and structural properties of precipitated ZnO fine particles. Jpn J. Appl. Phys. **42**, 481–485 (2003)
35. I.A. Palani, D. Nakamura, K. Okazaki, T. Shimogaki, M. Higashihata, T. Okada, Influence of ZnO buffer layer on growth of Sb doped ZnO nanowires using nano particle assisted pulsed laser deposition (NAPLD) using Sb as catalyst. Adv. Mat. Lett. doi:10.5185/amlett.2012.1302
36. T. Yang, B. Yao, T.T. Zhao, G.Z. Xing, H. Wang, H.L. Pan, R. Deng, Y.R. Sui, L.L. Gao, H.Z. Wang, T. Wu, D.Z. Shen, Sb doping behavior and its effect on crystal structure, conductivity and photoluminescence of ZnO film in depositing and annealing processes. J. Alloys. Compd **509**, 5426–5430 (2011)
37. I.A. Palani, D. Nakamura, K. Okazaki, M. Highasiata, T. Okada, Structural and optical properties of SbAl co-doped ZnO nanowires synthesized using Nanoparticle Assisted Pulsed Laser Deposition (NAPLD) with Sb as catalyst. J. Alloys. Compd. **527**, 112–116 (2012)
38. S.M.H. Hejazi, F. Majidi, M. Pirhadi Tavandashti, M. Ranjbar, The effect of heat treatment process on structure and properties of ZnO nano layer produced by sol–gel method. Mater. Sci. Semicond. Process. **13**, 267–271 (2010)
39. O. Lupan, L. Chow, G. Chai, B. Roldan, A. Naitabdi, A. Schulte, H. Heinrich, Nanofabrication and characterization of ZnO nanorod arrays and branched microrods by aqueous solution route and rapid thermal processing. Mater. Sci. Eng. B. **145**, 57–66 (2007)
40. L.C. Oleg, L.K. Lee, L. Ono et al., Synthesis and characterization of Ag- or Sb- doped ZnO nanorods by a facmile hydrothermal route. J. Phys. Chem. C **114**, 12401–12408 (2010)
41. J.M. Qin, B. Yao, Y. Yan, J.Y. Zhang, X.P. Jia, Z.Z. Zhang, B.H. Li, C.X. Shan, D.Z. Shen, Formation of stable and reporoducible low resistivity and high carrier concentration p-type ZnO doped at high pressure with Sb. App. Phys. Lett. **95**, 022101 (2009)
42. G.Z. Xing, B. Yao, C.X. Cong, T. Yang, Y.P. Xie, B.H. Li, D.Z. Shen, Effect of annealing on conductivity behavior of undoped ZnO prepared by rf magnetron sputtering. J. Alloys. Compd. **457**, 36–41 (2008)

Chapter 9
Time and Spatially Resolved Luminescence Spectroscopy of ZnO Nanostructures

Hideaki Murotani, Yoichi Yamada, Daisuke Nakamura and Tatsuo Okada

Abstract The optical properties of undoped, P-doped, and Sb-doped ZnO nanostructures (NSs) have been studied by means of photoluminescence (PL), time-resolved PL, and spatially resolved cathodoluminescence (CL) spectroscopy. The temperature dependence of the PL spectra of the P-doped and Sb-doped ZnO NSs was analyzed, and the binding energies of the P-acceptor- and the Sb-acceptor-bound excitons were estimated to be 15 and 11 meV, respectively. This indicated that the Sb impurities formed a shallower acceptor level than the P impurities in ZnO. PL lines due to the radiative recombination of biexcitons and the inelastic scattering processes of excitons were clearly observed in the undoped ZnO NSs, which enabled us to evaluate the binding energies of the excitons and biexcitons as 60 and 15 meV, respectively. These values were identical to the values in bulk ZnO. The radiative and nonradiative recombination lifetimes were estimated from the temperature dependence of the PL lifetime and the time-integrated PL intensity. Although the radiative recombination lifetimes for the undoped and P-doped ZnO NSs were almost equal, the nonradiative recombination lifetime for the P-doped ZnO NSs was longer than that for the undoped ZnO NSs. This suggested that the P doping suppressed the thermal activation of the nonradiative recombination processes. CL images revealed that the intensity of the side surface was much stronger than that of the interior in the P-doped ZnO NSs. On the other hand, the CL intensity was distributed almost uniformly in the Sb-doped

H. Murotani (✉) · Y. Yamada
Department of Materials Science and Engineering, Yamaguchi University,
2-16-1 Tokiwadai, Ube, Yamaguchi 755-8611, Japan
e-mail: murotani@toyota-ct.ac.jp

H. Murotani
Department of Electrical and Electronic Engineering, Toyota National College
of Technology, 2-1 Eisei-cho, Toyota, Aichi 471-8525, Japan

D. Nakamura · T. Okada
Graduate School of Information Science and Electrical Engineering, Kyushu University,
744 Motooka, Nishi-ku, Fukuoka 819-0395, Japan

M. S. R. Rao and T. Okada (eds.), *ZnO Nanocrystals and Allied Materials*,
Springer Series in Materials Science 180, DOI: 10.1007/978-81-322-1160-0_9,
© Springer India 2014

ZnO NSs. These observations suggested that the P impurities were distributed around the surface of the NSs and that the Sb impurities were distributed almost uniformly over the NSs.

9.1 Introduction

Among wide-gap II–VI compound semiconductors, ZnO has a large band gap energy of about 3.37 eV at room temperature, which makes it one of the key materials for applications in light-emitting devices operating in the ultraviolet spectral range [1]. So far, there have been several reports on the development of ZnO-based light-emitting devices. Recently, ZnO-based light-emitting diodes with a high output power of 70 μW were demonstrated [2]. However, the output power and the luminescence efficiency of these devices are still too low for commercial applications. The development of highly efficient devices based on ZnO has been impeded by the difficulty of achieving p-type conductivity. Many dopants such as nitrogen [3], phosphorous (P) [4], arsenic [5], antimony (Sb) [6, 7], and lithium [8] have been employed to obtain p-type ZnO. However, a p-type ZnO with a sufficient carrier concentration has not yet been obtained. Therefore, further study is necessary to achieve highly efficient ZnO-based light-emitting devices.

ZnO also has a small exciton Bohr radius ($a_B = 1.5$ nm) and a large exciton binding energy of about 60 meV, which is much larger than the thermal energy at room temperature ($k_B T = 26$ meV) and ensures that excitonic emissions are significant at room temperature. Therefore, ZnO is one of the most fruitful candidates for exploring the intrinsic recombination processes of high-density excitons. So far, there have been a number of reports on the radiative transition processes of high-density excitons, including the radiative recombination of biexcitons, and the inelastic scattering of excitons. Koch et al. reported optical gain due to the biexciton decay process in bulk ZnO [9]. Bagnall et al. suggested that inelastic exciton–exciton scattering contributed to stimulated emission at room temperature [10]. Therefore, ZnO is an ideal material for realizing room temperature excitonic devices.

In recent years, ZnO-based nanostructures (NSs) such as nanowires, nanorods, and nanobelts have attracted much interest owing to their numerous advantages, which include an increase in the radiative recombination rate, enhancement of excitonic effects, and the possibility to obtain high-quality crystals with extremely low defect densities. ZnO-based NSs also have potential applications in multifunctional nanodevices such as solar cells [11], nanolasers [12], and nanosensors [13]. There has been much work on the synthesis and the optical properties of ZnO-based NSs. ZnO-based NSs have been synthesized using several techniques, such as chemical vapor deposition (CVD) [14], physical vapor deposition (PVD) [15], molecular beam epitaxy [16], and nanoparticle-assisted pulsed laser deposition (NAPLD) [17–20]. The optical properties of ZnO NSs have been studied using a variety of methods such as photoluminescence (PL) [21–26], time resolved

PL [27–29], spatially resolved cathodoluminescence (CL) spectroscopy [30–33], and scanning near-field optical microscopy [34–36]. These studies have provided experimental insight into the optical properties of ZnO-based NSs. However, the optical properties of ZnO NSs are not fully understood. In particular, there are few studies on the effects of impurity doping on the optical properties of ZnO NSs.

In this chapter, we summarize our experimental studies on the optical properties of undoped, P-doped, and Sb-doped ZnO NSs by means of PL, time-resolved PL, and spatially resolved CL spectroscopy. First, we evaluate the binding energies of P-acceptor- and Sb-acceptor-bound excitons based on temperature-dependent PL measurements and discuss the ionization energies of P and Sb acceptors. Then, we study the excitonic optical properties of undoped ZnO NSs under high-density excitation and discuss the luminescence properties of the biexciton-exciton transition and exciton–exciton scattering processes. Moreover, the effects of impurity doping on the radiative and nonradiative recombination dynamics of excitons are studied by means of temperature-dependent time-resolved PL measurements. Finally, we analyze the CL intensity images of P-doped and Sb-doped ZnO NSs and discuss the spatial distribution of P and Sb impurities in ZnO NSs.

9.2 Experimental Procedure

The samples mainly used in the present work were undoped, P-doped, and Sb-doped ZnO NSs synthesized by the NAPLD technique. The undoped ZnO NSs were synthesized on a sapphire substrate using a pure ceramic ZnO target as the source material. The P-doped ZnO NSs were also synthesized on a sapphire substrate using a sintered ZnO:P_2O_5 target as the source material. The Sb-doped ZnO NSs were synthesized on a sapphire substrate after the deposition of a 1 μm thick ZnO buffer layer coated with a 100 nm thick Sb layer. A pure ceramic ZnO target was used as the target material for the synthesis of the Sb-doped ZnO NSs. Figure 9.1 shows the scanning electron microscopy (SEM) images of **a** undoped, **b** P-doped ZnO, and **c** Sb-doped NSs. As seen in Fig. 9.1, the undoped and P-doped ZnO NSs have pillar structures with diameters of 300–400 nm, and the Sb-doped ZnO NSs have pillar structures with diameters of 200–300 nm. The details of the growth procedure have been reported elsewhere [17–20, 37–41].

PL measurements were performed using the 325 nm line of a continuous-wave He-Cd laser and a Xe–Cl excimer laser ($\lambda = 308$ nm) as an excitation source. The pulse width and the repetition rate of the Xe–Cl excimer laser were 2.5 ns and 100 Hz, respectively. PL signals were detected by a liquid-nitrogen-cooled charge-coupled device camera in conjunction with a 50 cm single-grating monochromator with a 2400 groove/mm grating. The spectral resolution was better than 0.04 nm (i.e., better than 0.4 meV around 3.3500 eV). Time-resolved PL measurements were carried out by employing a synchroscan streak camera in conjunction with a 25 cm single-grating monochromator with a 1200 groove/mm grating. The excitation source was the third harmonic light (267 nm) of amplified Ti:sapphire laser

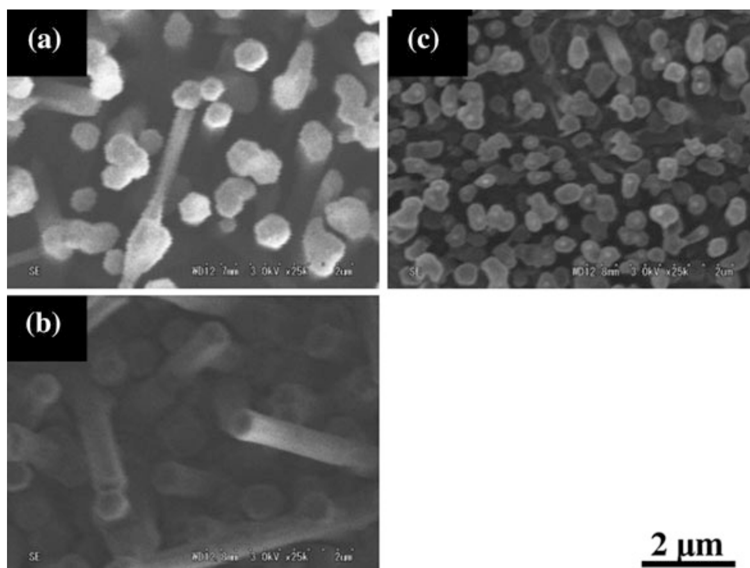

Fig. 9.1 Plan-view SEM images of **a** undoped, **b** P-doped, **c** Sb-doped ZnO NSs synthesized by NAPLD on sapphire substrates

pulses. The pulse duration and the repetition rate were 200 fs and 250 kHz, respectively. The instrumental response of our system was better than 5 ps. The spectral resolution was better than 0.12 nm (i.e., better than 1.1 meV around 3.3500 eV). Spatially resolved CL measurements were carried out in a field-emission scanning electron microscope operating at an accelerating voltage of 3 kV. The CL signals were detected by a photomultiplier tube in conjunction with a 30 cm single-grating monochromator with a 1200 groove/mm grating.

9.3 Temperature Dependence of PL Spectra

Figure 9.2 shows the temperature dependence of the PL spectra of the undoped ZnO NSs taken under an excitation power density of 32 W/cm^2. In this case, the 325 nm line of the continuous-wave He-Cd laser was used as an excitation source. The spectra were normalized by the maximum intensity of each spectrum. At the lowest temperature of 7 K, the spectrum is dominated by the PL line denoted by M. The M line is quenched with increasing temperature, and it cannot be resolved at temperatures above 140 K. The origin of the M line will be discussed later. In contrast to the quenching of the M line, the X line becomes prominent with increasing temperature, and it is predominant above 120 K. The 1LO and 2LO phonon replicas of the X line, which are denoted by X-1LO and X-2LO, respectively, are clearly observed at temperatures above 60 K. On the basis of these

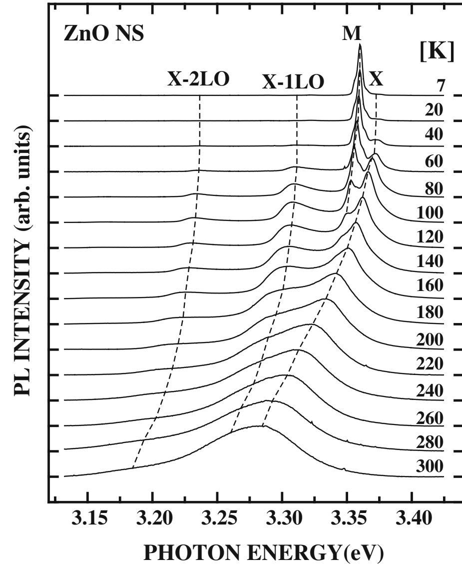

Fig. 9.2 Temperature dependence of PL spectrum taken from undoped ZnO NSs under an excitation power density of 32 W/cm^2 (after [42])

observations, we attribute the X line to the radiative recombination of free excitons. Then, the PL peak energy of free exciton luminescence, E_X, is estimated to be 3.3752 eV at 7 K. This value is almost consistent with the transition energy of free excitons in bulk ZnO at low temperatures [43–45]. This indicates that the ZnO NSs used in the present work are almost strain-free.

In order to confirm our assignment, we analyzed the temperature dependence of the PL peak energies of the X and X-1LO lines. Figure 9.3 shows the PL peak energies of the X and X-1LO lines taken from the undoped ZnO NSs as functions of temperature. The closed and open circles indicate the PL peak energies of the X line and the X-1LO line, respectively. The PL peak energy of the X line decreases gradually with increasing temperature from 7 to 150 K, and then a rapid decrease occurs above 160 K. Since the binding energy of excitons in ZnO is much larger than the thermal energy at room temperature, the temperature dependence of the transition energy of free excitons up to room temperature mainly reflects the temperature-dependent change in the band gap energy. Varshni's empirical model has often been used to describe the temperature-dependent variation of the band gap energy for a variety of semiconductors [46]:

$$E_X(T) = E_X(0) - \frac{\alpha T^2}{\beta + T}, \tag{9.1}$$

where α and β represent the Varshni coefficients and $E_X(0)$ is the transition energy at 0 K. The solid line shows the result of a least squares fit using the Varshni equation, where the obtained values are $\alpha = 3.6$ meV/K and $\beta = 3110$ K.

As seen in Fig. 9.3, the energy separation between the X line and the X-1LO line decreases with increasing temperature. According to Permogorov's theory, the

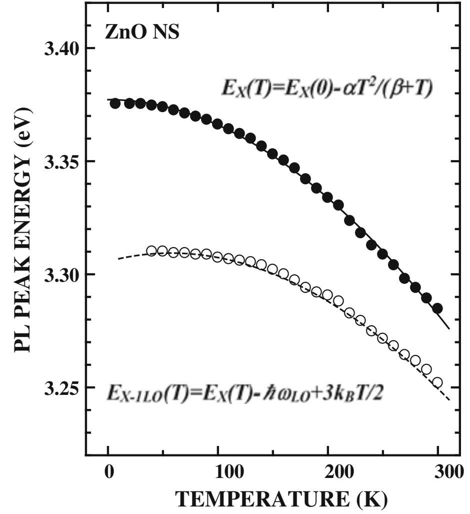

Fig. 9.3 PL peak energies of free exciton luminescence (X) and a 1LO phonon replica of the X line taken from the undoped ZnO NSs as functions of temperature. The solid line shows the result of a least squares fit using the Varshni equation [46]. The dashed line shows the predicted peak energy of the 1LO phonon replica of the X line

spectral peak energy of the 1LO phonon replica of the free excitons can be described as follows:

$$E_{\mathrm{X-1LO}}(T) = E_{\mathrm{X}}(T) - \hbar\omega_{\mathrm{LO}} + \frac{3}{2}k_{\mathrm{B}}T, \tag{9.2}$$

where $\hbar\omega_{\mathrm{LO}}$ and $E_{\mathrm{X}}(T)$ are the LO phonon energy and the transition energy of free excitons, respectively [47]. Thus, the energy separation between the free exciton luminescence and the 1LO phonon replica should decrease with increasing temperature. The dashed line in Fig. 9.3 represents the peak energy of the 1LO phonon replica of the free excitons predicted from Eq. (9.2), where the result of least squares fit using the Varshni equation (shown as the solid line) is used as the $E_{\mathrm{X}}(T)$ value and the value of $\hbar\omega_{\mathrm{LO}} = 72$ meV is used as the LO phonon energy of ZnO [1]. The PL peak energy of the X-1LO line coincides well with the predicted peak energy of the 1LO phonon replica of the free excitons. These observations support our assignment of the X line to the free exciton luminescence.

Next, we analyze the temperature dependence of the PL spectra of the P-doped and Sb-doped ZnO NSs in order to evaluate the binding energies of P-acceptor- and Sb-acceptor-bound excitons. Figures 9.4a, b show the temperature dependence of the PL spectra taken from the P-doped ZnO NSs and the Sb-doped ZnO NSs, respectively. These spectra were taken under an excitation power density of 32 W/cm^2. The spectra are normalized by the maximum intensity of each spectrum. At 7 K, the PL spectra of both the P-doped and the Sb-doped NSs are dominated by the radiative recombination of excitons bound to neutral acceptors [denoted by (A^0, X)]. With increasing temperature, the free exciton luminescence line (denoted X) is clearly observed in both NSs. The PL lines of the LO and 2LO phonon replicas of the line X are also observed at the lower energy side of line X in both ZnO NSs (denoted by X-1LO and X-2LO, respectively). Figures 9.5a, b

show the temperature dependence of the PL peak energy of the X, (A^0, X), and X-1LO lines taken from the P-doped and Sb-doped ZnO NSs, respectively. The closed and open circles indicate the PL peak energies of the X and the X-1LO lines, respectively, and the closed squares indicate the PL peak energies of the (A^0, X) line. The solid lines represent the results of a least squares fit to the experimental data using Eq. (9.1), and the dashed lines represent the peak energy of the 1LO phonon replica of the X line predicted from Eq. (9.2). Except for a slight deviation observed above 180 K for the X-1LO line in the P-doped ZnO NSs, the solid and the dashed lines are in good agreement with the experimental data. At 7 K, the PL peak energies of the (A^0, X) lines in the P-doped and the Sb-doped ZnO NSs are estimated to be 3.3600 and 3.3646 eV, respectively. The PL peak energy of the free exciton luminescence line at 7 K is also estimated to be 3.3756 eV for both NSs. Thus, the binding energies of the P-acceptor-bound exciton and the Sb-acceptor-bound exciton are estimated to be 15 and 11 meV, respectively. These observations suggest that the Sb impurity forms a shallower acceptor level than the P impurity in ZnO.

In order to confirm the value of the binding energy of the neutral-acceptor-bound excitons, we analyzed the PL intensity ratio of the (A^0, X) line relative to the X line as a function of temperature. Figures 9.6a, b show an Arrhenius plot of the relative PL intensity of the (A^0, X) line to the X line taken from the **a** P-doped and **b** Sb-doped ZnO NSs. The relative PL intensities of the (A^0, X) line to the X line in both ZnO NSs decrease with increasing temperature. These decreases in the relative PL intensity reflect the thermal dissociation of the neutral-acceptor-bound exciton into a neutral acceptor and free exciton. To estimate the activation energy, we perform a least squares fit using the following equation:

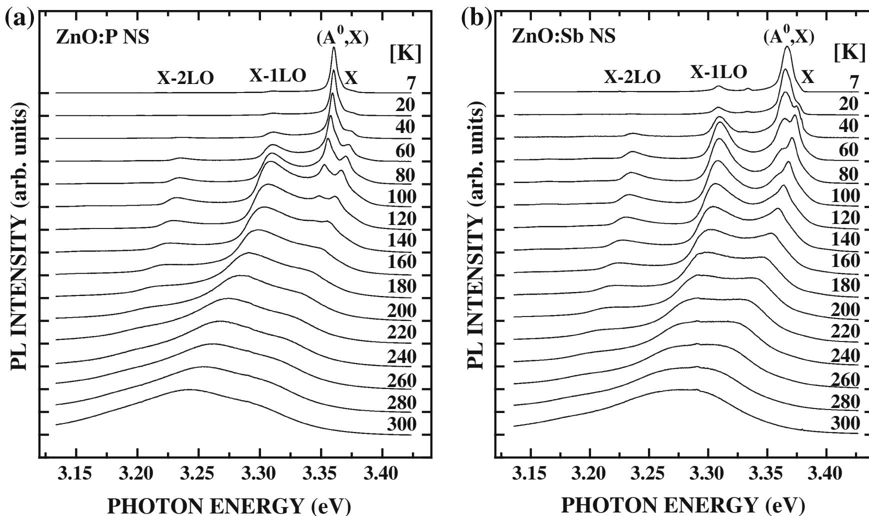

Fig. 9.4 Temperature dependence of PL spectra taken from **a** P-doped and **b** Sb-doped ZnO NSs under an excitation power density of 32 W/cm^2

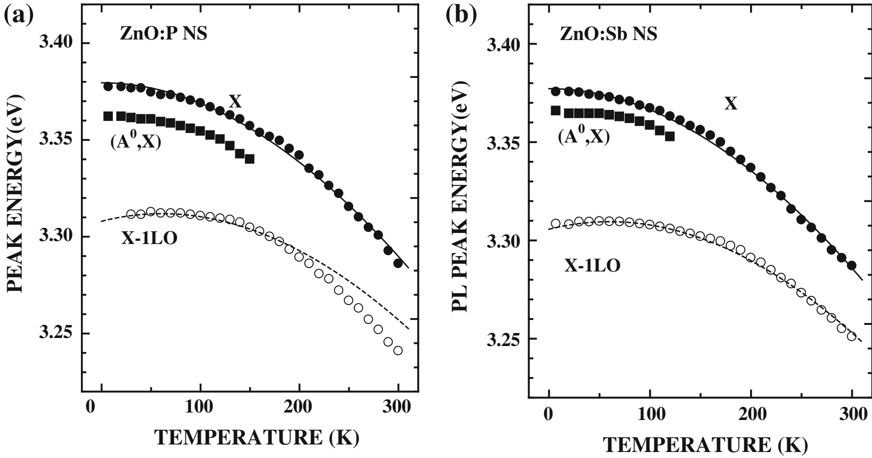

Fig. 9.5 Temperature dependence of PL peak energies of X, (A^0, X), and X-1LO lines taken from **a** P-doped and **b** Sb-doped ZnO NSs under an excitation power density of 32 W/cm^2. The closed circles, closed squares, and open circles indicate the PL peak energies of the X, (A^0, X), and X-1LO lines, respectively

$$I_{\mathrm{AX/FX}}(T) = \frac{I_{\mathrm{AX/FX}}(0)}{1 + A\exp(-E_a/k_B T)} \tag{9.3}$$

where $I_{\mathrm{AX/FX}}(0)$ represents relative PL intensity of the (A^0, X) line to the X line at 0 K, A is a constant, and E_a is the activation energy. The dashed lines in Fig. 9.6a, b indicate the results of the fitting, where the obtained values are $E_a = 15$ meV for

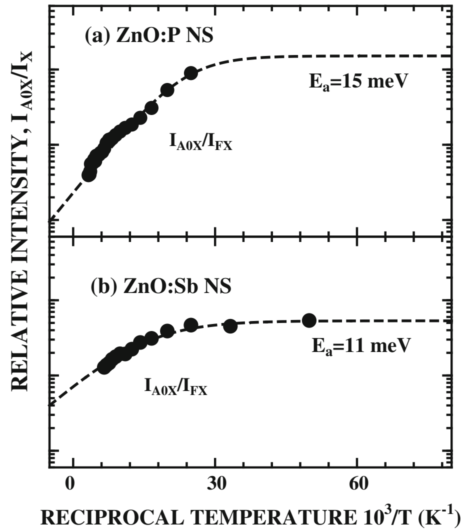

Fig. 9.6 Temperature dependence of integrated PL intensity ratio of accepter bound exciton luminescence related to free exciton luminescence taken from **a** P-doped and **b** Sb-doped ZnO NSs, respectively

Table 9.1 Ionization energies of P and Sb acceptors in ZnO

	P (meV)	Sb (meV)
Present work	150 ± 20	110
Allenic et al. [49]	120 ± 30	
Hwang et al. [50]	127	
Allenic et al. [51]	150	
Xiu et al. [52]	180	
Qin et al. [53]		113
Lopatiuk-Tirpak et al. [54]		135
Mandalapu et al. [55]		160

the P-doped ZnO NSs and $E_a = 11$ meV for the Sb-doped ZnO NSs. These values agree with the binding energy of the neutral-acceptor-bound excitons estimated from the energy separation between the (A^0, X) and X lines. Thus, these results confirm the acceptor-bound exciton binding energy of $E_{AX} = 15$ meV for the P acceptor and of $E_{AX} = 11$ meV for Sb acceptor. According to the Haynes rule [48], the ionization energies of P acceptors and Sb acceptors in ZnO NSs are estimated to be about 150 meV and 110 meV, respectively. The reported values of the ionization energies of P and Sb acceptors in ZnO are summarized in Table 9.1. The obtained value of the ionization energy of the P acceptor almost agrees with the value reported by Allenic et al. [51], and the obtained value of the ionization energy of the Sb acceptor almost agrees with the value reported by Qin et al. [53].

9.4 Excitonic Optical Properties Under High Density Excitation

The excitonic optical properties of the undoped ZnO NSs have been studied by means of PL and time-resolved PL spectroscopy. Figure 9.7 shows the PL spectra taken at 7 K from the undoped ZnO NSs under excitation power densities of **a** 0.045, **b** 0.21, **c** 0.35, **d** 1.9, **e** 3.6, **f** 17, and **g** 32 W/cm^2. Each spectrum is normalized by the peak height of the (A^0, X) line. At the excitation power density of 0.045 W/cm^2, the PL spectrum mainly consists of the PL lines observed at 3.3647 eV [denoted by (D_1^0, X)], 3.3605 eV (denoted by M), 3.3597 eV [denoted by (D_2^0, X)], and 3.3566 eV [denoted by (A^0, X)]. The (D_n^0, X) and (A^0, X) lines are attributed to the radiative recombination of excitons bound to neutral donors and acceptors, respectively. With increasing excitation power density, the M line grows rapidly compared to the other lines. The M line becomes predominant at excitation power densities above 1.9 W/cm^2. Based on this behavior, we attribute the M line to the radiative recombination of biexcitons. The binding energy of biexcitons, B_M, should correspond to the energy separation between the free exciton luminescence line and the biexciton luminescence line ($B_M = E_X - E_M$). Thus, the binding energy of biexcitons is estimated to be 14.7 meV. This value is consistent with the binding energy of biexcitons in bulk ZnO [56].

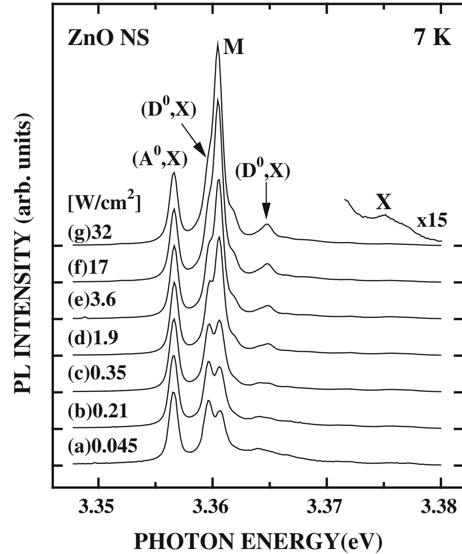

Fig. 9.7 Excitation power density dependence of PL spectrum taken at 7 K from the undoped ZnO NSs. The excitation power densities were estimated to be **a** 0.045, **b** 0.21, **c** 0.35, **d** 1.9, **e** 3.6, **f** 17, and **g** 32 W/cm^2 (after [42])

Figure 9.8 shows the excitation power density dependence of the PL spectrum taken at 7 K from the undoped ZnO NSs under excitation power densities of **a** 0.056, **b** 0.25, **c** 0.51, **d** 1.2, **e** 2.3, **f** 4.6, **g** 11, **h** 21, and **i** 42 MW/cm^2. In this case, the Xe–Cl excimer laser was used as an excitation source. The spectra are normalized by the maximum intensity of each spectrum. At the excitation power density of 0.056 MW/cm^2, the spectrum is dominated by the radiative recombination of biexcitons (denoted by M). With increasing excitation power density, the line width of the M line broadens, and the P line appears suddenly around $E_{\mathrm{P2}} = 3.332$ eV under the excitation power density of 4.6 MW/cm^2. The PL intensity of the P line increases superlinearly with further increases in the excitation power density. The energy separation between E_{X} and E_{P2} is estimated to be about 43 meV. This value is consistent with the energy difference between the ground ($n = 1$) state and the first excited ($n = 2$) state of free excitons in bulk ZnO. Based on these characteristics, the P line is attributed to the PL line due to exciton–exciton scattering processes.

As seen in Fig. 9.8, the PL peak energy of the P line shifts toward the higher energy side with increasing excitation power density. The PL peak energy of the exciton–exciton scattering process in which one of the excitons is scattered into the nth exciton state can be described by

$$E_{\mathrm{P}}^{n} = E_{\mathrm{X}} - B_{\mathrm{X}}\left(1 - \frac{1}{n^2}\right) - \frac{3}{2}k_B T_{\mathrm{eff}}, \tag{9.4}$$

where B_{X} represents the binding energy of free excitons and T_{eff} represents the effective temperature of the excitonic system [57]. Thus, blue shift of the PL peak energy of the P line reflects the filling of the excited states of free excitons ($n \geq 2$)

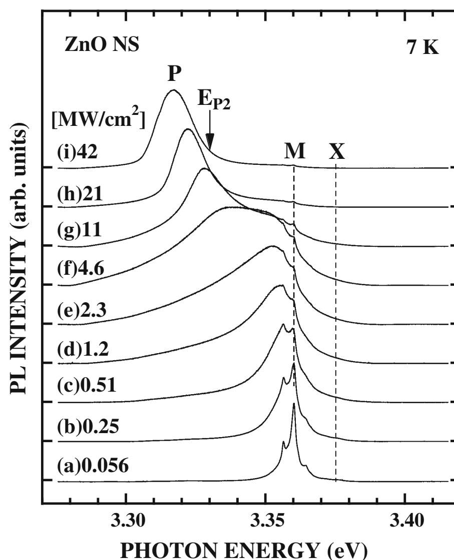

Fig. 9.8 Excitation power density dependence of PL spectrum taken at 7 K from the undoped ZnO NSs. The excitation power densities were estimated to be **a** 0.056, **b** 0.25, **c** 0.51, **d** 1.2, **e** 2.3, **f** 4.6, **g** 11, **h** 21, and **i** 42 MW/cm^2 (after [42])

as well as the increase in the effective temperature with increasing excitation power density.

In order to discuss the dynamics of exciton–exciton scattering processes, we performed time-resolved PL measurements. Figure 9.9 shows the time-integrated PL spectra taken at 7 K from the undoped ZnO NSs under excitation energy densities of **a** 0.7, **b** 1.3, **c** 2.9, **d** 5.9, **e** 7.2, **f** 14, **g** 33, and **h** 66 μJ/cm^2. In this case, the third harmonic light (267 nm) of amplified Ti:sapphire laser pulses was

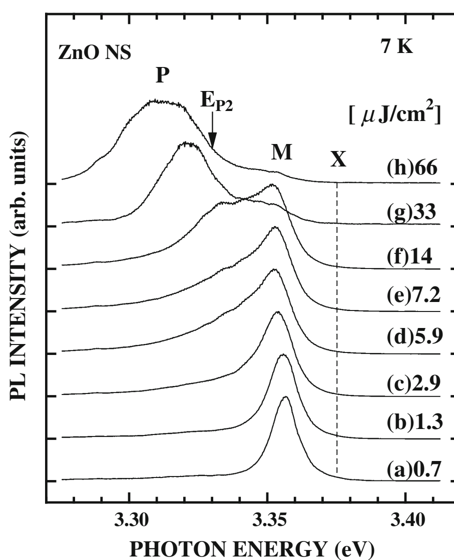

Fig. 9.9 Excitation energy density dependence of time-integrated PL spectrum taken at 7 K from the undoped ZnO NSs. The excitation energy densities were estimated to be **a** 0.7, **b** 1.3, **c** 2.9, **d** 5.9, **e** 7.2, **f** 14, **g** 33, and **h** 66 μJ/cm^2

used as an excitation source. The sweep range was about 800 ps. Each spectrum is normalized by the peak height. At the excitation energy density of 0.7 μJ/cm^2, the spectrum was dominated by the radiative recombination of biexcitons (denoted M). With increasing excitation energy density, the PL line due to exciton–exciton scattering processes (denoted by P) is clearly observed under excitation energy densities above 14 μJ/cm^2. Similar to the result under the Xe–Cl excimer laser excitation, the PL peak energy of the P line shifts toward the lower energy side with increasing excitation energy density.

Figure 9.10a shows the time-resolved PL spectra taken at 7 K from the undoped ZnO NSs under an excitation energy density of 66 μJ/cm^2. The spectra are recorded at different delay times from 6 to 48 ps in steps of 6 ps after arrival of the excitation pulse. The P line appears at a delay time within 6 ps and then shifts toward the higher energy side with increasing delay time. Figure 9.10b shows the PL peak energy of the P line as a function of delay time. At the delay time of 6 ps, the PL peak energy is estimated to be 3.309 eV. With increasing delay time, the PL peak energy shifts toward the higher energy side and approaches E_{P2}. The PL blue shift with increasing delay time reflects the cooling process of the excitonic system. The PL peak energy converges to E_{P2} at the delay time of 48 ps. This observation indicates that the exciton–exciton scattering process reaches equilibrium with the lattice temperature after 48 ps.

Figure 9.11a shows the PL decay of the P line taken from the undoped ZnO NSs under an excitation energy density of 66 μJ/cm^2. The closed circles indicate the PL intensity at 3.315 eV. The open circles indicate the system response measured under the same conditions. The PL decay curve of the P line can be well described by a single exponential function with a decay time of 6 ps, as shown by

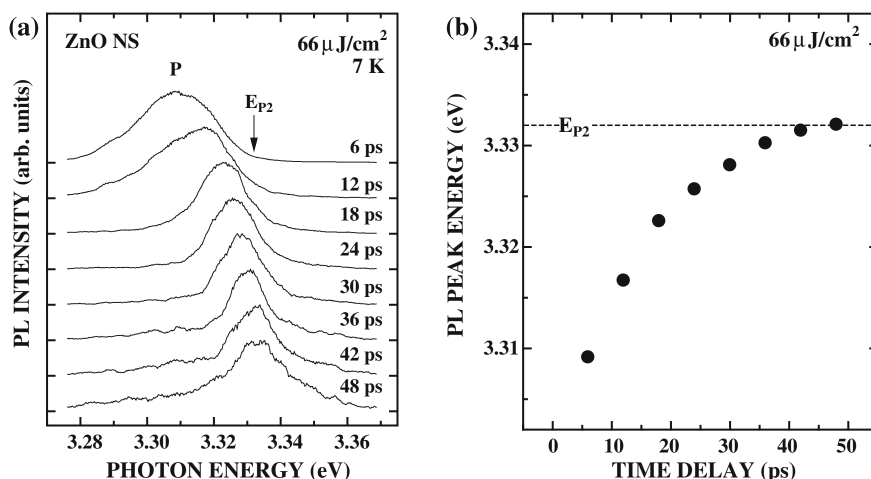

Fig. 9.10 **a** Time-resolved PL spectra taken at 7 K from the undoped ZnO NSs under an excitation energy density of 66 mJ/cm^2. **b** Temporal evolution of the PL peak energy of exciton–exciton scattering processes

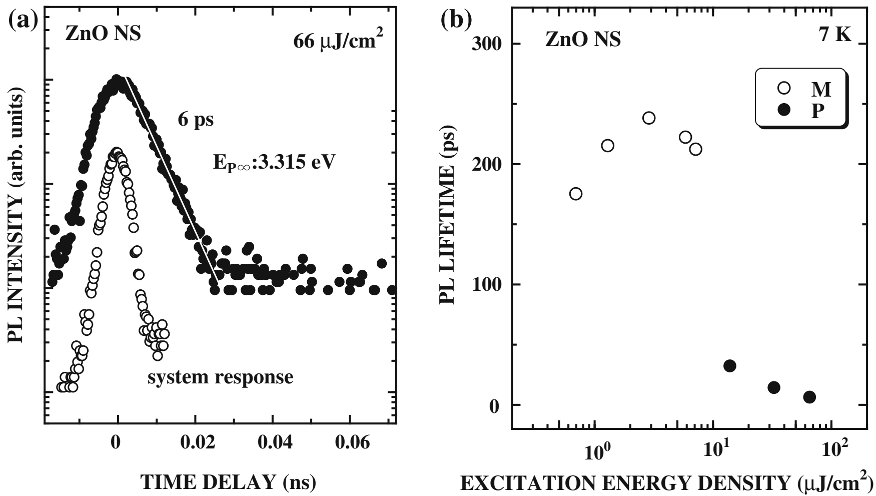

Fig. 9.11 **a** PL decay of exciton–exciton scattering processes taken at 7 K from the undoped ZnO NSs under an excitation energy density of 66 μJ/cm^2. **b** Excitation energy density dependence of the PL decay time of biexciton luminescence (*open circles*) and exciton–exciton scattering processes (*closed circles*) taken at 7 K from the undoped ZnO NSs

the solid line. The PL decay times of the M and the P lines are shown in Fig. 9.11b as functions of the excitation energy density. The PL decay time of the M line ranges from 175 to 238 ps. On the other hand, the PL decay time of the P line decreases from 14 to 6 ps with increasing excitation energy density. These values are one order of magnitude smaller than that of the M line, which ranges from 175 to 238 ps. In the exciton–exciton scattering process, one of the excitons is scattered into a higher excited state ($n \geq 2$) while the other is scattered into a bottleneck region of the lower polariton branch. Thus, the short PL decay time of the P line reflects the photon-like nature of the lower polariton branch.

9.5 Effects of Phosphorous Doping on Radiative and Nonradiative Recombination Dynamics of Excitons

The effects of the P doping on the recombination dynamics of free excitons have been studied by means of time-resolved PL measurements. Figure 9.12 shows the PL decay of the (a) undoped and (b) P-doped ZnO NSs taken at 60 K under an excitation energy density of 85 nJ/cm^2. The PL decays of both ZnO NSs can be well described by a double exponential function as

$$I(t) = A_1 \exp\left(-\frac{t}{\tau_1}\right) + A_2 \exp\left(-\frac{t}{\tau_2}\right), \tag{9.5}$$

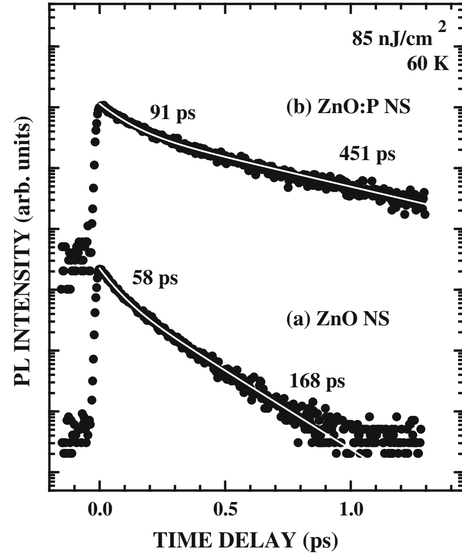

Fig. 9.12 PL decays of **a** undoped ZnO and **b** P-doped ZnO NSs at 60 K under an excitation energy density of 85 nJ/cm^2. The solid lines indicate the results of a least squares fit using a double exponential function

where A_1 and A_2 are adjustable constants and τ_1 and τ_2 are the fast and slow decay times, respectively. The solid lines show the results of a fit using Eq. (9.5). Based on the fitting, the fast and slow decay times are estimated to be 65 and 208 ps for the undoped ZnO NSs and 91 ps and 451 ps for the P-doped ZnO NSs, respectively. Figure 9.13 shows the temperature dependence of the PL decay time of the undoped and P-doped ZnO NSs under an excitation energy density of 85 nJ/cm^2. The closed and open circles in Fig. 9.13 indicate the fast decay times τ_1 of the undoped and P-doped samples, respectively. The PL lifetime of the P-doped sample is longer than that of the undoped sample at all temperatures. The PL lifetimes of both the undoped and P-doped samples first increase and then decrease with increasing temperature. These temperature-dependent behaviors reflect the increase in the radiative recombination lifetime and the decrease in the nonradiative recombination lifetime with increasing temperature.

In order to discuss the temperature dependence of radiative and nonradiative recombination processes, we estimated the radiative and nonradiative recombination lifetimes of free excitons. The measured PL decay time [$\tau_{PL}(T)$] can be expressed by the following equation:

$$\frac{1}{\tau_{PL}(T)} = \frac{1}{\tau_{rad}(T)} + \frac{1}{\tau_{nr}(T)}, \quad (9.6)$$

where $\tau_{rad}(T)$ and $\tau_{nr}(T)$ represent the radiative and nonradiative recombination lifetimes, respectively. The internal quantum efficiency $\eta_{int}(T)$ can also be described by

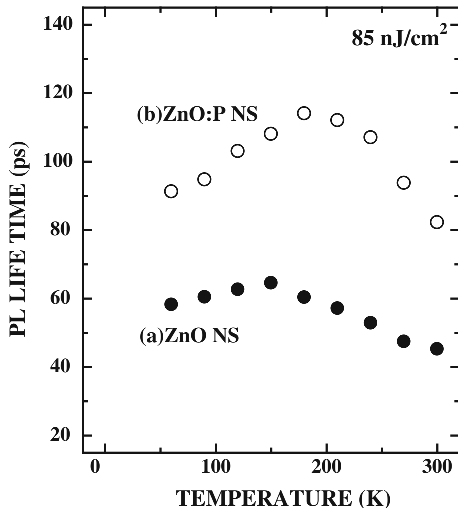

Fig. 9.13 Temperature dependence of PL decay time of **a** undoped and **b** P-doped ZnO NSs under an excitation energy density of 85 nJ/cm^2 (after [42])

$$\eta_{\mathrm{int}}(T) = \frac{\tau_{\mathrm{nr}}(T)}{\tau_{\mathrm{rad}}(T) + \tau_{\mathrm{nr}}(T)}. \tag{9.7}$$

Thus, the radiative and the nonradiative recombination lifetimes can be obtained from the internal quantum efficiency and the PL decay time by

$$\tau_{\mathrm{rad}}(T) = \frac{\tau_{\mathrm{PL}}(T)}{\eta_{\mathrm{int}}(T)}, \tag{9.8}$$

$$\tau_{\mathrm{nr}}(T) = \frac{\tau_{\mathrm{PL}}(T)}{1 - \eta_{\mathrm{int}}(T)}. \tag{9.9}$$

To evaluate the values of $\tau_{\mathrm{rad}}(T)$ and $\tau_{\mathrm{nr}}(T)$, the internal quantum efficiency $\eta_{\mathrm{int}}(T)$ is defined as the ratio of the time-integrated PL intensity at each temperature relative to that at low temperature, $\eta_{\mathrm{int}}(T) = I(T)/I_{\mathrm{LT}}$ [58].

Figure 9.14 shows the temperature dependence of τ_{rad} and τ_{nr} taken from the **a** undoped and **b** P-doped ZnO NSs under an excitation energy density of 85 nJ/cm^2. The closed and open circles indicate τ_{rad} and τ_{nr}, respectively. With increasing temperature from 60 to 300 K, τ_{rad} for the undoped ZnO NSs increases from 221 to 1.78 ns, and that for the P-doped ZnO NSs increases from 236 to 2.99 ns. The solid lines in Fig. 9.14 indicate the results of a linear least squares fit to the radiative recombination lifetime. Based on the fitting lines, the τ_{rad} of both samples increases superlinearly with increasing temperature, and the exponent values for the undoped and the P-doped samples are estimated to be 1.4 and 1.5, respectively ($\tau_{\mathrm{rad}} \propto T^{1.4-1.5}$). The temperature dependence of the radiative recombination lifetime is known to reflect the dimensionality of the excitons [59, 60]. For one-dimensional (1D) excitons, the radiative recombination lifetime is proportional to the square root of the temperature ($\tau_{\mathrm{rad}} \propto T^{1/2}$). On the other hand, the radiative recombination lifetime of

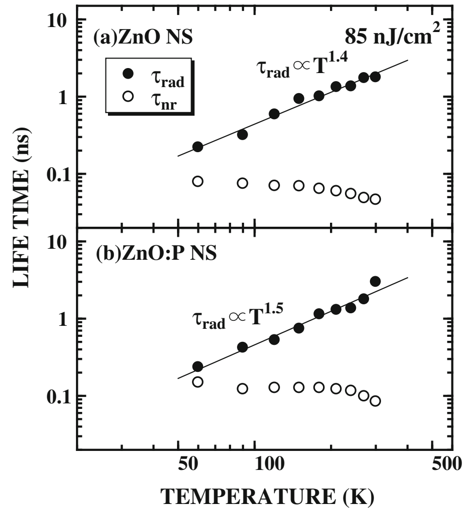

Fig. 9.14 Temperature dependence of radiative (*closed circles*) and nonradiative (*open circles*) recombination lifetimes taken from **a** undoped and **b** P-doped ZnO NSs under an excitation energy density of 85 nJ/cm^2 (after [42])

three-dimensional (3D) excitons increases as the 1.5th power of the temperature ($\tau_{rad} \propto T^{3/2}$). Therefore, we conclude that the excitons in both samples are nearly 3D excitons. This is consistent with the fact that the diameters of both samples (300–400 nm) are much larger than the Bohr radius of excitons in ZnO ($a_B = 1.5$ nm).

Next, we discuss the nonradiative recombination lifetime of free excitons as a function of temperature. With increasing temperature from 60 to 300 K, τ_{nr} for the undoped ZnO NSs decreases from 79 to 46 ps, and that for the P-doped ZnO NSs decreases from 149 to 85 ps. The decrease in the τ_{nr} reflects the thermal activation of nonradiative recombination processes with increasing temperature. The important point is that although the τ_{rad} values for the undoped and P-doped ZnO NSs are almost equal in the whole temperature range, τ_{nr} for the P-doped sample is about two times longer than that for the undoped sample. These observations suggest that the P doping suppresses the thermal activation of the nonradiative recombination processes. In fact, the PL intensity of the P-doped ZnO NSs is about 20 times stronger than that of the undoped ZnO NSs at room temperature.

9.6 Spatially Resolved Cathodoluminescence

In order to discuss the spatial distribution of impurities in ZnO NSs, we performed spatially resolved CL spectroscopy. Figure 9.15 shows the panchromatic CL intensity images of the **a** undoped, **b** P-doped, and **c** Sb-doped ZnO NSs (hereafter called sample Sb1) at 77 K. The CL intensity is distributed uniformly over both the sides and the top surfaces of the NSs in the undoped ZnO NSs, as shown in Fig. 9.15a. In contrast, the CL intensity from the side surface of the NSs is much

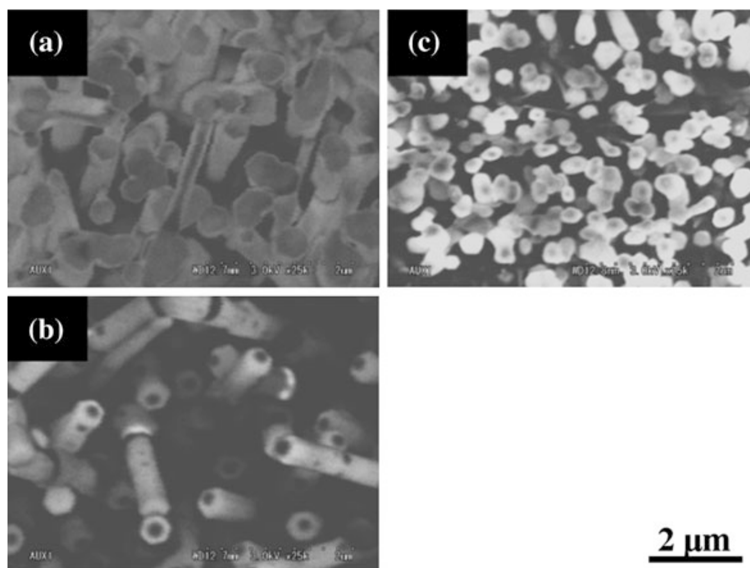

Fig. 9.15 Panchromatic CL intensity images of **a** undoped, **b** P-doped, and **c** Sb-doped ZnO NSs at 77 K (after [42])

stronger than that from the interior of the NSs in the P-doped ZnO NSs [Fig. 9.15b]. Since the PL spectrum of the P-doped sample taken at 77 K is dominated by the P-acceptor-bound exciton luminescence, as shown in Fig. 9.4a, we conclude that the CL from the side surface is due to the P-acceptor-bound exciton luminescence. Therefore, these observations indicate that the P impurities are mainly distributed on the side surface of the NSs. A similar distribution of impurities was observed in manganese-doped ZnO nanorods [61]. As seen in Fig. 9.15c, the CL intensity of the Sb-doped ZnO NSs is distributed uniformly over the pillar structures. Since the PL spectrum of the Sb-doped ZnO NSs is also dominated by the Sb-acceptor-bound exciton luminescence, as shown in Fig. 9.4b, this observation indicates that the Sb impurities are distributed almost uniformly over the NSs.

Next, we performed spatially resolved CL measurements of Sb-doped ZnO NSs produced under different synthesis conditions in order to discuss the spatial distribution of Sb impurities in detail. Figure 9.16 shows SEM images and CL images of Sb-doped ZnO NSs taken at room temperature. Figures 9.16a–c show the plan-view SEM images of samples Sb2–Sb4, respectively, and Figs. 9.16e–g show the panchromatic CL intensity images of samples Sb2–Sb4, respectively. Samples Sb2 and Sb3 were synthesized by NAPLD on a Si substrate coated with a 100–200 nm thick Sb layer using a sintered ZnO target as the source material [62]. The growth temperature was varied from 680 to 880 °C during the growth of sample Sb2. On the other hand, the growth temperature was constant at 750 °C during the growth of Sb3. Sample Sb4 was synthesized by NAPLD on a Si substrate using a sintered

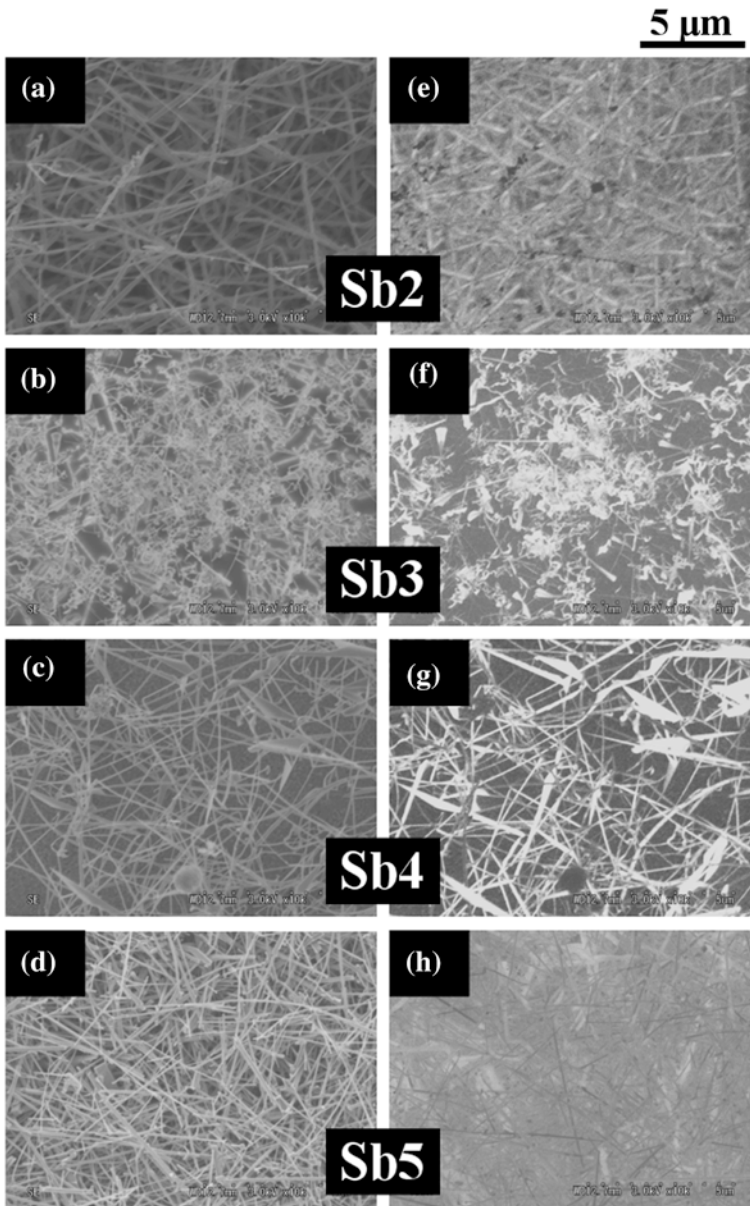

Fig. 9.16 Plan-view SEM images of samples **a** Sb2, **b** Sb3, **c** Sb4, and **d** Sb5. Panchromatic CL intensity images of samples **e** Sb2, **f** Sb3, **g** Sb4, and **h** Sb5 taken at room temperature

ZnO:Sb_2O_3:Al_2O_3 target as the source material [63]. The growth temperature was constant at 750 °C during the growth of Sb4. As seen in Figs. 9.16e–g, the CL intensity is distributed almost uniformly over the NSs in the three samples. Such a

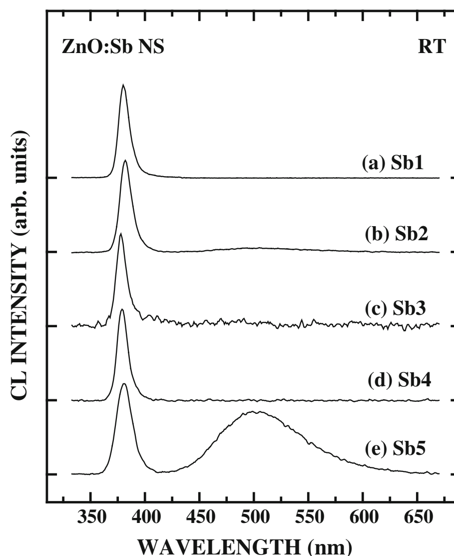

Fig. 9.17 CL spectra taken at room temperature from Sb-doped ZnO NSs of **a** Sb1, **b** Sb2, **c** Sb3, **d** Sb4, and **e** Sb5

CL intensity distribution has been observed for all the Sb-doped ZnO NSs, even at 77 K. Since the neutral-acceptor-bound exciton luminescence is dominant at 77 K in all three Sb-doped ZnO NSs, these observations suggest that the Sb impurities are distributed almost uniformly in all samples. Therefore, the difference in the spatial distribution of impurities between the P-doped and the Sb-doped ZnO NSs is not caused by a difference in the growth conditions.

Finally, we discuss the difference in the CL distribution between the Sb-doped ZnO NSs synthesized by NAPLD and CVD. Figures 9.16d–h shows the plan-view SEM image and the panchromatic CL intensity image of the Sb-doped ZnO NSs synthesized by CVD (Sb5). Sample Sb5 was synthesized by CVD on a Si substrate coated with a 10 nm thick Sb layer and a 1 nm thick Au layer [64]. As shown in Fig. 9.16h, the CL intensity from the NSs is weak and luminescence from the area surrounding the NSs is observed in sample Sb5. A similar tendency has been observed at 77 K. To clarify the origin of the difference in the CL distribution between sample Sb5 and the other samples (Sb1–Sb4), we compare the CL spectra of these Sb-doped ZnO NSs. Figure 9.17 shows the CL spectra taken at room temperature from samples **a** Sb1, **b** Sb2, **c** Sb3, **d** Sb4, and **e** Sb5. The spectra were normalized by the maximum intensity of each spectrum. The near-band-edge luminescence at around 380 nm is clearly observed in all the Sb-doped ZnO NSs. In addition to the near-band-edge luminescence, a broad luminescence band at around 450–600 nm was observed in sample Sb5. Such a broad luminescence band (a so-called green luminescence band) has been frequently observed in ZnO and is attributed to oxygen-vacancy-related emission [65]. Therefore, we attribute the luminescence from the area surrounding the NSs in sample Sb5 to the green

luminescence band. This observation suggests that the density of oxygen vacancies in the Sb-doped ZnO NSs synthesized by NAPLD is much lower than that in the NSs synthesized by CVD.

9.7 Conclusion

The optical properties of the undoped, P-doped, and Sb-doped ZnO NSs have been studied by means of PL, time-resolved PL, and spatially resolved CL spectroscopy. The temperature dependence of the PL spectra of the P-doped and Sb-doped ZnO NSs was analyzed, and the binding energies of the P-acceptor- and the Sb-acceptor-bound excitons were estimated to be 15 and 11 meV, respectively. This indicated that the Sb impurities formed a shallower acceptor level than the P impurities in ZnO. We observed the luminescence lines due to the radiative recombination of biexcitons and the exciton–exciton scattering processes and estimated the binding energies of excitons and biexcitons to be 60 and 15 meV, respectively. These values were almost identical to the values reported in bulk ZnO single crystals. The radiative and nonradiative recombination lifetimes were estimated from the temperature dependence of the PL lifetime and the time-integrated PL intensity. Although the radiative recombination lifetimes for each ZnO NSs were almost equal, the nonradiative recombination lifetime for the P-doped ZnO NSs was longer than that for the undoped ZnO NSs. We concluded that the P doping suppressed the thermal activation of the nonradiative recombination processes. CL images revealed that the intensity of the side surface was much stronger than that of the interior in the P-doped ZnO NSs. On the other hand, the CL intensity was distributed almost uniformly in the Sb-doped ZnO NSs. These observations suggested that the P impurities were distributed around the surface of the NSs, while the Sb impurities were distributed almost uniformly over the NSs.

Acknowledgments This work was supported by a Japanese national research fund sponsored by the Japan Science and Technology Agency.

References

1. Ü. Özgür, Y.L. Alivov, C. Liu, A. Teke, M. Reshchikov, S. Dogan, V. Avrutin, S.J. Cho, and H. Morkoç, J. Appl. Phys. **98**, 041301 (2005)
2. K. Nakahara, S. Akasaka, H. Yuji, K. Tamura, T. Fujii, Y. Nishimoto, D. Takamizu, A. Sasaki, T. Tanabe, H. Takasu, H. Amaike, T. Onuma, S.F. Chichibu, A. Tsukazaki, A. Ohtomo, M. Kawasaki, Appl. Phys. Lett. **97**, 013501 (2010)
3. D.C. Look, D.C. Reynolds, C.W. Litton, R.L. Jones, D.B. Eason, G. Cantwell, Appl. Phys. Lett. **81**, 1830 (2002)
4. K.-K. Kim, H.-S. Kim, D.-K. Hwang, J.-H. Lim, S.-J. Park, Appl. Phys. Lett. **83**, 63 (2003)

5. Y.R. Ryu, T.S. Lee, H.W. White, Appl. Phys. Lett. **83**, 87 (2003)
6. T. Aoki, Y. Shimizu, A. Miyake, A. Nakamura, Y. Nakanishi, Y. Hatanaka, Phys. Status Solidi B **229**, 911 (2002)
7. F.X. Xiu, Z. Yang, L.J. Mandalapu, D.T. Zhao, J.L. Liu, W.P. Beyermann, Appl. Phys. Lett. **87**, 152101 (2005)
8. Y.J. Zeng, Z.Z. Ye, W.Z. Xu, D.Y. Li, J.G. Lu, L.P. Zhu, B.H. Zhao, Appl. Phys. Lett. **88**, 062107 (2006)
9. S.W. Koch, H. Haug, G. Schmieder, W. Bohnert, C. Klingshirn, Phys. Status Solidi B **89**, 431 (1978)
10. D.M. Bagnall, Y.F. Chen, Z. Zhu, T. Yao, S. Koyama, M.Y. Shen, T. Goto, Appl. Phys. Lett. **70**, 2230 (1997)
11. M. Law, L.E. Greene, J.C. Johnson, R. Saykally, P.D. Yang, Nat. Mater. **4**, 455 (2005)
12. M.H. Huang, S. Mao, H. Feick, H. Yan, Y. Wu, H. Kind, E. Weber, R. Russo, P. Yang, Science **292**, 1897 (2001)
13. Q. Wan, Q.H. Li, Y.J. Chen, T.H. Wang, X.L. He, J.P. Li, C.L. Lin, Appl. Phys. Lett. **84**, 3654 (2004)
14. J.-J. Wu, S.-C. Liu, Adv. Mater. **14**, 215 (2002)
15. Y.C. Kong, D.P. Yu, B. Zhang, W. Fang, S.Q. Feng, Appl. Phys. Lett. **78**, 407 (2001)
16. Y.W. Heo, V. Varadarajan, M. Kaufman, K. Kim, D.P. Norton, F. Ren, P.H. Fleming, Appl. Phys. Lett. **81**, 3046 (2002)
17. A.B. Hartanto, X. Ning, Y. Nakata, T. Okada, Appl. Phys. A **78**, 299 (2004)
18. T. Okada, B.H. Agung, Y. Nakata, Appl. Phys. A **79**, 1417 (2004)
19. T. Okada, K. Kawashima, Y. Nakata, X. Ning, Jpn. J. Appl. Phys. **44**, 668 (2005)
20. T. Okada, K. Kawashima, Y. Nakata, Thin Solid Films **506–507**, 274 (2006)
21. Y. Li, G.W. Meng, L.D. Zhang, F. Phillipp, Appl. Phys. Lett. **76**, 2011 (2000)
22. W. Lee, M.-C. Jeong, J.-M. Myoung, Appl. Phys. Lett. **85**, 6167 (2004)
23. J. Jie, G. Wang, Y. Chen, X. Han, Q. Wang, B. Xu, J.G. Hou, Appl. Phys. Lett. **86**, 031909 (2005)
24. Y. Zhang, R.E. Russo, S.S. Mao, Appl. Phys. Lett. **87**, 043106 (2005)
25. K. Sakai, S. Oyama, K. Noguchi, A. Fukuyama, T. Ikari, T. Okada, Physica E **40**, 2489 (2008)
26. K. Sakai, A. Fukuyama, T. Ikari, T. Okada, Jpn. J. Appl. Phys. **48**, 085001 (2009)
27. Z. Qiu, K.S. Wong, M. Wu, W. Lin, H. Xu, Appl. Phys. Lett. **84**, 2739 (2004)
28. X. Han, G. Wang, Q. Wang, L. Cao, R. Liu, B. Zou, J.G. Hou, Appl. Phys. Lett. **86**, 223106 (2005)
29. W.M. Kwok, A.B. Djurišić, Y.H. Leung, W.K. Chan, D.L. Phillips, Appl. Phys. Lett. **87**, 093108 (2005)
30. T.-W. Kim, T. Kawazoe, S. Yamazaki, M. Ohtsu, T. Sekiguchi, Appl. Phys. Lett. **84**, 3358 (2004)
31. H.J. Fan, R. Scholz, M. Zacharias, U. Gösele, F. Bertram, D. Forster, J. Christen, Appl. Phys. Lett. **86**, 023113 (2005)
32. M. Foley, C. Ton-That, M.R. Phillips, Appl. Phys. Lett. **93**, 243104 (2008)
33. S.S. Kurbanov, G.N. Panin, T.W. Kang, Appl. Phys. Lett. **95**, 211902 (2009)
34. T. Yatsui, J. Lim, M. Ohtsu, S.J. An, G.-C. Yi, Appl. Phys. Lett. **85**, 727 (2004)
35. T. Yatsui, M. Ohtsu, J. Yoo, S.J. An, G.-C. Yi, Appl. Phys. Lett. **87**, 033101 (2005)
36. T. Yatsui, S. Sangu, K. Kobayashi, T. Kawazoe, M. Ohtsu, J. Yoo, G.-C. Yi, Appl. Phys. Lett. **94**, 083113 (2009)
37. T. Okada, K. Kawashima, M. Ueda, Appl. Phys. A **81**, 907 (2005)
38. R.Q. Guo, J. Nishimura, M. Ueda, M. Higashihata, D. Nakamura, T. Okada, Appl. Phys. A **89**, 141 (2007)
39. R. Guo, J. Nishimura, M. Matsumoto, D. Nakamura, T. Okada, Appl. Phys. A **93**, 843 (2008)
40. R. Guo, M. Matusmoto, T. Matsumoto, M. Higashihata, D. Nakamura, T. Okada, Appl. Surf. Sci. **225**, 9671 (2009)

41. A. Kumeda, K. Toya, K. Kubo, K. Tsuta, M. Higashihata, D. Nakamura, T. Okada, and K. Sakai, in Proceedings of 2010 IEEE Region 10 Conference, 446 (2011)
42. H. Murotani, D. Akase, Y. Yamada, T. Matsumoto, D. Nakamura, and T. Okada, Proceedings of 2010 IEEE Region 10 Conference, 1011 (2011)
43. K. Thonke, T. Gruber, N. Teofilov, R. Schönfelder, A. Waag, R. Sauer, Physica. B **308–310**, 945 (2001)
44. M.W. Allen, P. Miller, R.J. Reeves, S.M. Durbin, Appl. Phys. Lett. **90**, 062104 (2007)
45. B.K. Meyer, J. Sann, S. Lautenschläger, M.R. Wagner, A. Hoffmann, Phys. Rev. B **76**, 184120 (2007)
46. Y.P. Varshni, Physica **34**, 149 (1967)
47. S. Permogorov, in *Excitons*, ed. by E.I. Rashba, M.D. Sturge (North-Holland, Amsterdam, 1982)
48. J.R. Haynes, Phys. Rev. Lett. **4**, 361 (1960)
49. A. Allenic, W. Guo, Y.B. Chen, Y. Che, Z.D. Hu, B. Liu, X.Q. Pan, J. Phys. D Appl. Phys. **41**, 025103 (2008)
50. D.-K. Hwang, H.-S. Kim, J.-H. Lim, J.-Y. Oh, J.-H. Yang, S.-J. Park, K.-K. Kim, D.C. Look, Y.S. Park, Appl. Phys. Lett. **86**, 151917 (2005)
51. A. Allenic, W. Guo, Y.B. Chen, M.B. Katz, G.Y. Zhao, Y. Che, Z.D. Hu, B. Liu, S.B. Zhang, X.Q. Pan, Adv. Mater. **19**, 3333 (2007)
52. F.X. Xiu, Z. Yang, L.J. Mandalapu, J.L. Liu, W.P. Beyermann, Appl. Phys. Lett. **88**, 052106 (2006)
53. J.M. Qin, B Yao, Y. Yan, J.Y. Zhang, X.P. Jia, Z.Z. Zhang, B.H. Li, C.X. Shan, D.Z. Shen, Appl. Phys. Lett. **95**, 022101 (2009)
54. O. Lopatiuk-Tirpak, W.V. Schoenfeld, L. Chernyak, F.X. Xiu, J.L. Liu, S. Jang, F. Ren, S.J. Pearton, A. Osinsky, P. Chow, Appl. Phys. Lett. **88**, 202110 (2006)
55. L.J. Mandalapu, Z. Yang, S. Chu, J.L. Liu, Appl. Phys. Lett. **92**, 122101 (2008)
56. Y. Yamada, *Wide Bandgap Semiconductors: Fundamental Properties and Modern Photonic and Electronic Devices*, ed. by K. Takahashi, A. Yoshikawa, A. Sandhu (Springer, Berlin, 2007), p. 56
57. C. Klingshirn, Phys. Status Solidi B **71**, 547 (1975)
58. M. Gurioli, A. Vinattieri, M. Colocci, C. Deparis, J. Massies, G. Neu, A. Bosacchi, S. Franchi, Phys. Rev. B **44**, 3115 (1991)
59. J. Feldmann, G. Peter, E.O. Gobel, P. Dawson, K. Moore, C. Foxon, R.J. Elliot, Phys. Rev. Lett. **59**, 2337 (1987)
60. H. Akiyama, S. Koshiba, T. Someya, K. Wada, H. Noge, Y. Nakamura, T. Inoshita, A. Shimizu, H. Sakaki, Phys. Rev. Lett. **72**, 924 (1994)
61. H.L. Yan, J.B. Wang, X.L. Zhong, Y.C. Zhou, Appl. Phys. Lett. **93**, 142502 (2008)
62. I.A. Palani, D. Nakamura, K. Okazaki, M. Higashihata, T. Okada, Mater. Sci. Eng. B **176**, 1526 (2011)
63. D. Nakamura, K. Okazaki, I.A. Palani, M. Higashihata, T. Okada, Appl. Phys. A **103**, 959 (2011)
64. I.A. Palani, K. Okazaki, D. Nakamura, K. Sakai, M. Higashihata, T. Okada, Appl. Surf. Sci. **258**, 3611 (2012)
65. K. Vanheusden, W.L. Warren, C.H. Seager, D.R. Tallant, J.A. Voigt, B.E. Gnade, J. Appl. Phys. **79**, 7983 (1996)

Chapter 10
Synthesis of Polycrystalline Silicon Carbide (SiC) Thin Films Using Pulsed Laser Deposition

B. Venkataramesh and Nilesh J. Vasa

Abstract Silicon carbide (SiC), similar to diamond and other ceramic materials, is a material with excellent functional properties. SiC films based devices can be used for various applications ranging from automobile, aerospace industry, power delivery systems, photovoltaic, and microelectromechanical systems. The growth of bulk single crystals of SiC is difficult, but several techniques, such as chemical vapor deposition (CVD), electron beam CVD (EB-CVD), pulsed laser deposition (PLD), are used to produce SiC thin films for various functional applications. In the PLD technique, high substrate temperature (>600 °C) is required to produce crystalline SiC thin films and the onset of the large-scale crystallization has been detected above 800 °C. The PLD technique has been extended for SiC film deposition on various substrates, such as Si (100), alkali-free glass materials. A review on PLD of SiC thin film clearly show that it is possible to deposit 3C-SiC (β-SiC) and 4H-SiC (α-SiC) thin films by controlling various process parameters, such as laser fluence and substrate temperature. Recent advances in the PLD technique combined with the surface annealing can improve the characteristics of SiC thin films for photovoltaic and electronic device-related applications.

10.1 Introduction

Silicon carbide (SiC), similar to diamond and other ceramic materials, is a material with excellent physical, chemical, and mechanical properties. SiC possesses high hardness, resistance to thermal shock, high thermal conductivity (3.2–4.9 W/cm °C), wide band gap (2.4–3.3 eV), high breakdown field (2.1–2.5 MV/cm), and high electron mobility. As a result, crystalline SiC is of great importance in manufacturing of electronic components, photovoltaic cells, image sensors,

B. Venkataramesh · N. J. Vasa (✉)
Department of Engineering Design, Indian Institute of Technology Madras,
Chennai 600036, India
e-mail: njvasa@iitm.ac.in

M. S. R. Rao and T. Okada (eds.), *ZnO Nanocrystals and Allied Materials*,
Springer Series in Materials Science 180, DOI: 10.1007/978-81-322-1160-0_10,
© Springer India 2014

abrasion tooling, and microelectromechanical systems (MEMS) [1]. SiC also possesses high hardness, wear resistance, melting point (2,830 °C), oxidation resistance at high temperature, resistance to chemical and radiation exposure, and relatively low thermal coefficient of expansion. Hence, SiC film is also considered as a protective coating for metallic components under severe working environment in terms of tribological behavior (sliding friction or wear resistance) and high temperature applications [2]. SiC has large microhardness value (2,700 kg mm^{-2}) and can be applied to films, as protective surface for architectural, automotive and aircraft glass windows, as well as for transparent heating panels and anti-reflection coatings for solar arrays [3]. Technological fields ranging from the automobile and aerospace industry, to power delivery systems, microwave communications, and MEMS can use SiC-based devices as they can withstand harsh environments.

The above properties make SiC interesting for the fabrication of microelectronic, photovoltaic, and optoelectronic devices. It is also attractive for sensors working in adverse environments. In comparison to diamond, SiC can be doped with both p- and n-type and it allows a natural oxide to be grown on its surface. Further, some of the limitations of the current Si technology, such as relatively small band gap ($E_g = 1.1$ eV), Si possesses an indirect band gap, limited operating temperature (below 350 °C) due to the generation of thermal carriers, requirement of active cooling systems, moderate stability against chemical attack due to the small band gap etc., can be overcome by appropriately employing SiC material. One of the potential applications of SiC thin film is photovoltaics or in manufacturing of solar cells. The primary aim is to develop a solar cell which can overcome loss mechanisms, such as lattice thermalization of generated carriers that have energy greater than the bandgap of the semiconductor, and for sub-bandgap photons that are not absorbed. The reasons for an interest in SiC for a future semiconducting material for the photovoltaic industry include: both carbon and silicon are abundant, as with silicon-based technology, SiO_2 passivation layers can be thermally grown, and tandem cell can provide multi-wavelength photon absorption. Figure 10.1 shows a schematic diagram of a photovoltaic device consisting of *p*-type SiC thin film deposited on c–Si wafer.

The growth of bulk single crystals of SiC is difficult as SiC single crystals can exist in numerous prototypes and SiC cannot be grown from stoichiometric melt. In the past, various favorable properties of SiC were difficult to realize because of the

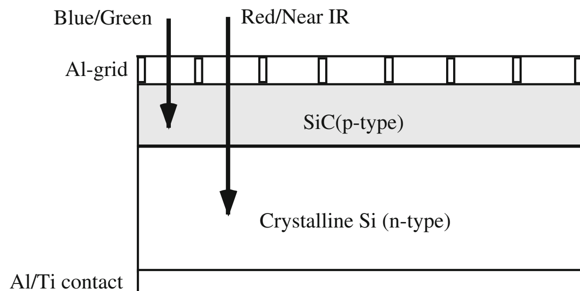

Fig. 10.1 Schematic diagram of a (*p*) SiC/(*n*) c–Si tandem photovoltaic cell

Table 10.1 Physical properties of SiC polytypes

SiC Polytype	3C–SiC (or) β–SiC	4H–SiC	6H–SiC (or) α-SiC
Crystal structure	Zinc blend (cubic)	Hexagonal	Hexagonal
Lattice constants (Å)	$a = 4.3596$	$a = 3.0730$; $b = 10.053$	$a = 3.0730$; $b = 15.11$
Band gap (eV)	2.36	3.23	3.05
Density (g/cm^3)	3.21	3.21	3.21
Thermal conductivity (W/(cm·K))	3.6	3.7	4.9

polytypism supported by the SiC, difficulties in material preparation and problems in processing of devices made from SiC. The polytypes have the same chemical composition but exhibit different crystallographic structures and stacking sequences along the principal crystal axis. All SiC prototypes consist of carbon atoms covalently bonded with equal numbers of Si atoms. However, all SiC polytype has its own distinct set of electrical semiconductor properties. Several important polytypes of SiC are hexagonal (4H– and 6H–SiC) (α-SiC) and cubic (3C–SiC or β-SiC) polytypes. Typical characteristics of SiC polytypes are described in Table 10.1. The hexagonal polytype 4H–SiC exhibits large band gap energy of 3.23 eV, while possessing a large critical breakdown field and high thermal conductivity. However, the 4H–SiC and 6H–SiC-based metal–oxide–semiconductor field-effect transistor (MOSEFT) devices have exhibited low channel mobility, which is attributed to the high density of interface traps. In contrast, 3C–SiC possesses high effective channel mobility (165–229 cm^2/V s). In comparison with 4H–SiC, the 3C–SiC (β-SiC) prototype has the advantages, such as isotropic properties (cubic structure), isotropic electron mobility of 1,000 cm^2/V s, low mass density and thermal expansion, high thermal conductivity and flexural strength, thermal shock resistance, oxidation, and rain erosion resistance potential. An application of an p-type 3C–SiC thin film on a n-type Si wafer has been considered for a hetero-junction solar cell where 3C–SiC is used as an emitter [4].

One of the factors that have inhibited the development of SiC device technology is the absence of low-cost SiC substrates. To provide relatively inexpensive and large-area substrate of SiC for electronic devices, growth of SiC film on Si substrates has been considered. However, there is a considerable scope for improving the growth techniques of appropriate SiC film and device fabrication technologies. The use of Si substrates for SiC thin film growth is challenged by the large lattice mismatch (20 %) between SiC and Si, which leads to strain and poor film adhesion.

Several techniques, such as chemical vapor deposition (CVD), electron beam CVD (EB-CVD), and pulsed laser deposition (PLD), are used to produce SiC thin films for various functional applications. The PLD technique, which has been used for deposition of various types of functional thin films, has various advantages, such as low substrate temperature, production of stoichiometric films, and multiple-layer deposition. In this chapter, advances in SiC film deposition techniques for various applications is described.

10.2 SiC Thin Film Deposition Techniques

There are various deposition techniques for producing SiC thin films on different substrates. These techniques are basically categorized into two types: namely physical vapor deposition (PVD) and CVD.

10.2.1 Chemical Vapor Deposition Technique

The CVD technique involves formation of thin films via chemical reactions from gaseous precursors. The action of the chemical reaction is initiated by thermal or electrical discharge plasma treatment. CVD technique is commonly used for SiC thin film synthesis, which forms epitaxial SiC layers [5–8]. CVD method is used to produce SiC by thermal decomposition and chemical reaction of gaseous precursor compounds. It involves convective heat and mass transfer as well as diffusion, with which chemical reactions occur at the substrate surface. The CVD technique and its modified techniques, such as metal organic CVD (MOCVD), plasma enhanced CVD (PECVD), and hot-filament CVD (HFCVD) produce crystalline SiC thin films. However, the process temperature is above 1,400 °C. Further, mixture of silane and hydrocarbons or various organo–silicon compounds are used in hydrogen flow for an epitaxial growth of the film. The films deposited by the CVD technique usually contain hydrogen and stoichiometric yield is difficult to obtain. Studies have reported that, the hydrogenated a-SiC: H films deposited by various CVD techniques results in reduction of the Si–C bond density, and lowering of mechanical properties such as hardness and Young modulus of the thin film.

10.2.2 Physical Vapor Deposition Techniques

The most important characteristic feature of the PVD technique is that the transport of vapor from the source to the substrate takes place by physical means and it can be achieved by carrying out the deposition essentially in a vacuum of such magnitude that the mean free path of the ambient gas molecule is greater than the dimensions of the deposition chamber and the source to substrate distance. By thermal evaporation or by using energetic particles mechanically knocking out the atoms or molecule from the surface, the vapor species of a solid material can be created. Recently, electron beam-physical vapour deposition (EB-PVD), direction deposition, and combined metal vapor vacuum arc (MEVVA) ion-source implantation with ion beam-assisted deposition technique are also considered for SiC deposition [9].

On the other hand, PLD is a potential technique for deposition of amorphous and crystalline SiC films on various substrates. It offers several advantages over

other techniques, such as simple experimental setup with flexibility and control, stoichiometric film deposition, wide deposition parameter control, such as temperature, ambient pressure; multiple layer deposition with different target material is possible. In PLD, both neutral and ionized species within the vapor plume can have kinetic energies in the range of 10–100 eV, which is several orders of magnitude larger than other methods, such as the molecular beam epitaxy technique. As a result, a smoother surface morphology at low substrate temperatures is expected by PLD, in comparison to other thin film deposition techniques. PLD technique can also be used to achieve composite materials in several ways, which include the ablation of composite target material, deposition in a reactive gas atmosphere, or by using two or more targets. Different research groups have demonstrated the PLD technique for SiC thin film deposition [9–14].

10.2.3 PLD of SIC Films

In recent years, PLD has emerged laser fluence, frequency, substrate material, the chemical composition of the buffer gas, and finally the substrate temperature and the distance between the target and the substrate influence the PLD technique and the properties of the deposited SiC films. Studies show that the pulse energy and substrate temperature are the main parameters which influence the deposition process [15, 16]. In most reports, it has been found that substrate temperature during film growth is the main parameter that influences the crystallinity of films. Typically, high substrate temperature (>600 °C) is required to produce crystalline SiC thin films. It has been found that, around a temperature bandwidth 600–650 °C, the nanostructure of the films undergoes significant modifications resulting in a reduced disorder Si–C bonds. The onset of the large-scale crystallization has been detected above 800 °C. Some attempts have also been made for a furnace annealing of PLD SiC films. The annealing at high temperature above 1,100 °C in high vacuum has resulted in stress relief in the crystalline SiC films, reduced disorder in the layers and increased SiC bonding. Hence, PLD technique can be utilized to grow epitaxial, polycrystalline, and hydrogen-free SiC films. In PLD experiments, SiC films have been deposited using SiC targets or silicon–carbon alloy film and two-component targets [12] onto heated substrates in a controlled ambient condition.

10.2.3.1 Experimental Studies

Most of research groups have employed experimental apparatus as shown in Fig. 10.2. Different types of pulsed lasers, such as excimer lasers (XeCl 308 nm, KrF 248 nm, ArF 193 nm), and Nd^{3+}:YAG laser with different output wavelength via harmonic conversion (1,064, 532, 355 nm), have been used. In most of the studies reported, the nanosecond (ns) pulsed laser beam is focused on a rotating

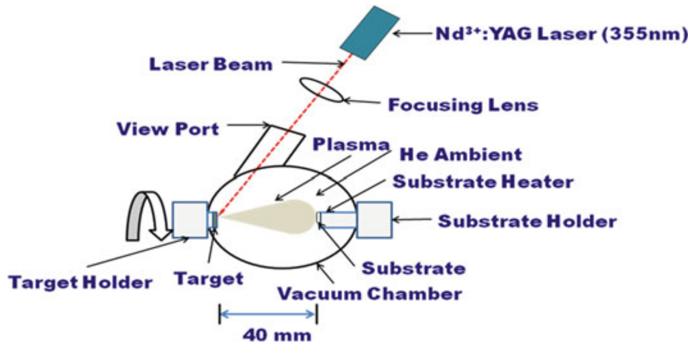

Fig. 10.2 Experimental setup for PLD of SiC thin film

SiC target with the laser fluence ranging from 1 to 4 J/cm^2. As a substrate, crystalline-silicon (100) is placed parallel to the SiC target surface and the target-to-substrate distance ranges from 30 to 50 mm. In some cases, both the target and the substrate are rotated during the PLD process in order to obtain uniform film thickness. The substrates are heated to the deposition temperature ranging from 400 to 1,000 °C. As an ambient gas Ar, N_2 has been introduced with the chamber pressure at around 1.3×10^{-2} Pa. The duration of deposition ranges from 20 to 60 min. Various parameters generally employed during the PLD of SiC film are described in Table 10.2.

We have also attempted PLD studies for SiC film deposition on different substrates, such as Si(100), and alkali-free glass (AFG). SiC target used in the PLD studies was prepared by compacting SiC powder (Carborundum Universal Ltd., Grit Size 120) using a hydraulic press with a binder. Subsequently, pellets were sintered to attain a required handling strength and remove the binder, which might interfere with the PLD process.

Figure 10.2 shows the schematic of the experimental setup of the PLD process. A pulsed Nd^{3+}:YAG laser with a repetition rate of 10 Hz and pulse width of 8 ns

Table 10.2 Pulsed laser deposition of SiC thin film: parameter description

Parameter	Range
Target	SiC compound in pellet form
Substrate	c–Si (100) or (111), Sapphire (0001), Glass
Substrate-to-target distance	30–50 mm
Substrate temperature	Room temperature to 1200 °C
Laser beam	Excimer lasers (XeCl: 308 nm; KrF: 248 nm, ArF 193 nm), Nd^{3+}:YAG laser (1,064, 532, 355 nm)
Laser fluence	1–5 J/cm^2 (0.5–1 J/cm^2 in [9])
Laser pulse width	10–25 ns
Laser repetition rate	10–30 Hz
Ambient gas	Ar, N_2, High vacuum ($\approx 10^{-5}$ Pa)
Ambient gas pressure	$\approx 10^{-3}$ Pa

Table 10.3 Experimental parameters used for SiC PLD on different substrates

Parameters	Specifications
Laser used	Nd^{3+}:YAG (355 nm)
Pulse duration	8 ns
Pulse frequency	10 Hz
Laser fluence	2 J/cm^2
Target diameter	30 mm
Target thickness	5 mm
Target density	1.475 μgm/mm^3
Base pressure	9.9×10^{-3} Pa
Chamber pressure	Varied from 2 to 2×10^{-2} Pa
Substrates	Alkali free glass, c–Si
Substrate area	10 × 10 mm
Inert atmosphere	He
Target-to-substrate distance	40 mm
Substrate temperature	Varied from 400 to 800 °C
Duration of deposition	30 min, 1 h

was used. The output wavelength and the energy were 355 nm and around 54 mJ, respectively. The Nd^{3+}:YAG laser was focused using a plano-convex lens (focal length = 300 mm) in a vacuum chamber. SiC pellets prepared by compacting and sintering processes were mounted on a target holder. The laser irradiation intensity was estimated to be $\approx 2 \times 10^8$ W/cm^2, considering a laser focused spot size of 1 mm. The PLD process was performed at substrate temperature ranging from 400 to 800 °C in He ambience with a chamber pressure varying from 2 to 2×10^{-2} Pa. Table 10.3 shows experimental parameters used for the PLD of SiC thin films on different substrates.

The influence of deposition conditions on the morphology and the structural changes in thin films was studied by various techniques, such as X-ray diffraction (XRD), scanning electron microscopy (SEM), Raman spectroscopy, surface profilometry, and nano-indentation techniques.

10.2.3.2 Results and Discussion

Figure 10.3 shows surface profile of SiC thin films deposited on c–Si at 650 °C at different pressure level. Surface profiles of as deposited SiC thin film along with substrate edge were measured by using an optical surface profilometer (Veeco, Vision 32-[Dataset 2:2D Analysis], North America) which is a noncontact type profilometer. Based on Fig. 10.3, an average thickness of SiC thin films was estimated to be 35 and 110 nm for the deposition time of 30 and 60 min, respectively, at the substrate temperature of 650 °C and at different pressure values.

Figures 10.4(a), (b), and (c) shows the typical SEM (Quanta FEG 200, FEI) microphotograph of film at different c–Si substrate temperatures, ranging from 400

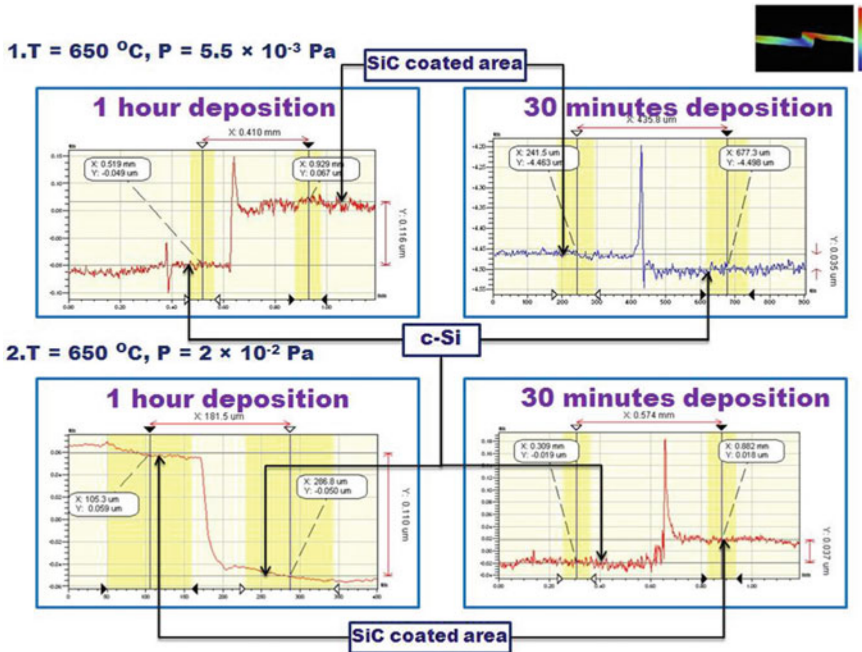

Fig. 10.3 Surface profile of SiC deposited on c–Si

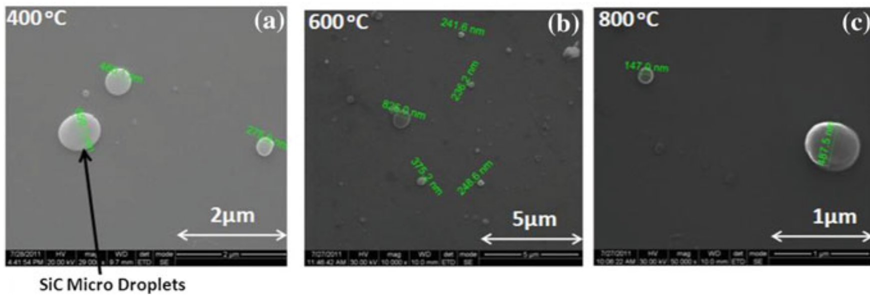

Fig. 10.4 SEM image of SiC deposited on c–Si substrate at different deposition temperature ranging from 400 to 800 °C

to 800 °C with the laser irradiation fluence of 2.0 J/cm^2 (irradiation intensity of 2×10^8 W/cm^2). The formation of microdroplets is observed when SiC deposited on c–Si at 400 °C. Gradual increase of temperature resulted nucleation growth of SiC particles. The microdroplets formed on the c–Si substrates with different temperatures were smooth and spherical in shape [11]. The size distribution of SiC particles was estimated to be around 100–900 nm based on the SEM analysis. According to EDS analysis, the percentage weights of Si and C were maintained equal up to the substrate temperature of 400 °C. However, with increase in the

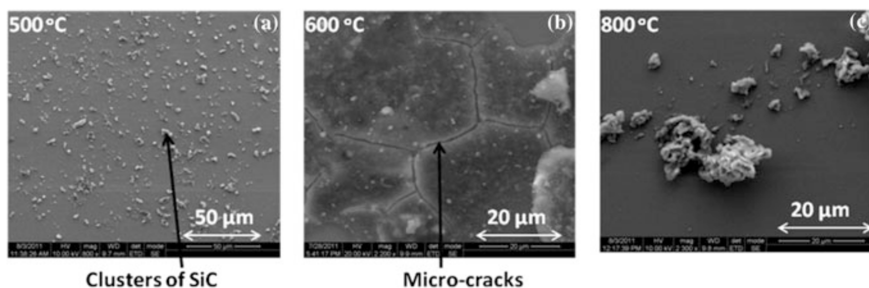

Fig. 10.5 SEM images of SiC deposited on alkali-free glass (AFG) at different deposition temperatures

substrate temperature, the carbon percentage was decreased. This observation was in accordance with the XRD analysis. Figure 10.5 shows SEM analysis of SiC thin films deposited on AFG substrates at different substrate temperatures (a) 500 °C, (b) 600 °C, and (c) 800 °C, respectively. As shown in Fig. 10.5(a), clusters of SiC were observed at lower substrate temperature values. When the temperature was increased to 600 °C and higher, microcracks were also observed on the thin-film surface. This might be due to amorphous nature of the AFG substrates and different expansion coefficient of the substrate and the thin film. The elemental distribution was also disturbed at substrate temperatures of 500 °C and above. Urban et al. have also reported on excimer laser deposition of SiC thin film on glass near a soft point of 600 °C followed by laser annealing of SiC film. The pulsed laser energy and laser fluence play a significant role in controlling the film thickness. Based on experimental studies reported by Elgazzar et al. it was shown that as the KrF laser (248 nm) with a pulse width of 25 ns, pulse repetition rate of 50 Hz and with the laser spot of 2 mm^2, as the laser fluence increased from 0.5 to 1 J/cm^2, the thickness of the as deposited SiC film also increased from 50 to 170 nm [10]. In the study, the laser fluence values used were much lower than those used in similar PLD elsewhere and the target-to-substrate distance of 33 mm was also less. Higher laser beam energy was absorbed for a longer length. As a result, the ablation propagated deeper in the target, and hence the ablated amount from the target was increased. Further, based on Elgazzar et al., at the lowest laser fluence the film thickness was nonuniform as compared to the films deposited with higher laser fluence values. Further, the surface morphology studies based on SEM indicated that lower laser fluence value (0.5 J/cm^2) lead to the lack of good adherence of the ablated particles at the film–substrate interface, which resulted in the formation of voids. On the other hand, at the higher laser fluence value of 1 J/cm^2, higher temperature of the deposited particles on the substrate was expected. Due to Ar ambience aiding to the cooling effect, high thermal stresses and hence cracking of the film were resulted. In the case of the lower energy fluence, although the thermal stresses produced at the film-substrate interface were expected to be lower, the lack of adhesion of the ablated particles, due to low temperature, to the surface results in the void structure.

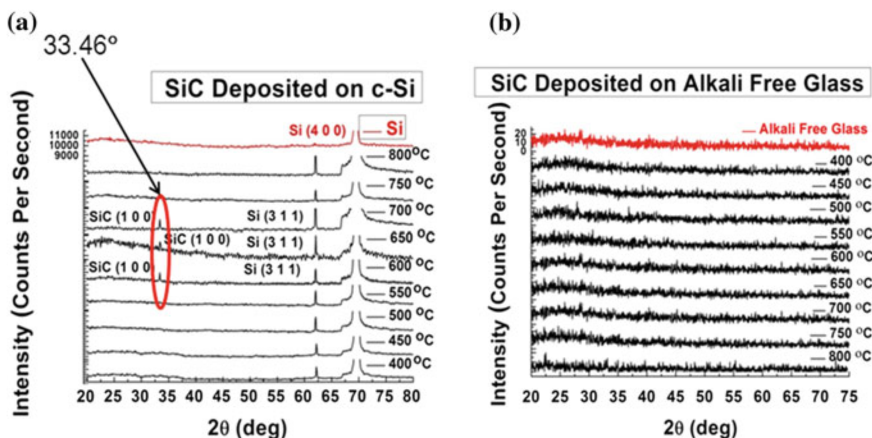

Fig. 10.6 X-ray diffraction patterns of SiC thin films obtained with different substrates **a** c–Si and **b** alkali-free glass (AFG) at different temperatures

Figure 10.6 shows the XRD patterns of SiC thin films deposited on both c–Si and AFG. The XRD peak of $2\theta = 33.46°$ corresponding to SiC (100) along with peaks corresponding to c–Si were obtained. In contrast, in the case of SiC deposited on AFG, no diffraction peaks were observed. As shown in Fig. 10.6, the characteristic diffraction peak corresponding to SiC thin film around $2\theta = 33.46°$ at the c–Si substrate temperature ranging from 600 to 700 °C. When the substrate temperature was either higher or lower than the above range, the characteristic X-ray diffraction peak corresponding to SiC thin film was not observed. At lower substrate temperature, the surface energy might not be sufficient for SiC to form crystalline film.

Influence of pressure on the crystalline structure of SiC thin films was studied at with c–Si substrates at different temperatures from 600 to 700 °C. The chamber pressure was varied from 2×10^{-2} to 2 Pa. Figure 10.7 shows the XRD analysis results at different pressure and deposition duration with the substrate temperature of 600 °C. SiC (100) peak was observed at $2\theta = 33.46°$. Further, Confocal Raman spectroscopy technique was used to measure the Raman scattering spectra from the as deposited SiC thin film. Based on the spectroscopy studies with an Nd^{3+}:YAG laser (532 nm), Raman scattering peaks around 308, 433 , 521, 610, 675, 817, and 978 cm^{-1} band were observed. The Raman scattering peaks at 308, 521, and 978 cm^{-1} band were correspond to c–Si substrate, 433 and 675 cm^{-1}, broadband were correspond to amorphous Si and impurity, respectively. Raman scattering peaks at 610 and 817 cm^{-1} correspond to 4H–SiC and 3C–SiC, respectively [17, 18].

Wang et al. [17] have reported on single-crystal 4H–SiC film by pulsed XeCl laser deposition. In the work, by ablating ceramic SiC target with pulsed XeCl laser, SiC films were prepared on Si (100) substrate at temperature 850 °C and post deposition annealing at high temperature above 1,100 °C in high vacuum (1.5×10^{-7} Pa) [19]. The XRD peak at $2\theta = 33.2°$ was observed. Based on the

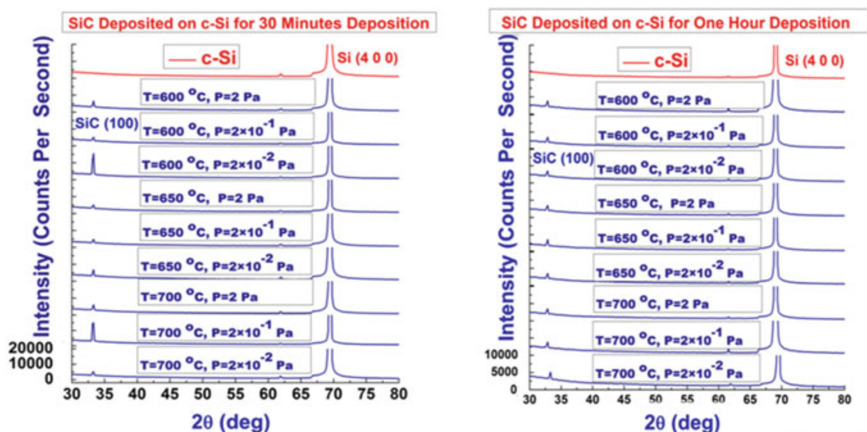

Fig. 10.7 X-ray diffraction patterns of SiC thin films deposited on c–Si at different deposition time

analysis, the films consisted of polycrystal 4H–SiC structure before annealing and of oriented single-crystal epitaxial 4H–SiC after annealing. Further, when the films were excited by the 290 nm laser at room temperature, the films give out two emissions peak at 377 and 560 nm. The emission at 377 nm was assigned to the combination of the transmission between the valence band and conductor band, and the other at 560 nm was assigned to the exciton emission.

Figure 10.8 shows the typical SEM microphotograph of SiC deposited on c–Si for 30 min deposition at different pressures ranging from 2×10^{-2} to 2 Pa at the temperature 600 °C. All samples show spherical particles (laser droplets) that were in-homogeneously dispersed on the surface of the thin film. When the ambient pressure was decreased from 2 to 2×10^{-2} Pa, the particle density also decreased. The same observation made at the substrate temperature ranging from 600 to 700 °C. The influence of the SiC grit size may also be studied to reduce the droplet formation.

To minimize the number of the droplets, a reduction of the laser repetition rate was also tried by Elgazzar et al. [10]. The number of droplets was reduced when the laser repletion rate was reduced from 50 to 25 Hz. This was attributed to the decrease in the deposition rate, diminished plasma effect, and possible travel of the deposited species to the just right sites.

The mechanical properties, such as Young's modulus and hardness of SiC thin films, were estimated using the nano-indentation technique. To eliminate the influence of the substrate on the produced results the film's modulus and hardness were measured at 30–50 % of the total film thickness for each sample. The experimental study was performed using the nanoindenter (TI950, Hysitron). The peak load was chosen as 10 mN and the pattern of loading was chosen to be trapezoidal. The force versus displacement curves as obtained by nano-indentation

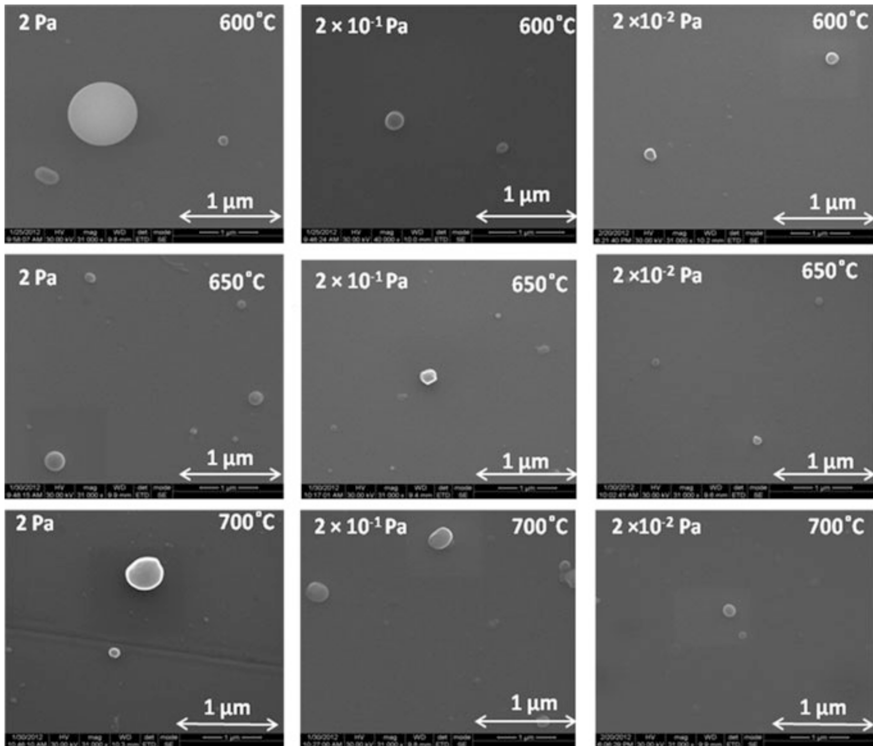

Fig. 10.8 SEM image of SiC deposited on c–Si for 30 min deposition at different ambient pressure values ranging from 2 to 2×10^{-2} Pa

equipment are shown in Fig. 10.9. Based on the above experimental study, the average elastic modulus of the thin films deposited on the substrate c–Si wafer is found to be 300 GPa and average Hardness value of 45 GPa, the experiment was conducted at constant pressure of 2×10^{-2} Pa for 1h deposition time and different substrate temperatures 600, 650, and 700 °C as shown in Fig. 10.9. The mechanical characteristics of the SiC films were indicative of low porosity structure.

10.3 Recent Advances in PLD of SiC Thin Film

There are no suitable substrates in order to grow epitaxial SiC films. Various attempts have been made to grow epitaxial 3C–SiC (β-SiC, a = 4.3596 Å) on Si (100) substrates, although the mismatch lattice constant is around 20 % and mismatch of thermal expansion coefficient is around 8 %. Most of the early reports on PLD of 3C–SiC (β-SiC) on Si (100) substrates have used the substrate

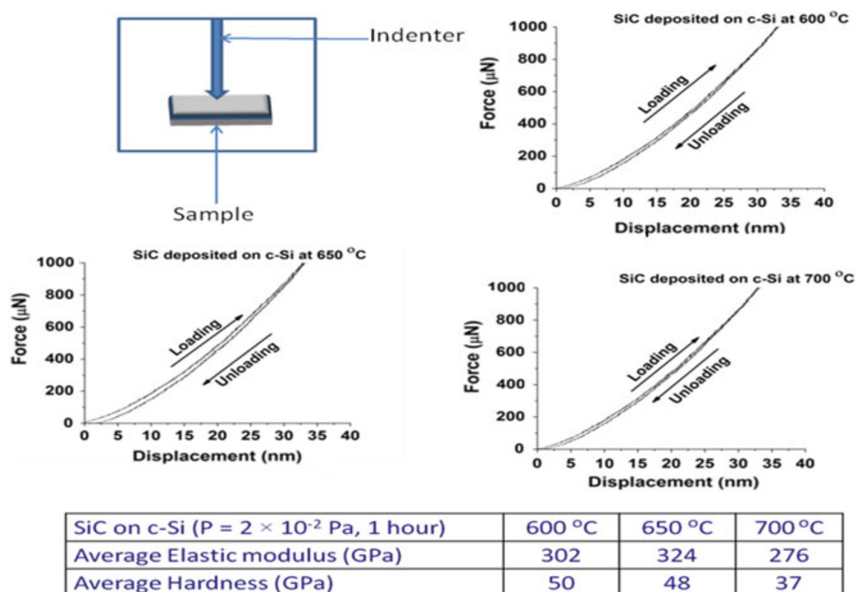

SiC on c-Si (P = 2 × 10-2 Pa, 1 hour)	600 °C	650 °C	700 °C
Average Elastic modulus (GPa)	302	324	276
Average Hardness (GPa)	50	48	37

Fig. 10.9 Typical load versus displacement curves

temperature around 1,000 °C. Recently, a Ti:sapphire ($\lambda = 800$ nm, pulse width ≈ 50 fs) laser source is used to ablate the SiC pellet. The pulsed laser beam with a repetition rate of 1 kHz and an energy per pulse in the range 20–60 μJ, was focused in spots of 0.02 mm^2, corresponding to a laser fluence in the range 100–300 mJ/cm^2. The target-to-substrate distance was maintained at 40 mm and the deposition was carried out in vacuum (10^{-4} Pa) at 500–800 °C substrate temperature for 20–25 min. Based on the structural investigation, the films were not fully crystallized. With this approach, crystalline grains with elongated shapes were obtained at the substrate temperature around 750 °C [20]. In an another study, a Ti:sapphire pulsed laser (120 fs) was used to ablate a SiC target in an high vacuum (7×10^{-5} Pa) chamber. The laser-induced plasma species were then driven and grown to form 3C–SiC films of about 1 μm thick on c–Si wafer at 20 and 500 °C [21]. The distinctive features of fs-PLD films are their extremely smooth surfaces, stoichiometry, amorphous structure, and low defect density compared to CVD films, along with higher growth rates than ns-PLD films.

Other study involves PLD at medium substrate temperature around 400 °C and post-annealing under inert environment [22]. Nano structured SiC films with nanoholes, nanowires of SiC can be synthesized and controlled by varying the substrate temperatures from 1,000 to 1,200 °C and the substrate material [23]. The variation of nanostructure was explained based on the large strain from the misfit in lattices between the SiC films and the substrate. An application of SiC film as a buffer layer has also been considered. The films of ZnO/SiC/Si (111) were grown by the PLD technique [24]. A compliant SiC buffer layer can relax partial stress

induced by large lattice and thermal mismatch between ZnO and Si which can improve the crystalline quality of ZnO thin film grown on Si substrate. The results show that the SiC buffer not only leads to better crystalline quality and higher intensity of luminescence at 380 nm of ZnO thin film, but induces lower leakage current and improved photoresponse of UV detectors. PLD of SiC films followed by high temperature thermal annealing in Ar ambience around 800 °C resulted in the growth of 3C–SiC precipitates. Recently, to avoid the particulate problems usually met in the PLD, an application of an off-axis PLD method by placing the sample at 90° and 45° with respect to the target has been reported using an Nd^{3+}:YAG laser at the fundamental wavelength [25]. The study was performed using a pure 3C–SiC target and Si (100) at a moderate temperature of around 650 °C. It was possible to grow well adherent, particulate free 3C–SiC thin film.

10.4 Summary

SiC possesses excellent physical and electrical properties. Hence, it is a promising material for use in high-temperature, high-power, and high-radiation environment conditions under which devices made from conventional semiconductors cannot perform adequately. PLD technique can be considered for a growth of SiC film on Si or sapphire substrate with a moderate temperature. PLD is also a high vacuum process and therefore contamination is almost nonexistent. SiC thin films were grown on Si (100) and AFG substrates by PLD technique in vacuum. The influence of substrate temperature and laser fluence on both structure and morphology of SiC thin film was studied by different characterization techniques. SiC deposited on c–Si film, thickness is varying 35 nm for 30 min and 110 nm for 1 h deposition when substrate temperature at 650 °C. XRD analysis of the characteristic crystalline peak corresponding to SiC thin film was obtained in the temperature range from 600 to 700 °C at constant pressure 5.5×10^{-3} Pa. SEM analysis of micro droplets observed when SiC deposited on c–Si, and microcracks are observed at higher temperatures when SiC deposited on AFG. The particle density and size of the particle are decreasing when the pressure is decreasing from 2 to 2×10^{-2} Pa. Based on nano-indentation analysis, the average hardness of the SiC thin film decreased with increase in the substrate temperature. The PLD technique for SiC thin film deposition promises its use in smaller devices which operate at high power and temperature than standard silicon components. A review on PLD of SiC thin film clearly show that it is possible to deposit 3C–SiC (β-SiC) and 4H–SiC (α-SiC) thin films by controlling various process parameters, such as laser fluence and substrate temperature. Recent advances in the PLD technique combined with the surface annealing can improve the characteristics of SiC thin films for photovoltaic applications.

Acknowledgments Authors are grateful to Prof. M. Singaperumal (IIT Madras) and Dr. I. A. Palani (IIT Indore) for their discussions at various stages. Authors are also grateful to Mr. Xavier from Carborundum Universal Ltd., India for providing SiC powder with different grit sizes.

References

1. G. Muller, G. Krotz, SiC for sensors and high-temperature electronics. Sens. Actuators, A **43**, 259–268 (1994)
2. J.W. Palmour, J.A. Edmond, H.S. Kong, C.H. Carter Jr, 6H-silicon carbide devices and applications. Physics B **185**, 461–465 (1993)
3. W. Slusark Jr., B. Lalevic, G. Taylor, Hard transparent dielectric coatings. Thin Solid Films, **39**, 155–163 (1976)
4. C. Banerjee, K.L. Narayanan, K. Haga, J. Sritharathikhun, S. Miyajima, A. Yamada, M. Kongai, Fabrication of microcrystalline cubic silicon carbide/crystalline silicon heterojunction solar cell by hot wire chemical vapour deposition. Jpn. J. Appl. Phys. **46**, 1–6 (2007)
5. H. Matsunami, S. Nishino, H. Ono, Hetero-epitaxial growth of cubic silicon-carbide on foreign substrates. IEEE Trans. Electron Devices **28**, 1235–1236 (1981)
6. A. Tabata, Y. Komura, T. Narita, A. Kondo, Growth of silicon carbide thin films by hot-wire chemical vapor deposition from $SiH_4/CH_4/H_2$. Thin Solid Films **517**, 3516–3519 (2009)
7. I.A. Yunaz, K. Hashizume, S. Miyajima, A. Yamada, M. Konagai, Fabrication of amorphous silicon carbide films using VHF-PECVD fortriple-junction thin-film solar cell applications. Sol. Energy Mater. Sol. Cells **93**, 1056–1061 (2009)
8. I. Golecki, F. Reidinger, J. Marti, Single-crystalline, epitaxial cubic SiC films grown on (100) Si at 750-degree-C by chemical vapor deposition. Appl. Phys. Lett. **60**, 1703–1705 (1992)
9. Y.S. Katharria, S. Kumar, F. Singh, J.C. Pivin, D. Kanjilal, Synthesis of buried SiC using an energetic ion beam. J. Phys. D-Appl. Phys. **39**, 3969–3973 (2006)
10. H. ElGazzar, E.A. Rahaman, H.G. Salem, F. Nassar, Preparation and characterization of amorphous nanostructured SiC thin films by low energy pulsed laser deposition. Appl. Surf. Sci. **256**, 2056–2060 (2010)
11. Y.S. Katharria, S. Kumar, R.J. Choudhary, R. Prakash, F. Singh, N.P. Lalla, D.M. Phase, D. Kanjilal, Pulsed laser deposition of SiC thin films at medium substrate temperatures. Thin Solid Films **516**, 6083–6087 (2008)
12. I. Hanyecz, J. Budai, A. Oszko, E. Szilagyi, Z. Toth, Room-temperature pulsed laser deposition of SizC thin films in different compositions. Appl. Phys. A **100**, 1115–1121 (2010)
13. Y.H. Tang, T.K. Sham, D. Yang, L. Xue, Preparation and characterization of pulsed laser deposition (PLD) SiC films. Appl. Surf. Sci. **252**, 3386–3389 (2006)
14. J.S. Pelt, M.E. Ramsey, S.M. Durbin, Characterization of crystalline SiC films grown by pulsed laser deposition. Thin Solid Films **371**, 72–79 (2000)
15. M. Tabbal, A. Said, E. Hannoun, T. Christidis, Amorphous to crystalline phase transition in pulsed laser deposited silicon carbide. Appl. Surf. Sci. **253**, 7050–7059 (2007)
16. T. Kasumori, H. Muto, M.E. Brito, Control of polytype formation in silicon carbice heteroepitaxial films by pulsed-laser deposition. Appl. Phys. Lett. **84**, 1272–1274 (2004)
17. Y. Wang, J. Wen, Z. Guo, Y. Tang, H. Tang, J. Wu, The preparation of single-crystal 4H-SiC film by pulsed XeCl laser deposition. Thin Solid Films **338**, 93–99 (1999)
18. J.C. Burton, L. Sun, M. Pophristic, S.J. Lukacs, F.H. Longa, Spatial characterization of doped SiC wafers by Raman spectroscopy. J. Appl. Phys. **84**, 6268–6273 (1998)
19. A. Debernardi, C. Ulrich, K. Syassen, M. Cardona, Raman linewidths of optical phonons in 3C-SiC under pressure First-principles calculations and experimental results. Phys. Rev. B **59**, 6774–6783 (1999)
20. C. Ghica, C. Ristoscu, G. Socol, D. Brodoceanu, L.C. Nistor, I.N. Mihailescu, A. Klini, C. Fotakis, Growth and characterization of β-SiC films obtained by fs laser ablation. Appl. Surf. Sci. **252**, 4672–4677 (2006)
21. M. Vendan, P. Molian, A. Bastawros, J. Anderegg, Ultra-short pulsed laser deposition and patterning of SiC thin films for MEMS fabrication. Mater. Sci. Semicond. Process. **8**, 630–645 (2005)

22. Y.S. Latharria, S. Kumar, R. Prakash, R.J. Choudhary, F. Singh, D.M. Phase, D. Kanjilal, Characterization of pulsed laser deposition of SiC thin films. J. Non-Cryst. Solids **353**, 4660–4665 (2007)
23. H.X. Zhang, P.X. Feng, V. Makarov, B.R. Weiner, G. Morell, Synthesis of nanostructured SiC using the pulsed laser deposition technique. Mater. Res. Bull. **44**, 184–188 (2009)
24. C.Y. Zhao, Z.R. Liu, B. Sun, J. Tang, P.S. Xu, J.C. Xie, Effects of SiC buffer on the structural and photoelectrical properties of ZnO thin films grown on Si (111) by PLD. Physica E **41**, 479–482 (2009)
25. G. Monaco, D. Garoli, M. Natali, M.G. Pelizzo, P. Nicolosi, Synthesis of heteroepytaxial 3C-SiC by means of PLD. Appl. Phys. A **105**, 225–231 (2011)

Chapter 11
Preparation and Characterization of ZnO Nanorods, Nanowalls, and Nanochains

T. Premkumar, Y. F. Lu and K. Baskar

Abstract The vertically aligned zinc oxide (ZnO) nanorods were synthesized on silicon (Si) substrate using high-pressure pulsed laser deposition (HPPLD). The aligned ZnO nanorods were obtained at the substrate temperature of 650 °C, oxygen partial pressure of 7 Torr, and the target–substrate distance of 25 mm. The influence of substrate lattice mismatch including gallium nitride (GaN-2 %), sapphire (Al_2O_3-18 %), and Si (40 %) on the growth of ZnO nanowalls was examined. The interlinked ZnO nanowalls were obtained on GaN substrate, whereas ZnO nanorods were obtained on Al_2O_3 and Si substrates. The magnesium (Mg) doping has influenced the morphological transition of ZnO from nanorods to nanochains. The chain-like structures were obtained for Mg-doped ZnO target. The growth mechanism has been proposed for the formation of ZnO nanorods, nanowalls, and nanochains. The strong (0002) peak and E_{2H} mode confirmed that the ZnO nanorods, nanowalls, and nanochains are preferentially oriented along *c*-axis and have good crystalline quality. The near band edge emission (NBE) at 3.27 eV revealed the good optical properties of ZnO nanorods, nanowalls, and nanochains.

11.1 Introduction

Recently, ZnO has attracted great interest because of its strong potential applications in nano-electronics, nano-optoelectronics, nano-piezotronics, gas/chemical sensing, and field emission displays. ZnO has a direct band gap of 3.4 eV in the

T. Premkumar · K. Baskar (✉)
Crystal Growth Centre, Anna University, Chennai 600 025, Tamilnadu, India
e-mail: drbaskar2009@gmail.com

T. Premkumar · Y. F. Lu
Department of Electrical Engineering, University of Nebraska-Lincoln,
Lincoln, NE 68503, USA

M. S. R. Rao and T. Okada (eds.), *ZnO Nanocrystals and Allied Materials*,
Springer Series in Materials Science 180, DOI: 10.1007/978-81-322-1160-0_11,
© Springer India 2014

near-UV region and a large exciton binding energy of 60 meV, so that exciton related emission processes could persist at or even above room temperature [1]. ZnO is available as large bulk single crystals in contrast to III-nitride materials such as GaN, aluminum nitride (AlN), and indium nitride (InN). Hence, the epitaxy of ZnO films on native substrates can result in reduced defects and, consequently better performance in electronic and photonic devices. In addition to this, low symmetry of the ZnO crystal structure combined with a large electromechanical coupling gives rise to strong piezoelectric and pyroelectric properties [2].

All these excellent properties together with new synthesis approaches, e.g., control over synthesis of ZnO nanostructures, led to substantial interest in the fabrication of ZnO nanodevices. Novel ZnO nanostructures including nanorods, nanowires, nanowalls, nanobelts, nanohelix, nanotubes, and nanonails have been reported using various physical and chemical methods [2]. Among them, one of the versatile approaches to grow oxide thin film is PLD. It has several attractive features, including stoichiometric transfer of material from the target, strong interaction between the cation and molecular oxygen in the ablated plasma, and good compatibility with background pressures ranging from UHV to 100 Torr. The primary advantages of high-pressure PLD growth are; (i) the high oxygen background pressure enhances the oxidation of material (ii) reduces the kinetic energy of ablated species and improves the controllability [3]. In the present investigation, ZnO nanostructures of various morphologies have been synthesized using HPPLD. The vertically well-aligned ZnO nanorods were grown on the Si substrate. The effect of substrate lattice mismatch on the growth ZnO nanowalls was examined using GaN, Al_2O_3, and Si substrates. Finally, the influence of Mg (4 %) doping on the growth ZnO nanochains was discussed in detail.

11.2 Experimental Implementation

ZnO nanostructures were grown on GaN (0001), Al_2O_3 (0001), and Si (100) substrates using a HPPLD. The chamber was evacuated to a base pressure of 8×10^{-6} Torr, after loading the ZnO target and substrates. A KrF excimer laser ($\lambda = 248$ nm, laser fluence of 3 J/cm^2, pulse duration of 30 ns, and repetition rate of 10 Hz) was used to irradiate the ZnO target, through a quartz window at an incidence angle of 45°. The substrate temperature (T_{sub}) was varied from 500 to 700 °C. The substrates were placed at 25 mm away from the target. The chamber was maintained at an oxygen pressure (PO_2) of 7 Torr during the deposition. The growth was terminated at 30 min, unless/otherwise mentioned. A 4 % of Mg was doped into ZnO to study the influence of Mg doping on the morphology of ZnO. The surface morphology, structural, and optical properties of the ZnO nanowalls and nanorods were investigated using field emission scanning electron microscope (FESEM), high-resolution transmission electron microscope (HRTEM), X-ray diffraction, micro-Raman and fluorescence spectroscope. The composition of ZnO was analyzed using laser-induced breakdown spectroscopy (LIBS).

11.3 Results and Discussion

11.3.1 Synthesis of Vertically Aligned ZnO Nanorods on Si Substrate

The surface of ZnO film was imaged through FESEM. Figure 11.1(a–e) shows the top view of ZnO grown on Si at the T_{sub} of 500, 550, 600, 650, and 700 °C, respectively. The film deposited at 500 °C shows a sheet-like structure. The morphology turned into grain-like structures with the average diameter of ~ 1 μm at 550 °C. As the T_{sub} increased to 600 °C, the films were covered by randomly aligned hexagonal grains, which have a diameter of ~ 400 nm. ZnO films deposited at 650 °C show the well-separated vertically aligned hexagonal nanorods with tapered tip at the top. The tapered tip can be clearly seen in the cross-sectional view of ZnO nanorods in Fig. 11.1f. The average diameter of ZnO nanorods was around 300 nm. As the T_{sub} increased to 700 °C, the nanorods diameter further increased and started to touch the neighboring nanorods. The ZnO nanorods lost its ordered alignment and led to the formation of continuous ZnO film at 700 °C. The cross-sectional images clearly show the vertically aligned growth of ZnO nanorods.

11.3.1.1 Growth Mechanism of Aligned ZnO Nanorods

The schematic diagram for ZnO nanorod's growth mechanism is shown in Fig. 11.2. A high-power laser beam interacts with ZnO target (Step-I), during laser ablation. The strong laser–material interaction leads to the evaporation of Zn, O and neutrals atoms from the target. The background gas pressure determines the number of collision between the ablated species and gaseous atoms. At a high

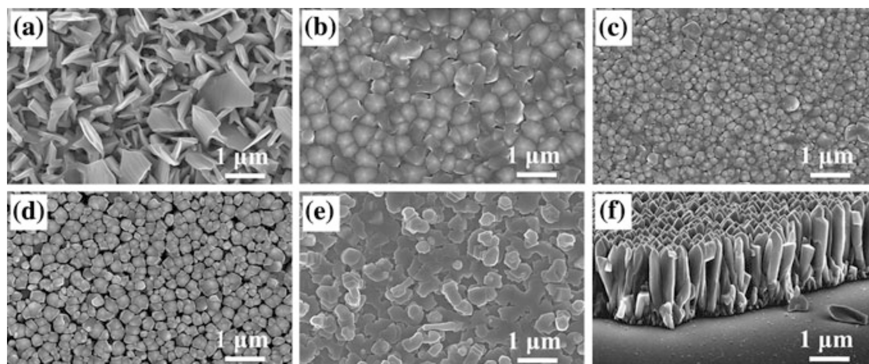

Fig. 11.1 FESEM images of ZnO grown at **a** 500 **b** 550 **c** 600 **d** 650, **e** 700 °C and **f** cross-sectional view of ZnO grown at 650 °C

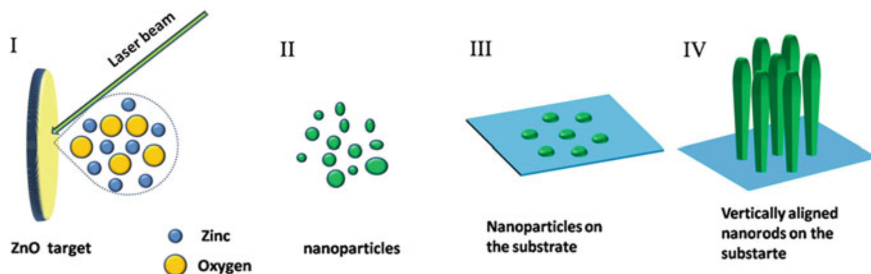

Fig. 11.2 Schematic diagram represents the growth mechanism of ZnO nanorods

oxygen pressure, above 1 Torr, the increased collisions lead to the condensation of ablated species, which results the formation of nanoparticles (Step-II). The nanoparticles which reach the Si substrate acts as a nucleation site for the growth of ZnO nanorods [4, 5] (Step-III). The nucleation can occur at any possible site on the substrate. Since ZnO nanoparticles are thermodynamically favorable site for the growth of ZnO nanostructures, the nanorods growth can be attributed to the formation of nanoparticles in the gas phase at high pressure (Step-VI).

The nanoparticles formed in the gas phase play an important role in the growth of vertically aligned nanorods. Figure 11.3a, b shows the XRD pattern and micro-Raman spectrum of ZnO nanorods grown at 650 °C. The strong (0002) peak and E_{2H} mode at 439 cm^{-1} confirmed that the preferred orientation of nanorods along c-axis and it is highly crystalline wurtzite ZnO.

11.3.2 Effect of Substrate Lattice Mismatch on the Growth of ZnO Nanowalls

The lattice mismatch between the substrate and the film has strong influence on the alignment of nanostructures [6]. The GaN (a = 3.18 Å, c = 5.18 Å) and Al_2O_3 (a = 4.75 Å, c = 12.99 Å) substrates have close lattice match with ZnO

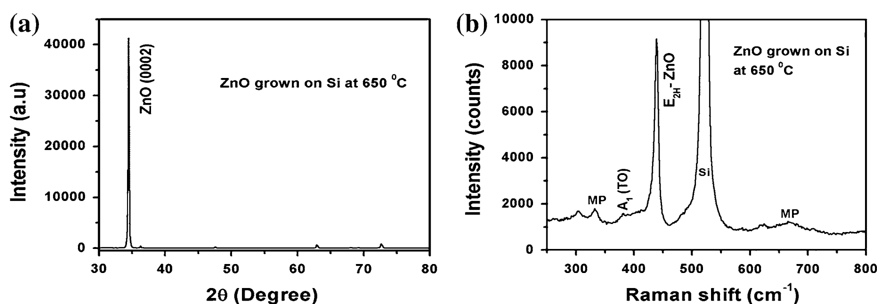

Fig. 11.3 **a** XRD pattern and **b** Raman spectra of ZnO nanorods

(a = 3.24 Å, c = 5.20 Å) than Si substrate. The lattice constant of Si is a = 5.43 Å [1]. The alignment/orientation of the nanostructures can be tuned by utilizing the lattice mismatch. In comparison with the growth of ZnO nanorods/wires, the growth of two-dimensional (2D) ZnO nanowalls is difficult due to its polar nature along c-axis. The (0001) basal plane has highest surface energy that induces fast growth along c-axis, which results in one-dimensional (1D) nanorods/wire growth. Until now, few papers have reported the growth of ZnO nanowalls using carbothermal reduction process [7], gold-catalyzed epitaxial growth [7] and catalyst free MOVPE [8]. Kim et al. [9] confirmed the formation of ZnO thin film prior to the growth of ZnO nanowalls on GaN substrates. The origin of the growth of ZnO nanowalls is still under debate. In this study, the effect of lattice mismatch on the growth of ZnO nanowalls was examined in detail [10].

Figure 11.4a–c shows the 45° tilted view, and Fig. 11.4d–f shows the cross-sectional view of nanowalls and nanorods grown on GaN, Al_2O_3 and Si substrates, respectively. The vertically aligned nanorods were obtained on Al_2O_3 and Si substrates. The diameter and length of the ZnO nanorods were 300 ± 50 nm and 3 ± 0.1 μm, respectively. Interlinked ZnO nanowalls were obtained on GaN substrate. The width and height of the ZnO nanowalls were 120 ± 50 nm and 1.2 ± 0.1 μm, respectively.

11.3.2.1 Growth Mechanism of ZnO Nanowalls

Several parameters would influence the nucleation of ZnO nanostructures including the lattice mismatch between the substrate and film, the T_{sub}, and PO_2. During the growth, at a fixed T_{sub} and PO_2, the key parameter affecting the nucleation process would be the lattice mismatch. Verma et al. [11] reported the

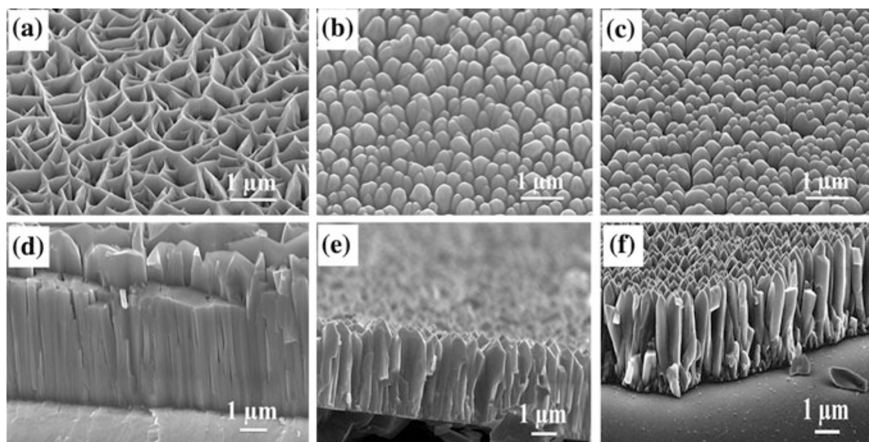

Fig. 11.4 FESEM images of ZnO nanowalls and nanorods grown on GaN, Al_2O_3 and Si substrates, (**a**–**c**) 45°-tilted view and (**d**–**f**) cross-sectional view, respectively

growth of well-separated ZnO nanocolumns on Al_2O_3 substrate and columnar thin films on yttrium stabilized zirconia (YSZ) substrate, and attributed the increase in diameter and coalescence of the nanocolumns with decrease in the lattice mismatch. The lattice mismatch between ZnO and GaN, Al_2O_3 and Si are 1.8, 18.4, and 40.1 %, respectively [1]. In this work, ZnO morphology transformed from nanorods to nanowalls with decrease in lattice mismatch. The results are in good correlation with the report of Verma et al. [11].

The cross-sectional view in Fig. 11.4d shows the growth of dense ZnO columnar film on GaN compared with Si and Al_2O_3. This behavior can be attributed to the low lattice mismatch between ZnO and GaN. This implies that the morphology of ZnO nanostructures can be tuned, during growth, by utilizing the lattice mismatch between the substrate and film. The schematic diagram in Fig. 11.5 represents the growth mechanism for ZnO nanowalls. The ablation at high PO_2 of $\sim$7 Torr leads to the formation of nanoparticles in the gas phase due to increase in number of collisions between Zn^{2+} and O_2. These nanoparticles acted as a nucleation sites for the growth of nanorods (Fig. 11.5a, b) [4]. The growth rate of ZnO crystals in different directions has been reported to be $[0001] > [01\bar{1}\bar{1}] > [10\bar{1}0] > [01\bar{1}1]$, resulting in crystals being bounded by $(10\bar{1}0)$ facets with $[01\bar{1}1]$ caps [12, 13]. The growth rate along $< 0001 >$ directions is higher than that of $<10\bar{1}0>$ and $< 01\bar{1}1 >$ directions. Similarly, $(10\bar{1}0)$ and (0001) facets are generally observed in ZnO nanostructures, this correlates well with the present results. While nanorods grow along $< 0001 >$ direction, the incoming Zn and O species contributed to the radial growth of nanorods along $<10\bar{1}0>$ direction. The radial growth leads to coalescence of neighboring nanorods, after

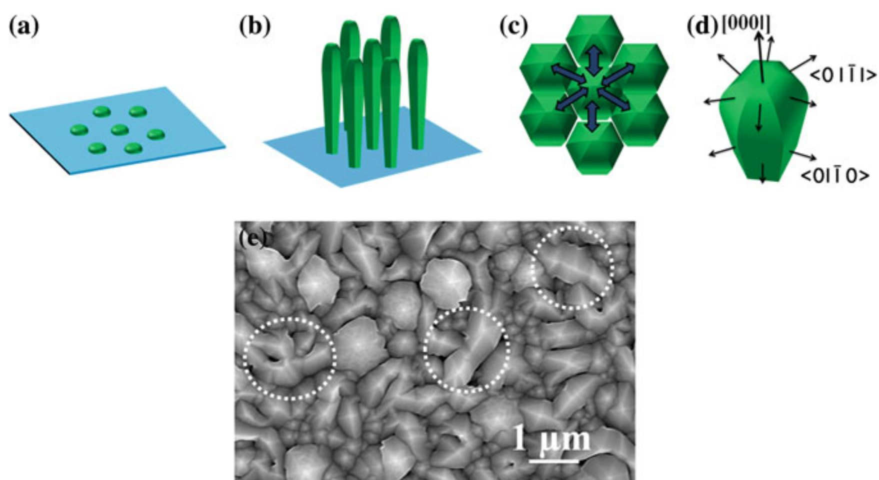

Fig. 11.5 Schematic representation of growth mechanism of ZnO nanowalls, **a** ZnO nanoparticles deposited on the substrate, **b** growth of ZnO nanorods, **c** left–right arrow represents the formation of nanobridges/walls, **d** hexagonal ZnO planes and **e** FESEM image of ZnO grown on GaN for 20 min

coalescence there is no growth along $<10\bar{1}0>$ direction. The growth is presumed to continue along $<01\bar{1}1>$ direction as shown in Fig. 11.5c, d. Laudise et al. [14]. reported that the growth rate for $<01\bar{1}1>$ direction seems to be intermediate between those of $<10\bar{1}0>$ and $< 0001 >$ directions. Further growth along $<01\bar{1}1>$ direction among the tips of the nanorods leads to formation of bridges [15]. Finally, the interlinked network of nanowalls was formed over the dense columnar ZnO films. ZnO was deposited for 20 min by keeping other growth parameters constant to confirm the formation of bridges between the tips of ZnO nanorods. Figure 11.5e shows the top view of ZnO nanowalls grown on GaN substrates. The circle represents an initial stage of the formation of ZnO nanowalls/bridges. The lateral growth of nanorods along $<01\bar{1}1>$ direction connects all of them together and evolves as nanowalls.

Figure 11.6a–c shows the XRD pattern, micro-Raman spectra and fluorescence spectra of ZnO nanowalls and nanorods grown on GaN, Al_2O_3, and Si substrates, respectively. The strong (0002) peak in XRD shows that the ZnO nanowalls were

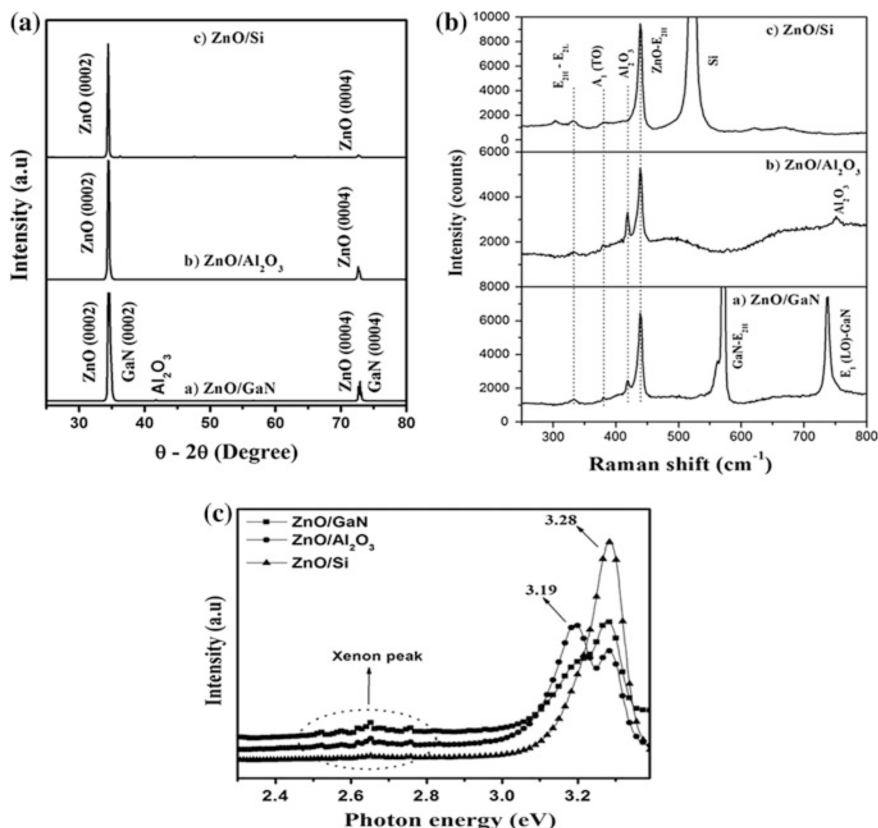

Fig. 11.6 **a** XRD pattern, **b** micro-Raman spectra and **c** fluorescence spectra of ZnO

preferentially oriented along c-axis. The Raman modes of ZnO were observed at 331 (E_{2H}–E_{2L}), 380 (A_1 (TO)), and 439 cm^{-1} (E_{2H})[16]. The Raman shifts observed at 417, 521, 571 and 736 cm^{-1} correspond to Al_2O_3, Si, GaN (E_{2H}) and GaN (A_1 (LO)), respectively. The E_{2H} mode of ZnO nanowalls and nanorods were observed at 439 cm^{-1}. The strong E_{2H} mode can be attributed to low intrinsic defects associated with oxygen e.g., oxygen vacancies (V_O), since E_{2H} mode is only associated with the vibration of O atoms [17]. The low V_O in the ZnO nanorods and nanowalls can be attributed to high oxygen pressure during PLD growth.

The PL spectra show a strong NBE emission of ZnO at 3.28 eV, which is closer to the bandgap of bulk ZnO (3.36 eV). In addition to the NBE emission, a peak at 3.19 eV was observed for ZnO grown on GaN and Al_2O_3. Similarly, Lin et al. [18] reported the energy level of zinc vacancy (V_{Zn}) at 3.06 eV. In this study, the peak located at 3.19 eV closely matched with V_{Zn}. The formation of oxygen vacancy (V_O) and zinc interstitials (Zn_i) is high in ZnO grown under low oxygen pressures. The formation of zinc vacancy (V_{Zn}), oxygen interstitials (O_i) and oxygen antisite (O_{Zn}) is high in ZnO grown under high oxygen pressures [19]. Though formation of O_i and O_{Zn} is also favorable in the present case, the energy intervals between these defect levels and the conduction band edge are 2.28 and 2.38 eV, respectively. Hence, these energy levels are too small to assign to the violet emission. Therefore, emission peak at 3.19 eV observed in this study can be assigned to electron transition from the bottom of the conduction band to the Zn vacancy level [18]. The presence of V_{Zn} and absence of visible emissions in ZnO nanowalls and nanorods can be due to high oxygen pressure growth. These results are in good agreement with the micro-Raman result.

11.3.2.2 Field Emission Characteristics of ZnO Nanorods and Nanowalls

The vertically aligned ZnO nanowalls and nanorods are suitable for field electron emission. The field-emission (FE) characteristics of ZnO nanowalls and nanorods deposited on GaN and Si substrates were measured in a two-parallel-plate configuration. The vacuum chamber was evacuated to a base pressure of 1.5×10^{-5} Torr. The voltage was swept by automatic sweep option of source meter from 0 to 1000 V. The experiment was repeated for several times to check the consistence of the results.

Figure 11.7a, b shows the FE plot between current density and electric field (J-E) for ZnO nanowalls and nanorods, with cathode-to-anode spacing of 40 and 150 μm, respectively. The turn-on fields of ZnO nanorods and nanowalls were 2 V/μm (at 7.1 mA/cm^2) and 12.5 V/μm (at 7 $\mu A/cm^2$), respectively. The threshold fields of ZnO nanorods and nanowalls were 6.7 V/μm (at 7.7 mA/cm^2) and 25 V/μm (14 $\mu A/cm^2$), respectively. A low turn-on field of 2 V/μm was achieved for ZnO nanorods compared with ZnO nanospikes [10, 20]. The turn-on field of ZnO nanorods is lower than nanowalls. In addition to that, the current density (J) of ZnO nanorods (7.7 mA/cm^2) is higher compared to ZnO nanowalls

(in the present work) and the previous reports. Pradhan et al. [20]. achieved a J of 1.3 mA/cm^2 at 7 V/μm for ZnO nanospikes which is six times smaller than the J of the ZnO nanorods. Figure 11.7c, d shows the Fowler–Nordheim (F–N) plot of the J–E curves, i.e., ln(J/E^2) $\sim$ 1/E, for ZnO nanorods and nanowalls. The F–N plot of ZnO nanostructures shows the two-slope behavior, as reported earlier. The non-linearity in the F–N plot is the typical characteristic of the semiconductor material. The estimated β-factor of ZnO nanorods (10×10^5) is higher than that of ZnO nanowalls (16,862), which is also consistent with the lower turn-on field of the nanorods. Hence, the low turn-on field, high current density, and large β value of ZnO nanorods can be attributed to high aspect ratio of tapered nanorods tip and good vertical alignment compared with ZnO nanowalls [10].

11.3.3 *Influence of Mg Doping on the Growth of ZnO Nanochains*

The metal catalysts have been used to control the orientation and dimension of ZnO nanostructures [21]. In addition to this, doping or alloying of specific element also leads to increase/decrease in the dimension of nanostructures [22]. There are

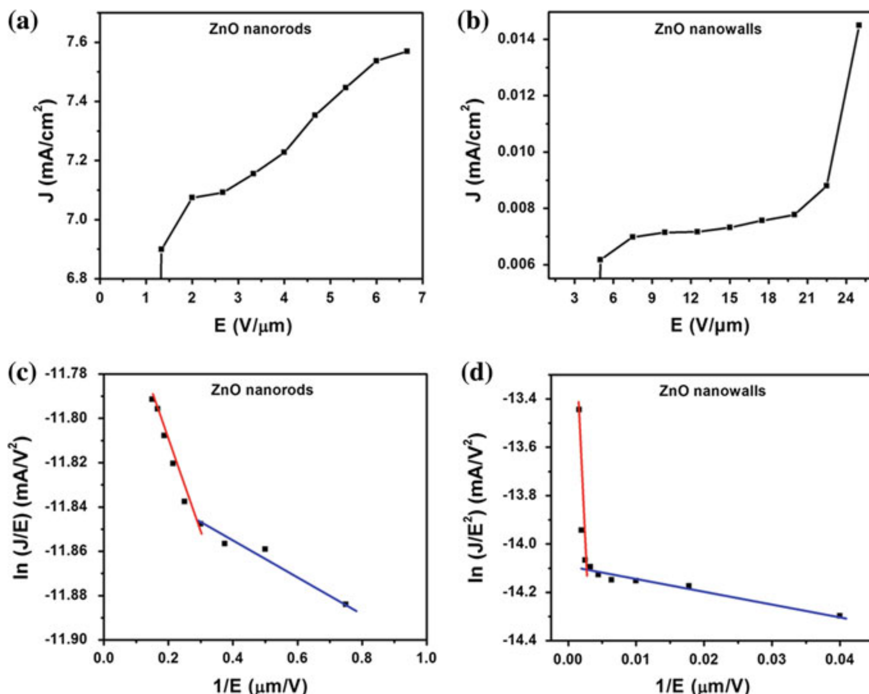

Fig. 11.7 **a**, **b** J-E plots and **c**, **d** F–N plots of ZnO nanorods and nanowalls

few reports available on the growth of ZnO nanochains [23]. In this study, we report the influence of Mg doping on the morphological transition of ZnO from nanorods to nanochains [24]. Compared with the previous experiments, here, the Mg-doped ZnO target was used instead of ZnO target.

The as grown ZnO film was scanned through FESEM. ZnO film grown using Mg:ZnO target shows the formation of chain-like structures. Figure 11.8a, b illustrates the formation of distinct and well-separated beaded ZnO nanochains. The nanochains appear like connecting the beads of ZnO nanoparticles in series along c-axis. Figure 11.8c shows a low-magnification TEM image of ZnO nanochains and the nanochains beads are clearly visible in the inset. The diameter of nanobeads is ~110 nm which is in close agreement with diameter measured from FESEM ~120 nm. The lattice fringes are clearly visible in Fig. 11.8d and the inter spacing was measured to be 0.52 nm, which confirms the single crystallinity of nanochains with preferential growth along [0001] direction.

11.3.3.1 Growth Mechanism of ZnO Nanochains

The possible growth mechanism of ZnO nanochains is depicted as follows. Figure 11.9 represents a schematic diagram of nanochain growth. At high PO_2,

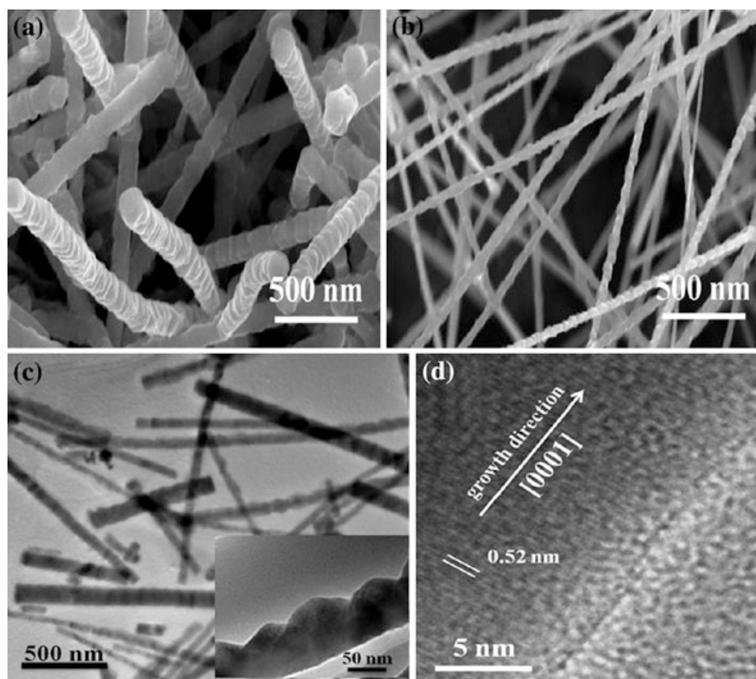

Fig. 11.8 **a**, **b** FESEM and **c**, **d** HRTEM images of ZnO nanochains

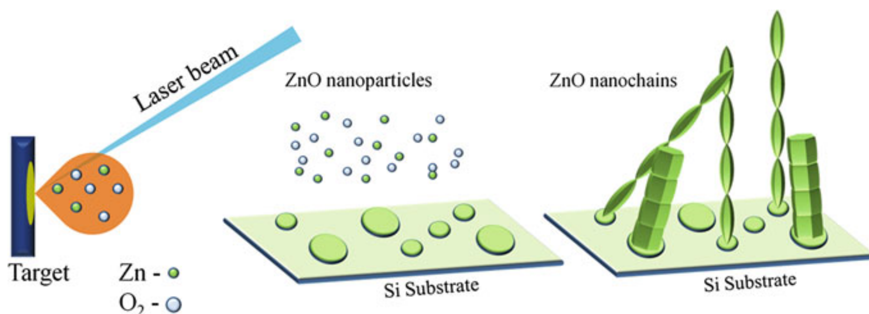

Fig. 11.9 Schematic representation of growth mechanism of ZnO nanochains

ZnO tends to form nanoparticles in gas phase due to the condensation of ablated particles. Hartanato et al. [4] claimed that the nanoparticles, which reach the substrate, played an important role in growing nanorods. They confirmed the deposition of nanoparticles on the nanorods surface at 300 °C and melting of these nanoparticles at 700 °C. The incoming nanoparticles reach the substrate and fuse into the nanorods at a high substrate temperature, which leads to the growth of nanorods.

In this study, ZnO nanochains appear like stacking of nanoparticles along c-axis. The possible reasons can be, change in the vapor pressure of Zn due to Mg doping, since the morphologies of ZnO nanostructures are mainly influenced by the concentration of Zn [22], and the incomplete fusion of nanoparticles due to low T_{sub} (650 °C) during the growth. This led to the stacking of nanoparticles along [0001] direction as represented in Fig. 11.9. The reason for the formation of various ZnO nanostructures is ascribed to different Zn vapor pressure [25, 26]. Hierarchical ZnO nanostructures including nanobelts, nanohelix, nanotetrapod, nanomultipod, nanobridges, nanonails, and nanorods have been reported by depositing mixtures of ZnO with graphite, SnO_2, GeO_2, and Li_2O. Shen et al. [27] reported the morphology transition of ZnO from nanonails (Zn/S = 25:1) to nanowires (Zn/S = 10:1) by varying zinc and sulfur molar ratio. The mixing/doping/alloying of specific element plays a major role in modifying or increasing/decreasing the dimension of nanostructures [22]. In the ZnO : Mg (4 %) ratio, the concentration of Zn vapor was tuned for growing chain-like structures. No chain-like growth was observed using primitive ZnO target. The formation of the nanoparticles in the gas phase is the preliminary condition for the subsequent growth of nanochains. This can be easily achieved through gas-phase condensation by increasing the gas pressure in the HPPLD [24]. This implies that the novel ZnO nanochains morphology can be realized by modifying the concentration of Zn in HPPLD.

The composition of nanochains was analyzed using laser-induced breakdown spectroscopy (LIBS). The LIBS spectra confirmed the presence of Mg in ZnO nanochains (not shown here). Figure 11.10a shows the XRD patterns of the ZnO nanorods and nanochains. The diffraction peaks of both patterns are indexed to

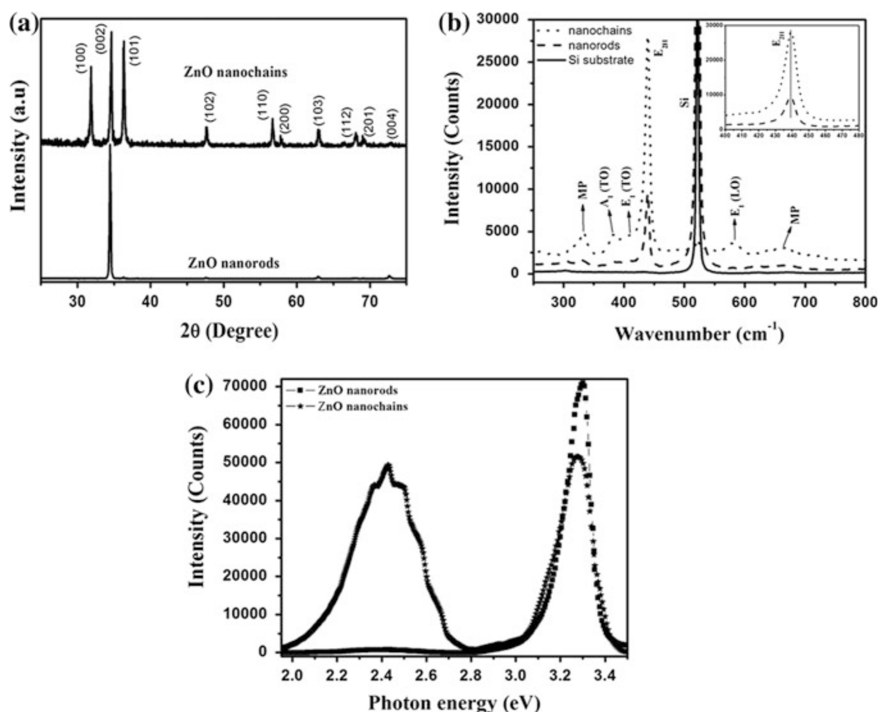

Fig. 11.10 **a** XRD pattern, **b** micro - Raman spectra and **c** PL spectra of ZnO nanorods and nanochains

wurtzite ZnO. The strong (0002) peak confirmed that the nanochains were preferentially oriented along c-axis.

The micro-Raman spectra of ZnO nanochains, nanorods, and Si are shown in Fig. 11.10b. ZnO nanochains exhibit A_1 (TO), E_1 (TO), E_{2H} and E_1 (LO) modes at 382, 411, 439, and 584 cm^{-1}, respectively, whereas ZnO nanorods shows A_1 (TO) and E_{2H} modes at 382 and 439 cm^{-1}, respectively. The FWHM of E_{2H} mode of ZnO nanorods and nanochains are 6.6 and 8.3 cm^{-1}, respectively. The FWHM increases with decrease in diameters of the nanochains, diameter of the nanorods and nanochains were 350 nm and 120 nm, respectively. The broadening of the E_{2H} mode can be attributed to the size effect and residual stress in the nanochains. The E_1 (LO) mode of ZnO nanochains has been observed at 584 cm^{-1}, which originated due to the formation of zinc and oxygen-related defects in the nanochains. Hence, the presence of strong E_{2H} mode with a weak E_1 (LO) mode confirmed that ZnO nanochains have good crystallinity. The photoluminescence (PL) spectra of the ZnO nanorods and nanochains were illustrated in Fig. 11.10c. ZnO nanorods and nanochains exhibit NBE emission at 3.28 eV. The NBE emission can be assigned to the recombination of bound ZnO excitons. The FWHM of NBE emission of ZnO nanorods and nanochains are 98 and 120 meV, respectively. The FWHM increases with decrease in nanochain diameter. A broad deep level

emission peaking at 2.42 eV was observed for ZnO nanochains. The deep level emission of nanochains can be attributed to zinc interstitial, oxygen vacancies, and surface state defects. This trend is in good agreement with the presence of E_1 (LO) mode of ZnO nanochains in micro-Raman spectra. The experiments were also performed with different concentration of Mg doped ZnO. The diameter of the nanochains increased with the increase of Mg concentration. The growth at various substrate temperatures also influenced the morphology of ZnO nanochains (not shown here).

11.4 Conclusions

Growth of aligned ZnO nanorods, effect of lattice mismatch on the growth of ZnO nanowalls, and influence of Mg doping on the formation of ZnO nanochains have been demonstrated using HPPLD. ZnO nanorods and nanowalls exhibit a strong E_{2H} vibration mode in the micro-Raman spectra. The XRD pattern confirmed the preferred orientation of ZnO nanorods and nanowalls along c-axis. High aspect ratio, good vertical alignment, and better crystallinity of ZnO nanorods exhibited promising field emission performance with a low turn-on field of 2 V/μm, a high current density of 7.7 mA/cm^2, and a large field enhancement factor of 10×10^5. The FESEM and HRTEM images revealed the growth of beaded nanochains along [0001] direction. The micro-Raman spectra have confirmed the good crystallinity of ZnO nanochains. The ZnO nanorods, nanowalls, and nanochains exhibited good optical properties.

References

1. U. Ozgur, Y.I. Alivov, C. Liu, A. Teke, M.A. Reshchikov, S. Doğan, V. Avrutin, S.J. Cho, H. Morkoç, J. Appl. Phys. **98**, 041301 (2005)
2. Z.L. Wang, J. Phys. Condens. Matter. **16**, R829 (2004)
3. D.B. Chrisey, G.K. Hubler, *Pulsed laser deposition of thin films* (Wiley-Interscience, New York, 1994), pp. 327–356
4. A.B. Hartanto, X. Ning, Y. Nakata, T. Okada, Appl. Phys. A **78**, 299 (2004)
5. M. Kawakami, A. Hartanto, Y. Nakata, T. Okada, Jpn. J. Appl. Phys. **42**, L33 (2003)
6. X. Wang, J. Song, Z.L. Wang, J. Mater. Chem. **17**, 711 (2007)
7. H.T. Ng, J. Li, M.K. Smith, P. Nguyen, A. Cassel, J. Han, M. Meyyappan, Science **300**, 1249 (2003)
8. Y.J. Hong, H.S. Jung, J. Yoo, Y.J. Kim, C.H. Lee, M. Kim, G.C. Yi, Adv. Mater. **21**, 222 (2009)
9. S.W. Kim, H.K. Park, M.S. Yi, N.M. Park, J.H. Park, S.H. Kim, S.L. Maeng, C.J. Choi, S.E. Moon, Appl. Phys. Lett. **90**, 033107 (2007)
10. T. Premkumar, Y.S. Zhou, Y.F. Lu, K. Baskar, ACS Appl. Mater. Interfaces **2**, 2863 (2010)
11. H. Verma, D. Mukherjee, S. Witanachchi, P. Mukherjee, M. Batzill, J. Cryst. Growth **312**, 2012 (2010)
12. W.J. Li, E.W. Shi, W.Z. Zhong, Z.W. Yin, J. Cryst. Growth **203**, 186 (1999)

13. J.S. Jeong, J.Y. Lee, J.H. Cho, C.J. Lee, S.J. An, G.C. Yi, R. Gronsky, Nanotechnology **16**, 2455 (2005)
14. R.A. Laudise, A.A. Ballman, J. Phys. Chem. **64**, 688 (1960)
15. C.C. Wu, D.C. Wu, P.R. Lin, T.N. Chen, R.H. Horng, Nanoscale. Res. Let. **4**, 377 (2009)
16. S. Singamaneni, M. Gupta, R. Yang, M.M. Tomczak, R.R. Naik, Z.L. Wang, V.V. Tsukruk, ACS Nano **3**, 2593 (2009)
17. X. Zhu, H. Wu, Z. Yuan, J. Kong and W. Shen **40**, 2155 (2009)
18. B. Lin, Z. Fu, Y. Jia, Appl. Phys. Lett. **79**, 943 (2001)
19. S.H. Jeong, B.S. Kim, B.T. Lee, Appl. Phys. Lett. **82**, 2625 (2003)
20. D. Pradhan, M. Kumar, Y. Ando, K.T. Leung, ACS Appl. Mater. Interfaces **1**, 789 (2009)
21. M. Lorenz, E.M. Kaidashev, A. Rahm, T. Nobis, J. Lenzner, G. Wagner, D. Spemann, H. Hochmuth, M. Grundmann, Appl. Phys. Lett. **86**, 143113 (2005)
22. M.H. Choi, T.Y. Ma, Mater. Lett. **62**, 1835 (2008)
23. M. Dutta, D. Basak, Nanotechnology **20**, 475602 (2009)
24. T. Premkumar, Y.S. Zhou, Y. Gao, K. Baskar, L. Jinag, Y.F. Lu, Appl. Surf. Sci. **258**, 2297 (2012)
25. Y.H. Leung, A.B. Djurisic, J. Gao, M.H. Xie, W.K. Chan, Chem. Phys. Lett. **385**, 155 (2004)
26. P.C. Chang, Z.Y. Fan, D.W. Wang, W.Y. Tseng, W.A. Chiou, J. Hong, J.G. Lu, Chem. Mater. **16**, 5133 (2004)
27. G. Shen, J.H. Cho, J.K. Yoo, G.C. Yi, C.J. Lee, J. Phys. Chem. B. **109**, 5491 (2005)

Chapter 12
Synthesis and Characterization of ZnO-Based Phosphors and Related Phosphor Composites in Bulk, Thin Film and Nano Form

P. Thiyagarajan, M. Kottaisamy and M. S. Ramachandra Rao

Abstract Phosphors are light emitting solids that play an important role in the lighting industry. The physics of doping suitable elements plays an equally important role in controlling the emission properties. The choice of host lattice is the key in controlling the charge transfer mechanism. Zn_2SiO_4 is a useful host material, and in this chapter we discuss on the effect of doping in various forms of this host material. Zn_2SiO_4:Mn powder (bulk) phosphors have been synthesized by sol–gel [1] and solid-state method, and thin films grown by pulsed laser deposition [2]. The optimization parameters like growth temperature, vacuum, and oxygen partial pressure (in case of thin films) that determine the luminescent efficiency of the phosphors will be highlighted. The defect and its related emission in ZnO encapsulated SiO_2 nanocomposites [3] synthesized using urea assisted sol–gel techniques projecting toward the fabrication of UV-LED pumped white LED will be discussed in detail.

12.1 Introduction

α-Zn_2SiO_4, known as Willeminite, crystallizes in phenacite structure and belongs to the group of orthosilicates [4]. Mn-doped Zn_2SiO_4 phosphor can be easily prepared as the ionic size and valence state of Zn is identical to that of Mn.

P. Thiyagarajan (✉)
Crystal Growth Centre, Anna University, Chennai 600025, India
e-mail: thiyagarajan@annauniv.edu

M. Kottaisamy
Department of Chemistry, Thiagarajar College of Engineering, Madurai, India
e-mail: mmksamy66@yahoo.com

M. S. Ramachandra Rao
Department of Physics, Materials Science Research Centre,
Indian Institute of Technology Madras, Chennai 600036, India
e-mail: msrrao@iitm.ac.in

M. S. R. Rao and T. Okada (eds.), *ZnO Nanocrystals and Allied Materials*,
Springer Series in Materials Science 180, DOI: 10.1007/978-81-322-1160-0_12,
© Springer India 2014

This silicate phosphor emits an efficient green colour and can find potential applications in various display devices such as plasma display panels, vacuum fluorescent displays (VFD), thin film electroluminescent devices, field emission displays, and medical imaging radiation detectors [5–11]. Zn_2SiO_4 can also be used as a luminescent material in fluorescent lamps and cathode ray tubes because of its high luminance efficiency and chemical stability [12]. Mere controlling of the chemical composition of multi-component oxide phosphors, high luminance, and superior luminous efficiency can be realized with tunable Commission International de l'Eclairage (CIE) chromaticity coordinates of the emitted light [13]. The Zn_2SiO_4:Mn phosphor prepared by the conventional solid-state route involves crushing, grinding, ball milling, and firing the raw materials at elevated temperature (1300 °C). However, realizing device-worthy luminescent intensities by this method is hard due to the problem of phase separation and inhomogeneous distribution of the activator ions. Various routes such as aqueous medium, [14] single polymer precursor route, [15] sol–gel process, [16–18] spray pyrolysis, [19] charge liquid cluster beam technique, [20] hydrothermal method, [16] mesophorous template route, [21] and solution combustion synthesis [22–24] have been utilized to tune the luminescent properties in these materials. The advantage of the sol–gel method over solid-state reaction is the need for low calcination temperature ($\sim$1000 °C) and homogeneous distribution of the activator ions that leads to improved emission efficiency of the phosphors [25, 26].

Until recently, phosphor thin films have reported to have been prepared using the sol–gel process [25]. Among the various thin film growth techniques employed, pulsed laser deposition (PLD) have proved to be one of the most versatile techniques due to its ability to produce homogeneous and stoichiometric films [27]. However, the role of oxygen that significantly affects the luminescent properties in the PLD-grown phosphor films has not been studied in detail hitherto [28].

Zinc oxide is a wide-band-gap semiconductor ($Eg = 3.5$ eV) with the excitonic emission at near-UV [390 nm]. It exhibits an intense greenish-yellow emission because of the presence of intrinsic and extrinsic defects in its lattice [29]. Moreover, due to its excellent stability and emission aided by defects, ZnO has been widely used as a phosphor in VFD [30]. In the near future, it is expected that ZnO has the ability to replace the expensive GaN-based LEDs. Researchers have been contemplating the utility of ZnO as an alternative source to GaN-based-LEDs, the most important aspect is that ZnO should, along with the near-UV excitonic emission, exhibit intense light emission in the greenish-yellow–red regions when excited at the excitation wavelength of this near-UV and blue regions. It is important to note that the greenish-yellow emission is essential for LUCOLED to realize white light emission. Recently, it has been demonstrated that the ZnO-based composites showed predominant greenish-yellow emission [31, 32]. It is imperative that synthesis technique plays an important role in improving the defect emission intensity. There are a number of reports on sol gel-prepared ZnO-particles which exhibit a variety of optical properties when the ZnO nanoparticles are embedded in amorphous and semicrystalline SiO_2 matrix [33–37].

In order to enhance the PL emission, it is important to tune the parameters of chemical reaction to produce the requisite properties. The interface between such phases play a crucial role.

This chapter reports on the low temperature sol–gel-combustion-synthesis of powder Zn_2SiO_4:Mn phosphor in a silica gel matrix and the characterization of its physical properties. As mentioned above, the silica-phosphor matrix is important to realize tunability in emission properties. Moreover, the optimization of the Zn_2SiO_4:Mn thin film growth conditions during the PLD growth process using various oxygen partial pressures (O_2 pp) on different substrates with detailed structural and luminescence properties have been examined and reported. In addition, white light emitting ZnO–SiO_2 nanocomposites were prepared using urea assisted sol–gel combustion that can serve as a new phosphor for white LED applications upon capping with UV-LEDs. All the samples were subjected to characterization studies such as thermogravimetric analysis (TGA), differential thermal analysis (DTA), X-ray diffraction (XRD), scanning electron microscopy (SEM), Fourier transform infrared (FTIR), diffuse reflectance spectroscopy (DRS), and photoluminescence (PL) and the results were discussed in detail.

This chapter is split into three sections, Section I focuses on the powder Zn_2SiO_4:Mn phosphor, Section II discusses the thin film growth aspects of Zn_2SiO_4:Mn phosphor, and Section III highlights results on ZnO–SiO_2 nanocomposites for white light emission.

12.2 Synthesis of $Zn_{2(1-x)}Mn_xSiO_4$ ($1 < x < 7$ mol %) Phosphor

$Zn_{2(1-x)}Mn_xSiO_4$ ($1 < x < 7$ mol %) phosphors were synthesized in an alcohol medium using high pure starting chemicals such as zinc nitrate ($Zn(NO_3)_2 \cdot 6H_2O$), manganese acetate [$(CH_3COO)_2Mn \cdot 4H_2O$], tetraethoxysilane ($Si(OR)_4$) and urea ($NH_2CONH_2$) [1]. The calculation was carried out using total oxidizing (*O*) and reducing (*R*) valence states of the elements constituting the compounds [25]. Stoichiometric quantities of zinc nitrate, manganese acetate and urea, were taken in a beaker and ethyl alcohol was added. This mixture was stirred continuously until complete dissolution occurred. Then the required quantity of tetraethoxysilane was added and the stirring was continued for about 5 h to ensure homogeneity followed by the addition of the required amount of water and HNO_3 to maintain a pH of 3. This solution was heated slowly and kept at 110 °C so as to evaporate alcohol to form the gel mixture. This mixture was then heated at 300 °C for 5 h (precursor material). This precursor material was heated at different temperatures in the range 500–1100 °C for 5 h in ambient to analyze the growth of Zn_2SiO_4 phase [1].

The entire preparation process is given in the flow chart below:

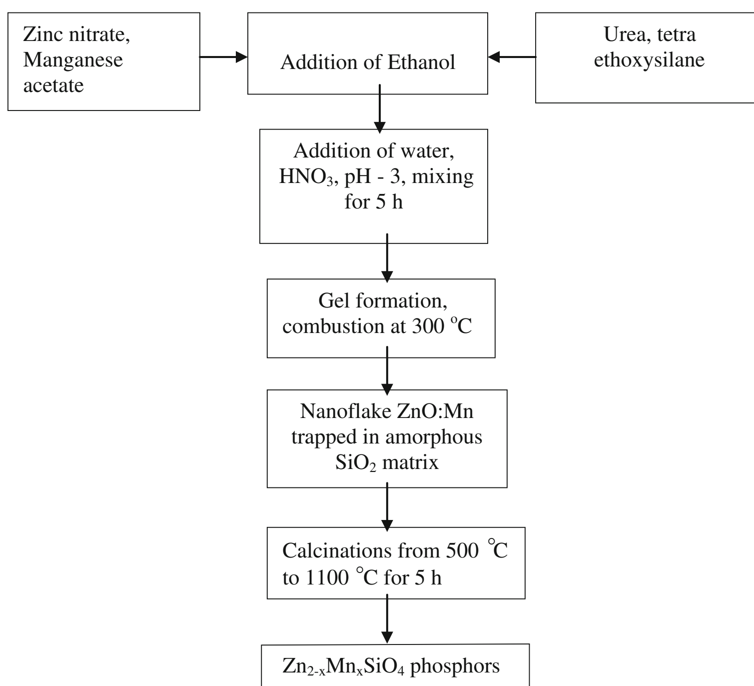

In addition, the $Zn_{2(1-x)}Mn_xSiO_4$ ($x = 3$ mol %) phosphor powder was prepared by solid-state reaction route to compare PL emission intensity against the phosphor synthesized by urea gel combustion synthesis method. For the solid-state reaction route, the stoichiometric compositions of $MnCO_3$, ZnO, and SiO_2 were taken and mixed thoroughly in an agate mortar and pestle. The resultant mixture was then heated in the temperature range 900–1100 °C for 5 h.

Characterization of $Zn_{2(1-x)}Mn_xSiO_4$ ($1 < x < 7$) mol % Phosphors: The phase purity and crystallinity of $Zn_{2(1-x)}Mn_xSiO_4$ ($1 < x < 7$) mol % were analyzed [1] by XRD (Rich Seifert, Germany). TGA and DTA studies were performed on the precursor gel. The FTIR spectral studies have been performed using a Perkin-Elmer spectrometer (spectrum 1000) with KBr pellets. The diffuse reflectance spectroscopic studies were carried out using an Ocean Optics USB2000 spectrophotometer. PL emission and excitation spectra were recorded at room temperature using (Fluorolog) fluorescence spectrophotometer equipped with a 450 W Xenon lamp as the excitation source.

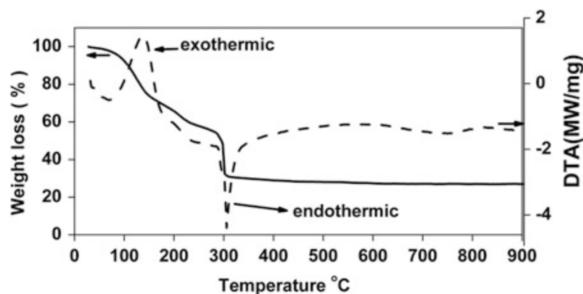

Fig. 12.1 TGA and DTA of the $Zn_{2(1-x)}Mn_xSiO_4$ ($x = 3$ mol %) precursor obtained at 110 °C

12.3 TGA and DTA Analysis

The existence of various phases during the formation of Zn_2SiO_4:Mn^{2+} green phosphor from the gel precursor was studied from the weight loss and the corresponding energy (release) exothermic or (absorbed) endothermic reaction from the TGA and DTA, respectively, as shown in Fig. 12.1. From the figure, an abrupt weight loss of about 72.73 % is seen up to the temperature of 300 °C.

This weight loss could be due to the evaporation of water and release of gases like nitrogen and carbon dioxide as a result of the occurrence of combustion reaction between $Zn(NO_3)_2$ and urea. Thereafter no weight loss takes place even up to 1200 °C resulting in the formation of pure oxide phases without any decomposable intermediates. Exothermic and endothermic reactions happen at 100 and 300 °C, respectively, and the latter reaction leads to the formation of ZnO phase. X-ray powder diffraction studies of gel combustion synthesized ceramic product revealed the evolution of various crystalline phases, with respect to variation of calcination temperature (Fig. 12.2).

No diffraction peaks due to Zn_2SiO_4 are observed for the sample calcined at 500 °C, and ZnO phase alone is seen which is found to persist up to 700 °C. Only

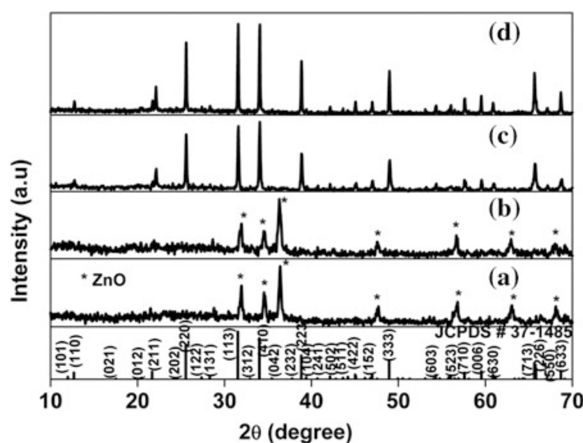

Fig. 12.2 Powder X-ray diffraction patterns of $Zn_{2(1-x)}Mn_xSiO_4$ ($x = 3$ mol %) phosphor combustion synthesized by technique followed by calcination at various temperatures. **a** 500 °C, **b** 700 °C, **c** 800 °C, and **d** 1100 °C for 5 h. The lower most pattern shows the standard JCPDS pattern for the parent compound

above 800 °C, the formation of Zn_2SiO_4 phase is seen. In any case, the synthesis temperature of 800 °C is about 300 °C lower than that required in the solid-state reaction method [17] and about 100 °C lower than that required in solution combustion synthesis method as reported earlier [16]. Upon further increase in the calcination temperature to about 1100 °C, the diffraction peak intensity has been found to increase indicating an increase in crystallinity of the phosphor. The XRD patterns obtained on the calcined powder phosphors confirmed the formation of rhombohedral structure with lattice constant ($a = 13.93$ Å and $c = 9.31$ Å) having ($R\bar{3}H$) space group (JCPDF 37-1485).

12.4 FTIR Measurements

The FTIR spectra of the precursor material obtained at 110 °C and subsequently calcined at different temperatures from 300 to 1100 °C for 5 h are shown in Fig. 12.3 [1]. The spectra obtained for gel heat treated sample at 110 °C can be split into two major components: the first region starts from 800 to 1125 cm^{-1} corresponding to the absorption of Si–O–Si due to the asymmetric stretching vibrations and the second part arises as a result of the presence of urea and acetate groups that show absorption in the range 1250–1750 cm^{-1} [38]. The sample heated at 300 °C shows a broad absorption band around 750–1250 cm^{-1} due to the

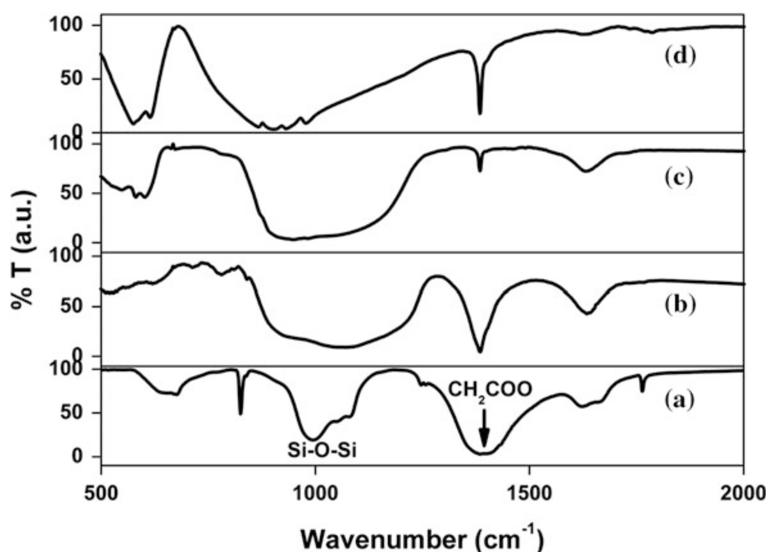

Fig. 12.3 FT-IR spectra of $Zn_{2(1-x)}Mn_xSiO_4$ ($x = 3$ mol %) phosphor precursors formed at 110 °C and heat treated at different temperatures. **a** 100 °C, **b** 300 °C, **c** 700 °C, and **d** 1100 °C for 5 h

Si–O–Si groups. The powders heated at 500 and 700 °C showed two broad peaks having maxima in the regions around 590 and 920 cm^{-1} that arise due to the asymmetric stretching vibration of SiO_4 group and symmetric stretching vibration of ZnO_4 group, respectively [39]. The SiO_4 group shows broadband absorption due to its amorphous nature. Importantly, the powder heated at 1100 °C shows that the main absorption peaks that fall in the frequency range between 500 and 1,200 cm^{-1} and a sharp absorption occurs at 1,384 cm^{-1}. The IR bands and the corresponding vibrational modes for willemite are 870 cm^{-1} (υ_1 SiO_4); 978, 934, and 900 cm^{-1} (υ_3 SiO_4); 578 cm^{-1} (υ_1 ZnO_4) and 616 cm^{-1} (υ_3 ZnO_4), where υ_1 corresponds to the total symmetric stretching, υ_3 is asymmetric stretching and υ_4 is asymmetric deformation [39, 40].

12.5 Photoluminescence Measurements

The room temperature PL excitation spectra, of $Zn_{2(1-x)}Mn_xSiO_4$ ($x = 3$ mol %) phosphors synthesized by urea gel combustion method and calcined at various temperatures, monitored at the emission wavelength ($\lambda_{em} = 522$ nm) are shown in Fig. 12.4a. It has been reported that Zn_2SiO_4 has a strong host absorption band with a maximum at 196 nm [18], which could not be detected in the present sample due to the limitations of the instrument (excitation source starts from 220 to 800 nm). A broadband strong excitation peak at 260 nm could be attributed to a charge transfer band (CTB) transition [that is from ground state of Mn^{2+} to the lower energy of conduction band (CB) (O^{2-})]. The excitation maxima beyond the CTB correspond to Mn^{2+} ions. The peak positions of these excitation maxima are determined by the crystal field experienced by Mn^{2+} ion as it occupies the Zn^{2+}

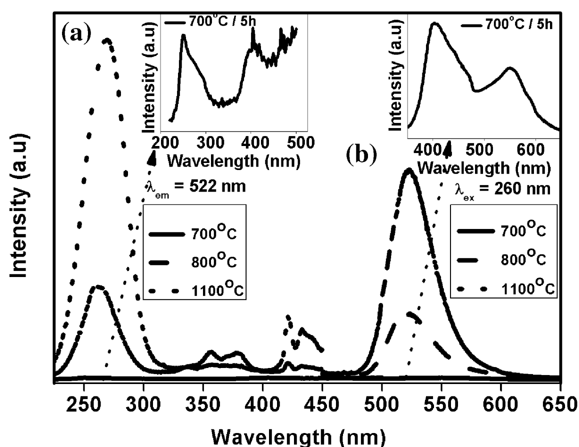

Fig. 12.4 Powder PL excitation (**a**) and emission (**b**) spectra of the urea gel combustion synthesized $Zn_{2(1-x)}Mn_xSiO_4$ ($x = 3$ mol %) phosphor. *Inset* shows the spectrum corresponding to the powder calcined at 700 °C for 5 h

site. As the Mn^{2+} ion experiences crystalline electric field and splits the $3d^5$ orbital into t_{2g} and e_g orbitals with electronic states $^6A_{1g}$, $^4A_{1g}$, ^4E_g, $^4T_{1g}$, $^4T_{2g}$ in which $^6A_{1g}$ is the lowest state, giving rise to five excitation peaks. Hence, in Fig. 12.4a, all the excitation peaks other than the CTB are due to various excited levels of Mn^{2+} ion, which will be either doublets or quartets and the luminescence occurs only due to spin forbidden transitions [1].

The room temperature PL emission spectra of $Zn_{2(1-x)}Mn_xSiO_4$ ($x = 3$ mol %) phosphors, calcined at various temperatures and monitored at the excitation wavelength of 260 nm, are shown in Fig. 12.4b. The sample calcined at 700 °C does not yield significant emission from Mn^{2+}. However, a feeble emission takes place at 400 nm possibly due to the recombination of electrons with holes (excitonic pair formation) of ZnO phase. In addition to this, another emission occurs at 550 nm which originates because of the ZnO:Zn phase (inset in Fig. 12.4b) which is another proof for the existence of ZnO defect phase. It is reported that the physical properties of a semiconductor such as the density of states, valence and CB do not change even in amorphous state since the gross feature of electronic states is determined by the short range order [41]. The phosphor heated at 800 °C shows the emission spectrum with a peak wavelength at 522 nm due to Zn_2SiO_4:Mn phase with a minor ZnO excitonic emission ($\sim$400 nm). Similarly, the phosphor heated at 1100 °C shows improvement in the green emission intensity as compared with that of phosphors heated at lower temperatures. This indicates that increasing the calcination temperature, increases emission intensity leading to the formation of highly crystalline defect free, Mn^{2+}-doped Zn_2SiO_4 willeminite phosphor. The Mn^{2+}-doped Zn_2SiO_4 phosphors excited under UV photons realize green emission that has been assigned to an electronic transition $^4T_1(G)$–$^6A_1(S)$ of Mn^{2+} with peak at 522 nm, which is a parity forbidden emission transition [42].

As mentioned above, due to similar ionic radii and oxidation states of Zn^{2+} and Mn^{2+} ions, Mn^{2+} can very well substitute for Zn^{2+} and distribute uniformly in the Zn_2SiO_4 lattice. Depending upon the type of crystal field, either a weak or strong splitting of excited d energy levels will occur. If the crystal field of Mn^{2+} is weak, then the splitting of the excited *d* energy levels will be small, giving rise to blue shift of the emission peak. On the other hand, strong crystal field results in Mn^{2+} emission at lower energy. In general, tetrahedrally coordinated Mn^{2+} (weak crystal field) ions give rise to green emission, whereas, octahedrally (or higher) coordinated Mn^{2+} (strong crystal field) ions show an orange to red emission [43]. Willeminite (α-Zn_2SiO_4) with phenacite structure that belongs to rhombohedral space group $R\bar{3}H$ has both Zn^{2+} and Si^{4+}, which are tetrahedrally coordinated to four oxygen atoms [44]. The Mn^{2+} ion in Zn_2SiO_4 has fourfold coordination since it replaces Zn^{2+} in the host and hence the green emission occurs.

12.6 Study on Mn Concentration Quenching: A Realization of Optimum Emission Intensity

The $Zn_{2(1-x)}Mn_xSiO_4$ phosphors were synthesized with various Mn concentrations which were then studied to understand the effect of Mn concentration on PL emission intensity (figure not shown). The study shows that increase of Mn content from 1 to 3 mol % increases the PL emission intensity, the maximum PL intensity is observed for 3 mol % of Mn-doped Zn_2SiO_4. Upon further increase in concentration to a value of 5 and 7 mol %, decrease in emission intensity was observed due to concentration quenching. Therefore, 3 mol % is found to be the optimum concentration. However, this value varies with respect to the method of synthesis [17, 22, 25]. In addition to the quenching phenomenon, a red shift of emission band occurring with the increase in Mn^{2+} concentration [45, 46] has been observed, which could be due to a stronger exchange interaction between Mn ion pairs [47, 48]. The influence of preparation methods of Zn_2SiO4:Mn powder phosphors that bring about structural and optical properties are reported by Thiyagarajan et al. [1].

12.7 Effect of Phosphor Preparation Routes and the Optical Properties

In order to compare the PL intensity of $Zn_{2(1-x)}Mn_xSiO_4$ ($x = 3$ mol %) phosphor based on the method of preparation, we have compared the urea sol–gel combustion synthesis phosphor with that of the phosphor prepared using solid-state reaction method. The XRD patterns of phosphors prepared by solid-state route calcined at 900 and 1100 °C respectively are shown in Fig. 12.5a, b, whereas, the XRD patterns of phosphors prepared by urea sol–gel route calcined at 900 and 1100 °C, respectively are shown in Fig. 12.5c, d. The phosphor prepared by solid-state reaction method at 900 °C contains ZnO and SiO_2 phases along with minor Zn_2SiO_4 phase. Even on heating to higher temperature (1100 °C), crystalline Zn_2SiO_4 phase could be seen along with impurity ZnO phase. Whereas, for the phosphor prepared by urea gel combustion synthesis method, single phase Zn_2SiO_4 could be realized even at 800 °C (refer Fig. 12.2c). Complete crystallization with increase in crystallinity is realized for samples heated through 900 to 1100 °C.

12.8 Dependence of PL Intensity with Respect to Synthesis Method

PL studies were performed on both (sol–gel and solid-state method) samples to compare the excitation and emission intensity with a motive to examine the dependence on preparation route. The annealing temperature was varied from 900

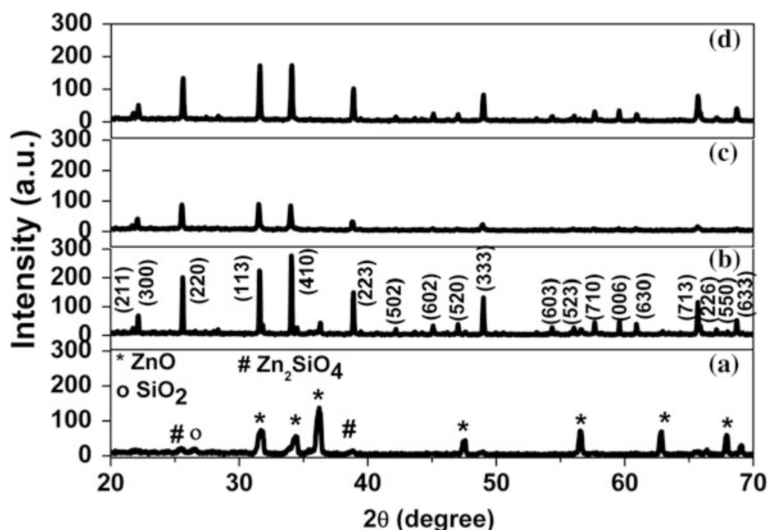

Fig. 12.5 X-ray diffraction patterns of $Zn_{2(1-x)}Mn_xSiO_4$ ($x = 3$ mol %) phosphor prepared by solid state reaction method (**a** and **b**) and urea gel combustion synthesis method (**c** and **d**), followed by calcination at various temperatures [**a**, **c**] 900 °C and [**b**, **d**] 1100 °C, respectively for 5 h

to 1100 °C in both cases. The origin of emission and excitation spectrum of $Zn_{2(1-x)}Mn_xSiO_4$ ($x = 3$ mol %) phosphor prepared by urea sol–gel chemical method is discussed in the above section (refer to Fig. 12.4a, b). In both the cases, the samples calcined at 1100 °C for 5 h is used as the standard for the comparative study. The phosphor prepared by urea gel method shows higher intensity compared to that of the phosphor prepared by solid-state method (figure not included). No green emission from Mn^{2+} is seen on the sample prepared using solid-state method at 900 °C. However, an intense defect emission from ZnO:Zn and the ZnO excitonic emission is seen. For the sample prepared by gel combustion an excellent green emission was observed whose emission intensity has been found to increase with increase in calcinations temperatures (up to 1100 °C). This occurs due to increase in crystallinity and homogeneous doping of Mn in Zn_2SiO_4 phosphors [1].

12.9 Pulsed Laser Deposited $Zn_{2(1-x)}Mn_xSiO_4$ ($x = 3$ mol %) Thin Film Phosphors and its Characterization Studies

In order to examine the structural and optical properties of Zn_2SiO_4:Mn phosphors in thin film form, different substrates were used to grow the Zn_2SiO_4:Mn thin films to optimize the growth conditions under various oxygen partial pressures (O_2 pp)

using the PLD technique. The Mn dopant content was taken as 3 mol %, that was already optimized while studying the Zn_2SiO_4:Mn powder phosphors. A pulsed Nd:YAG laser with a fluence of 2.0 J cm^{-2} was used for the growth of thin film on Si (100) and quartz substrates. The chamber was initially evacuated to 3×10^{-5} Torr. Oxygen gas of purity ~99.9 % was then introduced so as to study the change in the emission properties with respect to variations in O_2 pp ~ 100, 300, 500, and 700 mTorr. The Zn_2SiO_4:Mn target was rotated at a constant speed during the impingement of the pulsed laser beam. The time and the temperature of deposition were fixed as 10 min and 750 °C, respectively. After the deposition, the films were in situ annealed for 1 h under the same conditions as that used during the growth process [2].

Figure 12.6 shows the XRD patterns of $Zn_{2(1-x)}Mn_xSiO_4$ ($x = 3$ mol %) phosphor thin film deposited under different O_2 pp (100, 300, 500, and 700 mTorr) at a fixed substrate temperature (750 °C). The patterns show that the diffraction planes correspond to the Zn_2SiO_4 phase which crystallizes at a temperature which is 50 °C less than that required for the bulk counterpart [1]. It is clear that the film grown at 300 mTorr O_2 pp shows high intense reflections indicating a relatively better crystallinity compared to that of films grown at lower (100 mTorr) and at higher oxygen partial pressures (500 and 700 mTorr). The crystallite size calculated using the Scherrer formula for films grown at 100, 300, and 500 mTorr are found to be approximately 79, 94, and 75 nm, respectively. Moreover, the film grown at 300 mTorr O_2 pp gives the highest PL intensity (discussed below), corroborating well with the XRD result and hence it is considered that 300 mTorr is the optimum O_2 pp. The reflection at $2\theta = 51.75°$ is due to the (003) plane of SiO_2.

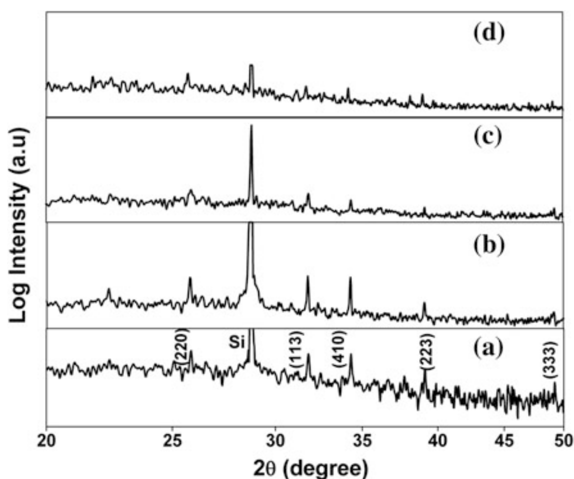

Fig. 12.6 X-ray diffraction patterns of the $Zn_{2(1-x)}Mn_xSiO_4$ ($x = 3$ mol %) thin film phosphors grown on Si substrate at 750 °C under various partial pressures; **a**) 100 mTorr, **b**) 300 mTorr, **c**) 500 mTorr, and **d**) 700 mTorr followed by in situ annealing for 1 h at the same temperature and atmosphere

12.10 Influence of O_2 Partial Pressure on PL Properties

Figure 12.7a, b shows the PL emission spectra of $Zn_{2(1-x)}Mn_xSiO_4$ ($x = 3$ mol %) thin film phosphors and the image of green emission of the thin film phosphor grown on Si substrate (dark portion) excited with UV- 254 nm [2]. Thin films grown at all the oxygen pressures show green emission. The film grown at 300 mTorr shows maximum PL intensity and is seen to decrease for films grown at higher O_2 pp. The variation in spectral shape between the films grown at the optimized O_2 pp (300 mTorr) and the other films (grown at 100, 500, and 700 mTorr) is observed in the region between 320 and 480 nm along with the appearance of ZnO excitonic emission. The film grown at 300 mTorr has shown a predominant emission peak at 399 nm that originates due to electron-hole recombination in ZnO lattice. Minor peaks accompany the major peak at 377 and 420 nm. Whereas, for the films grown below and above the optimized O_2 pp (300 mTorr), the above peaks appear with less intensity. The occurrence of multiple blue emissions are attributed to various defect levels within ZnO namely shallow donor levels formed due to oxygen vacancies and interstitial Zn [49]. The origin of multiple emissions can be attributed to zinc vacancies [50] and interstitial oxygen [51].

12.11 Improvement in Certain Intrinsic Properties Upon Ex-situ Annealing of Thin Films: Crystal Structure and Photoluminescence Intensity Analysis

Systematic studies were performed to examine the effect of ex-situ annealing at atmospheric pressure on the structural and luminescent properties of $Zn_{2(1-x)}Mn_xSiO_4$ ($x = 3$ mol %) at various temperatures. As seen in Fig. 12.7

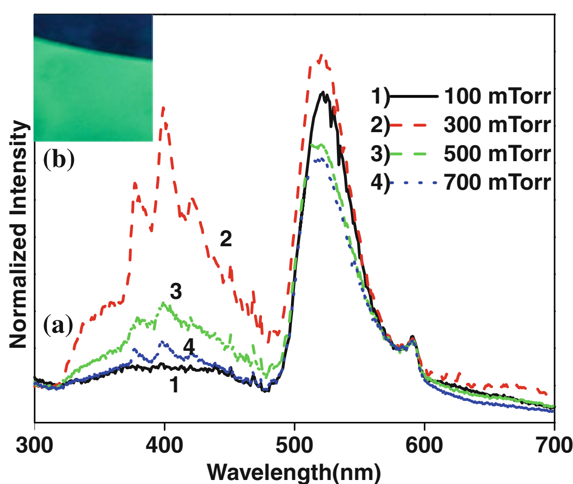

Fig. 12.7 **a** Dependence of PL intensity on O_2 pp of $Zn_{2(1-x)}Mn_xSiO_4$ ($x = 3$ mol %) thin film grown on Si substrate and **b** picture of green PL emission of the thin film phosphor grown on Si substrate (*dark portion*) excited with UV- 254 nm (reprinted after permission from Elsevier Publishers group [2])

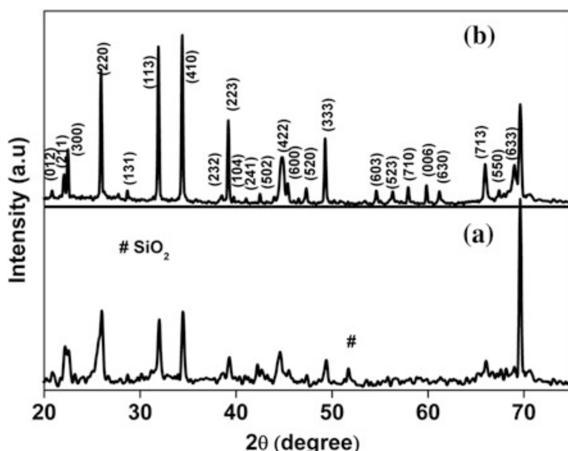

Fig. 12.8 X-ray diffraction patterns of $Zn_{2(1-x)}Mn_xSiO_4$ ($x = 3$ mol %) thin film phosphor grown on silicon substrate at 700 °C in 300 mTorr oxygen, followed by ex-situ annealing for 1 h at **a**) 800 °C and **b**) 900 °C in air

even though PL emission occurs, the phase formation is not good in the as-deposited condition. Hence, the thin films grown at the optimized conditions were ex-situ annealed in air at 800 and 900 °C for 1 h [2]. The XRD patterns recorded on these samples are shown in Fig. 12.8. The XRD patterns reveal that the film grown at 800 °C shows diffraction peaks corresponding to SiO_2 and Zn_2SiO_4 phases. These peaks have been found to match well with those of the standard pattern (JCPDS No.37-1485) for Zn_2SiO_4 phase that crystallizes in the willemite structure. The single phase of crystalline Zn_2SiO_4 host lattice is attained at 900 °C without any secondary phase inclusions.

A comparative study of PL excitation and emission spectra has been analyzed for ex-situ annealed Zn_2SiO_4:Mn thin films in air up to 900 °C [2]. Figure 12.9a, b shows such patterns in which excitation spectra is monitored at $\lambda_{em} = 522$ nm whereas emission spectra is monitored at $\lambda_{em} = 251$ nm. PL emission occurs because of the transitions of $3d^5$ electrons of Mn^{2+}. The spectra showed an intense and a broadband peak, which is ascribed to the CTB (strong dipolar e → t_2) of Mn^{2+} in Zn_2SiO_4 system as reported by Mishra et al. [52]. With increase in temperature from 700 to 900 °C, an increase in CTB peak excitation intensity along with other bands of Mn^{2+} (*d*-*d*) transition at higher wavelength has also been observed. These multiple excitations are due to the splitting of the ^4D and ^4G levels because of the crystal field effect, as discussed by Orgel diagram for Mn^{2+} [42, 45, 53]. The electrons at the $^6A_1$ (^6S) ground state of Mn^{2+} ions are photo-excited to the CB of Zn_2SiO_4 and the free electrons in the CB relax back to the $^4T_1(^4G)$ excited state through a non-radiative process [21]. Finally, this is followed by radiative transition from the $^4T_1(^4G)$ excited state to the $^6A_1$ (^6S) ground state, emitting green light (522 nm). The energy level scheme of Zn_2SiO_4:Mn in which the excitation through CTB and the corresponding radiative and non-radiative transitions to realize green emission is shown in Fig. 12.9c.

As the temperature increases, the intensity of the green emission increases progressively. This result indicates that defect-free crystalline Mn^{2+}-doped

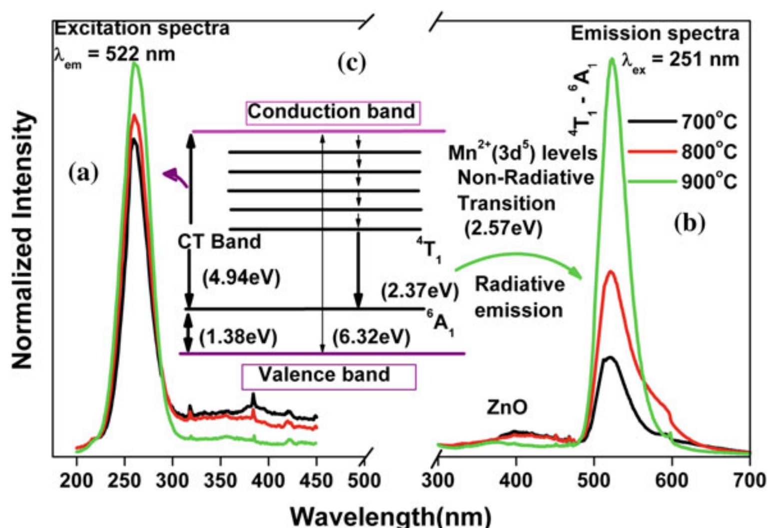

Fig. 12.9 **a**) PL excitation and **b**) emission spectra of $Zn_{2(1-x)}Mn_xSiO_4$ ($x = 3$ mol %) thin film phosphor grown on Si substrate at 700 °C followed by ex-situ annealing at different temperatures in air and **c**) corresponding energy level scheme to explain the excitation and emission spectra (Reprinted after permission from Elsevier Publishers group [2])

Zn_2SiO_4 phosphor thin films are formed using PLD technique and on ex-situ annealing.

12.12 White Light Emitting Material Synthesis Using Near Ultraviolet Light Excitation on Zinc Oxide–Silicon Dioxide Nanocomposite

This part of the work reports on white light generation using ZnO–SiO_2 nanocomposite coupled with UV 405 and 465 nm LEDs. To the best of our knowledge we are first people to report on ZnO–SiO_2 nanocomposites that are suitable for white LED application. The ZnO–SiO_2 nanocomposites were prepared using urea sol–gel combustion synthesis route [3]. This synthesis route involves dissolving zinc nitrate, urea and tetraethoxy silane in ethanol. In order to form a sol–gel, nitric acid is used as an acid catalyst and the pH of the solution was maintained at 3. In the ZnO–SiO_2 nanocomposites, the ZnO concentration was varied from 0.25 to 1 mol with respect to 1 mol of SiO_2. For a stoichiometric conversion of zinc nitrate to zinc oxide, the concentration of urea was calculated with respect to zinc nitrate based on the self-propagating high temperature combustion synthesis [54]. The above mixed solution was stirred for 10 h to get a transparent gel and the gel was slowly evaporated to remove the ethanol and then dried at 100 °C. Then the

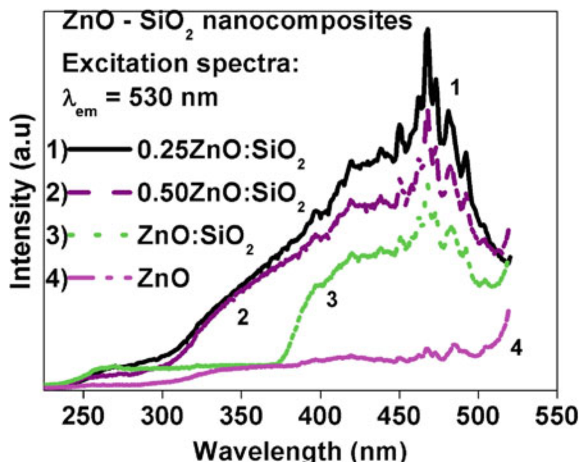

Fig. 12.10 PL excitation spectra of ZnO–SiO_2 with different ZnO content

dried mass was heat treated at 300–700 °C for 3 h. During the heat treatment, the urea in the gel induces the zinc nitrate to decompose to zinc oxide nano-crystals at low temperature. Among the heat treated samples at various temperatures, the composite which was heat treated at 300 °C only showed maximum PL emission intensity. All the ZnO–SiO_2 nanocomposites were characterized by XRD, SEM, DRS, and PL excitation and emission spectroscopy. In order to study the EL emission spectra of the composites for white LED applications, the materials were mixed with epoxy resin and coated over the 405 and 465 nm LEDs. The spectra and CIE color co-ordinate were measured using the Ocean Optics Spectrophotometer, USB 2000 at room temperature at the rated current of 20 $mAcm^{-2}$.

Figure 12.10 shows the PL excitation spectra of the ZnO–SiO_2 nanocomposites for various values of ZnO content with a fixed concentration of SiO_2 [3]. From the figure, it can be seen that at the lower concentration of ZnO (0.25 mol), the composite has yielded the highest excitation intensity and when the concentration increased, the intensity decreased. The excitation intensity of 0.25ZnO–SiO_2 is almost seven times higher than that of ZnO. Moreover, it is interesting to observe that the composite showed excitation spectra in the wavelength of 260–480 nm with a maximum intensity at 465 nm, a wavelength at which the commercial white LEDs are fabricated.

The excitation wavelengths of the composites over a wide range of values are further confirmed by diffuse reflectance spectra as shown in Fig. 12.11 [3]. The spectra confirm that the composites consisting of different ratios of ZnO over SiO_2 did not yield well defined band edges as compared to bulk commercial ZnO. It is seen that the spectra showed strong defect absorption in the near UV and blue wavelength regions for a lower content of ZnO in the matrix. This result confirms that the composites can be excited in the UV to blue wavelength range.

It was observed earlier by Bouguerra et al. [32] that ZnO shows a much strong intense band gap excitation (378 nm) than the defect excitation at blue light

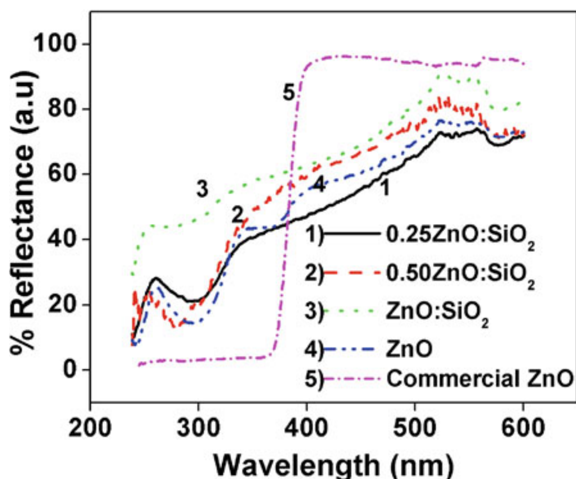

Fig. 12.11 Diffuse reflectance spectra of ZnO–SiO_2 composites with different ZnO content

region, presumably due to V_o (oxygen vacancy) defects. However, in the ZnO–SiO_2 nanocomposites, we have observed a strong defect excitation in the region of 260–480 nm due to dominant oxygen vacancies created by highly defective ZnO obtained by sol–gel combustion synthesis.

Figure 12.12 shows PL emission spectra of ZnO–SiO_2 nanocomposites recorded at the maximum excitation wavelength at 465 nm. The spectra show broadband emission in the wavelength range 465–650 nm with an emission maximum at 525 nm. PL emission spectra of 0.25ZnO–SiO_2 nanocomposite showed a well defined broad peak with maximum intensity. The same broadband emission spectra were also observed for this composite at different emission maxima at different excitation wavelengths in the range from 260 to 465 nm. It is observed that at high-energy excitation (UV region: 260–400 nm), the composite showed a less intense broadband emission between 400 and 600 nm with dominant blue emission [3]. At low energy excitation (400–480 nm), a dominant broadband greenish-yellow defect emission is observed. It is interesting to observe that all these defect emission peaks exhibited a major red shift with increase in excitation wavelength and no characteristic excitonic emission is observed from ZnO. This indicates that most of the excited carriers recombine at deeply trapped sites and are attributed to the radiative recombination of electron from shallow donor levels created by various oxygen vacancies in the valence band of ZnO and emit in the blue and greenish region [31]. This is due to the reason that there are several optically active defect centers formed in ZnO lattice in SiO_2 matrix during the combustion synthesis which produce significant amount of porosity due to the sudden release of high energy gases [55]. This result contradicts the earlier reports in which ZnO trapped in an oxygen-rich SiO_2 matrix enhances the UV emission and reduces the defect emission by surface passivation [34]. In our case, ZnO in SiO_2 matrix shows a strong and stable blue and greenish-yellow defect emission depending on the excitation. This is due to the reason that the growth of ZnO by

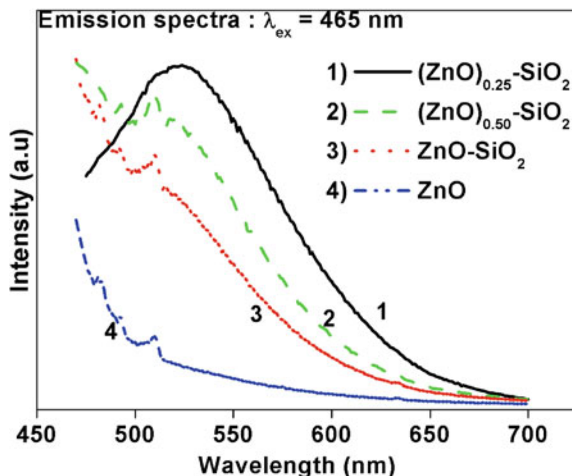

Fig. 12.12 PL emission spectra of ZnO–SiO_2 nanocomposites with various ZnO content at ($\lambda_{ex} = 465$ nm)

combustion of zinc nitrate by urea in a confined SiO_2 matrix creates more surface defects, which leads to an increase in emission intensity, because of the number moles of gases (N_2, CO_2, H_2O) evolved. This was confirmed by the preparation of the same ZnO–SiO_2 composite without using urea resulting in the same defect emission but with poor emission intensity. Further, it is also confirmed that ZnO prepared by using zinc acetate as a zinc source along with urea and silica gel, showed poor emission. Hence, it is concluded that the presence of nitrate supports the gaseous combustion reaction in the presence of urea at low temperature (300 °C) to form ZnO–SiO_2 nanocomposite with high surface–volume ratio. Even though the samples exhibit strong luminescence due to highly defective ZnO, the XRD patterns do not reveal any intense diffraction peaks, possibly because of the nano-scale dispersion of ZnO in the amorphous SiO_2 matrix [3].

Figure 12.13 shows the scanning electron microscope images of porous ZnO–SiO_2 nanocomposites obtained by the combustion of zinc nitrate and urea in the silica gel, which show the growth of ZnO nano rods and particles dispersed in the amorphous silica matrix. The energy-dispersive X-ray analysis of the composite confirms the presence of Zn, O, and Si in the nanocomposites.

Figure 12.14a, b shows the white light EL emission spectra of ZnO–SiO_2 nanocomposites with various concentrations of ZnO along with one mole SiO_2 (0.25:1, 0.5:1, and 1:1) and with that of ZnO alone obtained by urea based combustion synthesis, excited by the near-UV LED (404 nm) and blue LED (465 nm), respectively at the rate of 20 $mAcm^{-2}$. The EL emission spectra recorded at the excitation of 404 nm LED shows a wide cover of the entire visible wavelength which starts from violet to green–yellow regions with a full width at half maximum of 115 nm. The inset picture shows the white light generated by coating the 0.25ZnO–SiO_2 nanocomposites over the 404 nm commercial LED. As observed from the PL excitation and emission spectra of 0.25ZnO–SiO_2 nano-composites, the white light realized through EL emission (404 nm LED pumped

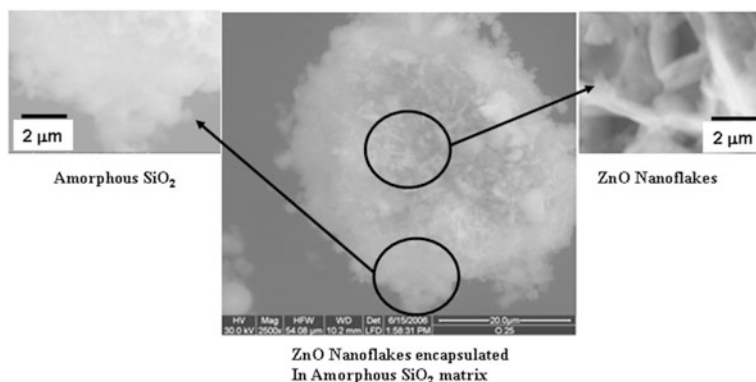

Fig. 12.13 Scanning electron microscopy images of ZnO–SiO_2 nano-composite prepared at 300 °C

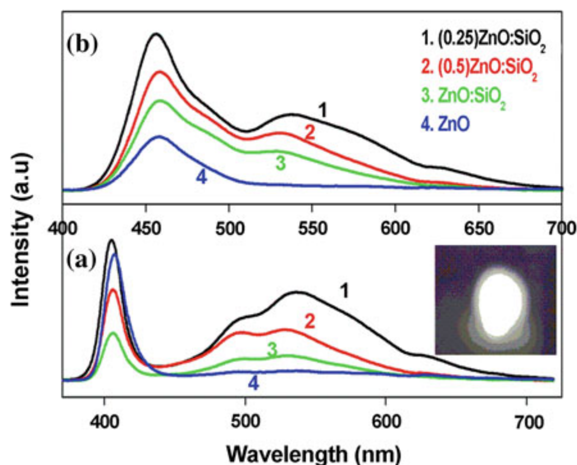

Fig. 12.14 **a**, **b**) EL spectra of ZnO as well as ZnO–SiO_2 nanocomposites with various contents of ZnO at $\lambda_{ex} = 404$ and 465 nm LED source, respectively. *Inset* in **a**) shows a bright white light in 0.25ZnO–SiO_2 composite (Reprinted after permission from Elsevier Publishers group [3])

nanocomposites) is greatly enhanced while compared to the rest of ZnO–SiO_2 composite and ZnO alone. Figure 12.14b depicts the EL emission spectra recorded at an excitation wavelength of 465 nm for the various ZnO–SiO_2 composites and compared with the commercial white LEDs coated with YAG:Ce phosphor. From the spectra, it can be seen that the composition of 0.25ZnO–SiO_2 yields the highest EL intensity and the emission spectrum is the same as that obtained from a commercial white LED. The ZnO–SiO_2-based white LED showed bluish-green white light and its emission efficiency was only 10 % when compared to the commercial white LEDs. Although the PL efficiency of ZnO trapped in SiO_2 matrix is low, the possibility of using ZnO–SiO_2 nanocomposite, as a phosphor material for near UV and blue light converted white LED, is seen to be feasible.

From the above spectral studies, it is observed that an enormous quantity of ZnO nanoparticles in SiO_2 matrix reduces the efficiency of the white light emission whereas the minimum quantity with high surface area enhances the emission intensity.

Figure 12.15a, b shows the schematic energy level diagram of different defect levels in ZnO nanocrystals embedded in an amorphous SiO_2 matrix and Lorentzian curve fit by fitting the PL emission spectra using a Lorentzian equation [3]. Deconvoluting the PL emission peaks reveal six spectral peaks corresponding to excitonic emission (P_1) and defect emission viz., violet (P_2), blue (P_3), green (P_4), deep green (P_5), and orange (P_6) emission from various ZnO trap levels. The violet–blue emission is attributed to the existence of two V''_{Zn} defects, green emission is attributed to the radiative recombination of electrons from the CB edge to V'_{Zn} and the deep green and orange emission is related to the transition of electrons from CB to the deeply trapped holes ($V_{\ddot{O}}$) in the bulk ZnO nanoparticles [32].

Figure 12.16 shows the CIE chromaticity coordinate (*x*, *y*) of ZnO–SiO_2 nanocomposites measured at the excitation of 405 and 465 nm LEDs using ocean optics spectrophotometer and compared with commercial YAG based white LEDs. At 465 nm LED excitation, all the nanocomposites show almost the same coordinate (*x*, *y*) values irrespective of ZnO concentration. The CIE color coordinates (0.216, 0.143) show a large difference when compared with that of commercial GaInN-YAG:Ce combined white LEDs (0.295, 0.275). However, at 404 nm LED excitation, the composite shows a CIE coordinate (0.270, 0.308), which is close to the standard white light (0.333, 0.333) coordinates. Therefore, the white light realized by using 0.25ZnO–SiO_2 nanocomposites coated on 404 nm emitting GaInN based UV LED can be useful for the solid-sate white light emitting diode applications.

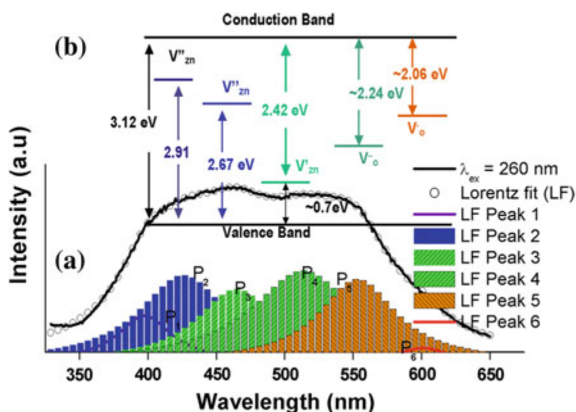

Fig. 12.15 **a**) Lorentzian curve fit of 0.25ZnO:SiO_2 spectrum excited at 260 nm and **b**) Schematic of the defect levels in ZnO nanocrystals embedded in amorphous SiO_2 matrix: Energy level diagram (Reprinted after permission from Elsevier Publishers group [3])

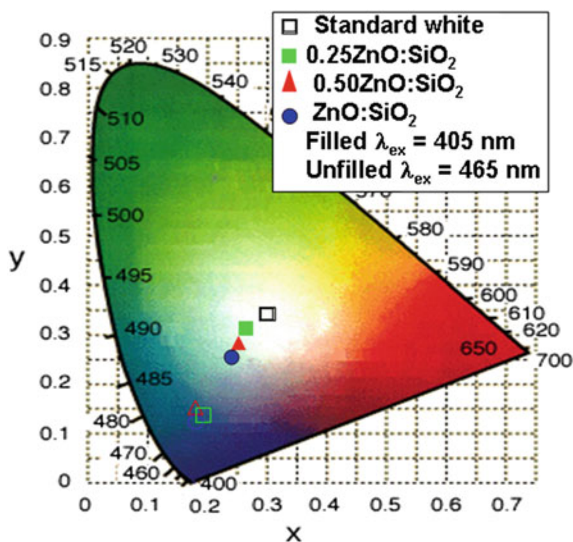

Fig. 12.16 CIE chromaticity co-ordinates for various contents of ZnO in SiO_2 nanocomposites measured at the excitation of 404 nm (*filled symbol*) and 465 nm (*unfilled symbol*) LED source (Reprinted after permission from Elsevier Publishers group [3])

12.13 Conclusions

Mn^{2+}-doped Zn_2SiO_4 green emitting phosphors were prepared by urea sol–gel combustion synthesis and conventional solid-state reaction method whose crystallinity and PL properties were compared. TGA and DTA studies of sol–gel precursor showed the presence of decomposable products by means of weight loss as a function of temperature and the existence of different phases throughout the reaction process. Lattice parameters calculated from XRD confirmed that $Zn_{2(1-x)}Mn_xSiO_4$ crystallizes in a rhombohedral structure with a space group of $R\bar{3}H$. ZnO nano flakes dispersed in an amorphous silica matrix were prepared. The PL emission intensity was optimized and the maximum green emission intensity was achieved at 3 mol % of Mn concentration along with red shift. Occupation of Mn in tetrahedrally coordinated site of Zn_2SiO_4 is seen to be responsible for green emission. The phosphor prepared by urea gel combustion synthesis results in an enhancement in spectral properties suitable for display applications.

Thin film deposition and luminescent properties of PLD-grown Zn_2SiO_4:Mn ($x = 3$ mol %) phosphors have been systematically studied with respect to variation in oxygen partial pressure to achieve optimal emission intensity. It was observed that films grown on Si substrate and in situ annealed at 300 mTorr O_2 pp exhibited better PL properties. In the in situ annealed film, the luminescence intensity occurs between 320 and 480 nm as a result of ZnO excitonic emission. Thin films ex-situ annealed to higher temperatures (900 °C) showed a good improvement in PL properties.

ZnO–SiO_2 nanocomposites synthesized by sol–gel combustion emit a stable broadband greenish-yellow light emission at UV (260–360 nm), near UV (360–400 nm), violet (400–430 nm) and blue light (430–470 nm) excitation wavelengths. The EL intensity of 0.25ZnO–SiO_2 composition showed much higher intense white light compared to other concentration of the ZnO (0.50 and 1.00) in ZnO–SiO_2 nanocomposites. The phosphor-coated-white LED fabricated using 404 and 465 nm LED with ZnO–SiO_2 nanocomposite exhibited CIE chromaticity coordinates (0.304, 0.308) and (0.216, 0.143), respectively. Therefore, white LED fabricated using 404 nm UV LED with optimized nanocomposite can be considered as a potential candidate for solid-state lighting device application.

References

1. P. Thiyagarajan, M. Kottaisamy, M.S. Ramachandra Rao, J. Electrochem. Soc. **154**(4), H297–H303 (2007)
2. P. Thiyagarajan, M. Kottaisamy, M.S. Ramachandra Rao, Scripta Mater. **57**, 433–436 (2007)
3. P. Thiyagarajan, M. Kottaisamy, M.S. Ramachandra Rao, Scripta Mater. **59**, 722–725 (2008)
4. J.A. Speer, P.H. Ribbe, in *Reviews in Mineralogy*, vol. 5, 2nd ed. by P.H. Ribbr (Mineralogical Society of America, Washington, 1982), p. 429
5. J. McKittrick, L.E. Shea, C.F. Bacalski, E.J. Bosze, Displays **19**, 169 (1999)
6. Y.C. Kang, I.W. Lenggoro, S.B. Park, K. Okuyama, J. Phys. Chem. Solids **60**, 1855 (1999)
7. L.E. Shea, J. McKittric, O.A. Lopez, J. Am. Ceram. Soc. **79**, 3257 (1996)
8. S. Shionoya, W.M. Yen (eds.), *Phosphor Handbook* (Phosphor Research Society (Japan), CRC, Boca Raton, 1999)
9. H.C. Swart, T.A. Trottier, J.S. Sebastian, S.L. Jones, P.H. Holloway, J. Appl. Phys. **83**, 4578 (1998)
10. T. Minami, T. Miyata, S. Tanaka, I. Fukuda, Jpn. J. Appl. Phys., Part 2, **30**, L117 (1991)
11. I. Kandarakis, D. Cavouras, P. Prassopoulos, E. Kanellopoulos, C.D. Nomicos, G.S. Panayiotakis, Appl. Phys. A **67**, 521 (1998)
12. T. Miyata, T. Minami, S. Tanaka, I. Fukuda, Digest of Technical Papers 1991 SID International Symposium, p. 286 (1991)
13. T. Minami, Solid-State Electron. **47**, 2237 (2003)
14. T.S. Ahmad, M. Haase, H. Weller, Mater. Res. Bull. **35**, 1869 (2002)
15. K. Su, D.T. Tilley, M.J. Sailor, J. Am. Chem. Soc. **118**, 3459 (1996)
16. Q.H. Li, S. Komarneni, R. Roy, J. Mater. Sci. **30**, 2358 (1995)
17. T.H. Cho, H.J. Chang, Ceram. Int. **29**, 611 (2003)
18. J. Lin, D.U. Sanger, M. Mennig, K. Barner, Mater. Sci. Eng. *B*, **B64**, 73 (1999)
19. Y.C. Kang, S.B. Park, Mater. Res. Bull. **35**, 1143 (2000)
20. M. Cich, K. Kim, H. Choi, S.T. Hwang, Appl. Phys. Lett. **73**, 2116 (1998)
21. L. Xiong, J. Shi, J. Gu, L. Li, W. Huang, J. Gao, M. Ruan, J. Phys. Chem. B **109**, 731 (2005)
22. R.P. Sreekanth Chakradhar, B.M. Nagabhushana, G.T. Chandrappa, K.P. Ramesh, J.L. Rao, J. Chem. Phys. **121**, 10250 (2004)
23. Y. Hao, Y. Wan, Z. Zhang, J. Rare Earths, **21** (Suppl), 28 (2003)
24. V.B. Bhatkar, S.K. Omanwa, S.V. Moharil, Phys. Status Solidi A **191**, 272 (2002)
25. R. Morimo, K. Matae, Mater. Res. Bull. **24**, 175 (1989)
26. J. Lin, Q. Su, J. Mater. Chem. **5**, 1 (1996)
27. M. McLaughlin, H. Sakeck, P. Macquire, W. Graham, J. Molloy, T. Morrow, S. Lavery, J. Anderson, Appl. Phys. Lett. **63,** 1865 (1993)

28. D. Kumar, J. Sankar, K.G. Cho, V. Craciun, R.K. Singh, Appl. Phys. Lett. **77**(16), 2518 (2000)
29. X.L. Wu, G.G. Siu, C.L. Fu, H.C. Ong, Appl. Phys. Lett. **78**, 2285 (2001)
30. S. Shionoya, W.M. Yen (eds.), *Phosphor Hand Book* (CRC press, Boca Raton, 1999), p. 565
31. L. Guo, J.X. Cheng, X.Y. Li, Y.J. Yan, S.H. Yang, C.L. Yang, J.N. Wangand, K. Wu, Mater. Sci. Eng. **C-16**, 123 (2001)
32. Y.-Y. Peng, T.-E. HSieh, C.-H. Hsu, Nanotechnology **17**, 174–180 (2006)
33. Z. Fu, B. Yang, L. Li, W. Dong, C. Jia, W. Wu, J. Phys.: Condens. Matter **15**, 2867 (2003)
34. Y. Kayanuma, H. Momiji, Phys. Rev. B **41**, 10261 (1990)
35. M. Bouguerra, M. Samah, M.A. Belkhir, A. Chergui, L. Gerbous, G. Novet, D. Chateigner, R. Madelon, Chem. Phys. Lett. **425**, 77 (2006)
36. B.D. Yao, H.Z. Shi, H.J. Bi, L.D. Zhnag, J. Phys.: Condens. Matter **12**, 6265 (2000)
37. S.R. Jain, K.C. Adiga, V.R. Paiverneker, Combust. Flame **40**, 71 (1981)
38. D.R. Brezinski (ed.), *An Infrared Spectroscopy Atlas for the Coatings Industry*, vol. 1, 4th edn. (Federation of Society for Coating Technology, Philadelphia, 1991)
39. C.C. Lin, P. Shen, J. Non-Cryst, Solids **281**, 171 (1994)
40. G.T. Chandrappa, S. Ghosh, K.C. Patil, J. Mater. Synth. Process. **7**, 273 (1999)
41. S. Kondo, T. Itoh, T. Saito, Phys. Rev. B **57**, 13235 (1998)
42. A. Morell, N. El Khiati, J. Electrochem. Soc. **140**, 2019 (1993)
43. G. Blasse, B.C. Grabmaier (eds.), *Luminescent Materials* (Springer, Berlin, 1994)
44. H. Kigperking, M.J. Sienko, J. Chem. Phys. **46**, 2398 (1967)
45. C. Barthou, J. Benoit, P. Benalloul, A. Morell, J. Electrochem. Soc. **141**, 524 (1994)
46. A.L.N. Stevels, A.T. Vink, J. Lumin. **8**, 443 (1974)
47. C.R. Ronda, T. Amrein, J. Lumin. **69**, 245 (1996)
48. A.P. Wink, M.A. deBruin, S. Roke, P.S. Peijzel, A. Meijerink, J. Electrochem. Soc. **148**, E313 (2001)
49. D.H. Zhang, Z.Y. Xue, Q.P. Wang, J. Phys. D **35**, 2837 (2002)
50. Z.X. Fu, C.X. Guo, B.X. Lin, G.H. Liao, Chin. Phys. Lett. **15**, 457 (1998)
51. W. Li, D.S. Mao, Z.H. Zheng et al., Surf. Coat. Technol. **128–129**, 346 (2000)
52. K.C. Mishra, K.H. Johnson, B.G. DeBoer, J.K. Berkowitz, J. Olsen, E.A. Dale, J. Lumin. **47**, 197 (1991)
53. L.E. Orgel, J. Chem. Phys. **23**, 1004 (1955)
54. S.R. Jain, K.C. Adigao, V.R. Pai Verneker, Combust. Flame **40**, 1 (1981)
55. M. Kottaisamy, M. Mohan Rao, D. Jeyakumar, J. Mater. Chem. **7**, 345 (1997)

Chapter 13
Zinc Oxide Nanomaterials as Amylase Inhibitors and for Water Pollution Control

Rohini Kitture, Sandip Dhobale and S. N. Kale

Abstract Zinc oxide has been one of the most popular materials in the range of inorganic materials. In its bulk form, it has shown promises to the coatings and device industries. With the advent of nanotechnology, ZnO has expanded its range of applications to sensors, semiconductors, magnetic semiconductors, cosmetics, and also biomedicine. Last decade has witnessed tremendous research in all these domains, especially due to widening of the band gap and the ability to manipulate the nanostructures in various sizes and shapes. Some issues are still being evaluated; such as evolution of magnetic semiconducting nature and *p*-type or *n*-type origins of this fascinating material. However, in the biomedical domain, the material has shown interesting promises; namely as antimicrobial, antioxidant, and also as a sensor. In this article, we discuss on the ability of ZnO nanoparticles to work as amylase inhibitors and also as an efficient water pollution controlling agent. The ZnO candidature has been compared with TiO_2 nanoparticles for water treatment. The amylase inhibitor activity has been compared with standard drug's ability to control the conversion of starch to sugar. A strategy to make ZnO work as a probable selective biosensor is also discussed.

13.1 Introduction

ZnO as a fascinating material: Zinc oxide has been a material of tremendous scientific research due to its property range, ease of synthesis, and its long shelf life. As is known, Zinc oxide is a wide band gap (3.4 eV) II–VI compound

R. Kitture · S. Dhobale
Department of Electronic-Science, Fergusson College, Pune 411004, India

S. N. Kale (✉)
Department of Applied Physics, Defence Institute of Advanced Technology (DIAT-DU), Girinagar, Pune 411025, India
e-mail: sangeetakale2004@gmail.com

M. S. R. Rao and T. Okada (eds.), *ZnO Nanocrystals and Allied Materials*, Springer Series in Materials Science 180, DOI: 10.1007/978-81-322-1160-0_13,
© Springer India 2014

semiconductor, along with the array of other binary compounds like of Cd and Hg with O, S, Se, and Te and their ternary or quaternary alloys. Most of the group II–VI binary compound semiconductors crystallize in either cubic zinc blende or hexagonal-wurtzite structure, where each cation is surrounded by four anions at the corners of a tetrahedron, and vice versa. Although this tetrahedral coordination is typical of sp^3 covalent bonding, these materials also have appreciable ionic character. ZnO is known to be stable in various structural forms such as wurtzite (B4), zinc blende (B3), and rocksalt (B1) as schematically shown in Fig. 13.1. However, the wurtzite phase is known to be thermodynamically stable under ambient conditions. The zinc-blende ZnO structure can be stabilized only by growth on cubic substrates, and the rocksalt NaCl structure may be obtained at relatively high pressures. Özgür et al. have elaborated this analysis in their documentation [1].

ZnO, with its wide bandgap, possess large excitons binding energy of 60 meV which is appreciably larger in comparison with that of its competitor GaN which is just 25 meV. Apart from excitons binding energy, ZnO has several other advantages like, having a native substrate, ease of wet chemical processing, and not the least that it is more resistant to radiation damage. This makes ZnO a better candidate for optoelectronic lasing applications. Also it has got several remarkable applications [2] in high density data storage systems, solid-state lighting (where white light is obtained from phosphors excited by blue or UV light-emitting diodes), secure communications, integrated sensors, drug delivery agents and many more. The material possesses high refractive index, high thermal conductivity, semiconducting nature, and good binding ability. Hence, the material is being harnessed for such applications, both in its single crystal as well as polycrystalline forms.

Materials in nanoforms: With the advent of Nanotechnology, the researchers have obtained a handle over the growth protocols to make the materials in smaller dimensional regime. The growth can be controlled in such a way that the shape and size can be engineered. Various wet and dry synthesis tools have been utilized and almost all elements in the periodic table have been tried to convert in their nano

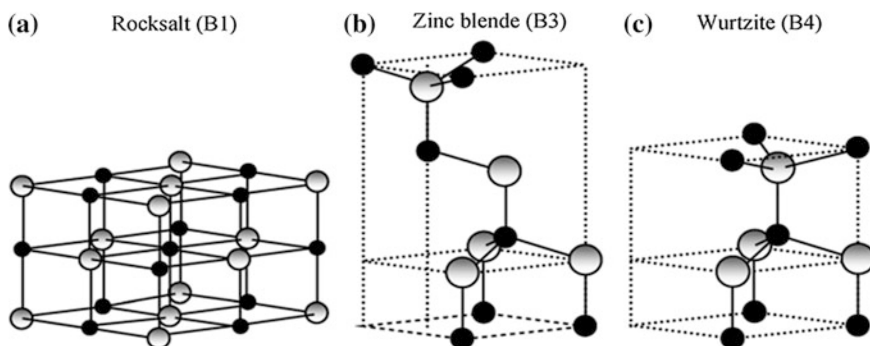

Fig. 13.1 Stick-and-ball representation of ZnO crystal structures: **a** Cubic rocksalt (B1). **b** Cubic zinc blende (B3). **c** Hexagonal wurtzite (B4). Shaded *gray* and *black spheres* denote Zn and O atoms, respectively

forms. This is almost like expanding the periodic table, basically because the properties exhibited by such nanoforms are seen to be phenomenally different from their counterparts; which could be put to use, provided the modified properties are conducive.

Nanostructures, as is known, exhibit quantum confinement which changes the intrinsic properties of the bulk counterpart which leads to several interesting applications. One of the important effects of converting a bulk into nano material is the increase in surface to volume ratio, which adds better scope for surface-related interactions. However, with the lesser particle size, the stable substances can become highly reactive and unstable. The stability can be achieved through various mechanisms, such as surfactant coatings, imparting charge on the particles surface, and so on. This requires good coating strategy and hence good chemistry protocols have come in picture. Upon coating with surfactant, the material gains several other advantages as well. Additional surface groups for further functionalization is one major advantage, which makes the material useful in the area of drug delivery and sustained drug release. Surface groups could also be compensated by adsorbing gas moieties on them, thereby making the material work as a sensor. Such and many other applications can hence be envisaged; which we will see in the coming paragraphs. Another aspect of nanomaterials is the optical property modification. The optical properties may get affected with the quantum confinement giving rise to increase in band-gap energy and wavelength of the light emitted. This property which is been highly explored make the corresponding materials work as white light emitters in lasers.

ZnO in their nanoforms: Out of many materials which have been affected positively due to this technology, Zinc oxide is the most popular one. This is due to its structural stability in various forms and the good engineering ability developed by the researchers all around the globe. By simple chemical routes, too, one is able to tune the shapes right from simple spherical nanoparticles, to rods, rings, columns, and spirals. Schematic in Fig. 13.2 shows all such structures already envisaged, and as observed by Wang et al. [3]. Since ZnO shows tendency toward higher growth rate along c-axis, due to its polar nature (this semiconductor material have two opposite polarity crystallographic planes with different surface relaxation energy), the structure easily assumes nanorod-like vertical structures [2].

Figure 13.3 shows this effect through the photoluminescence (PL) spectrum of ZnO nanobelts as discussed by Wang et al. in their communication [3]. The particle size effect introduces blue shift in the PL spectrum, when the particle size changes from 200 to 6 nm. Not only optical, but conductivity, specific heat, hardness, and surface reactivity also get modified in ZnO in their nanoforms. Nanostructured semiconductors are known to show various nonlinear optical properties. Semiconductor Q-particles also show quantum confinement effects which may lead to special properties, like the luminescence in silicon powders and silicon germanium quantum dots as infrared optoelectronic devices. Nanostructured semiconductors are used as window layers in solar cells. Andrievski et al. [4] have summarized these property variations in various materials in their nanoforms in their book chapter.

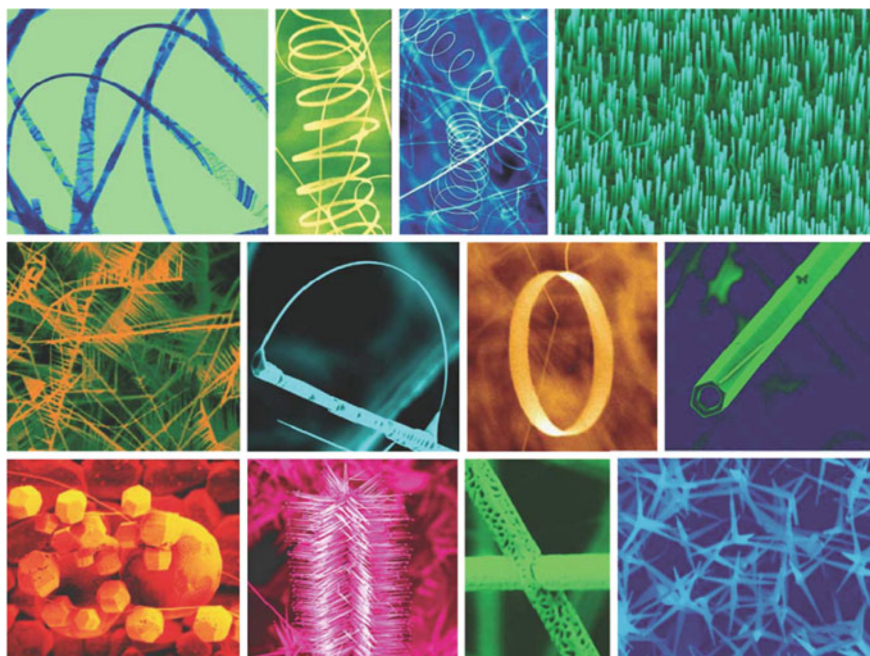

Fig. 13.2 A collection of nanostructures of ZnO synthesized under controlled conditions. [Reprinted with permission from Wang [2]]

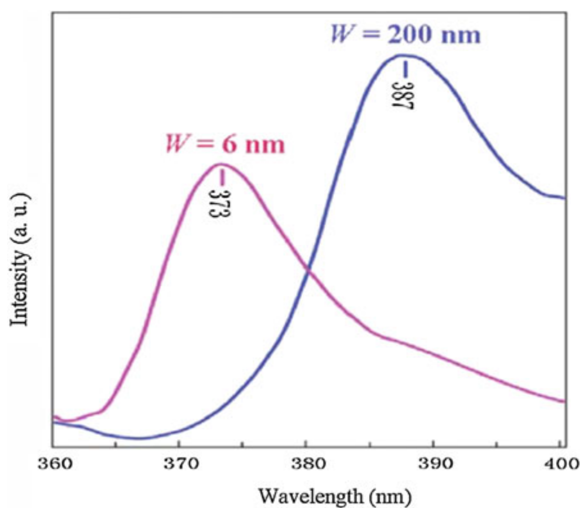

Fig. 13.3 PL spectra of ZnO nanobelts, *blue* shift in the emission peak results from reduction in the width of the nanobelt from 200 to 6 nm [Reprinted with permission from Wang [2]]

Applications of ZnO nanomaterials: There are several thought flows of various researchers on this material and hence this material is one of the most popular and well sought, amongst both the researchers and technocrats. [2, 5–8].

ZnO nanoparticles show improved heat conductivity which is required to dissipate the heat produced in the rubber of the tire by the deformation when it rolls along the street and also it positively influences the vulcanization process. Further, the admixture of ZnO improves resistance of the concrete against water and allows increased processing time. A large fraction of the ZnO is utilized in the concrete and rubber industries as well [6].

Extensive research work is going on ZnO, due to its evident promise as a semiconductor to the device industry. Several works have been reported on this ability of the material, right since 1930, which still continues with lot of rigor. Exploring them as *n*-type and *p*-type semiconductor (for electronic devices), magnetic semiconductor (as spintronic devices), white light emitters, photonic material (lasing devices), photovoltaic devices is well under way. There have been additional attempts to explore these materials as sensors, especially gas sensors. Such works have been documented very well in the recent literatures [9–11].

Though this particular chapter is not dealing with gas-sensing applications, it is important to state here that the best application of ZnO in its nanoforms has been for sensing. There are umpteen numbers of papers on this particular topic and the work is still in progress [12–15]. Issues such as sensitivity, selectivity, and operating temperatures are being resolved by doping the materials, or forming their compounds with other oxides or forming composites. Fan et al. [16] have reported ZnO to be used in varistors in its mixed oxide form. ZnO is also reported to be used as photovoltaic devices and in/as lasers [17–19].

ZnO nanomaterials in biomedical domain—issues and opportunities: Until very recent times, inorganic materials, in general, and ZnO, in particular, have not been a very strong candidate for biomedical applications. One of the basic reasons is this that, generally, inorganic materials are very rarely accommodated by the organic medical community. This is quite justified due to their issues on toxicity, bio-degradable ability, therapeutic values, and in vivo complexities. Their in ability to get cleared from the biological systems is a big issue, which has always needed good attention, and hence these materials have been less explored. However, two avenues have been witnessed in recent times:

1. With the advent of the same materials in their nanoforms, the toxicity of the materials could be different in nanoforms (as compared to their toxicity in bulk forms). The therapeutic values could be enhanced. Their conjugational protocols could make them good “in vivo” candidates for many applications such as drug delivery and bio imaging.
2. With the enhanced property regimes, the in vitro applications could also be radically different. For example, water pollution control could be achieved by the ability of the nanomaterials as heavy-ion/toxic dye degrading (or chelating) agents. They could be harnessed for toxic gas sensing. The diagnostic kits could also be newly designed using these nanomaterials as the base and conjugating bioentities onto them for better diagnostics, using lesser samples.

Zno in biomedicine: ZnO is been extensively used in cosmetics industries [20, 21]. It has these applications mainly due to its capacity to block UV

radiations, which is a part of sun-screen requirement [22]. A fine ZnO coat gives a good finishing to the surface on which it is applied; therefore, it has added advantage as a cosmetic product ingredient. It is also reported to be an additive in human and animal food [23, 24]. Several bioapplications of ZnO material have also been explored [25–29] such as for antimicrobial agents, in vivo imaging, food supplements (as modulators due to their hydrolase activity), as a probable MRI agent (due to its projected magnetic property upon doping with magnetic dopants). As a sensor, along with conventional gas-sensing property as mentioned before, ZnO has also been investigated as cholesterol sensor [25].

Apart from these applications, being biocompatible, nontoxic as compared to several other oxide semiconductor counterparts, several other applications like drug delivery, photocatalysis, and p type ZnO for device application have been reported. For example, Zhou et al. reported the first study on biodegradability and biocompatibility of ZnO wires [30]. Fan and Freer have studied carbon-decorated ZnO nanowires for biosensing and electrochemistry of enzymes [16]. Ghoshal et al. have reported medical applications of ZnO like dental filling materials and wound healing [31].

On the lines of issues pertaining to health, water pollution control and air-pollution sensing, can also be a part of health issues. Zinc oxide has significantly contributed on these fronts as well. For water pollution control, ZnO bulk and nanoparticles have been explored as catalysts [32, 33]. They have been used along with either the visible light or with UV light for these explored applications. The process of water pollution control is mainly via the degradation of the pollutants. The pollutants can also be “physically removed” by adsorbing the molecules on the nanomaterials and then filtering the nanomaterials out. However, this procedure requires filtering and constant resupply of the nanomaterials. We will briefly review the works done along with ZnO on these lines first and then cover some of the recent results from our group.

Zinc oxide for water pollution control: Environmental pollution, typically air and water pollution has hazardous consequences on the human life. Particularly water pollution occurs due to variety of reasons, namely dirt-incorporated water storage tanks, contaminants from atmosphere retained in drinking water, and so on. One of the most dangerous categories of water pollutants is industrial wastewater release; typically that arising due to release of dye compounds during the dyeing and finishing operation in textile industries. In addition to these dyes, the textile wastewater contains heavy metals, which are also hazardous to human being. In order to make the polluted water reusable, degradation of such organic pollutants, which have deleterious effect on the wellbeing of mankind, has become the center of the research efforts in today’s scientific world. The conventional approach include physical methods (e.g. adsorption) [34], chemical methods (e.g. chlorination, ozonation) [35], and biological methods (e.g. biodegradation) [36]. The major drawback of physical methods is that they leave behind more concentrated pollutant-containing phase. Due to the fluctuation in wastewater composition, chemical, and biological methods are less adopted [37]. In this sense, these methods cannot be considered to provide complete solution. Hence, the scope to search for better and

promising methods is still well open. It is at this juncture that semiconductor inorganic materials working as photocatalysts are well in demand.

It was the discovery of the photocatalytic splitting of water on TiO_2 electrode by Fujishima and Honda [38] in 1972 that attracted researchers to study effect of light illumination on TiO_2 and its various potential applications, such as for photocatalysis and photovoltaics. Later on several other simple oxide and sulfide semiconductors have been studied for their potential use as photocatalyst. To list a few of them-apart from TiO_2 ($E_g = 3.2$ eV) are WO_3 ($E_g = 2.8$ eV), $SrTiO_3$ ($E_g = 3.2$ eV), alpha-Fe_2O_3 ($E_g = 3.1$ eV), ZnO ($E_g = 3.2$ eV), and ZnS ($E_g = 3.6$ eV) [39–45]. TiO_2 has been extensively used as a photocatalyst, as reported by many [46–48].

The photocatalytic degradation process can be explained as follows: when mixed with contaminated water, let us say, an organic industrial dye mixed in water, the dye and water gets adsorbed onto the surface of the semiconductor. Each semiconductor is characterized by a conduction band and valance band (CB and VB respectively); the gap in them is known as bandgap, E_g. When illuminated by a photon with energy of hν that equals or exceeds the energy of the band gap, an electron hole pair is generated in the semiconductor. The fate of the separated electron and hole can follow several pathways. The separated electron and hole can recombine on the surface or in the volume of the semiconductor particle or with the release of heat. The photo-induced electron/hole can migrate to the semiconductor surface. The pairs those escaped through this recombination process diffuse to the surface of the semiconductor and take part in the chemical reaction with the surface adsorbed donor (D) or acceptor (A) molecules. The holes can oxidize donor molecules (1) to form hydroxyl radical, whereas the conduction band electrons can reduce appropriate electron acceptor molecules (usually oxygen in an aerated solution) e.g., produce superoxide radical (2). The schematic is shown in Fig. 13.4.

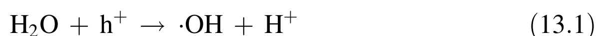

$$H_2O + h^+ \rightarrow \cdot OH + H^+ \quad (13.1)$$

$$O_2 + e^- \rightarrow O_2^{\cdot -} \quad (13.2)$$

These radicals being highly reactive can be used to degrade most of the organic contaminants. The degraded products eventually get desorbed from the surface of the catalyst [46].

For better photocatalysis process, the photogenerated carriers need to have higher mobility. Also, deeper valance band plays crucial role in the process via stronger oxidative activity. TiO_2, fulfilling almost all the criteria required by a better photocatalyst, has been extensively studied for years, typically in the near-UV or in UV range. However, it is important to realize that UV occupies merely ca. 4 % of whole solar energy which brings difficulties in the widespread application of TiO_2. Therefore, it is indispensable and urgent to develop a particular photocatalyst sensitive to sunlight for making the technology widely applied. Increasing surface area could increase number of surface adsorbed dye and water

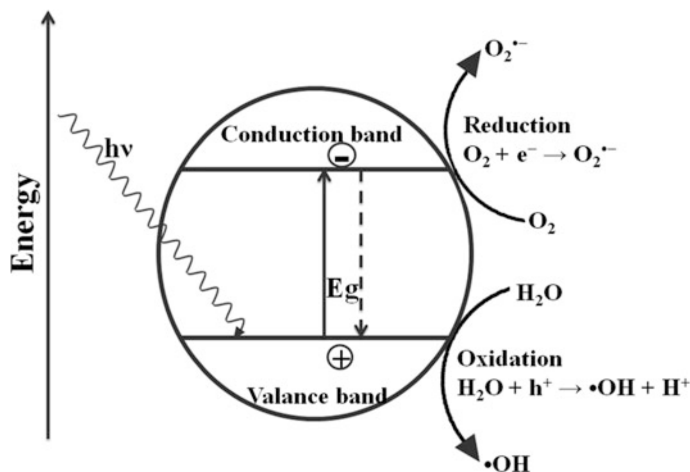

Fig. 13.4 Simplified schematic photocatalysis process

hence increasing reaction rate, but this gives blue shift on the activity. This has developed the need of appropriately band-gap engineered material or the material to possess these characteristics which are brought out by its defect nature. Recently, the photocatalytic performance of ZnO has attracted much attention which was considered as an alternative to TiO_2 [49–51]. This study was done with UV light as activator. Several other attempts have been done for dye degradation in solar light. Figure 13.5 shows one such works done with different nanoparticles on methylene blue dye [51]. Kitture et al. [52] have presented a comparative study of few reports. It is important to note that this comparison was done with the respect to few literature findings and necessarily does not portray all works. The table below summarizes such partial literature survey [53–57].

Ref.	Dye	Dye concentration (mg/l)	Catalyst	Catalyst concentration (mg/l)	Activation	Time (min)	% Degradation
[53]	MO	10	ZnO	1	Solar	30	~100
		10		1	UV	120	~100
		25		1	Solar	90	98.9
		25		1	UV	90	50
[54]	MB	27	P 25	0.375	UV	120	~100
[55]	MB	100	TiO_2	1000	UV	80	~95
		100	TiO_2	1000	Solar	220	~100
	MB	100	TiO_2	1000	Solar	225	95
[56]	MO	20	TiO_2-mordenite	4	UV	100	96.58
[57]	MO	32.7	P25	1.1	Solar	540	~100

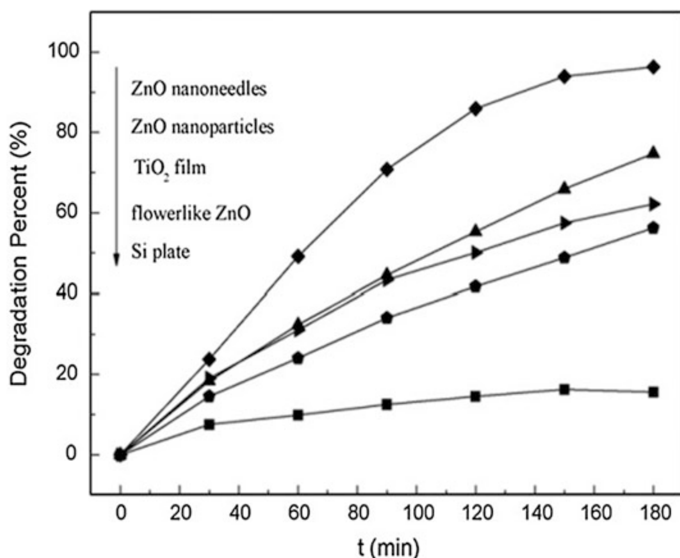

Fig. 13.5 Decomposition ratio of methylene blue with different forms of ZnO, TiO_2 film and Si plate. [Reprinted with permission from [51]]

From the analysis of this table, it was derived that solar and UV light has been used by various researchers for their photocatalytic activity to do dye degradation.

To approach this issue, we did works with two different dyes, namely Methylene Blue [MB] and Methyl Orange [MO]. Two different photocatalysts were used, namely P25 (P25, which is a commercial grade of TiO_2 nanoparticles) and ZnO (submicron particles, synthesized either as tetrapods (abbreviated as ZnO1000) or spherical (abbreviated as ZnO600)). Studies were done for normal sunlight dye degradation. Careful studies revealed that ZnO was able to not only decolorize both the dyes, but was also able to completely degrade them. This was done merely in 20 min in normal sunlight. The dye-degraded water was analyzed to be safe for re-use, as confirmed through the WHO and CPCB (India) standard charts on safe water. TiO_2, on the other hand, could decolorize the dyes and adsorb on the nanoparticles, rather than degrading. Figure 13.6a, b shows these effects. The insets of both graphs show pictorial representation of fresh and decolorized dyes (MO/MB), with different materials.

The reusability and photostability of the ZnO and P25 was compared and it was interesting to know that tetrapod structured ZnO was significantly stable against photocorrosion and also that it could be used several times as against the other counterparts. Figure 13.7 shows these results of reuse and photostability of catalysts ZnO1000 (a), ZnO600 (b) and P25 (c), and inset shows expanded view of reuse trials of ZnO1000. The lines indicate the fitted curves.

The results were understood from the UV-vis spectrum data of the obtained ZnO samples. The UV-vis spectrum of ZnO particles showed broad range of

absorption (data not shown here). The range extended from visible to UV regime, probably due to the defect driven states. This generates a probability that the material absorb from around 380 nm to cover the complete visible spectrum of sunlight. Though ZnO, in its pure form has high excitonic energy, with its spectra showing a characteristic signature at 380 nm, their broad-range absorption has been observed by many [58–60]. For example, Singh et al. [58] have seen broad green emission around 500 nm, covering the signature at 380 nm. Hence, the photocatalytic activity seen in our studies could be attributed to the donor states caused by the large number of defect sites such as oxygen vacancies and interstitial zinc atom. It could also be due to the acceptor states that arise from zinc vacancies and interstitial oxygen atoms [61]. Oxygen vacancies, which are located at energy positions 2.35–2.50 eV, are also responsible for the UV-light response as is seen by the green luminescence. Since our samples were polydispersed, these defect states dominate to get excellent photocatalytic dye degradation. Such defect states engineering in ZnO powders can give much practical solution for industrial dye effluent treatments.

Zinc oxide as anti-diabetic material: Diabetes is one of the most dreaded diseases of the time. There have been significant breakthroughs in the research related to both control and diagnostics of the levels of sugar in human body. The efforts though have been significant, the scope is still much wide, mainly due to the requirements on both fronts: for diagnostics and therapy. For diagnostics, the search is well on to fabricate the kits for faster sugar-level detection and with minimum blood sample [62–64]. Such kits, as of now, are to be used only once and thrown away; indicating a demand for re-usable kits. For therapeutics, there are several ways to control; typically, either to control via insulin supply or by using inhibitors. Use of sustained-drug release via microcapsules [65–67] is also been investigated in this context.

Use of nanoparticles in such contexts has been investigated by many research groups worldwide. Nanoparticles can be used for diabetic patients to tolerate transplanted insulin producing cells. They can be loaded with immunosuppressive agents (anti-rejection drugs) and because they are so small, sent precisely to cells in the body that regulate the immune system's response. By pinpointing the delivery of the drug to a specific cell, we can potentially dampen or modify an immune response that would be triggered by the introduction of foreign tissue and allow diabetic patients to tolerate transplanted insulin-producing cells. The use of nanoparticles may play a significant role in our ability to achieve transplant tolerance, maintain long-term insulin function and improve the quality of life of diabetes patients. The lipid matrices can be used to load and deliver anti-diabetic drugs since these are high pH and enzymatic proteolysis which cannot be taken oral [68]. Vijayan et al. have reported preparation and characterization of solid-lipid nanoparticles for delivery of anti-diabetic drug [69]. Hyperglycemia or high-blood sugar creates more complications in diabetic patients, biologically synthesized gold nanoparticles (Au NPs) used to control the hyperglycemic conditions in streptozotocin-induced diabetic mice [70]. Phytochemically synthesized gold nanoparticles are used in hypoglycemic treatment for diabetes mellitus [71].

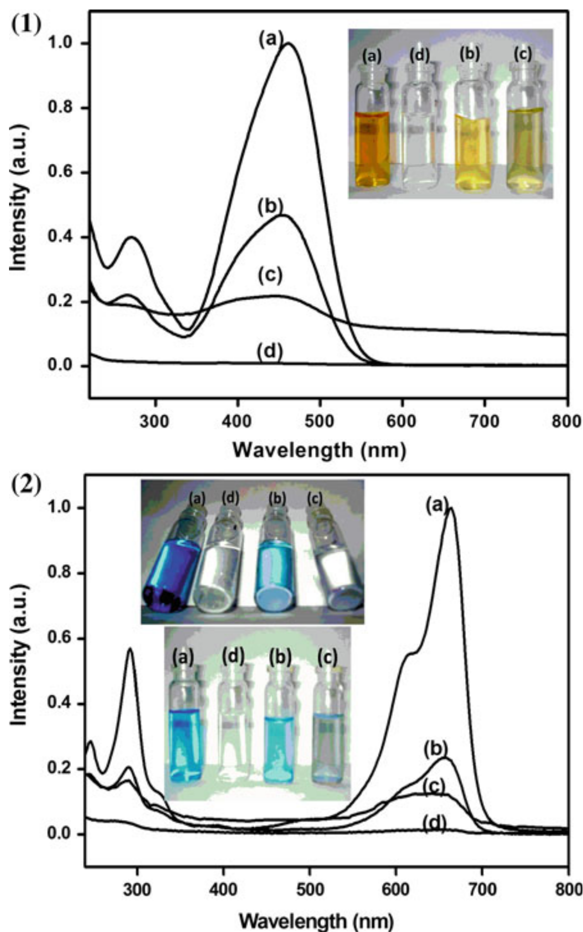

Fig. 13.6 1. UV-vis data for photocatalytic decolorization of MO with ZnO and P25 samples after 20 min of solar exposure using UV-vis spectrum. **a** Shows initial signature of MO, **b**, **c** and **d** shows signature MO after exposure to sunlight for 20 min with the catalysts ZnO600, P25, and ZnO1000, respectively. Inset is pictorial representation of fresh and decolorized MO. The picture in inset clearly exhibits visual decolorizing effect. [Reprinted with permission from [52]]. 2. Photocatalytic decolorization of MB with ZnO samples after 20 min of solar exposure. (a) Shows initial signature of MB (b), (c) and (d) show signature MB after exposure to sunlight with the catalysts ZnO600, P25, and ZnO1000, respectively. Inset is pictorial representation of fresh and decolorized MB. Another inset shows bottom view, to give evidence of adsorption of the dye MB on P25, unlike ZnO1000 and ZnO600, showing the catalyst in its original white powder form. [Reprinted with permission from [52]]

Polymeric nanoparticles are used for insulin carrying. These polymers are biodegradable, polymer-insulin matrix is enclosed by nanoporous membrane contains glucose oxidase. A rise in blood glucose level triggers a change in the surrounding

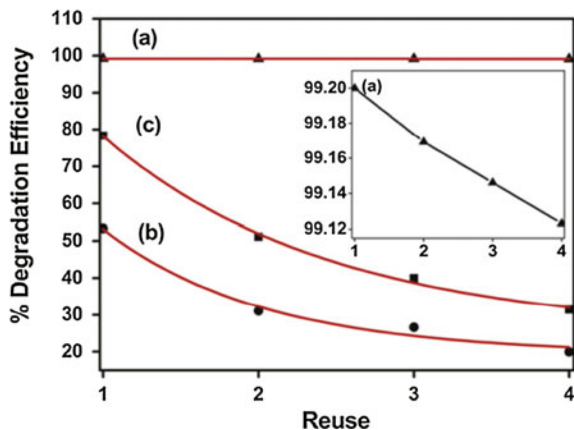

Fig. 13.7 Reuse and photostability of catalysts ZnO1000 (a), ZnO600 (b) and P25 (c), and inset shows expanded view of reuse trials of ZnO1000. The lines indicate the fitted curves. [Reprinted with permission from [52]]

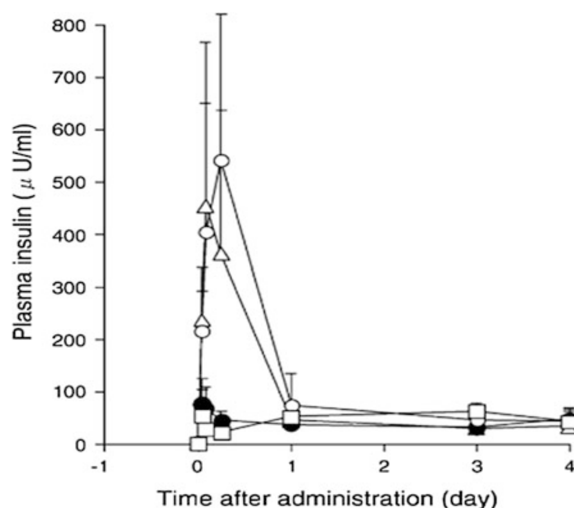

Fig. 13.8 Effect of insulin particle size. Insulin-containing PLGA microcapsules were prepared using human insulin (Δ) lyophilized human insulin (O) or Zn-free insulin (·). ZnO was added at a 12-fold molar excess over insulin, and glycerin and water were used as the other additives. [Reprinted with permission from [79]]

nanoporous membrane, resulting in biodegradation and subsequently releases insulin. Many groups have worked on similar lines [72–78].

Takenaga et al. have studied sustained insulin release though microcapsules. Further, they have also studied the effect of ZnO on initial profile of insulin release from the microcapsules. Figure 13.8 shows the compilation of their results. The biological activity of insulin extracted from the microcapsules was confirmed to be similar to that of normal insulin. The interesting outcome was that, with ZnO as an additive to the microcapsule containing insulin, initial rapid insulin release could be suppressed. This could also be improved by controlling the insulin particle size [79].

Starch blockers are good candidates for controlling the conversion of starch into sugar. Several organic materials have been investigated in this context and recently the interest has been shifted to inorganic materials. Some of the reports mentioned

below are those which have already explored many organic and inorganic materials as starch blockers [80, 81].

These agents inhibit alpha amylases. Alpha amylases are major digestive enzymes in animals/humans which play key role in breaking down long-chain carbohydrates polysaccharide starch, a major sugar obtained from diet into maltose and glucose. So the organic compounds when inhibit alpha amylase, will in turn prevent dietary starches from being absorbed by the body via inhibiting breakdown of complex sugars to simpler ones. This will, in other way control the amount of sugar available for assimilation, thereby helping in controlling diabetes. Such kind of amylase inhibitors are mainly proteins, isolated from plants, mainly from legumes and microorganisms [82–84]. Alpha amylase and its inhibitors have been the targets of drug design for developing compounds for treatment of diabetes, obesity, and hyperlipemia [85].

Feng et al. have successfully purified four types of different alpha-amylase inhibitors from wheat flour. Further, they studied the activity against alpha amylase from insects and human, where HAS stands for alpha amylase from human saliva [86]. Such and many similar studies have been performed, typically by botanists and biologists. The works done by physicists and chemists community have been comparatively, quite recent.

Our works, as documented in Dhobale et al., have done such works on similar lines using zinc oxide nanoparticles as alpha-amylase inhibitor [87]. We have studied the application of ZnO nanoparticles as alpha-amylase inhibitor. The nanoparticles were coated with thioglycerol (TG), which was duly characterized to study the conjugation chemistry using molecular spectroscopy. The ZnO nanoparticles have been synthesized using soft-chemistry approach and thioglycerol was used as a surfactant to yield polycrystalline nanoparticles of size $\sim$18 nm, stabilized in wurtzite structure. Cytotoxicity studies on human fibrosarcoma (HT-1080) and skin carcinoma (A-431) cell lines as well as mouse primary fibroblast cells demonstrate that up to a dose of 20 μg/ml, ZnO nanoparticles are nontoxic to the cells. Figure 13.9 shows these results, which are important to be evaluated for such bio-activity studies. The alpha-amylase inhibitory activity of ZnO nanoparticles has been documented in this work wherein an optimum dose of 20 μg/ml was sufficient to exhibit 49 % glucose inhibition at neutral pH and 35 °C temperature. This inhibitory activity was similar to that obtained with acarbose, a standard alpha-amylase inhibitor, thereby projecting ZnO nanoparticles as novel alpha-amylase inhibitors.

Figure 13.10 shows these results. These results showed that ZnO-TG exhibited alpha-amylase inhibitory activity similar to that of a standard alpha-amylase inhibitor, thereby paving way to the use of this nontoxic inorganic material in the domain of biomedicine.

Such activity enhancement by using zinc oxide nanoparticles was comparatively less explored. Since amylase, being a protein, has an amine and a carboxyl group at its N-terminus and C-terminus ends, respectively, conjugation to these proteins could occur at either of these sites. However, on the other hand, formation of covalent bond with the starch molecules is rather difficult since these are highly

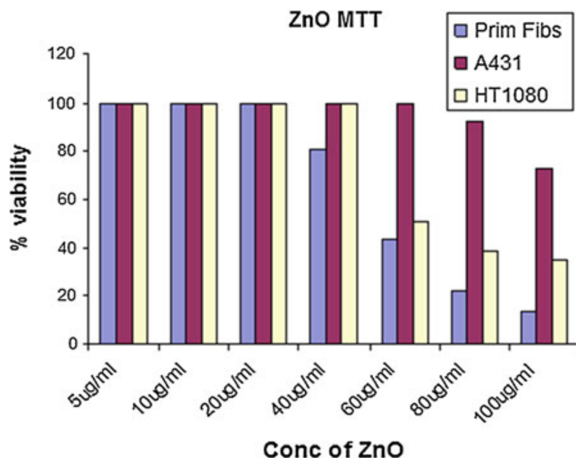

Fig. 13.9 Cytotoxicity studies on human fibrosarcoma (HTT-1080) and skin carcinoma (A-431) cell lines as well as mouse primary fibroblasts cells demonstrating that up to a dose of 20 μg/ml ZnO-TG nanoparticles are nontoxic to the cells. [Reprinted with permission from [87]]

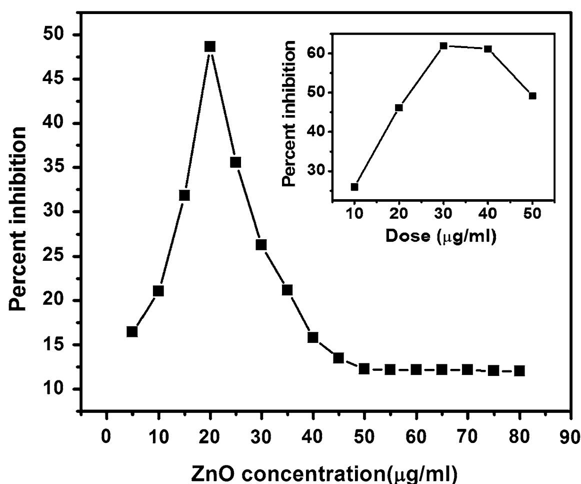

Fig. 13.10 DNS acid assay test for ZnO-TG nanoparticles dosage compared with a standard acarbose drug shown in the inset, which shows that at 20 μg/ml, the percentage inhibition for both materials is comparable. [Reprinted with permission from [87]]

stable carbon–hydrogen–oxygen rings. Hence, it has been proposed that the reaction of amylase with ZnO-TG takes place through bonding of $-NH_2$ facilitating primary carbocation formation due to leaving of –SH. Such an interaction may be rendering the enzyme unavailable for the substrate (starch in this case), thereby resulting into its inhibition consequently arresting glucose formation from starch. Since ZnO nanoparticles depict similar properties like that of standard alpha-amylase inhibitors, it could be a prospective drug for diabetes [83–85].

13.2 Conclusions and Future Prospects

The article discusses zinc oxide as a potential candidate in the area of healthcare. A brief introduction of the material in its bulk and nanoform has been discussed. Several application areas have been touched upon in this article. The property regimes which have been harnessed for their applications in the area of biomedicine and healthcare have also been analyzed. Typical role of zinc oxide as a catalyst and as an inhibitory molecule has been detailed in this review. Several areas of other applications such as in cosmetics, biosensing, antimicrobials, and antifungal materials have been mentioned. Though the material promises to be a good candidate for such and similar applications, there should be a word-of-caution whilst using these for in vivo applications. Many reports have addressed this worry, which is toxicity. Up to a certain microgram (per ml) quantity the material exhibits "biosafe" property. The cytotoxicity is much higher for higher concentration. Hence, even though their catalytic activities are good, their composition cannot be concentrated. Functionalization strategies may improve the viability of such molecules; however, the stability of the conjugates and their excretion mechanisms have to be carefully looked into. Since the materials tend to chelate in biological environments, the worry is still more and hence careful analysis is surely needed before using them for such applications as imaging and inhibitors. However, the material shows immense promise as a sensor and surely enough, as a biosensor it should show wonderful potential. Such works are well underway and selective biosensing would be well within reach of the researchers in coming times. Reusability and shelf-life could be the issues which have be carefully addressed. In conclusion, zinc oxide can be considered as a good candidate in biomedical applications. The in vitro applications are well established and show good promise as a catalyst and therapeutic material.

Acknowledgments It is a pleasure to thank Dr. M. S. R. Rao, the Editor of this book published by the Springer Publishers, for his kind invitation to write this chapter. SK would like to thank Dr. Prahlada, Vice Chancellor, Defence Institute of Advanced Technology (DIAT) for his constant encouragement and support. SK would also acknowledge "DRDO-DIAT programme on Nanomaterials" by ER&IPR, DRDO, New Delhi.

References

1. U. Özgür, I. Alivov Ya, C. Liu, A. Teke, M.A. Reshchikov, A comprehensive review of ZnO materials and devices. J. Appl. Phys. **98**, 04130-1-103 (2005)
2. C.F. Klingshirn, B.K. Meyer, A. Waag, A. Hoffmann, J. Geuts, *Zinc Oxide: From Fundamental Properties Towards Novel Applications* (Springer, Berlin, 2010)
3. Z.L. Wang, Nanostructures of zinc oxide. Mater. Today **7**, 26–33 (2004)
4. R.A. Andrievski, A.M. Glezer, Size effects in Properties of Nanomaterials. Elsevier Science Ltd. **44**, 1621–1623 (2000)

5. P.H. Miller Jr. in ed. H.K. Henisch, Proceedings of the International Conference on Semiconducting Materials, Reading (1950) (Butterworths Scientific Publications, London, 1951), p. 172
6. H.E. Brown, *Zinc Oxide Rediscovered* (The New Jersey Zinc Company, New York, 1957)
7. H. Heiland, E. Mollwo, F. Stöckmann, Electronic processes in zinc oxide. Solid State Phys. **8**, 191–323 (1959)
8. C. Klingshirn, ZnO: Basic to application. Phys. Status Solidi B **244**, 3027–3073 (2007)
9. A. Tiwari, C. Jin, D. Kumar, J. Narayan, Rectifying electrical characteristics of $La_{0.7}Sr_{0.3}MnO_3$/ZnO heterostructure. Appl. Phys. Lett. **83**, 1773–1775 (2003)
10. Z.L. Wang, Zinc oxide nanostructures: Growth, properties and applications. J. Phys.: Condens. Matter **16**, R829–R858 (2004)
11. S.J. Pearton, D.P. Norton, Y.W. Heo, T. Steiner, Recent progress in processing and properties of ZnO. Prog. Mater Sci. **50**, 293–340 (2005)
12. W. Shen, Y. Zhao, C. Zhang, The preparation of ZnO based gas-sensing thin films by ink-jet printing method. Thin Solid Films **48**, 382–387 (2005)
13. N. Kumar, A. Dorfmann, J. Hahm, Ultrasensitive DNA sequence detection using nanoscale ZnO sensor arrays. Nanotech **17**, 2875–2881 (2006)
14. J. Suehiro, N. Nakagawa, S.-I. Hidaka, M. Ueda, K. Imasa, M. Higashihata, T. Okada, M. Hara, Dielectrophoretic fabrication and characterization of a ZnO nanowire-based UV photosensor. Nanotech **17**, 2567–2573 (2006)
15. M.C. Larciprete, D. Haertle, A. Belardini, M. Bertolotti, F. Sarto, P. GFnter, Characterization of second and third order optical nonlinearities of ZnO sputtered films. Appl. Phys. B **82**, 431–437 (2006)
16. J. Fan, R. Freer, The roles played by Ag and Al dopants in controlling the electrical properties of ZnO varistors. J. Appl. Phys. **77**, 4795–4801 (1995)
17. K.S. Leschkies, R. Divakar, J. Basu, E. Enache-Pommer, J.E. Boercker, C.B. Carter, U.R. Kortshagen, D.J. Norris, E.S. Aydil, Photosensitization of ZnO Nanowires with CdSe quantum dots for photovoltaic devices. Nano Lett. **7**(6), 1793–1798 (2007)
18. Z.W. Pan, Z.R. Dai, Z.L. Wang, Nanobelts of semiconducting oxides. Science **291**, 1947–1949 (2001)
19. M.H. Huang, S. Mao, H. Feick, H.Q. Yan, Y.Y. Wu, H. Kind, E. Weber, R. Russo, P.D. Yang, Room-temperature ultraviolet nanowire nanolasers. Science **292**, 1897–1899 (2001)
20. FDA, Sun Protection, Available from: http://www.fda.gov/Radiation-EmittingProducts/RadiationEmittingProductsandProcedures/Tanning/ucm116445.htm
21. M.A. Mitchnick, D. Fairhurst, S.R. Pinnell, Microfine zinc oxide (Z-Cote) as a photostable UVA/UVB sunblock agent. J. Am. Acad. Dermatol. **40**, 85–90 (1999)
22. G.J. Nohynek, J. Lademann, C. Ribaud, M.S. Roberts, Grey goo on the skin? Nanotechnology, cosmetic and sunscreen safety. Crit. Rev. Toxicol. **37**, 251–277 (2007)
23. K.H. Brown, K.R. Wessells, S.Y. Hess, Zinc bioavailability from zinc-fortified foods. Int. J. Vitam. Nutr. Res. **77**, 174–181 (2007)
24. D. Clark, E. Gillis, H. Gobble, N. Francisco, J. Kincaid, Fortified edible compositions and process of making, U.S. Patent 6168811, 2001
25. R. Khan, A. Kaushik, P.R. Solanki, A.A. Ansari, M.K. Pandey, B.D. Malhotra, Zinc oxide nanoparticles-chitosan composite film for cholesterol biosensor. Anal. Chim. Acta **616**, 207–213 (2008)
26. K.M. Reddy, K. Feris, J. Bell, D.G. Wingett, C. Hanley, A. Punnoose, Selective toxicity of zinc oxide nanoparticles to prokaryotic and eukaryotic systems. Appl. Phys. Lett. **90**, 213902-1-3 (2007)
27. C. Bárcena, A.K. Sra, G.S. Chaubey, C. Khemtong, J.P. Liu, J. Gao, Zinc ferrite nanoparticles as MRI contrast agents. Chem. Commun. **19**, 2224–2226 (2008)
28. J. Szabo, M. Hegedus, G. Bruckner, E. Kosa, E. Andrasofszky, E. Berta, Large doses of zinc oxide increases the activity of hydrolases in rats. J. Nutr. Biochem. **15**, 206–209 (2004)

29. H.M. Xiong, Y. Xu, Q.G. Ren, Y.Y. Xia, Stable aqueous ZnO@polymer core-shell nanoparticles with tunable photoluminescence and their application in cell imaging. J. Am. Chem. Soc. **130**, 7522–7523 (2008)
30. J. Zhou, N. Xu, Z.L. Wang, Dissolving behavior and stability of ZnO wires in biofluids. Adv. Mater. **18**, 2432–2435 (2006)
31. T. Ghoshal, S. Kar, S. Chaudhuri, Synthesis and optical properties of nanometer to micrometer wide hexagonal cones and columns of ZnO. J. Cry. Growth **293**, 438–446 (2006)
32. N. Daneshvar, D. Salari, A.R. Khataee, Photocatalytic degradation of Azo Dye Acid Red14 in water—investigation of the effect of operational parameters. J. Photochem. Photobiol., A **157**, 111–116 (2003)
33. M.M. Uddin, M.A. Hasnat, A.J.F. Samed, R.K. Majumdar, Influence of TiO_2 and ZnO photocatalysts on adsorption and degradation behaviour of erythrosine. Dyes Pigm. **75**, 207–212 (2007)
34. B. Zargar, H. Parham, A. Hatamie, Fast removal and recovery of amaranth by modified iron oxide magnetic nanoparticles. Chemosphere **76**, 554–557 (2009)
35. Y.M. Slokar, A.M. Le Marechal, Methods of decoloration of textile wastewaters. Dyes Pigm. **37**, 335–356 (1998)
36. S.S. Patil, V.M. Shinde, Biodegradation studies of aniline and nitrobenzene in aniline plant wastewater by gas chromatograph. Environ. Sci. Technol. **22**, 1160–1165 (1988)
37. S.K. Mohapatra, S.U. Sonavane, R.V. Jayaram, P. Selvam, Reductive cleavage of azo dyes and reduction of nitroarenes over trivalent iron incorporated hexagonal mesoporous aluminophosphate molecular sieves. Appl. Catal. B: Environ. **46**, 155–163 (2003)
38. A. Fujishima, K. Honda, Electrochemical photolysis of water at a semiconductor electrode. Nature **238**, 37–38 (1972)
39. Y.Y. Wu, H.Q. Yan, P.D. Yang, Synthesis and property of mesoporous tantalum oxides. Top. Catal. **19**, 197–202 (2002)
40. A. Houas, H. Lachheb, M. Ksibi, E. Elaloui, C. Guillard, J.M. Herrmann, Photocatalytic degradation pathway of methylene blue in water. Appl. Catal. B: Environ. **31**, 145–157 (2001)
41. Yumin CUI, Photocatalytic degradation of MO by complex nanometer particles WO_3/TiO_2 Rare Metals **25**, 649–653 (2006)
42. C.L. Torres-Martinez, R. Kho, O.L. Mian, R.K. Mehra, Efficient photocatalytic degradation of environmental pollutants with mass-produced ZnS nanocrystals. J. Colloids Interf. Sci. **240**, 525–532 (2001)
43. X. Ren, D. Han, D. Chen, F. Tang, Large-scale synthesis of hexagonal cone-shaped ZnO nanoparticles with a simple route and their application to photocatalytic degradation. Mater. Res. Bull. **42**, 807–813 (2007)
44. H.H. Yin, J. Wada, T. Kitamura, S. Yanamuda, Photoreductive dehalogenation of halogenated benzene derivatives using ZnS or CdS nanocrystallites as photocatalysts. Environ. Sci. Tech. **35**, 227–231 (2001)
45. W. Chen, Z. Wang, Z. Lin, L. Lin, Absorption and luminescence of the surface states in ZnS nanoparticles. J. Appl. Phys. **82**, 3111–3115 (1997)
46. J.M. Herrmann, Heterogeneous photocatalysis: Fundamentals and applications to the removal of various types of aqueous pollutants. Catal. Today **53**, 115–129 (1999)
47. M. Anpo, Utilization of TiO_2 photocatalysts in green chemistry. Pure Appl. Chem. **72**, 1265–1270 (2000)
48. D. Chattergee, Visible light assisted photodegradation of halocarbons on the dye modified TiO_2 surface using visible light. Sol. Energy Mater. Sol. Cells **90**, 1013–1020 (2006)
49. T. Pauporte, J. Rathousky, Electrodeposited mesoporous ZnO thin films as efficient photocatalysts for the degradation of dye pollutants. J. Phys. Chem. C **111**, 7639–7644 (2007)
50. C.H. Ye, Y. Bando, G.Z. Shen, D. Golberg, Thickness-dependent photocatalytic performance of ZnO nanoplatelets. J. Phys. Chem. B **110**, 15146–15151 (2006)

51. H. Yan, J. Hou, Z. Fu, B. Yang, P. Yang, K. Liu, M. Wen, Y. Chen, S. Fu, F. Li, Growth and photocatalytic properties of one-dimensional ZnO nanostructures prepared by thermal evaporation. Mater. Res. Bull. **44**, 1954–1958 (2009)
52. R. Kitture, S.J. Koppikar, R. Kaul-Ghanekar, S.N. Kale, Catalyst efficiency, photostability and reusability study of ZnO nanoparticles in visible light for dye degradation. J. Phys. Chem. Sol. **72**, 60–66 (2011)
53. S.K. Kansal, M. Singh, D. Sud, Studies on photodegradation of two commercial dyes in aqueous phase using different photocatalysts. J. Hazard. Mater. **141**, 581–590 (2007)
54. H. Lachheb, E. Puzenat, A. Houas, M. Ksibi, E. Elaloui, C. Guillard, J.M. Herrmann, Photocatalytic degradation of various types of dyes (Alizarin S, Crocein Orange G, Methyl Red, Congo Red, Methylene Blue) in water by UV-irradiated titania. Appl. Catal. B: Environ. **39**, 75–90 (2002)
55. G. Sivalingam, K. Nagaveni, M.S. Hegde, G. Madras, Photocatalytic degradation of various dyes by combustion synthesized nano anatase TiO_2. Appl. Catal. B: Environ. **45**, 23–38 (2003)
56. F. Li, S. Sun, Y. Jiang, M. Xia, M. Sun, B. Xue, Photodegradation of an azo dye using immobilized nanoparticles of TiO_2 supported by natural porous mineral. J. Hazard. Mater. **152**, 1037–1044 (2008)
57. M.N. Rashed, A.A. El-Amin, Photocatalytic degradation of methyl orange in aqueous TiO_2 under different solar irradiation sources. Int. J. Phys. Sci. **2**, 073–081 (2007)
58. S. Singh, P. Thiyagarajan, K. Mohan Kant, D. Anita, S. Thirupathiah, N. Rama, B. Tiwari, M. Kottaisamy, M.S.R. Rao, Structure, microstructure and physical properties of ZnO based materials in various forms: Bulk, thin film and nano. J. Phys. D: Appl. Phys. **40**, 6312–6327 (2007)
59. J. Lim, K. Shin, H.W. Kim, C. Lee, Photoluminescence studies of ZnO thin films grown by atomic layer epitaxy. J. Lumin. **109**, 181–185 (2004)
60. J. Zhang, Z. Zhang, T. Wang, A new luminescent phenomenon of ZnO due to the precipitate trapping effect of MgO. Chem. Mater. **16**, 768–770 (2004)
61. F. Tuomisto, K. Saarinen, Introduction and recovery of point defects in electron-irradiated ZnO. Phys. Rev. **72**, 085206-1-11 (2005)
62. M. Shichiri, Y. Yamasaki, R. Kawamori, N. Hakui, H. Abe, Wearable artificial endocrine pancreas with needle-type glucose sensor. The Lancet. **8308**,1129–1131 (1982)
63. F. M. Matschinsky, Glucokinase as Glucose Sensor Metabolic Signal Generator in Pancreatic {beta}-Cells and Hepatocytes. Diabetes. **39**, 647–652 (1990)
64. D. S. Bindra, Y. Zhang, G. S. Wilson, R. Sternberg, D. R. Thevenot, D. Moatti, G. Reach, Design and in vitro studies of a needle-type glucose sensor for subcutaneous monitoring. Anal. Chem. **63**, 1692–1696 (1991)
65. B. Feldman, R. Brazg, S. Schwartz, R. Weinstein, “A continuous glucose sensor based on wired enzyme technology – results from a 3-day trial in patients with type 1 diabetes. Diabetes. Technol. Ther. **5**, 769–779 (2003)
66. S. Freiberg, X. X. Zhu, Polymer microspheres for controlled drug release. Int. J. Pharm. **282**, 1–18 (2004)
67. R. Jalil, J. R. Nixon, Biodegradable poly(lactic acid) and poly(lactide-coglycolide) microcapsules: problems associated with preparative techniques and release properties. J. Microencapsulation. **7**, 297–325 (2008)
68. Eliana B. Souto, Joana F. Fangueiro and Selma S. Souto, in, ed. by Lan-Anh Le, Ross J. Hunter and Victor R. Preedy, Lipid Matrix Nanoparticles in Diabetes, Nanotechnology and Nanomedicine in Diabetes. Chapter 2 (Science Publishers, 2012), pp. 14–33
69. V. Vijayan, D.S. Rao, E. Jayachandran, J. Anburaj, Preparation and characterization of anti diabetic drug loaded solid lipid nanoparticles. JITPS **1**, 320–328 (2010)
70. S. BarathManiKanth, K. Kalishwaralal, M. Sriram, S.B.R. Pandian, H. Youn, S. Eom, S. Gurunathan, Anti-oxidant effect of gold nanoparticles restrains hyperglycemic conditions in diabetic mice. J. Nanobiotech. **8**, 16–30 (2010)

71. P. Daisy, K. Saipriya, Biochemical analysis of Cassia fistula aqueous extract and phytochemically synthesized gold nanoparticles as hypoglycemic treatment for diabetes mellitus. Int. J. Nanomed. **7**, 1189–1202 (2012)
72. D. Attivi, P. Wehrle, N. Ubrich, C. Damge, M. Hoffman, P. Maincent, Formulation of insulin-loaded polymeric nanoparticles using response surface methodology. Drug Dev. Ind. Pharm. **31**, 179–189 (2005)
73. P. Venugopalan, A. Sapre, N. Venkatesan, S.P. Vyas, Pelleted bioadhesive polymeric nanoparticles for buccal delivery of insulin: Preparation and characterization. Pharmazie **56**, 217–219 (2001)
74. Y. Pan, Y. Li, H. Zhao, J. Zheng, H. Xu, G. Wei, J. Hao, F. Cui, Bioadhesive polysaccharide in protein delivery system: Chitosan nanoparticles improve the intestinal absorption of insulin in vivo. Int. J. Pharm. **249**, 139–147 (2002)
75. M. Morishita, I. Morishita, K. Takayama, Y. Machida, T. Nagai, Novel oral microspheres of insulin with protease inhibitor protecting from enzymatic degradation. Int. J. Pharm. **78**, 1–7 (1992)
76. T. Kuzuya, S. Nakagawa, J. Satoh, Y. Kanazawa, Y. Iwamoto, M. Kobayashi, K. Nanjo, A. Sasaki, Y. Seino, C. Ito, K. Shima, K. Nonaka, T. Kadowaki, Report of the Committee on the classification and diagnostic criteria of diabetes mellitus. Diabetes Res. Clin. Pract. **55**, 65–85 (2002)
77. J. Kost, T.A. Horbett, B.D. Ratner, Joseph Kost, M. Singh, Glucose-sensitive membranes containing glucose oxidase: Activity, swelling, and permeability studies. J. Biomed. Mater. Res. **19**, 1117–1133 (1985)
78. R. Pandey, A. Sharma, A. Zahoor, S. Sharma, G.K. Khuller, B. Prasad, Poly(dl-lactide-co-glycolide) nanoparticle-based inhalable sustained drug delivery system for experimental tuberculosis. J. Antimicrob. Chemother. **52**, 981–986 (2003)
79. M. Takenaga, Y. Yamaguchi, A. Kitagawa, Y. Ogawa, S. Kawai, Y. Mizushima, R. Igarashi, Optimum formulation for sustained-release insulin. Int. J. Pharm. **271**, 85–94 (2004)
80. G.W. Bo-Linn, C.A.S. Ana, S.G. Morawski, J.S. Fordtran, Starch blockers—their effect on calorie absorption from a high-starch meal. N. Engl. J. Med. **307**, 1413–1416 (1982)
81. C.B. Hollenbeck, A.M. Coulston, R. Quan, T.R. Becker, H. Vreman, D.K. Stevenson, G.M. Reaven, Effects of a commercial starch blocker preparation on carbohydrate digestion and absorption: In vivo and in vitro studies. Am. J. Clin. Nutr. **38**, 498–503 (1983)
82. S. Ignacimuthu, S. Prakash, Agrobacterium-mediated transformation of chickpea with alpha-amylase inhibitor gene for insect resistance. J. Biosci. **31**, 339–345 (2006)
83. R.J. Henry, V.G. Battershell, P.S. Brennan, K. Oono, Control of wheat α-amylase using inhibitors from cereals. J. Sci. Food Agric. **58**, 281–284 (1992)
84. P. Layer, G.L. Carlson, E.P. DiMagno, Partially purified white bean amylase inhibitor reduces starch digestion in vitro and inactivates intraduodenal amylase in humans. Gastroenterology **88**(6), 1895–1902 (1985)
85. O.L. Franco, D.J. Rigden, F.R. Melo, C. Bloch Jr., C.P. Silva, M.F. Grossi de Sá, Activity of wheat alpha-amylase inhibitors towards bruchid alpha-amylases and structural explanation of observed specificities. Eur. J. Biochem. **267**, 2166–2173 (2000)
86. G.H. Feng, M. Richardson, M.S. Chen, K.J. Kramer, T.D. Morgan, G.R. Reeck, α-Amylase inhibitors from wheat: Amino acid sequences and patterns of inhibition of insect and human a-amylases insect biochem. Mol. Biol. **26**, 419–426 (1996)
87. S. Dhobale, T. Thite, S.L. Laware, C.V. Rode, S.J. Koppikar, R. Kaul Ghanekar, S.N. Kale, Zinc oxide nanoparticles as novel alpha-amylase inhibitors. J. Appl. Phys. **104**, 094907-1-5 (2008)

Chapter 14
Zinc Oxide: From Optoelectronics to Biomaterial—A Short Review

R. Suryanarayanan

Abstract Zinc oxide is a well-known wide bandgap semiconductor that has attracted recent attention in part because of its large exciton binding energy (60 meV) which could lead to lasing action even above room temperature. Further interest has arisen because of the availability of good quality single crystals, improved technologies for thin film growth and nanorods or fibres, the possibility of *p*-type conduction, and some papers claiming ferromagnetism above room temperature. In addition, it is being proposed that ZnO might exhibit an antibacterial activity even under the dark condition. I review work pertaining to material growth and point out possible emerging applications in fields ranging from optoelectronics to biomaterials.

14.1 Introduction

Zinc oxide (ZnO) is a well-known wide bandgap (E_g ~3.3 eV) semiconductor. The interest in this material has increased rapidly as can be seen from a rapid increase in the number of publications. An exhaustive review covering the material preparation in various forms ranging from single crystal growth to thin films and to nanoribbons and rods pointing to numerous applications mainly in the field of optoelectronics has been recently published [1]. There have also been some recent studies to evaluate ZnO as a suitable biomaterial. In particular, after quantitative evaluation of antibacterial activities of some metal oxide powders (ZnO, MgO, and CaO), ZnO was found to be very effective for Staphylococcus aureus [2, 3]. In what follows, after a brief historical introduction, preparation of bulk crystal growth, thin films and nanocrystals, nature of defects in ZnO, problems related to

R. Suryanarayanan (✉)
Université Paris-sud, 91405 Orsay, France
e-mail: sury39@gmail.com

M. S. R. Rao and T. Okada (eds.), *ZnO Nanocrystals and Allied Materials*,
Springer Series in Materials Science 180, DOI: 10.1007/978-81-322-1160-0_14,
© Springer India 2014

p-type doping, examples of some optoelectronic devices, and ZnO as a possible candidate for dilute magnetic semiconductor (DMS) applications will be presented. This will be followed by a short discussion on ZnO as a biomaterial. As the title indicates, this work does not by any means claim to be an exhaustive review. However, most of the results presented here are taken from the papers published after 2005 and hence not discussed in Ref. [1].

14.2 Historical

As an aside, it is interesting to look at the history of Zinc [4]. Centuries before zinc was discovered in the metallic form, its ores were used for making brass and zinc compounds were used for healing wounds and sore eyes. Although the word brass frequently occurs in the Old Testament, there is little evidence that an alloy of zinc and copper was known in early times. The word translated "brass" might equally well be rendered bronze or copper, both of which were in common use. In the latter part of the thirteenth century, Marco Polo described the manufacture of zinc oxide in Persia and how the Persians prepared tutia (a solution of zinc vitriol) for healing sore eyes. The Roman writer Strabo (66 B.C.–24 A.D.) mentioned in his writings that only the Cyprian ore contained "the cadmian stones, copper vitriol, and tutty", that is to say, the constituents from which brass can be made. It is believed that the Romans first made brass in the time of Augustus (20 B.C.–14 A.D.) by heating a mixture of powdered calamine, charcoal, and granules of copper. Roman writers observed that coins made from orichalcum were undistinguished from gold.

The production of metallic zinc was described in the Hindu book *Rasarnava* which was written around 1200 A.D. However, we find the word *trapu* which means zinc cited in a prayer (Yajurveda 18.13) while doing fire sacrifice by the ancient Hindus as can be seen from the following verse in Sanskrit "*ashmaa cha me mrittikaa cha me girayashcha meparvataashcha me sikataashcha me vanaspatayashcha me hiraNyam cha me ayashcha me shyaamam cha me loham cha me seesam cha me trapu cha me yajyen kalpantaam*". It means may all the following things come to me through *yajnya*, *fire sacrifice*, Stone, the upper layer of earth, hills, mountains, sand, vegetation, gold, lodestone, blackstone, iron, lead, and **zinc**. This verse dates to around 2500–3000 B.C.

The fourteenth century Hindu work *Rasaratnassamuchchaya* describes how the new "tin-like" metal was made by indirectly heating calamine with organic matter in a covered crucible fitted with a condenser. Zinc vapor was evolved and the vapor was air cooled in the condenser located below the refractory crucible (Fig 14.1). By 1374, the Hindus had recognized that zinc was a new metal, the eighth known to man at that time, and a limited amount of commercial zinc production was underway. At Zawar, in Rajasthan, great heaps of small retorts bear testimony to extensive zinc production from the twelfth to the sixteenth centuries. The tubular retorts are about 25 cm long and 15 cm in diameter with

Fig. 14.1 Schematic representation of Indian method of producing Zinc. (*Courtesy* Fathi Habashi, International Zinc Association, Belgium)

walls about 1 cm thick. A small diameter tube was sealed onto the open end and the zinc vapors likely condensed in this. The retorts were closely spaced in a furnace which was probably heated with charcoal fanned by bellows. Both zinc metal and zinc oxide were produced. Zinc was used to make brass, whereas the oxide was used as a medicine. Over 130,000 tons of residues remain at Zawar (Rajasthan, India) and this represents the extraction of the equivalent of 1,000,000 tons of metallic zinc and zinc oxide. From India, zinc manufacture moved to China where it developed as an industry to supply the needs of brass manufacture. The Chinese apparently learned about zinc production sometime around 1600 A.D. An encyclopaedia issued in the latter half of the sixteenth century makes no mention of zinc, but the book *Tien-kong-kai-ou* published early in the seventeenth century related a procedure for zinc manufacture. Calamine ore, mixed with powdered charcoal, was placed in clay jars and heated to evolve zinc vapor. The crucibles are piled up in a pyramid with lump coal between them, and, after being brought to redness, are cooled and broken. The shining metal is found in the center. Soon, Zinc production expanded and began to be exported.

Agricola in 1546 reported that a white metal was condensed and scraped off the walls of the furnace when Rammelsberg ore was smelted in the Harz Mountains to obtain lead and silver to which he gave the name "contrefey" because it was used to imitate gold. This often consisted of metallic zinc, although he did not recognize it as such. He observed, furthermore, that a similar metal called "zincum" was being produced under similar circumstances in Silesia by the local people.

Paracelsus (1493–1541) was the first European to state clearly that "zincum" was a new metal and that it had properties distinct from other known metals. Thus, by about 1,600, European scientists were aware of the existence of zinc. All the

metal they had examined, however, had likely been imported from the East by Portuguese, Dutch, and Arab traders.

However, there was a profusion of names quite unrelated to the local names for zinc ores. These included tutenag—derived from the Persian tutiya, calamine, which became the English tutty, zinc oxide—and spelter, likely from the similar colored lead–tin alloy, pewter, or the Dutch equivalent, spiauter or Indian tin which the British scientist Robert Boyle latinised to spectrum in 1690 from which originates spelter, the commercial term for zinc. The word tutia, an old name for zinc oxide, is derived from a Persian word that means smoke and refers to the fact that ZnO is evolved as white smoke when zinc ores are roasted with charcoal.

In Renaissance times, latten (or laten, laton, and lattyn) became the common English word for brass, akin to the French laiton (= brass) and Italian latta (= sheet brass), and probably based on the Latin latte or lathe (= sheet). The origins of the German word for brass, Messing, may be related to the Latin massa (= lump of metal). The modern English brass may be related to the French braser (= braze or solder). The word "zinc" may be derived from the Persian word sing meaning stone. In Arabic, zinc is known as kharseen, i.e. Khar from Al-Ghar = mine, seen from Al-Seen = China, hence kharseen, and the metal from Chinese mines. The spelter trade with the East flourished throughout the seventeenth and first half of the eighteenth centuries, although there seem to be no records concerning the tonnages involved.

In an extensive research "On the method of extracting zinc from its true mineral, calamine", Andreas Marggraf in 1746 reduced calamine from Poland, England, Breslau, and Hungary with carbon in closed retorts and obtained metallic zinc from all of them. He described his method in detail, and established the basic theory of zinc production. Marggraf also showed that the lead ores from Rammelsberg contained zinc and that zinc can be prepared from sphalerite. Marggraf was probably unaware that in 1742, the Swedish chemist Anton von Swab (1703–1768) had distilled zinc from calamine and that, 2 years later, he had even prepared it from blende.

The knowledge of deliberate zinc smelting in a retort was acquired by an Englishman on a visit to China just prior to 1740. A vertical retort procedure was developed by William Champion (1709–1789) and by 1743 a zinc smelter had been established at Bristol in the United Kingdom. A charge of calamine and carbon was sealed into a clay crucible having a hole in the bottom. This was luted onto an iron tube extending below the crucible furnace into a cool chamber below. The closed end of the iron tube sat in a tub of water and it was here that the metallic zinc was collected. The distillation took a total of about 70 h to yield 400 kg of metal from all 6 crucibles positioned in the furnace. An annual production rate of 200 tons has been suggested for the works at that time. This type of apparatus continued to be employed until 1851 although it was fuel inefficient, consuming 24 tons of coal for every ton of spelter produced. In 1758, William's brother, John, patented the calcination of zinc sulfide to oxide for use in the retort process, thereby laying the foundation for the commercial zinc practice which continued well into the twentieth century. A major technological improvement

came with the development of the German process by Johann Ruberg (1751–1807) who built the first zinc smelting works in Wessola in Upper Silesia in 1798 which used the horizontal retort process developed by him. The principal advantage of this technique is that the retorts were fixed horizontally into the furnace allowing them to be charged and discharged without cooling. By placing the retorts in large banks, fuel efficiency was greatly increased. The raw material initially used was zinc galmei (calamine), a byproduct of lead and silver production. Later, it became possible to produce zinc directly from smithsonite, an easily smelted ore. This was shortly followed by the use of zinc blende, which had first to be converted into the oxide by roasting. After this development, other smelting works were soon erected in Silesia near the deposits, in the areas around Liège in Belgium, in Aachen, in the Rhineland, and Ruhr regions in Germany. The first Belgian plant was built by Jean-Jacques Daniel Dony (1759–1819) in 1805 and also used horizontal retorts but of slightly different design. A larger plant was built in 1810. This was the predecessor of the Societé de la Vieille Montagne which a few years later became the largest zinc producing company in the world.

Zinc production in the United States started in 1850 using the Belgium process and soon became the largest in the world. In 1907, world production was 737,500 tons of which the USA contributed 31 %, Germany 28 %, Belgium 21 %, the United Kingdom 8 %, and all other countries 12 %. Zinc was produced for about 500 years from its oxide ores which are far less abundant than the sulfides, before the sulfides became the major source of supply. The technology of zinc production changed gradually during the centuries toward a more pyrometallurgical route. However, this tendency underwent a radical change during World War I when the roasting-leaching-electrowinning process was introduced in the 1980s, when pressure leaching-electrowinning offered another practical route to zinc production.

14.3 Material Growth

14.3.1 Single Crystal Growth

The preparation of cm-size single crystals are important not only for carrying out fundamental studies such as nature of defects but also because these can be used as substrates for achieving homo or hetero epitaxial growth of thin films. For example, it is interesting to note that ZnO single crystal can be used to grow GaN, another promising material for electronic applications since their lattice mismatch is less than 1.8 %. However, the very high melting point of ZnO ($\sim$2000 °C) makes it difficult to achieve melt growth. Several years ago, hydrothermal [5, 6] and flux growth techniques have been used to grow small size single crystals. There were also attempts to grow crystals by chemical vapor transport (CVT) but again the crystals were of small size see for example [7]. However, CVT of ZnO crystals using chlorine as a gaseous transporting agent carried out in a closed system seemed to

have produced crystals of cm-size by Ntep et al. [8]. In the CVT process, a temperature gradient is used to achieve mass transport which occurs using a chemical reaction between the solid and a gaseous transporting agent. In principle, unlimited amounts of the starting material can be transported with a small amount of a transporting agent. Ntep et al. made use of the following reaction: $ZnO + Cl_2 \leftrightarrow ZnCl_2 + ½ O_2$. In order to get a significant amount of transported material, it is necessary to work in a region where the energy change of reaction is small keeping the equilibrium constant close to unity. This will result in the reverse reaction to an appreciable extent. In their experiments, these authors used 3 g of 5N5 purity ZnO powder in graphitized ampoules of 15 cm^3 volume. The ampoules were sealed off under a residual chlorine pressure of 100 mbar. ZnO crystal growth occurred at a source temperature in the range of 950–1000 °C. A maximum growth rate of 35 mg/h could be attained. These authors also found that the carbon also participated in the formation of ZnO through the reaction $ZnO + C \leftrightarrow Zn + CO$. The well-resolved Kikuchi lines indicated the good quality of crystals. Through Hall effect measurements, room temperature electron concentration as high as 3×10^{19} cm^{-3} and a mobility of 500 cm^2/V s at 90 K were determined.

Another method for producing bulk ZnO is that of melt growth which is employed at Cermet, Inc. [9]. It is based on a pressurized induction melting. The melt is contained in a cooled crucible. Zinc oxide powder is used as the starting material. The heat source used during the melting operation is radio frequency (rf) energy, induction heating. The rf energy produces joule heating until the ZnO is molten at about 1900 °C. Once the molten state is attained, the crucible is slowly lowered away from the heated zone to allow crystallization of the melt. A FWHM of about 125 arc s was reported for the (0004) X-ray rocking curve. The room temperature electron concentration and mobility were 5.04×10^{17} cm^{-3} and 131 cm^2 V^{-1} s^{-1}, respectively.

14.3.2 Thin Films

Thin films form an integral part of any optoelectronic device. The main problem concerns the selection of a suitable substrate. The lattice mismatch between ZnO and GaN, AlN, α-Al_2O_3, 6H–SiC, Si, $ScAlMgO_4$, and GaAs is respectively 1.8 %, 4.5 %, 18.4 %, 3.5 %, 40.1 %, 0.09 % and 42.4 %. Several techniques such as dc, rf-sputtering, molecular beam epitaxy(MBE) using thermal evaporation, and pulsed laser MBE are used for the preparation of thin films of ZnO (undoped and doped) on different substrates [1]. High quality films are obtained on ZnO or $ScAlMgO_4$ as discussed below.

14.3.3 Nanoparticles

Park and Park [10] have synthesized ZnO nanoparticles during carbon dioxide (CO_2) decomposition using a DC plasma jet. The oxygen molecules obtained from CO_2 decomposition and microsized Zn powders were used as raw materials. The operating variables were CO_2 flow rate, the carrier gases, and the inside diameters of the reaction tube. The morphologies of the synthesized ZnO were varied depending on the inside diameter of the reaction tube. The diameter of the rod-shaped ZnO ranged from 25 to 100 nm with an average diameter of 50 nm. These authors have not reported production time. On the other hand, an extremely short production time of 18 s was reported by Ohara et al. [11] on the synthesis of highly crystalline ZnO nanoparticles by the supercritical water hydrothermal synthesis method. Zinc nitrate aqueous solution at room temperature was pressurized to 30 MPa and then mixed with potassium hydroxide solution under the same conditions to generate metal hydroxides. This mixture was then rapidly heated to 673 K by mixing with supercritical water and then fed into a tubular reactor. Residence time is about 18 s. The reaction was terminated by cooling at the exit of the reactor. Production of nanosize particles with uniform particle size distribution (50 nm) showed a highly crystalline ZnO phase. Room temperature photoluminescence (PL) measurements showed near band edge emission at 380 nm. For the preparation of ZnO rods and whiskers, see below.

14.4 Defects

As in any semiconductor, the electrical and optical properties of ZnO are affected by the presence of point defects. Kohan et al. [12] and Van de Walle [13] have calculated formation energies and electronic structure of point defects and hydrogen in ZnO from first principles. It is shown that the concentration (c) of a defect in a crystal depends upon its formation energy (E^f)

$$c = N_s \exp\left\{-E^{\mathrm{f}} / k_B T\right\}$$

where N_s is the concentration of sites in the crystal where the defect can occur. Whereas a low formation energy implies a high concentration of defects, a high formation means defects are unlikely to form.

The formation energy of a point defect in a charge state q is given by $E^f (q)_ = E^{\mathrm{tot}}(q) - n_{\mathrm{Zn}}_\mu_{\mathrm{Zn}} - n_{\mathrm{O}}_\mu_{\mathrm{O}} - qE_F$, where $E^{\mathrm{tot}}(q)$ is the total energy of a system containing n_{Zn} and n_{O} zinc and oxygen atoms, μ_{Zn} and μ_{O} are the chemical potentials for zinc and oxygen, respectively, and E_F is the Fermi energy. Note that there are two possible interstitial sites in the wurtzite ZnO: one is tetrahedrally coordinated and another is octahedrally coordinated. It can be

concluded that, depending on the partial pressure of Zn, the two most common defects in ZnO are likely to be oxygen and zinc vacancies. In particular, oxygen vacancies V_O have lower formation energy than the zinc interstitials Zn_i and hence should be more abundant in Zn-rich conditions. This model allows to identify transitions observed in luminescence. Transitions are observed from the conduction band or a shallow donor to the V_{Zn} acceptor at around 2.6 eV in *n*-type ZnO. Thus, the broad green luminescence (GL) commonly observed in *n*-type ZnO can be attributed to V_{Zn}. Hydrogen in ZnO has been also investigated by the above-mentioned first-principles calculations. Unlike other semiconductors (where hydrogen is amphoteric, i.e., occurs as H^+ in *p*-type material and H^- in *n*-type material), hydrogen in ZnO is always positive, i.e., always acts as a donor. Hydrogen is tightly bound to an oxygen atom in ZnO, forming an O–H bond with a length of about 1.0 Å. In *n*-type ZnO, the formation energy for hydrogen is only 1.56 eV. In *p*-type ZnO, incorporation of hydrogen is even more favorable. In fact, this may be beneficial for obtaining *p*-type ZnO [1].

Low-temperature PL data are very useful to identify and control various defects. In undoped ZnO, the well-known GL band peaking at about 2.5 eV usually dominates the defect-related part of the PL spectrum. Some information is available about the shallow donor–acceptor pair (DAP) band having its main peak at about 3.22 eV. There are a few reports about other PL bands, in particular, the yellow luminescence (YL) in Li-doped ZnO. Besides strong and rich exciton-related emissions in the photon energy range of 3.25–3.4 eV, PL spectrum of undoped high quality ZnO usually contains a sharp peak at about 3.22 eV followed by at least two LO-phonon replicas. This emission has been attributed to the DAP transitions involving a shallow donor and a shallow acceptor [14]. The ionization energy of the unintentional shallow acceptor in ZnO has been estimated to be 195 ± 10 meV. The shallow acceptor is assumed to be N_O. In ZnO intentionally doped with N _with concentration up to 10^{19} cm^{-3}, a relatively broad line at 3.315 eV dominates the PL spectrum. Look et al. [15]. attributed this line to an acceptor-bound exciton (A^0X), associated with the N_O acceptor. A weaker and broader line (or shoulder) appearing at 3.238 eV has been attributed to the DAP emission, involving the N_O acceptor, superimposed with the LO-phonon replica of the dominant (A^0X) emission. The activation energy of the N_O acceptor has been estimated at 0.17–0.20 eV from the above PL experiments. In another study, [16] the PL spectrum of the *p*-type ZnO samples, doped with Nitrogen by using NO gas also contained a strong line at 3.309 eV followed by two LO-phonon replicas, that could be attributed to the shallow N_O acceptor (Fig. 14.2). The acceptor binding energy has been estimated at 165 ± 10 meV.

The nature of the GL, appearing at about 2.5 eV in undoped ZnO, remained controversial for decades. Although in the early studies it was unambiguously attributed to copper impurities, strong evidence was later presented in favor of the oxygen vacancy (V_O) as the defect responsible for the GL band. The architects of both mechanisms make compelling arguments. The controversy could perhaps be resolved if one assumes that while similar in position and width, these PL bands may actually be of different origins. Indeed, it was shown [1] that the GL band with a

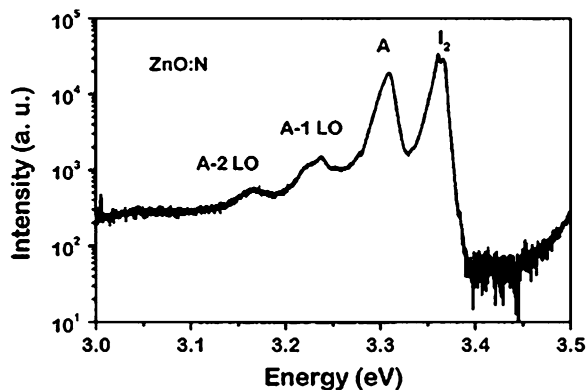

Fig. 14.2 Photoluminescence spectrum at 2 K of a ZnO layer annealed in a high pressure NO/O_2 atmosphere. (Reprinted with permission from american institute of physics, Rommeluère et al. [16])

characteristic fine structure is most likely related to the copper impurities, whereas the structure less GL band with nearly the same position and width may be related to a native point defect such as V_O or V_{Zn}. Doping ZnO with Li acceptor results in the YL band with a peak at about 2.2 eV and a FWHM of 0.5 eV. In contrast to the GL band, the YL band decays very slowly after switching off the excitation source, and can be observed also in the thermo luminescence spectrum [17]. Li-doped ZnO is highly resistive due to the deep location of the Li acceptor level, about 0.8 eV above the valence band. The YL is polarized at low temperatures, which was explained by two metastable orientations of the Li_{Zn} center in the ZnO lattice.

14.5 Doping of ZnO

As has been already pointed out ZnO has a strong potential for various short-wavelength optoelectronic device applications. In order to attain the potential offered by ZnO, both high-quality *n*- and *p*-type ZnO are indispensable. However, difficulty in bipolar carrier doping both *n*- and *p*-types is a major obstacle as seen in other wide bandgap semiconductors such as GaN and II–VI compound semiconductors including ZnS, ZnSe, and ZnTe. Unipolar doping has not been a surprising issue in wide bandgap semiconductors: ZnO, GaN, ZnS, and ZnSe are easily doped to *n*-type, while *p*-type doping is difficult. The situation is opposite for ZnTe where *p*-type doping is easily obtained, while *n*-type doping is difficult.

14.5.1 n-Type Doping

ZnO with a wurtzite structure is naturally an *n*-type semiconductor because of a deviation from stoichiometry due to the presence of intrinsic defects such as V_O and Zn interstitials (Zn_i). Undoped ZnO shows intrinsic *n*-type conductivity with

very high electron densities of about 10^{21} cm^{-3}. Although it is experimentally known that unintentionally doped ZnO is *n*-type, whether the donors are Zn_i and V_O is still controversial. The first-principles study suggested that none of the native defects show high concentration shallow donor characteristics [12, 13]. However, Look et al. [18] suggested that Zn_i rather than V_O is the dominant native shallow donor in ZnO with an ionization energy of about 30–50 meV. It has also been suggested that the *n*-type conductivity of unintentionally doped ZnO films is only due to hydrogen (H) which acts as a shallow donor with an ionization energy about 30 meV. This assumption is valid since hydrogen is always present in all growth methods and can easily diffuse into ZnO in large amounts due to its large mobility. First-principles calculations also suggested that unintentionally incorporated hydrogen acts as a source of conductivity and behaves as a shallow donor in ZnO. *n*-type doping of ZnO is relatively easy compared to *p*-type doping. Group-III elements Al, Ga, and In as substitutional elements for Zn and group-VII elements Cl and I as substitutional elements for O can be used as *n*-type dopants [19]. Doping with Al, Ga, and In has been attempted by many groups, resulting in high quality, highly conductive *n*-type ZnO films [1]. Singh and Rao [20] have recently reported on the optical and electrical transport studies of TM ion (Ni, Ti, V, Fe, Cr, Mn, and Co) doped ZnO polycrystalline samples. Diffuse reflectance spectroscopy of doped ZnO showed the existence of absorption bands which were attributed to the *d*–*d* transitions of respective dopants. Electrical resistivity was found to decrease in case of Ti-, V-, Fe-, and Ni-doped ZnO bulk samples as compared to undoped. This was explained on the basis of impurity *d*-band splitting model. Only the Fe-doped sample showed a cusp at 12 K indicating anti-ferromagnetic interaction.

In a very recent study, a very different doping approach has been used by Falson et al. [21]. These authors demonstrate that extremely low levels of magnesium doping in $Mg_xZn_{1-x}O$/ZnO (for $0.0025<x<0.105$) heterostructures grown by MBE can be utilized to achieve diluted electron density (n) and high-mobility (μ) samples. Carrier density control results in a monotonic decrease to 5.6×10^{10} cm^{-2} with reducing the Mg content to $x = 0.0038$ with retaining a mobility of 200,000 cm^2 V^{-1} s^{-1} (Fig. 14.3). On the other hand, integrating an optimal magnesium content ($x \sim 0{:}01$) results in mobility enhancement to over 700,000 cm^2 V^{-1} s^{-1}, where all heterostructures display clear 2D quantum transport features such as the fractional quantum Hall effect. Unique to this study was the use of distilled pure ozone (O3) as the source of oxygen. O3 flow was controlled using a piezoelectric leak valve and supplied through a water-cooled delivery tube to the vicinity of the substrate. Samples were grown across a temperature range of 750–900 °C. The configuration of heterostructures is $Mg_xZn_{1-x}O$ capping layer/ZnO buffer layer/ZnO substrate, where both the capping layer and buffer layer are typically 200–300 nm thick. The authors point out that in such a diluted heterostructure, the Wigner–Seitz radius defined as $r_S = \{\pi\, e^2/h^2\, \varepsilon\}\{m^*/\pi^{1/2}\, n^{1/2}\}$ where h is the Planck's constant, ε is the dielectric constant, and m^* is the effective mass, approaches a value of 15, suggesting significant electron–

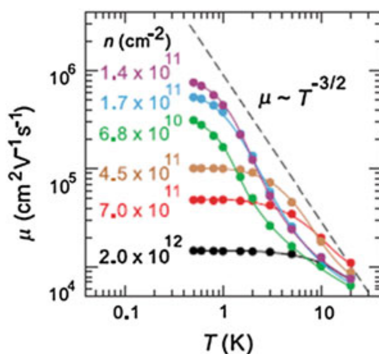

Fig. 14.3 Temperature dependence of electron mobility (μ) for representative samples with various charge carrier densities (n). The broken line represents $\mu \sim T^{-3/2}$ scaling ruled by phonon scattering. (Reprinted with permission from Japan society of Applied Physics, Falson et al. [21])

electron interaction, and extending high mobilitytwo-dimensional electron gas into new territories.

14.5.2 p-Type Doping

As mentioned repeatedly, it is very difficult to obtain *p*-type doping in wide bandgap semiconductors, such as GaN and ZnSe. The difficulties can arise due to compensation of dopants by low-energy native defects, such as Zn_i or V_O, or background impurities (H), low solubility of the dopant in the host material and deep impurity level. Known acceptors in ZnO include group-I elements such as Li, Na, and K, Cu, Ag, Zn vacancies, and group-V elements such as N, P, and As. However, many of these form deep acceptors and do not contribute significantly to *p*-type conduction. It has been believed that the most promising dopants for *p*-type ZnO are the group-V elements, although theory suggests some difficulty in achieving shallow acceptor level.

We will mention here a few recent reports which demonstrate *p*-type doping in ZnO. Tsukazhaki et al. [22] have prepared high quality ZnO and nitrogen-doped *p*-type ZnO films by laser MBE on $ScAlMgO_4$ substrates kept at 1000 °C. The undoped ZnO films show excellent optical and electronic properties. The lifetime of free-exciton emission reaches 2.5 ns. Such a long lifetime indicates very low density of nonradiative defects and negligible carrier trapping to deep radiative defects, such as the GL band frequently seen in poor quality crystals and films. The value of n is about 1×10^{16} cm^{-3} at 300 K. The value of μ is 300 cm^2 V^{-1} s^{-1} and 5,000 cm^2 V^{-1} s^{-1} at 300 K and 100 K, respectively, surpassing the best value for a ZnO bulk single crystals. Nitrogen doping was performed at low temperature (450 °C) and the temperature of the substrate was immediately ramped to a higher temperature of 1000 °C. The hole concentration was 2×10^{16} cm^{-3}. These authors have succeeded in making a *p–i–n* junction and observed a fairly good rectification with a threshold voltage of 7 V at 300 K. The electroluminescence (EL) spectrum shows luminescence from violet to green

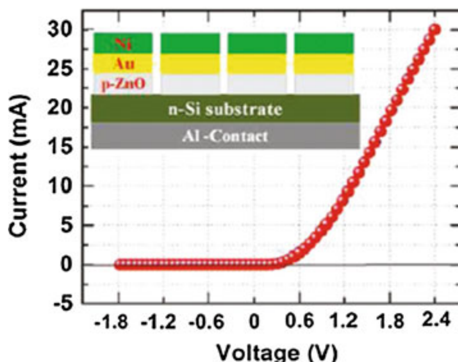

Fig. 14.4 Current–voltage (*I*–*V*) characteristics of the *p*-ZnO/*n*-Si junction diode and the inset shows the schematic of the p–n junction device; (Reprinted with permission from American Chemical Society, Kumar et al. [23])

regions with multi-reflection interference fringes. Attempts are being made to increase the hole concentration.

Kumar et al. [23] have grown thin films of ZnO, Zn_{1-x} Li_x O, $Zn_{1-y}Ni_yO$ and Zn_{1-x-y} Li_xNi_yO ($x = 0.02$ and $y = 0.02$) by pulsed laser deposition (PLD) technique. And 300 nm thick films were grown on quartz substrates kept at a temperature of 400 °C while the O_2 partial pressure was 0.15 mbar during deposition. The films were polycrystalline. Room temperature electrical transport measurements show that 2 mol % of Li-mono doped ZnO thin film is highly resistive in nature with a resistivity of 3.6×10^3 Ω cm. Ni mono-doped ZnO thin film shows resistivity ~0.21 Ω cm, whereas room temperature resistivity of Li–Ni co-doped ZnO thin film is ~0.15 Ω cm, which is four orders of magnitude less compared with Li-mono doped ZnO thin film. Because of high resistivity, Hall effect measurements were not reported on Li-mono-doped ZnO thin film. Ni mono-doped ZnO thin films were *n*-type (3.1×10^{17} cm^{-3}) with a mobility of ~96 cm^2 V^{-1} s^{-1}, whereas Li–Ni co-doped ZnO thin film exhibited a stable *p*-type conductivity with a hole concentration of 3.2×10^{17} cm^{-3} and a high mobility of 130 cm^2 V^{-1} s^{-1}. The positive magnetic field variation (from 0 to 7 T) of the Hall voltage for the Li–Ni co-doped ZnO thin films further confirmed the *p*-type conduction. *p*-ZnO/*n*-Si heterojunction diodes were also fabricated. The I–V characteristics demonstrated clearly the formation of the heterojunction diode. The diode showed a typical rectifying behavior, with a turn on voltage of 0.8 V (Fig. 14.4).

Another method to induce *p*-type conductivity in ZnO is by anion doping. Some preliminary work has been reported bulk $ZnO_{1-y}S_y$ ($y < 0.05$ and $y > 0.96$) crystals grown using CVT technique [24] ZnO was also doped with Te and N which showed an enhancement in photoconductivity [25]. The advantages of anion doping for band-gap engineering and devices have been pointed out by Maksimov [26].

14.6 Can Ferromagnetism be Induced in ZnO?

If ZnO can be made ferromagnetic by doping with transition metals (TM) such as Mn, Fe, Cr, Co, etc., or when spin injecting contacts to ZnO can be found, the material would be suitable for spin Field Effect Transistors. This has prompted many laboratories to investigate magnetic properties of TM-doped ZnO [1, 27]. Further, the calculations by Dietl et al. [28] predict a ferromagnetic Curi temperature (T_c) of around 300 K for *p*-type (3.5×10^{20} holes/cm^3) ZnO. Though there are so many reports confirming this prediction (mostly with no anomalous Hall Effect data), it is not clear if the dopants used really go into the lattice. However, Thakur et al. [29] have used Raman and high resolution electron microscope structural investigations on Co (< 5 %) doped ZnO films and show that the ferromagnetism arises because of oxygen vacancies and not because of Co segregation. To make the situation worse, there are reports wherein even undoped TiO_2 [30, 31] and In_2O_3 films show signs of ferromagnetism [32]. It is interesting to note that Pangaluri et al. [32] have used, for the first time, point contact Andreev reflection measurements to directly determine the spin polarization, which was found to be approximately 50 % also in the case of undoped In_2O_3 films (Fig. 14.5). These results are consistent with suggestions that the ferromagnetism observed in certain oxide semiconductors may be carrier mediated. However, this field is still open.

14.7 Devices

We have already seen above hetrostructures and *p–i–n* structures have been built using both *n*- and *p*-type ZnO. We will mention briefly some more results on devices obtained recently using both thin films and nanoparticles.

Sonmezoglu [33] has fabricated *n*-TiO_2/*p*-ZnO heterojunction diode. The materials were prepared by dip coating sol–gel solutions on to an Indium–Tin–Oxide substrate. The *n*-type TiO_2 solution was prepared by adding 2.4 mL of titanium tetraisopropoxide, to 50 mL of ethanol, then 5 mL of glacial acetic acid and 1.5 mL of triethlyamine. To prepare the *p*-type ZnO solution, a 0.4 M sol of zinc acetate dihydrate in isopropyl alcohol was prepared and stabilized by diethanolamine. Ammonium acetate as nitrogen source was added to the sol. The sample was annealed at 300 °C. It is interesting to note that this structure showed rectifying properties with an ideal factor of 3.62.

Zinc 20 wt % cadmium oxide (ZnCdO) transparent thin film transistors (TFTs) have been fabricated with a back-gate structure using highly *p*-type Si (001) substrate [34]. For the active channel, 30 nm, 50 nm, and 100 nm thick ZnCdO thin films were grown by PLD. The optical gap was around 3 eV. Good characteristics were obtained: threshold voltage of 4.69 V, a subthreshold swing of 4.2 V/decade, mobility of 0.17 cm^2/Vs, and on-to-off current ratios of 3.37×10^4.

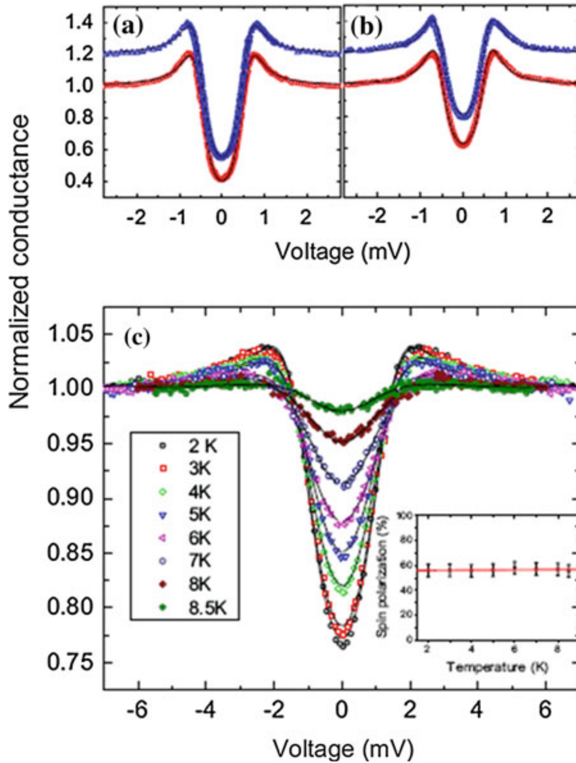

Fig. 14.5 **a** and **b** Normalized conductance curves for two different Sn contacts for **a** Cr: In_2O_3 and **b** In_2O_3 samples at $T = 1.2$ K. One curve in each plot is offset for clarity. Solid lines are the numerical fits obtained with the diffusive model using the BCS gap of bulk Sn, $\Delta = 0.57$ meV. **a** Contact resistance $R_c = 48\ \Omega$ (*open circles*) with fitting parameters: $Z = 0.44$ and $P = 47$ %; $R_c = 35\ \Omega$ (*open triangles*) with $Z = 0.47$ and $P = 52$ %. **b** $R_c = 75\ \Omega$ (*open circles*) with $Z = 0$ and $P = 40$ %; $R_c = 87\ \Omega$ (*open triangles*) with $Z = 0$ and $P = 42$ %. **c** A single Nb contact with the In_2O_3 thin film at different temperatures $R_c = 61\ \Omega$. The BCS temperature dependence of the gap with $\Delta(0) = 1.2$ mV was used for all the fits. The inset shows the temperature dependence of the resulting spin polarization in In_2O_3 with an average $P = 56$ %. (Reprinted with permission from American Physical Society, Pangaluri et al. [32])

Mohan and Kim [35] have argued recently that the development of ZnO-based RRAM would be of both scientific and commercial interest. According to these authors, ZnO with good resistive switching behavior has advantages. They used a horizontal tube furnace for the growth of ZnO single crystal whiskers. A mixture of ZnO and graphite in 1:1 ratio (by weight) were used as a source material. It was loaded on a quartz boat and placed in the center of a 1-m long quartz tube. High-purity argon and oxygen gases were introduced through one side of the furnace (1100 °C) and other side of the quartz tube was connected to a water bubbler. Transparent colourless needle-shaped whiskers with a hexagonal cross-section were found to grow in the boat. The device was structured over SiO_2/Si substrates

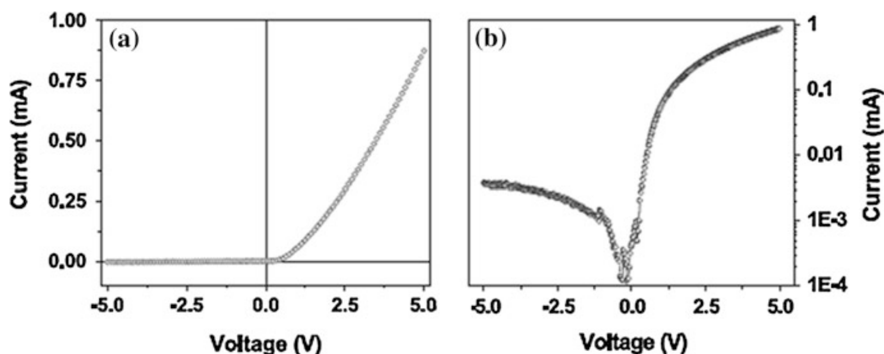

Fig. 14.6 *I–V* characteristics of the EL device in linear and semilog form: (**a**), (**b**) *n*-ZnO nanorod/*p*-Si, (Reprinted with permission from Institute of Physics, Rout and Rao [38])

and Ag was used for contacts. The ratio R_{OFF}/R_{ON} increases with decreasing diameter (d) of the whisker. For $d = 50$ µm, the ratio was = 1:37 and for $d = 5$ µm, the ratio increased to 235. The observed behavior was explained on the basis of the formation and migration of oxygen vacancies at the Ag/ZnO interface.

Before closing this section, we would like to mention a few applications of ZnO nanorods (NRs). An extensive review has been recently published [36]. ZnO NRs and needles can be easily grown. High purity ZnO power is heated at elevated temperatures in the presence of hydrogen, which then leads to the reduction and creation of Zn vapor in the presence of pure oxygen or air, Zn vapor is oxidized to form ZnO. The ZnO vapor before nucleation is transported by nitrogen and the nucleation is located at sites with lower temperature. Using this simple approach, high quality pure hexagonal needles of a few millimetres in diameter and several centimetres in length can be obtained [37]. Besides the ease of growing ZnO even in the nanostructure form, the advantage for light-emitting diodes (LEDs) would be the integration of *n*-ZnO NRs on other *p*-type substrates due to the fact that NRs of ZnO have no need for a lattice matched substrate for the overgrowth, in contrast to thin films. This implies that even amorphous and flexible substrates can be used and heterostructure devices can be built. For example, Rout and Rao [38] have grown *n*-ZnO NR/*p*-Si and *n*-ZnO NR/*p*-PEDOT/PSS heterojunction LEDs with ZnO NRs grown by a low-temperature method as well as by employing PLD. The low-temperature method involves growing the ZnO NRs by the reaction of water with zinc metal. The current–voltage (*I–V*) characteristics of the heterojunctions show good rectifying diode characteristics (Fig. 14.6). The EL spectra of the NRs show an emission band at around 390 nm and defect related bands in the 400–550 nm region. Room temperature EL is detected under forward bias for both the heterostructures. With the low-temperature grown NRs, the defect-related bands in the 400–550 nm range are more intense in the EL spectra, whereas with the PLD grown NRs, only the 390 nm band is prominent. For *n*-ZnO NR/*p*-Si heterojunctions, the leakage current is only 3.6 μA at a reverse bias of 5 V, and the

ratio of the forward-to-reverse bias current is 243 at a bias voltage of ± 5 V. For the *n*-ZnO/*p*-PEDOT/PSS structure, the rectification ratio of the forward-to-reverse bias current is 3.8 and 4574 at ±5 and ±50 V, respectively. Finally, it is interesting to note that the ZnO NRs can also be doped. Singh et al. [39] have recently shown that Ni-doped ZnO needles can be grown by PLD and which show RT PL.

14.8 Biomedical Applications

We present here a short review on biomedical applications of ZnO. Every human beings body possesses small proportions of this mineral, and hence it is known as a trace element. This common mineral is essential for performing simple, but vital functions in our body. In India, the Ayurvedic medicinal system for more than 12 centuries has been using *Pushpanjana* (ZnO) to cure conjunctivitis, trachoma, and chronic severe hiccough [40]. Zinc has also been used in Homeopathy. It has been claimed that this homeopathic medication helps the body to regulate the bladder and helps in curing minor urogenital problems. Recent research has shown that Zinc has a unique role in thymus dependent "*T*" cell-mediated immune response. In addition to combining with thymic hormone to form the biologically active thymic hormone molecule, even a mild reduction of circulating zinc levels is associated with reduced T cell production of certain critical proteins called cytokines which regulate immune response and act as growth factors for the immune system. Now, as a result of much research, zinc is included in human nutrient solutions and infant formulae. The benefit of normal levels of zinc on immune response is clear and the use of supplements to achieve this is well established [41].

Methicillin-resistant staphylococcus aureus (MRSA) commonly linked with both hospital-associated infections and new community-acquired strains, which is brought by a variety of disease-causing bacteria, such as Enterococcus, Staphylococcus, and Streptococcus, have been thought to be a serious threat to public health worldwide [42]. Therefore, new strategies need to identify and develop the next generation of drugs or agents to control bacteria infections, bacteriostatic, antimicrobial, or biocidal action [43]. For example, it is well-known that illuminated suspensions containing TiO_2 are effective at killing Escherichia coli (E. coli), which activity is originated from its photocatalytic disinfection. However, the disadvantage of utilizing TiO_2 is that UV light is required to activate the photocatalyst and initiate the killing of the bacteria and viruses. Hirota et al. [44] have fabricated ZnO ceramics starting from fine ZnO powders which were hydrothermally treated. Sustainability in antibacterial activity was evaluated using a colony count method with E. coli bacteria on nutrient agar medium in a Na–P-buffer solution. Antibacterial activity f was defined as the following equation: $f = -\log(N/N_0)$, where N_0 (10^7) the number of the colony before the addition of ZnO. f was found to be equal to seven indicating all the colonies were perfectly

disappeared after the antibacterial activity test. Thus, ZnO exhibits an antibacterial activity even under the dark condition.

Another recent application is in the field of bone and dental substitution materials. These materials should be porous to serve as a scaffold for capillary growth and further should have excellent biocompatibility, osteoconductivity, and a complete lack of antigenicity. Ideally, a scaffold will offer mechanical support and will be resorbed as new bone and tissue growth occur. Tri Calcium phosphate (TCP) materials have been widely studied for their use in orthopedic and dental implant applications and tissue scaffolds due to their excellent biocompatibility, controllable bioresorbability, and compositional similarity to bone see for example [45]. However, one of the major disadvantages of ceramic scaffolds is their low strength, especially at high volume percentages of porosity. In this respect, it is interesting to note the influence of a SiO_2/ZnO binary dopant system (SiO_2) (0.5 wt %) and zinc oxide (ZnO) (0.25 wt %)—on the mechanical and biological properties of designed macroporous TCP scaffolds fabricated using commercial 3D printing technology [46]. The addition of dopants decreased the β to α phase transformation of TCP sintered at 1250 °C, increased densification and as a result, showed up to 250 % increase in compressive strength when compared to pure TCP scaffolds. A maximum compressive strength of 10.21 ± 0.33 MPa was achieved in doped scaffolds with 500 μm interconnected macropores. Further, this additive facilitated faster cell proliferation when compared to pure TCP scaffolds.

We conclude this section by pointing out that ease of fabrication of ZnO and its biocompatibility has lead to several applications of ZnO as biosensors. In particular, mention should be made of glucose and cholesterol sensors [47].

14.9 Conclusion

In this brief review, I have tried to cover the following topics most of which have not been covered by Ozgur et al. [1] in their review paper: single crystal growth, thin films growth, nanoparticle production of ZnO, nature of defects, and identification of these by PL, preparation of high device quality *n*-type ZnO films, successful *p*-type doping of ZnO films, demonstration of thin film field effect transistors. In addition, a few selected useful applications of ZnO as biomaterials have been pointed out. There has been very notable progress in achieving *p*-type doping of ZnO and a few laboratories have even succeeded in making devices based on *p–i–n* junctions. It is quite possible that high quality *n*-type ZnO with a high mobility may be used as heterojunction devices. Devices using nano zinc oxide are in the process of development. Though it is clear that the silicon transistor is not going to be replaced very soon, the integration of new devices with conventional silicon electronics will open up a diverse range of applications [48]. One is tempted to predict that Si-based nano ZnO *n*-type heterostructures have a bright future. ZnO as a biomaterial could be an attractive substitute for TiO_2 in certain applications.

Acknowledgments I would like to thank Prof. M. S. Ramachandra Rao for encouraging me to write this review and for the hospitality shown to me during my visit to IIT Madras in January 2012.

References

1. U. Ozgur, Ya.I. Alivov, C. Liu, A. Teke, M.A. Reschikov, S. Dogan, V. Avrutin, S.-J. Cho, H. Morkoc, J. Appl. Phys. **98**, 041301 (2005)
2. J. Sawai, T. Yoshikawa, J. Appl. Microbiol. **96**, 803 (2004)
3. K. Horota, M. Sugimoto, M. Kato, K. Tsukagoshi, T. Tanigawa, H. Sugimoto, Ceram. Int. **36**, 497 (2010)
4. A history of Zinc by Fathi Habashi, International Zinc Association (IZA), www.zincworld.org
5. R.A. Laudise, A. Ballman, J. Phys. Chem. **64**, 688 (1960)
6. J.W. Nielson, E.F. Dearborn, J. Phys. Chem. **64**, 1762 (1960)
7. K. Matsumoto, K. Noda, J. Cryst. Growth **102**, 137 (1990)
8. J.-M. Ntep, S. Said Hassani, A. Lusson, A. Tromson-Carli, D. Ballutaud, G. Didier, R. Triboulet, J. Cryst. Growth **207**, 30 (1999)
9. Cermet, inc. http://www.cermetinc.com
10. J.-S. Park, D.-W. Park, Surf. Coat. Technol. **205**, S79 (2010)
11. S. Ohara et al., Solid State Ionics **172**, 261 (2004)
12. A.F. Kohan, G. Ceder, D. Morgan, C.G. Van de Walle, Phys. Rev. **B 61**, 15019 (2000)
13. C.G. Van de Walle, Physica B **899**, 308–310 (2001)
14. K. Thonke, T. Gruber, N. Trofilov, R. Schönfelder, A. Waag, R. Sauer, Physica B **945**, 308–310 (2001)
15. D.C. Look, D.C. Reynolds, C.W. Litton, R.L. Jones, D.B. Eason, G. Cantwell, Appl. Phys. Lett. **81**, 1830 (2002)
16. J.F. Rommeluère, L. Svob, F. Jomard, J. Mimila-Arroyo, A. Lusson, V. Sallet, Y. Marfaing, Appl. Phys. Lett. **83**, 287 (2003)
17. O.F. Schirmer, D. Zwingel, Solid State Commun. **8**, 1559 (1970)
18. D.C. Look, J.W. Hemsky, J.R. Sizelove, Phys. Rev. Lett. **82**, 2552 (1999)
19. H. Kato, M. Sano, K. Miyamoto, T. Yao, J. Cryst. Growth **538**, 237–239 (2002)
20. S. Singh, M.S.R. Rao, Phys. Rev. **B 80**, 045120 (2009)
21. J. Falson, D. Maryenko, Y. Kozuka, A. Tsukazaki, M. Kawasaki, Appl. Phys. Express **4**, 091101 (2011)
22. A. Tsukazhaki et al., Nat. Mat. **4**, 42 (2005)
23. E.S. Kumar, J. Chatterjee, N. Rama, N. DasGupta, and M.S.R. Rao, ACS Appl. Mater. Interfaces **3**, 1974 (2011)
24. S. Locmelis, C. Brunig, M. Binnewies, A. Borger, K.D. Becker, T. Homann, T. Bredow, J. Mater. Sci. **42**, 1965 (2007)
25. H.L. Porter, A.L. Cai, J.F. Muth, J. Narayan, Appl. Phys. Lett. **86**, 211918 (2005)
26. O. Maksimov, Rev. Adv. Mater. Sci. **24**, 26 (2010)
27. J.M.D. Coey, Curr. Opin. Solid State Mater. Sci. **10**, 83 (2006)
28. T. Dietl, H. Ohno, F. Matsukura, J. Cibert, D. Ferrand, Science **287**, 1019 (2000)
29. J. Thakur et al., J. Appl. Phys. **102**, 093904 (2007)
30. N.H. Hong, J. Sakai, N. Poirot, V. Brize, Phys. Rev. **B 73**, 132404 (2006)
31. C. Sudakar et al., J. Mag. Mag. Mat. **320**, L1 (2008)
32. R.P. Panguluri et al., Phys. Rev. **B 79**, 165208 (2009)
33. S. Sonmezoglu, Appl. Phys. Express **4**, 104104 (2011)
34. D.-H. Lee, S. Kim, S.Y. Lee, Thin Solid Films **519**, 4361 (2011)
35. R. Mohan, S.-J. Kim, Jpn. J. Appl. Phys. 50, 04DJ01 (2011)

36. M. Williander et al., Nanotechnology **20**, 332001 (2009)
37. E. Scharowski, Z. Phys. **135**, 318 (1953)
38. C.S. Rout, C.N.R. Rao, Nanotechnology **19**, 285203 (2008)
39. S. Singh et al., New J. Phys. 12 (2010)
40. A.K. Panda, S. Rout, Nat. Prod. Radiance **5**, 284 (2006)
41. S. Cunningham, Rundles. International Zinc Association, Belgium
42. U. Desselberger, J. Infect. **40**, 3 (2000)
43. P.K. Stoimenov, R.L. Klinger, G.L. Marchin, K.J. Klabunde, Langmuir **18**, 6679 (2002)
44. K. Hirota et al., Ceram. Int. **36**, 497 (2010)
45. R. Enderlea et al., Biomaterials **26**, 3379 (2005)
46. G. A. Fielding et al., *to be published*; Dental Materials, doi:10.1016/j.dental.2011.09.010
47. S.A. Kumar, S.-M. Chen, Anal. Lett. **41**, 141 (2008)
48. I. Ferain, C.A. Colinge, J.-P. Colinge, Nature **479**, 310 (2011)

Chapter 15
On the Optical and Magnetic Properties of Doped-ZnO

J. Kumar, S. Ramasubramanian, R. Thangavel and M. Rajagopalan

Abstract Investigations on the modifications of the optical and magnetic properties in ZnO due to different dopants have been carried out. First principle calculations were performed to understand the effect of dopants on the magnetic properties of ZnO. The studies revealed addition of nitrogen with cobalt enhances the total magnetic moment of the system. While considering the position of occupation of the dopants in the ZnO matrix, cobalt and nitrogen bonded pair is found to be energetically favorable. Likewise, lithium and cobalt co-doping in ZnO has been predicted to increase the magnetic moment of the system. Room temperature ferromagnetism has been observed in the Co and N, Li and Co co-doped ZnO films. Due to selective doping in ZnO, the bandgap can be tuned to the desired applications. Cadmium and magnesium co-doping is found to effectively modify the bandgap energy in the range between 3.3 eV and 3.66 eV.

15.1 Introduction

As a wide bandgap (3.2 eV), transparent semiconducting oxide, zinc oxide (ZnO) has been widely studied for a variety of optoelectronic devices such as solar cells, electrodes, sensors, transparent UV-protection films, and UV light emitting devices. It shows high thermal and chemical stability. ZnO is of wurtzite crystal structure at ambient conditions with a strong ionic bonding where the conduction band mainly comes from Zn^{2+} 4*s* states and the upper valence band arises from O^{2-} 2*p* states together with Zn^{2+} 3*d* states. Undoped ZnO exhibits n-type

J. Kumar (✉) · S. Ramasubramanian · M. Rajagopalan
Crystal Growth Centre, Anna University, Chennai 600 025, India
e-mail: marsjk@annauniv.edumarsjk@yahoo.com

R. Thangavel
Research Centre for Applied Sciences, Academia Sinica, Taipei 115, Taiwan

M. S. R. Rao and T. Okada (eds.), *ZnO Nanocrystals and Allied Materials*,
Springer Series in Materials Science 180, DOI: 10.1007/978-81-322-1160-0_15,
© Springer India 2014

conductivity due to donor-type defects such as oxygen vacancies and zinc interstitials. Considerable work has been carried out on transition metal (TM) doped ZnO for developing it as a dilute magnetic semiconductor (DMS). DMS needs localized magnetic moments that couple with the charge carriers without changing the semiconducting behavior of the host material. As the valence of Zn in ZnO is +2, it can be readily replaced by TM ions, enabling interesting magnetic, optical, and electrical properties. Diet et al. [1] predicted theoretically that room temperature ferromagnetism should exist in TM-doped ZnO. Among them, Mn and Co are mostly studied to realize room temperature ferromagnetism. There are many experimental reports available on the magnetic properties of TM-doped ZnO, but their origin remains unclear. In fact, the magnetic properties reported so far for TM-doped ZnO ranges from intrinsic ferromagnetism with different critical temperature Tc, [2–6] extrinsic ferromagnetism, [7–9] paramagnetic (or) super paramagnetic [10–12] to anti-ferromagnetism [13–15].

15.2 Doped ZnO System

Cobalt doped ZnO exhibit room temperature ferromagnetism. Unlike the case of manganese doped ZnO [1], cobalt doped ZnO does not show magnetism with dependence on the carrier type (n or p) and cobalt has also relatively more solubility in the system. We have carried out theoretical studies to evaluate magnetism in cobalt doped ZnO based on density functional theory (DFT). To find the energy of the system, the following Schrödinger equation is to be solved:

$$H\psi = E\psi \tag{15.1}$$

For many electron problem of a crystal,

$$\left[-\nabla^2 + V_{Ne} + V_{ee} + V_{xe}\right]\psi_{ik} = \varepsilon_{ik}\psi_{ik} \tag{15.2}$$

where V_{Ne} is the nuclear–electron attraction potential, V_{ee} is the electron–electron repulsion potential and V_{xe} is the exchange–correlation potential. Density functional theory is the basis for most of the band structure methods to calculate the ground state properties of crystalline solids and is based on the Hohenberg-Kohn theorem. According to the theorem, the external potential is a unique function of the electron density.

i.e.,

$$V(n(r)) < --- > n(r) \tag{15.3}$$

By knowing the electron density of a system and applying suitable wave function, the energy of the system can be determined. A super cell of 72 atoms in wurtzite ZnO was first optimized to construct the doped system. The electronic structure and magnetic calculations of these doped systems were performed using full potential linear augmented plane wave (FPLAPW) method as implemented in

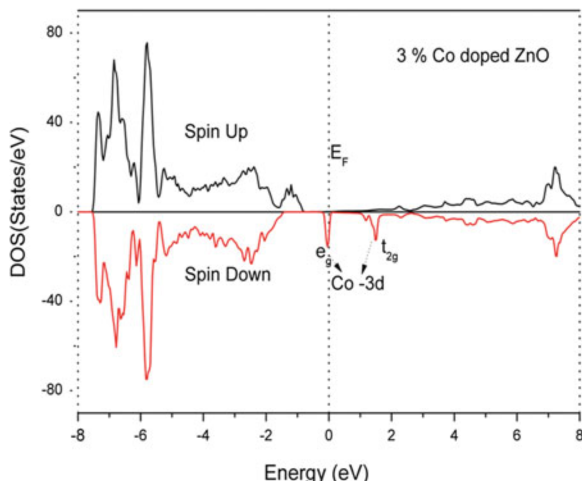

Fig. 15.1 Density of States (DOS) for 3 % cobalt doped ZnO

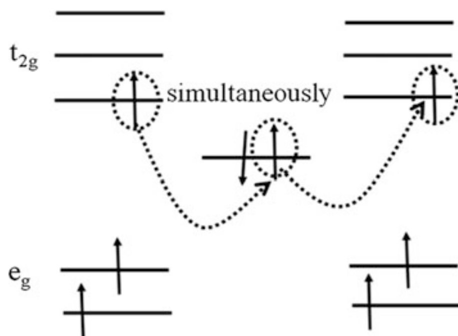

Fig. 15.2 Schematic representation of the exchange mechanism

Wien2K code [16]. Generalized gradient approximation (GGA) functional in the form of Perdew-Burke-Ernzherof (PBE) was employed here for the exchange–correlation potential. When cobalt (∼3 %) is substituted in Zn site, there is a delocalization of the 3*d* states of cobalt due to its p-d hybridization with O 2*p*-like states. This causes cobalt to be spin polarized. Cobalt 3*d* orbital's are split into double e_g states ($d_{x2\text{-}y2}$ and d_{z2}) with lower energy and triple t_{2g} (*dxy, dyz, and dxz*) states with higher energy by the crystal field in tetrahedral symmetry. From the Density of states (DOS) (Fig. 15.1) one can infer that the exchange splitting (∼2 eV) is large compared to the crystal splitting. The system shows the half-metallic behavior due to the partial occupation of t_{2g} states (↓).

This feature is also one of the shortcomings in GGA which amplifies the hybridization and shrinks the gap. The magnetic moment is calculated as 2.63 μ_B for each doped cobalt atom. The magnetic moment arises in the system due to the exchange of the spin in between the split cobalt *d* states through the bonded oxygen (Fig. 15.2).

According to Hund's rule on the intra-atomic exchange, the carriers do not change their spin orientation when moving from one ion to the next, so they can only move if the spins of the two ions are parallel. Therefore, this parallel spin alignment induces ferromagnetism.

Using Korringa–Kohn–Rostoker (KKR) Green function calculations based on DFT, Sato and Katayama [17] studied the stabilization of ferromagnetic states by electron doping in TM-doped ZnO. Lee and Chang [18] have also predicted that heavy electron doping and high Co concentration are required for obtaining ferromagnetism in cobalt doped ZnO. In another study [19] the hydrogen mediated spin–spin interaction is predicated to induce high temperature ferromagnetism in Co-doped ZnO. Thus the origin for stabilization of ferromagnetic state by electron doping comes from electron participating in a double exchange mechanism, lowering the energy of the ferromagnetic state. Hence, the study on the impact of an additional dopant on the spin exchange will lead to interesting results. We chose Lithium and Nitrogen separately, as a co-dopant in the ZnO:Co, as they do not contain d-electrons to interfere much with magnetic calculations of the host and to study the effect of hole in the ferromagnetic state of the system. The size of the N atom is suitable to substitute the oxygen position and that of Li is suitable to occupy the Zn atom in the ZnO:Co system.

First principle calculations have been performed to study the effect of N and Co co-doping on the electronic spin alignment of ZnO. The calculations are carried out for different combinations of Co occupying the Zn site and N occupying O site. The doping percentage and the resultant magnetic moment are summarized in Table 15.1. We introduced only nitrogen in the ZnO lattice and studied the magnetic property. Anionic substitution of N ($\sim$3 %) in oxygen position shows weak magnetism of 0.99 μ_B(Fig. 15.3).

The magnetism arises from the charge (spin) imbalance created by the nitrogen at oxygen site. Irrespective of the position of N doping in the ZnO, the magnetic moment at N site is 0.35 μ_B. It shows that magnetism arises mainly due to delocalized 2*p* orbital of the anions due to their by p–p interaction.

In order to find the best path for ferromagnetism for (Co, N) co-doped ZnO, different possible bonding combinations in a ZnO matrix have been studied [20], i.e., the substitution was done in different positions and their interactions have been carried out. Two favorable positions in the nitrogen substitution are (i) when

Table 15.1 Magnetic moments of the cobalt and nitrogen co-doped ZnO

$Zn_{36-x}Co_xO_{36-y}N_y$		Magnetic moment (Bohr Magnetron)			
		Total	**Cobalt site**	**Nitrogen site**	**Oxygen site**
$x = 1$, $y = 0$ ($\sim$3 %Co: doped)		3.02	2.63	–	–
$x = 0$, $y = 1$ ($\sim$3 % N: doped)		0.99	–	0.35	–
$x = 1$, $y = 1$	Case (i)	4	2.67	0.36	0.12
($\sim$3 % Co and N co-doped)	Case (ii)	4	2.64	0.17	0.22
$x = 2$, $y = 1$ ($\sim$ 6% Co and $\sim$ 3% N : co - doped)		7	2.58	0.38	0.09

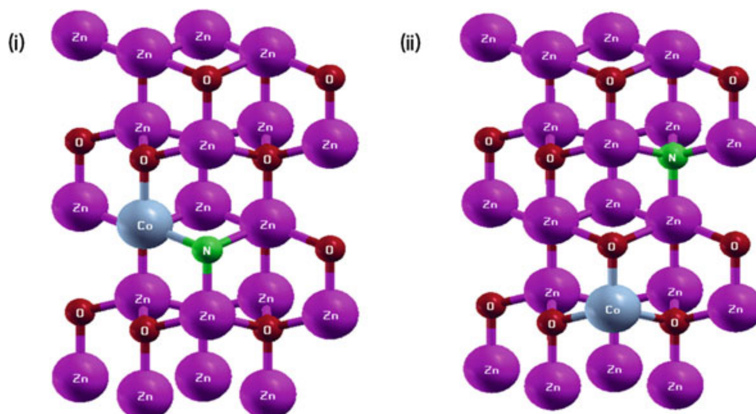

Fig. 15.3 Cobalt and nitrogen co-doped ZnO

there is a bonding between the cobalt and nitrogen, i.e.,–O–Co–N–Zn–, (ii) when there is no bonding between the cobalt atom and nitrogen –O–Co–O–Zn–N– (Fig. 15.4).

The combination reveals that the spin polarized Co atom increases the magnetic moment of the shortest bonded atom with not much change in the total magnetic moment of the system. There is a mutual exchange of spin between Co–N in their p–d hybridization leads a slight increase in the magnetic moment at Co site.

When the percentage of Co-dopant (∼6 % Co) is increased by means of introducing (i) Co-dimer with equal distance from O in the tetrahedral bonding and (ii) Co-dimer with unequal distance from O, there is increase in total magnetic moment in the system but there is no significant change in the magnetic moment at Co site. Here too the N substitution between the two Co atoms increases the spin magnetic moment of the system. There is exchange of the spin between Co atoms happens through the oxygen or nitrogen. Our calculation shows there is a

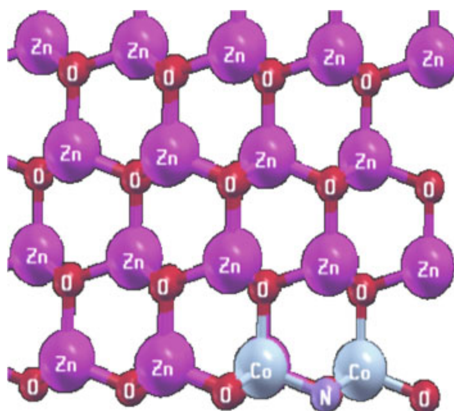

Fig. 15.4 Cobalt dimer in the ZnO bonded via nitrogen atom

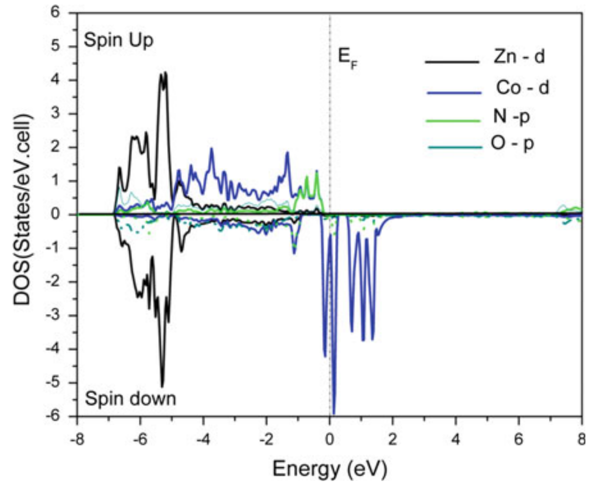

Fig. 15.5 Partial density of states of 3 % (Co, N) co-doped ZnO

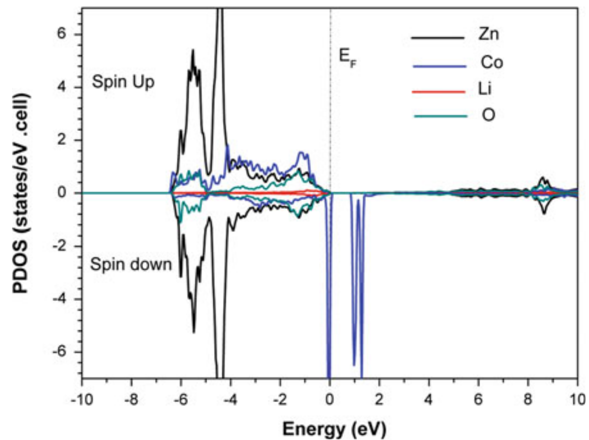

Fig. 15.6 Partial density of states of 3 % (Li, Co) co-doped ZnO

possibility of slight increase in the magnetic moment when the direct exchange happens through nitrogen instead of oxygen atom. Figure 15.5 shows the partial density of states of Co and N co-doped ZnO. In the spin down state, there is a hybridization of nitrogen p-orbital, oxygen p-orbital, and cobalt d-orbital.

In the case of Li co-doped ZnO, unlike N it contributes to magnetism as an individual dopant. We used a different occupancy site for Li and found that there is not much variance in the magnetic moment with respect to the position of the Li atom in the ZnO:Co system. But when Li is introduced in ZnO:Co it increases the magnetic moment of the cobalt to 2.74 μ_B. Sluiter et al. [21] have also predicted that Li doping promotes the ferromagnetic state in the ZnO:Co system. They studied the following cases: (1) two Co atoms with an intermediate or neighboring Li atom, (2) two Co atoms with a distant Li atom, and (3) two Co atoms with a distant interstitial Li with Zn vacancy. The former was found to be most energetically favorable, while the latter was least favorable. Surprisingly, in all three

cases they found that Li amplifies the couplings between Co pairs, and for distant pairs the FM couplings are much enhanced (Fig. 15.6).

15.3 Experiment

Dopant ions were provided by transition metal: Manganese Chloride ($MnCl_2 \cdot 4H_2O$) and Cobalt acetate [$CoCH_3(COO)_2 4 \cdot H_2O$]. Zinc acetate and dopant salts were dissolved completely in 2-methoxyethanol with monoethanolamine as stabilizing agent by stirring at room temperature. Sapphire (0001) substrates were cleaned using methanol, trichloroethylene and acetone before the deposition of the films for 15 min, followed by rinsing with deionized water and drying in air. Each film consisted of 10 layers, each spun at 3000 rpm for 30 s. After deposition, each layer was dried in a furnace at 373 K for 10 min to evaporate the solvent followed by a thermal treatment at 673 K for 10 min to decompose the organic component from the film before spinning the next layer. The complete ten-layer film was annealed at 873 K for 30 min in air in a quartz tube furnace and then cooled to room temperature (RT). We also carried out experiments with Mn, Li, and Co as well Co and N co-doped in ZnO.

(i) **Mn doped ZnO**

Figure 15.7 shows the XRD patterns of undoped and doped ZnO thin films with 1 wt% of manganese concentration on sapphire substrates. The XRD pattern of these samples is in close agreement with the JCPDS standard (No. 36-1451) data of wurtzite (hexagonal) ZnO powder.

The diffraction pattern of the sample doped with Mn suggests that Mn is incorporated at the Zn lattice site in the hexagonal wurtzite structure of ZnO. Few weaker peaks labeled by arrow can also be seen in Mn doped sample in the XRD pattern as shown in Fig. 15.7.

The peaks may be assigned to Mn_3O and they correspond to the (112) and (004) diffraction peaks respectively. That is to say, not all the Mn has entered the ZnO

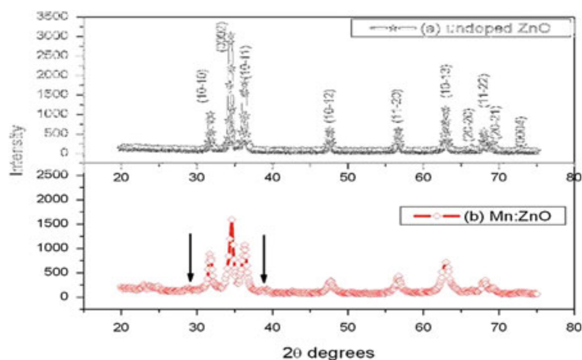

Fig. 15.7 X-ray diffraction of **a** undoped and **b** Mn doped ZnO thin films

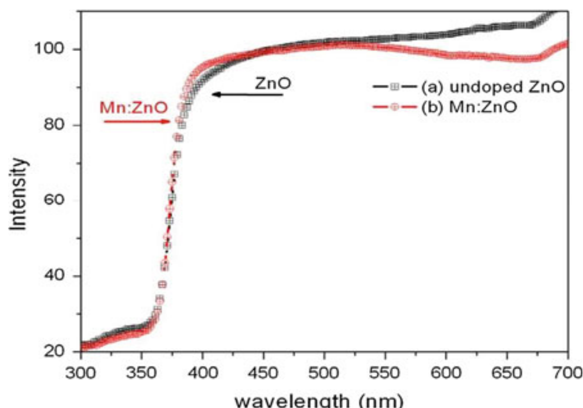

Fig. 15.8 UV-visible spectrum of **a** undoped and **b** Mn doped ZnO thin films

lattice and some of the Mn has been oxidized into the manganese oxide. Ivill et al. [22] reported the precipitation of Mn_3O_4 in $Zn_{1-x}Mn_xO$ film deposited on sapphire by pulsed laser deposition (PLD) at the Mn concentration of 3 at % only. No peak corresponding to Mn_3O phase has been found in the report of Fukumura et al. (1999) [23], who also reported the absence of oxide phases of Mn in $Zn_{1-x}Mn_xO$ films, up to $x = 0.35$, deposited by PLD.

Optical transmission spectra of the undoped and Mn doped ZnO films recorded in the wavelength region of 300–700 nm is shown in Fig. 15.8. The transmission is found to be the maximum for undoped ZnO film and decreased with in Mn doped film. The decrease in optical transmission is associated with the loss of light due to (i) oxygen vacancies and (ii) scattering at grain boundaries. A characteristic difference in the absorption edge was observed with Mn incorporation in ZnO. A sharp absorption edge has been observed for undoped ZnO and Mn doped films at 380 nm. The position of the absorbance spectra is observed to shift toward the lower wavelength side for Mn doped ZnO thin film. This indicates that bandgap of ZnO material increases with the doping concentration of Mn_{2+} ion [24]. According to Mandal and Nath [25] the value of the bandgap (E_g) is enhanced from 3.27 eV for $x = 0$ film to 3.52 eV in the case of highest Mn doped ($x = 0.25$) ZnO epitaxial thin film. Similar observations of enhancement of the bandgap of ZnO with Mn_{2+} ion concentration in epitaxial films have also been reported earlier [23].

(ii) **Li, Co co-doped ZnO**

Cobalt doped ZnO powders were synthesized by heat treating stoichiometric amounts of Co_3O_4 and ZnO at 940 °C for 10 h. For (Li and Co) co-doped ZnO, Lithium carbonate is taken in addition to Co_3O_4 and ZnO. In both cases, the dopant percentage is maintained as 3 %. An X-ray diffraction study has been performed to study the structure of the synthesized samples and is shown in Fig. 15.9.

The lattice parameters were calculated as $a = 3.268$ Å, $c = 5.125$ Å for cobalt doped ZnO and as $a = 3.278$ Å, $c = 5.143$ Å for the lithium and cobalt co-doped samples. No secondary phase has been detected. Room temperature magnetic

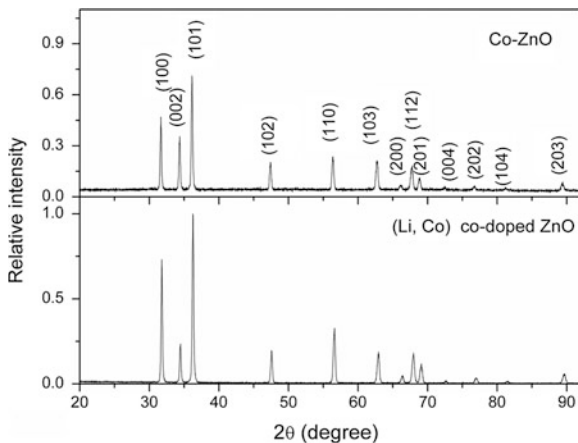

Fig. 15.9 XRD of the synthesized 3 % Co-doped and 3 % (Li, Co) doped ZnO powder

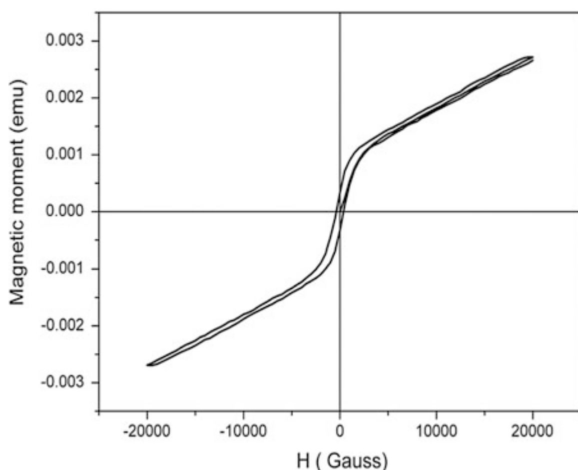

Fig. 15.10 M–H curve of the 3 % (Li, Co) doped ZnO powder

properties of the samples were studied using vibrating sample magnetometer (VSM). The cobalt doped ZnO showed paramagnetic property, while Li, Co co-doped ZnO showed ferromagnetism (Fig. 15.10).

The synthesized materials were mixed with a small amount of polyethylene glycol binder, cold pressed, and sintered for 6 h at 1,100 °C in air. These targets were used for making thin film using PLD. The targets were preablated in oxygen prior to every deposition to remove surface contaminants.

A KrF excimer (laser $\lambda = 248$ nm, $\tau = 25$ ns) with a pulse energy density of 2.8 J/cm^2 at a repetition rate of 10 Hz was used to deposit the thin films. The distance between target and substrate was maintained at 45 mm during the film deposition. Generally, a lower substrate temperature (<600 °C) and higher oxygen pressure (>10^{-5} mbar) have been reported to produce films with homogeneous cobalt distribution [8]. The substrate was maintained at a temperature of 400 °C

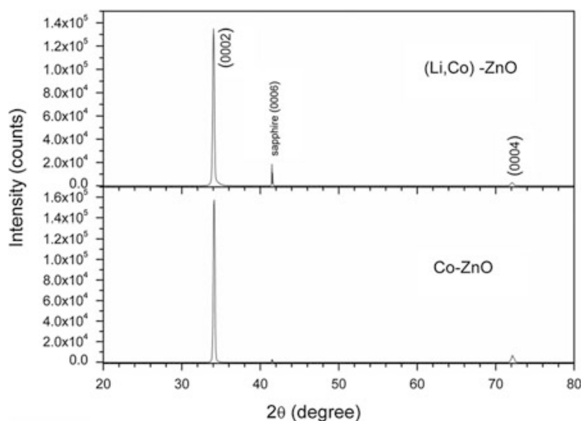

Fig. 15.11 XRD pattern of 3 % Co and (Li, Co) doped ZnO thin film

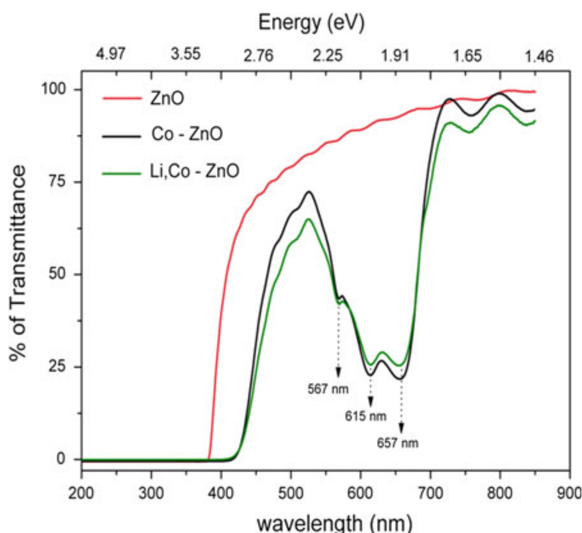

Fig. 15.12 Transmittance spectra of 3 % Co and (Li, Co) doped ZnO thin film

and an optimized oxygen partial pressure of 10^{-3} mbar was used for the deposition.

X-ray pattern in Fig. 15.11 reveals that the films are more epitaxial in nature orienting along (0002) direction of the wurtzite hexagonal structure. No trace of any secondary phases is found in the films within the limit of X-ray detections. The (0002) peak position of the films got shifted compared to the single crystalline peak of ZnO at 34.42°.

In the transmittance spectra shown in Fig. 15.12, doped ZnO samples exhibited absorption peaks in the visible region in addition to the absorption edge. An undoped ZnO film is included as reference. Absorption bands observed at 567, 615, and 657 nm are characteristic of d–d transition of tetrahedral coordination of Co^{2+} ions. These absorption peaks confirm the presence of cobalt as Co^{2+} and

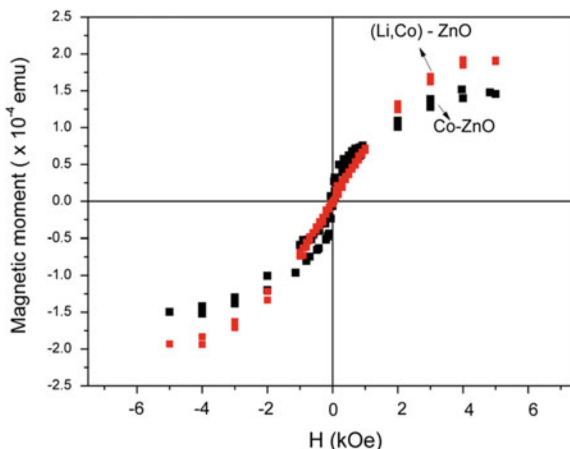

Fig. 15.13 M–H curve of the 3 % (Li, Co) doped ZnO thin film

indicate it has substituted Zn in the host lattice. Specifically, the peaks located at 567, 615, and 657 nm correspond to $^4A_2(F) \rightarrow {}^2A_1(G)$, $^4A_2(F) \rightarrow {}^4T_1(P)$ and $^4A_2(F) \rightarrow {}^2E(G)$ transitions respectively [26]. Red shift is observed in the transmission edge of the spectrum comparing pure ZnO and it is due to the sp–d exchange between the ZnO band electrons and localized d-electrons associated with the doped Co^{2+} cations, so that the introduction of cobalt into ZnO lattice will lower the conduction band and raise the valence band results in shrinking the bandgap.

M–H curve of the Co-doped and (Li, Co) doped ZnO films at 5 K are shown in Fig. (15.13). The diamagnetic contribution was corrected to eliminate the contribution of the substrate. This has been carried out by correcting the data by a slope equal to the slope of the magnetization loop at high field (50 kOe) and low temperature (5 K) where the diamagnetic contribution of the substrate is predominant.

(iii) **Co, N co-doped ZnO**

In our theoretical study the nitrogen doping itself shows weak ferromagnetism. To verify our results, the nitrogen implantation was done on the ZnO thin films prepared by PLD. 100 keV accelerated N^+ ion is chosen so that the nitrogen would distribute over a depth range of around 150 nm. In the M–H curve (Fig. 15.14) the dose of 10^{17} ions/cm^2 N^+ implanted shows weak ferromagnetism. Primarily, the magnetism arises mainly due to delocalized 2p orbitals of the anions when nitrogen got substituted in the place of oxygen in the ZnO lattice.

Nitrogen implantation was also done on the cobalt doped ZnO thin films. Although the films showed ferromagnetism, the magnetic results were too noisy. One of the ways to realize this co-doping in ZnO with even distribution of dopants in the film can be done using sol–gel technique. Zinc acetate dihydrate, Cobalt acetate tetrahydrate, Ammonium acetate, 2-methoxethanol, and monoethanolamine (MEA) were used as the starting materials, solvent and stabilizer,

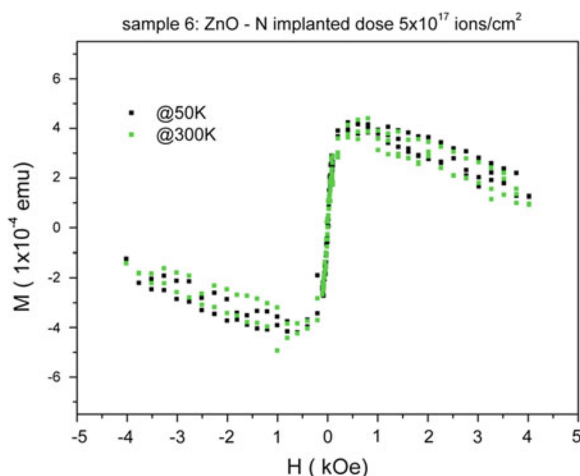

Fig. 15.14 M-H curve of the N (dose 10^{17} ions/cm^2) implanted ZnO thin film

respectively. Zinc acetate dehydrate, Cobalt acetate, and Ammonium acetate were first dissolved in 2-methoxyethanol. The molar ratio of MEA to zinc acetate dihydrate was maintained at 1.0 and the concentration of zinc acetate was 0.5 M. Then, the resulting mixture was stirred at 60 °C for 2 h. After aging for a day period, the solution was dropped onto the sapphire substrate, which was rotated at 3,000 rpm for 30 s by using a spin coater. After spin-coating, the film was dried at 300 °C for 10 min on a hot plate to evaporate the solvent and remove organic residuals. The procedure from coating to drying was repeated ten times. The grown film was then kept in a furnace and post annealed in air at 600 °C for 1 h.

X-ray photoelectron spectroscopy (XPS) studies have been carried out to confirm cobalt and nitrogen doping in ZnO. Figure 15.15 shows the XPS spectra of the ZnO: (Co, N) films. The core level peaks of Zn 2p, O 1s, Co 2p, and N 1s are observed. It can be well fitted by Gaussian lines. The binding energies of Zn 2p3/2 and Co 2p3/2 are located at 1021.27 and 779.21 eV, respectively, suggesting a single component of Zn^{2+} ions in the films. The Co 2p main peaks indicate a divalent state of the Co ions in ZnO : (Co, N) films [27–29]. The Co 2p1/2 peak is located at 795.12 eV. The difference between Co 2p1/2 and 2p3/2 is 15.9 eV, showing large chemical shifts compared to that of pure Co metal 15.05 eV. This indicates that Co ions have a 2+ valence and evident for its substitution of Zn in the ZnO lattice. Satellite peaks also appear at about 786.8 and 802.6 eV, respectively, which originate from the charge-transfer band structure characteristic of the 3*d* transition metal monoxides [27]. The differences between the main peaks and the corresponding satellites further prove that Co ions are in a tetrahedral crystal field surrounded by oxygen atoms and have a chemical valence of the +2 state. A clear peak at 396.6 eV was observed for the N 1s, reflecting the formation of Zn–N bonds as a result of N ion substitution [28–30]. Figure (15.13) shows stronger peak at 530.9 eV which may be attributed to O^{2-} ions in Zn–O and Co–O bonds, while another at 531.8 eV is usually associated with the loosely bound oxygen

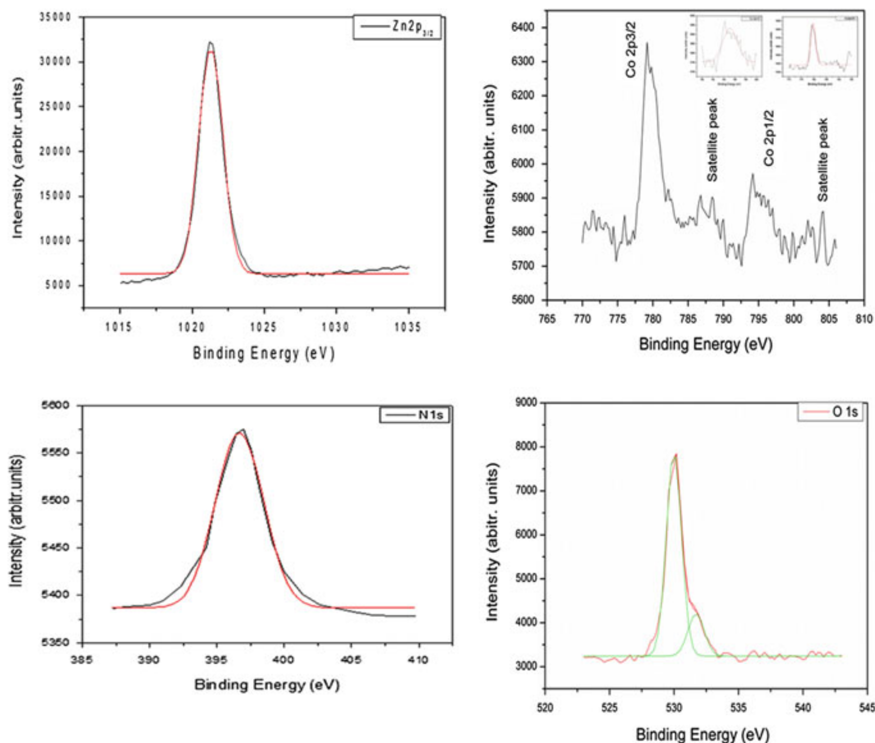

Fig. 15.15 XPS spectrum of 3 % (Co, N) co-doped ZnO

(e.g., adsorbed O_2,–OH) chemisorbed on the surface and/or grain boundary of polycrystalline film [31, 32].

The magnetization of films was measured as function of magnetic field (M–H) as shown in Fig. 15.16. The diamagnetic contribution from sapphire substrate has been subtracted from the raw data. When assigning the origin of ferromagnetism, one should carefully consider the possibility of material phase segregation even though no secondary phases have been detected in XRD measurements. The saturation magnetization of the film is estimated to be 0.45 μ_B/Co site from the M–H curve at 300 K.

(iv) **Cd, Mg co-doped ZnO**

ZnO and $Zn_{1-x}Mg_xO$ have been subjects of intense scientific research as wide bandgap optoelectronic materials. Their excellent material properties are promising for blue and UV photon emitters and detectors [33]. Also, they possess unique figures of merit, such as availability of lattice-matched single crystal substrates (ZnO and MgO for hexagonal and cubic $Zn_{1-x}Mg_xO$ films, respectively), tunable bandgap energy of 3.3–7.8 eV [34–36] and relatively low growth temperatures (100–750 °C) which are crucial for practical optoelectronic devices. Despite the

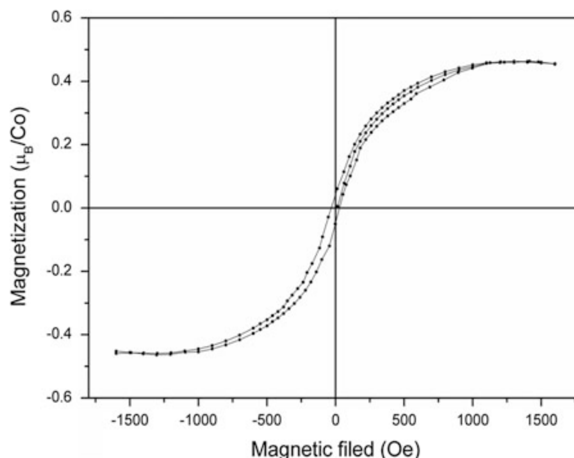

Fig. 15.16 Room temperature M-H curve of 3 % (Co, N) co-doped ZnO

challenges of reliable p-type doping of ZnO and $Mg_xZn_{1-x}O$ that hinder the realization of p-n junction-based devices, UV photodetectors, quantum wells, and superlattices based on ZnO and $Mg_xZn_{1-x}O$ have been successfully demonstrated [37]. The large exciton binding energy has enabled the observation of laser action and the stimulated emission of excitons at temperatures well above room temperature in ZnO thin films [38, 39]. These observations indicate that exciton-related recombination process can be utilized in optoelectronic devices based on ZnO. In principle, a lower pumping threshold can be expected, if exciton-related recombination is used rather than electron–hole recombination. The fabrication and characterization of alloys such as Cd-doped ZnO and Mg-doped ZnO are important from the viewpoint of bandgap engineering. The co-dopants of (Mg, Cd) are believed to allow a fine energy tuning in ZnO [40].

Undoped ZnO, Cd-doped ZnO ($Cd_{0.1}Zn_{0.9}O$), Mg-doped ZnO ($Mg_{0.1}Zn_{0.9}O$) and (Cd, Mg) co-doped ZnO ($Cd_{0.07}Mg_{0.03}Zn_{0.9}O$, $Cd_{0.03}Mg_{0.07}Zn_{0.9}O$) thin films were deposited on sapphire substrates using the sol–gel method and a spin-coating technique. Zinc acetate dihydrate was used as the precursor while cadmium acetate and magnesium acetate were used as source materials for Cd and Mg dopants respectively. The precursor and the dopant source were dissolved in 2-methoxyethanol (solvent) and monoethanolamine (stabilizing agent) at room temperature. The concentration of zinc acetate was 1 mol per liter and the molar ratio of monoethanolamine to zinc acetate was kept at 1:1. Using a magnetic stirrer, the solution was stirred at 333 K for 45 min. The films were spin-coated on sapphire substrates at 3,000 rpm for 30 s and were dried at 623 K for 15 min for evaporating the solvent and to remove the organic components present in the films. The entire process was repeated ten times. The films were then annealed at 773 K for 30 min.

Figure 15.17 shows the XRD pattern of $Cd_{0.1}Zn_{0.9}O$, $Cd_{0.07}Mg_{0.03}Zn_{0.9}O$, $Cd_{0.03}Mg_{0.07}Zn_{0.9}O$, $Mg_{0.1}Zn_{0.9}O$ and ZnO thin films deposited on sapphire substrates (substrate peak is not shown in the figure). The $Cd_{0.1}Zn_{0.9}O$, $Mg_{0.1}Zn_{0.9}O$ and ZnO thin films showed prominent (10-10), (0002) and (10-11) planes while the

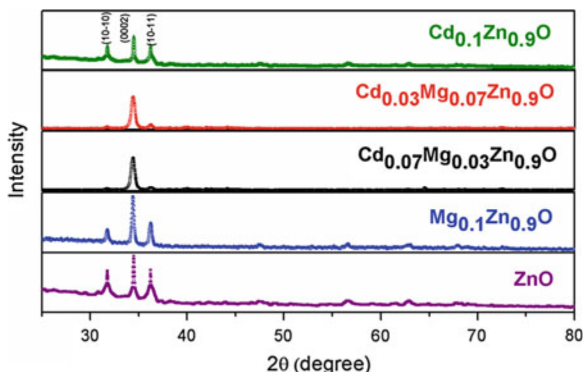

Fig. 15.17 XRD pattern of pure ZnO, $Cd_xMg_yZn_{1-x-y}O$ (x, y = 0.03, 0.07, 0.1)

$Cd_{0.07}Mg_{0.03}Zn_{0.9}O$ and $Cd_{0.03}Mg_{0.07}Zn_{0.9}O$ films showed a preferred c-axis orientation. No peaks relating to other materials such as CdO or MgO appear in the graph. This reveals that the introduction of Cd or Mg into the films could not change the wurtzite structure of ZnO films grown by this method. For the hexagonal ZnO structure, the lattice constants 'a' and 'c' are given by

$$\frac{1}{d_{hkl}^2} = \frac{4}{3}\left[\frac{h^2 + hk + k^2}{a^2}\right] + \frac{l^2}{c^2}$$

In the first order approximation, $n = 1$,

$$\sin^2\theta = \frac{\lambda^2}{4}\left[\frac{4}{3}\left(\frac{h^2 + hk + k^2}{a^2}\right) + \frac{l^2}{c^2}\right]$$

For the (100) orientation, the lattice constant 'a' was calculated using the formula

$$a = \frac{\lambda}{\sin\theta\sqrt{3}}$$

For the (002) orientation, the lattice constant 'c' was calculated using the formula

$$c = \frac{\lambda}{\sin\theta}$$

The grain size of $Cd_{0.1}Zn_{0.9}O$, $Cd_{0.07}Mg_{0.03}Zn_{0.9}O$, $Cd_{0.03}Mg_{0.07}Zn_{0.9}O$, $Mg_{0.1}Zn_{0.9}O$ and ZnO thin films were calculated from the (0002) diffraction plane using Scherrer's formula

$$d = \frac{0.9\lambda}{\sqrt{\beta^2 - \beta_0^2}\cos\theta}$$

Table 15.2 Lattice parameter, interplanar spacing (d), FWHMs, and average crystal size obtained from XRD pattern

	$Cd_{0.1}Zn_{0.9}O$	$Cd_{0.07}Mg_{0.03}Zn_{0.9}O$	$Cd_{0.03}Mg_{0.07}Zn_{0.9}O$	$Mg_{0.1}Zn_{0.9}O$	ZnO
Lattice parameter, a (Å), c (Å)	3.246 5.201	3.257 5.213	3.255 5.210	3.246 5.209	3.248 5.192
Interplanar spacing, d (Å)	2.601	2.607	2.605	2.604	2.596
FWHM, β (°)	0.3500	0.4100	0.4800	0.3200	0.4900
Average crystallite size (nm)	39	33	28	44	27 27

where β is the measured broadening of the (0002) diffraction peak, full width at half its maximum intensity (FWHM), β_0 is the FWHM of the spectral width caused by instrumental broadening (0.1° in our experiment), λ is the wavelength of the X-rays (1.5406 Å) and θ is the angle of diffraction. The average grain size and lattice parameters of the deposited films are given in Table 15.2. The lattice parameters of the ZnO thin films were found to be comparable to that obtained for powdered ZnO (JCPDS # 029272). Mg tends to be incorporated on the position of Zn lattice since the difference ionic radii of the tetrahedrally coordinated Mg^{2+} (0.71 Å) and Zn^{2+} (0.74 Å). The ionic radii of tetrahedrally coordinated Cd^{2+} (0.92 Å) is much larger than that of Zn^{2+} and hence the lattice parameter of the co-doped ZnO is expected to change as the system get more strained (Table 15.2). However, the incorporation of an isovalent alloying element (Mg and Cd) leads to a slight degradation of the crystalline quality only, whereas the incorporation of doping atoms (Li, Al, Ga and Sb) results in a significant degradation of the crystalline quality even at low doping concentrations [41].

The incorporation of Cd and Mg into the Cd and Mg co-doped ZnO lattice was confirmed by XPS measurement. Figure (15.18a shows the XPS spectra corresponding to Zn 2p1/2 and 2p3/2 peaks. The binding energies of the Zn 2p 1/2 and Zn 2p 3/2 are located at 1,045 and 1,021 eV respectively. The O 1s peak shown in Fig. 4.6b is observed with two components positioned at 529.6 and 531.9 eV. The relative ratio of the two components was found to be 1.2. The O 1s component at 529.6 eV can be attributed to the oxygen bound to four zinc atoms within the ZnO matrix. The O 1s peak forming a shoulder at higher energy of 531.9 eV as seen in the figure is a result of chemisorbed oxygen species on the sample surface [42]. The energy of the Cd 3d5 level in CdO is 403 eV [43]. Occurrence of the peak at 404.6 eV shown in Fig. 15.18c indicates the absence of CdO in the sample. The chemical shift of the peaks confirmed that Cd is really doped into ZnO. The asymmetry in the peak corresponding to Cd $3d_5$ is due to the superposition of two peaks corresponding to Cd 3d5/2 and Cd 3d since the energy difference between these peaks is very small. Figure (15.16d shows that the Mg 2p peak was observed at energy of 50.1 eV. There was no appreciable change in the chemical state of Mg

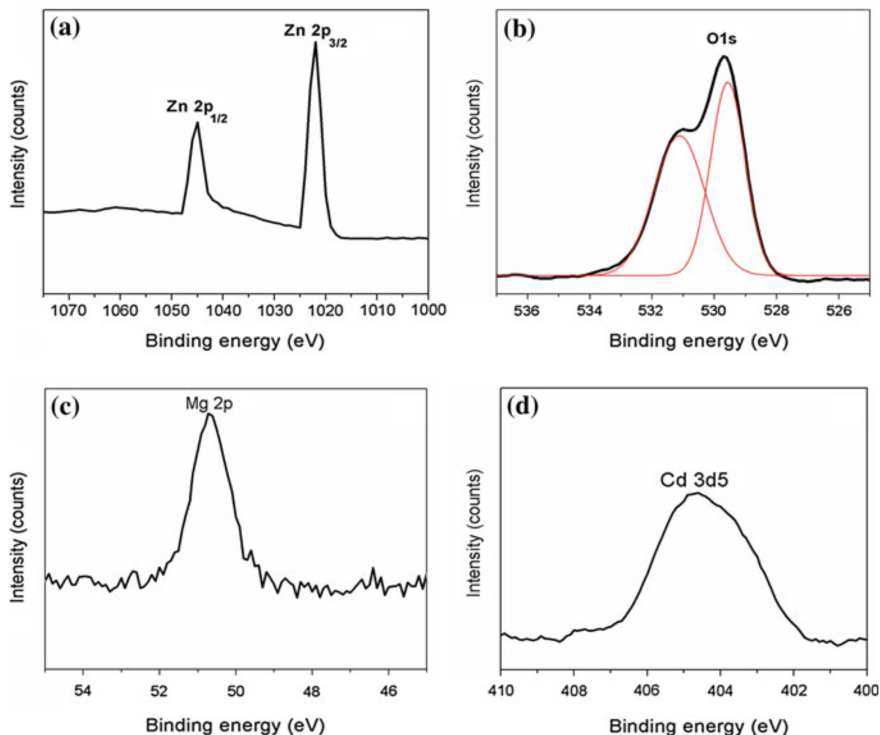

Fig. 15.18 XPS spectra of $Cd_{0.07}Mg_{0.03}Zn_{0.9}O$ ZnO thin film

in the $Cd_{0.07}Mg_{0.03}Zn_{0.9}O$ or $Cd_{0.03}Mg_{0.07}Zn_{0.9}O$ films in comparison with the parent ZnO and MgO spectra.

Figure 15.19 shows the transmittance spectra of $Cd_{0.1}Zn_{0.9}O$, $Cd_{0.07}Mg_{0.03}Zn_{0.9}O$, $Cd_{0.03}Mg_{0.07}Zn_{0.9}O$, $Mg_{0.1}Zn_{0.9}O$ and ZnO thin films measured at room temperature. As can be seen, all the films show high transmittance in the visible region.

The transmittance data was normalized so that $T_{\text{normalised}} = 100\ \%$ in the transparent region ($hv - E_g$). The absorption coefficient (α) was calculated using the relation

$$\alpha(E) = -\frac{1}{d}\ln(T_{normalised}(E))$$

where d is the film thickness. In order to calculate the bandgap energies of the deposited films, a plot was made of square of absorption coefficient as a function of photon energy. The optical bandgap energies of $Cd_{0.1}Zn_{0.9}O$, $Cd_{0.07}Mg_{0.03}Zn_{0.9}O$, $Cd_{0.03}Mg_{0.07}Zn_{0.9}O$, $Mg_{0.1}Zn_{0.9}O$ and ZnO thin films were found to be 3.13, 3.50, 3.57, 3.64, and 3.26 eV respectively. The bandgap values

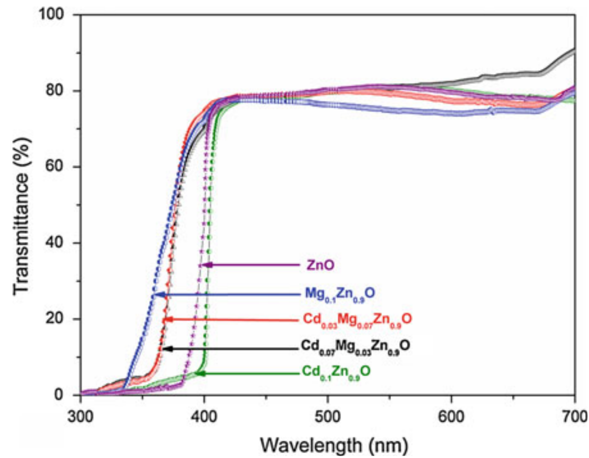

Fig. 15.19 Transmittance spectra of ZnO, $Cd_xMg_yZn_{1-x-y}O$ (x, y = 0.03, 0.07, 0.1) thin film

of the doped films was also calculated from the virtual crystal approximation using the formula

$$E_g\left(Cd_xMg_yZn_{1-x-y}O\right) = xE_g(CdO) + yE_g(MgO) + (1-x-y)E_g(ZnO)$$

The bandgap energies of $Cd_{0.1}Zn_{0.9}O$, $Cd_{0.07}Mg_{0.03}Zn_{0.9}O$, $Cd_{0.03}Mg_{0.07}Zn_{0.9}O$ and $Mg_{0.1}Zn_{0.9}O$ thin films were found to be 3.3, 3.41, 3.55 and 3.66 eV respectively. The experimental values and the calculated values of the bandgap of the deposited films agree well. Similar bandgap values for the mono-doped and co-doped ZnO thin films have been reported [44, 45].

Room temperature PL spectra for the deposited films are shown in Fig. 15.20. A strong near-band-edge (NBE) emission peak was observed for all samples, which originated from the radiative recombination of excitons in ZnO films [46]. The deep level around 2.4 eV is due to defects such as oxygen vacancies. It is well known that ZnO films always possess some oxygen vacancy regardless of the growth technique [47]. PL spectra of ZnO-based films depend on the stoichiometry and microstructure of the materials. The Cd-doped ZnO exhibited an NBE emission at 398 nm, while the Mg-doped ZnO thin films exhibited NBE-UV emission at 350 nm. A distinct blue shift of the NBE emission peak was observed for the Mg-doped ZnO and a distinct red shift of the NBE emission peak was observed for Cd-doped ZnO. This trend of blue shift and red shift of NBE peak has been observed previously in $Zn_{1-x}Mg_xO$ and $Zn_{1-x}Cd_xO$ films respectively and is thought to be due to the augmentation (reduction) of the $Zn_{1-x}Mg_xO$ ($Zn_{1-x}Cd_xO$) bandgap caused by the incorporation of Mg (Cd) [48, 49]. In other words, the NBE peak of the (Cd, Mg) co-doped ZnO films can be precisely controlled between 3.1 and 3.6 eV. The Cd and Mg-doped ZnO films are promising light emitting materials over a broad spectrum and can also be considered as a suitable barrier layer for bandgap engineering.

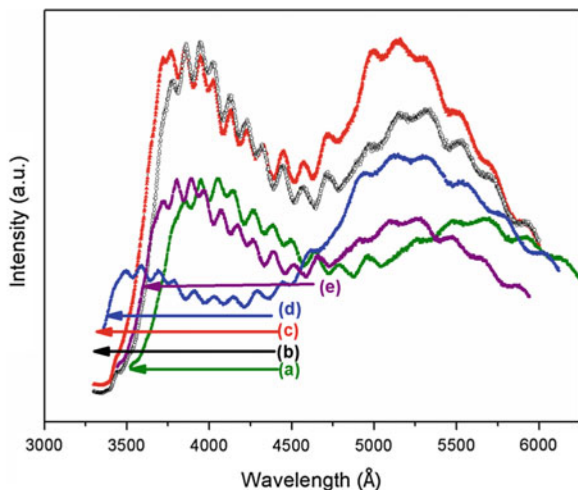

Fig. 15.20 Room temperature PL spectra of **a** $Cd_{0.1}Zn_{0.9}O$ **b** $Cd_{0.07}Mg_{0.03}Zn_{0.9}O$, **c** $Cd_{0.03}Mg_{0.07}Zn_{0.9}O$, **d** $Mg_{0.1}Zn_{0.9}O$ and **e** ZnO

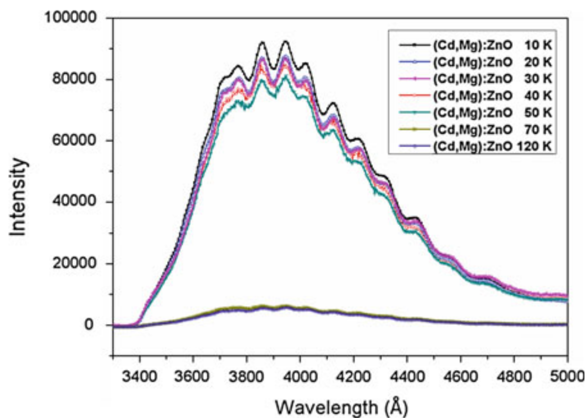

Fig. 15.21 NBE emission of the $Cd_{0.07}Mg_{0.03}Zn_{0.9}O$ films at different temperature

Figure 15.21 shows the NBE emission of the $Cd_{0.07}Mg_{0.03}Zn_{0.9}O$ films at various temperatures. As can be seen from the figure, the intensity of the NBE emission decreases while the FWHM increases, as the temperature increases. This is due to the thermally activated non-radiative recombination mechanisms [50–53].

The strongest PL peaks, at 3.333 and 3.307 eV are assigned to neutral donor bound exciton (D^0X) and ionized donor bound exciton transitions (D^+X). The shoulder at the higher energy of 3.395 eV is identified as the ground state emission of A free exciton (FX_A). The two peaks on the low-energy side of (D^+X) are assigned to FX LO phonon replicas.

Acknowledgments The authors thank the significant contributions from several researchers who collaborated in this work and in particular our thanks are due to Dr. G. Srinivasan, Dr. V. Ravichandran, and Dr. R. Thangavel

References

1. T. Dietl, H. Ohno, F. Matsukura, J. Cibert, D. Ferrand, Science **287**, 1019 (2000)
2. K. Ueda, H. Tabata, T. Kawai, Appl. Phys. Lett. **79**, 988 (2001)
3. S.G. Yang, A.B. Pakhomov, S.T. Hung, C.Y. Wong, IEEE Trans. Magn. **38**, 2877 (2002)
4. R. Thangavel, M. Rajagopalan, J. Kumar, J. Magn. Magn. Mater. **320**, 172 (2008)
5. H.J. Lee, S.Y. Jeong, C.R. Cho, C.H. Park, Appl. Phys. Lett. **81**, 4020 (2002)
6. M. Venkatesan, C.B. Fitzgerald, J.G. Lunney, J.M.D. Coey, Phys. Rev. Lett. **93**, 177206 (2004)
7. J.H. Park, M.G. Kim, H.M. Jang, S.W. Ryu, Y.M. Kim, Appl. Phys. Lett. **84**, 1338 (2004)
8. J.H. Kim, H. Kim, D. Kim, Y.E. Ihm, W.K. Choo, J. Appl. Phys. **92**, 6066 (2002)
9. S. Deka, P.A. Joy, Solid State Comm. **134**, 665 (2005)
10. Z. Jin, T. Fukumura, M. Kawasaki, K. Ando, H. Saito, T. Sekiguchi, Y.Z. Yoo, M. Murakami, Y. Matsumoto, T. Hasegawa, H. Koinuma, Appl. Phys. Lett. **78**, 3824 (2001)
11. M.H. Kane, K. Shalini, C.J. Summers, R. Varatharajan, J. Nause, C.R. Vestal, Z.J. Zhang, I.T. Ferguson, J. Appl. Phys. **97**, 023906 (2005)
12. J. Alaria, H. Bieber, S. Colis, G. Schmerber, A. Dinia, Appl. Phys. Lett. **88**, 112503 (2006)
13. M. Kobayashi, Y. Ishida, J.I. Hwang, T. Mizokawa, A. Fujimori, K. Mamiya, J. Okamoto, Y. Takeda, T. Okane, Y. Saitoh, Y. Muramatsu, A. Tanaka, H. Saeki, H. Tabata, T. Kawai, Phys. Rev. B **72**, 201201R (2005)
14. A.S. Risbud, N.A. Spaldin, Z.Q. Chen, S. Stemmer, R. Seshadri, Phys. Rev. B **68**, 205202 (2003)
15. M. Bouloudenine, N. Viart, S. Colis, J. Kortus, A. Dinia, Appl. Phys. Lett. **87**, 052501 (2005)
16. P. Blaha, K. Schwarz, G. K. H. Madsen, D. Kvasnicka , J. Luitz, *WIEN2k*, *An Augmented Plane Wave + Local Orbitals Program for Calculating Crystal Properties* (2001)
17. K. Sato, H.K. Yoshida, Physica E **10**, 251 (2001)
18. E.C. Lee, K.J. Chang, Phys. Rev. B **69**, 085205 (2004)
19. C.H. Park, D.J. Chadi, Phys. Rev. Lett. **94**, 127204 (2005)
20. M. Rajagopalan, S. Ramasubramanian, J. Kumar, AIP Conf. Proc. **1447**, 1155 (2012)
21. M.H.F. Sluiter, Y. Kawazoe, P. Sharma, A. Inoue, A.R. Raju, C. Rout, U.V. Waghmare, Phys. Rev. Lett. **94**, 187204 (2005)
22. M. Ivill, S.J. Pearton, D.P. Norton, J. Kelly, A.F.J. Hebard, Appl. Phys. **97**, 53904–53908 (2005)
23. T. Fukumura, Z. Jin, A. Ohtomo, H. Koinuma, M. Kawasaki, Appl. Phys. Lett. **75**, 3366–3368 (1999)
24. G. Srinivasan, J. Kumar, J. Cryst. Growth **310**(7–9), 1841–1846 (2008)
25. S.K. Mandal, T.K. Nath, Thin Solid Films **515**, 2535–2541 (2006)
26. P. Koidl, Phys. Rev. B **15**, 2493 (1977)
27. Z.L Lu, Z.R. Mo, W.Q. Zou, S.Wang, G.Q. Yan, X.C. Liu, Y.B. Lin, J.P. Xu, L. Y. Lv, X.M. Wu, Z.H. Xia, M.X. Xu, F.M. Zhang, Y.W. Du, J. Phys. D: Appl. Phys. **41**, 115008 (2008)
28. H.Y. Xu, Y.C. Liu, C.S. Xu, Y.X. Liu, C. L. Shao, R. Mu. Appl. Phys. Lett. **88**, 242502 (2006)
29. H.J. Lee, S.Y. Jeong, C.R. Cho, C.H. Park, Appl. Phys. Lett. **81**, 4020 (2002)
30. G.A. Garson, M.H. Nassir, M.A. Langell, J. Vac. Sci. Technol., A **14**, 1637 (1996)
31. J.G. Ma, Y.C. Liu, R. Mu, J.Y. Zhang, Y.M. Lu, D.Z. Shen, X.W. Fan, J. Vac. Sci. Technol. B **22**, 94 (2004)

32. Craig L. Perkins, S. Lee, X. Li, Sally E. Asher, Timothy J. Coutts, J. Appl. Phys. 97, 034907 (2005)
33. M. Chen, X. Wang, Y.H. Yu, Z.L. Pei, X.D. Bai, C. Sun, R.F. Huang, L.S. Wen, Appl. Surf. Sci. **158**, 134 (2000)
34. D.C. Look, Mater. Sci. Eng. B **80**, 383 (2001)
35. J. Narayan, A.K. Sharma, A. Kvit, C. Jin, J.F. Muth, O.W. Holland, Solid State Commn. **121**, 9 (2002)
36. A. Ohtomo, M. Kawasaki, T. Koida, K. Masubuchi, H. Koinuma, Y. Sakurai, Y. Yoshida, T. Yasuda, Y. Segawa, Appl. Phys. Lett. **72**, 2466 (1998)
37. S. Choopun, R.D. Vispute, W. Yang, R.P. Sharma, T. Venkatesan and v.H. Shen, Appl. Phys. Lett. 80, 1529 (2002)
38. H.D. Sun, T. Makino, Y. Segawa, M. Kawasaki, A. Ohtomo, K. Tamura, H. Koinuma, J. Appl. Phys. **91**, 1993 (2002)
39. P. Zu, Z.K. Tang, G.K.L. Wong, M. Kawasaki, A. Ohtomo, H. Koinuma, Y. Segawa, Solid State Comm. **103**, 459 (1997)
40. D.M. Bagnall, Y.F. Chen, Z. Zhu, T. Yao, S. Koyama, M.Y. Shen, T. Goto, Appl. Phys. Lett. **70**, 2230 (1997)
41. W.I. Park, G.C. Yi, H.M. Jang, Appl. Phys. Lett. **79**, 2022 (2001)
42. D. Spemann, E.M. Kaidashev, M. Lorenz, J. Vogt, T. Butz, Nucl. Instr. Meth. B**219–220**, 891 (2004)
43. Y.F. Lu, H.Q. Ni, Z.H. Mai, Z.M. Ren, J. Appl. Phys. **88**, 498 (2000)
44. D.N. Bose, M.S. Hedge, S. Basu, K.C. Mandal, Semicond. Sci. Tech. **4**, 866 (1989)
45. Y.S. Choi, C.G. Lee, S.M. Cho, Thin Solid Films **289**, 153 (1996)
46. M. Lorenz, E.M. Kaidashev, von Wenckstern, V. Riede, C. Bundesmann, D. Spemann, G. Benndorf, H. Hochmuth, A. Rahm, H. C. Semmelhack, M. Grundmann. Solid State Electron. **47**, 2205 (2003)
47. X. Zhang, X.M. Li, T.L. Chen, J.M. Bian, C.Y. Zhang, Thin Solid Films **492**, 248 (2005)
48. U. Ozgur, A. Ya, I. Alivov, C. Liu, A. Teke, M.A. Reshchikov, S. Dogan, V. Avrutin, S.J. Cho, H. Morkood, J. Appl. Phys. **98**, 041301 (2005)
49. C. Jianlin, D. Chen, J. He, S. Zhang, Z. Chen, Appl. Surf. Sci. **255**, 9413 (2009)
50. V. Osinsky, J.W. Dong, J.Q. Xie, B. Hertog, A.M. Dubrian, P.P. Chow, S.J. Pearton, D. P. Norton, D. C. Look, W. Schoenfeld, O. Lopatiuk, L. Chernyak, M. Cheung, A. N Cartwright, M. Gerhold, Mater. Res. Soc. Symp. Proc. 892, FF 18-01 (2006)
51. W.L. Xu, M.J. Zheng, G.Q. Ding, W.Z. Shen, Chem. Phys. Lett. **411**, 37 (2005)
52. X.Y. Zhang, J.Y. Dai, H.C. Ong, N. Wang, H.L.W. Chan, C.L. Choy, Chem. Phys. Lett. **393**, 17 (2004)
53. H. Priller, R. Hauschild, J. Zeller, C. Klingshirn, H. Kalt, R. Kling, F. Reuss, Ch. Kirchner, A. Waag, J. Lumin. **112**, 173 (2005)

Chapter 16
Low-Temperature Photoluminescence of Sb-doped ZnO Nanowires Synthesized on Sb-coated Si Substrate by Chemical Vapor Deposition Method

K. Sakai, K. Ishikura, A. Fukuyama, I. A. Palani, M. S. Ramachandra Rao, T. Okada and T. Ikari

Abstract The fabrication of *p*-type ZnO crystal is motivated by the need to develop ZnO semiconductor devices. On the other hand, it is well-known that high-quality nano-sized ZnO crystal can be easily obtained by various crystal growth techniques. Consequently, we tried to grow *p*-type Sb-doped ZnO nanowires by the chemical vapor deposition under various deposition temperature conditions and investigated their optical properties by photoluminescence (PL) spectroscopy. Multiple emission peaks caused by free excitons, excitons bound to donors and structural defects, and acceptors formed by Sb-doping were observed. The temperature dependence of PL confirmed the existence of acceptor level due to Sb-doping, and the activation energy of the acceptor level was estimated to be 125 meV.

16.1 Introduction

Zinc oxide (ZnO) semiconductor is one of the most promising materials for device applications such as transparent conductive oxide, ultraviolet (UV)-emitting, and UV-sensing devices. However, intrinsic defects such as oxygen vacancies (V_O) are

K. Sakai (✉)
Center for Collaborative Research and Community Cooperation, University of Miyazaki, 1-1 Gakuen Kibanadai-nishi, Miyazaki, Japan
e-mail: k-sakai@cc.miyazaki-u.ac.jp

K. Ishikura · A. Fukuyama · T. Ikari
Faculty of Engineering, University of Miyazaki, 1-1 Gakuen Kibanadai-nishi, Miyazaki, Japan

I. A. Palani · M. S. Ramachandra Rao
Department of Physics, Nano Functional Materials Technology Centre and Materials Science Research Centre, Indian Institute of Technology Madras, Chennai 600036, India

T. Okada
Graduate School of Information Science and Electrical Engineering, Kyushu University, Fukuoka 812-8581, Japan

M. S. R. Rao and T. Okada (eds.), *ZnO Nanocrystals and Allied Materials*, Springer Series in Materials Science 180, DOI: 10.1007/978-81-322-1160-0_16,
© Springer India 2014

inevitably formed in ZnO crystals during crystal growth, and ZnO subsequently exhibits n-type conduction. Therefore, it is important to control such defects in the ZnO crystal growth process. Recently, nano-sized ZnO semiconductors such as nanorods, nanobelts, and nanowires have attracted considerable attention owing to their importance in both scientific research studies and potential technological applications. We have previously investigated the optical properties of ZnO nanorods and nanowires synthesized by a pulsed laser deposition (PLD) technique [1, 2]. Our photoluminescence (PL) measurements demonstrated intense ultraviolet luminescence (UVL) around 3.3 eV for the ZnO nanorods and nanowires at RT [1]. This UVL peak was due to a near-band-edge free-exciton (FX) transition [3]. Another broad PL peak around 2.4 eV was also observed for these samples [1]. This peak was due to the deep-level emission from the ZnO crystal and is well-known as green luminescence (GL) [3]. GL is mainly related to V_O. To examine the effects of growth conditions on the optical properties of these samples, the ratio of the PL peak intensity of GL to that of UVL of the nanorods and nanowires was investigated as a function of the gas pressure during crystal growth [1]. The GL/UVL ratio exhibited a downward trend with increasing gas pressure for both the samples. A suitable gas pressure for inhibiting the formation of a defect level in the growth process was estimated for both the samples.

Furthermore, we have studied the emission properties at low temperature around the band gap of the nanorod and nanowire samples in detail [2]. The UVL band consists of several sharp emission lines due to FXs, donor-bound excitons, donor–acceptor pair (DAP) transitions, and their longitudinal optical (LO)phonon replicas. The FX binding energy was estimated to be 59 meV, and the band gap of the ZnO crystals was determined to be 3.435 eV at 10 K [2]. The temperature variation in the energy positions of FX emission was fitted by the Manoogian–Woolley equation, and the Debye temperature was estimated to be 505 K [2]. By investigating the low-temperature PL, we demonstrated that our nano-sized ZnO crystals had excellent crystallinity, and that these crystals can be applied to UV-emitting devices, solar cells, and other nanodevices.

On the other hand, the fabrication of *p*-type ZnO semiconductor is motivated by the need to develop semiconductor devices, such as a homopolar ZnO light-emitting diode (LED). Group V and I elements, N, P, As, Sb, and Li are typically used as dopants to realize the *p*-type conduction of ZnO semiconductor. In particular, a model for large-size-mismatched group-V dopants such as As and Sb in ZnO was proposed by Limpijumnong et al. by performing a first-principles calculation [4]. They suggested that As (Sb) would substitute for Zn instead of O and subsequently produce two corresponding Zn vacancies, which are As_{Zn}–$2V_{Zn}$ (Sb_{Zn}–$2V_{Zn}$) complexes. Some groups have reported the successful growth of *p*-type Sb-doped ZnO [5, 6]. Subsequently, we tried to grow *p*-type Sb-doped ZnO nanowires by chemical vapor deposition (CVD). In this study, an attempt has been made for the first time to carry out Sb-doping in ZnO crystals by using a sandwich-type substrate, where Si coated with Sb and Au is used as substrate for the synthesis of Sb-doped ZnO nanowires. The nanowires are generated from the sandwich-type substrate under different deposition temperatures.

Incidentally, it is very difficult to measure the electrical properties of nano-sized semiconductors owing to the limited size of the related nanowires. Consequently, it is necessary to study the electronic structure of semiconductors by investigating their optical properties. Since the conductivity of semiconductors is greatly affected by impurities and/or defect levels formed in the band gap, the PL technique is a powerful tool for investigating electronic states owing to its high sensitivity and high spatial resolution. In this study, we report on the growth of Sb-doped ZnO nanowires using CVD under various deposition temperatures as well as the luminescence properties of these nanowires by using PL spectroscopy. We also discuss impurity levels formed in the band gap of ZnO because of Sb-doping and the possibility for materializing *p*-type conduction.

16.2 Experimental Procedure

Sb-doped ZnO nanowire crystals were synthesized by CVD. Mixed powders of Zn, Sb, and C in the ratio 20:4:4 were prepared and placed in an Al_2O_3 boat. Single crystal Si wafer was used as the substrate. The Si substrate was coated with 60–100 nm thick antimony and then coated with 1 nm thick gold particles. The deposition was performed at various temperatures between 750 and 1000 °C for 30 min and the temperatures were lowered by the ambient condition induced by Ar flow. Further, we annealed the same batch of these samples at 750 °C for 30 min to carry out Sb-doping in ZnO crystals.

The surface morphology of the Sb-doped ZnO nanowires was investigated by using a scanning electron microscope (SEM). For PL measurements, a He–Cd laser (325 nm) was used as the excitation light source. The laser beam was focused on the sample placed in a cryostat for low-temperature measurements. The PL signal dispersed by a monochromator was detected by a charge coupled device (CCD) and a photomultiplier. The PL measurements were performed between 10 K and RT.

16.3 Results and Discussion

Figure 16.1 shows the SEM images of the obtained Sb-doped ZnO nanowires. Figure 16.1a, b shows the surface morphologies of the samples synthesized at 1000 °C before and after annealing, respectively. Web-like straight and curly nanowires were observed at a high deposition temperature. The diameter and length of the nanowires were in the order of 100 nm and 1 μm, respectively. A large number of straight nanowires were observed across the board. Figure 16.1c, d shows the surface morphologies of the samples synthesized at 750 °C before and after annealing, respectively. Straight and curly nanowires were observed at a low deposition temperature as well. However, the number of straight nanowires was less

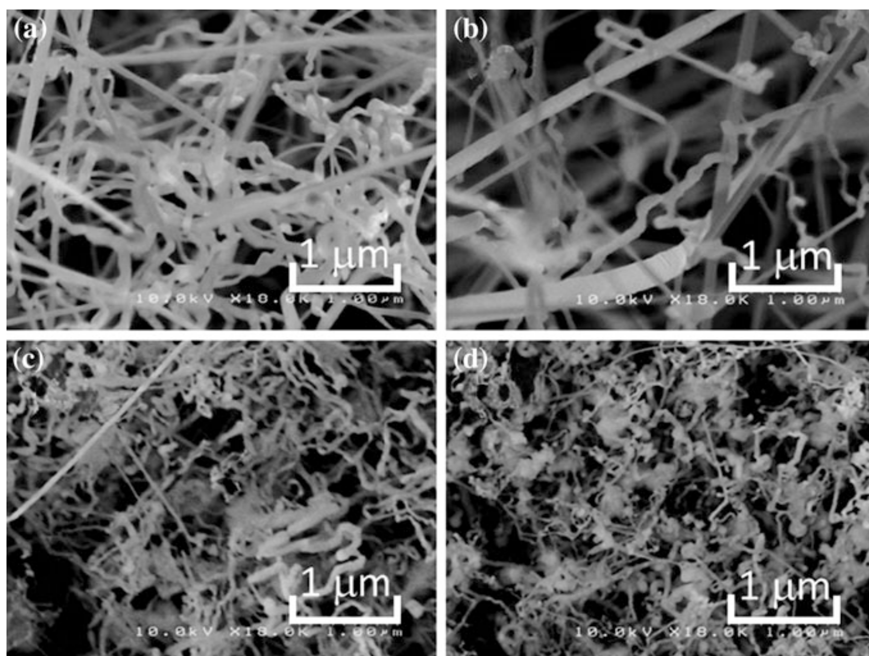

Fig. 16.1 SEM images of Sb-doped ZnO nanowires (**a**), (**b**) shows the surface morphologies of the samples synthesized at 1000 °C before and after annealing, respectively (**c**), (**d**) shows the surface morphologies of the samples synthesized at 750 °C before and after annealing, respectively

than that grown at a higher temperature of 1000 °C. In addition to the short curly nanowires, seaweed-like crystals were also confirmed. After annealing, the number of short curly nanowires reduced, and seaweed-like ZnO crystals became dominant. The effect of annealing at 750 °C for 30 min was not confirmed from the SEM observations for both the samples synthesized at 1000 and 750 °C.

Next, we investigated the temperature dependence of PL properties in the UVL region for the Sb-doped ZnO nanowire samples between 10 and 300 K. Figure 16.2 shows the temperature variations of the PL spectra for the as-grown nanowire sample synthesized at 1000 °C, where the vertical scale is logarithmic. Since the diameter of the excitation laser beam was considerably larger than that of the nanowire crystals, the observed PL spectra were those averaged over many different crystals. The multiple emission peaks in the UVL region were observed for low temperatures. The related optical transition mechanisms for the observed emission peaks are shown in Fig. 16.2. The emission peaks at 10 K were assigned to the ground-state FX at 3.376 eV, the neutral donor-bound excitons (BEs) defined as $I_{6/6a}$ and I_9 at 3.362 and 3.358 eV, respectively, and the ionized donor BE (I_3) at 3.366 eV [7]. PL spectra were dominated by the emissions related to donor levels because of the impurities that were unintentionally incorporated into the raw materials, i.e., ZnO, C, and Sb powders.

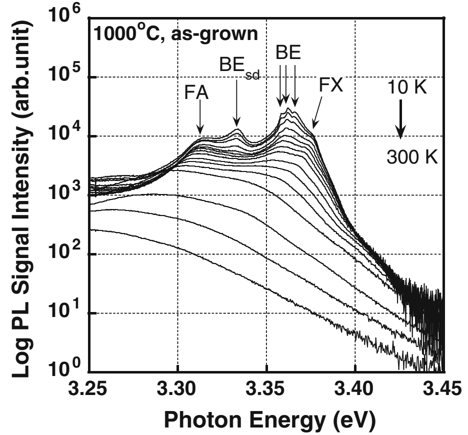

Fig. 16.2 Temperature variations in PL spectra of as-grown Sb-doped ZnO nanowires deposited at 1000 °C

New PL peaks at 3.334 and 3.314 eV were observed, as shown in Fig. 16.2; these peaks could not be observed for the nondoped ZnO nanowire. As for the 3.334 eV PL peak labeled BE_{sd}, Thonke et al. [8] observed a similar peak at 3.333 eV in nondoped bulk ZnO crystal and assigned it to the two-electron satellite (TES) transitions of the neutral donor BEs. However, according to the cathodoluminescence investigations of Mayer et al., this PL peak was related to excitons bound to the structural defects (BE_{sd}) [7]. Although the details are not yet clear, our results agree with the model of Mayer et al., since this peak was not observed for our nondoped ZnO nanowire samples. Next, we consider the broader PL peak at 3.314 eV. TES emissions of BE as well were observed at 3.324 eV near this peak [3]. Although it is expected that the TES transitions of I_6 and I_9 should be observed by first separating their emission energies, the shape of the PL spectra of Sb-doped ZnO nanowires was different from that of nondoped ZnO nanowires. On the other hand, the ZnO sample doped with group-V elements exhibited a free-to-acceptor (FA) emission centered around 3.310 eV [9, 10]. FA transition of PL for Sb-doped ZnO crystals has been observed at 3.296 (8.5 K) [11], 3.312 (10 K) [12], 3.301 eV, and (125 K) [13] by other research groups, and these peak positions almost agree with our results. Consequently, we deduce that this peak is due to the transition of free electrons to a neutral acceptor, i.e., FA transition.

The plots of temperature variations in the FX and FA peaks are denoted by closed circles in Fig. 16.3. First, we fitted the temperature dependence of FX peaks by using the Manoogian–Woolley equation [14]:

$$E = E_0 + UT^S + V\theta[\coth(\theta/2T) - 1], \qquad (16.1)$$

where T and E_0 are the sample temperature and energy value at $T = 0$ K. θ approximately equals $3/4\theta_D$ where θ_D is the Debye temperature. The second term UT^S describes the energy shift due to lattice dilatation with temperature. The third term $V\theta[\coth(\theta/2T)\text{-}1]$ represents the contribution of the electron–phonon interaction. Since the FX transition energy in ZnO exhibited the same temperature

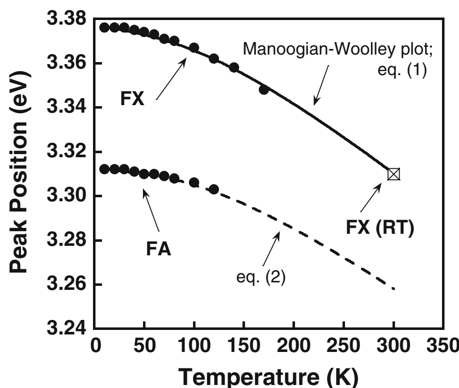

Fig. 16.3 Temperature variations in FX and FA peaks for Sb-doped ZnO nanowires deposited at 1000 °C

variation as that for the band gap, we could use this form in Eq. (16.1) to examine the temperature variation in the FX transition energy instead of the band gap energy. We obtained the best fit curve for the Sb-doped ZnO nanowire sample grown at 1000 °C by using $E_0 = 3.377$ eV, $U = -2.8 \times 10^{-5}$ eV/K, $V = -9.4 \times 10^{-5}$ eV/K, $S = 1.3$, and $\theta = 412$ K. The fitted curve is shown as the solid line in Fig. 16.3. The FX transition energy at 300 K was calculated from the conventional band gap energy (3.37 eV) of the ZnO crystal, and the temperature-independent exciton binding energy of 60 meV was used as in the Ref. [15]. Although the FX peak could not be observed experimentally at RT, the estimated value of 3.31 eV fitted well in the best fitted curve, as shown in Fig. 16.3. The fitting parameters were in good agreement with those reported by Hanby et al. [16] and Su et al. [17].

Further, the activation energy of the acceptor was estimated from the temperature variation in the FA peak. The acceptor activation energy can be calculated using the following equation [11–13].

$$E_{\mathrm{A}} = E_{\mathrm{g}} + E_{\mathrm{FA}} + \frac{1}{2}k_{\mathrm{B}}T, \tag{16.2}$$

where, E_{g} was calculated from the sum of the FX peak energies obtained using the aforementioned Manoogian–Wooley equation. The curve fitting result is shown by the dashed line in Fig. 16.3. The best fit was obtained when E_{A} was 125 meV. This result is in good agreement with that reported in some other studies [11–13]. In any case, the crystal growth conditions do not affect the temperature variations in FX and FA.

Next, we discuss the deposition temperature variation in the PL spectra. Figure 16.4a, b shows the PL spectra of as-grown and annealed Sb-doped ZnO nanowire samples under various deposition temperatures, respectively. The PL spectra were normalized by the FX peak intensity. Hereafter, we refer to the normalized intensity as the PL peak intensity ratio. Although the observed PL peak positions such as FX, BE, $\mathrm{BE_{sd}}$, and FA for the as-grown and annealed samples

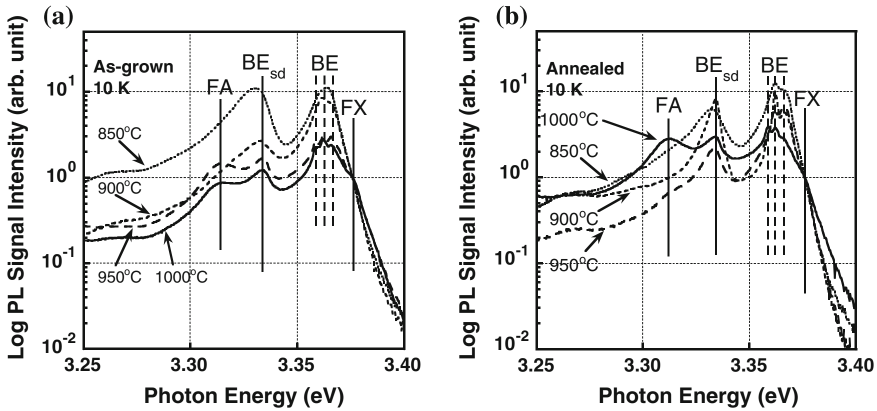

Fig. 16.4 Comparison of PL spectra for as-grown (**a**) and annealed (**b**) samples under various deposition temperatures

were the same under various deposition temperatures, the PL intensity ratios of the observed peaks varied.

Figure 16.5a, b shows the deposition temperature variations in the PL intensity ratios for the as-grown and annealed samples, respectively. Below a deposition temperature of 800 °C, the PL intensity was very weak and could not be detected. The reason for this could be poor crystallinity, because as shown by the energy-dispersive X-ray (EDX) measurements, the concentration of Sb_2O_3 increased over 50 and 80 % for the samples deposited at 800 and 750 °C, respectively. Hence, we disregarded this region in our investigations. The PL intensity ratio of BE and BE_{sd} decreased when the deposition temperature increased. Since the BE and BE_{sd} peaks were attributed to the donor levels due to the unintentionally incorporated impurities and structural defects formed in the band gap of ZnO, respectively, the

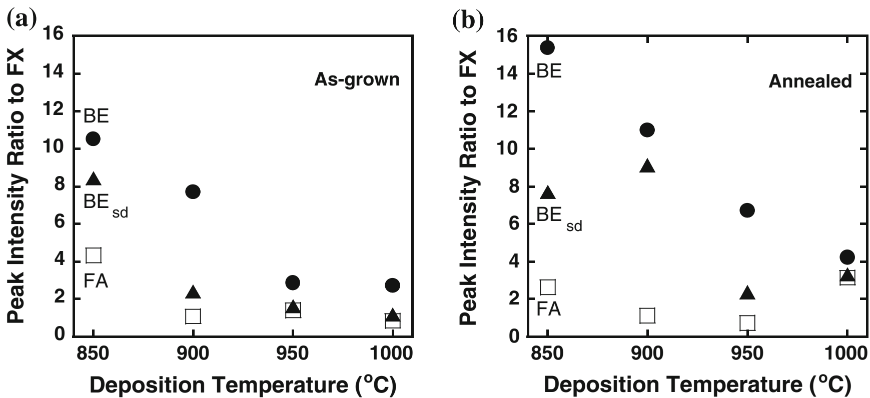

Fig. 16.5 Deposition temperature variations in PL intensity ratios of as-grown (**a**) and annealed (**b**) samples, respectively

concentration of impurities and defects in the ZnO crystal must have reduced with increasing deposition temperature. On the other hand, the FA peak intensity ratio was almost constant. According to the first-principles calculations by Limpijumnong et al., an Sb_{Zn}–$2V_{Zn}$ complex represents a new class of defects with low formation energy, which serves as shallow acceptor levels [4]. In this complex, the core Sb occupies the Zn site, which is energetically favorable for spontaneously inducing two Zn vacancies [4]. We believe that the FA peak corresponds to the acceptor level induced by this complex formed in our Sb-doped ZnO nanowires. However, we found that deposition temperature variations did not affect the acceptor concentration formed in the band gap of ZnO by Sb-doping. Annealing dependence of the PL peak intensity ratios is shown in Fig. 16.5b. The intensity ratios for BE and BE_{sd} decreased with increasing deposition temperature, as in the case for as-grown samples. However, the intensity ratios increased and their slopes became steeper. As mentioned above, BE and BE_{sd} correspond to the donor levels caused by the unintentionally incorporated impurities and the structural defects formed in the band gap of ZnO, respectively, which indicates that the impurity and defect concentrations in the ZnO crystal increases by sample annealing. However, only the FA peak intensity ratio remained almost constant, as shown in the figures for both as-grown and annealed samples. This means that the acceptor concentration formed by Sb-doping does not increase even by sample annealing. Although the conduction type of our Sb-doped ZnO nanowires could not be determined at the time of conducting the present experiments due to difficulty in performing Hall measurements, it was found that a *p*-type conduction may be obtained by suppressing donor levels such as those corresponding to BE and BE_{sd} peaks, which compensate for hole carriers released from the acceptor level in this study.

16.4 Conclusion

We grew Sb-doped ZnO nanowires under various deposition conditions by CVD. The optical properties of these nanowires were investigated by PL measurements. The PL spectra of these samples were dominated by the emissions related to donor levels due to unintentionally incorporated impurities. However, the appearance of the FA PL peak, FA, by Sb-doping suggests that impurity level due to Sb acceptor could certainly be formed. The activation energy of the acceptor level was estimated to be 125 meV. Since the impurity concentration contributing to the donor level decreased with increasing deposition temperature, acceptor doping can be carried out in ZnO crystal nanowires by using the proposed growth technique.

Acknowledgments This work was partially supported by the Special Coordination Funds for Promoting Science and Technology from the Japan Science and Technology Agency, and a Grant-in-Aid by the Ministry of Education, Science, Sports, and Culture.

References

1. K. Sakai, S. Oyama, K. Noguchi, A. Fukuyama, T. Ikari, T. Okada, Phys. E **40**, 2489 (2008)
2. K. Sakai, K. Noguchi, A. Fukuyama, T. Ikari, T. Okada, Jap. J. Appl. Phys. **48**, 085001 (2009)
3. Ü. Özgür, Y.I. Alivov, C. Liu, A. Teke, M.A. Reshchikov, S. Doğan, V. Avrutin, S.-J. Cho, H. Morkoç, J. Appl. Phys. **98**, 041301 (2005)
4. S. Limpijumnong, S.B. Zhang, S.H. Wei, C.H. Park, Phys. Rev. Lett. **92**, 155504 (2004)
5. T. Aoki, Y. Shimizu, A. Miyake, A. Nakamura, Y. Nakanishi, Y. Hatanaka, Phys. Stat. Sol. B **229**, 911 (2002)
6. F.X. Xiu, Z. Yang, L.J. Mandalapu, D.T. Zhao, J.L. Liu, Appl. Phys. Lett. **87**, 152101 (2005)
7. B.K. Meyer, H. Alves, D.M. Hofmann, W. Kriegseis, D. Forster, F. Bertram, J. Christen, A. Hoffmann, M. Straßburg, M. Dworzak, U. Haboeck, A.V. Rodina, Phys. Stat. Sol. B **241**, 231 (2004)
8. K. Thonke, T. Gruber, N. Teofilov, R. Schonfelder, A. Waag, R. Sauer, Phys. B **308–310**, 945 (2001)
9. Y. Dongqi, H. Lizhong, Q. Shuangshuang, Z Heqiu, S. Len, and L. Len, J. Phys. D: Appl. Phys. 42 (2009) 055110
10. D. Hwang, H. Kim, J. Lim, J. Oh, J. Yang, S. Park, K. Kim, D.C. Look, Y.S. Park, Appl. Phys. Lett. **86**, 151917 (2005)
11. F.X. Xiu, Z. Yang, L.J. Mandalapu, D.T. Zhao, J.L. Liu, Appl. Phys. Lett. **87**, 252102 (2005)
12. H. Zhang, L. Hu, Z. Zhao, J. Ma, Y. Qiu, B. Wang, H. Liang, J. Bian, Vacuum **85**, 718 (2011)
13. G. Hong, Z. Mingyu, J. Hong, W. Xuanzhang, Z. Zhiguo, J. Alloys Compd. **464**, 234 (2008)
14. A. Manoogian, J.C. Wooly, Can. J. Phys. **62**, 285 (1984)
15. Y. Chem, D.M. Bagnall, H. Koh, K. Park, K. Hiraga, Z. Zhu, T. Yao, J. Appl. Phys. **84**, 3912 (1998)
16. D.W. Hamby, D.A. Lucca, M.J. Klopfstein, G. Cantwell, J. Appl. Phys. **93**, 3214 (2003)
17. F. Su, W. Wang, K. Ding, G. Li, Y. Liu, A.G. Joly, W. Chen, J. Phys. Chem. Solids **67**, 2376 (2006)

Chapter 17
Experimental and Theoretical Investigations of Dopant, Defect, and Morphology Control on the Magnetic and Optical Properties of Transition Metal Doped ZnO Nanoparticles

O. D. Jayakumar, C. Persson, A. K. Tyagi and C. Sudakar

Abstract The control of size, shape, and physical properties by surface modifications are of immense interest in materials which are of technological importance. The ZnO-based wide bandgap semiconductor nanoparticles have gained significant interest in the research community due to its large exciton binding energy (60 meV). Further substantial renewed interest in ZnO-based compounds is due to the possible realization of *p*-type conduction and ferromagnetic behavior when doped with transition metals. In this report we present interesting results on the ZnO nanoparticle system in which the control of dopants, morphology, and the surface modification can influence significantly the physical properties of the ZnO nanoparticles. First, we present the methods to control the morphology of the ZnO particle to obtain nanorods. As an example we show the effect of Li dopant on the morphology control of Co and Ni doped ZnO. The effect of morphology on the magnetic properties of these compounds is discussed further. We also demonstrate the effect of the *n*-type charge carriers on the magnetic and optical properties by doping aliovalent cations in Zn(Co)O. Following this we comment on the magnetic property manipulations by surfactant treatment of transition metal (TM) doped ZnO and defect stabilization in ZnO by Mg doping. The magnetic coupling is RKKY-like both with and without Li co-doping. Finally, we provide the

O. D. Jayakumar · A. K. Tyagi
Chemistry Division, Bhabha Atomic Research Centre, Mumbai 400085, India

C. Persson
Department of Physics, University of Oslo, P.O. Box 1048 Blindern 0316 Oslo, Norway

C. Persson
Department of Materials Science and Engineering, Royal Institute of Technology, SE-100 44 Stockholm, Sweden

C. Sudakar (✉)
Deparment of Physics, Indian Institute of Technology Madras,
Chennai 600036, India
e-mail: csudakar@iitm.ac.in

M. S. R. Rao and T. Okada (eds.), *ZnO Nanocrystals and Allied Materials*,
Springer Series in Materials Science 180, DOI: 10.1007/978-81-322-1160-0_17,
© Springer India 2014

significant implications of these results on the nanorods structures of room temperature ferromagnetic materials by first-principles modeling. These theoretical analyses demonstrate that Li co-doping has primarily two effects in bulk $Zn_{1-x}M_xO$ (with M = Co or Ni). First, the Li-on-Zn acceptors increase the local magnetic moment by depopulating the M 3d minority spin-states. Second, Li-on-Zn prefer to be closer to the M atoms to compensate the M–O bonds and to locally depopulate the 3d states, and this will help in forming high aspect nanostructures. The observed room temperature ferromagnetism in Li co-doped $Zn_{1-x}M_xO$ nanorods can therefore be explained by the better rod morphology in combination with locally ionizing the magnetic M atoms.

17.1 Introduction

Zinc oxide (ZnO) is a wide bandgap semiconductor (direct bandgap of 3.37 eV) with a large exciton binding energy (60 meV) at room temperature [1]. It exhibits near UV emission, transparent conductivity, and piezoelectricity. In its one-dimensional form it exhibits unique electrical, thermal, optical, mechanical properties due to size reduction or quantum confinement [2]. The research on the one-dimensional ZnO nanostructured materials [3] is sprouting to a new level due to promising novel applications. Excellent optoelectronic and piezoelectric properties of ZnO is leading to a wide variety of applications including ultraviolet (UV) lasers [4, 5], light emitting diodes [6], field emission devices [7, 8], nanosensors [9, 10], dye and semiconductor sensitized solar cells [11–13], piezoelectric nanogenerators, and piezotronics [14–18]. In addition, a range of nanodevices such as UV photodetectors [19–23], sensors [24–26], field effect transistors [27], intramolecular p-n junction diodes [28], Schottky diodes [29], and light emitting devices [6] fabricated using ZnO nanorods or nanowires have been reported by a large number of researchers [2]. In the last decade intense research is being carried out on the fabrication approaches and size and shape controlled properties of one-dimensional ZnO nanostructures [2]. Of the various ZnO nanostructures reported ZnO nanorods and nanowires have been studied more often due to their easy fabrication and device application [2, 30].

In addition to optoelectronic and piezoelectric devices, transition metal (TM) (Fe, Co, Mn, Ni, Cr, and V) doped ZnO materials are shown to be promising for newly proposed spintronics devices. Relatively long room temperature spin-coherence time [31], and the possibility of fabricating p-type ZnO [32–34] in addition to well-established n-type ZnO fabrication with low resistivity give bipolar spintronics a realistic option. However, there are lot of controversies on the hole [35, 36] and electron [37–39] mediated ferromagnetism and needs both experimental and theoretical clarifications [40]. More extensive research has been carried out to realize and understand the homogeneous doping of magnetic elements in the semiconducting matrix, and above room temperature ferromagnetic ground state in ZnO [41, 42]. More generally the magnetic properties of bulk TM

doped ZnO are paramagnetic, on the other hand the majority of the work reported on the same system in thin film and nanostructure forms show the existence of ferromagnetic nature. The role of dopant, morphology of the ZnO particles, and the native defects including the surface defect states collectively play the role in determining the magnetic properties.

In this chapter, we present optical and magnetic properties of TM doped ZnO nanorods, nanoparticles, and surface modified nanoparticles. We first report the methods of fabricating ZnO nanorods, nanoparticles, and surface modification by using surfactant treatment and different annealing conditions including hydrogenation. We show that morphology of ZnO plays a significant role in controlling the magnetic and optical properties in addition to the dopant and native defects. We also demonstrate the effect of the *n*-type charge carriers on the magnetic and optical properties by doping aliovalent cations in ZnO. Following this we discuss the magnetic property manipulations by surfactant treatment of TM doped ZnO and defect stabilization in ZnO by Mg doping. Finally, we show from theoretical studies the implication of the shape, size, dopant concentration, etc., on the magnetic properties of TM doped ZnO.

17.2 Preparation of ZnO Nanoparticles/Nanorods

There are several approaches for preparing nanoparticles and nanorods. This includes many of the physical and chemical vapor deposition techniques [43–47] and wet chemical synthesis techniques [3, 48–51]. Exotic ZnO nanostructures have been prepared by the reaction of Zn metal vapor with oxygen gas [52]. The growth mechanisms include the vapor–liquid–solid process [53] and vapor–solid process [43]. However, the solution chemical syntheses offer flexibility to obtain the nanorods at room temperature at much lower cost [3, 54–56]. The ZnO nanoparticles and nanorods presented in this work were synthesized by standard solid-state reaction [57] followed by surfactant treatment [58, 59], sol–gel route followed by pyrolysis or by solvothermal method [60, 61]. A brief description of the experimental procedure for the above three methods is discussed below.

17.2.1 Surfactant Coated Polycrystalline Transition Metal Doped ZnO

$Zn_{1-x}M_xO$ (M is metal cation; x is typically less than 0.1) bulk samples were prepared by a standard solid-state reaction route [57], using high purity ZnO and metal oxide (e.g. MnO_2) powders. The ZnO and metal oxide powders were mixed in appropriate proportions. These mixtures were calcined at 400 °C for 8 h followed by sintering in air at 450 °C for 12 h and cooled to room temperature

normally to obtain nominal $Zn_{1-x}Mn_xO$ bulk powder. Any other co-dopants such as Li in $Zn_{1-x}M_xO$ were prepared by a similar method by reacting the co-dopant parent solid, i.e., LiOH in the procedure discussed above. Surfactants used during the synthesis process significantly change the particle properties. To make surfactant coating on ZnO or $Zn_{1-x}M_xO$ particles we used AOT (sodium bis-2-ethylhexyl sulfosuccinate, 99.9 %)- or triblock copolymer (poly(ethylene glycol)-block-poly(propylene glycol)- block-poly(ethylene glycol); Pluronic 123). The samples were mixed with AOT or copolymer with sample to surfactant weight ratio of 1:10 and heated at 400 °C for 1 h in air. After heat treatment the samples were washed and dried, followed by heating at 400 °C for 2 h in air.

17.2.2 Nanoparticles of Doped ZnO by Sol-Gel Route Followed by Pyrolytic Reactions

To prepare $Zn_{1-x}M_xO$ or $Zn_{1-x-y}M_xLi_yO$ (x and y typically below 0.1) nanoparticles by the pyrolysis process of gels obtained from the sol–gel process, we used high pure zinc acetate dihydrate, metal (e.g. M = Co or Mn) acetate tetrahydrate, lithium acetate dihydrate, sodium bicarbonate ($NaHCO_3$), and alcohol as a solvent without any further purification. As an example, to prepare $Zn_{1-x-y}Mn_xLi_yO$ nanoparticles, zinc acetate dihydrate, manganese acetate tetrahydrate, lithium acetate dihydrate, and $NaHCO_3$ taken in appropriate proportions were mixed using 2-propoxy ethanol as the solvent and monoethanolamine as the dissolution agent at room temperature [62]. The mixture was pyrolyzed at 150–175 °C for 1–2 h. The resulting product was washed thoroughly with deionized water and absolute ethanol to remove the unwanted sodium acetate and other impurities. The samples were oven-dried subsequently at 125 °C for 24 h [63]. The dried product was heated at 300 °C for 1 h to remove organic residuals and further annealed at 500–600 °C for 1 h to obtain the desired $Zn_{1-x-y}M_xLi_yO$ nanoparticles. Co-doping of two metal cations such as (Co:In), (Co:Ga), (Co:Al) in ZnO was done by similar process either using appropriate metal chlorides or metal acetate as the starting material.

17.2.3 $Zn_{1-x-y}M_xLi_yO$ Nanorods by Solvothermal Method

ZnO nanowires/rods were prepared by solvothermal method. This process involves rapidly heating a mixture of high pure zinc acetate dihydrate (10 mmol) with 15 mL of trioctylamine in a round-bottomed flask to 320 °C. The reaction was maintained at 320 °C for 2 h with continuous refluxing. Finally the mixture was cooled to room temperature. For preparing $Zn_{1-x-y}M_xLi_yO$ (M = Co, Ni) the above process was carried out with metal acetates taken in appropriate proportions in the mixture. We have maintained the duration of reaction same for all the

samples so that the effect of metal dopants on the nanorod length and aspect ratio can be studied. The precipitate obtained in these reactions were washed thoroughly with acetone and absolute ethanol and dried.

17.2.4 Effect of Hydrogenation, Vacuum, and Air Annealing Treatment

The characteristic properties of doped ZnO can be modified by treating them in H_2, vacuum, or air ambient at temperature ranging from 30 to 400 °C. Significant changes in the morphologies and associated defect emissions and magnetic property changes take place on such treatments, in particular on treatment in H_2 at room temperature. For hydrogen treatment samples were loaded in a Sievert-type hydriding reactor unit made of stainless steel [64, 65]. Hydrogenation of the samples was done at room temperature and at 400 °C after evacuating to 10^{-6} torr and subsequently applying hydrogen pressure of around 5–15 atmospheres for several hours. The samples were removed from the reactor after cooling the hydriding unit to liquid N_2 temperature and excess H_2 was removed by evacuation. The samples were exposed to air at liquid N_2 temperatures. The hydriding unit is warmed up to room temperature before collecting the sample.

17.3 Effect of Morphology on the Doped ZnO

Nanomaterials have significant differences in the physical and chemical properties compared to conventional bulk compound. ZnO with one-dimensional attributes and ferromagnetic properties are proposed to be potential material for developing nanoscale spintronic devices [41, 66–68]. In spite of such promising devices fundamental understanding including spin effects in nanoscale magnetic semiconductors need to be developed. This can partly be accomplished by applying novel synthesis approaches for preparing TM doped ZnO nanostructures and studying their properties. Several methods including template-assisted synthesis for large area patterning of metal oxide nanowire arrays [69], surfactant-assisted template free methods [70], sonochemical [71], and hydrothermal processes [72–74] have been reported [43]. Low temperature solution phase growth processes have been employed to prepare TM doped ZnO nanowires/nanorods [54–56]. ZnO nanorods which are otherwise stable can become unstable when doped with metal cations. Therefore, it is important to understand the morphological stability of the ZnO nanorods in presence of intrinsic defects and extrinsic dopants to tailor the magnetic, electrical, and optical properties.

Monophasic $Zn_{1-x-y}M_xLi_yO$ (M = Co or Ni; x = 0, 0.03, 0.05; y = 0.03, 0.05, 0.10) nanorods were prepared by the solvothermal process described above. The Li

substitution in ZnO increases the lattice parameter slightly compared to the Co or Ni doped ZnO. Ni doping decreases the cell parameters compared to pure ZnO due to smaller ionic radius of Ni^{2+} (0.55 Å) compared to Zn^{2+} (0.60 Å). Transmission electron micrographs show the nanorod morphology of pure ZnO with 500–3,000 nm long rods with a diameter in the range of 100–150 nm (Fig. 17.1a). The high aspect ratio (15–20) of pure ZnO reduces significantly with $x = 0.03$ of Co (with Li concentration $y = 0$) and with $x = 0.05$ Co doping the majority of the particles become almost spherical in shape (Fig. 17.1b). With Ni doping for $x = 0.03$ the aspect ratio of the particle decreases to 1–3 with hexagonally faceted particles morphology (Fig. 17.1c). This clearly indicates the instability of the nanorod morphology brought in by the presence of Co or Ni in ZnO. With only Li doping (up to $y = 0.1$) the nanorod shape is retained with slightly higher aspect ratio (20–25) (Fig. 17.2a). In presence of Li, adding Co (5 at.%) in ZnO lattice does not alter the nanorod shape. The observation is the same with Ni, where co-doping Li ($y = 0.03$) with Ni ($x = 0.03$) retained the original nanorod shape of

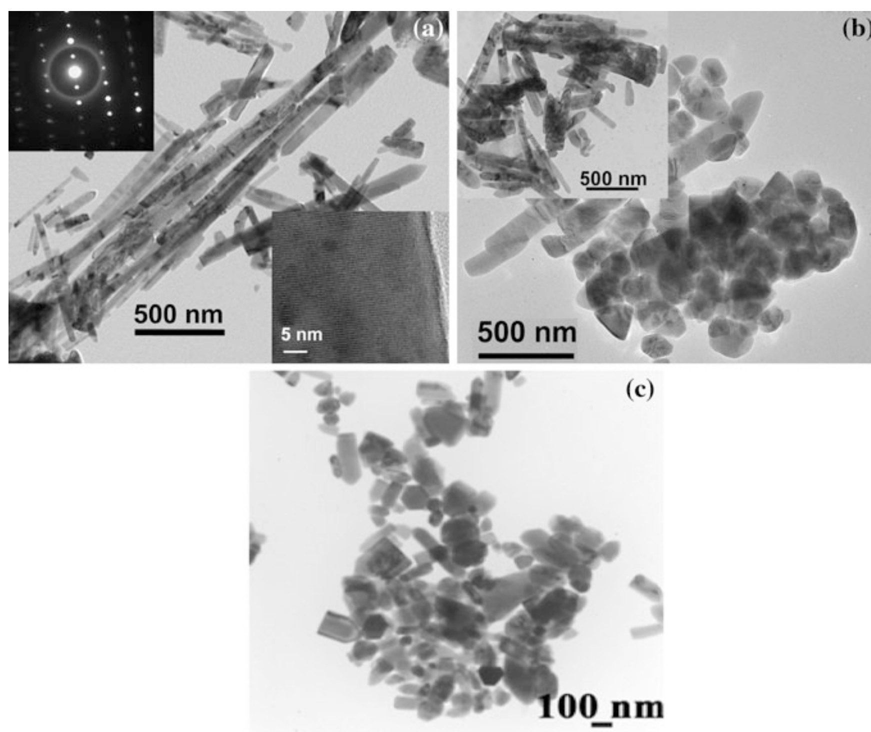

Fig. 17.1 Bright field transmission electron microscopy (TEM) images of **a** pristine ZnO, **b** $Zn_{0.95}Co_{0.05}O$, **c** $Zn_{0.97}Ni_{0.03}O$. The inset in **a** shows the selected area electron diffraction (SAED) pattern and high resolution TEM image of one of the nanoparticles. The inset in **b** shows the TEM image of $Zn_{0.97}Co_{0.03}O$

ZnO with much high aspect ratio of 15–30. This clearly shows the role of Li in stabilizing the shape and morphology of the ZnO particle. In general the particles are highly crystalline without any impurity phases. However, $Zn_{0.85}Co_{0.05}Li_{0.10}O$ nanoparticles showed occasional planar defects that can potentially break the long particles (inset Fig. 17.2b). The stability of the nanorod morphology due to Li could be due to the localization of mobile Li at Zn site close to Co during the growth of nanorods as predicted by the first principle theoretical modeling [61, 75]. However, the precise reason that affects the morphology is not clear. Anisotropic growth can promote the ZnO particles to grow in a specific direction more rapidly than the other directions. The growth of ZnO along the *c*-axis to form nanorod-shaped elongated particles is favored by the lowest density of surface energy along c-axis (9.9 eV/nm^2) [76]. Ni and Co doping can affect the overall free energy leading to more isotropic growth of the particles. With Li addition, the

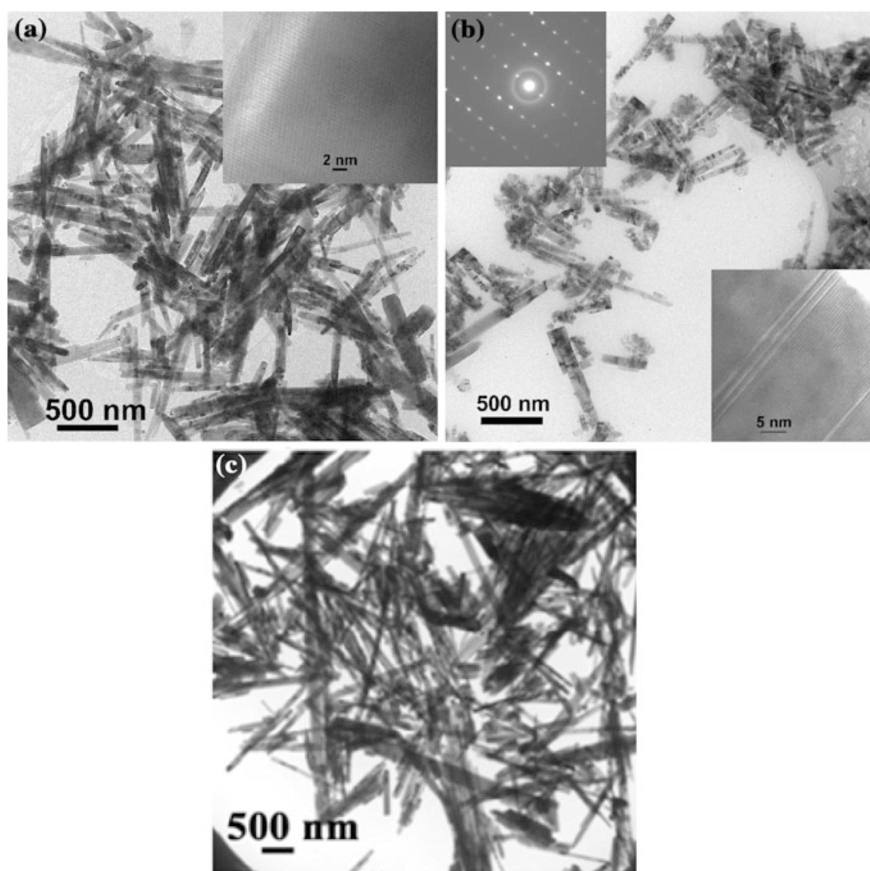

Fig. 17.2 Bright field TEM images of **a** $Zn_{0.90}Li_{0.10}O$, **b** $Zn_{0.85}Co_{0.05}$ $Li_{0.10}O$, **c** $Zn_{0.94}$ $Li_{0.03}Ni_{0.03}O$. Insets: **a** High resolution TEM image of $Zn_{0.90}Li_{0.10}O$ crystallite; **b** Selected area electron diffraction (*top left*) and HRTEM (*bottom right*) of $Zn_{0.85}Co_{0.05}$ $Li_{0.10}O$ crystallite

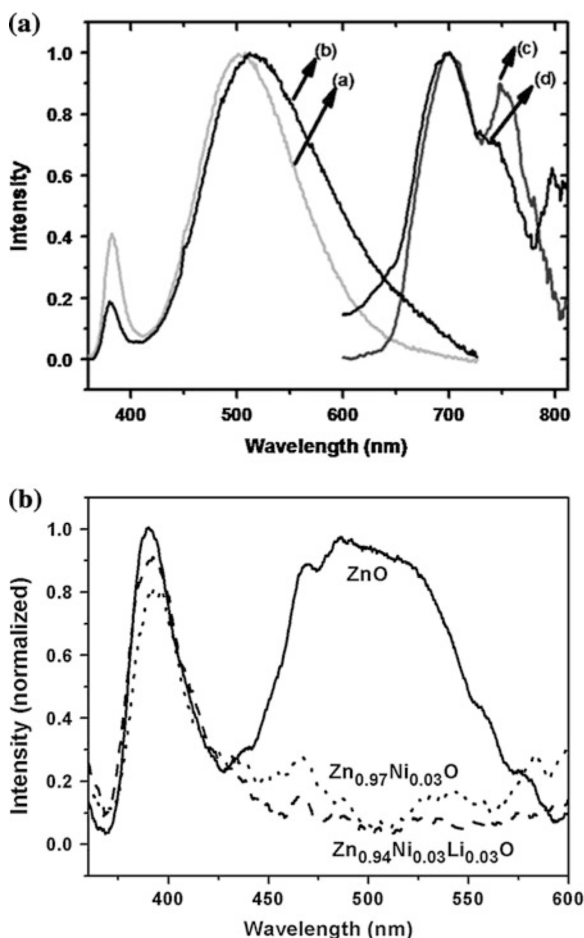

Fig. 17.3 **a** Photoluminescence emission spectra of (*a*) pristine ZnO, (*b*) $Zn_{0.90}Li_{0.10}O$, (*c*) $Zn_{0.95}Co_{0.05}O$, (*d*) $Zn_{0.85}Co_{0.05}$ $Li_{0.10}O$ obtained after 280 nm excitation. **b** Photoluminescence emission spectra of (*a*) pristine ZnO, (*b*) $Zn_{0.97}Ni_{0.03}O$, and (*c*) $Zn_{0.94}$ $Li_{0.03}Ni_{0.03}O$ obtained after 345 nm excitation

oxygen vacancies that get created can stabilize the ZnO lattice, again favoring the anisotropic growth. With increasing concentration of Li in ZnO the particles also get wider in addition to being longer, which indicate that the nanorods can get bundled together and sinter to form wider particles.

The optical properties get modified by the dopant, defect and the morphology. The latter is prominent in pure ZnO that will be discussed in Sect. 17.6. The photoluminescence emission spectra obtained on the $Zn_{1-x-y}M_xLi_yO$ ($M = $ Co, Ni) are shown in Fig. 17.3a. The band edge luminescence around 380 nm with a broad defect emission $\sim$510 nm is seen in ZnO and $Zn_{0.9}Li_{0.10}O$. The broad

defect emission is due to recombination of conduction electron with the hole trapped at the oxygen vacancies [77]. In presence of Co ($x = 0.03, 0.05$) the band edge emission gets completely quenched. New bands due to transition between localized d-levels of Co^{2+} occupying the tetrahedral environment are seen around 697 and 747 nm [77, 78]. The decrease in the relative intensity of 747 nm with Li doping ($y = 0.1$) indicate that co-doping of Li^{+} ions in $Zn_{0.95}Co_{0.05}O$ results in the distortion around Co^{2+} luminescence center. This could be due to the additional anion vacancies created by Li^{+} ions incorporation in the lattice. When Ni is substituted in ZnO, the defect emission gets completely suppressed (Fig. 17.3b). The emission pattern is the same with Li co-doping. The suppression of the defect emission can be due to increased nonradiative process [79] thereby reducing the extent of electron hole recombination by trapping of the electron by the Ni^{2+} centers in the lattice.

Recently, it has been evidenced that the magnetic properties of nanoparticular systems turn out to be very different from their respective bulk systems [80]. We have investigated the magnetic properties of TM doped for $Zn_{1-x-y}M_xLi_yO$ nanorods in which aspect ratio of the nanorods vary significantly with metal cation and Li concentration. The magnetization versus magnetic field (M–H) measurements for $Zn_{1-x-y}M_xLi_yO$ (M = Co, Ni) are summarized in Fig. 17.4. Pure ZnO and Li doped ZnO are diamagnetic in characteristics. Whereas clear hysteresis is observed in Co-doped ZnO samples. With Li co-doping in Co doped ZnO, a six fold increase in magnetization is observed. Similar enhancement in Li co-doped ZnCoO nanoparticle system has been shown [81]. The increase is attributed to the additional charge carriers that are needed in addition to the random magnetic ions and defects for the cooperative exchange interactions that result in ferromagnetic coupling [81]. Similarly, the M–H measurements (Fig. 17.4b) at room temperature for $Zn_{0.97-y}Ni_{0.03}Li_yO$ ($y = 0$–0.1) show a saturation magnetization of 0.55 emu/g (0.26 μ_B/Ni) for $Zn_{0.97}Ni_{0.03}O$ ($y = 0$) which increased to 0.8 emu/g (0.39 μ_B/Ni) by increasing 'y' to 0.03. Further increase in Li concentration (y) resulted in a

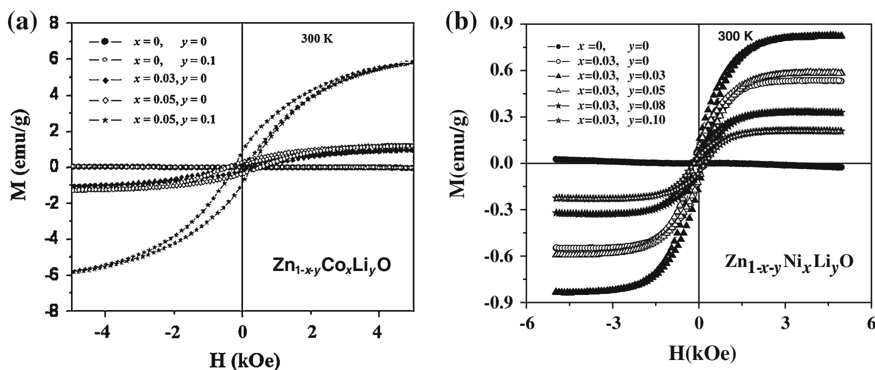

Fig. 17.4 Magnetization (M) versus magnetic field (H) plots for **a** $Zn_{1-x-y}Co_xLi_yO$ and **b** $Zn_{1-x-y}Ni_xLi_yO$

monotonous decrease in the magnetization showing a lowest value of 0.2 emu/g (0.09 μ_B/Ni) compared to the $Zn_{0.97}Ni_{0.03}O$ samples for $y = 0.10$. The increase in magnetization with Li co-doping and monotonous decrease in the magnetization with further increase in Li concentration has a direct correlation to the changes observed in the nanorod morphology with the changes in the concentration of Li. These studies clearly point out the interdependence of magnetization with the TM doping concentration, the carrier concentration modifying dopants, and the morphology of the nanoparticles that are influenced by these dopants. Such interdependency arises from the role of Li to stabilize the strained M–O bond in $Zn_{1-x-y}M_xLi_yO$ which in turn stabilize the nanorod morphology [61, 75].

17.4 Effect of Aliovalent (In, Ga, Al) co-dopants on the Magnetic Properties of Zn(Co)O Nanoparticles

The TM dopants are introduced in dilute concentration in the ZnO to realize the magnetic property. However, at dilute concentration the dopant magnetic atoms are far from each other, under homogeneous distribution, than the distance required for the conventional exchange interaction that would result in ferromagnetic property [82]. Therefore, the role played by the free carriers in stabilizing the ferromagnetic interaction is very important and is taken into consideration in many of the theoretical models. Theoretical models based on the Ruderman-Kittel-Kasuya-Yoshida (RKKY) interaction have been developed for systems where the magnetic ions interact among each other through the delocalized charge carriers [83, 84]. For insulating systems a bound magnetic polaron model has been proposed [85–88]. In such systems the charge carriers localized on oxygen vacancies interact with the magnetic metal cations forming "magnetic polarons." The magnetic polarons interact ferromagnetically. When the magnetic polarons form a percolative network, long-range ferromagnetic interaction arises leading to ferromagnetic nature in these oxides. As the role of carriers is important as proposed in mechanisms based on carrier mediation, controlling the magnetic property by manipulating the carrier concentration can be a promising approach. Carrier concentration can be tuned by doping aliovalent cations, for e.g., Al^{3+}, In^{3+}, Ga^{3+} in $Zn_{0.95}Co_{0.05}O$ has been used in the examples we discuss here, which can be expected to influence significantly the resulting ferromagnetic properties in these oxides. We have chosen Co doped ZnO as it has attracted considerable interest with many reports, mostly in the thin films and nanostructures, showing room temperature ferromagnetism [39, 89–91]. Neutron scattering studies show that the cobalt doping up to 5 at. % is single phase [92].

Many reports showed the absence of ferromagnetism in bulk polycrystalline samples of Co doped ZnO [93–97]. However, thin films made from colloidal nanocrystals show the switching from a paramagnetic state to ferromagnetic state while introducing and removing *n*-type interstitial Zn defect of ZnO [38].

Therefore, understanding the role of carriers in nanocrystalline samples has important implications on the control of magnetic properties of TM doped ZnO. We discuss below the magnetic properties of Al^{3+}, In^{3+}, Ga^{3+} doped $Zn_{0.95}Co_{0.05}O$ nanoparticular systems. Nanoparticles of $Zn_{0.95-x}Co_{0.05}A_xO$ (A = In, Ga, Al; $x = 0.0$–0.1) were prepared by pyrolytic reaction of sol–gels obtained by the procedure discussed in Sect. 17.2.2.

17.4.1 In Doped $Zn_{0.95}Co_{0.05}O$ Nanoparticles

Nanoparticles of In doped $Zn_{0.95-x}Co_{0.05}A_xO$ made up to $x = 0.07$ were all single phase with no secondary phases discerned as examined from X-ray diffraction and selected area electron diffraction. The bright field TEM images of these samples are shown in Fig. 17.5. The crystallite size ranged from ~25 to ~10 nm [62]. The crystallite size decreased with increasing In concentration, i.e., ~25 nm for $x = 0$ to ~12 nm for $x = 0.07$. The TEM images show the particles of ZnO and $Zn_{0.95}Co_{0.05}O$ are made of hexagonal facets of size ~23 nm (Fig. 17.5). For In-doped $Zn_{0.95-x}Co_{0.05}A_xO$ samples the particle size was ~18–20 nm. The cobalt in all these samples is in 2+ oxidation state as inferred from the X-ray photoelectron spectroscopy. The M–H plots show that pure ZnO is diamagnetic and $Zn_{0.95}Co_{0.05}O$ is paramagnetic (Fig. 17.6). As the In concentration increases in

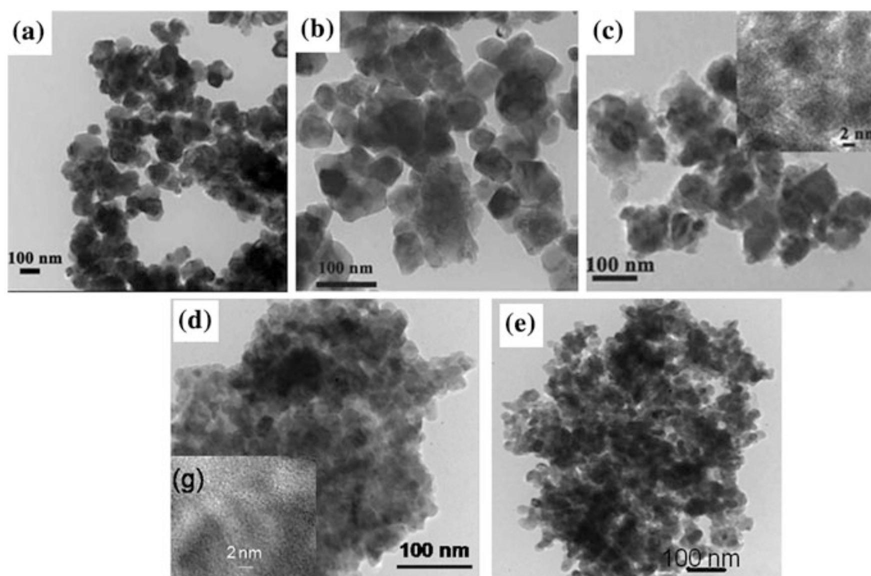

Fig. 17.5 Bright field TEM images of **a** ZnO, **b** $Zn_{0.95}Co_{0.05}O$, **c** $Zn_{0.88}Co_{0.05}$ $Al_{0.07}O$, **d** $Zn_{0.90}Co_{0.05}$ $In_{0.05}O$, and **e** $Zn_{0.92}Co_{0.05}$ $Ga_{0.03}O$. Inset in **c** and **d** show the HRTEM images of the crystallites

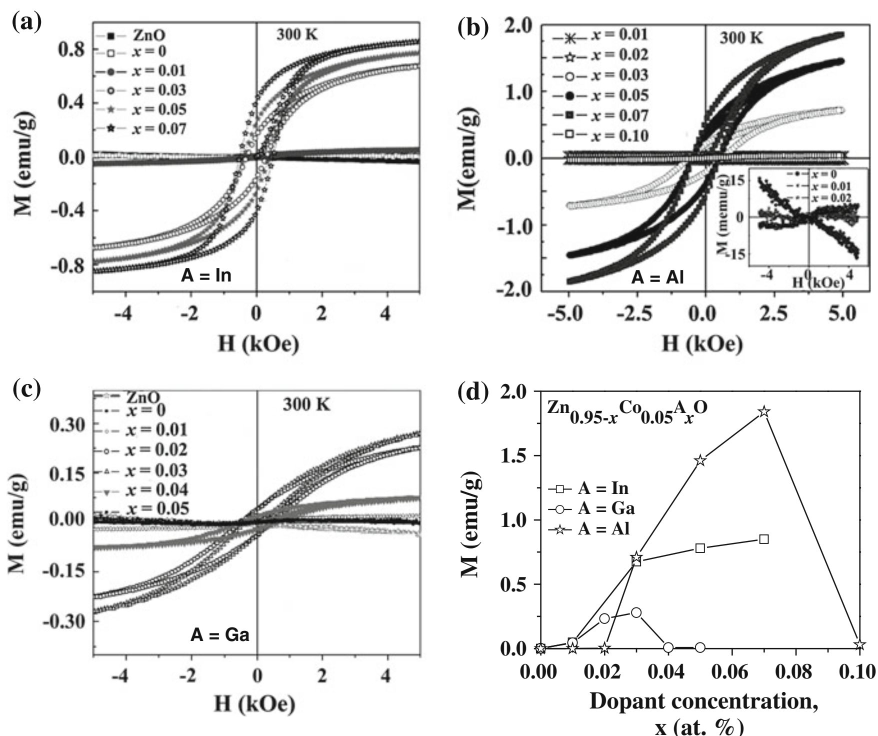

Fig. 17.6 **a**–**c** Magnetization versus magnetic field plots for $Zn_{0.95-x}Co_{0.05}A_xO$ (A = In, Ga, Al; $x = 0.0$–0.1) measured at 300 K. **d** The change in the magnetization with dopant concentration of A (In, Ga, Al) in $Zn_{0.95-x}Co_{0.05}A_xO$

$Zn_{0.95-x}Co_{0.05}In_xO$ the saturation magnetization increased and a maximum saturation magnetization of ~ 0.8 emu/g was obtained for $x = 0.07$ in $Zn_{0.95-x}Co_{0.05}In_xO$. The coercivity also increased from 50 Oe for $x = 0.01$ to 520 Oe for $x = 0.07$. The hysteresis in magnetization plots of In doped samples clearly indicate that the ferromagnetism in $Zn_{0.95-x}Co_{0.05}A_xO$ is not due to any superparamagnetic clusters. Further, the systematic increase in the magnetization with In concentration can be directly correlated to the increased carriers or defects introduced in the samples.

17.4.2 Al Doped $Zn_{0.95}Co_{0.05}O$ Nanoparticles

Similar to In, Al doping in ZnO can alter the carrier concentration. It should be noted that Al doped ZnO thin film is one of the competing transparent conducting oxide electrodes used in photovoltaic and optoelectronic applications [98]. In general the solubility of Al in ZnO is low (≤ 3 at.%) [99–102]. In our study the

samples prepared by sol–gel route followed by pyrolysis show an increased solubility up to 7 at.%. Samples prepared with Al concentration $x \leq 0.07$ are homogeneous and monophasic. Above $x = 0.07$ secondary phases including Al_2O_3 and $ZnAl_2O_4$ were observed. Since our interest was to understand the Al doping effect on the magnetic property, we will focus on the observed magnetic properties of $Zn_{0.95-x}Co_{0.05}Al_xO$ ($x = 0$–0.1). Up to $x = 0.02$ the change in the magnetization is insignificant although the diamagnetic M–H trace for $Zn_{0.95}Co_{0.05}O$ changes to a ferromagnetic S-shaped trace for $Zn_{0.93}Co_{0.05}Al_{0.02}O$. The magnetization is around 0.003 emu/g for $x = 0.02$ sample with no significant hysteresis. As x increases from 0.02 to 0.07, a systematic increase in the magnetization from 0.003 emu/g for $x = 0.02$ to 1.84 emu/g for $x = 0.07$ of Al doping is seen (Fig. 17.6b). The coercivity also increases to $\sim$500 Oe for $x = 0.07$ Al doping. This clearly shows that the ferromagnetism is not due to any superparamagnetic clusters or nanoparticles. The magnetization decreased to almost zero with further increase in Al concentration, i.e., above $x = 0.07$. This is coincident with the considerable phase segregation inferred from the XRD and TEM studies. It has been observed that the ferromagnetic hysteresis loop observed in $Zn_{0.88}Co_{0.05}Al_{0.07}O$ annealed at 600 °C disappears on annealing at 800 °C. Therefore, we believe the ferromagnetism is not due to secondary phase such as $Zn_{1-x}Co_xAl_2O_4$ identified from XRD analysis. The solubility limit of Al in $Zn_{0.95}Co_{0.05}O$ is of about 3 at.% and, beyond that, segregation of Al_2O_3 phase has been reported earlier [99–101]. Comparison of magnetic behavior of the Al doped samples with that of In doping in $Zn_{0.95}Co_{0.05}O$ suggests a commonality in the origin of ferromagnetism. A systematic increase in saturation magnetization in M–H curves up to $x = 0.07$ is attributed to the increasing amount of Al dissolved in the $Zn_{0.95}Co_{0.05}O$. The concentration dependence shows that below $x = 0.02$ of Al doping in $Zn_{0.95}Co_{0.05}O$ does not induce ferromagnetism as the carriers introduced may not be sufficient to mediate strong ferromagnetism. Whereas above $x = 0.02$ of Al doping, significant increase in the carrier concentration increases the magnetization. However, above $x = 0.07$ of Al doping, the ferromagnetism suddenly vanishes due to the large fraction of Al getting phase segregated into non-magnetic phase. Therefore, the Al doping does effectively contribute to the charge carriers leading to the magnetization behavior of $Zn_{0.95}Co_{0.05}O$.

17.4.3 Ga Doped $Zn_{0.95}Co_{0.05}O$ Nanoparticles

Ga doping in ZnO is also another possible dopant to modulate the carrier concentration and therefore tune the magnetic properties. Studies on the polycrystalline bulk [102] and thin films [103] have been reported at low doping levels. We have studied the structural and magnetic properties of $Zn_{0.95-x}Co_{0.05}Ga_xO$ ($x = 0$–0.05) prepared by pyrolytic reaction of the sol-gels [104]. The samples are monophase with wurtzite structure. Ga doping decreases the lattice parameters '*a*' and '*c*' due to the smaller ionic radii of Ga^{3+} (0.47 Å) compared to Zn^{2+} in

tetrahedral coordination for x up to 0.03. Above this the cell parameters show an increasing trend possibly due to the limit in the solubility of Ga in ZnO. However, no secondary phases were discerned from XRD, SAED, and high resolution TEM studies [104]. Similar to our earlier observations on the magnetic properties of In and Al doping in $Zn_{0.95}Co_{0.05}O$ samples, increasing the Ga concentration (from 0 to 5 at.%) showed a systematic increase in the magnetization and coercivity values (Fig. 17.6c). A maximum in the magnetization of 0.27 emu/g is observed for $x = 0.03$ before showing the decreasing trend in the magnetization with further increase in Ga concentration.

Interestingly, we observe different values of maximum saturation magnetization that can be achieved in $Zn_{0.95}Co_{0.05}O$ by doping In, Al, and Ga (Fig. 17.6d). Such differences cannot be due to secondary phases as our detailed analysis on the structural and magnetic properties on all the three different set of samples prompt to the possible role played by these dopants to create the carriers. This is also supported by the absence of ferromagnetism in $Zn_{0.95}Co_{0.05}O$ sample. Since In, Ga, and Al have different levels of solubility, the amount of secondary phases that can result locally in the form of clusters may vary. Further, it is important to note that the contribution to magnetization values need not necessarily arise from all the Co-atoms in the samples. This is more prominently observed in the case of Ga where the M–H loops show linear increase in the magnetization at higher fields indicating a major fraction of Co^{2+} in paramagnetic state. In addition, the compensation of the charge carriers by the creation defects can also influence to some extent the effective charge carriers available for the interaction. Considering the high level of inconsistencies reported in many oxides [82], systematic increase in the magnetization with the increase in charge carrier producing dopants shows that carrier-mediated interaction plays a major role in establishing the ferromagnetism in these oxides. From these studies Al doping is very promising as a large magnetization of $\sim$2 emu/g was observed. Indium doping resulted in magnetization $\sim$0.8 emu/g, whereas Ga doping only give a maximum magnetization of $\sim$0.3 emu/g. We believe that these compounds prepared under appropriate conditions in proper device structures can be useful for several spintronics applications.

17.5 Effect of Surfactants on the Properties of TM Doped ZnO

Many of the intriguing magnetic properties in TM doped oxides are shown to arise from the influence of various defect states including point, extended, and surface defects [82, 105–107]. The ferromagnetism in many of the nanostructured materials are believed to be influenced significantly by the surface and interface defects [108]. Therefore, it is necessary to understand the specific role the surface plays on deciding the magnetic properties of TM doped ZnO, especially in nanostructured form. We carried out surface modification in the bulk and nanoparticles of Mn and Co doped ZnO. Mn (2.2 at.%) and Co (5 at.%) doping are presented as a case

study here, since the magnetization in these samples is the highest observed in comparison to the different concentrations we have studied [58, 59, 109]. The nanoparticle and bulk samples were prepared by pyrolytic reaction and solid-state reaction respectively. The details of the synthesis methods and the surfactant treatment are given in Sect. 17.2.1. We also added small amounts of Li^+ in these samples to see the effect of additional carriers that might get introduced in the system. Figure 17.7 shows the HRTEM images of the surface after surfactant treatment of typical nanoparticles of $Zn_{0.978}Mn_{0.022}O$ and $Zn_{0.85}Co_{0.05}Li_{0.10}O$. The single crystalline, structural defect-free particles are coated with $\sim$1 nm thick uniform layers of surfactant. Figure 17.8a shows the M–H loop for $Zn_{0.978}Mn_{0.022}O$ bulk samples which increase five times on treating with AOT. It is to be noted that pure ZnO treated in a similar way shows only diamagnetic nature in M–H plots. The same sample treated with a different surfactant, pluronic 123 instead of AOT, also showed three times increase in the magnetization. For nanoparticles also we observed substantial increase in magnetization. For Li co-doped system, $Zn_{0.96}Mn_{0.03}Li_{0.01}O$, the AOT treatment yields much larger magnetization of $\sim$0.15 emu/g. Similar studies of surface treatment with AOT on $Zn_{0.95}Co_{0.05}O$ did not show much change in the magnetization, although more linear M–H plot for uncoated $Zn_{0.95}Co_{0.05}O$ tend to show some S-shaped curve after AOT surface treatment (see inset of Fig. 17.8c). However, drastic increase in magnetization (fivefold) is observed when $Zn_{0.85}Co_{0.05}Li_{0.10}O$ samples are treated with AOT surfactants. The pluronic 123 surface treatment also showed three times increase in magnetization of $Zn_{0.85}Co_{0.05}Li_{0.10}O$.

The increase in the magnetization of TM doped ZnO on treating with surfactant is surprising and is difficult to explain. We believe that some alteration in the defects at the interface between nanocrystals in addition to the homogenization of dopant ions in the host matrix can account for the enhancement in the magnetization. Similar unambiguous conclusion of interfacial or grain-boundary defects in activating the ferromagnetism at room temperature on broad spectrum of TM doped oxides including cobalt doped ZnO has been shown by Gamelin's group

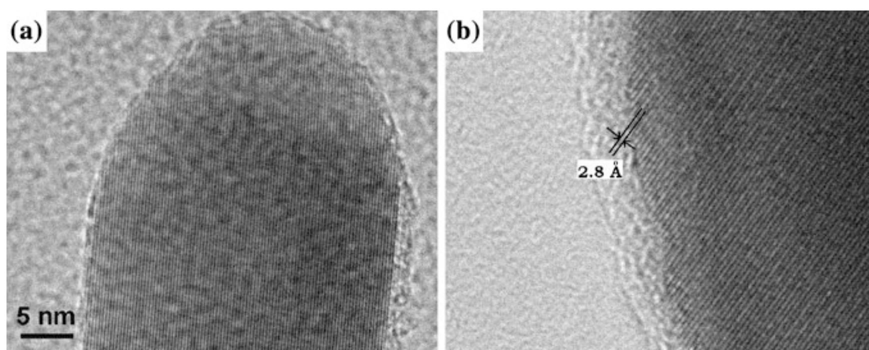

Fig. 17.7 High resolution TEM images of **a** nanoparticle $Zn_{0.85}Co_{0.05}$ $Li_{0.10}O$, **b** bulk $Zn_{0.978}Mn_{0.022}O$ after treating with AOT surfactant

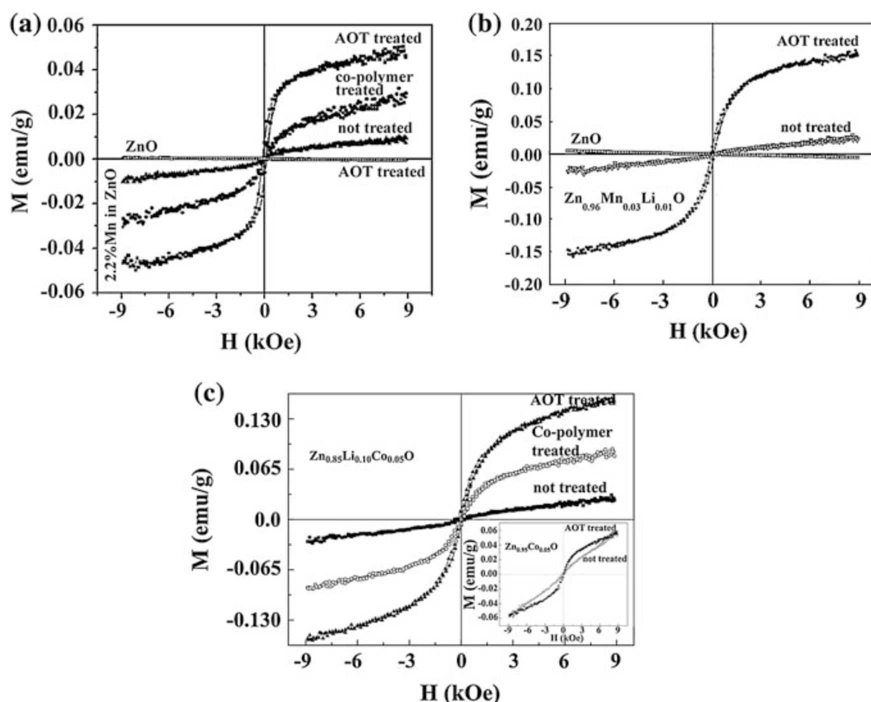

Fig. 17.8 Magnetization versus magnetic field plots at 300 K of **a** $Zn_{0.978}Mn_{0.022}O$, **b** $Zn_{0.96}Mn_{0.03}Li_{0.01}O$, **c** $Zn_{0.85}Co_{0.05}Li_{0.10}O$ with and without AOT (co-polymer) treatment

[35, 38, 91, 110]. Studies on carbon-encapsulated Co doped ZnO also showed ferromagnetism at 300 K [111]. The treatment of particles with surfactant can homogenize the magnetic ions as the surfactants reduce the interfacial tension between the host and the dopant [112, 113]. AOT is sulfur containing ionic surfactant with a thiol group at the end. The reports of ferromagnetism in thiol-capped gold nanoparticles [114, 115] and coating ZnO nanoparticles with thiol [116] also suggest that the enhanced magnetic moment observed in $Zn_{0.95}Co_{0.05}O$ and $Zn_{0.85}Co_{0.05}$ $Li_{0.10}O$ on treating with AOT could be due to M–S bond formation that may take place in addition to the homogenization of the samples. Further, higher magnetization observed in Li co-doped samples indicates that presence of carriers in addition to these may favor the ferromagnetic state.

17.6 Role of Defects in Pure and Mg Doped ZnO

As evidenced from several studies the control on the magnetic and optical properties in ZnO is highly dependent on the rich details of intrinsic and extrinsic defects. The optical properties of ZnO are shown to depend on the point defects. The green

emission peak, which can be controlled by oxidation or reduction, has been attributed to a variety of impurities and defects in ZnO. Several luminescence centers such as oxygen vacancies located below the conduction band edge, zinc interstitials located at 2.5 eV below the conduction band, and various other native defects have been reported in the ZnO [117–119]. The photoluminescence emission in ZnO nanoislands has been attributed to zinc vacancy complex defect [120]. Although oxygen vacancies form readily in ZnO, it has been proposed that O vacancies are unlikely cause for the *n*-type conductivity in ZnO [121, 122]. To address such variations and also to stabilize the defects in ZnO we studied the photoluminescence properties of ZnO and $Zn_{0.95}Mg_{0.05}O$ nanorods prepared by solvothermal method [65, 123]. To understand the origin of green emission we further manipulated the defects in these samples by subjecting these nanorod samples to treatments, with H_2 at 300 and 673 K, under vacuum and in air at 400 °C.

On heat-treating the samples under different ambient we also observed that the nanorod shape of ZnO and $Zn_{0.95}Mg_{0.05}O$ changes significantly (Figs. 17.9, 17.10). The air annealing does not change the particle morphology. However, hydrogenation and vacuum annealing breaks the nanorods into fine particles. The TEM images show that these broken fine particles remain connected (in spite of the ultrasonication done to disperse the particles in a solution during the TEM sample preparation) along the long axis. At high temperatures they also coalesce and sinter forming spherical particles. The emission spectra of treated samples (Figs. 17.9, 17.10) show that after hydrogen treatment and vacuum annealing treatment the emission intensity decreases significantly. On air annealing the emission spectra does not get affected much. From this we infer that the zinc vacancies are responsible for the green emission. The presence of Zn vacancies in ZnO nanoparticles is reported by McCluskey [121]. If oxygen vacancies were reasoned for the green emission peak the relative intensity should have improved. In Mg doped ZnO nanorod, we observed that the green emission intensity does not get modified significantly by hydrogen or air annealing treatment. This also points to the fact that presence of Mg stabilizes the Zn vacancies in ZnO, which can be understood due to the high ionic nature of Mg–O bonds compared to Zn–O bonds and associated increase in lattice energy [123]. Our conclusion is also supported by McCluskey and Jokela's report [121] that the green-emission need not necessary come from the oxygen vacancy. In addition to green emission, red and orange emission has been shown by Kwok et al. [124]. These studies show that modifying the emission characteristics of ZnO can be done by changing the concentration and type of defects. Such tunable optical property in ZnO will lead to the exploration of functional properties.

17.7 Theoretical Studies on Co Doped ZnO

The theoretical analyses of $Zn_{1-x-y}M_xLi_yO$ (with M = Co or Ni) and $Zn_{0.94-y}Co_{0.06}B_yO$ (with B = Ga or In) are based on atomistic first-principles modeling, using the Kohn–Sham method within the density functional theory (DFT).

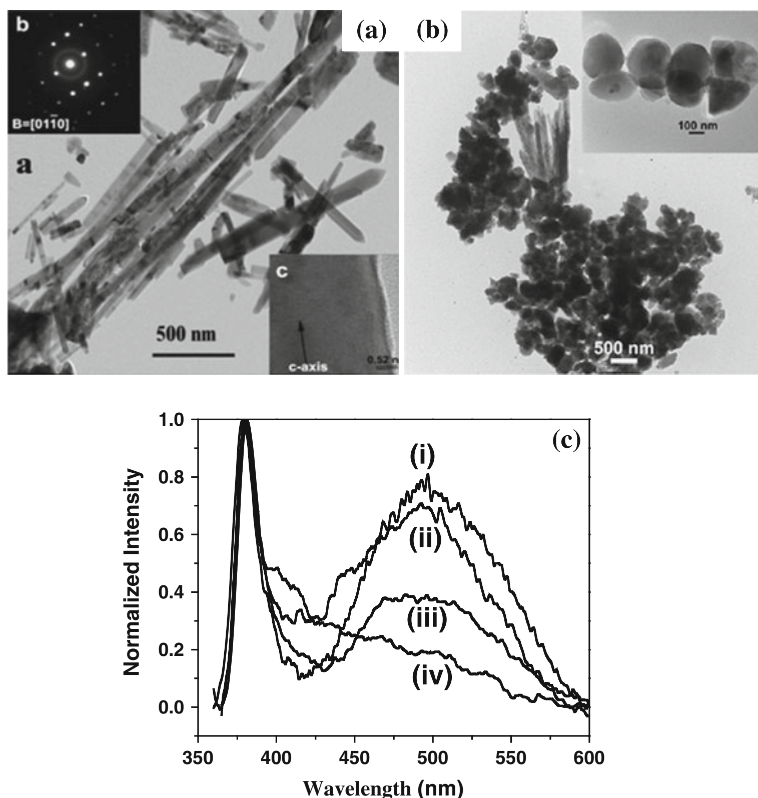

Fig. 17.9 TEM micrographs of as synthesized ZnO nanorod (**a**) and hydrogenated nanorod (**b**). **c** Shows the room temperature PL spectra of ZnO nanorods treated under different annealing conditions. In **c** (*i*)–(*iv*) represent the following conditions: (*i*) as synthesized ZnO nanorod, (*ii*) after annealing at 400 °C/2 h in air of (*i*), (*iii*) vacuum annealed at 400 °C/2 h, (*iv*) hydrogenated at room temperature. Insets: (**a**) selected area diffraction (top right) and HRTEM (bottom right) of ZnO nanorod; (**b**) high magnification image of hydrogenated ZnO nanorod

17.7.1 Computational Details

The $Zn_{1-x-y}M_xB_yO$ compounds are modeled by a supercell wurtzite-like crystalline bulk structures. Study on these bulk systems is justified by the primarily bulk-like property of the relatively large nanostructures. The crystalline, electronic, and magnetic properties are calculated by the projector augmented wave (PAW) method [125, 126] with the local spin-density approximation (LSDA) in the DFT. This LDA exchange-correlation functional is corrected by an on-site Coulomb potential within the rotationally invariant LSDA + U approach [127] with the effective Coulomb interaction parameters U_d(Zn) = 6 eV and U_d(Co; Ni; Ga; In) = 4 eV. The correction of the Zn *d*-states within LDA + U has been found to significantly improve the Zn $d - O\ p$ valence-band hybridization,

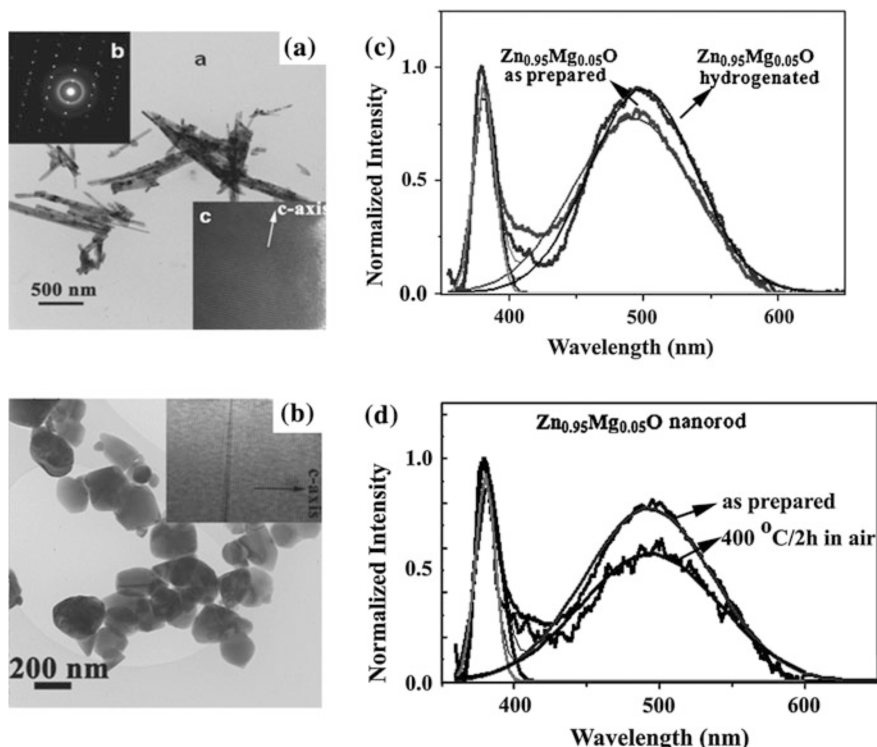

Fig. 17.10 TEM micrographs of as synthesized $Zn_{0.95}Mg_{0.05}O$ nanorod (**A**) and hydrogenated nanorod (**B**).**C** and **d** shows room temperature PL spectra of $Zn_{0.95}Mg_{0.05}O$ nanorods treated in air and hydrogenated conditions. **A** shows the SAED and HRTEM of the nanorods. **B** shows the HRTEM image of a particle

especially the Zn d – O p hybridization at 7 eV below the valence band maximum [128]. The correction of the Ni and Co d-states follow earlier studies on similar compounds [129–131], and it has been shown that this on-site Coulomb potential is crucial to accurately describe ground-state magnetic properties of d-state TM binaries [132].

The supercell is constructed by 3 × 3 × 2 wurtzite structures consisting of 72 atoms (Fig. 17.11). The variation of the doping concentrations in $Zn_{1-x-y}M_xB_yO$ is obtained by $x = 0$, 1/32, and 2/32 (thus ~0, 3, and 6 at.% M = Ni or Co) and $y = 0$, 1/32, 2/32, and 3/32 (~0, 3, 6, and 9 at.% B = Ga or In, respectively). Experimental lattice constants are used, and ions are fully relaxed by means of both the conjugate gradient algorithm and the quasi-Newton algorithm, and the convergence is 0.1 meV for the total energy of the unit cell and 8 meV/Å for the forces of each atom. The energy cutoff is 400 eV. The total energy, the local charge distribution, the spin-dependent density-of-states (DOS) as well as the magnetic moment are obtained from a tetrahedron integration with Blöchl corrections using a Γ-centered 6 × 6 × 6 Monkhorst–Pack type **k**-mesh in the

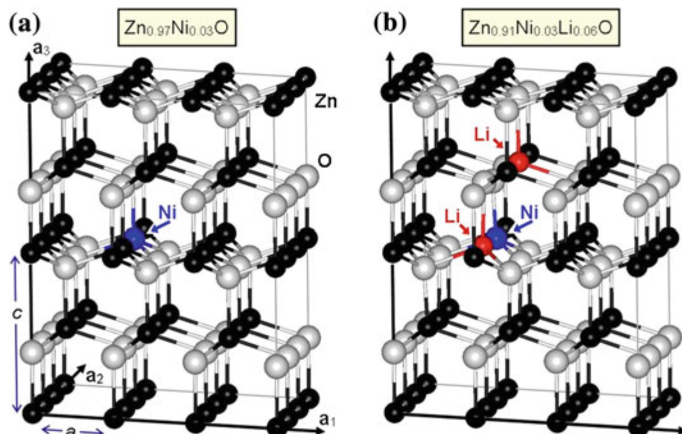

Fig. 17.11 Crystal structure of **a** $Zn_{0.97}Ni_{0.03}O$ and **b** $Zn_{0.91}Ni_{0.03}Li_{0.06}O$ demonstrating the relaxation effects due to the presence of Li dopants. Li-on-Zn is energetically favored by a location close to the magnetic Ni defect. Similar result is found for $Zn_{0.91}Co_{0.03}Li_{0.06}O$ [61]

irreducible Brillouin zone. The atomic muffin-tin radii are 1.27, 0.82, 1.28, 1.30, 1.36, 1.22, and 1.68 Å for Zn, O, Ni, Co, Li, Ga, and In respectively.

17.7.2 Li Doped $Zn_{0.94-y-x}M_xO$ with M = Co or Ni

The calculations of total energies of Li-free $Zn_{0.94}Ni_{0.06}O$ (6 at.% Ni) supports that the compound is paramagnetic with a local magnetic moment at the Ni atoms of $\sim 1.6\ \mu_B$/Ni and zero total magnetic moment for the antiferromagnetic configuration. For the ferromagnetic configuration the crystal cell with two Ni atoms (each $\sim 1.6\ \mu_B$/Ni) has a total magnetic moment of 4.0 μ_B. The four neighboring O atoms to the Ni dopants are induced by at most only $\sim 0.06\ \mu_B$/oxygen on the p-like states. The total energy difference between ferro- and antiferromagnetic configurations is very small: $\Delta E = E_{FM}–E_{AFM} \approx$ 13 meV/cell. This small energy difference suggests that $Zn_{0.94}Ni_{0.06}O$ should be regarded as ZnO with a magnetic dopant rather than a material with magnetic phase. Thereby, additional doping and/or structural reconstruction can relatively easily change the magnetic properties. This discussion holds also for Li-free $Zn_{0.94}Co_{0.06}O$ (6 at.% Co) for which $\Delta E = E_{FM}–E_{AFM} \approx$ 16 meV/cell and the local magnetic moment of about 2.7 μ_B/Co.

Ni and Co have both similar covalent radii 1.24 and 1.26 Å, respectively, compared with Zn with 1.22 Å. Therefore, it is expected that Ni and Co doping does not reconstruct the ZnO lattice. Ni-on-Zn distorts the ZnO host only moderately. Additional co-doping by Li will also only moderately affect the crystalline structure since covalent radius of Li is 1.28 Å. However, Li-on-Zn dopants will directly affect the electronic structure since group-I Li substituting group-II Zn

atoms implies acceptor-type defects. The Pauling electro-negativity of Li is ~0.98 and the corresponding data for Zn is ~1.65. Thereby, charge redistribution near Li-on-Zn can affect the crystalline relaxation near the dopants. Moreover, the acceptor-type Li-on-Zn defect can also depopulate the 3*d* state of Ni (with configuration [Ar]–$4s^2 3d^8$) and Co (configuration [Ar]–$4s^2 3d^7$). This can thereby impact the magnetic moment of the magnetic *M* atoms.

From the crystalline relaxation of $Zn_{0.97}Ni_{0.03}O$, we find that the Ni–O bond length of δ(Ni–O) ≈ 1.99 Å is similar to the bond length of δ(Zn–O) = 1.98 Å (see also Fig. 17.11). The total magnetic moment is 2.0 μ_B. Additional co-doping by Li-on-Zn (e.g., 3 at.% Li and 3 at.% Ni) impacts both the crystal relaxation as well as the magnetic properties. The calculated total energy reveals that Li prefers a Zn site next to the Ni-on-Zn atom, and the Li–O bond lengths are relatively large δ(Li–O) ≈ 2.03–2.32 Å. The total energy E_t is ~0.2 eV/Li lower for the system where Li is located close to Ni compared to being located further away from Ni. Moreover, Li induces a somewhat larger magnetic moment of Ni. In Li-free $Zn_{0.97}Ni_{0.03}O$, the magnetic Ni has a distinct local magnetic moment of ~1.7 μ_B/Ni. In Li co-doped $Zn_{0.94}Ni_{0.03}Li_{0.03}O$, the local magnetic moment of Ni increases to 1.9 μ_B. In addition, there is magnetic moment of the O by (0.16–0.23) μ_B/oxygen. This additional magnetization occurs on the four O 2*p*-like states next to the Ni atom through hybridization with the Ni 3*d*-like states. The total magnetic moment increases thereby by 1.0 μ_B to a value of 3.0 μ_B. The total energy calculations also reveal that further co-doping by Li (i.e., 6, and 9 at.% Li) preferably will form Li cluster around the Ni dopant, but the energy cost for Li to be away from Ni–O–Li cluster is small (<50 meV/Li).

The topmost and partially filled Ni 3*d* states are well above the host ZnO valence-band maximum; see DOS in Fig. 17.12. Li-on-Zn dopants act as an acceptor and decrease the valence electrons. For 3 at.% Li (that is, one Li per Ni atom), the acceptor will empty the Ni 3*d*-states and increases the magnetization by 1.0 μ_B according to Hund's rule. The same effect occurs by varying the valence population by ionization instead of Li incorporation; see cross marks in Fig. 17.13. With completely filled or empty Ni 3*d*-bands, the filled 3*d* states become more localized well below the ZnO host topmost bands. Further, Li-on-Zn incorporation (6 and 9 at.% Li) will however mainly affect the ZnO host rather than the population of the Ni 3*d*-bands. The Fermi level will now decrease below the ZnO valence-band maximum and, as a consequence, the empty host states will start to screen the Ni atoms and thus the total magnetization decreases. Thus, the theoretical analyses can explain the experimental findings that for low Li-on-Zn concentrations the total magnetization is increased by depopulation of the Ni 3*d*-states in the ZnO bandgap region, whereas for higher Li concentrations the total magnetization is decreased due to the depopulation of ZnO host states that screens the magnetic coupling.

The theoretical modeling of Co–Li co-doped $Zn_{1-x-y}Co_xLi_yO$ reveals qualitatively similar material physics as Ni–Li co-doped $Zn_{1-x-y}Ni_xLi_yO$. Crystal relaxation of $Zn_{0.97}Co_{0.03}O$ demonstrates that Co energetically prefers Zn sites forming substitutional Co-on-Zn dopants. The Co–O bond length of δ(Co–

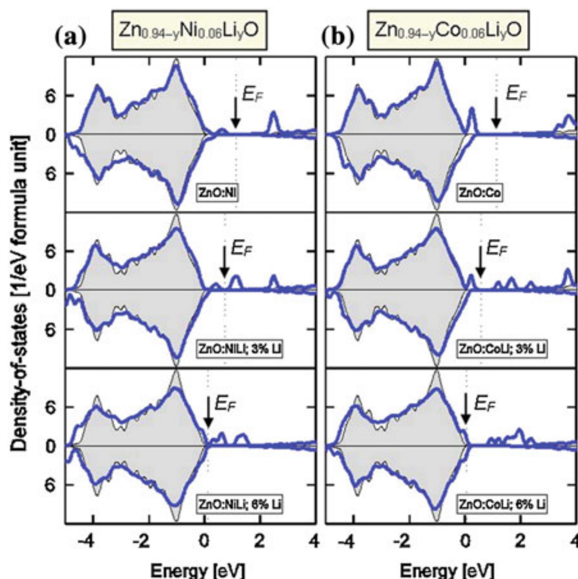

Fig. 17.12 Spin-dependent valence DOS of ferromagnetic configurations of **a** $Zn_{0.94-y}Ni_{0.06}Li_yO$ and **b** $Zn_{0.94-y}Co_{0.06}Li_yO$. The energy is referred to the valence-band maximum of ZnO (*gray area*) and *vertical dotted lines* indicate the Fermi level. The main difference in DOS between the Ni and Co containing compounds originates from the energy location and population of the Ni (with $4s^23d^8$) and Co ($4s^23d^7$) valence states. DOS of antiferromagnetic configurations [62] show qualitatively similar results, though spin-dependent differences in the defect states at the valence-band maximum

O) = 1.91 Å to the four neighboring O atoms in the tetrahedral coordination. This bond length is smaller than δ(Zn–O) = 1.98 Å of the host ZnO compound. Thus, there is a strong local relaxation effect around the co-dopant in $Zn_{0.97}Co_{0.03}O$. Additional co-doping by Li-on-Zn (e.g., 3 at.% Li and 3 at.% Co) impacts both the crystal relaxation as well as the magnetic properties. Li doping compensates the Co–O bond by forming Li-on-Zn close to the Co-on-Zn dopant, partly due to δ(Li–O) = 2.01 Å in $Zn_{0.97}Li_{0.03}O$ which is somewhat larger than the Zn–O bond length. Moreover, in $Zn_{0.94}Co_{0.03}Li_{0.03}O$, the co-dopant Li is energetically favored to form Li-on-Zn close to the Co-on-Zn dopant. Also, in $Zn_{0.91}Co_{0.03}Li_{0.06}O$ with high Li concentrations, Li-on-Zn close to Co-on-Zn is favored, although an Li-on-Zn dopant can easily be located away from Co (with only ~0.3 eV higher total energy). The relaxation of the neighboring O atoms of Co is much stronger in $Zn_{0.91}Co_{0.03}Li_{0.06}O$ compared with $Zn_{0.97}Co_{0.03}O$, demonstrating stability in the Co–O bond in the Co–Li co-doped compounds. This can thus explain the improved aspect ratio and morphology in the Li rich nanoparticles.

The calculated spin-dependent DOS of ferromagnetic $Zn_{0.97}Co_{0.03}O$ reveals that (Fig. 17.12) Co forms the empty and partially 3*d* states above the host ZnO Fermi energy. This is similar to Ni $3d^8$ in $Zn_{0.97}Ni_{0.03}O$, but even though Co $3d^7$ has less

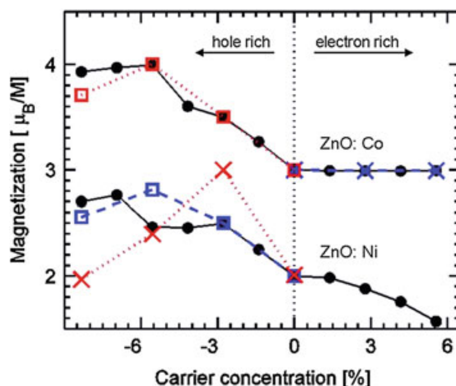

Fig. 17.13 Magnetic moment per M atom of $Zn_{0.94}M_{0.06}O$ (M = Co and Ni) as function of free carrier doping concentration (*black solid circles*). Positive and negative values of the concentration represent electron and hole doping, respectively. The magnetic M atoms are in the ferromagnetic configuration. *Red square* marks show Li-on-Zn acceptor doping in $Zn_{0.94-y}Co_{0.06}Li_yO$ ($y \approx$ 0, 3, and 6 %). The corresponding result for Ga-on-Zn in $Zn_{0.94-y}Co_{0.06}Ga_yO$ ($y \approx$ 0, 3, and 6 %) indicates no impact on the magnetic moment for donor doping (*blue crosses*). *Blue square* marks $Zn_{0.94-y}Ni_{0.06}Li_yO$ show similar trends as the Co-based alloys, however, both $Zn_{0.94-y}Ni_{0.06}Li_yO$ (*blue squares*) and especially the moderately Ni doped alloy $Zn_{0.97-y}Ni_{0.03}Li_yO$ (*red crosses*) demonstrates that magnetic moment decreases for high Li doping as a consequence of band filling of host states

valence electrons, the Co-based compound is more filled 3d states above the ZnO host valence-band maximum in $Zn_{0.97}Co_{0.03}O$. According to Fig. 17.13 and the discussion above for Li–Ni co-doping, more filled 3d states above the valence-band maximum imply that the material can be co-doped with Li-on-Zn to a higher acceptor concentration before the host valence bands start to be depopulated. Thus, Co-based $Zn_{1-y}Co_{0.03}Li_yO$ will retain magnetic character to a higher Li concentration compared with corresponding Ni-based $Zn_{1-y}Ni_{0.03}Li_yO$.

The magnetic moment in $Zn_{0.91}Co_{0.03}Li_{0.03}O$ is 3.0 μ_B per Co-atom as expected. Additional Li doping changes the DOS of the topmost 3d states (Fig. 17.12). These states are split by the Li dopants and only the lowest band is partially filled. The origin to this is twofold: first, lower crystal symmetry and relaxation effects enhance a split of the bands. Second, both Co 3d and the surrounding O 2p compensate the missing Li-on-Zn's contribution in the cation–anion bond. Thereby, Co induces a magnetic moment of the O p-like states of the four neighboring anions. This charge-transfer-induced magnetic moment is $\sim$0.3 μ_B per O atom, whereas the magnetic moment of Co decreases slightly to 2.9 μ_B. Thus, an enhanced ferromagnetism in the Co and Li co-doped ZnO can be explained by magnetization of the surrounding O atoms. Heavier Li-doping, however, will lower the magnetic moment, as the host ZnO valence bands start to be depopulated and thereby screen the magnetic Co-atom (Fig. 17.13).

The theoretical analysis points towards a probable scenario where substitutional Li-on-Zn stabilizes the strained M–O bond in $Zn_{1-x-y}M_xLi_yO$ (M = Co or Ni) and

stabilize thereby the morphology of the material. The magnetization of $Zn_{1-x}M_xO$ is increased by additional co-doping with Li as a consequence of depopulation of M 3d states and a charge-induced magnetic moment of neighboring O atoms. Further Li-doping, however, implies a too strong depopulation of the ZnO host states, and this decreases the local magnetic moment of the magnetic M atom.

17.7.3 Ga or In Doped $Zn_{0.94-x}Co_{0.06}O$

The analysis of $Zn_{0.94-y}Co_{0.06}B_yO$ (doped with $B =$ Ga or In) follow the same methodology as in the previous section for Li doping. The difference in Ga/In doping with respect to Li doping is primarily related to the valence configurations of the dopants. Whereas Li-on-Zn is an acceptor-like dopant, both Ga and In are group-III elements and the corresponding Ga-on-Zn and In-on-Zn dopants are donor like. Moreover, Ga and In are isovalent with similar electron affinities ($\sim$30 kJ/mol) and similar electron negativities ($\sim$1.80), and the main difference between incorporating Ga and In in $Zn_{0.94}Co_{0.06}O$ is therefore related to the size of the dopants. Ga with a covalent radius of $\sim$1.22 Å has the same size as Zn (also $\sim$1.22 Å) and Ga substituting Zn has thus minor impact on the crystalline structure, whereas the larger In atom ($\sim$1.42 Å) causes larger structural relaxation effects that may easily induce additional defects.

Cobalt in $Zn_{0.94}Co_{0.06}O$ has a relatively moderate local magnetic moment (2.7 μ_B/Co-atom), and the total energy difference between the ferro- and antiferromagnetic configurations is small ($\Delta E \approx$ 16 meV/cell). The incorporation of Ga-on-Zn donors in $Zn_{0.94-y}Co_{0.06}Ga_yO$ suppresses the antiferromagnetic coupling slightly, but still the energy difference between the two magnetic phases is small: $\Delta E \approx$ 10 meV/cell. For both with the ferro- and antiferromagnetic configurations, the local magnetic moment remains $\sim$2.7 μ_B/Co-atom independent of Ga concentration. Moreover, there is only a small difference between the DOS of the two magnetic configurations; see Fig. 17.14. These small differences between the two configurations suggest that additional doping and/or structural reconstruction can relatively easily change the magnetic phase.

The main effect of the Ga-on-Zn doping is an additional band filling of free carriers in the conduction band, and thereby the Fermi level (dotted lines in Fig. 17.14) is energetically increased. Similar results were found for $Zn_{0.94-y}Co_{0.06}In_yO$ with In-on-Zn donors [62]. This free electron concentration does not mediate additional ferromagnetic interaction, instead it is expected that localized holes are responsible for the magnetic phase in doped ZnO. This is demonstrated in Fig. 17.13 where the total magnetic moment is shown for $Zn_{0.94-y}Co_{0.06}Ga_yO$ as well as for $Zn_{0.94}Co_{0.06}O$ as function of free electron concentration, that is, with additional electrons in the material. Only with additional holes the magnetic moment increases. Since Ga-on-Zn is a donor, ferromagnetic coupling will not be enhanced by the Ga-on-Zn donors, at least not in uncompensated bulk $Zn_{0.94-y}Co_{0.06}Ga_yO$ materials. This is demonstrated in Fig. 17.13 where Ga doping does

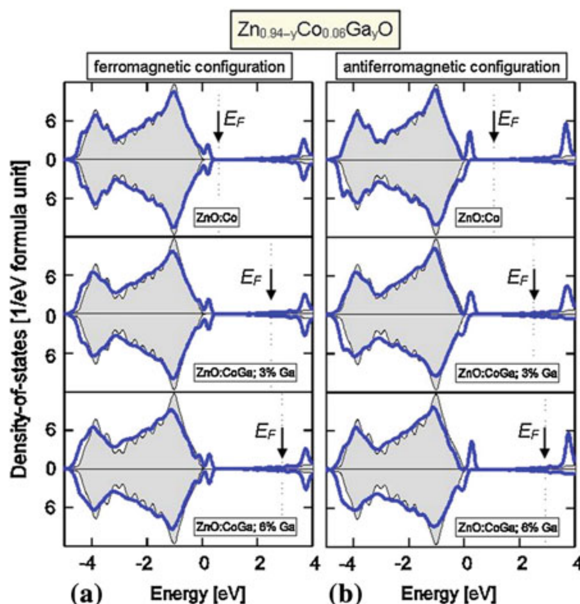

Fig. 17.14 Spin-resolved density-of-states of $Zn_{0.94y}Co_{0.06}Ga_yO$ for **a** antiferromagnetic and **b** ferromagnetic configuration of the two Co-atoms. The energies are referred to the valence-band maximum of intrinsic ZnO (*gray area*) and *vertical dotted lines* indicate the Fermi level. Comparable results were found for $Zn_{0.94y}Co_{0.06}In_yO$ [62]

not increase the total magnetic moment. Instead, observed measured ferromagnetic phase generated by Ga co-doping (or In co-doping) of $Zn_{0.94}Co_{0.06}O$ should be an effect from a change in crystalline structure of the nanoparticles and/or the presence of induced acceptor-type defects.

17.8 Conclusion

We have summarized a brief overview of the morphology control of ZnO by metal dopants and how the dopant and defect modify the magnetic and optical properties of ZnO system. Li dopant stabilizes the nanorod shape which is otherwise not favored by the Co and Ni doping. Li addition also improves the magnetic properties of Co and Ni doped ZnO system. The first-principles atomistic modeling of bulk $Zn_{1-x-y}M_xLi_yO$ (with M = Co or Ni) demonstrate two effects due to the presence of Li. Li-on-Zn act as acceptors and depopulating the M 3d minority spin-states, thereby local magnetic moment is increased. Moreover, since Li-on-Zn prefers to be closer to the M atoms, Li doping also impacts the local crystalline structure and stabilizes nanorods with high aspect nanostructures. The observed room temperature ferromagnetism in Li co-doped $Zn_{1-x}M_xO$ nanorods can

therefore be explained by the better rod morphology in combination with locally ionizing the magnetic M atoms.

Further, doping aliovalent cations such as In, Al, and Ga, in $Zn_{0.95}Co_{0.05}O$ nanoparticles show increase in the magnetization up to a certain concentration. Typically above the miscibility point drastic decrease in magnetization is observed. The theoretical analyses of bulk $Zn_{0.94-y}Co_{0.06}B_yO$ (with B = Ga or In) reveal that Ga/In-on-Zn act as donors and generate free carriers in the conduction band, and thereby energetically increase the Fermi level. The total energy calculations of Ga- or In doped bulk $Zn_{0.94}Co_{0.06}O$ indicate a local magnetic coupling with the paramagnetic phase for all doping concentrations. This suggests that the observed ferromagnetic phase in these materials should originate from the crystalline structure of the nanoparticles and/or from the presence of compensating acceptor defects.

In addition to the dopants the surface modification by surfactant treatment and hydrogenation also significantly alters the magnetic properties. The surface treatment could alter the distribution of dopants and infuse surface defects which could enhance the magnetization. Hydriding the samples also brings in the ferromagnetic nature, although at high temperature magnetic metal clusters are unambiguously responsible for the ferromagnetic signal. Hydriding Mg doped ZnO also shows increased green emission which gets suppressed in ZnO. Zinc vacancies which are responsible for the green emission is stabilized in Mg doped ZnO. From these studies it is clear that the role of dopants, defects, and morphology of ZnO can be tailored to modify physical properties.

Acknowledgments C. Sudakar would like to thank Prof. R. Naik, Prof. V. M. Naik, and Prof. G. Lawes and members of their group at Wayne State University (WSU). The author would like to acknowledge the Jane and Frank Warchol Foundation and the Institute for Manufacturing Research at WSU for support to TEM works carried out at WSU. C. Persson is supported by the Swedish Energy Agency, and the Swedish Research Council, and he acknowledges access to high-performance computing resources at the HPC2N and NSC centers through SNIC/SNAC and Matter network.

References

1. U. Ozgur, Y.I. Alivov, C. Liu, A. Teke, M.A. Reshchikov, S. Dogan, V. Avrutin, S.J. Cho, H. Morkoc, J. Appl. Phys. **98**(4) (2005)
2. G.-C. Yi, C. Wang, W.I. Park, Semicond. Sci. Technol. **20**(4), S22 (2005)
3. S. Xu, Z. Wang, Nano Res. **4**(11), 1013–1098 (2011)
4. M.H. Huang, S. Mao, H. Feick, H. Yan, Y. Wu, H. Kind, E. Weber, R. Russo, P. Yang, Science **292**(5523), 1897–1899 (2001)
5. K. Govender, D.S. Boyle, P. O'Brien, D. Binks, D. West, D. Coleman, Adv. Mater. **14**(17), 1221–1224 (2002)
6. W.I. Park, G.C. Yi, Adv. Mater. **16**(1), 87–90 (2004)
7. W.Z. Wang, B.Q. Zeng, J. Yang, B. Poudel, J.Y. Huang, M.J. Naughton, Z.F. Ren, Adv. Mater. **18**(24), 3275–3278 (2006)

8. Y.W. Zhu, H.Z. Zhang, X.C. Sun, S.Q. Feng, J. Xu, Q. Zhao, B. Xiang, R.M. Wang, D.P. Yu, Appl. Phys. Lett. **83**(1), 144–146 (2003)
9. T.-Y. Wei, P.-H. Yeh, S.-Y. Lu, Z.L. Wang, J. Am. Chem. Soc. **131**(48), 17690–17695 (2009)
10. P.-H. Yeh, Z. Li, Z.L. Wang, Adv. Mater. **21**(48), 4975–4978 (2009)
11. C. Lévy-Clément, R. Tena-Zaera, M.A. Ryan, A. Katty, G. Hodes, Adv. Mater. **17**(12), 1512–1515 (2005)
12. B. Weintraub, Y. Wei, Z.L. Wang, Angew. Chem. Int. Ed. **48**(47), 8981–8985 (2009)
13. Y. Wei, C. Xu, S. Xu, C. Li, W. Wu, Z.L. Wang, Nano Lett. **10**(6), 2092–2096 (2010)
14. X. Wang, J. Song, J. Liu, Z.L. Wang, Science **316**(5821), 102–105 (2007)
15. Z.L. Wang, Adv. Funct. Mater. **18**(22), 3553–3567 (2008)
16. Z.L. Wang, Adv. Mater. **19**(6), 889–892 (2007)
17. Z.L. Wang, Mater. Today **10**(5), 20–28 (2007)
18. Z.L. Wang, J. Song, Science **312**(5771), 242–246 (2006)
19. O. Harnack, C. Pacholski, H. Weller, A. Yasuda, J.M. Wessels, Nano Lett. **3**(8), 1097–1101 (2003)
20. H. Kind, H. Yan, B. Messer, M. Law, P. Yang, Adv. Mater. **14**(2), 158–160 (2002)
21. H. Ohta, M. Kamiya, T. Kamiya, M. Hirano, H. Hosono, Thin Solid Films **445**(2), 317–321 (2003)
22. S.E. Ahn, J.S. Lee, H. Kim, S. Kim, B.H. Kang, K.H. Kim, G.T. Kim, Appl. Phys. Lett. **84**(24), 5022–5024 (2004)
23. K. Keem, H. Kim, G.-T. Kim, J.S. Lee, B. Min, K. Cho, M.-Y. Sung, S. Kim, Appl. Phys. Lett. **84**(22), 4376–4378 (2004)
24. Q. Wan, Q.H. Li, Y.J. Chen, T.H. Wang, X.L. He, X.G. Gao, J.P. Li, Appl. Phys. Lett. **84**(16), 3085–3087 (2004)
25. Q. Wan, Q.H. Li, Y.J. Chen, T.H. Wang, X.L. He, J.P. Li, C.L. Lin, Appl. Phys. Lett. **84**(18), 3654–3656 (2004)
26. Q.H. Li, Q. Wan, Y.X. Liang, T.H. Wang, Appl. Phys. Lett. **84**(22), 4556–4558 (2004)
27. M.S. Arnold, P. Avouris, Z.W. Pan, Z.L. Wang, J. Phys. Chem. B **107**(3), 659–663 (2002)
28. C.H. Liu, W.C. Yiu, F.C.K. Au, J.X. Ding, C.S. Lee, S.T. Lee, Appl. Phys. Lett. **83**(15), 3168–3170 (2003)
29. W.I. Park, G.-C. Yi, J.-W. Kim, S.-M. Park, Appl. Phys. Lett. **82**(24), 4358–4360 (2003)
30. Z.L. Wang, Mater. Today **7**(6), 26–33 (2004)
31. S. Ghosh, V. Sih, W.H. Lau, D.D. Awschalom, S.-Y. Bae, S. Wang, S. Vaidya, G. Chapline, Appl. Phys. Lett. **86**(23), 232507 (2005)
32. D.C. Look, Semicond. Sci. Technol. **20**(4), S55 (2005)
33. J. Wang, R. Martins, N.P. Barradas, E. Alves, T. Monteiro, M. Peres, E. Elamurugu, E. Fortunato, J. Nanosci. Nanotechnol. **9**(2), 813–816 (2009)
34. E. Senthil Kumar, J. Chatterjee, N. Rama, N. DasGupta, M.S.R. Rao, ACS. Appl. Mater. and Interfaces **3**(6), 1974–1979 (2011)
35. K.R. Kittilstved, N.S. Norberg, D.R. Gamelin, Phys. Rev. Lett. **94**(14), 147209 (2005)
36. N.S. Norberg, K.R. Kittilstved, J.E. Amonette, R.K. Kukkadapu, D.A. Schwartz, D.R. Gamelin, J. Am. Chem. Soc. **126**(30), 9387–9398 (2004)
37. H. Saeki, H. Tabata, T. Kawai, Solid State Commun. **120**(11), 439–443 (2001)
38. D.A. Schwartz, D.R. Gamelin, Adv. Mater. **16**(23–24), 2115–2119 (2004)
39. M. Venkatesan, C.B. Fitzgerald, J.G. Lunney, J.M.D. Coey, Phys. Rev. Lett. **93**(17), 177206 (2004)
40. I. Djerdj, Z. Jaglicic, D. Arcon, M. Niederberger, Nanoscale **2**(7), 1096–1104 (2010)
41. H. Ohno, Science **281**(5379), 951–956 (1998)
42. K.R. Kittilstved, W.K. Liu, D.R. Gamelin, Nat. Mater. **5**(4), 291–297 (2006)
43. J.G. Lu, P. Chang, Z. Fan, Mater. Sci. Eng: R: Reports **52**(1–3), 49–91 (2006)
44. Z.R. Dai, Z.W. Pan, Z.L. Wang, Adv. Funct. Mater. **13**(1), 9–24 (2003)
45. W.I. Park, D.H. Kim, S.-W. Jung, G.-C. Yi, Appl. Phys. Lett. **80**(22), 4232–4234 (2002)

46. G. Malandrino, S.T. Finocchiaro, R. Lo Nigro, C. Bongiorno, C. Spinella, I.L. Fragalà, Chem. Mater. **16**(26), 5559–5561 (2004)
47. H.W. Kim, N.H. Kim, Appl. Phys. A: Mater. Sci. Process. **81**(4), 763–765 (2005)
48. Y.C. Choi, W.S. Kim, Y.S. Park, S.M. Lee, D.J. Bae, Y.H. Lee, G.S. Park, W.B. Choi, N.S. Lee, J.M. Kim, Adv. Mater. **12**(10), 746–750 (2000)
49. H. Wang, H.B. Wang, F.J. Yang, Y. Chen, C. Zhang, C.P. Yang, Q. Li, S.P. Wong, Nanotechnology **17**(17), 4312 (2006)
50. M.H. Huang, Y. Wu, H. Feick, N. Tran, E. Weber, P. Yang, Adv. Mater. **13**(2), 113–116 (2001)
51. Y. Li, G.W. Meng, L.D. Zhang, F. Phillipp, Appl. Phys. Lett. **76**(15), 2011–2013 (2000)
52. Z.L. Wang, J. Phys. Condens. Matter **16**(25), R829 (2004)
53. S.Y. Bae, H.W. Seo, J. Park, J. Phys. Chem. B **108**(17), 5206–5210 (2004)
54. L. Vayssieres, K. Keis, A. Hagfeldt, S.-E. Lindquist, Chem. Mater. **13**(12), 4395–4398 (2001)
55. L.W. Yang, X.L. Wu, T. Qiu, G.G. Siu, P.K. Chu, J. Appl. Phys. **99**(7), 074303 (2006)
56. J. Song, S. Baek, S. Lim, Phys. B **403**(10–11), 1960–1963 (2008)
57. P. Sharma, A. Gupta, K.V. Rao, F.J. Owens, R. Sharma, R. Ahuja, J.M.O. Guillen, B. Johansson, G.A. Gehring, Nat. Mater. **2**(10), 673–677 (2003)
58. O.D. Jayakumar, C. Sudakar, I.K. Gopalakrishnan, J. Cryst. Growth **310**(13), 3251–3255 (2008)
59. O.D. Jayakumar, C. Sudakar, A. Vinu, A. Asthana, A.K. Tyagi, J. Phys. Chem. C **113**(12), 4814–4819 (2009)
60. O.D. Jayakumar, C. Sudakar, C. Persson, V. Sudarsan, R. Naik, A.K. Tyagi, J. Phys. Chem. C **114**(41), 17428–17433 (2010)
61. O.D. Jayakumar, C. Sudakar, C. Persson, V. Sudarsan, T. Sakuntala, R. Naik, A.K. Tyagi, Cryst. Growth Des. **9**(10), 4450–4455 (2009)
62. O.D. Jayakumar, C. Sudakar, C. Persson, H.G. Salunke, R. Naik, A.K. Tyagi, Appl. Phys. Lett. **97**(23), 232510 (2010)
63. Z. Wang, H. Zhang, L. Zhang, J. Yuan, S. Yan, C. Wang, Nanotechnology **14**(1), 11 (2003)
64. O.D. Jayakumar, I.K. Gopalakrishnan, K. Shashikala, S.K. Kulshreshtha, C. Sudakar, Appl. Phys. Lett. **89**(20), 202507 (2006)
65. O.D. Jayakumar, V. Sudarsan, C. Sudakar, R. Naik, R.K. Vatsa, A.K. Tyagi, Scr. Mater. **62**(9), 662–665 (2010)
66. S.A. Wolf, D.D. Awschalom, R.A. Buhrman, J.M. Daughton, S. von Molnar, M.L. Roukes, A.Y. Chtchelkanova, D.M. Treger, Science **294**(5546), 1488–1495 (2001)
67. G.A. Prinz, Science **282**(5394), 1660–1663 (1998)
68. S.J. Pearton, C.R. Abernathy, M.E. Overberg, G.T. Thaler, D.P. Norton, N. Theodoropoulou, A.F. Hebard, Y.D. Park, F. Ren, J. Kim, L.A. Boatner, J. Appl. Phys. **93**(1), 1–13 (2003)
69. J.C. Hulteen, C.R. Martin, J. Mater. Chem. **7**(7), 1075–1087 (1997)
70. C. Xu, G. Xu, Y. Liu, G. Wang, Solid State Commun. **122**(3–4), 175–179 (2002)
71. Q.L. Tao Gao, T. Wang, Chem. Mater. **17** (2005)
72. J. Wang, L. Gao, J. Mater. Chem. **13**(10), 2551–2554 (2003)
73. M. Guo, P. Diao, S. Cai, J. Solid State Chem. **178**(6), 1864–1873 (2005)
74. B. Liu, H.C. Zeng, J. Am. Chem. Soc. **125**(15), 4430–4431 (2003)
75. C. Persson, O.D. Jayakumar, C. Sudakar, V. Sudarsan, A.K. Tyagi, Acta Phys. Plolonica A **119**(2), 95–98 (2011)
76. N. Fujimura, T. Nishihara, S. Goto, J. Xu, T. Ito, J. Cryst. Growth **130**(1–2), 269–279 (1993)
77. B.D. Yuhas, D.O. Zitoun, P.J. Pauzauskie, R. He, P. Yang, Angew. Chem. Int. Ed. **45**(3), 420–423 (2006)
78. P. Lommens, F. Loncke, P.F. Smet, F. Callens, D. Poelman, H. Vrielinck, Z. Hens, Chem. Mater. **19**(23), 5576–5583 (2007)
79. S. Shubra, N. Daisuke, S. Kentaro, O. Tatsuo, M.S.R. Rao, New J. Phys. **12**(2), 023007 (2010)

80. A. Sundaresan, R. Bhargavi, N. Rangarajan, U. Siddesh, C.N.R. Rao, Phys. Rev. B **74** (Copyright (C) 2010 Am. Phys. Soc.), 161306 (2006)
81. O.D. Jayakumar, I.K. Gopalakrishnan, S.K. Kulshreshtha, Adv. Mater. **18**(14), 1857–1860 (2006)
82. S.B. Ogale, Adv. Mater. **22**(29), 3125–3155 (2010)
83. M.J. Calderon, G. Gomez-Santos, L. Brey, Phys. Rev. B **66**, 075218 (2002)
84. T. Dietl, H. Ohno, F. Matsukura, Phys. Rev. B **63**(19), 195205 (2001)
85. J.M.D. Coey, M. Venkatesan, C.B. Fitzgerald, Nat. Mater. **4**, 173 (2005)
86. T. Dietl, A. Haury, Y.M. d'Aubigne, Phys. Rev. B **55**, R3347 (1997)
87. A.C. Durst, R.N. Bhatt, P.A. Wolff, Phys. Rev. B **65**, 235205 (2002)
88. A. Kaminski, S. Das Sarma, Phys. Rev. Lett. **88**, 247202 (2002)
89. K. Ueda, H. Tabata, T. Kawai, Appl. Phys. Lett. **79**(7), 988–990 (2001)
90. H.-J. Lee, S.-Y. Jeong, C.R. Cho, C.H. Park, Appl. Phys. Lett. **81**(21), 4020–4022 (2002)
91. D.A. Schwartz, N.S. Norberg, Q.P. Nguyen, J.M. Parker, D.R. Gamelin, J. Am. Chem. Soc. **125**(43), 13205–13218 (2003)
92. H.-J. Lee, G.-H. Ryu, S.-K. Kim, S.A. Kim, C.-H. Lee, S.-Y. Jeong, C.R. Cho, Phys. Status Solidi (B) **241**(12), 2858–2861 (2004)
93. A.S. Risbud, N.A. Spaldin, Z.Q. Chen, S. Stemmer, R. Seshadri, Phys. Rev. B **68**(20), 205202 (2003)
94. S.C. Wi, J.-S. Kang, J.H. Kim, S.-B. Cho, B.J. Kim, S. Yoon, B.J. Suh, S.W. Han, K.H. Kim, K.J. Kim, B.S. Kim, H.J. Song, H.J. Shin, J.H. Shim, B.I. Min, Appl. Phys. Lett. **84**(21), 4233–4235 (2004)
95. M. Bouloudenine, N. Viart, S. Colis, A. Dinia, Chem. Phys. Lett. **397**(1–3), 73–76 (2004)
96. G. Lawes, A.S. Risbud, A.P. Ramirez, R. Seshadri, Phys. Rev. B **71**(4), 045201 (2005)
97. C.N.R. Rao, F.L. Deepak, J. Mater. Chem. **15**(5), 573–578 (2005)
98. T. Minami, MRS Bulletin August *58* (2000)
99. X.C. Liu, E.W. Shi, Z.Z. Chen, H.W. Zhang, B. Xiao, L.X. Song, Appl. Phys. Lett. **88**(25), 252503 (2006)
100. T. Zhang, L.-X. Song, Z.-Z. Chen, E.-W. Shi, L.-X. Chao, H.-W. Zhang, Appl. Phys. Lett. **89**(17), 172502 (2006)
101. L. Liao, H.B. Lu, L. Zhang, M. Shuai, J.C. Li, C. Liu, D.J. Fu, F. Ren, J. Appl. Phys. **102**(11), 114307 (2007)
102. Y. He, P. Sharma, K. Biswas, E.Z. Liu, N. Ohtsu, A. Inoue, Y. Inada, M. Nomura, J.S. Tse, S. Yin, J.Z. Jiang, Phys. Rev. B **78**(15), 155202 (2008)
103. Z. Lu, H.-S. Hsu, Y. Tzeng, J.-C.-A. Huang, Appl. Phys. Lett. **94**(15), 152507 (2009)
104. O.D. Jayakumar, C. Sudakar, A.K. Tyagi, Nanosci. Nanotechnol. Lett. **3**(2), 140–145 (2011)
105. C. Sudakar, in *Magnetic Thin Films*: *Properties*, *Performance and Applications,* ed. by J.P. Volkerts (Nova Science Publishers, Inc., Huntington, 2011)
106. C. Sudakar, S. Singh, M.S.R. Rao, G. Lawes, in *Functional Metal Oxide Nanostructures*, ed. by J. Wu, J. Cao, W.-Q. Han, A. Janotti, H.-C. Kim, Vol. 149 (Springer, New York, 2012), pp. 37–68
107. A. Brinkman, M. Huijben, M. van Zalk, J. Huijben, U. Zeitler, J.C. Maan, W.G. van der Wiel, G. Rijnders, D.H.A. Blank, H. Hilgenkamp, Nat. Mater. **6**(7), 493–496 (2007)
108. C. Sudakar, P. Kharel, G. Lawes, R. Suryanarayanan, R. Naik, V.M. Naik, Appl. Phys. Lett. **92**(6), 062501–062503 (2008)
109. O.D. Jayakumar, I.K. Gopalakrishnan, C. Sudakar, R.M. Kadam, S.K. Kulshreshtha, J. Alloy. Compd. **438**(1–2), 258–262 (2007)
110. J.D. Bryan, D.A. Schwartz, D.R. Gamelin, J. Nanosci. Nanotechnol. **5**(9), 1472–1479 (2005)
111. S. Bhattacharyya, A. Gedanken, J. Phys. Chem. C **112**(12), 4517–4523 (2008)
112. W. Zhu, H.H. Weitering, E.G. Wang, E. Kaxiras, Z. Zhang, Phys. Rev. Lett. **93**(12), 126102 (2004)
113. S.C. Erwin, L. Zu, M.I. Haftel, A.L. Efros, T.A. Kennedy, D.J. Norris, Nature **436**(7047), 91–94 (2005)

114. P. Crespo, R. Litrán, T.C. Rojas, M. Multigner, J.M. de la Fuente, J.C. Sánchez-López, M.A. García, A. Hernando, S. Penadés, A. Fernández, Phys. Rev. Lett. **93**(8), 087204 (2004)
115. P. Crespo, M.A. García, E. Fernández Pinel, M. Multigner, D. Alcántara, J.M. de la Fuente, S. Penadés, A. Hernando, Phys. Rev. Lett. **97**(17), 177203 (2006)
116. M.A. Garcia, J.M. Merino, E. Fernández Pinel, A. Quesada, J. de la Venta, M.L. Ruíz González, G.R. Castro, P. Crespo, J. Llopis, J.M. González-Calbet, A. Hernando, Nano Lett. **7**(6), 1489–1494 (2007)
117. D.M. Bagnall, Y.F. Chen, M.Y. Shen, Z. Zhu, T. Goto, T. Yao, J. Cryst. Growth **184–185**, 605–609 (1998)
118. E.G. Bylander, J. Appl. Phys. **49**(3), 1188–1195 (1978)
119. N.Y. Garces, L. Wang, L. Bai, N.C. Giles, L.E. Halliburton, G. Cantwell, Appl. Phys. Lett. **81**(4), 622–624 (2002)
120. X. Zhou, S. Gu, Z. Wu, S. Zhu, J. Ye, S. Liu, R. Zhang, Y. Shi, Y. Zheng, Appl. Surf. Sci. **253**(4), 2226–2229 (2006)
121. M.D. McCluskey, S.J. Jokela, J. Appl. Phys. **106**(7), 071101 (2009)
122. A.F. Kohan, G. Ceder, D. Morgan, C.G. Van de Walle, Phys. Rev. B **61**(22), 15019–15027 (2000)
123. O.D. Jayakumar, V. Sudarsan, K. Shashikala, C. Sudakar, R. Naik, R.K. Vatsa, A.K. Tyagi, J. Nanosci. Nanotechnol. **11**(4), 3273–3277 (2011)
124. W.M. Kwok, A.B. Djurisic, Y.H. Leung, D. Li, K.H. Tam, D.L. Phillips, W.K. Chan, Appl. Phys. Lett. **89**(18), 183112 (2006)
125. G. Kresse, D. Joubert, Phys. Rev. B **59**(3), 1758–1775 (1999)
126. P.E. Blöchl, Phys. Rev. B **50**(24), 17953–17979 (1994)
127. A.I. Liechtenstein, V.I. Anisimov, J. Zaanen, Phys. Rev. B **52**(8), R5467–R5470 (1995)
128. C. Persson, C.L. Dong, L. Vayssieres, A. Augustsson, T. Schmitt, M. Mattesini, R. Ahuja, J. Nordgren, C.L. Chang, A. Ferreira da Silva, J.H. Guo, Microelectron. J. **37**(8), 686–689 (2006)
129. W.E. Pickett, S.C. Erwin, E.C. Ethridge, Phys. Rev. B **58**(3), 1201–1209 (1998)
130. T. Archer, R. Hanafin, S. Sanvito, Phys. Rev. B **78**(1), 014431 (2008)
131. W. Setyawan, R.M. Gaume, S. Lam, R.S. Feigelson, S. Curtarolo, ACS Comb. Sci. **13**(4), 382–390 (2011)
132. P. Mohn, C. Persson, P. Blaha, K. Schwarz, P. Novák, H. Eschrig, Phys. Rev. Lett. **87**(19), 196401 (2001)

Editors Biography

Prof. M.S. Ramachandra Rao is heading the ‘Nanostructured Thin Films and Advanced Materials group’ at IIT Madras, Chennai, India. His research activities are primarily focused on Physics and Applications of Nanostructures and Nanomaterials. Prof. Rao obtained his M.Sc. (Physics) and Ph.D. (experimental solid-state physics) from IIT Kharagpur, India. He was a research scientist at CNRS, Bellevue, France, Alexander von Humboldt fellow, JSPS fellow and Erasmus Mundus foreign academician and Visiting Faculty at UMCP, USA. Prof. Rao is the Fellow of Institute of Physics (FInstP), UK and the editorial board member (from India) of J. Phys. D. Appl. Phys (IoP).
His research areas: PLD grown-doped ZnO nanostructures to realize light emission; Magnetic nanoparticles for hyperthermia and water purification applications; Synthesis of Nanoink of selenide-based photovoltaics; Nanocrystalline diamond for mechanical applications; Study of diffusion process in nanoscale metal oxides; CVD grown Graphene layers for transport study. He has 17 years of teaching experience and published about 140 research publications, obtained 10 patents and 4 technology transfers, guided 10 Ph.D. students and 65 UG and PG project students.

Prof. Tatsuo Okada is associated as Professor with Department of Electrical Engineering, Kyushu University, Japan. Currently, he is Invited Professor at Jinan University, China. Prof. Okada has received his doctoral degree from Department of Electrical Engineering, Kyushu University in 1981. He has authored more than 100 articles in last 10 years and also authored two books “Lasers in Chemistry” and “Lasers in Material Sciences”. His field of specialization is Laser Engineering.

M. S. R. Rao and T. Okada (eds.), *ZnO Nanocrystals and Allied Materials*,
Springer Series in Materials Science 180, DOI: 10.1007/978-81-322-1160-0,
© Springer India 2014

Author Index

B
Baskar, K., 233

D
Dhobale, S., 269

F
Fukuyama, A., 91, 331

H
Hashimoto, T., 125
Higashihata, M., 39, 101, 149
Highasiata, M., 175
Hirashima, A., 125

I
Ikari, T., 91, 331
Ishida, Y., 39
Ishikura, K., 91, 331

J
Jayakumar, O. D., 341

K
Kale, S. N., 269
Kitture, R., 269
Kottaisamy, M., 247
Kukreja, L. M., 49
Kumar, J., 309

L
Lu, Y. F., 233

M
Matsuda, Y., 125
Matsuoka, D., 125
Mine, K., 125
Misra, P., 49
Murotani, H., 195

N
Nakamura, D., 39, 91, 101, 149, 175

O
Ohori, D., 91
Okada, T., 39, 91, 101, 125, 149, 175, 195, 331
Okazaki, K., 39, 101, 149, 175

P
Palani, I. A., 101, 149, 175, 331
Persson, C., 341
Premkumar, T., 233

R
Rajagopalan, M., 309

M. S. R. Rao and T. Okada (eds.), *ZnO Nanocrystals and Allied Materials*,
Springer Series in Materials Science 180, DOI: 10.1007/978-81-322-1160-0,
© Springer India 2014

Ramachandra Rao, M. S., 1, 91, 247, 331
Ramasubramanian, S., 309

S
Sakai, K., 91, 331
Senthil Kumar, E., 1
Shimogaki, T., 39, 101, 149
Shinohara, M., 125
Singh, S., 1
Sudakar, C., 341
Suryanarayanan, R., 289

T
Thangavel, R., 309
Thiyagarajan, P., 247
Tyagi, A. K., 341

V
Vasa, N. J., 217
Venkataramesh, B., 217

Y
Yamada, Y., 195